

# Interactions of Small Functional Molecules with Metal-Organic Frameworks

Dardan Ukaj

Vollständiger Abdruck der von der TUM School of Natural Sciences der Technischen Universität München zur Erlangung des akademischen Grades eines

**Doktors der Naturwissenschaften (Dr. rer. nat.)**

genehmigten Dissertation.

Vorsitzender: Prof. Dr. Torben Gädt

Prüfer der Dissertation: 1. Prof. Dr. Dr. h. c. Roland A. Fischer

2. Prof. Dr. Tom Nilges

Die Dissertation wurde am 17.11.2022 bei der Technischen Universität München eingereicht und durch die TUM School of Natural Sciences am 12.12.2022 angenommen.





Die vorliegende Dissertation wurde am Lehrstuhl für Anorganische und Metallorganische Chemie der Technischen Universität München im Zeitraum von April 2018 bis Dezember 2022 angefertigt.



*“Whatever it is you’re seeking  
won’t come in the form you’re expecting.”*

HARUKI MURAKAMI



*Për familjen time.*



# *Danksagung*

Zahlreiche Menschen haben mich in den letzten Jahren während meiner Promotion begleitet, ohne die es diese Arbeit in ihrer jetzigen Form nicht gegeben hätte und ich nicht der Mensch geworden wäre, der ich heute bin. Deshalb freue ich mich nun über die Gelegenheit an dieser Stelle, diesen Menschen von Herzen zu danken.

Zuerst gilt mein Dank natürlich Herrn **Prof. Dr. Dr. h.c. Roland A. Fischer**. Ich habe es sehr geschätzt, wie Sie mir während meiner Zeit an Ihrem Lehrstuhl Ihr volles Vertrauen entgegengebracht und mir gleichzeitig völlige wissenschaftliche Freiheit in der Auswahl und Durchführung meiner Projekte gewährt haben. Diese Möglichkeit, selbstständig Ideen zu entwickeln und daran zu forschen, neue Problemstellungen zu entdecken und versuchen, diese zu lösen, hat mich sowohl wissenschaftlich, als auch ganz persönlich enorm weitergebracht und wird mir trotz mancher Hindernisse bei meinem Versuch, „Bäume in der Arktis zu pflanzen“, immer als wunderbare Zeit in Erinnerung bleiben. Gleichzeitig hatten Sie immer Interesse an meinen Fortschritten und haben mir Besuche von diversen Konferenzen und Summer Schools in Paris und Como ermöglicht, wofür ich ebenfalls sehr dankbar bin.

Als nächstes möchte ich mich bei Herrn **Dr. Gregor Kieslich** bedanken, für Dein stets konstruktives und zielgerichtetes Feedback bei allerlei Problemstellungen und Dein immer offenes Ohr. Insbesondere hat das Schreiben und Überarbeiten von Manuskripten unter Deiner Betreuung wirklich Spaß gemacht, ich war sehr beeindruckt von Deinem Talent gute Texte zu schreiben und denke bzw. hoffe, dass ich das eine oder andere davon mitnehmen kann für die Zukunft.

Damit verbunden möchte ich unserem gesamten „Mittelbau“, **Dr. Gregor Kieslich, Dr. Alexander Pöthig, Dr. Christian Gemel, Dr. Gabriele Raudaschl-Sieber, Dr. Markus Drees, Dr. Mirza Cokoja, Dr. Julien Warnan** und **Dr. Dominik Halter**,

sowie unserem Sekretariat mit **Martin Schellerer** und **Dr. Dana Weiß** für ihre Unterstützung in wissenschaftlichen und technischen Fragen danken.

Ebenso gilt mein Dank dem technischen Personal der Fakultät für Chemie an der TUM, darunter **Katia Rodewald**, **Jürgen Kudermann**, **Olaf Ackermann**, **Rodica Dumitrescu**, **Tobias Kubo**, **Cihangir Agacdeviren**, **Daniel Lemma**, **Ulrike Ammari**, **Petra Ankenbauer** und **Bircan Dilki** für ihre Unterstützung im Laboralltag, bei der Betreuung von Laborpraktika und der Durchführung von Auftragsmessungen.

Der Gesellschaft deutscher Chemiker danke ich für die finanzielle Unterstützung in Form eines Reisestipendiums.

Allen meinen Bachelor- und Masterstudenten, insbesondere **Sonia Mackewicz** und **Alexandros Tholiotis**, danke ich für ihr Engagement und der Unterstützung bei meiner Forschung.

Meine Entscheidung zur Promotion am AMC Lehrstuhl wäre wohl nie ohne das damalige Forschungspraktikum und die spätere Masterarbeit bei Herrn **Dr. Christian Schneider** gefallen. Christian, ich danke Dir für Deine tolle Betreuung, die sowohl wissenschaftlich konstruktive Diskussionen über ein spannendes Thema, aber auch ein sehr angenehmes persönliches Verhältnis umfasste. Ohne diese Erfahrung wäre ich nie auf mein Promotionsthema gekommen.

In diesem Sinne möchte ich den gesamten damaligen und jetzigen Lehrstuhlmitgliedern für die positive Arbeitsatmosphäre, den freundschaftlichen Umgang und all die schönen, gemeinsamen Erfahrungen danken. Ich habe mich bei AMC sehr wohl gefühlt und werde diese Zeit nie vergessen. Ganz besonderer Dank gilt an dieser Stelle **Laura Kronthaler** und **Thomas Pickl**, für eure perfekte Mischung aus konstruktiver Zusammenarbeit und vollkommenem Unfug im Laboralltag und auch außerhalb davon. Ihr seid wirklich die Besten.

Zu guter Letzt bin ich unendlich dankbar für die stete Unterstützung und Liebe von meiner **Familie**, auf die ich mich immer verlassen kann egal wohin mich die Zukunft führt. Ihr habt immer an mich geglaubt und mir jedes Mal neuen Mut und neue Kraft gegeben, weiterzumachen. An dieser Stelle danke ich auch **Svenja** für Deine Liebe und Geduld mit mir, Deiner Unterstützung und all unserer bisherigen schönen Zeit, die hoffentlich noch lange andauern wird.

---



# *Abstract*

A society of growing complexity inevitably faces challenges that demand increasingly sophisticated solutions to enable further technological progress. In this spirit, multifunctional materials that provide solutions for multiple problems simultaneously are on the rise, and metal-organic frameworks (MOFs) are a part of these endeavors. Their highly modular building principle has led to the preparation of myriad new structures with different material properties and porosity. In recent years, this porosity was recognized as a new possibility to expand their modularity even further by introducing any functional molecule into the MOF pores, thereby adding new desired material properties. In principle, any functional guest can be introduced in every MOF, and the resulting properties are simply the sum of the two. However, guests can also interact with the framework and these interactions can give rise to material properties that enhance the inherent MOF performances or create a system with divergent characteristics. The work presented in this thesis focuses on the rationalization of these interactions between porous MOFs and functional guest molecules that lead to interesting features such as electrical conductivity or influence negative thermal expansion (NTE).

Different systems were analyzed towards their host-guest interactions and correlated with their material properties. For example, the first study focuses on the tetrathiafulvalene tetrabenzoate (TTFTB)-based MOF  $M_2$ TTFTB ( $M^{2+} = \text{Zn}, \text{Cd}$ ) and its charge-transfer (CT) interaction with redox-active tetracyanoethylene (TCNE), and how this influences the electrical properties of the resulting host-guest complex. A thorough vibrational spectroscopic analysis of this system provides answers to the observed performance trends. The second study tackles the design of a tetraselenafulvalene (TSF)-based linker that could be used for MOF synthesis and is expected to exhibit interesting electrical properties. It was found that a copper catalyzed direct arylation gives arylated TSF in moderate yields, whereas other synthesis strategies are completely ineffective. The third study deals with the guest-dependent changes of NTE in  $\text{Cu}_3$  benzene tricarboxylate ( $\text{BTC}$ )<sub>2</sub> and illustrates how simple modifications of the guest can lead to

interesting differences in the material properties, despite their similar structures. At the heart of this thesis are the efforts to establish reliable characterization procedures that can visualize host-guest interactions and correlate them with changes of their material properties in a rational manner. While many underlying mechanism remain unclear, this thesis provides some insights into the possibilities of tuning MOF properties.

---

# Zusammenfassung

Eine immer komplexer werdende Gesellschaft steht zwangsläufig vor Herausforderungen, die immer ausgefeiltere Lösungen erfordern, um weiteren technologischen Fortschritt zu ermöglichen. In diesem Sinne sind multifunktionale Materialien, die Lösungen für mehrere Probleme gleichzeitig bieten, auf dem Vormarsch, und Metallorganische Gerüstverbindungen (MOFs) sind ein Teil dieser Bemühungen. Ihr hochgradig modulares Bauprinzip hat zur Herstellung von unzähligen neuen Strukturen mit unterschiedlichen Materialeigenschaften und Porosität geführt. In den letzten Jahren wurde diese Porosität als neue Möglichkeit erkannt, ihre Modularität noch weiter zu erweitern, indem beliebige funktionelle Moleküle in die MOF-Poren eingebracht werden, wodurch neue gewünschte Materialeigenschaften hinzugefügt werden. Im Prinzip kann jeder funktionelle Gast in jedes MOF eingeführt werden, und die resultierenden Eigenschaften sind einfach die Summe der beiden. Gäste können jedoch auch mit dem Gerüst interagieren, und diese Interaktionen können zu Materialeigenschaften führen, die die inhärenten Eigenschaften von MOFs verbessern oder ein System mit abweichenden Eigenschaften schaffen. Die in dieser Arbeit vorgestellten Arbeiten konzentrieren sich auf die Rationalisierung dieser Wechselwirkungen zwischen porösen MOFs und funktionellen Gastmolekülen, die zu interessanten Eigenschaften wie elektrische Leitfähigkeit führen oder negative thermische Expansion (NTE) beeinflussen. Verschiedene Systeme wurden auf ihre Wirt-Gast-Wechselwirkungen hin analysiert und mit ihren Materialeigenschaften in Beziehung gesetzt. So konzentriert sich die erste Studie auf das Tetrathiafulvalentetrazolato (TTFTB)-basierte MOF  $M_2\text{TTFTB}$  ( $M^{2+} = \text{Zn}, \text{Cd}$ ) und dessen Charge-Transfer (CT)-Wechselwirkung mit dem redoxaktiven Tetracyanoethylen (TCNE), und wie dies die elektrischen Eigenschaften des resultierenden Wirt-Gast-Komplexes beeinflusst. Eine gründliche schwingungsspektroskopische Analyse dieses Systems liefert Antworten auf die beobachteten Eigenschaftstrends. Die zweite Studie befasst sich mit der Entwicklung eines Linkers auf Tetraselenafulvalen (TSF)-Basis, der für die MOF-Synthese verwendet werden könnte und interessante elektrische Eigen-

schaften aufweisen dürfte. Es wurde festgestellt, dass eine kupferkatalysierte direkte Arylierung aryliertes TSF in mäßiger Ausbeute liefert, während andere Synthesestrategien völlig ineffektiv sind. Die dritte Studie befasst sich mit den gastabhängigen Veränderungen von NTE in  $\text{Cu}_3$  Trimesat ( $\text{BTC}$ )<sub>2</sub> und veranschaulicht, wie einfache Modifikationen des Gastes trotz ähnlicher Struktur zu interessanten Unterschieden in den Materialeigenschaften führen können. Im Mittelpunkt dieser Arbeit stehen die Bemühungen zum Hervorbringen zuverlässiger Charakterisierungsverfahren, mit denen die Wechselwirkungen zwischen Wirt und Gast sichtbar gemacht und auf rationale Weise mit den Änderungen ihrer Materialeigenschaften in Beziehung gesetzt werden können. Obwohl viele zugrundeliegende Mechanismen noch unklar sind, bietet diese Arbeit einige Einblicke in die Möglichkeiten der Kontrolle von MOF-Eigenschaften.

---

# Contents

Danksagung	i
Abstract	iii
Zusammenfassung	v
Acronyms	xiii
List of Tables	xix
List of Figures	xxi
List of Schemes	xxxiii
<b>I Empirical Research</b>	<b>1</b>
1 Introduction	3
2 Guest-Induced Charge-Transfer in Tetrathiafulvalene-Based Metal-Organic Frameworks	7
2.1 Introduction . . . . .	7
2.2 Synthesis and Structural Characterization of $(\text{TCNE})_x\text{M}_2\text{TTFTB}$	11
2.2.1 Vapor-Phase Infiltration of $\text{M}_2\text{TTFTB}$ with TCNE and Determination of TCNE Content . . . . .	11
2.2.2 Crystallinity of TCNE-loaded $\text{M}_2\text{TTFTB}$ Metal-Organic Frameworks . . . . .	13
2.2.3 TCNE Distribution in $\text{M}_2\text{TTFTB}$ Crystals . . . . .	15
2.2.4 Porosity Changes of TCNE-Loaded $\text{M}_2\text{TTFTB}$ . . . . .	20
2.3 Redox-Sensitive Vibrations as a Probe for Charge-Transfer . . .	20
2.3.1 FTIR of TCNE Species in $(\text{TCNE})_x\text{M}_2\text{TTFTB}$ . . . . .	22
2.3.2 Raman of TTFTB Species in $(\text{TCNE})_x\text{M}_2\text{TTFTB}$ . . . . .	24
2.4 Influence of the Host-Guest Interactions on the Electrical Conductivity of . . . . .	28
2.5 Conclusion . . . . .	30

---

3	Tetraselenafulvalene-Linkers for Metal-Organic Frameworks	33
3.1	Introduction	33
3.2	Synthesis of Tetraselenafulvalene	41
3.3	Direct Arylation	43
3.3.1	Palladium Catalysis	43
3.3.2	Copper Catalysis	44
3.4	Cross Coupling of Functionalized Tetraselenafulvalene	50
3.4.1	Negishi Coupling	50
3.4.2	Dechalcogenative Coupling	51
3.5	Conclusion	52
4	Tuning Negative Thermal Expansion in Metal-Organic Frameworks	55
4.1	Introduction	55
4.2	Guest Infiltration of $\text{Cu}_3\text{BTC}_2$ with Open Metal Site Bridging Dinitriles	60
4.3	Vibrational Analysis of Retrofitted $(\text{Guest})_x\text{Cu}_3\text{BTC}_2$	63
4.4	Conclusion	65
5	Conclusion	67
6	Experimental	71
6.1	General	71
6.2	Analytical Methods	72
6.2.1	Infrared Spectroscopy	72
6.2.2	Raman Spectroscopy	72
6.2.3	Nuclear Magnetic Resonance Spectroscopy	73
6.2.4	X-Ray Diffraction	73
6.2.5	Gas Sorption	74
6.2.6	Elemental Analysis	74
6.2.7	Electron Microscopy	76
6.2.8	Mass Spectrometry	76
6.2.9	Electrical Conductivity	76
6.3	Synthetic Procedures	77
6.3.1	Tetraethyl tetrathiafulvalene tetrabenzoate ( $\text{Et}_4\text{TTFTB}$ )	77
6.3.2	Tetrathiafulvalene tetrabenzoic acid ( $\text{H}_4\text{TTFTB}$ )	78
6.3.3	$\text{Zn}_2\text{TTFTB}$	78
6.3.4	$\text{Cd}_2\text{TTFTB}$	79
6.3.5	$(\text{TCNE})_x\text{M}_2\text{TTFTB}$	79
6.3.6	Acetaldehyde semicarbazone	80
6.3.7	1,2,3-Selenadiazole	81
6.3.8	2-Methylene-1,3-diselenole	82

---

---

6.3.9	Tetraselenafulvalene . . . . .	83
6.3.9.1	Sodium acetylide route . . . . .	83
6.3.9.2	Semicarbazone route . . . . .	85
6.3.10	Direct Arylation of Tetraselenafulvalene . . . . .	86
6.3.10.1	Palladium catalysis . . . . .	86
6.3.10.2	Copper Catalysis . . . . .	86
6.3.11	Cross Coupling of Functionalized Tetraselenafulvalene .	87
6.3.11.1	Negishi Coupling of Zincated Tetraselenafulvalene . . . . .	87
6.3.11.2	Tetra(methylthio)tetraselenafulvalene . . . . .	87
6.3.11.3	Tetra(phenylseleno)tetraselenafulvalene . . . . .	88
6.3.11.4	Tetra(butylseleno)tetraselenafulvalene . . . . .	88
6.3.11.5	Liebeskind-Srogl Type Coupling . . . . .	89
6.3.12	Other Functionalizations of Tetraselenafulvalene . . . . .	89
6.3.12.1	Bromination with <i>N</i> -Bromosuccinimide . . . . .	89
6.3.12.2	Bromination with Bromine . . . . .	90
6.3.12.3	Tetracarboxylation . . . . .	90
6.3.12.4	Tetraboronation . . . . .	91
6.3.12.5	Tetrasilylation . . . . .	91
6.3.13	$\text{Cu}_3\text{BTC}_2$ . . . . .	92
6.3.14	$(\text{Dinitrile})_x\text{Cu}_3\text{BTC}_2$ . . . . .	92
6.4	Characterization . . . . .	93
<b>II</b>	<b>Theory and Methodology</b>	<b>151</b>
7	Metal-Organic Frameworks	153
7.1	Introduction . . . . .	153
7.2	Topological Description . . . . .	153
7.3	Formation of Metal-Organic Frameworks . . . . .	155
7.4	Reticular Chemistry . . . . .	156
7.4.1	Historical Background . . . . .	156
7.4.2	Stable and Variable Metal-Organic Frameworks . . . . .	157
7.5	Responsiveness to External Stimuli . . . . .	159
7.6	Isoreticular Expansion . . . . .	160
7.7	Chemical Modifications . . . . .	164
7.7.1	Pre-Synthetic Modifications . . . . .	164
7.7.2	Post-Synthetic Modifications . . . . .	164
7.8	Guests in Metal-Organic Frameworks . . . . .	165
7.8.1	Solvent Effects . . . . .	165
7.8.2	Counter Ions . . . . .	167

---

---

7.8.3	Non-Native Guests . . . . .	167
7.8.4	Retrofitting . . . . .	168
8	Electrically Conductive Metal-Organic Frameworks . . . . .	171
8.1	Introduction . . . . .	171
8.2	Through-Bond Approach . . . . .	172
8.3	Mixed-Valency . . . . .	174
8.4	Through-Space Approach . . . . .	177
8.5	Extended Conjugation . . . . .	180
8.5.1	Dihydroxybenzoquinone Linkers . . . . .	181
8.5.2	Aromatic Catecholates . . . . .	184
8.5.3	Aromatic Dithiolenes . . . . .	186
8.5.4	Aromatic Diimines . . . . .	187
8.5.5	Further Extended Metal-Organic Frameworks . . . . .	189
8.6	Guest-Induced Electrical Conductivity . . . . .	189
9	Electron Theory . . . . .	193
9.1	Introduction . . . . .	193
9.2	Quantum Mechanics of the Electron . . . . .	193
9.2.1	Free Electron . . . . .	194
9.2.2	Electron in a Box . . . . .	194
9.2.3	Tunnel effect . . . . .	196
9.2.4	Electron in the Solid State . . . . .	196
9.2.5	Energy Bands in Crystals . . . . .	197
9.2.6	Fermi Distribution Function and Density of States . . . . .	199
9.3	Electrical Conductivity . . . . .	202
9.3.1	Classical Definition . . . . .	202
9.3.2	Quantummechanical Aspects . . . . .	203
9.3.3	Semiconductors . . . . .	204
9.3.4	Hopping Transport . . . . .	207
9.4	Measurement of Electrical Conductivity . . . . .	209
10	X-Ray Diffraction . . . . .	213
10.1	Introduction . . . . .	213
10.2	Crystallography . . . . .	213
10.3	X-Rays . . . . .	214
10.3.1	Generation of X-Rays . . . . .	214
10.3.2	Scattering at a Crystal - Bragg Conditions . . . . .	217
10.3.3	Reciprocal Lattice and Ewald's Sphere . . . . .	218
10.3.4	Powder X-Ray Diffraction . . . . .	221

---



---

11	Gas Sorption	223
11.1	Introduction . . . . .	223
11.2	General Experimental Procedure . . . . .	224
11.3	Sorption Isotherms . . . . .	224
11.4	Hysteresis . . . . .	225
11.5	BET Model and Surface Area Determination . . . . .	226
12	Vibrational Spectroscopy	233
12.1	Introduction . . . . .	233
12.2	Molecular Vibrations . . . . .	233
12.3	Infrared Spectroscopy . . . . .	236
12.4	Raman Spectroscopy . . . . .	237
13	Electron Microscopy	239
13.1	Introduction . . . . .	239
13.2	Electron Scattering . . . . .	240
13.2.1	Elastic scattering . . . . .	242
13.2.2	Inelastic scattering . . . . .	244
13.3	Electron Microscopes . . . . .	245
13.3.1	General . . . . .	245
13.3.2	Transmission Electron Microscope . . . . .	246
13.3.3	Scanning Electron Microscope . . . . .	247
13.3.4	Scanning Transmission Electron Microscope . . . . .	247
13.3.5	Energy-Dispersive X-ray Spectroscopy . . . . .	247
14	Nuclear Magnetic Resonance Spectroscopy	251
14.1	Introduction . . . . .	251
14.2	Nuclear Spin . . . . .	251
14.3	Nucleus in the Magnetic Field . . . . .	252
14.4	Chemical Shift . . . . .	252
14.5	Fine Structure . . . . .	254
15	Mass Spectrometry	259
15.1	Introduction . . . . .	259
15.2	Ion Sources . . . . .	259
15.2.1	Electron/Chemical Ionization . . . . .	259
15.2.2	Field Ionization/Desorption . . . . .	261
15.2.3	Electrospray Ionization . . . . .	261
15.2.4	Matrix-Assisted Laser Desorption Ionization . . . . .	261
15.3	Mass Analyzers . . . . .	262
15.3.1	Time-of-Flight . . . . .	262
15.3.2	Magnetic Sectors . . . . .	262

---

15.3.3	Quadrupoles . . . . .	263
15.3.4	Ion Traps . . . . .	263
15.3.5	Fourier-Transform Ion Cyclotron Resonance . . . . .	264
15.3.6	Orbitrap . . . . .	264
<b>References</b>		<b>265</b>
<b>List of Scientific Contributions</b>		<b>305</b>

---

# Acronyms

ADF	Annular Dark-Field
BDC	Benzene Dicarboxylate
BDP	1,4-Benzenedipyrazolate
BDT	5,5'-(1,4-Phenylene)bis(1 <i>H</i> -Tetrazole)
BEDT-TSF	Bis(ethylenedithio)tetraselenafulvalene
BET	Brunauer, Emmett And Teller
BF	Bright-Field
BHT	Benzene-1,2,3,4,5,6-Hexathiol
BINAP	2,2'-Bis(diphenylphosphino)-1,1'-Binaphthyl
BPDC	Biphenyl Dicarboxylic Acid
BPTC	Biphenyl-3,3',5,5'-Tetracarboxylic Acid
Br <sub>2</sub> dhbq	Bromoanilate
BSE	Back-Scattered Electrons
BTB	Benzene Tribenzoate
BTC	Benzene Tricarboxylate
Cl <sub>2</sub> dhbq	Chloroanilate
CP	Coordination Polymer
Cp	Cyclopentadiene
CT	Charge-Transfer
CuTC	Copper(I) Thiophene-2-Carboxylate
DavePhos	2-Dicyclohexylphosphino-2'-( <i>N,N</i> -Dimethylamino)biphenyl
dba	Dibenzylideneacetone
DCB	1,2-Dicyanobenzene
DCM	Dichloromethane
DCN	2,3-Dicyanonaphthalene

DCP	4,5-Dichlorophthalonitrile
DCT	3,4-Dicyanothiophene
DF	Dark-Field
DFT	Density Functional Theory
dhbq	2,5-Dihydroxybenzoquinone
<b>dia</b>	Diamond
DMA	<i>N,N</i> -Dimethyl Acetamide
DMAD	Dimethyl Acetylenedicarboxylate
DMF	<i>N,N</i> -Dimethyl Formamide
DMSO	Dimethyl Sulfoxide
DOBDC	2,5-Dioxidoterephthalate
DPE-Phos	(oxydi-2,1-Phenylene)bis(diphenylphosphine)
dppf	1,1'-Ferrocenediyl-Bis(diphenylphosphine)
DSBDC	2,5-Dimercaptobenzene-1,4-Dicarboxylate
DTGS	Deuterated Triglycine Sulfate
EDS	Energy-Dispersive X-Ray Spectroscopy
EPR	Electron Paramagnetic Resonance Spectroscopy
FTIR	Fourier Transform Infrared Spectroscopy
HAADF	High-Angle Annular Dark-Field
HAB	1,2,3,4,5,6-Hexaaminobenzene
HHTP	2,3,6,7,10,11-Hexahydroxytriphenylene
HITP	2,3,6,7,10,11-Hexaiminotriphenylene
HKUST-1	Hong Kong University Of Science And Technology-1
HMPA	Hexamethylphosphoramide
HR-TEM	High-Resolution Transmission Electron Microscopy
IRMOF	Isorecticular Metal-Organic Framework
IVCT	Intervalence Charge-Transfer
LDA	Lithium Diisopropylamide
LIFDI	Liquid Injection Field Desorption Ionization
LiTMP	Lithium 2,2,6,6-Tetramethylpiperidide
MIL	Matériaux De L'Institut Lavoisier
MLCT	Metal-To-Ligand Charge-Transfer
MOF	Metal-Organic Framework
MS	Mass Spectrometry

---

---

MTV-MOF	Multi-Variate Metal-Organic Framework
NBS	<i>N</i> -Bromosuccinimide
NDI-py	<i>N,N'</i> -Di(4-Pyridyl)-1,4,5,8-Naphthalenetetracarboxdiimide
NMP	1-Methyl-2-Pyrrolidone
NMR	Nuclear Magnetic Resonance Spectroscopy
<i>np</i>	Narrow Pore
NTE	Negative Thermal Expansion
OCV	Open Circuit Voltage
OMS	Open Metal Sites
ORR	Oxygen Reduction Reaction
PCN	Porous Coordination Network
<b>pcu</b>	Primitive Cubic
pd <sub>t</sub>	2,3-Pyrazinedithiolate
PEPPSI-IPr	1,3-Bis(2,6-Diisopropylphenyl)imidazol-2-Ylidene(3-Chloro-pyridyl)palladium(II) Dichloride
phen	1,10-Phenanthroline
phz	Phenazine
PSLI	Post-Synthetic Ligand Incorporation
PSM	Post-Synthetic Modification
PSME	Post-Synthetic Metal-Exchange
PSMI	Post-Synthetic Metal Incorporation
<b>pto</b>	Platinum Oxide
PXRD	Powder X-Ray Diffraction
RT	Room Temperature
RUM	Rigid-Unit Mode
RuPhos	2-Dicyclohexylphosphino-2',6'-Diisopropoxybiphenyl
SALE	Solvent-Assisted Linker Exchange
SBU	Secondary Building Unit
<i>scsc</i>	Single Crystal To Single Crystal
SCXRD	Single-Crystal X-Ray Diffraction
SE	Secondary Electrons
SEM	Scanning Electron Microscopy
SPhos	2-Dicyclohexylphosphino-2',6'-Dimethoxybiphenyl
<b>sra</b>	SrAl <sub>2</sub>

---

STEM	Scanning Transmission Electron Microscopy
TATB	Triazine Tribenzoate
TBAPy	1,3,6,8-Tetrakis( <i>p</i> -Benzoate)pyrene
<b>tbo</b>	Twisted Boracite
TCB	1,2,4,5-Tetracyanobenzene
TCNE	Tetracyanoethylene
TCNQ	7,7,8,8-Tetracyanoquinodimethane
TEM	Transmission Electron Microscopy
tfp	Tri-(2-Furyl)phosphine
THF	Tetrahydrofuran
THT	Triphenylene-2,3,6,7,10,11-Hexathiol
TLC	Thin-Layer Chromatography
TMPMgCl · LiCl	2,2,6,6-Tetramethylpiperidinylmagnesium Chloride Lithium Chloride
TMPZnCl · LiCl	2,2,6,6-Tetramethylpiperidinylzinc Chloride Lithium Chloride
TMS	Tetramethylsilane
TMTSF	Tetramethyltetraselenafulvalene
TOF	Time-Of-Flight
tri	1,2,3-Triazolate
TRTS	Time-Resolved Terahertz Spectroscopy
TSF	Tetraselenafulvalene
TSF(SeBu) <sub>4</sub>	Tetra(butylseleno)tetraselenafulvalene
TSF(SePh) <sub>4</sub>	Tetra(phenylseleno)tetraselenafulvalene
TSF(SMe) <sub>4</sub>	Tetra(methylthio)tetraselenafulvalene
TSFTB	Tetraselenafulvalene Tetrabenzoate
TTeF	Tetratellurafulvalene
TTeFTB	Tetratellurafulvalene Tetrabenzoate
TTF	Tetrathiafulvalene
TTFTB	Tetrathiafulvalene Tetrabenzoate
VPI	Vapor Phase Infiltration
VT	Variable Temperature
<i>wp</i>	Wide Pore
XAS	X-Ray Absorption Spectroscopy
XPhos	2-Dicyclohexylphosphino-2',4',6'-Triisopropylbiphenyl

---

XPS	X-Ray Photoelectron Spectroscopy
XRD	X-Ray Diffraction
ZIF	Zeolitic Imidazolate Framework

---





## List of Tables

1	VPI of M <sub>2</sub> TTFTB with varying eq. TCNE, temperature, and reaction time. <i>x</i> in (TCNE) <sub><i>x</i></sub> M <sub>2</sub> TTFTB was experimentally determined via elemental analysis (Table 9). . . . .	12
2	Integrals of the fitted FTIR peaks corresponding to TCNE <sup>-</sup> or TCNE <sup>0</sup> and their ratio in (TCNE) <sub><i>x</i></sub> M <sub>2</sub> TTFTB. . . . .	24
3	Attempted Pd-catalyzed direct arylation of TSF with ethyl 4-bromobenzoate. <sup>a</sup> 45 mol%. <sup>b</sup> 60 mol%. <sup>c</sup> 120 mol%. <sup>d</sup> ethyl 4-iodobenzoate was used. <sup>e</sup> 30 mol%. . . . .	44
4	Cu-catalyzed direct arylation of TSF with ethyl 4-iodobenzoate. <sup>a</sup> 12 eq. <sup>b</sup> 40 mol%. <sup>c</sup> NMR yield. <sup>d</sup> ethyl 4-bromobenzoate was used. <sup>e</sup> based on NMR, less side product detected. <sup>f</sup> based on NMR, less side product detected. <sup>g</sup> worse than CuI, more side products. <sup>h</sup> 1 g scale, incomplete conversion to tetra-substituted TSF, tri-substituted was detected as major, inseparable product. . . . .	46
5	Attempted Pd-catalyzed Negishi coupling of zincated TSF with ethyl 4-iodobenzoate. <sup>a</sup> No ZnCl <sub>2</sub> . <sup>b</sup> MgCl <sub>2</sub> used instead of ZnCl <sub>2</sub> . <sup>c</sup> 1-methyl-2-pyrrolidone (NMP). <sup>d</sup> 50 mol%. <sup>e</sup> 10 mol%. <sup>f</sup> 4 eq. <sup>g</sup> Tri-(2-furyl)phosphine (tfp). <sup>h</sup> addition at 0 °C. <sup>i</sup> addition at RT. <sup>j</sup> ethyl 4-bromobenzoate was used. . . . .	51
6	Attempted Pd-catalyzed Liebeskind-Srogl couplings of tetrachalcogenated TSF derivatives. <sup>a</sup> Copper(I) thiophene-2-carboxylate. <sup>b</sup> with Zn(OAc) <sub>2</sub> (2 eq.). <sup>c</sup> with Cs <sub>2</sub> CO <sub>3</sub> (6 eq.). <sup>d</sup> 2-dicyclohexylphosphino-2',6'-dimethoxybiphenyl (SPhos). <sup>e</sup> Cs <sub>2</sub> CO <sub>3</sub> (8 eq.) was used. <sup>f</sup> 2-dicyclohexylphosphino-2',4',6'-triisopropylbiphenyl (XPhos). <sup>g</sup> 2-dicyclohexylphosphino-2',6'-diisopropoxybiphenyl (RuPhos). <sup>h</sup> 1,1'-ferrocenediyl-bis(diphenylphosphine) (dppf). <sup>i</sup> (oxydi-2,1-phenylene)bis(diphenylphosphine) (DPE-Phos). . . . .	52
7	VPI of Cu <sub>3</sub> BTC <sub>2</sub> with 0.5 and 1.0 eq. of dinitriles at 180 °C for 10 d.	62

8	VPI of $M_2$ TTFTB (200 mg) with varying eq. TCNE, temperature, and reaction time. . . . .	80
9	Elemental analysis of $(TCNE)_xM_2$ TTFTB with experimental values in wt.%, and simulated values in parentheses. $x$ is calculated using equation 6.8, and simulated values using equation 6.6. . . . .	81
10	VPI of $Cu_3BTC_2$ (100 mg) with varying eq. of dinitriles at 180 °C for 10 d. . . . .	93
11	Fitting parameters and crystallographic information for $Cu_3BTC_2$ . . . . .	122
12	Fitting parameters and crystallographic information for <b>I</b> . . . . .	123
13	Fitting parameters and crystallographic information for <b>II</b> . . . . .	124
14	Fitting parameters and crystallographic information for <b>III</b> . . . . .	125
15	Fitting parameters and crystallographic information for <b>IV</b> . . . . .	126
16	Fitting parameters and crystallographic information for <b>V</b> . . . . .	127
17	Fitting parameters and crystallographic information for <b>VI</b> . . . . .	128
18	Fitting parameters and crystallographic information for <b>VII</b> . . . . .	129
19	Fitting parameters and crystallographic information for <b>VIII</b> . . . . .	130
20	Fitting parameters and crystallographic information for <b>IX</b> . . . . .	131
21	Fitting parameters and crystallographic information for <b>X</b> . . . . .	132
22	Fitting parameters and crystallographic information for <b>XI</b> . . . . .	133
23	Fitting parameters and crystallographic information for <b>XII</b> . . . . .	134

---

## List of Figures

1	Crystal structure and stacking geometry of donors and acceptors in TTF-TCNQ. . . . .	8
2	Crystal structure and stacking geometry of donors and acceptors in TTF-TCNE. . . . .	8
3	(a) Crystal structure of $M_2$ TTFTB viewed along the $c$ axis. (b) Connectivity of TTFTB linkers and $MO_6$ -octahedra in $M_2$ TTFTB. (c) Rod-SBU of $M_2$ TTFTB consisting of corner-sharing $MO_6$ -octahedra. (d) Helical $\pi$ -stacks of TTF moieties. . . . .	10
4	PXRD patterns of $(TCNE)_xM_2$ TTFTB (Zn: top, Cd: bottom). The blue highlighted area emphasizes the (100) reflection (and the absence thereof in the Cd-series). . . . .	14
5	Cell parameters of $(TCNE)_xM_2$ TTFTB determined via Pawley profile fits. . . . .	15
6	Relative reflection intensities of $(TCNE)_xM_2$ TTFTB. . . . .	16
7	(a) DF-STEM images of <b>1</b> and EDS mapping of the K lines of elements (b) C (purple), (c) N (red), (d) O (blue), (e) S (yellow), and (f) Zn (green). . . . .	17
8	(a) DF-STEM images of <b>3</b> and EDS mapping of the K lines of elements (b) C (purple), (c) N (red), (d) O (blue), (e) S (yellow), and (f) Zn (green). . . . .	18
9	(a) DF-STEM images of <b>5</b> and EDS mapping of the K lines of elements (b) C (purple), (c) N (red), (d) O (blue), (e) S (yellow), and (f) Zn (green). . . . .	19
10	Sorption isotherms of $(TCNE)_xM_2$ TTFTB. Probe gases are shown in the graph titles, the respective MOFs in the legends. Filled and empty marker branches correspond to the adsorption and desorption branch, respectively. . . . .	21
11	FTIR spectra of $(TCNE)_xM_2$ TTFTB (Zn: top, Cd: bottom). . . . .	23

---

12	Deconvolution of CN stretching peak in FTIR spectra of <b>1-6</b> (see titles of subfigures), showing the experimentally observed (black) and simulated peak (orange), the latter consisting of the individual contributions P1-5. . . . .	25
13	Deconvolution of CN stretching peak in FTIR spectra of <b>7-10</b> (see titles of subfigures), showing the experimentally observed (black) and simulated peak (orange), the latter consisting of the individual contributions P1-5. . . . .	26
14	Raman spectra of (TCNE) <sub>x</sub> M <sub>2</sub> TTFTB (Zn: top, Cd: bottom). The wave-like intensities in the spectrum of Zn <sub>2</sub> TTFTB from 1650–2500 cm <sup>-1</sup> are caused by heating of the sample during the laser irradiation. . . . .	27
15	Summary of the electrical conductivities. . . . .	30
16	Crystal structure and stacking geometry of donors and acceptors in TTeF-TCNQ. . . . .	34
17	Proposed linkers H <sub>4</sub> TSFTB and H <sub>4</sub> TTeFTB (X = Se, Te). . . . .	34
18	NMR spectrum of the crude product obtained after Cu-catalyzed direct arylation of TSF with ethyl 4-iodobenzoate. . . . .	47
19	NMR spectrum of the Et <sub>4</sub> TSFTB. . . . .	47
20	LIFDI-MS of Et <sub>4</sub> TSFTB (purple) and simulated pattern (orange). . . . .	48
21	NMR spectra of the crude products obtained after Cu-catalyzed direct arylation of TSF with ethyl 4-iodobenzoate at 130 °C (blue), 110 °C (green), and 100 °C (orange). . . . .	48
22	LIFDI-MS of tri-arylated TSF (purple) and simulated (orange). . . . .	49
23	Illustration of the mean bond length ( $r_e$ ) increase with increasing temperature due to population of energetically higher vibrational states. The dashed line indicates the mean bond length at the initial temperature. . . . .	56
24	Illustration of volume shrinkage caused by rotation of equally sized tiles. The orange square on the right spans across the new tile centers and is smaller than the former (dark green) square when tile angles are 90°. . . . .	57
25	Crystal structure of ZrW <sub>2</sub> O <sub>8</sub> with corner-sharing ZrO <sub>6</sub> octahedra (green) connected to six WO <sub>4</sub> tetrahedra (blue). WO <sub>4</sub> tetrahedra contain one terminal oxygen atom. . . . .	57
26	Retrofitting of Cu <sub>3</sub> BTC <sub>2</sub> with TCNQ. The guests are oriented within the crystallographic (111) plane of Cu <sub>3</sub> BTC <sub>2</sub> . . . . .	59
27	Cross-linkers used for the synthesis of (Guest) <sub>x</sub> Cu <sub>3</sub> BTC <sub>2</sub> ( $x = 0.5, 1.0$ ) . . . . .	60

---

---

28	Absolute and relative volume changes of (Guest) <sub>x</sub> Cu <sub>3</sub> BTC <sub>2</sub> as a function of temperature. Guests are denoted above the subplots and different <i>x</i> are depicted in blue and green for 0.5 and 1.0 eq., respectively. Filled and empty markers correspond to the heating branch between 100 and 400 K in steps of 20 K and the cooling branch between 390 and 110 K in steps of 20 K, respectively. . . . .	61
29	Thermal expansion coefficient $\alpha_V$ and unit cell volume <i>V</i> at 100 K of (Guest) <sub>x</sub> Cu <sub>3</sub> BTC <sub>2</sub> . . . . .	63
30	FTIR spectra of (Guest) <sub>x</sub> Cu <sub>3</sub> BTC <sub>2</sub> with focus on the nitrile stretching frequency region at 2100–2300 cm <sup>-1</sup> . Nitrile signals of free-standing guests are indicated as a black dashed line. . . . .	66
31	Simulated and as synthesized PXRD data of Zn <sub>2</sub> TTFTB in a range of 5° to 50°. . . . .	94
32	Simulated and as synthesized PXRD data of Cd <sub>2</sub> TTFTB in a range of 5° to 50°. . . . .	94
33	Simulated and activated PXRD data of Cu <sub>3</sub> BTC <sub>2</sub> in a range of 2° to 25°. . . . .	95
34	VT-PXRD data of Cu <sub>3</sub> BTC <sub>2</sub> in a range of 2° to 25° from 100–400 K. During heating between 100 and 400 K, measurements were performed in temperature steps of 20 K. For the cooling, measurements were performed between 390 and 110 K with the same temperature steps of 20 K. . . . .	96
35	VT-PXRD data of <b>I</b> in a range of 2° to 25° from 100–400 K. During heating between 100 and 400 K, measurements were performed in temperature steps of 20 K. For the cooling, measurements were performed between 390 and 110 K with the same temperature steps of 20 K. . . . .	97
36	VT-PXRD data of <b>II</b> in a range of 2° to 25° from 100–400 K. During heating between 100 and 400 K, measurements were performed in temperature steps of 20 K. For the cooling, measurements were performed between 390 and 110 K with the same temperature steps of 20 K. . . . .	98
37	VT-PXRD data of <b>III</b> in a range of 2° to 25° from 100–400 K. During heating between 100 and 400 K, measurements were performed in temperature steps of 20 K. For the cooling, measurements were performed between 390 and 110 K with the same temperature steps of 20 K. . . . .	99

---

- 
- 38 VT-PXRD data of **IV** in a range of 2° to 25° from 100–400 K. During heating between 100 and 400 K, measurements were performed in temperature steps of 20 K. For the cooling, measurements were performed between 390 and 110 K with the same temperature steps of 20 K. . . . . 100
- 39 VT-PXRD data of **V** in a range of 2° to 25° from 100–400 K. During heating between 100 and 400 K, measurements were performed in temperature steps of 20 K. For the cooling, measurements were performed between 390 and 110 K with the same temperature steps of 20 K. . . . . 101
- 40 VT-PXRD data of **VI** in a range of 2° to 25° from 100–400 K. During heating between 100 and 400 K, measurements were performed in temperature steps of 20 K. For the cooling, measurements were performed between 390 and 110 K with the same temperature steps of 20 K. . . . . 102
- 41 VT-PXRD data of **VII** in a range of 2° to 25° from 100–400 K. During heating between 100 and 400 K, measurements were performed in temperature steps of 20 K. For the cooling, measurements were performed between 390 and 110 K with the same temperature steps of 20 K. . . . . 103
- 42 VT-PXRD data of **VIII** in a range of 2° to 25° from 100–400 K. During heating between 100 and 400 K, measurements were performed in temperature steps of 20 K. For the cooling, measurements were performed between 390 and 110 K with the same temperature steps of 20 K. . . . . 104
- 43 VT-PXRD data of **IX** in a range of 2° to 25° from 100–400 K. During heating between 100 and 400 K, measurements were performed in temperature steps of 20 K. For the cooling, measurements were performed between 390 and 110 K with the same temperature steps of 20 K. . . . . 105
- 44 VT-PXRD data of **X** in a range of 2° to 25° from 100–400 K. During heating between 100 and 400 K, measurements were performed in temperature steps of 20 K. For the cooling, measurements were performed between 390 and 110 K with the same temperature steps of 20 K. . . . . 106
-

---

45	VT-PXRD data of <b>XI</b> in a range of 2° to 25° from 100–400 K. During heating between 100 and 400 K, measurements were performed in temperature steps of 20 K. For the cooling, measurements were performed between 390 and 110 K with the same temperature steps of 20 K. . . . .	107
46	VT-PXRD data of <b>XII</b> in a range of 2° to 25° from 100–400 K. During heating between 100 and 400 K, measurements were performed in temperature steps of 20 K. For the cooling, measurements were performed between 390 and 110 K with the same temperature steps of 20 K. . . . .	108
47	Pawley profile fit of activated Zn <sub>2</sub> TTFTB. The experimental data (black) was fitted (red) using the hexagonal space group <i>P6<sub>5</sub></i> . The difference curve is given in blue and the R <sub>wp</sub> values are shown in the top right corner. . . . .	109
48	Pawley profile fit of activated Cd <sub>2</sub> TTFTB. The experimental data (black) was fitted (red) using the hexagonal space group <i>P6<sub>5</sub></i> . The difference curve is given in blue and the R <sub>wp</sub> values are shown in the top right corner. . . . .	109
49	Pawley profile fit of <b>1</b> . The experimental data (black) was fitted (red) using the hexagonal space group <i>P6<sub>5</sub></i> . The difference curve is given in blue and the R <sub>wp</sub> values are shown in the top right. . . .	110
50	Pawley profile fit of <b>2</b> . The experimental data (black) was fitted (red) using the hexagonal space group <i>P6<sub>5</sub></i> . The difference curve is given in blue and the R <sub>wp</sub> values are shown in the top right. . . .	110
51	Pawley profile fit of <b>3</b> . The experimental data (black) was fitted (red) using the hexagonal space group <i>P6<sub>5</sub></i> . The difference curve is given in blue and the R <sub>wp</sub> values are shown in the top right. . . .	111
52	Pawley profile fit of <b>4</b> . The experimental data (black) was fitted (red) using the hexagonal space group <i>P6<sub>5</sub></i> . The difference curve is given in blue and the R <sub>wp</sub> values are shown in the top right. . . .	111
53	Pawley profile fit of <b>5</b> . The experimental data (black) was fitted (red) using the hexagonal space group <i>P6<sub>5</sub></i> . The difference curve is given in blue and the R <sub>wp</sub> values are shown in the top right. . . .	112
54	Pawley profile fit of <b>6</b> . The experimental data (black) was fitted (red) using the hexagonal space group <i>P6<sub>5</sub></i> . The difference curve is given in blue and the R <sub>wp</sub> values are shown in the top right. . . .	112
55	Pawley profile fit of <b>7</b> . The experimental data (black) was fitted (red) using the hexagonal space group <i>P6<sub>5</sub></i> . The difference curve is given in blue and the R <sub>wp</sub> values are shown in the top right. . . .	113

---

- 
- 56 Pawley profile fit of **8**. The experimental data (black) was fitted (red) using the hexagonal space group  $P6_5$ . The difference curve is given in blue and the  $R_{wp}$  values are shown in the top right. . . . 113
- 57 Pawley profile fit of **9**. The experimental data (black) was fitted (red) using the hexagonal space group  $P6_5$ . The difference curve is given in blue and the  $R_{wp}$  values are shown in the top right. . . . 114
- 58 Pawley profile fit of **10**. The experimental data (black) was fitted (red) using the hexagonal space group  $P6_5$ . The difference curve is given in blue and the  $R_{wp}$  values are shown in the top right. . . . 114
- 59 Pawley profile fit of  $\text{Cu}_3\text{BTC}_2$  at 100 K. The experimental data (black) was fitted (red) using the cubic space group Fm-3m. The difference curve is given in blue and the  $R_{wp}$  values are shown in the top right corner. . . . . 115
- 60 Pawley profile fit of **I** at 100 K. The experimental data (black) was fitted (red) using the cubic space group Fm-3m. The difference curve is given in blue and the  $R_{wp}$  values are shown in the top right corner. . . . . 115
- 61 Pawley profile fit of **II** at 100 K. The experimental data (black) was fitted (red) using the cubic space group Fm-3m. The difference curve is given in blue and the  $R_{wp}$  values are shown in the top right corner. . . . . 116
- 62 Pawley profile fit of **III** at 100 K. The experimental data (black) was fitted (red) using the cubic space group Fm-3m. The difference curve is given in blue and the  $R_{wp}$  values are shown in the top right corner. . . . . 116
- 63 Pawley profile fit of **IV** at 100 K. The experimental data (black) was fitted (red) using the cubic space group Fm-3m. The difference curve is given in blue and the  $R_{wp}$  values are shown in the top right corner. . . . . 117
- 64 Pawley profile fit of **V** at 100 K. The experimental data (black) was fitted (red) using the cubic space group Fm-3m. The difference curve is given in blue and the  $R_{wp}$  values are shown in the top right corner. . . . . 117
- 65 Pawley profile fit of **VI** at 100 K. The experimental data (black) was fitted (red) using the cubic space group Fm-3m. The difference curve is given in blue and the  $R_{wp}$  values are shown in the top right corner. . . . . 118
-



---

66	Pawley profile fit of <b>VII</b> at 100 K. The experimental data (black) was fitted (red) using the cubic space group Fm-3m. The difference curve is given in blue and the $R_{wp}$ values are shown in the top right corner. . . . .	118
67	Pawley profile fit of <b>VIII</b> at 100 K. The experimental data (black) was fitted (red) using the cubic space group Fm-3m. The difference curve is given in blue and the $R_{wp}$ values are shown in the top right corner. . . . .	119
68	Pawley profile fit of <b>IX</b> at 100 K. The experimental data (black) was fitted (red) using the cubic space group Fm-3m. The difference curve is given in blue and the $R_{wp}$ values are shown in the top right corner. . . . .	119
69	Pawley profile fit of <b>X</b> at 100 K. The experimental data (black) was fitted (red) using the cubic space group Fm-3m. The difference curve is given in blue and the $R_{wp}$ values are shown in the top right corner. . . . .	120
70	Pawley profile fit of <b>XI</b> at 100 K. The experimental data (black) was fitted (red) using the cubic space group Fm-3m. The difference curve is given in blue and the $R_{wp}$ values are shown in the top right corner. . . . .	120
71	Pawley profile fit of <b>XII</b> at 100 K. The experimental data (black) was fitted (red) using the cubic space group Fm-3m. The difference curve is given in blue and the $R_{wp}$ values are shown in the top right corner. . . . .	121
72	SEM picture of $Zn_2TTFTB$ . . . . .	135
73	SEM picture of <b>1</b> . . . . .	135
74	SEM picture of <b>2</b> . . . . .	136
75	SEM picture of <b>3</b> . . . . .	136
76	SEM picture of <b>4</b> . . . . .	137
77	SEM picture of <b>5</b> . . . . .	137
78	SEM picture of <b>6</b> . . . . .	138
79	SEM picture of $Cd_2TTFTB$ . . . . .	138
80	SEM picture of <b>7</b> . . . . .	139
81	SEM picture of <b>8</b> . . . . .	139
82	SEM picture of <b>9</b> . . . . .	140
83	SEM picture of <b>10</b> . . . . .	140
84	NMR spectrum of $Et_4TTFTB$ . . . . .	141
85	NMR spectrum of $H_4TTFTB$ . . . . .	141
86	NMR spectrum of acetaldehyde semicarbazone. . . . .	142

---

87	NMR spectrum of 1,2,3-selenadiazole. . . . .	142
88	NMR spectrum of 2-Methylene-1,3-diselenole in (a) CDCl <sub>3</sub> , and (b) CD <sub>2</sub> Cl <sub>2</sub> . . . . .	143
89	NMR spectrum of TSF(SMe) <sub>4</sub> . . . . .	144
90	NMR spectrum of TSF. . . . .	144
91	NMR spectrum of TSF(SePh) <sub>4</sub> . . . . .	145
92	NMR spectrum of TSF(SeBu) <sub>4</sub> . . . . .	145
93	Current-voltage curves of (TCNE) <sub>x</sub> M <sub>2</sub> TTFTB. . . . .	146
94	FTIR spectra of (Guest) <sub>x</sub> Cu <sub>3</sub> BTC <sub>2</sub> . . . . .	147
95	FTIR spectra of guests used for the VPI of Cu <sub>3</sub> BTC <sub>2</sub> . The peak maxima are indicated with a black dashed line. . . . .	148
96	(a) Crystal structure of MOF-5. The different pore sizes of 15.1 and 11.0 Å are illustrated using an orange and a green sphere, respectively. (b) Illustration of the underlying <b>pcu</b> topology of MOF-5. Green spheres indicate the empty pore space. The Vesta3 software was used for crystal structure visualization. . . . .	155
97	(a) Crystal structure of [Cu <sup>I</sup> [C(C <sub>6</sub> H <sub>4</sub> CN) <sub>4</sub> ]][BF <sub>4</sub> ] · x PhNO <sub>2</sub> . H, BF <sub>4</sub> <sup>-</sup> , and PhNO <sub>2</sub> are omitted. The orange sphere indicates the void space. (b) Illustration of the underlying <b>dia</b> topology in the cationic framework [Cu <sup>I</sup> [C(C <sub>6</sub> H <sub>4</sub> CN) <sub>4</sub> ]][BF <sub>4</sub> ] · x PhNO <sub>2</sub> . . . . .	157
98	(a) Crystal structure of Cu <sub>3</sub> BTC <sub>2</sub> . The different pore sizes of are illustrated using an orange, green, and pink spheres. (b) Illustration of the underlying <b>tbo</b> topology of MOF-5. Orange and pink spheres indicate the empty pore space. . . . .	159
99	Breathing behavior of flexible MIL-53 in the presence of water. . .	160
100	Isorecticular expansion of MOF-5. . . . .	162
101	Dependence of the topology of MOFs obtained via isorecticular expansion on the linker symmetry. . . . .	163
102	Conceptual illustration of MTV-MOF-5 containing (a) mixed-metal SBUs and (b) multiple linkers with a variety of functional groups (indicated with different colors). . . . .	164
103	Retrofitting of BPDC in MOF-520. . . . .	169
104	Crystal structures of M <sub>2</sub> (DSBDC) (a) M = Mn, (b) M = Fe. . . . .	174
105	(a) SBU of Fe <sup>II</sup> (tri) <sub>2</sub> . (b) Structure of Fe <sup>II</sup> <sub>0.67</sub> Fe <sup>III</sup> <sub>0.33</sub> (tri) <sub>2</sub> (BF <sub>4</sub> ) <sub>0.33</sub> with <b>dia</b> topology. . . . .	175
106	(a) One-dimensional chains of FeN <sub>6</sub> octahedra bridged by pyrazolates as SBU. (b) Crystal structure of Fe <sub>2</sub> BDP <sub>3</sub> . . . . .	176
107	(a) Crystal structure and (b) π-stacking of TTF units in Ln <sub>6</sub> TTFTB <sub>5</sub> (Ln = Tm, Yb, Lu). . . . .	178

108	Crystal structures of (a) $\text{La}_4\text{HTTFTB}_4$ , (c) $\text{LaHTTFTB}$ , and (e) $\text{La}_4\text{TTFB}_3$ , and their respective TTF-TTF $\pi$ -stacking motifs in (b), (d), and (f). . . . .	179
109	(a) Crystal structure and (b) $\pi$ -stacking arrangement in $\text{Cd-NDI-py}$ . . . . .	180
110	(a) Molecular structure of chloroanilic acid, $\text{H}_2\text{Cl}_2\text{dmbq}$ . (b) Crystal structure of the MOF family $[\text{M}_2(\text{Cl}_2\text{dmbq})_3]^{2-}$ with view of the $ab$ plane. (c) Stacking of two-dimensional sheets in $[\text{M}_2(\text{Cl}_2\text{dmbq})_3]^{2-}$ along the crystallographic $c$ axis. . . . .	181
111	Crystal structure of $(\text{NBu}_4)_2[\text{Fe}^{\text{III}}_2(\text{dmbq})_3]$ . For clarity, only one of the two entangled frameworks is shown. H atoms and tetrabutylammonium cations are omitted. . . . .	184
112	(a) Crystal structure of $\text{Co}_3(\text{HHTP})_2$ viewed along the crystallographic $c$ axis. (b) Stacking of extended and isolated layers of HHTP perpendicular to the $c$ axis. . . . .	185
113	(a) Crystal structure of $\text{Ln}_{1+x}\text{HHTP}$ . View of the hexagonal sheets in the $ab$ plane. (b) $\pi$ -stacking and edge-sharing $\text{LnO}_6$ octahedra perpendicular to the sheets. . . . .	186
114	Simulated structure of $\text{Ni}_3\text{HITP}_2$ (a) within the plane, (b) slipped-parallel stacking of the extended coordination sheets. . . . .	190
115	Crystal structure of $\text{Cr}^{\text{III}}\text{Cl}_2(\text{pyrazine})_2$ . . . . .	191
116	(a) Crystal structure and (b) helical rod-SBU in $\text{V}_2(\text{OH})_2\text{BPTC}$ . . . . .	192
117	Schematic illustration of a bound electron in a potential well with infinitely large potential barriers. The probability function of the electron, $\psi\psi^*$ , is zero in the forbidden blue area and on the border to the permitted white area. . . . .	195
118	(a) Wave functions, and (b) probability functions for the energy levels of the bound electron with infinitely large potential barriers. . . . .	195
119	Tunneling of an electron through a potential barrier. . . . .	196
120	Formation of band gaps for an electron in a periodically varying potential field, also known as the Kronig-Penney model. (a) Function $y = \cos(\alpha a) + P \frac{\sin(\alpha a)}{\alpha a}$ vs. $\alpha a$ for $P = 4$ . (b) Cutout of the above graph between $-1 \leq y \leq 1$ . . . . .	197
121	Energy profile of an electron in a crystal. (a) Repetition of the energy profile of a free electron with periodicity of $\frac{2\pi}{a}$ . (b) Summation of the individual energy profiles into a periodic zone scheme. (c) Reduced zone scheme between $k_x = \pm \frac{\pi}{a}$ . (d) Extended zone scheme showing both first and second Brillouin zones. . . . .	198

122	Fermi distribution functions. The line changes its shape from a horizontal line at $T = 0$ (purple) to a curve with increasing temperature (yellow). Note that at $E = E_F$ , $F(E) = 0.5$ for every temperature. . . . .	199
123	Energy state in quantum number space. . . . .	200
124	(a) Density of states and (b) population density within a band. . . . .	201
125	Band population and density of states for (a) insulators, semiconductors, and (b) metals. . . . .	203
126	Band formation and overlap in a covalent solid with $N$ atoms and interatomic bond distance $a_{eq}$ . $E_g$ is the energetic band gap between the filled valence band and empty conduction band. . . . .	204
127	Relationships of charge carrier mobility, density, and electrical conductivity of intrinsic semiconductors vs. temperature. . . . .	206
128	Donor and acceptor levels in (a) $n$ -type and (b) $p$ -type extrinsic semiconductors, respectively. . . . .	206
129	Relationship of charge carrier density and electrical conductivity with temperature for extrinsic semiconductors. The dashed lines indicate the temperature at which intrinsic effects become apparent. High doping increases the electrical conductivity. . . . .	207
130	Dependence of the Fermi level on the temperature of $n$ -type (blue) and $p$ -type (yellow) extrinsic semiconductors. . . . .	208
131	Measurement techniques for electrical conductivity. (a) Two-contact probe method. (b) Four-contact probe method. (c) Four-point probe method. (d) Van-der-Pauw method. . . . .	211
132	Crystal systems and Bravais lattices. Triclin: $a \neq b \neq c$ , $\alpha \neq \beta \neq \gamma \neq 90^\circ$ , $120^\circ$ . Monoclin: $a \neq b \neq c$ , $\alpha = \gamma = 90^\circ$ , $\beta \neq 90^\circ$ , $120^\circ$ . Orthorhombic: $a \neq b \neq c$ , $\alpha = \beta = \gamma = 90^\circ$ . Tetragonal: $a = b \neq c$ , $\alpha = \beta = \gamma = 90^\circ$ . Hexagonal: $a = b \neq c$ , $\alpha = \beta = 90^\circ$ , $\gamma = 120^\circ$ . Trigonal: $a = b = c$ , $\alpha = \beta = \gamma \neq 90^\circ$ , $<120^\circ$ . Cubic: $a = b = c$ , $\alpha = \beta = \gamma = 90^\circ$ . P: primitive, C: base-centered, I: body-centered, F: face-centered, R: rhombohedral. . . . .	215
133	Schematic illustration of an x-ray source. . . . .	216
134	X-radiation spectrum for Cu. The green line indicates the absorption profile of Ni, with its absorption edge located between the $K_\alpha$ and $K_\beta$ lines indicated as a dashed green line. . . . .	217
135	(a) Geometric illustration of Bragg's law. (b) Constructive interference. (c) Destructive interference. . . . .	218
136	(a) Unit cell in real space. (b) Conversion of the real unit cell into the reciprocal unit cell. Each point in the reciprocal space corresponds to one family of planes in the real space. . . . .	220

---

137	(a) Formation of diffraction cones from polycrystalline samples. (b) One-dimensional diffractogram obtained by scanning the $2\theta$ diffraction range using a typical PXRD detector. . . . .	221
138	Isotherm types (volumetric uptake vs. relative pressure). . . . .	225
139	Hysteresis loops (volumetric uptake vs. relative pressure). . . . .	226
140	Schematic illustration of a BET plot. . . . .	231
141	Vibrational modes: (a) symmetric stretching; (b) asymmetric stretching, (c) scissoring, (d) rocking, (e) wagging (out of plane), (f) twisting (out of plane). . . . .	234
142	(a) Model for a chemical bond. (b) Harmonic potential energy of a bond with an equilibrium distance $r_0$ and energetically equidistant vibrational states of the energy increment $E_i = h\nu(0.5 + \nu_i)$ . (c) Anharmonic (Morse) potential with an equilibrium distance $r_0$ , finite vibrational states and bond dissociation energy $D$ . . . . .	236
143	Model for an excitation of a vibration from the ground state to the first excited state using infrared light. . . . .	236
144	(a) Elastic (Rayleigh) scattering; Raman effect: (b) Inelastic (Stokes) scattering. (c) Inelastic (Anti-Stokes) scattering. . . . .	237
145	Scattering process of a primary electron (trajectory indicated in green) by atomic nucleus (surrounded by electron shells according to the Bohr atom model). The electric field is stronger closer to the nucleus, so the deflection angle $\theta_1$ is greater for an electron passing closer to the nucleus than for one passing further away at an angle $\theta_2$ . . . . .	241
146	Relationship of (a) cross section $\sigma$ and scattering angle $\theta$ with varying beam energy $eV$ , increasing beam energies decrease cross sections, (b) $\sigma$ and $\theta$ with varying atomic number $Z$ , increasing $Z$ increases $\sigma$ , (c) the mean-free path $\lambda$ and beam energy $eV$ with varying $Z$ , $\lambda$ decreases with increasing $Z$ . . . . .	243
147	Penetration depth $R$ of a primary electron (also a BSE) in a solid after impact with the surface <b>S</b> and characteristic pear-shape interaction volume $V$ . $R$ increases with increasing beam energy and decreasing $Z$ (mass-thickness) of the specimen. . . . .	244
148	Oblique angle $\phi$ of incident electron beam increases the specimen volume between the surface <b>S</b> and escape depth <b>E</b> , giving rise to higher SE yields. . . . .	245
149	Schematic setups of (a) TEM, (b) SEM, and (c), STEM. Purple lines: electron trajectory, ellipses: magnetic electron lenses, green rectangles: scanning coils, orange rectangles: specimen. . . . .	248

---

150	Energetic splitting of the magnetic orientations $m_I$ in the field $\mathcal{B}_0$ . . . . .	253
151	(a) Spin-spin coupling in an $AX$ -system. (b) Illustration of the signal splitting in the NMR spectrum. . . . .	256
152	Spin-spin coupling in a (a) $AX_2$ , (b) $AX_3$ . . . . .	257
153	Names and intensity ratios of multiplets defined by Pascal's triangle for $n$ neighbors. . . . .	257

---

## List of Schemes

1	First reported synthesis of TSF. . . . .	35
2	Alternative synthesis of TSF based on CSe <sub>2</sub> . . . . .	35
3	New synthesis routes of TSF from diselenafulvene. . . . .	36
4	Synthesis of <i>E/Z</i> -diphenyltetraselenafulvalene. . . . .	36
5	CSe <sub>2</sub> -free synthesis of tetrasubstituted tetraselenafulvalenes. . . .	37
6	Titanocene-route to 4,5-dicarbomethoxy-1,3-diselenole-2-thione. .	37
7	Synthesis of BEDT-TSF. . . . .	38
8	Titanocene complexes as intermediates for the synthesis of mixed tetrachalcogenafulvalenes. . . . .	38
9	Titanocene complexes obtained from selenadiazoles. . . . .	38
10	Synthesis of dibenzotetraselenafulvalene. . . . .	39
11	Tetralithiation of TSF and quenching with dimethyl disulfide. . . . .	39
12	Homo coupling of stannylated TSF to bi-TSF. . . . .	39
13	Proposed direct arylation of zincated TSF using Pd catalyzed Negishi coupling. . . . .	40
14	Proposed direct arylation of TSF using Pd catalysis. . . . .	40
15	Conversion of TSF to diaryl selenide at direct arylation reaction conditions. . . . .	43
16	Reaction scheme for the synthesis of tetraethyl tetrathiafulvalene tetrabenzoate (Et <sub>4</sub> TTFTB). . . . .	77
17	Reaction scheme for the synthesis of tetrathiafulvalene tetraben- zoate (H <sub>4</sub> TTFTB). . . . .	78
18	Reaction scheme for the synthesis of acetaldehyde semicarbazone. . . . .	80
19	Reaction scheme for the synthesis of 1,2,3-selenadiazole. . . . .	81
20	Reaction scheme for the synthesis of 2-methylene-1,3-diselenole. . . . .	82
21	Reaction scheme for the synthesis of TSF from sodium acetylide. . . . .	83
22	Reaction scheme for the synthesis of TSF, starting from acetalde- hyde semicarbazone. . . . .	85
23	Reaction scheme for the synthesis of TSF(SMe) <sub>4</sub> . . . . .	87

---

24	Reaction scheme for the synthesis of $\text{TSF}(\text{SePh})_4$ . . . . .	88
25	Reaction scheme for the synthesis of $\text{TSF}(\text{SeBu})_4$ . . . . .	88
26	Reaction scheme for the failed bromination of TSF using NBS. . .	89
27	Reaction scheme for the failed bromination of TSF with bromine. .	90
28	Reaction scheme for the failed tetracarboxylation of TSF. . . . .	90
29	Reaction scheme for the failed tetraboronation reaction of TSF with $i\text{PrO}-\text{Bpin}$ . . . . .	91
30	Reaction scheme for the failed tetrasilylation of TSF with various silyl chlorides. . . . .	92
31	Illustration of the topological reduction of paddle-wheel complexes and linear dicarboxylates into squares and links and their connectivity. . . . .	154
32	Conceptual illustration of the diverse PSM strategies for MOF-5 analogs. . . . .	166
33	Preparation of electrically conductive $\text{Cu}^{\text{II}}[\text{Cu}^{\text{II}}(\text{pdt})_2]$ from $\text{CuI}$ and $\text{Na}[\text{Cu}^{\text{III}}(\text{pdt})_2]$ in $\text{MeCN}$ . . . . .	173
34	Reduction reaction of mixed-valent $[\text{Me}_2\text{NH}_2][\text{Fe}_2(\text{Cl}_2\text{dhbq})_3]$ to mono-valent $(\text{Cp}_2\text{Co})_{1.43}(\text{Me}_2\text{NH}_2)_{1.57}(\text{Fe}_2(\text{Cl}_2\text{dhbq})_3)$ with cobaltocene. . . . .	182
35	Structure of the coordination polymer (a) $\text{Cu}_3\text{BHT}$ , (b) $\text{Ni}_3\text{BHT}_2$ . . .	188
36	Structure of $\text{Fe}_3\text{THT}_2(\text{NH}_4)_3$ . . . . .	189
37	Ionization and subsequent fragmentation pathways during electron ionization. Uncharged $\text{X}^\bullet$ and $\text{N}$ are not detected by MS. . . . .	260
38	Ionization of the reagent gas and subsequent formation of the pseudomolecular ion $\text{MH}^+$ in $\text{Cl}$ . . . . .	260

---







# I

EMPIRICAL RESEARCH



# 1

## *Introduction*

Functional materials are the epitome of technological progress. This is perhaps best illustrated by how entire ancient eras are referred to as the age of the material which has revolutionized the common lifestyle of humans at the time. Crucial to the development of new materials is the ever-growing understanding of the physical and chemical laws of nature that shed light on further technological possibilities. Likewise, this process is codependent on the application of sophisticated materials as a means of reaching technological goals which constantly gain in complexity. Consequently, what has come to be known as "smart materials" are the efforts to design materials that meet consistently higher standards, fulfill functions that exceed the common state-of-the-art and expand the field of possible applications.<sup>1</sup> Following this trend, multifunctional materials have recently emerged in the pursuit of combining even more physical and chemical properties in one tailored material that serves several custom purposes.<sup>2</sup> At the center of attention is the understanding of structure-property relationships between structural motifs on a microscopic scale that translate to physicochemical functions in the solid state. However, materials science is usually limited to this direction of the chain of causation: new materials are obtained with the aid of the toolbox of known chemical transformations, and their physical properties are deduced from the results of analytical experiments. Although highly desirable, the opposite direction, i.e. the access to a material with priorly predicted physical properties, is very difficult to achieve.<sup>3</sup> This would require synthetic control of materials with specific structural motifs, either known or predicted via computational methods for certain physical properties. Such chemical directionality, where the outcome of an unknown synthetic transformation is somewhat predictable, is mostly limited to the area of organic synthetic chemistry. In contrast, inorganic and materials synthesis is usually limited to the "trial and error" method, and even more so the rationalization of

structure-property relationships of the obtained materials.<sup>4</sup> A major step towards a better understanding of these relationships is achieved by providing a means of directionality in the synthesis of new functional materials.

Metal-organic frameworks (MOFs) are a comparably new class of materials that have emerged in the last twenty years.<sup>5</sup> These hybrid organic-inorganic materials seem to be the bridge between the multifunctionality of inorganic materials and the chemical directionality of the synthesis of organic molecules, for their preparation follows rational guidelines. Their modular composition of inorganic structural units with different geometries that are interconnected by coordinating organic ligands, also known as linkers, give rise to a rich structural diversity that is generally dependent on the geometry and connectivity of the applied components but not on the nature of the atoms in these components per se. Therefore, isostructural frameworks with different connectors are easily obtained. This synthetic principle, which was coined as "reticular synthesis", provides an unprecedented synthetic control in the design of new materials, the functions of which stem from the employed organic and inorganic struts of the MOF and are interchangeable depending on the desired function the material chemist wants to introduce.<sup>6</sup>

Furthermore, MOFs are porous as a result of the connector sizes that create coordination frameworks with voids in between the struts when these self-assemble to higher-dimensional architectures.<sup>7</sup> While initial research on MOFs has focused on taking advantage of this porosity for directly related applications such as gas storage and separation,<sup>8</sup> it was later discovered that their material properties can be tuned in ways that combine seemingly contradicting physical functions such as porosity and electrical conductivity.<sup>9</sup> This is one of many examples that emphasizes the potential of MOFs as a multifunctional material platform in which structures can be attained and their physical properties tuned by rational means. In addition, their porosity also opens up the field of tuning the physical properties of the MOF by introducing a functional molecule — or "guest" — into these framework voids, giving rise to yet another parameter space in the control of multifunctionality.<sup>10</sup> Guests can be either simple gases that induce structural changes of the MOF,<sup>11</sup> or more complex molecules which are subject to electronic interactions with the MOF, leading to improved electrical conductivity or photophysical properties, all of which are not inherent in the pristine MOF and are easily tuned by employing different guests.<sup>12</sup> Here, the additional tuning possibility via the pore space offers orthogonality in materials design, which is commonly not feasible in traditional material classes.

However, the exact processes occurring in the MOF host-guest complexes that lead to new physical properties are often only poorly understood, if studied at all. Nevertheless, insights into the interaction mechanisms would open up further

---

possibilities of fine-tuning certain material properties towards the desired function and generally contribute to better structure-property relationship statements. Seemingly small changes in the employed guest, the studied MOF host, or the reaction conditions at which the host-guest complexes are obtained may exert a significant influence on the resulting material properties based on the changing structural or electronic interactions, which can be easily overlooked. Hence, this thesis aims at answering the following research questions:

*“How can interactions between MOFs and guests be probed beyond a qualitative manner?”*

*“Can these interactions be tuned even further in the same host-guest system by varying the reaction conditions?”*

*“How do slight changes of the MOF or the guest affect their interaction?”*

This thesis is divided in two parts. In the first part, the three chapters therein present the outcomes of three different projects, which are all guided by the goal of answering the above-mentioned research questions and some of them will be tackled simultaneously. Each chapter begins with a introduction to provide all the necessary topic-related knowledge the reader needs to understand the project and its outcome. In the beginning of this thesis, MOF systems were sought that are suitable for performing electronic or structural interactions with specific guest molecules, and thus the work has focused on the tetrathiafulvalene tetrabenzoate (TTFTB)-based MOFs  $M_2$ TTFTB ( $M^{2+} = \text{Zn}, \text{Cd}$ )<sup>13,14</sup> for investigating electronic interactions with redox-active guests such as TCNE and its influence with respect to the electrical conductivity of the host-guest complex as the first project (Chapter 2). The interesting properties of TTFTB-based MOFs led to the question of how the electrical properties of possible isostructural systems would be affected by employing an isostructural linker with a tetraselenafulvalene (TSF) core in the center, and a synthetic route to this linker was developed in the second chapter (Chapter 3). On the other hand,  $\text{Cu}_3$  benzene tricarboxylate ( $\text{BTC}$ )<sub>2</sub> was chosen to study interaction of different guests on the negative thermal expansion (NTE) behavior of this MOF<sup>15</sup> to gain insight into how small variations in guest design leads to property changes in the third and final project (Chapter 4). What follows after the conclusion is a description of experimental procedures and presentation of additional data (Chapter 6).

The second part of this thesis serves the purpose of providing all the background information that is necessary to understand the general chemistry of the materials studied here and the principles of the analytical techniques used to readers that are less familiar with MOFs and material characterization techniques. Chapter 7

is dedicated to the description and chemistry of MOFs, as well as their manifold functionalization possibilities. Next, the focus lies solely on electrically conductive MOFs, for they play an important role in developing the motivation to study host-guest interactions in MOFs in more detail (Chapter 8). What follows after that is a brief summary of electron theory that is needed to understand the origins of electrical conductivity and the concepts discussed in the first two chapters of this thesis (Chapter 9). In the following chapters, similarly brief overviews of the characterization techniques, which have been used in this thesis, are meant to provide a recapitulation of working principles of these techniques to readers who are less familiar with them in order to provide a sufficient knowledge for understanding the experimental data presented in this thesis. Beginning with x-ray diffraction (XRD) (Chapter 10) and gas sorption (Chapter 11), the most commonly employed techniques in MOF characterization are introduced before moving on to Fourier transform infrared spectroscopy (FTIR)- and Raman spectroscopy (Chapter 12), which has been of crucial importance for the deduction of host-guest reactivities as presented in the first chapter. MOFs are also often analyzed via electron microscopy to investigate the distribution of guests within the framework, which is a relevant issue in the first chapter, and so the theory related to this technique is summarized in Chapter 13. Finally, nuclear magnetic resonance spectroscopy (NMR) (Chapter 14) and mass spectrometry (MS) (Chapter 15) have been important for the development of a TSF-based linker in the second chapter. For a more detailed perspective into these techniques, the author refers to the references cited herein.

---



# 2

## *Guest-Induced Charge-Transfer in Tetrathiafulvalene-Based Metal-Organic Frameworks*

### 2.1 INTRODUCTION

Tetrathiafulvalene (TTF)-based charge-transfer (CT) complexes are a class of organic metals that can exhibit large electrical conductivity and even superconductivity.<sup>16,17</sup> Crucial to these — for organic materials typically uncommon — electrical properties is the partial degree of TTF oxidation in the formation of the CT complex, as well as the structural arrangement of the donor and acceptor molecules within the crystal.<sup>18</sup> For example, TTF reacts with 7,7,8,8-tetracyanoquinodimethane (TCNQ) to form the quasi-one-dimensional organic metal TTF-TCNQ of 1:1 stoichiometry in which segregated infinite, one-dimensional  $\pi$ -stacks of slipped-parallel TTF molecules are aligned in parallel to one-dimensional  $\pi$ -stacks of TCNQ (Figure 1).<sup>19,20</sup> Essential is the degree of CT,  $\rho$ , that is smaller than one (i.e., full electron transfer from the donor to the acceptor molecule) and TTF-TCNQ is best described as  $(\text{TTF})^{+0.59}(\text{TCNQ})^{-0.59}$  with a mixture of neutral and charged species is present in each of the stacks.<sup>21</sup> The electrical conductivity is highly anisotropic due to the dimensionality of the stacking, in which the intermolecular interactions between the mixed-valent donor (and acceptor) molecules are greatest along the  $\pi$ -interaction direction and significantly reduced perpendicular to the  $\pi$ -stacking axis.<sup>22</sup> For sub-integer values of  $\rho$ , the conduction band of the solid is only partially filled with electrons and the resulting activation energy for an electronic transition is very small, giving rise to metallic electrical conductivity (*cf.* chapter 9).<sup>23</sup> Importantly, CT salts with full electron transfer from the donor to

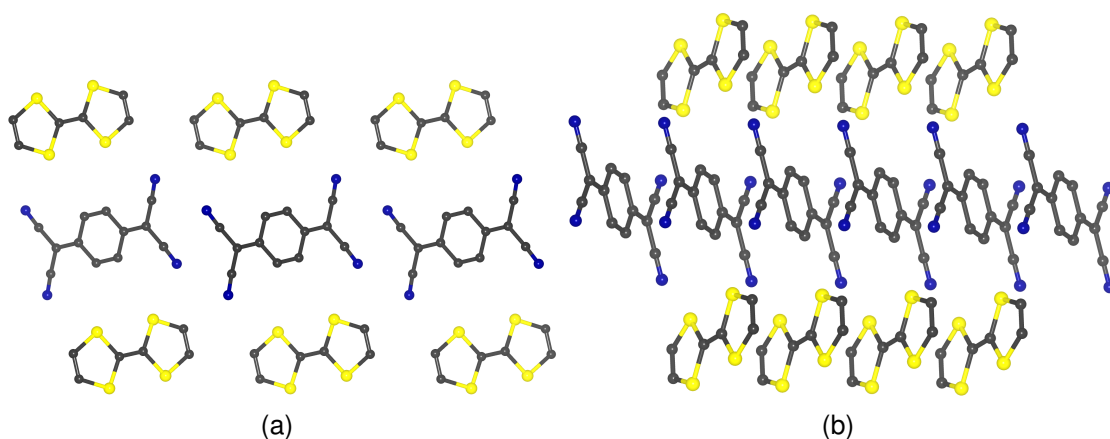


**Figure 1.** Crystal structure and stacking geometry of donors and acceptors in TTF-TCNQ.

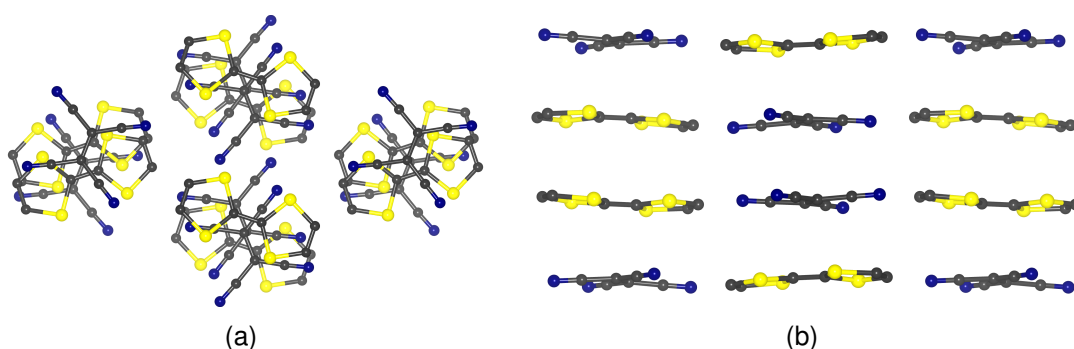


**Figure 2.** Crystal structure and stacking geometry of donors and acceptors in TTF-TCNE.

the acceptor yield mono-valent systems consisting of only charged species in the stacks (i.e., radical-cations in the donor stack and radical-anions in the acceptor stack) in which the band is half-filled and electrical conduction would be expected according to band theory; however, these materials are found to be insulating.<sup>23</sup> These so called "Mott insulators" are not electrically conductive because of strong electron-electron repulsive interactions if two electrons were placed on the same molecule during the conduction process, resulting in the localization of the charge on each molecule and electrical insulation.<sup>24</sup> Of equal importance for electrical conductivity in organic metals is the arrangement of donor and acceptor molecules within the crystal. This is best illustrated by the CT complex TTF-TCNE in which  $\rho$  is similar to TTF-TCNQ ( $\rho = 0.54$ ), but the solid exhibits a room temperature (RT) electrical conductivity of  $10^{-9} \text{ S cm}^{-1}$  compared to  $500 \text{ S cm}^{-1}$  of the latter.<sup>25</sup> Here, the crystal structure consists of TTF<sup>•+</sup> radical cation dimers alternating with TCNE<sup>•-</sup> radical anion dimers within one  $\pi$ -stack in a  $\dots \text{DDAA} \dots$  (D: donor, A: acceptor) fashion (Figure 2).<sup>26</sup> As a consequence, the mobility of free charge carriers generated by the CT is limited to those dimers only, thereby inhibiting electron delocalization over the dimensions of the solid, and thus any possible electrical conductivity mechanism.<sup>26</sup>

Intermolecular  $\pi$ -interactions of redox-active molecular units as a means of creating electron delocalization pathways is one of the most successful strategies for the development of MOFs (chapter 7) with advantageous electrical properties (chapter 8).<sup>9,27</sup> A prototypical example for the beneficial effect of  $\pi$ -stacking of organic motifs on the electrical conductivity of MOFs is the TTF-based MOF-series  $M_2$ TTFTB ( $M^{2+} = \text{Mn, Co, Zn, Cd}$ ).<sup>13,14</sup> Most importantly, the hexagonal crystal structure of the isomorphous MOFs consist of rod-secondary building units (SBUs) in which corner-sharing  $\text{ZnO}_6$  octahedra are aligned in parallel to helical  $\pi$ -stacks of TTF moieties along the crystallographic  $c$  axis, together with cylindrical open pores (Figure 3). Some of the TTFTB linkers are autoxidized during the self-assembly formation process of the framework, leading to moderate semiconductivity.<sup>13</sup> The porosity of MOFs can serve as a platform to modulate the properties of the material even further via post-synthetic incorporation of guest species (*cf.* chapter 8). Having established the importance of partially oxidized donor and acceptor molecules, as well as their stacking arrangement, it is expected that the introduction of an electron-accepting guest with suitable electron affinity and stability of the resulting anion enhances the electrical conductivity of  $M_2$ TTFTB. Ideally, the guest induces the formation of a host-guest CT complex with partial electron transfer from the electron-donating TTFTB linkers to the electron-accepting guest molecule. Furthermore, the connectivity of the MOF may force a segregation of donor and acceptor radicals into separate stacks in which free charge carriers are delocalized over the stacks of radical-containing species along one crystallographic dimension, and thus are both able to contribute to the resulting electrical conductivity of the host-guest system. The small dimensions of the cylindrical pores ( $\approx 5 \text{ \AA}$ ) limit the scope of possible acceptors considerably,<sup>13</sup> but TCNE is suitable for entering the available pore volume of  $M_2$ TTFTB.

This chapter deals with the infiltration of the host structure  $M_2$ TTFTB ( $M^{2+} = \text{Zn, Cd}$ ) with TCNE via vapor phase infiltration (VPI)<sup>28</sup> in which stoichiometric amounts of TCNE are mixed with evacuated (activated) powders of  $M_2$ TTFTB and heated in a closed, evacuated reaction vessel, thereby forcing sublimation of rather volatile TCNE and diffusion of the same into the porous structure of the MOF. The obtained series of  $(\text{TCNE})_x M_2 \text{TTFTB}$  was structurally characterized using powder x-ray diffraction (PXRD), elemental analysis, Brunauer, Emmett and Teller (BET) gas sorption studies, and scanning transmission electron microscopy (STEM) to determine the influence of TCNE on material properties such as crystallinity and porosity in correlation with the amount of guest and its distribution within individual crystals of the framework. Electrical conductivities were measured and trends with respect to the TCNE loading amount in  $(\text{TCNE})_x M_2 \text{TTFTB}$  are established with data from FTIR and Raman spectroscopy of the redox-sensitive

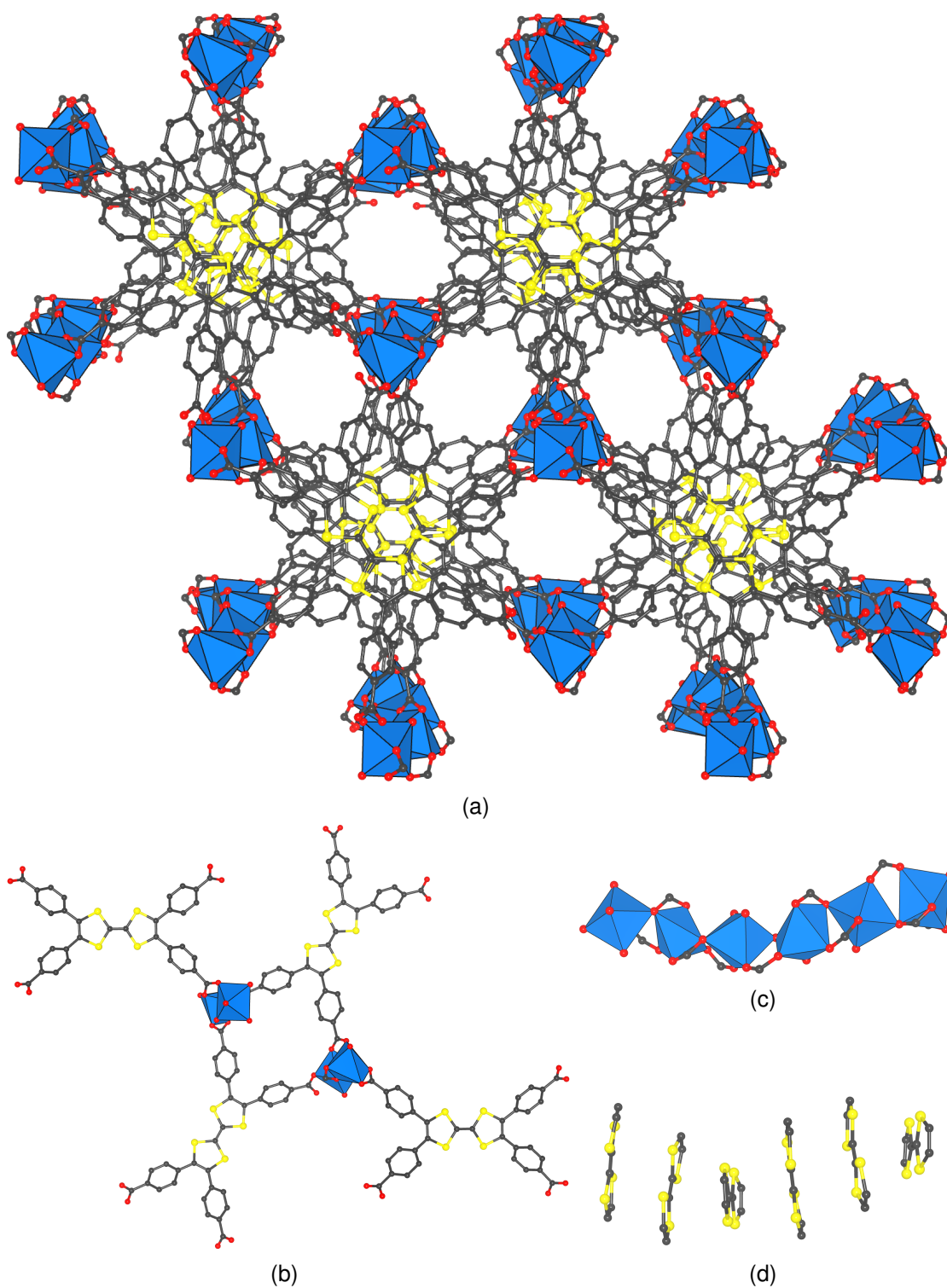


**Figure 3.** (a) Crystal structure of  $M_2$ TTFTB viewed along the  $c$  axis. (b) Connectivity of TTFTB linkers and  $MO_6$ -octahedra in  $M_2$ TTFTB. (c) Rod-SBU of  $M_2$ TTFTB consisting of corner-sharing  $MO_6$ -octahedra. (d) Helical  $\pi$ -stacks of TTF moieties.

vibrations in TTFTB and TCNE. The scope of this chapter comprises the VPI of polycrystalline  $\text{M}_2\text{TTFTB}$  MOFs based on redox-inactive  $\text{Zn}^{2+}$  and  $\text{Cd}^{2+}$  to avoid possible metal-based mixed valency. Single crystals of activated  $\text{M}_2\text{TTFTB}$  were not accessible to VPI. The results were published in *Chemistry of Materials*.<sup>29</sup>

## 2.2 SYNTHESIS AND STRUCTURAL CHARACTERIZATION OF $(\text{TCNE})_x\text{M}_2\text{TTFTB}$

### 2.2.1 Vapor-Phase Infiltration of $\text{M}_2\text{TTFTB}$ with TCNE and Determination of TCNE Content

The series  $(\text{TCNE})_x\text{M}_2\text{TTFTB}$  was obtained by exposing activated powders of  $\text{M}_2\text{TTFTB}$  to an atmosphere of stoichiometric amounts of TCNE in the gas phase. For this purpose,  $\text{M}_2\text{TTFTB}$  and TCNE are mixed and transferred to a borosilicate glass ampule, which is then flame-sealed under fine vacuum ( $p = 10^{-2}$  mbar) to obtain a closed, evacuated system. By heating the ampules to high temperatures of 200–300 °C, solid TCNE is brought into the gas-phase via sublimation and a fast diffusion of gas phase TCNE into the pores of  $\text{M}_2\text{TTFTB}$  is ensured until saturation is reached. The resulting black powders of  $(\text{TCNE})_x\text{M}_2\text{TTFTB}$  are analyzed towards their guest content by means of elemental analysis, in which the experimentally observed weight percentage of nitrogen, for example, allow the quantification of absorbed guest,  $x$ , in the phase-pure samples of MOF (*cf.* calculation of guest content via elemental analysis, section 6.2.6). The values of  $x$  for each sample, as well as their synthetic conditions, are summarized in Table 1. It was found that the maximum loading capacities of  $(\text{TCNE})_x\text{M}_2\text{TTFTB}$  for  $\text{M} = \text{Zn}$  and  $\text{Cd}$  are  $x \approx 0.8$  eq. and 0.6 eq. at 200 °C, respectively, and these maxima did not change with increasing the temperature to 300 °C for the Zn-series, whereas TCNE-loaded Cd-MOF amorphized at 300 °C. Excess TCNE resublimed at the ampule walls during the cooling process which allowed the product to be separated from the reactant and obtain phase-pure samples as evidenced by the absence of TCNE-related reflections in the diffractograms of  $(\text{TCNE})_x\text{M}_2\text{TTFTB}$  (*vide infra*). TCNE was adsorbed essentially quantitatively when 0.5 eq. were used in the VPI except for **1** where only a reduced amount of TCNE ( $x = 0.38$ ) was found via elemental analysis, indicating slower diffusion rates of TCNE in  $\text{Zn}_2\text{TTFTB}$  compared to **3** which was kept in the oven at the same temperature for 30 d instead of 10 d. These findings point at a surface area

**Table 1.** VPI of  $M_2$ TTFTB with varying eq. TCNE, temperature, and reaction time.  $x$  in  $(TCNE)_xM_2$ TTFTB was experimentally determined via elemental analysis (Table 9).
$$M_2\text{TTFTB (M = Zn, Cd)} \xrightarrow[\text{T, time}]{\text{TCNE}} (TCNE)_xM_2\text{TTFTB}$$

M	No.	TCNE eq. used	time/days	T/°C	$x$ found
Zn	1	0.5	10	200	0.38
	2	1.0	10	200	0.81
	3	0.5	30	200	0.46
	4	1.0	30	200	0.86
	5	0.5	30	300	0.50
	6	1.0	30	300	0.82
Cd	7	0.5	10	200	0.47
	8	1.0	10	200	0.58
	9	0.5	30	200	0.47
	10	1.0	30	200	0.60

limited uptake of TCNE, the discrepancy of maximum TCNE loadings between  $Zn_2$ TTFTB and  $Cd_2$ TTFTB being a result of the lower initial surface area of the Cd-MOF. This is further substantiated by the absence of any measurable porosity for fully loaded MOFs as evidenced by BET gas sorption experiments (*vide infra*). From a purely structural perspective, a higher loading amount would have been expected. Considering that one unit cell of  $M_2$ TTFTB contains in total one  $\pi$ -stack consisting of six TTFTB linkers and three cylindrical pores (Figure 3), each of these cylindrical pores could also accommodate  $\pi$ -stacks of six TCNE molecules, in theory, resulting in a theoretical maximum guest amount of " $(TCNE)_{3.0}M_2$ TTFTB". However, this is not desirable for achieving high electrical conductivity since electrically conductive CT complexes based on TTF derivatives of type  $D_mA_n$  are known only for stoichiometry ratios where  $m \geq n$ .<sup>17</sup> Even more, CT salts with complex stoichiometries (i.e.,  $m > n$ ) are usually better electrical conductors than their counterparts of equal ratio  $m : n$  since mixed-valency within the donor stack is always achieved even for full CT from the donor to the acceptor.<sup>17</sup> This is best illustrated by the significant differences in electrical conductivity between monovalent  $(TTF)Br$  ( $10^{-6} \text{ S cm}^{-1}$ ) and mixed-valent  $(TTF)Br_{0.71-0.76}$  ( $> 200 \text{ S cm}^{-1}$ ).<sup>23</sup> Therefore, it is expected that substoichiometric amounts of TCNE give rise to more significant increases of electrical conductivity in  $(TCNE)_xM_2$ TTFTB compared to higher amounts. This will be further supported by experimental data obtained from the electrical conductivity measurements of  $(TCNE)_xM_2$ TTFTB, see section 2.4.

### 2.2.2 Crystallinity of TCNE-loaded $\text{M}_2\text{TTFTB}$ Metal-Organic Frameworks

With the  $(\text{TCNE})_x\text{M}_2\text{TTFTB}$  series at hand, the crystallinity of the samples is evaluated via PXRD in dependence of the guest content. As shown in Figure 4, only small intensity changes are observed in the diffractograms of  $(\text{TCNE})_x\text{M}_2\text{TTFTB}$  compared to the pristine  $\text{M}_2\text{TTFTB}$  MOFs, which is expected for MOFs that maintain their structure upon guest loading. Pawley profile fits of the individual PXRD patterns of pristine and guest-loaded  $\text{M}_2\text{TTFTB}$  (chapter 6, Figure 49-58) reveal the absence of any significant changes of lattice parameters or trends thereof as a function of TCNE loading (Figure 5). On the other hand, there are considerable changes seen for the relative diffraction peak intensities, most notably for the (100) and (200) reflections which monotonically decrease with increasing TCNE content in the  $(\text{TCNE})_x\text{M}_2\text{TTFTB}$  series (Figure 6). This trend can be explained by the orientation of the helical  $\pi$ -stacks of the TTFTB in  $\text{M}_2\text{TTFTB}$  along the crystallographic  $c$  axis and in parallel to the (100) plane. A decrease in reflection intensity in PXRD corresponds to a lower electron density in that plane (chapter 10) and correlates well with the increase in TCNE content in  $(\text{TCNE})_x\text{M}_2\text{TTFTB}$  because of an increasing degree of TTFTB linker oxidation. Structural distortions causing relative intensity changes are unlikely in this case since there are no observable lattice parameter changes with increasing  $x$ , which points at relatively strong chemical interactions between TCNE and the TTFTB linker, this first indication being substantiated even further by the vibrational analysis of the redox-sensitive vibrations in TTFTB and TCNE (section 2.3). Similarly strong interactions between guests and MOFs resulting in continuous diffraction peak intensity changes were observed in the case of  $\text{TCNQ}@Cu_3\text{BTC}_2$ , in which case the (111) reflection intensity increases with increasing TCNQ content.<sup>28</sup> This was rationalized by the increase of electron density within the (111) plane when TCNQ coordinates to the open metal sites (OMS) of the  $\text{Cu}_2$  paddle-wheel SBUs in a bridging fashion, thereby being oriented in the (111) plane of  $\text{Cu}_3\text{BTC}_2$  (*cf.* chapter 4). In contrast to  $\text{TCNQ}@Cu_3\text{BTC}_2$ , however, the PXRD patterns of  $(\text{TCNE})_x\text{M}_2\text{TTFTB}$  show no additional reflections that might point at symmetry-lowering processes.<sup>15,28</sup> Based on this evidence,  $\text{M}_2\text{TTFTB}$  is confirmed to not undergo structural changes upon loading with TCNE, but is subject of strong electronic host-guest interactions. Importantly, the diffraction intensity changes are generally less pronounced in  $(\text{TCNE})_x\text{Cd}_2\text{TTFTB}$  than  $(\text{TCNE})_x\text{Zn}_2\text{TTFTB}$ , which serves as a first indication that the host-guest interactions in the former are less pronounced than in the latter (Figure 6). These will be also supported by the vibrational spectroscopic analysis of the MOFs.

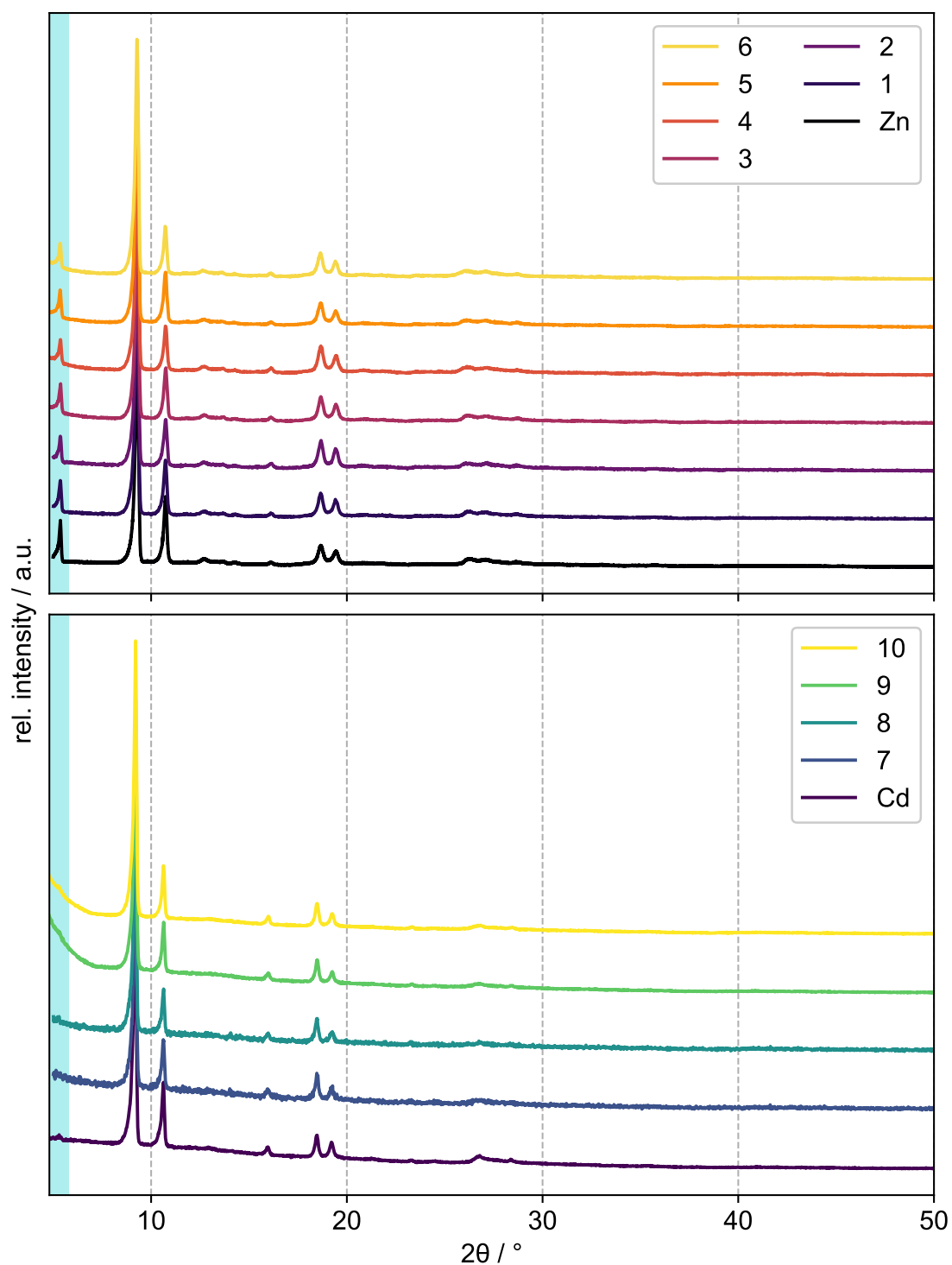


**Figure 4.** PXRD patterns of  $(\text{TCNE})_x\text{M}_2\text{TTFTB}$  (Zn: top, Cd: bottom). The blue highlighted area emphasizes the (100) reflection (and the absence thereof in the Cd-series).



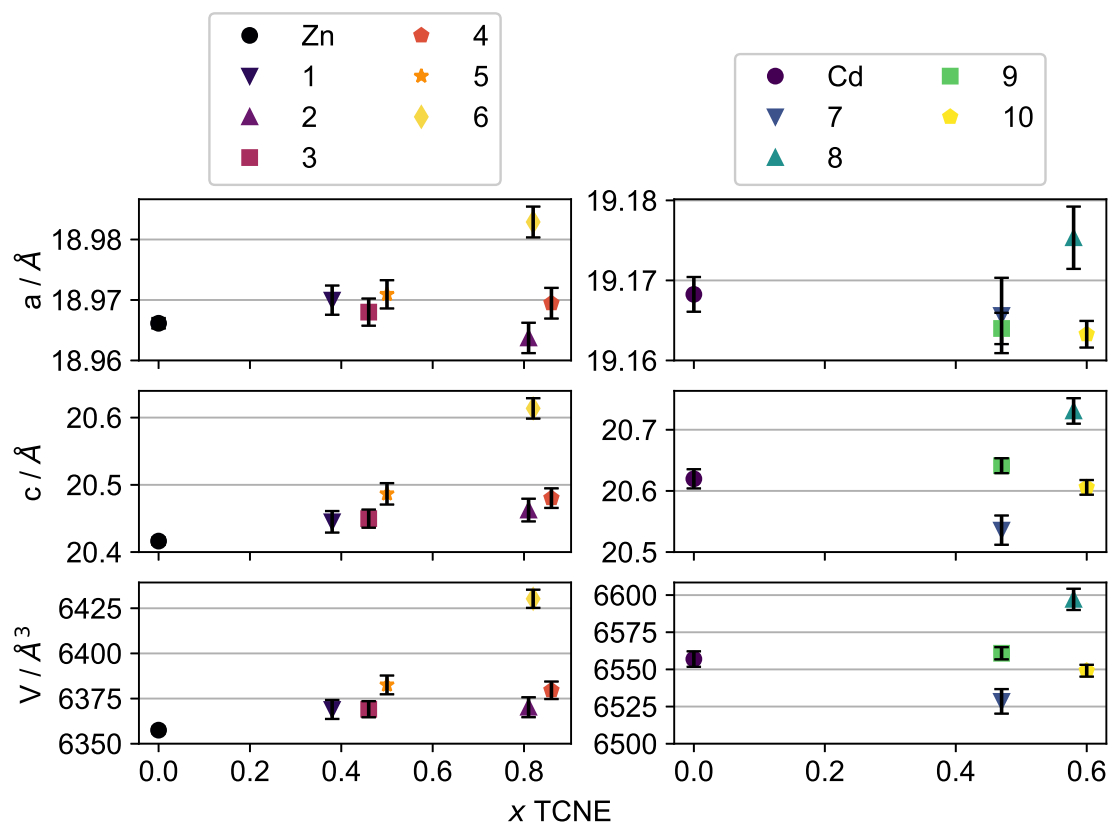


**Figure 5.** Cell parameters of  $(TCNE)_xM_2TTFTB$  determined via Pawley profile fits.

### 2.2.3 TCNE Distribution in $M_2TTFTB$ Crystals

Insights on the morphology of  $M_2TTFTB$  crystals in the presence of TCNE, as well as the phase homogeneity within individual crystallites are obtained by means of electron microscopy (chapter 13). In regard to the crystal morphology, scanning electron microscopy (SEM) images of  $(TCNE)_xM_2TTFTB$  were recorded (chapter 6, Figure 72-83). Upon infiltration of  $M_2TTFTB$  with TCNE, the hexagonal morphology of the MOF crystallites remains unchanged. Crystal morphologies different from the hexagonal structure of  $M_2TTFTB$  are not observed, this observation being in line with the phase purity as shown via PXRD. In the next step, the TCNE distribution in  $(TCNE)_xM_2TTFTB$  is probed using STEM in combination with energy-dispersive x-ray spectroscopy (EDS). The samples **1**, **3**, and **5** were chosen as representatives for each of the applied synthesis conditions (Figure 7-9). Note that the fluorescence yield of low- $Z$  elements, such as C, N, and O is much lower compared to heavy elements, so the experimental data does not allow to formulate quantitative statements about the distribution of these elements. The STEM-EDS maps do not show any significant concentration gradients of the respective elements for all tested samples, pointing at an only little pronounced diffusion limitation of TCNE in the pores of  $Zn_2TTFTB$  and its uniform

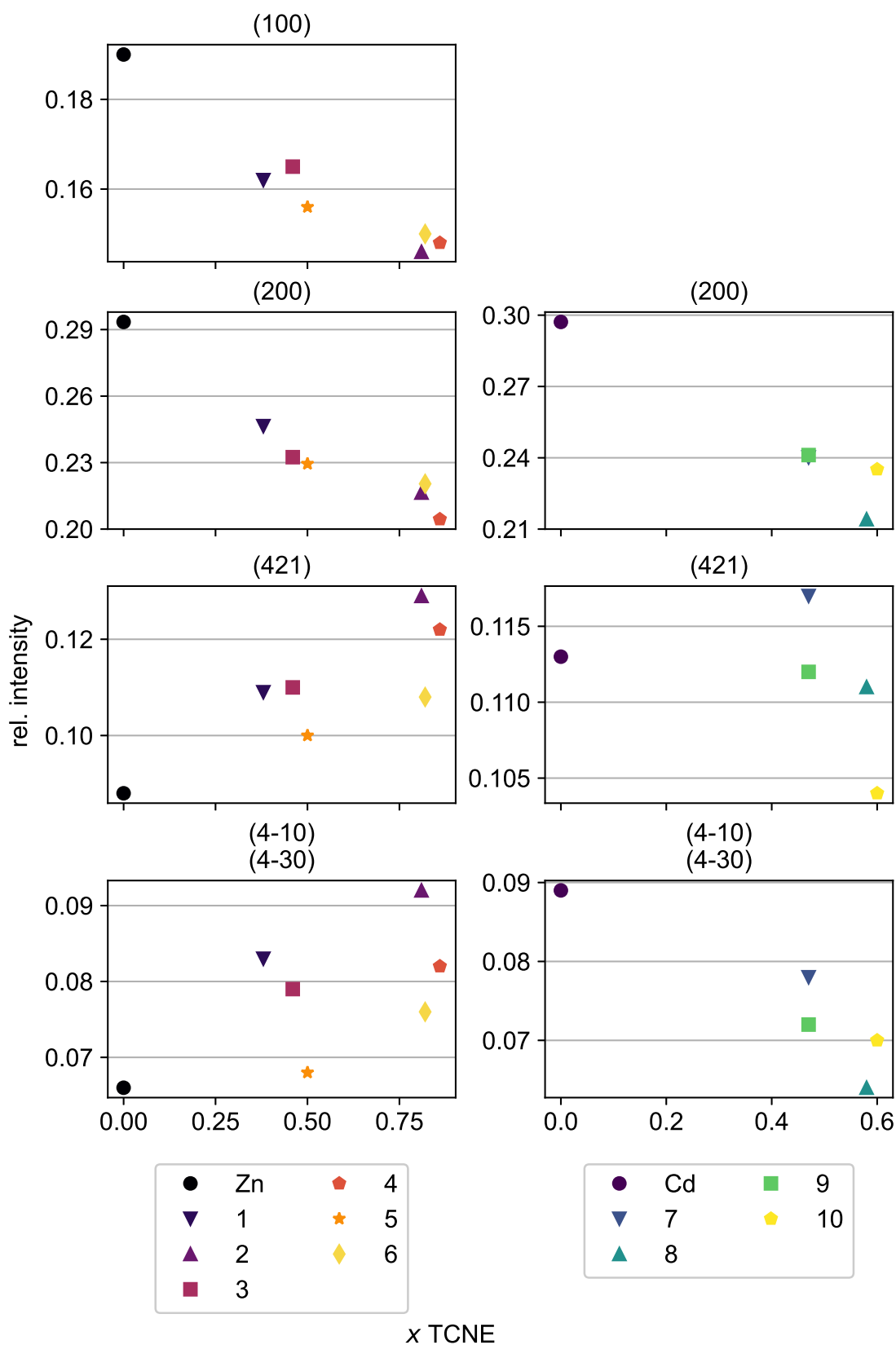


**Figure 6.** Relative reflection intensities of  $(\text{TCNE})_x\text{M}_2\text{TTFTB}$ .

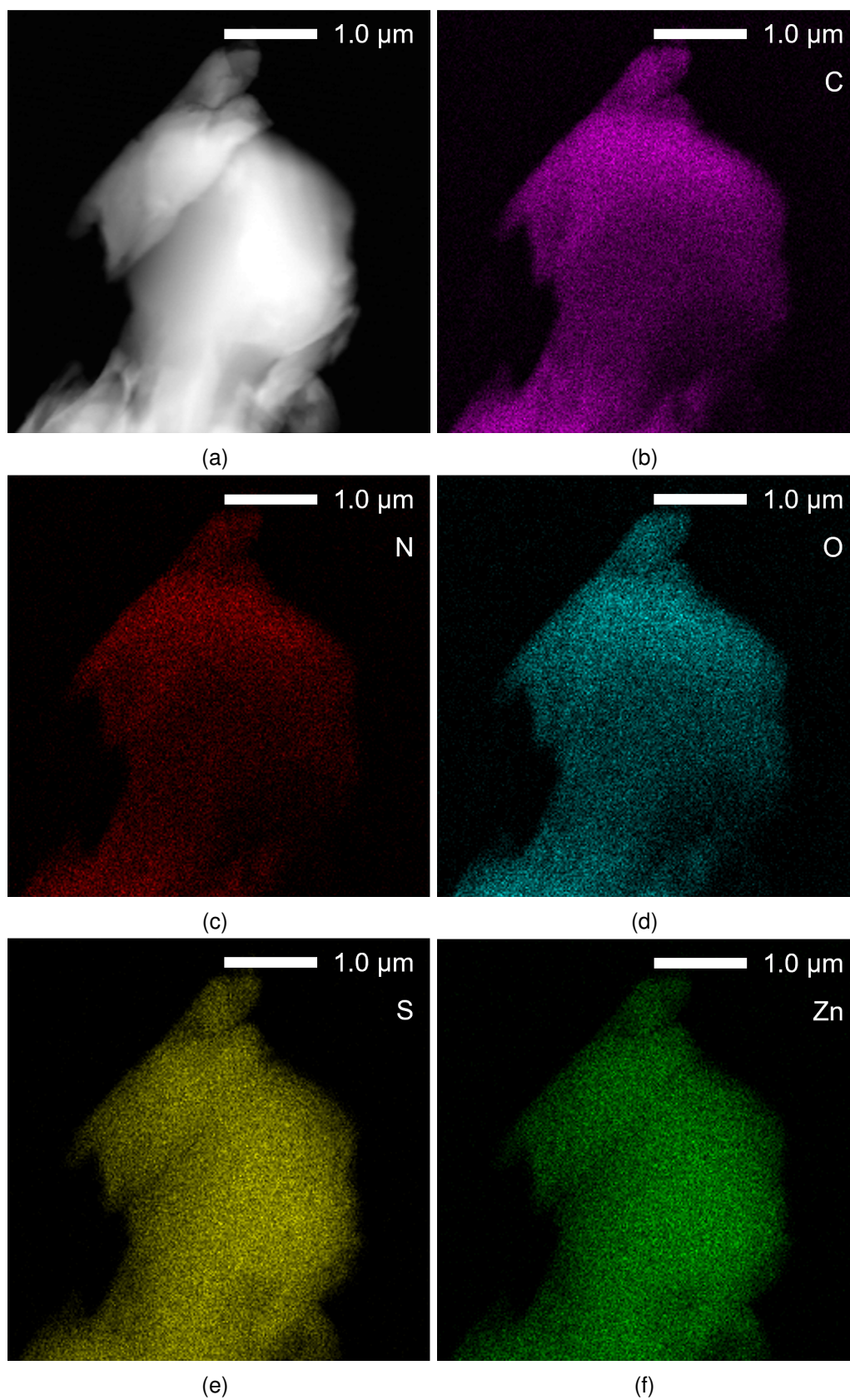


**Figure 7.** (a) dark-field (DF)-STEM images of **1** and EDS mapping of the K lines of elements (b) C (purple), (c) N (red), (d) O (blue), (e) S (yellow), and (f) Zn (green).

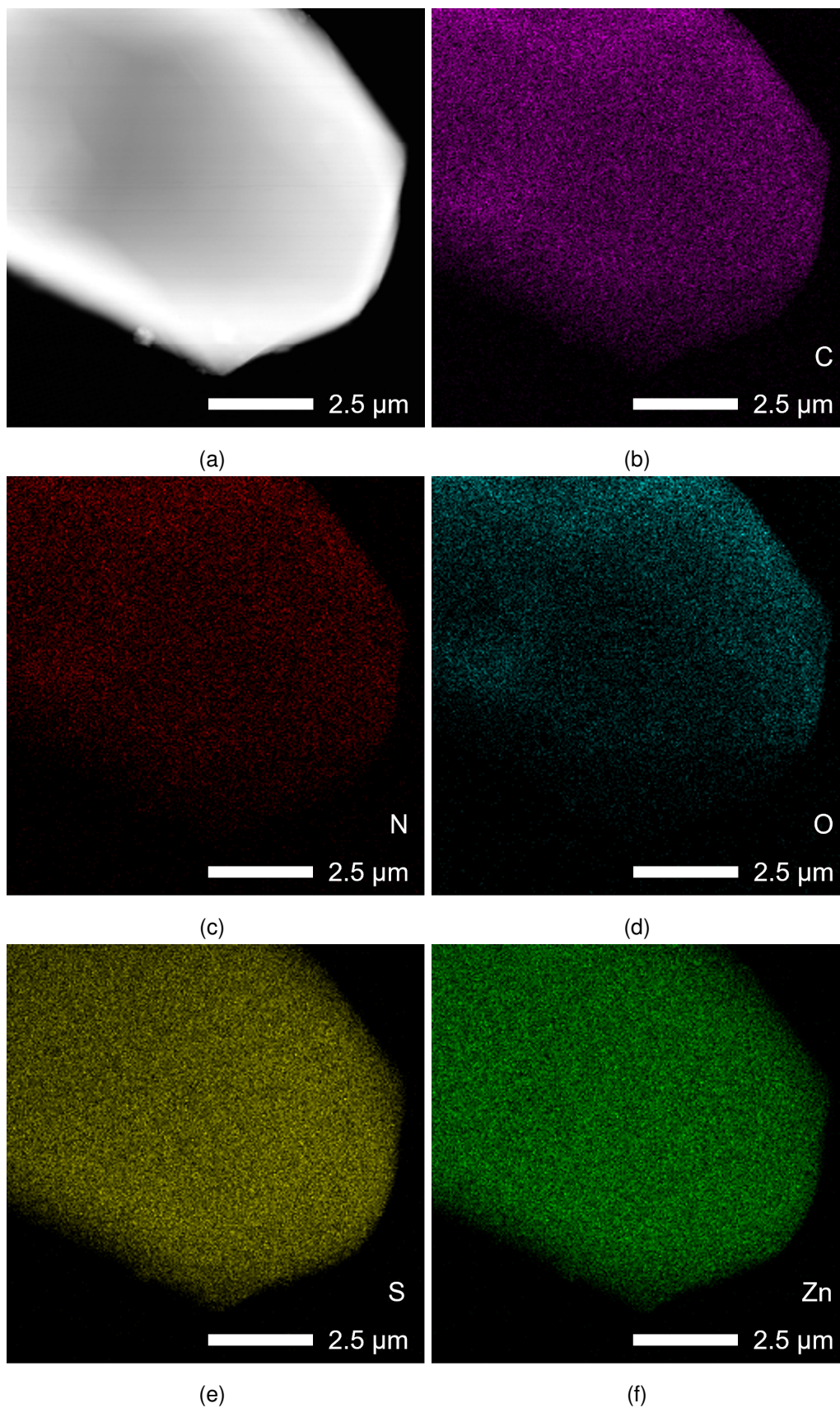


**Figure 8.** (a) DF-STEM images of **3** and EDS mapping of the K lines of elements (b) C (purple), (c) N (red), (d) O (blue), (e) S (yellow), and (f) Zn (green).

---



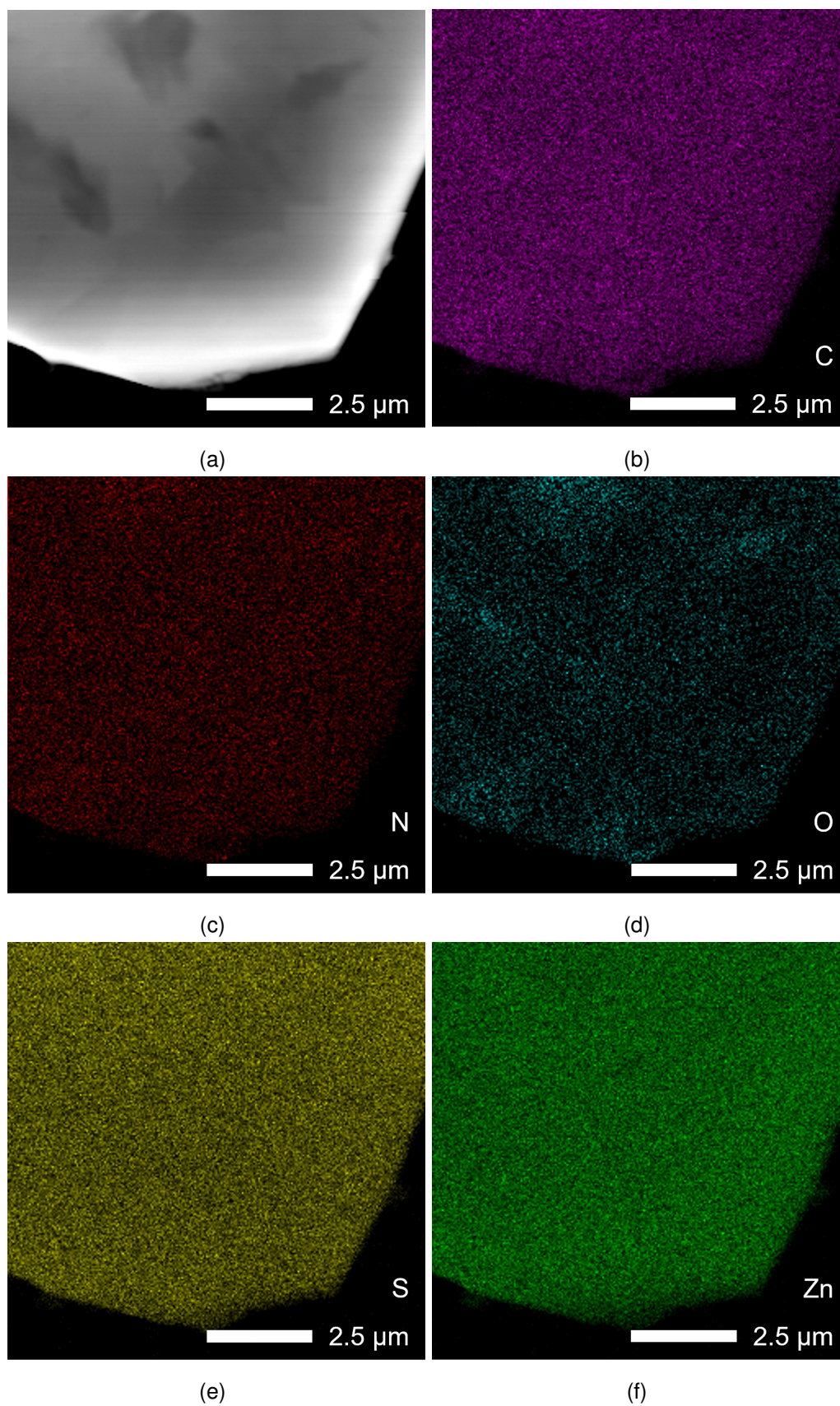


**Figure 9.** (a) DF-STEM images of **5** and EDS mapping of the K lines of elements (b) C (purple), (c) N (red), (d) O (blue), (e) S (yellow), and (f) Zn (green).

distribution throughout the MOF crystals. However, these findings are somewhat in conflict with CO<sub>2</sub> sorption experiments which show smaller equilibration times of **5** compared to **1** and **3** which translates to a better overall distribution of TCNE for samples prepared at high temperatures, and thus expectedly better diffusion of TCNE (*vide infra*). A likely explanation for this observation lies in the probable crystallite size in STEM which requires electron-transparent (i.e., thin) samples, whereas the average particle size of M<sub>2</sub>TTFTB MOFs ranging from 1–30 μm is much larger than that. It can be expected that diffusion limitations are more significant in bigger crystals and that surface concentrations are higher than bulk concentration, to some extent. This is probably most pronounced for sample **1** in which the experimentally observed TCNE content deviates the most from the expected value. Nonetheless, the absence of trends of TCNE distribution with time and temperature seen in STEM-EDS, the absence of strain effects in the diffraction patterns, and the almost quantitative loading in all samples points at a predominantly uniform distribution of guest throughout the MOFs crystals.

#### 2.2.4 Porosity Changes of TCNE-Loaded M<sub>2</sub>TTFTB

In agreement with the previous analytical data, the BET surface areas of (TCNE)<sub>x</sub>M<sub>2</sub>TTFTB further support the successful guest incorporation (Figure 10). Both Zn- and Cd<sub>2</sub>TTFTB exhibit type I N<sub>2</sub> and CO<sub>2</sub> adsorption isotherms in line with their microporosity (*cf.* chapter 11) and exhibit BET surface areas of 724±1 m<sup>2</sup> g<sup>-1</sup> and 537±1 m<sup>2</sup> g<sup>-1</sup>, respectively. In contrast, TCNE-infiltrated frameworks are nonporous for N<sub>2</sub>, and very long equilibration times are observed for CO<sub>2</sub> in the cases of **1**, **3**, **5**, which suggests some remaining porosity in these materials. Still, these long equilibration times hindered the measurement of the whole CO<sub>2</sub> sorption isotherm. On the other hand, all Cd-based MOFs remained nonporous even for CO<sub>2</sub>, from which is concluded that (TCNE)<sub>x</sub>M<sub>2</sub>TTFTB can be generally considered nonporous with uniform distribution of TCNE within the frameworks.

### 2.3 REDOX-SENSITIVE VIBRATIONS AS A PROBE FOR CHARGE-TRANSFER

By means of FTIR and Raman spectroscopy, it is possible to study the electronic interactions and CT between TCNE and M<sub>2</sub>TTFTB due to the sensitivity of the

---

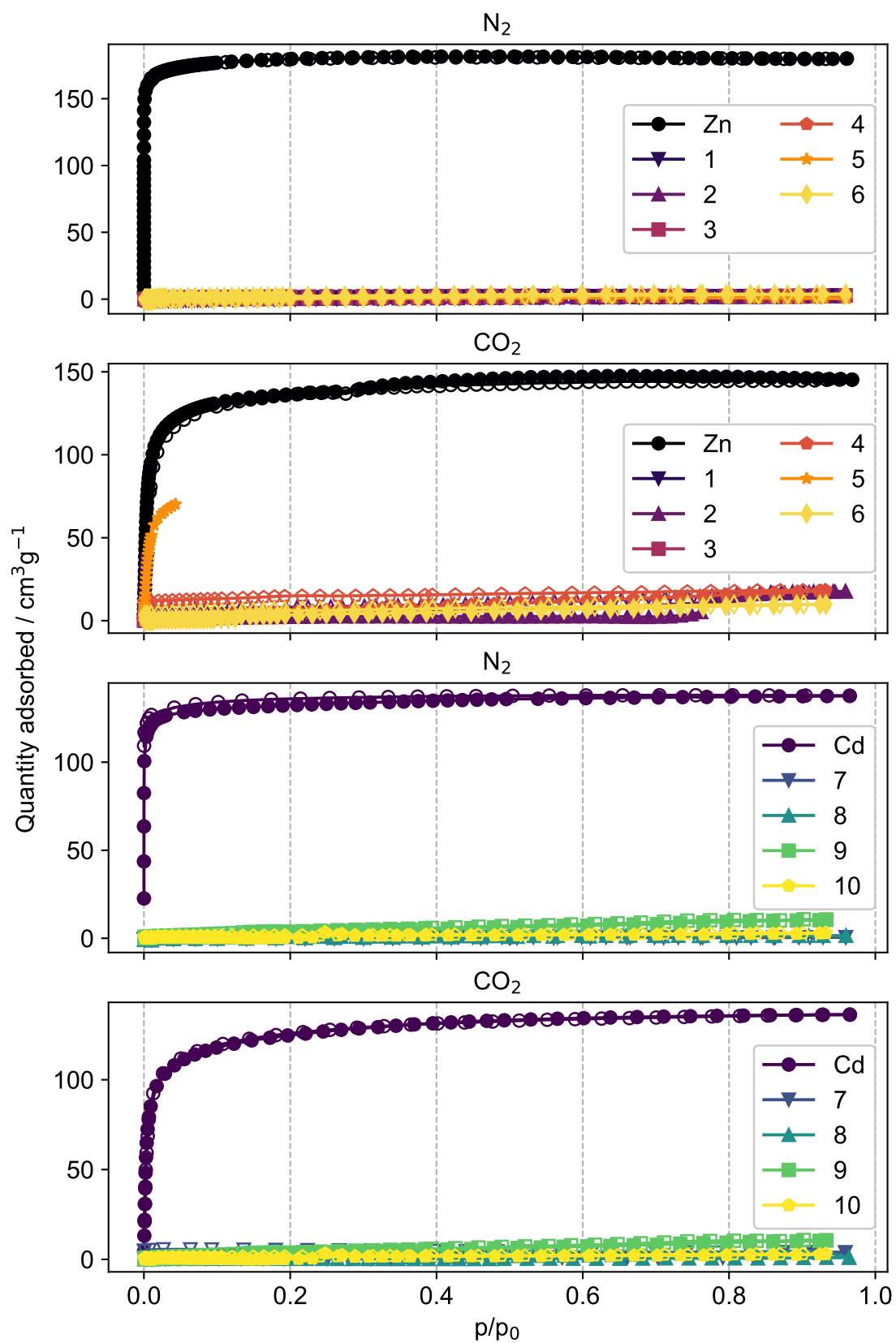


**Figure 10.** Sorption isotherms of  $(\text{TCNE})_x\text{M}_2\text{TTFTB}$ . Probe gases are shown in the graph titles, the respective MOFs in the legends. Filled and empty marker branches correspond to the adsorption and desorption branch, respectively.

C $\equiv$ N and internal C=C vibrational modes in TCNE and TTFTB to their oxidation state, respectively.<sup>30–34</sup>

### 2.3.1 FTIR of TCNE Species in (TCNE)<sub>x</sub>M<sub>2</sub>TTFTB

In full agreement with the previous data, FTIR spectra of (TCNE)<sub>x</sub>M<sub>2</sub>TTFTB show all signals of pristine M<sub>2</sub>TTFTB, confirming an intact MOF structure after TCNE incorporation (Figure 11). However, additional signals appear at 2250–2170 cm<sup>-1</sup>, 1360–1200 cm<sup>-1</sup>, and 1200–1040 cm<sup>-1</sup>. The region at 2250–2170 cm<sup>-1</sup> is assigned to the vibrational modes of the C $\equiv$ N group of TCNE, in which the individual contributions of neutral TCNE<sup>0</sup> and the radical-anion TCNE<sup>-</sup> overlap. Deconvolution of this broad signal results in five peaks at 2178, 2197, 2214, 2227 and 2245 cm<sup>-1</sup>, the first three being assigned to TCNE<sup>-</sup><sup>26,33</sup> and the other two to TCNE<sup>0</sup>.<sup>26,35</sup> By means of integration of the intensities for each peak, the relative contribution of TCNE<sup>-</sup> to the C $\equiv$ N signal can be calculated according to  $r = \int(\text{TCNE}^-) / \int(\text{TCNE}^0)$ , i.e., a higher  $r$  value corresponds to a higher concentration of TCNE<sup>-</sup> in (TCNE)<sub>x</sub>M<sub>2</sub>TTFTB, and thus to a higher degree of CT from TTFTB to the guest. Comparison of the FTIR spectra of the Zn- and Cd-series reveal that  $r$  is much larger in samples of the former series than in those of the latter, pointing to a higher reactivity of Zn<sub>2</sub>TTFTB (Figure 12) towards TCNE than Cd<sub>2</sub>TTFTB (Figure 13). The  $r$  values of each sample are summarized in Table 2. Remarkably, a substantial amount of TCNE<sup>-</sup> is present in **1** with  $r = 1.92$  (entry 2.1), which then decreases upon further increasing the loading in **2** ( $r = 1.36$ , entry 2.2). This suggests a certain saturation level of Zn<sub>2</sub>TTFTB with TCNE at which CT occurs; if this level is exceeded, the remaining TCNE is not reduced by TTFTB and contributes to the TCNE<sup>0</sup> signal. This may be explained by a reduction of the electron-donating strength of the TTFTB  $\pi$ -stack when electron-density is constantly withdrawn from the assembly. Furthermore, Raman analysis shows that the CT process is accompanied by the formation of electron-accepting TTFTB<sup>2+</sup> dications, for which the parent-dication TTF<sup>2+</sup> is known for its electron-accepting properties (*vide infra*).<sup>36,37</sup> Looking at (TCNE)<sub>x</sub>Cd<sub>2</sub>TTFTB,  $r$  is  $\approx 1$  in **7** (entry 2.7) and decreases even further at higher TCNE loadings, analog to the Zn-based series. This suggests that the previously mentioned saturation level of CT from Cd<sub>2</sub>TTFTB to TCNE is significantly lower, resulting in larger TCNE<sup>0</sup> contents of guest-loaded MOFs. Interestingly, consistently lower ratios are observed in (TCNE)<sub>x</sub>Zn<sub>2</sub>TTFTB when the samples are kept at 200 °C for 30 d (**3**:  $r = 1.44$ , entry 2.3) instead of 10 d, and even more so at 300 °C for 30 d (**5**:  $r = 1.19$ , entry 2.5). No clear trend was observed for (TCNE)<sub>x</sub>Cd<sub>2</sub>TTFTB. From these results



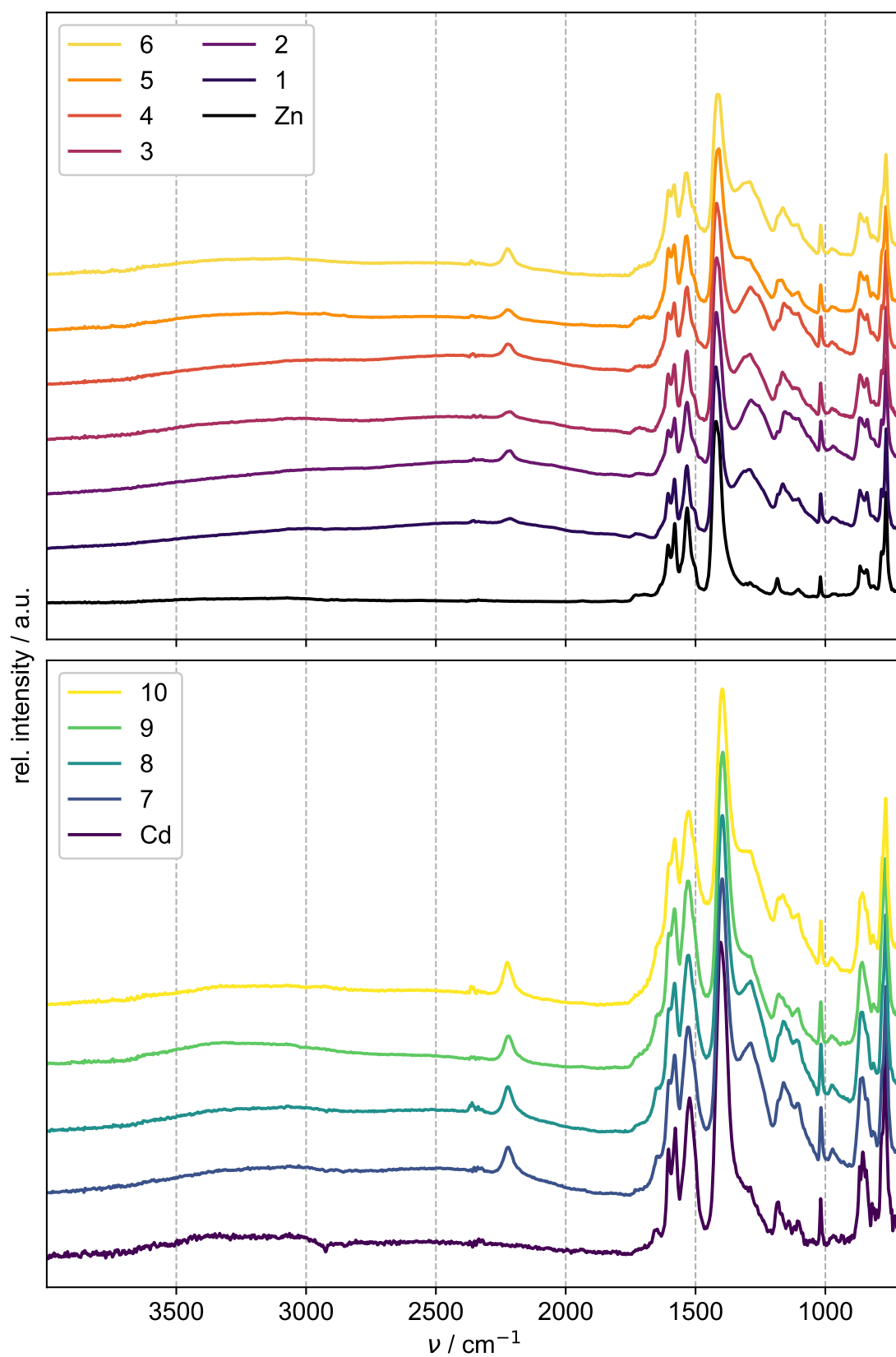


**Figure 11.** FTIR spectra of  $(\text{TCNE})_x\text{M}_2\text{TTFTB}$  (Zn: top, Cd: bottom).

**Table 2.** Integrals of the fitted FTIR peaks corresponding to TCNE<sup>-</sup> or TCNE<sup>0</sup> and their ratio in (TCNE)<sub>x</sub>M<sub>2</sub>TTFTB.

Entry	M	No.	$\int$ TCNE <sup>-</sup>	$\int$ TCNE <sup>0</sup>	$r = \text{TCNE}^- / \text{TCNE}^0$
2.1	Zn	<b>1</b>	28.21	14.66	1.92
2.2		<b>2</b>	24.49	17.99	1.36
2.3		<b>3</b>	27.22	18.91	1.44
2.4		<b>4</b>	21.44	18.95	1.13
2.5		<b>5</b>	23.77	19.99	1.19
2.6		<b>6</b>	20.39	18.79	1.09
2.7	Cd	<b>7</b>	21.39	20.88	1.02
2.8		<b>8</b>	19.32	20.54	0.94
2.9		<b>9</b>	23.44	18.10	1.30
2.10		<b>10</b>	17.38	20.83	0.83

follows that the anticipated CT occurs from TTFTB to TCNE, more pronounced in the Zn-series compared to the Cd-series.

### 2.3.2 Raman of TTFTB Species in (TCNE)<sub>x</sub>M<sub>2</sub>TTFTB

Proceeding with the TTFTB species, Raman spectroscopy is particularly useful for the identification of the redox-sensitive symmetric vibrations of the molecule.<sup>30,31</sup> In the Raman spectra of pristine M<sub>2</sub>TTFTB, prominent peaks appear at 1606, 1570, 1550, 1489, 1413 and 516 cm<sup>-1</sup> (Figure 14). With respect to CT, the most relevant are the C=C stretching modes of the TTF core in TTFTB corresponding to its neutral state, TTFTB<sup>0</sup>, at 1570 and 1550 cm<sup>-1</sup>, and the C-S stretching at 516 cm<sup>-1</sup>, while the remaining ones can be assigned to benzene C=C modes (1606 cm<sup>-1</sup>) and the carboxyl-related modes (1489 cm<sup>-1</sup>).<sup>38-40</sup> Moreover, the signal at 1413 cm<sup>-1</sup> comes from the C=C stretching mode of radical-cationic TTFTB<sup>+</sup>.<sup>31,38</sup> With increasing TCNE content, the bands at 1570 and 1550 cm<sup>-1</sup> in pristine M<sub>2</sub>TTFTB shift to 1534 and 1509 cm<sup>-1</sup> in (TCNE)<sub>x</sub>Zn<sub>2</sub>TTFTB, matching well with previous reports of the symmetric C=C stretching bands of the external C=C bonds in TTF<sup>+</sup>.<sup>35</sup> Furthermore, the signal of the internal C=C stretch of TTFTB<sup>+</sup> at 1413 cm<sup>-1</sup> splits into two bands at 1438 and 1393 cm<sup>-1</sup> when TCNE is introduced to Zn<sub>2</sub>TTFTB. Such a splitting can be ascribed to the formation of CT vibronic bands as a result of the electronic interaction between the donor and acceptor, a phenomenon that is also observed in the CT complex TTF-TCNE, where the equivalent bands are observed at 1453 and 1404 cm<sup>-1</sup>.<sup>35</sup> Consistent with the FTIR data of (TCNE)<sub>x</sub>Cd<sub>2</sub>TTFTB and other analytical results, the band at

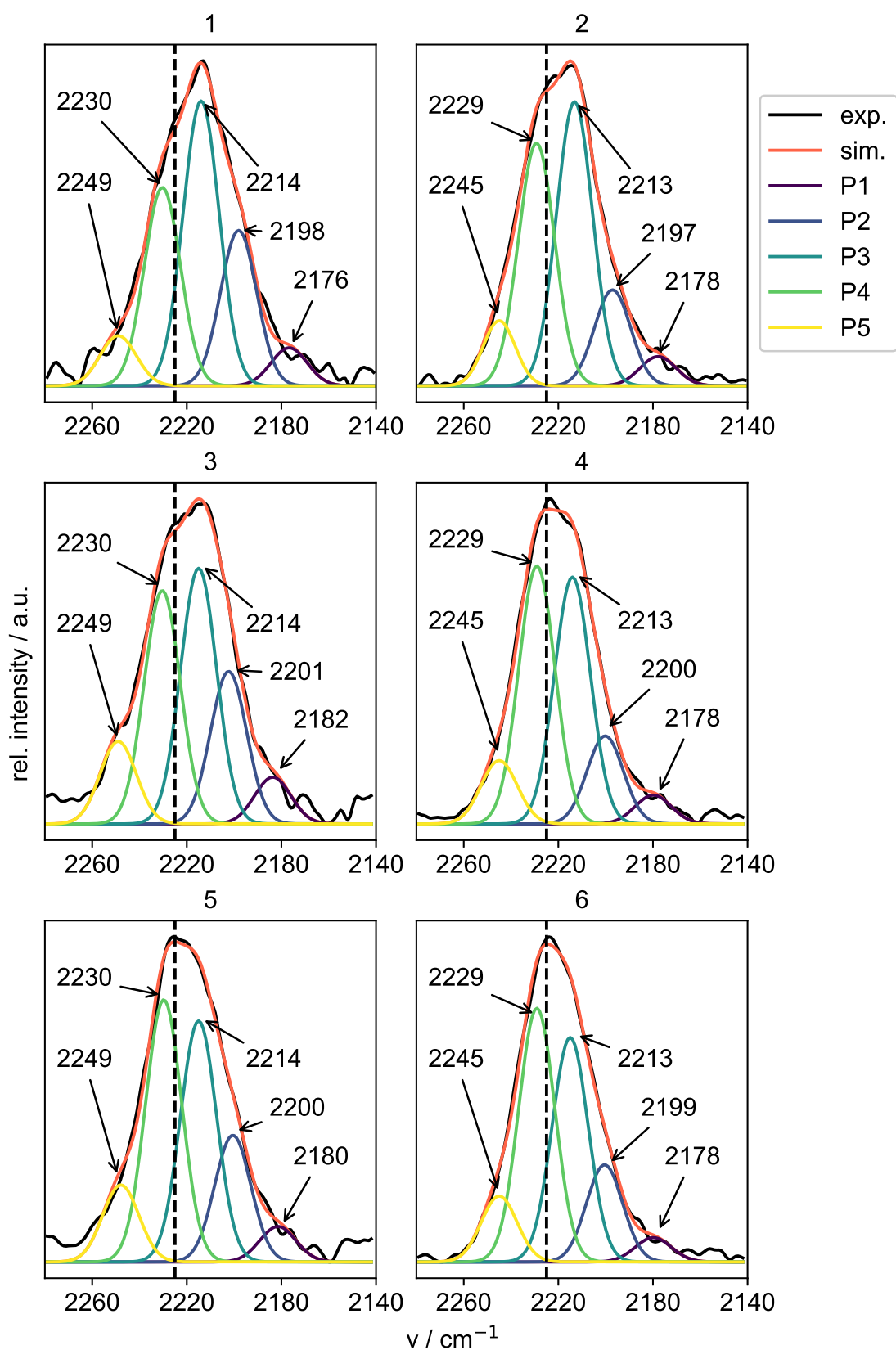


**Figure 12.** Deconvolution of CN stretching peak in FTIR spectra of 1-6 (see titles of subfigures), showing the experimentally observed (black) and simulated peak (orange), the latter consisting of the individual contributions P1-5.

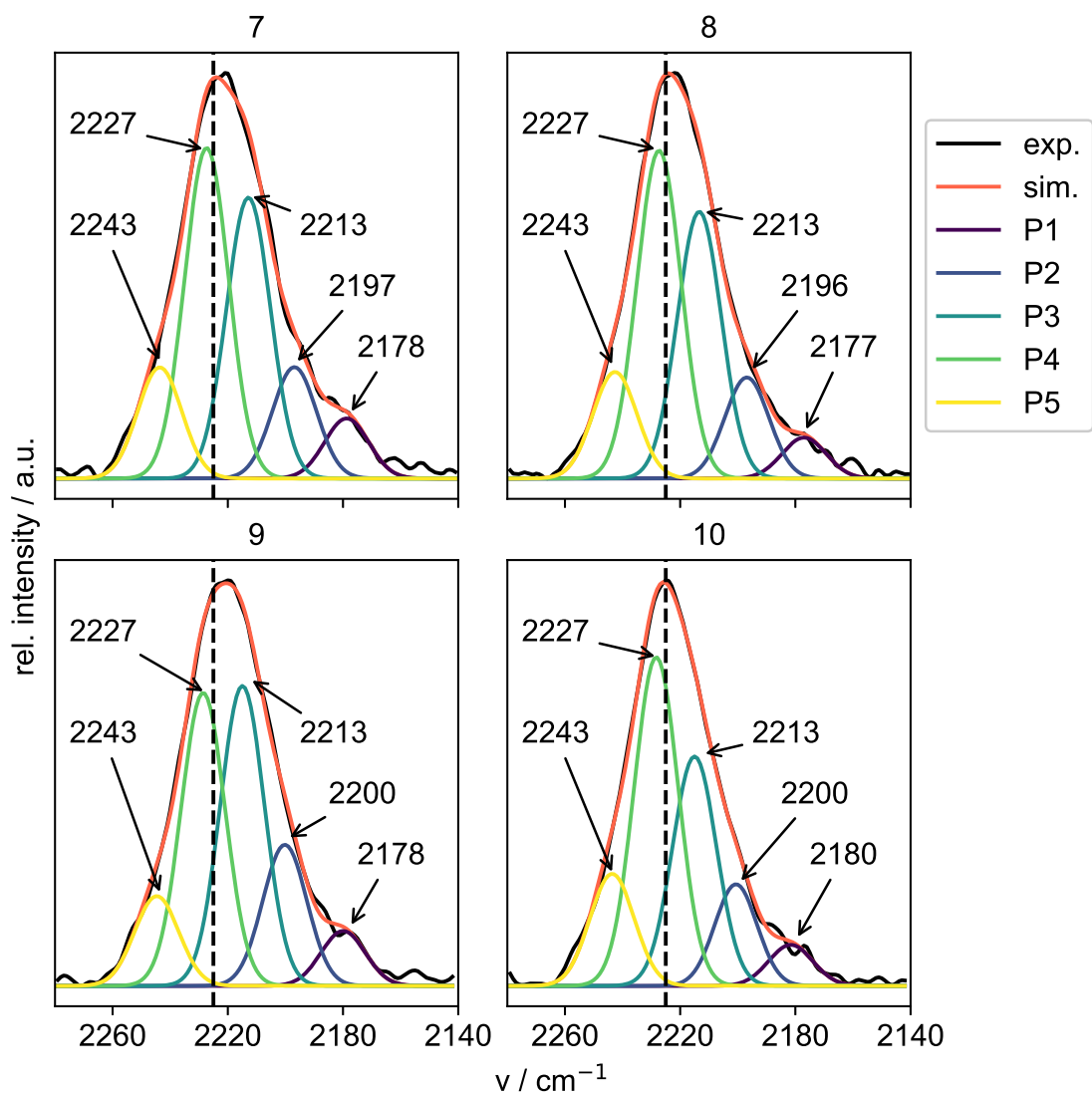


**Figure 13.** Deconvolution of CN stretching peak in FTIR spectra of **7-10** (see titles of subfigures), showing the experimentally observed (black) and simulated peak (orange), the latter consisting of the individual contributions P1-5.

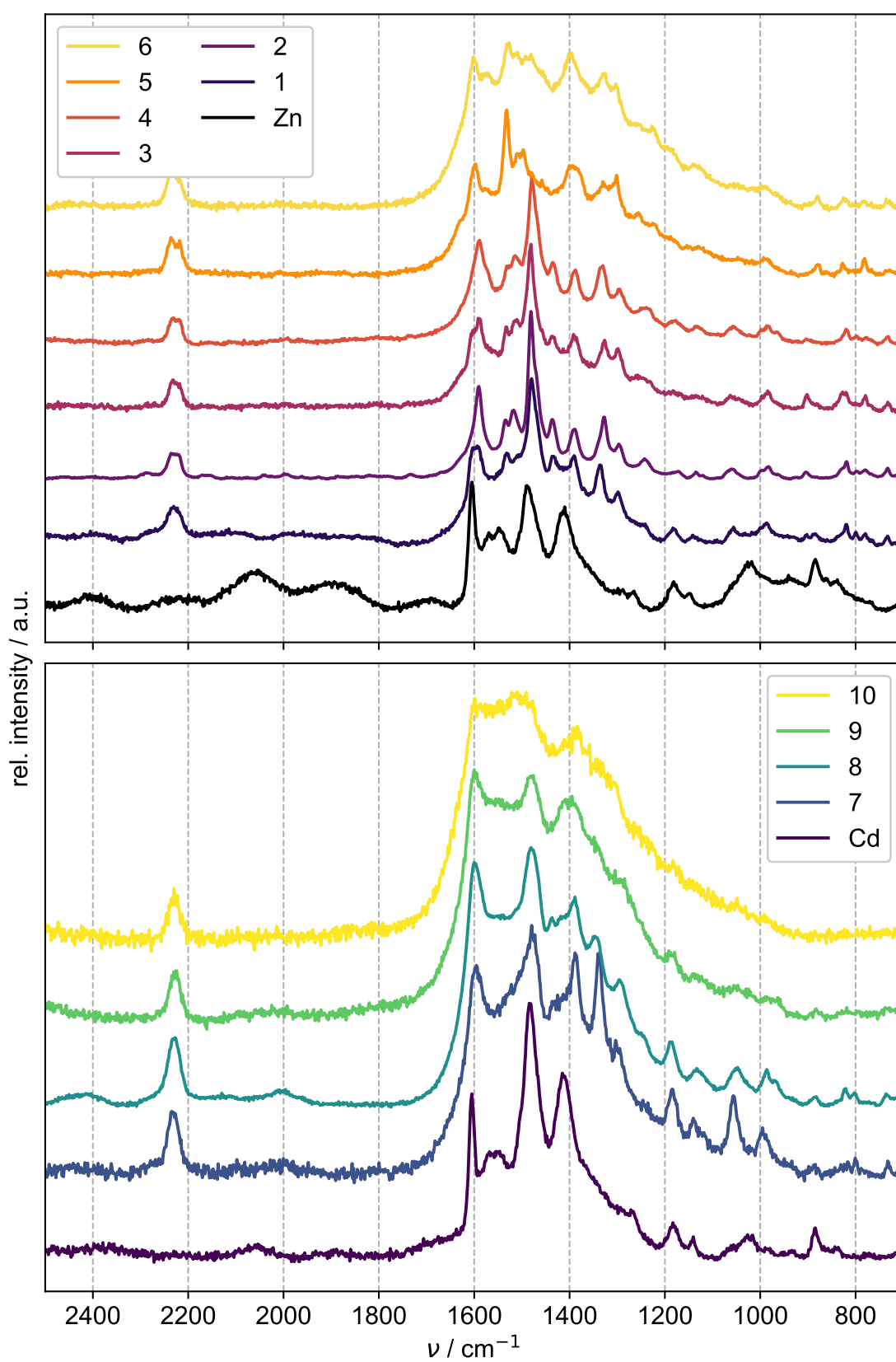


**Figure 14.** Raman spectra of  $(\text{TCNE})_x\text{M}_2\text{TTFTB}$  (Zn: top, Cd: bottom). The wave-like intensities in the spectrum of  $\text{Zn}_2\text{TTFTB}$  from 1650–2500  $\text{cm}^{-1}$  are caused by heating of the sample during the laser irradiation.

1438  $\text{cm}^{-1}$  in the Raman spectra of the same series is much less pronounced and the band at 1404  $\text{cm}^{-1}$  is more intense than in the Zn series, which amounts to a weaker interaction between the TCNE guest and  $\text{Cd}_2\text{TTFTB}$ . Additional signals were detected at 1340 and 1300  $\text{cm}^{-1}$  that match well with  $\text{TTFTB}^{2+}$  based on the expected wavenumber shift of the signal by  $\approx 100 \text{ cm}^{-1}$  for each oxidation step from  $\text{TTF}^0$  to  $\text{TTF}^+$ , and likewise from  $\text{TTF}^0$  to  $\text{TTF}^{2+}$ .<sup>41</sup> These bands become more intense with further loading of  $\text{Zn}_2\text{TTFTB}$  with TCNE, suggesting that more TTFTB units get oxidized to the dication. The dication formation is unexpected since TTF with its strong oxidizing power reacts to form TTF-TCNE that exhibits only a partial CT with  $\rho = 0.54$ , whereas the linkers in  $\text{M}_2\text{TTFTB}$  exhibit higher oxidation potentials relative to TTF, meaning that they should be more difficult to oxidize as a component of the framework.<sup>38</sup> However, the high synthesis temperature are a likely explanation for the oxidation to the dication, which was shown to be only a quasi-reversible process in solid-state cyclic voltammetry.<sup>38</sup> As previously mentioned,  $\text{TTF}^{2+}$  dications exhibit  $\pi$ -accepting properties that might decrease the electron-donating ability of TTFTB, and thus to a decreasing  $r$  value at higher TCNE contents in  $(\text{TCNE})_x\text{M}_2\text{TTFTB}$  when the CT saturation level inherent to  $\text{M}_2\text{TTFTB}$  is reached.<sup>36,37</sup> Interestingly, only one report has reported the unusual  $\text{TTF}^+/\text{TTF}^{2+}$  mixed-valency and the incorporation of  $\text{TTF}^{2+}$  in a hybrid organic-inorganic material,<sup>42</sup> while  $(\text{TCNE})_x\text{M}_2\text{TTFTB}$  is the first material with three-fold mixed-valency of  $\text{TTF}^0/\text{TTF}^+/\text{TTF}^{2+}$ . In closing, these results show that CT from TTFTB to TCNE in  $(\text{TCNE})_x\text{M}_2\text{TTFTB}$  yields mixed-valent host-guest complexes. Five different species can be observed in the vibrational spectra, namely  $\text{TTFTB}^0$ ,  $\text{TTFTB}^+$ , and  $\text{TTFTB}^{2+}$ , as well as  $\text{TCNE}^0$  and  $\text{TCNE}^-$ . Because of the higher reactivity of  $\text{Zn}_2\text{TTFTB}$ , the degree of CT,  $r$ , is consistently higher in the respective series than in  $\text{Cd}_2\text{TTFTB}$ .

## 2.4 INFLUENCE OF THE HOST-GUEST INTERACTIONS ON THE ELECTRICAL CONDUCTIVITY OF

Electrical conductivity measurements of  $(\text{TCNE})_x\text{M}_2\text{TTFTB}$  (two-contact pellet probe, *cf.* section 9.4) revealed ohmic behavior in the voltage range of  $-0.1$ – $0.1$  V (chapter 6, Figure 93). The specific conductivities were calculated based on the slope of the graphs and the geometry of the pellet and plotted against the series members (Figure 15). Here, the pristine MOFs exhibited electrical conductivities of  $1.34 \times 10^{-7}$  and  $1.74 \times 10^{-6} \text{ S cm}^{-1}$  for  $\text{Zn}_2\text{TTFTB}$  and  $\text{Cd}_2\text{TTFTB}$ , respectively, which are in general agreement with the trends of the single-crystal electrical con-

ductivities of  $\text{Zn}_2\text{TTFTB}$  ( $3.95 \times 10^{-6} \text{ S cm}^{-1}$ ) and  $\text{Cd}_2\text{TTFTB}$  ( $2.86 \times 10^{-4} \text{ S cm}^{-1}$ ).<sup>14</sup> Deviations from these values can be explained by intergrain boundary resistances between crystals in pressed pellets.<sup>43</sup> Both MOFs show increasing electrical conductivity upon TCNE infiltration (**1**:  $1 \times 10^{-5} \text{ S cm}^{-1}$ , **7**:  $7.85 \times 10^{-6} \text{ S cm}^{-1}$ ), which remain nearly constant at higher loadings (**2**:  $1.17 \times 10^{-5} \text{ S cm}^{-1}$ , **8**:  $8.12 \times 10^{-6} \text{ S cm}^{-1}$ ). In comparison, the electrical conductivities decrease again for longer reaction times (**3**:  $2.42 \times 10^{-6} \text{ S cm}^{-1}$ , **9**:  $2.28 \times 10^{-6} \text{ S cm}^{-1}$ ) and even more so at higher temperature (**5**:  $1.37 \times 10^{-6} \text{ S cm}^{-1}$ ). Discrepancies of the electrical conductivity of samples synthesized at equal conditions but with different TCNE loading amounts fall in the range of the measurement error influenced by the intergrain boundary resistances and inconsistent pellet thickness. Generally, increasing the loading amount of TCNE gives rise to a higher percentage of TCNE<sup>0</sup> in the materials as shown via FTIR, which does not contribute to the doping of the frameworks and the electrical conductivity. Remarkably,  $\text{Zn}_2\text{TTFTB}$  shows much higher responsiveness to TCNE infiltration compared to  $\text{Cd}_2\text{TTFTB}$ , with a nearly 100-fold higher electrical conductivity for **1** compared to  $\text{Zn}_2\text{TTFTB}$  vs. a 4-fold increase for **4** compared to  $\text{Cd}_2\text{TTFTB}$ . This is assigned to the higher reactivity of  $\text{Zn}_2\text{TTFTB}$  to TCNE according to vibrational spectroscopy. The Cd-based MOF series also exhibits  $\text{TTFTB}^{2+}$  dications, which implies that other mechanism might influence their electrical conductivity. Shorter interplanar distances found in single crystals of  $\text{Cd}_2\text{TTFTB}$ <sup>14</sup> than in  $\text{Zn}_2\text{TTFTB}$ <sup>13</sup> that can facilitate the formation of insulating  $\pi\text{-}[\text{TTFTB}]_2^{2+}$  dimers within the stack might be one possible explanation.<sup>38</sup> Another could be the potential disorder of the TTFTB units in the MOF linker  $\pi$ -stacks as indicated by the absence of the (100) reflection in the diffraction patterns of  $(\text{TCNE})_x\text{Cd}_2\text{TTFTB}$ , thereby reducing electron mobilities. Intriguingly, the electrical conductivities of the materials studied here are much larger than those of the CT complex TTF-TCNE mentioned in the introduction of this chapter. The striking difference between TTF-TCNE and  $(\text{TCNE})_x\text{M}_2\text{TTFTB}$  is that the connectivity of the MOF fixes the linkers in  $\text{M}_2\text{TTFTB}$  in  $\pi$ -stacks of short interplanar distances that do not allow intercalation of TCNE between the planes. Therefore, TCNE can only diffuse into the pores that are aligned in parallel to the TTFTB  $\pi$ -stacks, and the resulting segregation of donor and acceptor radicals gives rise to an increase of electrical conductivity.

---

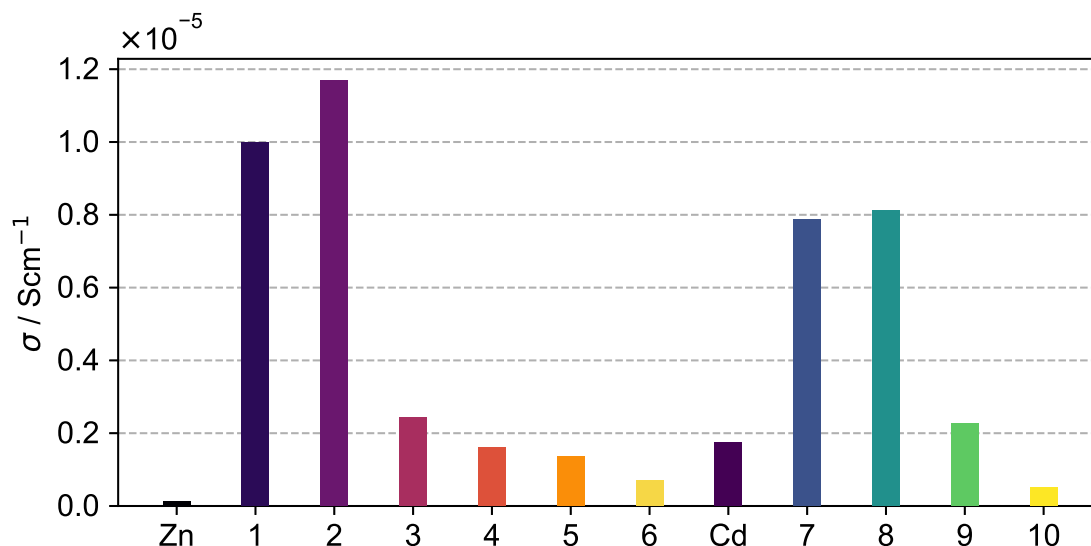


**Figure 15.** Summary of the electrical conductivities.

## 2.5 CONCLUSION

In conclusion,  $(\text{TCNE})_x\text{M}_2\text{TTFTB}$  is obtained via VPI of  $\text{M}_2\text{TTFTB}$  with stoichiometric amounts of TCNE. The resulting host-guest complexes are crystalline and exhibit a uniform distribution of TCNE throughout the crystals. Vibrational spectroscopy shows the formation of several species in these host-guest complexes, including neutral  $\text{TCNE}^0$  and the corresponding radical-anion  $\text{TCNE}^-$ , as well as neutral  $\text{TTFTB}^0$ , and the corresponding radical-cation  $\text{TTFTB}^+$  and dication  $\text{TTFTB}^{2+}$ . The ratio of  $\text{TCNE}^-$  and  $\text{TCNE}^0$ ,  $r$ , is highest at low loadings of TCNE and for samples synthesized at comparatively low reaction temperature and time (i.e., 200 °C, 10 d). For higher  $x$ , or samples synthesized at higher temperatures and longer reaction times, this ratio decreases. It turned out that  $r$  is an important measure for the electrical conductivity changes of  $(\text{TCNE})_x\text{M}_2\text{TTFTB}$  since samples of high  $r$  showed the strongest electrical conductivity changes, and samples that exceeded the CT saturation limit and contained more  $\text{TCNE}^0$  lead to only small differences. Remarkably,  $\text{Zn}_2\text{TTFTB}$  is much more reactive toward TCNE than  $\text{Cd}_2\text{TTFTB}$  and **1** exhibits high concentrations of  $\text{TCNE}^-$  with a concomitant increase of the electrical conductivity by two orders of magnitude, whereas  $\text{TCNE}^-$  concentrations are much lower in  $\text{Cd}_2\text{TTFTB}$ , with almost unaltered material properties after the infiltration with TCNE in effect. This work illustrates how an in-depth analysis of vibrational spectroscopic data of  $(\text{TCNE})_x\text{M}_2\text{TTFTB}$  explains electrical conductivity trends dependent on  $x$  and the nature of the metal cation, and how host-guest interactions in MOFs with non-innocent guest molecules, and in consequence their physical property changes, can be rationalized and



tuned. However, the reasons for the nonlinear CT behavior with higher loadings and electron-donor strength of the MOFs are still unknown. Here, computational studies on the electronic structure of these MOFs and their interaction with TCNE may give further insights into the complex CT processes and their origins.

---



# 3

## *Tetraselenafulvalene-Linkers for Metal-Organic Frameworks*

### 3.1 INTRODUCTION

The discovery of metallic electrical conductivity in the CT complex TTF-TCNQ marks a milestone in the development of electrically active materials beyond the scope of purely inorganic solids.<sup>19,44</sup> As mentioned in Chapter 2, the partial degree of CT from TTF to TCNQ leads to the formation of segregated stacks of mixed-valent donor and acceptor species that are arranged along one dimension. Consequently, the electrical conductivity was found to be strongly anisotropic, with maximum values observed along the  $\pi$ -stacking direction of the planar molecules in which the intrastack, intermolecular orbital overlap is much more pronounced as opposed to the interstack electronic interactions.<sup>16,17,24</sup> However, one-dimensional systems like TTF-TCNQ are prone to undergo a Peierls transition in which the band formed by the electronic interaction of equidistant members in a one-dimensional chain is perturbed by the dimerization of units at lower temperatures.<sup>45</sup> As a result, the electronic delocalization vanishes due to the formed energy gaps, leading to a metal-to-insulator transition below a certain critical temperature.<sup>46</sup> By increasing the extent of the intermolecular overlap within the  $\pi$ -stacks, the dimerization of units during the Peierls transition is energetically less favored than maintaining a delocalized electronic band and a metal-to-insulator transition occurs either at lower temperatures or not at all. One way of increasing the intermolecular overlap is using selenium- or tellurium-based donors, of which the orbitals are more diffuse compared to sulfur and allow more extensive intermolecular orbital interactions within the  $\pi$ -stack and between those.<sup>47,48</sup> For example, the donors TSF<sup>49</sup> and tetratellurafulvalene (TTeF)<sup>50,51</sup> form CT complexes with TCNQ; while

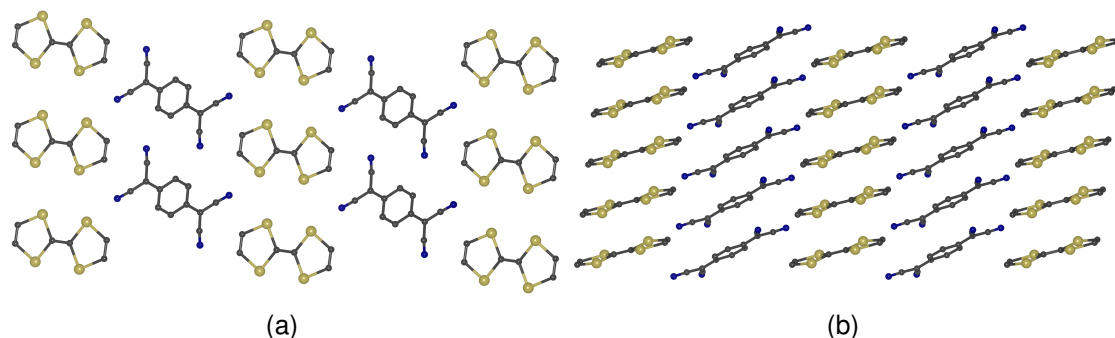


**Figure 16.** Crystal structure and stacking geometry of donors and acceptors in TTeF-TCNQ.

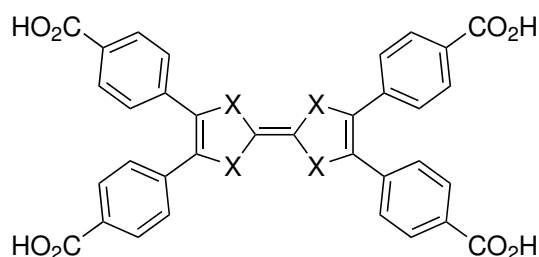


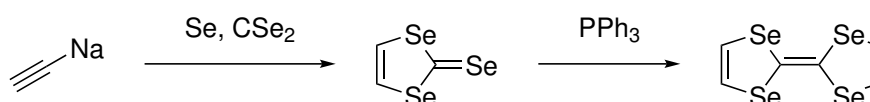
**Figure 17.** Proposed linkers  $H_4TSFTB$  and  $H_4TTeFTB$  ( $X = Se, Te$ ).

TSF-TCNQ<sup>49</sup> is isomorphous to TTF-TCNQ, the even heavier chalcogen-homolog TTeF-TCNQ<sup>48</sup> contains segregated  $\pi$ -stacks of donors and acceptors, with the significant difference of additional close chalcogen-chalcogen contacts between the TTeF-stacks (Figure 16). Accordingly, the electrical conductivities of these salts of 800 and 2200 S cm<sup>-1</sup>, respectively, are much larger than in TTF-TCNQ, and the metal-to-insulator transition temperature drops within the series from 59 K (S) to 40 K (Se) to 2 K (Te).<sup>48</sup>

In the quest of electrically conductive MOFs,  $\pi$ -stacking of redox-active donors was shown to be a successful strategy to impart electrical conductivity on these materials while maintaining their porosity at the same time.<sup>9</sup> In Chapter 2,  $M_2TFTB$  was introduced as the benchmark example for how organic motifs like TTF that are well-studied in electrically conductive CT salts can give rise to new hybrid materials with interesting electrical properties, albeit limited to semiconductivity so far. Inspired by the improved metallic character of CT salts based on heavy chalcogen analogs of TTF, one can envision that MOFs based on these analogs may show even higher electrical conductivities. More specifically, a potential isostructural series of  $M_2$ tetraselenafulvalene tetrabenzoate (TSFTB) or  $M_2$ tetratellurafulvalene tetrabenzoate (TTeFTB) (or other structures with  $\pi$ -interactions between the linkers) would be interesting examples for the systematic study of the chalcogen effect on the electrical conductivity within the scope of MOFs (Figure 17).

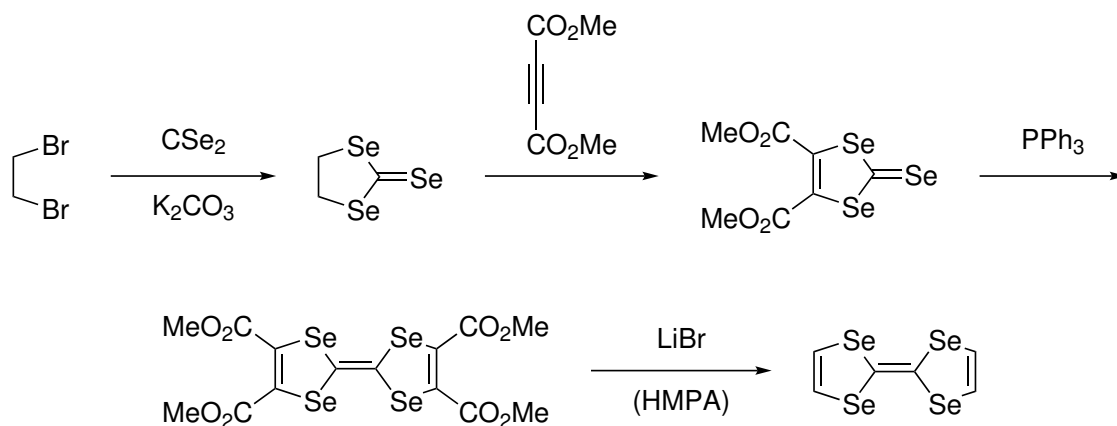
After screening of the available literature on these donors, it is not surprising that systems based on TSF and especially TTeF neither have found as much use

in the preparation of CT complexes, nor have ever been used in the construction of MOFs. Unlike TTF, the synthetic accessibility of TSF or TTeF and their derivatization is limited to a few chemical transformations and even fewer building blocks to use for their construction.<sup>52,53</sup> Focusing on TSF, its first synthesis was based on the cyclization reaction of sodium acetylide with selenium and carbon diselenide,  $CSe_2$ , to form 1,3-diselenole-2-selenone in a yield of 15–20%, which is then homo coupled with triphenylphosphine,  $PPh_3$ , to obtain TSF with a 70–80% yield (Scheme 1).<sup>49</sup>



**Scheme 1.** First reported synthesis of TSF.

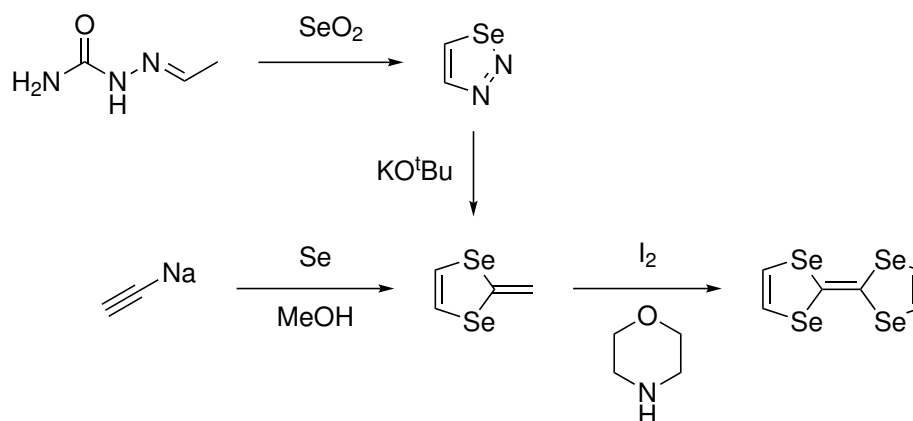
Alternatively, 1,3-diselenolane-2-selenone can be converted to the corresponding diester 4,5-dicarbomethoxy-1,3-diselenole-2-selenone by the action of dimethyl acetylenedicarboxylate (DMAD), which is then homo coupled with  $PPh_3$  and finally decarboxylated using lithium bromide in hexamethylphosphoramide (HMPA) (Scheme 2).<sup>54</sup>



**Scheme 2.** Alternative synthesis of TSF based on  $CSe_2$ .

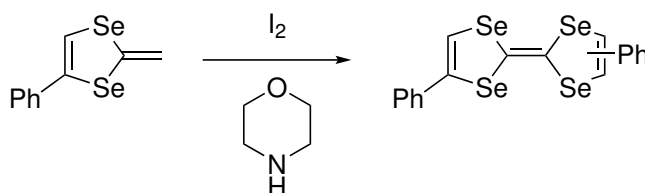
Generally, synthetic procedures using  $CSe_2$  are often limited to a few steps, for the central, five-membered building block containing a 1,3-diselenole-2-selenone unit is easily obtained as shown above. However, synthesis of  $CSe_2$  involves a complicated thermolysis of elemental selenium in a dichloromethane (DCM) atmosphere at 550 °C, and the compound is unstable and extremely toxic.<sup>55</sup> Therefore, preparations of TSF and its derivatives are often focused on substitution on  $CSe_2$  with less toxic selenium reagents. For example, the more recent synthesis strategy of parent TSF involves the intermediate 2-methylene-1,3-diselenole (or diselenafulvene) which is oxidized by iodine in the presence of an amine base

such as morpholine to TSF, following an unknown reaction mechanism.<sup>56,57</sup> Diselenafulvene, originally obtained by the oxidation of acetaldehyde semicarbazone with selenium dioxide,  $\text{SeO}_2$ , to 1,2,3-selenadiazole<sup>58</sup> and subsequent nitrogen abstraction and dimerization in the presence of potassium *tert*-butoxide,<sup>56</sup> was also reported to be accessible in one step by a selenium insertion into the carbon-sodium bond of sodium acetylide and subsequent dimerization of the obtained selenole in methanol (Scheme 3).<sup>57</sup>



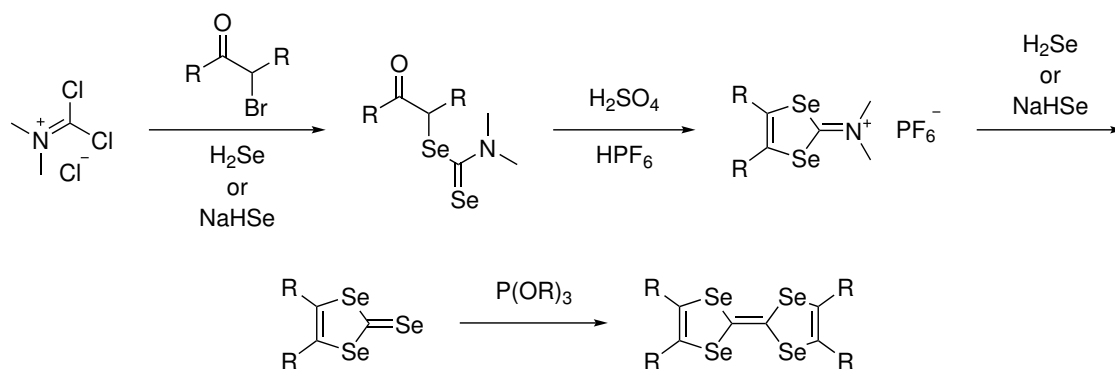
**Scheme 3.** New synthesis routes of TSF from diselenafulvene.

This reactivity can be also exploited in the synthesis of disubstituted tetraselenafulvalenes, for example in the synthesis of an *E/Z*-mixture of diphenyltetraselenafulvalene from 2-methylene-4-phenyl-1,3-diselenole, but tetrasubstituted TSF is not accessible (Scheme 4).<sup>59</sup>



**Scheme 4.** Synthesis of *E/Z*-diphenyltetraselenafulvalene.

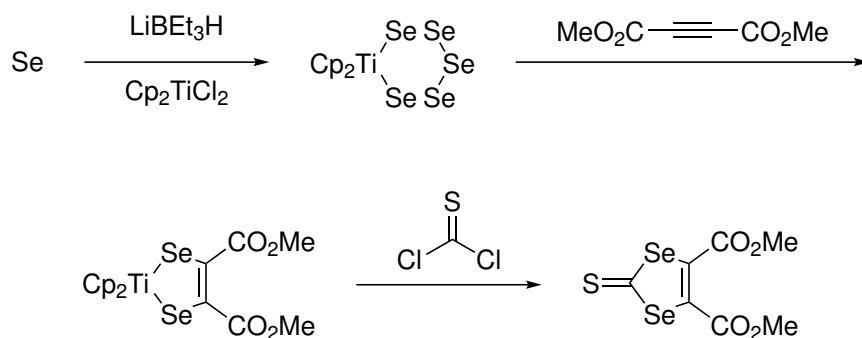
As for the preparation of functionalized TSF, the synthesis of tetramethyltetraselenafulvalene (TMTSF), for example, avoids the use of  $\text{CSe}_2$  by employing selenoureas for  $\text{S}_\text{N}2$ -like reactions with substituted  $\alpha$ -bromoketones, which are subsequently cyclized in concentrated sulfuric acid, then converted to the corresponding selenones by action of hydrogen selenide,  $\text{H}_2\text{Se}$ , and finally homo coupled with trialkyl phosphites,  $\text{P}(\text{OR})_3$  ( $\text{R} = \text{Me}, \text{Et}$ ) to obtain the tetrasubstituted tetraselenafulvalenes (Scheme 5).<sup>60–63</sup>  $\text{H}_2\text{Se}$  is synthetically much more accessible compared to  $\text{CSe}_2$  but poses similar health hazards due to its toxicity, and thus it was soon replaced with  $\text{NaHSe}$  generated *in situ* from the reduction of selenium with sodium borohydride,  $\text{NaBH}_4$  (Scheme 5).<sup>64</sup>



**Scheme 5.** CSe<sub>2</sub>-free synthesis of tetrasubstituted tetraselenafulvalenes.

To the best of the author's knowledge, the chemistry shown in Scheme 4 and 5 is the only example in the literature that yield TSF molecules with aromatic substituents that are not fused to the TSF core.

The "titanocene-route" is another strategy of synthesizing functionalized TSF.<sup>52</sup> Elemental selenium can be reduced with lithium triethylborohydride to obtain lithium pentaselenide, Li<sub>2</sub>Se<sub>5</sub>, which can be quenched with titanocene dichloride to obtain the stable titanocene pentaselenide and then converted to the corresponding 4,5-dicarbomethoxy-1,3-diselenole-2-titanocene using electrophilic DMAD in a Diels-Alder-like reaction (Scheme 6).<sup>65,66</sup> These titanocene complexes serve as masked 1,3-diselenolates which can be trapped with electrophilic reagents such as thiophosgene to obtain the corresponding 1,3-diselenole-2-thione (Scheme 6).<sup>66</sup>

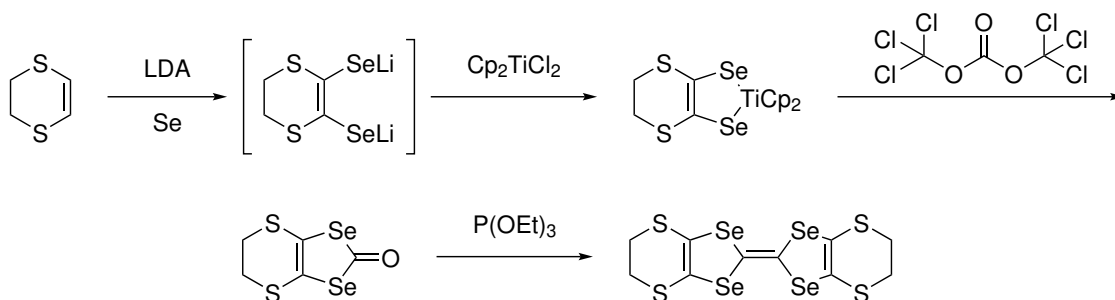


**Scheme 6.** Titanocene-route to 4,5-dicarbomethoxy-1,3-diselenole-2-thione.

However, when this 1,3-diselenole-2-thione with electron-withdrawing substituents is homo coupled using trialkyl phosphites, a "chalcogen-scrambling" occurs in which triselenathiafulvalenes are observed as the only products.<sup>67,68</sup> In order to keep the 1,3-diselenole functionality during the coupling reaction, a prior conversion of the 2-thiones to the 2-ones with mercuric acetate, Hg(OAc)<sub>2</sub>, is necessary.<sup>52,69</sup>

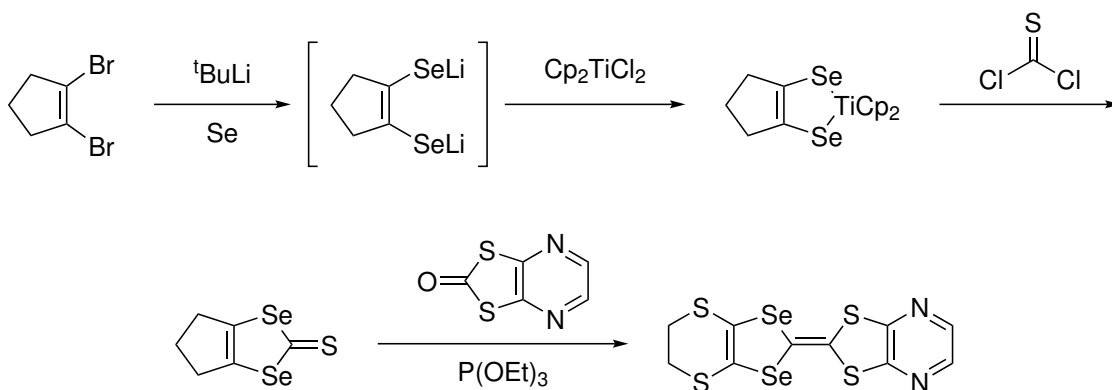
1,3-Diselenoles can be also synthesized via a deprotonation of acidic protons, subsequent selenium insertion into the carbon-metal bond, and trapping of the

intermediate with titanocene dichloride.<sup>70</sup> After phosgenation with triphosgene and homo coupling with triethylphosphite, bis(ethylenedithio)tetraselenafulvalene (BEDT-TSF) can be obtained (Scheme 7).



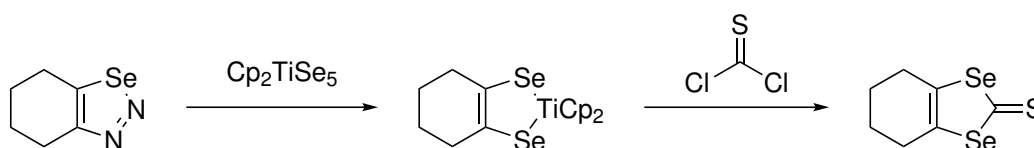
**Scheme 7.** Synthesis of BEDT-TSF.

Similarly, selenium insertion can also occur into lithiated species obtained by a bromine-lithium exchange, where complexation with titanocene dichloride serves as a purification and isolation step of the reactive intermediate (Scheme 8).<sup>71,72</sup>



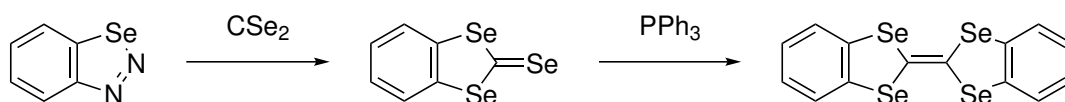
**Scheme 8.** Titanocene complexes as intermediates for the synthesis of mixed tetrachalcogenafulvalenes.

In addition, the previously introduced selenadiazoles are also useful precursors for the synthesis of functionalized tetraselenafulvalenes.<sup>73,74</sup> Serving as masked nucleophilic selenolates, they can be converted with titanocene dichloride and subsequent quenching with thiophosgene to the corresponding 1,3-diselenole-2-thiones (Scheme 9),<sup>73</sup> or directly with  $\text{CSe}_2$  to 1,3-diselenole-2-selenones, as in the synthesis of dibenzotetraselenafulvalene (Scheme 10).<sup>74</sup>



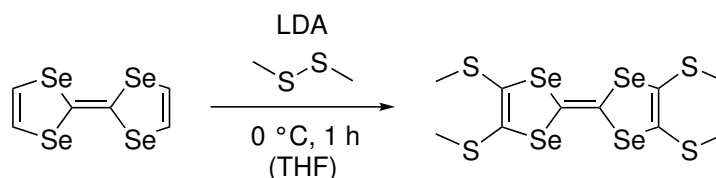
**Scheme 9.** Titanocene complexes obtained from selenadiazoles.





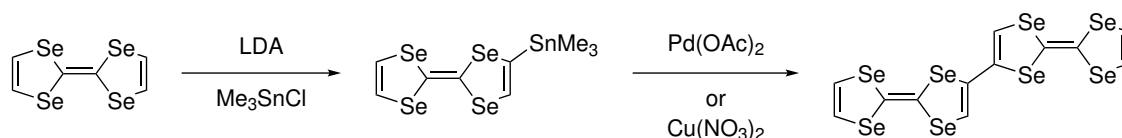
**Scheme 10.** Synthesis of dibenzotetraselenafulvalene.

The protons of TSF are sufficiently acidic for deprotonation with amide bases such as lithium diisopropylamide (LDA), which is particularly useful for the synthesis of tetrasubstituted TSF directly from the parent molecule.<sup>57,75–77</sup> The tetralithiotetraselenafulvalene intermediate is most often converted with disulfides or diselenides to obtain the corresponding tetrasubstituted alkyl- or arylthio- or selenoethers, but other electrophiles such as chloroformate or  $\text{CO}_2$  were reported, as well (Scheme 11).<sup>75</sup>



**Scheme 11.** Tetralithiation of TSF and quenching with dimethyl disulfide.

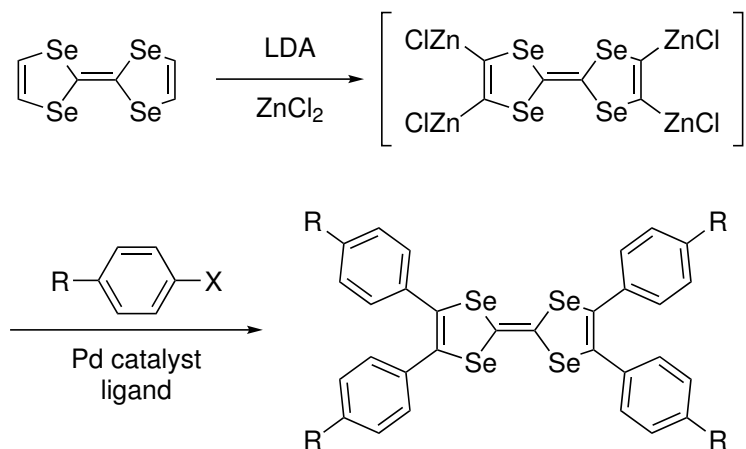
Looking beyond the scope of simple electrophiles, this reactivity opens up the possibility for the functionalization of TSF with more complex electrophiles such as aromatic halides which require transition-metal catalysis. For instance, the lithiated species could potentially be transmetalated with metals such as zinc or tin that are useful in Negishi or Stille couplings.<sup>78–80</sup> This would present the key synthetic transformation to tetra-aryl-substituted TSFs which are of interest for the preparation of new MOFs isostructural to  $\text{M}_2\text{TTFB}$ . Interestingly, no cross coupling reactions have been reported yet for TSF. The only available report for a transition-metal catalyzed coupling reaction of TSF is the homo coupling of mono-stannylated TSF in the presence of stoichiometric amounts of  $\text{Pd}(\text{OAc})_2$  or  $\text{Cu}(\text{NO}_3)_2 \cdot 3\text{H}_2\text{O}$  to bi-TSF (Scheme 12).<sup>81</sup>



**Scheme 12.** Homo coupling of stannylated TSF to bi-TSF.

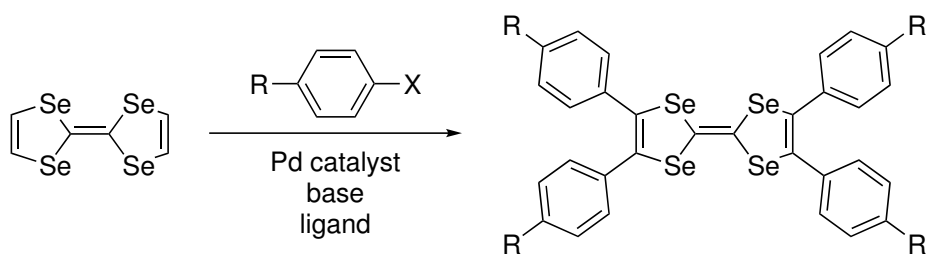
Due to the stability of tetralithiotetraselenafulvalene, transmetalation of the tetralithio species with zinc salts that may yield the corresponding zincated reagent accessible to Negishi couplings seems plausible. Similar Negishi coupling reaction conditions were already established for zincated TTF species.<sup>82</sup> Therefore,

Negishi coupling of zincated TSF appears to be a reasonable strategy for the preparation of tetrasubstituted aryl-TSFs (Scheme 13).



**Scheme 13.** Proposed direct arylation of zincated TSF using Pd catalyzed Negishi coupling.

On the other hand, a potential transition-metal catalyzed direct arylation of TSF would proceed without the use of pre-functionalization and yield the desired tetrasubstituted compounds in a one-step reaction.<sup>83–85</sup> The analogous direct arylation reaction of TTF yielded tetrasubstituted aryl-TTFs in high yield.<sup>86</sup> Therefore, direct arylation of TSF under similar reaction conditions to obtain arylated TSFs seems like a very promising strategy (Scheme 14).



**Scheme 14.** Proposed direct arylation of TSF using Pd catalysis.

The following chapter presents the author's efforts to synthesize tetra-arylated TSFs. Beginning with a critical discussion on the available modern synthetic routes to parent TSF, which are not straightforward, the following section will cover the attempted direct arylation of TSF. TTF can be arylated directly in high yield with aryl bromides in the presence of  $\text{Cs}_2\text{CO}_3$  as base, and tri-*tert*-butylphosphonium tetrafluoroborate,  $\text{P}^t\text{Bu}_3 \cdot \text{HBF}_4$  and  $\text{Pd}(\text{OAc})_2$  as the catalyst, using tetrahydrofuran (THF) or dioxane as solvent.<sup>86</sup> These results were a strong indicator that TSF might exhibit similar reactivity, for the chemistry of TTF and TSF is usually quite similar. Various catalysts, bases, additives, and reaction conditions were tested, and the results will be discussed in the following. After this, coupling reactions of functionalized TSF were examined. Two routes were considered as most promis-

ing: the first route was tetralithiation of TSF with subsequent transmetalation with zinc salts, followed by reaction with an aryl halide in the presence of a catalyst. The second route was desulfitative Liebeskind-Srogl type coupling reactions which make use of thio- and selenoethers as leaving groups during the oxidative addition of a catalyst into a comparatively weak C–S or C–Se bond, using zincated or boronated compounds as transmetalation reagents.<sup>87–90</sup> As previously mentioned, the tetrasubstituted thio- and selenoethers of TSF are readily available by tetralithiation and subsequent quenching with disulfides and diselenides, respectively. Next, various functionalizations of parent TSF were tested. In the last section, efforts to synthesize functionalized TSF in a "bottom-up" approach, i.e., attaching aryl groups to a 1,3-diselenole containing heterocycle without the need to synthesize parent TSF will be summarized and discussed.

### 3.2 SYNTHESIS OF TETRASELENAFULVALENE

The precursor of TSF, 2-methylene-1,3-diselenole or diselenafulvene, can be synthesized in a one-pot procedure from action of sodium acetylide with elemental selenium at  $-78-0$  °C, followed by a hydrolysis in methanol (Scheme 3).<sup>57</sup> Gram-scale yields of  $\approx 25\%$  were reported to be possible. Originally, diselenafulvene was obtained by the reaction of 1,2,3-selenadiazole with potassium *tert*-butoxide, which probably leads to the formation of an acetylenic selenolate that is able to dimerize after protonation.<sup>56,57</sup> The same reaction intermediate can also be obtained via a selenium insertion into the carbon-sodium bond of sodium acetylide. However, when the synthesis starting from sodium acetylide is reproduced following the same reaction conditions, TSF is only obtained in a yield of 2% at best (for more experimental details, Chapter 6). In comparison, if diselenafulvene is synthesized via the semicarbazone route (Scheme 3) and then converted to TSF with iodine/morpholine, acceptable gram-scale yields of 12% are obtained. Hence, it is likely that the purity of isolated diselenafulvene differs strongly between the two routes, and thus is responsible for the worse yields in the one-step reaction. The semicarbazone route employs  $\text{SeO}_2$  as the selenium source for the preparation of 1,2,3-selenadiazole and the product is distilled prior to the next step. Then, pure diselenafulvene is afforded after the reaction of the selenadiazole with  $\text{KO}^t\text{Bu}$  and crystallizes as big off-white platelets. On the other hand, selenium insertion into sodium acetylide is performed at 0 °C yielding a brown mixture, and hydrolysis of the reaction intermediates and work-up of the reaction gives a red-brown solid. Although not identified, it seems plausible that the colored

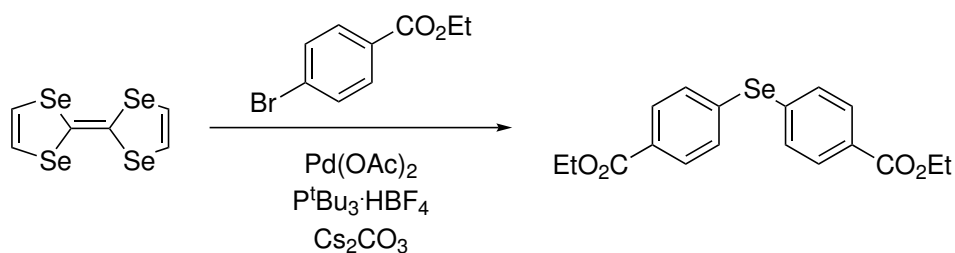
side products either correspond to a low purity of diselenafulvene which in turn results in an overall low yield of TSF in the following step, or they inhibit the following coupling reaction. Typical for selenium chemistry, brown colors often indicate the presence of polyselenide species, whereas fully reduced selenides are colorless.<sup>91</sup> Likewise, a quantitative insertion of selenium into sodium acetylide should also result in colorless solutions of sodium organoselenides. It seems plausible that the nucleophilicity of sodium acetylide is insufficient to cleave all Se–Se bonds of the polymeric chains in black selenium, and that the reaction intermediates consist of a large amount of acetylene substituted polyselenides,  $\text{HC}\equiv\text{C}-(\text{Se})_n-\text{Se}^-$  ( $n \geq 1$ ). After hydrolysis, the red-brown organic solution would then contain diselenafulvene as the dimerization product of acetylene selenol, but also other polyselenols which would not dimerize or yield big selenium heterocycles containing Se–Se bonds. Furthermore, selenols are prone to undergo aerobic oxidation, further underlying the instability of such compounds.<sup>92</sup> This may also serve as an explanation for the extensive decomposition observed during the work-up of the reaction concomitant with a coating of all glassware with what was most likely red selenium, even at lower temperatures. Although diselenafulvene was reported to be light-sensitive and only stable for two weeks even at low temperature under an inert atmosphere,<sup>56</sup> the compound turned out to be rather moderately temperature sensitive and storage at  $-32\text{ }^\circ\text{C}$  did not affect the quality of the product even after a period of months when synthesized via the semicarbazone route. Thus, the decomposition of products obtained via the sodium acetylide route are most likely caused by the unwanted polyselenide side products. A possible way to avoid the formation of these side products and increase the yield and purity of diselenafulvene could be the use of red selenium, which consists of small selenium rings and is more reactive than black or gray selenium, or by performing the selenium insertion into sodium acetylide at more forcing reflux conditions under an inert atmosphere until colorless solutions are observed. Nevertheless, the semicarbazone route was chosen for the synthesis of TSF during the course of this project, for it was more reliable and gave better yields of the final product.

---

### 3.3 DIRECT ARYLATION

#### 3.3.1 Palladium Catalysis

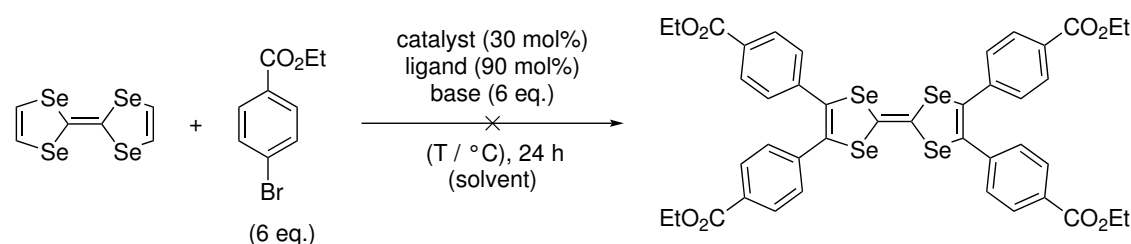
As previously mentioned, the chemistry of TTF and TSF is usually quite similar, so a direct arylation of TSF which employs the same reaction conditions of the direct arylation of TTF seemed highly promising to obtain the desired tetra-arylated TSFs. However, an analogous reaction of TSF with ethyl 4-bromobenzoate in THF showed only very little conversion of TSF (Table 3, Entry 3.1). In contrast, the same reaction in dioxane showed full conversion of TSF (Entry 3.3) and trace amounts of mono- and disubstituted products were observed via liquid injection field desorption ionization (LIFDI)-MS (*cf.* Chapter 15), but the main product was identified as bis(4-ethoxycarbonylphenyl) selenide via NMR (Scheme 15, for more information on NMR *cf.* Chapter 14).<sup>93</sup>



**Scheme 15.** Conversion of TSF to diaryl selenide at direct arylation reaction conditions.

A total destruction of TSF and conversion to the same diaryl selenide was also observed in other dipolar-aprotic solvents such as *N,N*-dimethyl formamide (DMF) (Entry 3.4). Changing the phosphine ligand to 2,2'-bis(diphenylphosphino)-1,1'-binaphthyl (BINAP) had no effect on the selectivity of the reaction (Entry 3.5). Weaker bases such as K<sub>2</sub>CO<sub>3</sub> or KOAc resulted in no reaction (Entries 3.6, 3.11), as did the replacement of the phosphine ligand with less electron-rich PPh<sub>3</sub> (Entry 3.7). N-heterocyclic carbene complexes of palladium like 1,3-bis-(2,6-diisopropylphenyl)imidazol-2-ylidene(3-chloropyridyl)palladium(II) dichloride (PEPPSI-IPr) did not catalyze the reaction at all (Entry 3.8). In highly dipolar-aprotic DMF, the conversion of TSF to diaryl selenide proceeded even without any phosphine ligand at higher temperatures when ethyl 4-bromobenzoate was used (Entry 3.9), whereas little conversion was observed for the analogous aryl iodide (Entry 3.10). Adding CuI did not improve the selectivity (Entries 3.12, 3.13). A possible explanation for the differences in reactivity between TTF and TSF is the weaker C–Se bond strength compared to C–S, which facilitates bond cleavage by means of either oxidative addition to an electron-rich metal atom or by Lewis acid assisted nucleophilic attack of basic species at electrophilic selenium. The

**Table 3.** Attempted Pd-catalyzed direct arylation of TSF with ethyl 4-bromobenzoate. <sup>a</sup>45 mol%. <sup>b</sup>60 mol%. <sup>c</sup>120 mol%. <sup>d</sup>ethyl 4-iodobenzoate was used. <sup>e</sup>30 mol%.



Entry	Catalyst	Ligand	Base	Additive	Solvent	T (°C)	Conv. (%)	Yield (%)
3.1	Pd(OAc) <sub>2</sub>	P <sup>t</sup> Bu <sub>3</sub> · HBF <sub>4</sub>	CS <sub>2</sub> CO <sub>3</sub>		THF	80	little	trace
3.2	Pd(OAc) <sub>2</sub>	P <sup>t</sup> Bu <sub>3</sub> · HBF <sub>4</sub>	CS <sub>2</sub> CO <sub>3</sub>		PhMe	110	little	trace
3.3	Pd(OAc) <sub>2</sub>	P <sup>t</sup> Bu <sub>3</sub> · HBF <sub>4</sub>	CS <sub>2</sub> CO <sub>3</sub>		dioxane	110	full	trace
3.4	Pd(OAc) <sub>2</sub>	P <sup>t</sup> Bu <sub>3</sub> · HBF <sub>4</sub>	CS <sub>2</sub> CO <sub>3</sub>		DMF	110	full	trace
3.5	Pd(OAc) <sub>2</sub>	BINAP <sup>a</sup>	CS <sub>2</sub> CO <sub>3</sub>		DMF	110	full	trace
3.6	Pd(OAc) <sub>2</sub>	P <sup>t</sup> Bu <sub>3</sub> · HBF <sub>4</sub>	K <sub>2</sub> CO <sub>3</sub>	<sup>t</sup> BuCO <sub>2</sub> H <sup>b</sup>	THF	110	little	0
3.7	Pd(OAc) <sub>2</sub>	PPh <sub>3</sub> <sup>c</sup>	CS <sub>2</sub> CO <sub>3</sub>		dioxane	110	little	0
3.8	PEPPSI-IPr	P <sup>t</sup> Bu <sub>3</sub> · HBF <sub>4</sub>	CS <sub>2</sub> CO <sub>3</sub>		dioxane	110	0	0
3.9	Pd(OAc) <sub>2</sub>		CS <sub>2</sub> CO <sub>3</sub>		DMF	150	full	trace
3.10	Pd(OAc) <sub>2</sub>		CS <sub>2</sub> CO <sub>3</sub>		DMF	120	little	0 <sup>d</sup>
3.11	Pd(OAc) <sub>2</sub>		KOAc		DMF	150	little	0
3.12	Pd(OAc) <sub>2</sub>		CS <sub>2</sub> CO <sub>3</sub>	CuI <sup>e</sup>	DMF	150	full	0
3.13	Pd(OAc) <sub>2</sub>		CS <sub>2</sub> CO <sub>3</sub>	CuI <sup>e</sup>	DMF	150	full	0 <sup>d</sup>

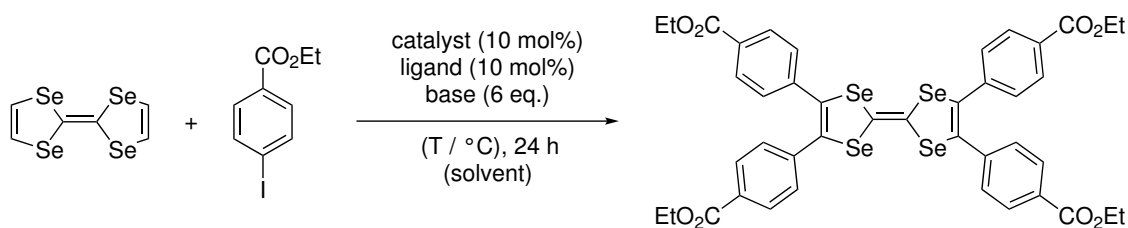
latter seems more reasonable, for diaryl selenides are often synthesized from aryl halides and various selenium sources such as elemental selenium or potassium selenocyanate, using copper salts as catalysts, carbonates or hydroxides as bases, in polar solvents such as DMF, dimethyl sulfoxide (DMSO), or water.<sup>94–98</sup> Based on this, several key aspects can be identified that need to be addressed for increasing the selectivity of the reaction towards the direct arylation of TSF. A possible oxidative addition of the C–Se bond that opens the heterocyclic ring should be avoided by employing less electron rich metals in higher oxidation states. The base needs to be strong enough to abstract the acidic protons of TSF, whereas excess basicity would favor nucleophilic attack at selenium and ring opening. Oxidative addition of the carbon-halide bond in the aromatic coupling partner should proceed at mild conditions.

### 3.3.2 Copper Catalysis

Copper catalyzed direct arylation are often performed for heterocyclic substrates with acidic protons.<sup>99–101</sup> The initial hint that copper might be catalytically active

in the direct arylation of TSF was the observation that TSF was fully converted when Pd(OAc)<sub>2</sub> was used without any ligand, although only the corresponding diaryl selenide was formed (Entry 3.9). By replacing Pd(OAc)<sub>2</sub> with CuI, the selectivity of the reaction could potentially be shifted more towards the direct arylation. Similarly to Pd catalysis, no reaction was observed in dioxane as solvent (Table 4, Entry 4.1). Interestingly, full conversion was observed when PPh<sub>3</sub> was added to the reaction, but it led to the full destruction of the molecule, even without formation of the diaryl selenide (Entry 4.8). When the solvent and temperature were changed to DMF and 130 °C, respectively, NMR revealed the presence of a new species which causes signals of aromatic protons at 7.23 and 7.87 ppm in CDCl<sub>3</sub>, both doublets with coupling constants of 8.3 Hz (Figure 18, purple). Due to the chemical similarity between TSFTB and TTFTB, and the latter causing NMR doublet signals of its aromatic protons at 7.26 and 7.91 ppm, it is very likely that the proton chemical shifts of TSFTB are found at similar positions since the distance between substituent protons and core chalcogen atoms is too large to inflict greater deshielding. Besides ethyl 4-iodobenzoate (Figure 18, yellow) and bis(4-ethoxycarbonylphenyl) selenide (green), another species is detected with doublets of aromatic protons at 7.60 and 8.04 ppm and coupling constants of 8.4 Hz (turquoise), of which the structure could not be identified. Separation of the compound of interest via column chromatography proved to be somewhat difficult, but a brown solid was finally obtained in a yield of 10% which showed only the expected NMR signals at 7.87 ppm (d, <sup>3</sup>J = 8.3 Hz, 8 H), 7.23 ppm (d, <sup>3</sup>J = 8.3 Hz, 8 H), 4.34 ppm (q, <sup>3</sup>J = 7.1 Hz, 8 H), and 1.37 ppm (t, <sup>3</sup>J = 7.1 Hz, 12 H) (Figure 19) and was identified as Et<sub>4</sub>TSFTB using LIFDI-MS (Figure 20). Variation of the reaction conditions were conducted to further increase the selectivity towards direct arylation. Bases stronger than Cs<sub>2</sub>CO<sub>3</sub>, such as K<sub>3</sub>PO<sub>4</sub> or LiO<sup>t</sup>Bu, led to the full destruction of TSF and isolation of an uncharacterizable slurry (Entries 4.6, 4.12), while other alkali carbonates or CsOAc were ineffective (Entries 4.9–4.13). The initial choice of CuI turned out to be the optimal catalyst because other copper sources such as copper powder or CuOAc were either too reactive (Entries 4.18, 4.21) or gave more side products like CuCl and CuBr (Entries 4.19, 4.20). Choosing the right reaction temperature is important since no reaction occurs below 90 °C (Entries 4.16, 4.24), whereas at 150 °C only diaryl selenide is formed (Entry 4.25). NMR yields of the product are significantly increased when the reaction is performed at 110 °C (Figure 21, green) and even more at 100 °C (Figure 21, orange). This observation is in line with the previous assumption that more forcing conditions lead to ring opening and subsequent side product formation. Unfortunately, it was impossible to separate the product from an unidentified side product with signals of aromatic protons at 8.02 and

**Table 4.** Cu-catalyzed direct arylation of TSF with ethyl 4-iodobenzoate. <sup>a</sup>12 eq. <sup>b</sup>40 mol%. <sup>c</sup>NMR yield. <sup>d</sup>ethyl 4-bromobenzoate was used. <sup>e</sup>based on NMR, less side product detected. <sup>f</sup>worse than CuI, more side products. <sup>g</sup>1 g scale, incomplete conversion to tetra-substituted TSF, tri-substituted was detected as major, inseparable product.



Entry	Catalyst	Ligand	Base	Solvent	T (°C)	Conversion (%)	Yield (%)
4.1	CuI		Cs <sub>2</sub> CO <sub>3</sub>	dioxane	100	0	0
4.2	CuI		Cs <sub>2</sub> CO <sub>3</sub>	DMF	130	full	10
4.3	CuI		Cs <sub>2</sub> CO <sub>3</sub> <sup>a</sup>	DMF	130	full	0
4.4	CuI <sup>b</sup>		Cs <sub>2</sub> CO <sub>3</sub>	DMF	130	full	10 <sup>c</sup>
4.5	CuI		Cs <sub>2</sub> CO <sub>3</sub>	DMF	150	full	0 <sup>d</sup>
4.6	CuI		K <sub>3</sub> PO <sub>4</sub>	DMF	130	full	0
4.7	CuI	PPh <sub>3</sub>	Cs <sub>2</sub> CO <sub>3</sub>	DMF	130	full	0
4.8	CuI	PPh <sub>3</sub>	Cs <sub>2</sub> CO <sub>3</sub>	dioxane	140	full	0
4.9	CuI		Li <sub>2</sub> CO <sub>3</sub>	DMF	140	little	0
4.10	CuI		Na <sub>2</sub> CO <sub>3</sub>	DMF	140	little	0
4.11	CuI		K <sub>2</sub> CO <sub>3</sub>	DMF	140	little	0
4.12	CuI		LiO <sup>t</sup> Bu	DMF	140	full	0
4.13	CuI		CsOAc	DMF	130	0	0
4.14	CuI		CsOAc	MeCN	110	0	0
4.15	CuI		Cs <sub>2</sub> CO <sub>3</sub>	DMF	25	0	0
4.16	CuI		Cs <sub>2</sub> CO <sub>3</sub>	DMF	80	0	0
4.17	CuI		Cs <sub>2</sub> CO <sub>3</sub>	DMF	110	full	10 <sup>e</sup>
4.18	Cu		Cs <sub>2</sub> CO <sub>3</sub>	DMF	130	full	0 <sup>f</sup>
4.19	CuCl		Cs <sub>2</sub> CO <sub>3</sub>	DMF	130	full	little <sup>f</sup>
4.20	CuBr		Cs <sub>2</sub> CO <sub>3</sub>	DMF	130	full	little <sup>f</sup>
4.21	CuOAc		Cs <sub>2</sub> CO <sub>3</sub>	DMF	130	full	0
4.22	CuI		Cs <sub>2</sub> CO <sub>3</sub>	DMF	130	full	10 <sup>g</sup>
4.23	CuI		Cs <sub>2</sub> CO <sub>3</sub>	DMF	100	full	10
4.24	CuI		Cs <sub>2</sub> CO <sub>3</sub>	DMF	90	little	trace
4.25	CuI		Cs <sub>2</sub> CO <sub>3</sub>	DMF	150	full	0



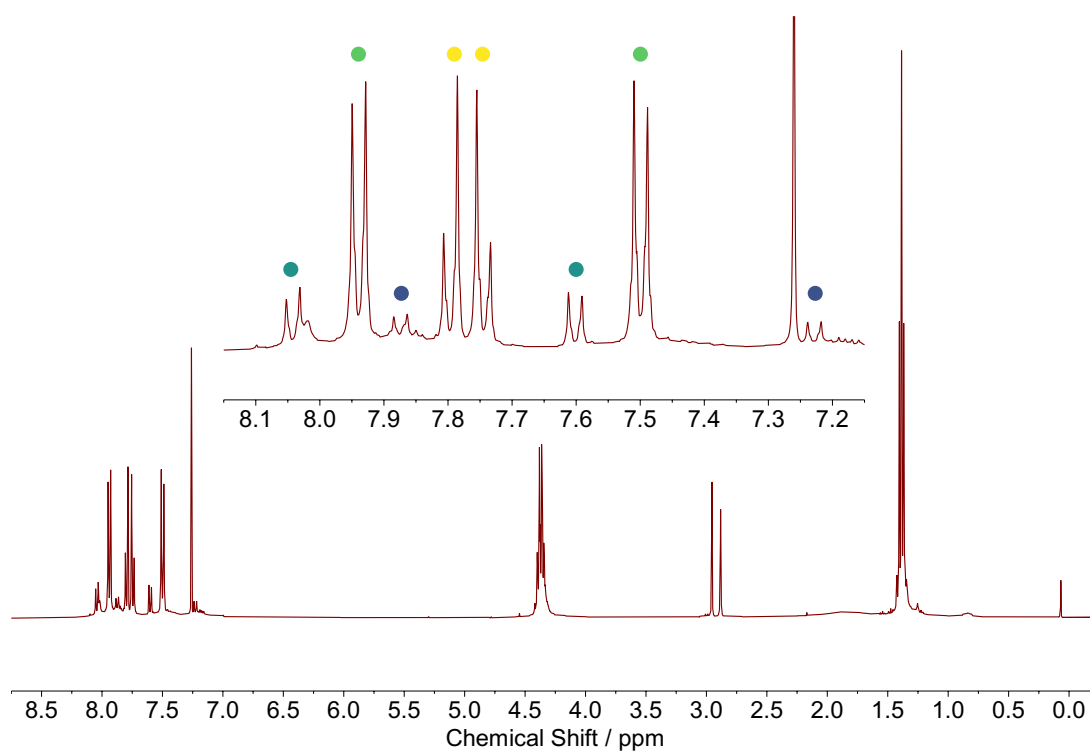


**Figure 18.** NMR spectrum of the crude product obtained after Cu-catalyzed direct arylation of TSF with ethyl 4-iodobenzoate.

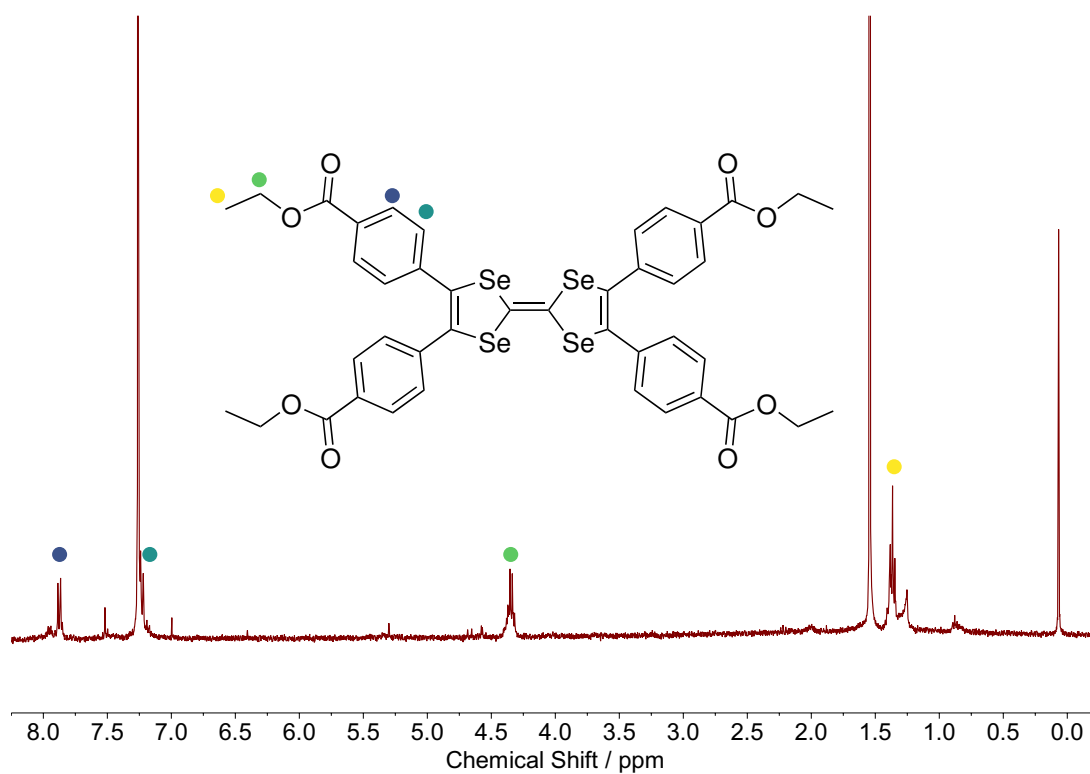


**Figure 19.** NMR spectrum of Et<sub>4</sub>TSFTB.

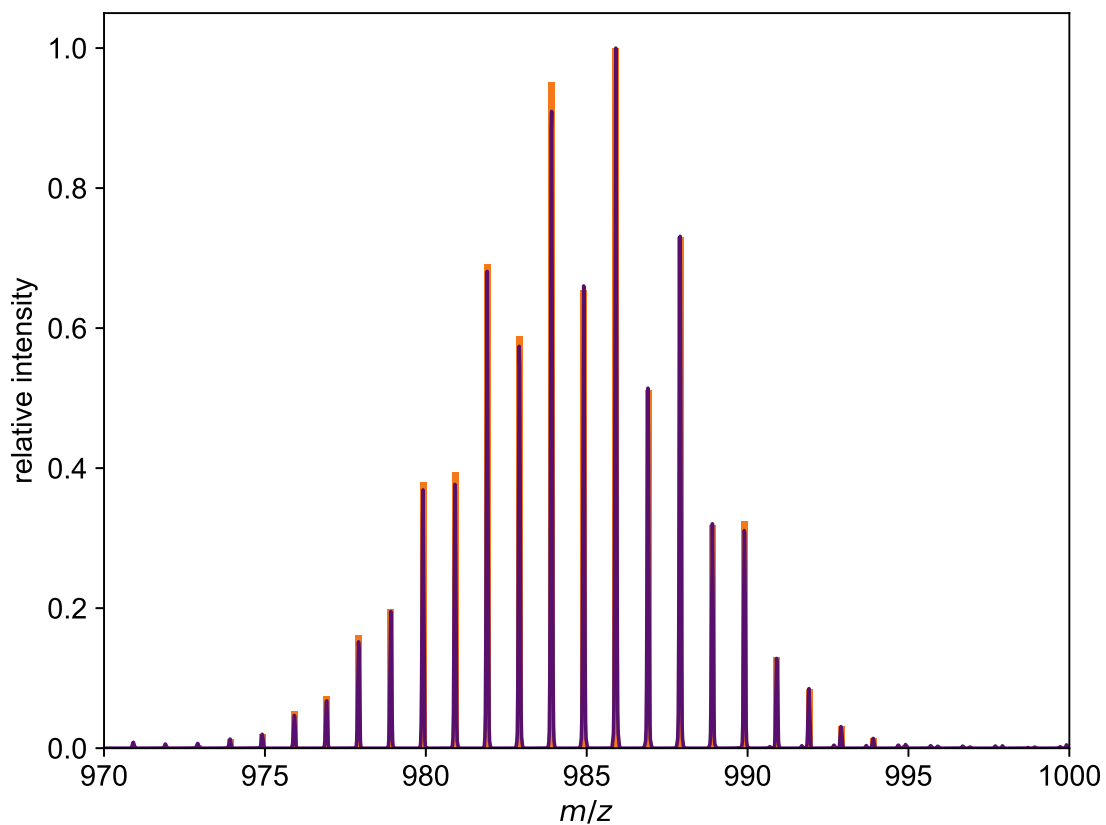


**Figure 20.** LIFDI-MS of Et<sub>4</sub>TSFTB (purple) and simulated pattern (orange).

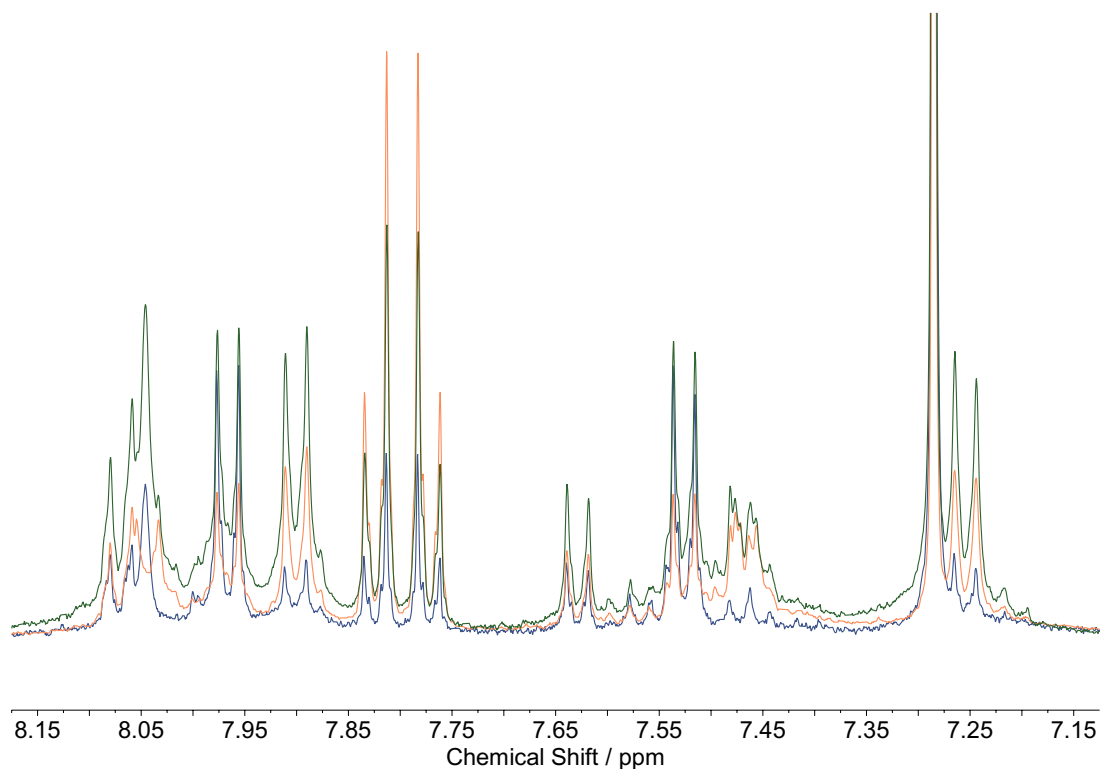


**Figure 21.** NMR spectra of the crude products obtained after Cu-catalyzed direct arylation of TSF with ethyl 4-iodobenzoate at 130 °C (blue), 110 °C (green), and 100 °C (orange).

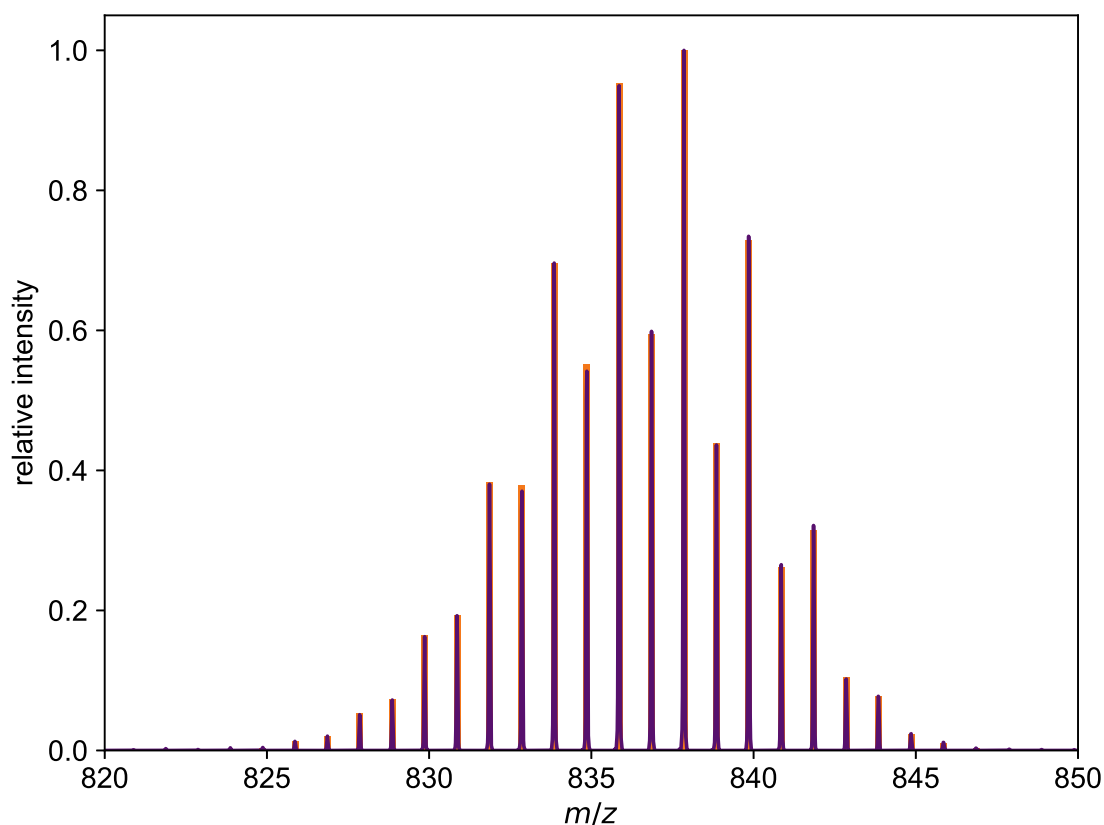


**Figure 22.** LIFDI-MS of tri-arylated TSF (purple) and simulated (orange).

7.45 ppm via column chromatography due to their equal retention times, which could be undersubstituted arylated TSFs, pointing at an incomplete reaction at these lower temperatures. Furthermore, upscaling of the synthesis at 130 °C to a 1 g scale led to similar problems where the incomplete reaction gave mixtures of the product and the presumably undersubstituted TSFs mentioned above. This is further supported by a LIFDI-MS analysis of the product where only tri-substituted TSF was observed (Figure 22).

In summary, simple CuI can catalyze the direct arylation of TSF with aryl iodides without the need of additional ligands, thereby presenting the first cross coupling reaction using TSF as substrate in general. The reaction temperature and time is the most important handle to drive the selectivity towards arylation and suppress the competing ring opening carbon-selenium coupling. Although this route is successful in producing arylated TSFs, other synthetic routes that could potentially produce arylation products more selectively without diaryl selenide formation and in higher yield were also examined and will be discussed in the next section.

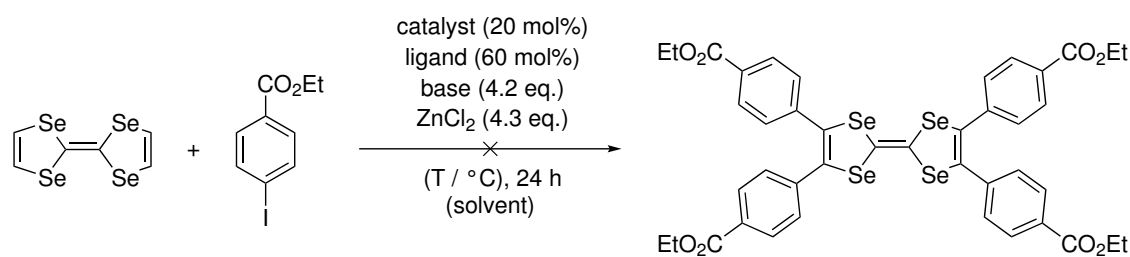
### 3.4 CROSS COUPLING OF FUNCTIONALIZED TETRASELENAFULVALENE

#### 3.4.1 Negishi Coupling

The Negishi coupling is an often used and mild cross coupling reaction for a broad variety of substrates.<sup>102–104</sup> Like most cross coupling reactions, it is based on the oxidative addition of a palladium catalyst to a weak carbon-halide bond of an aromatic substrate, using aryl zinc reagents for transmetalation and transfer of the coupling agent to the palladium catalyst prior to reductive elimination of the desired product. Aryl zinc reagent are often prepared via the transmetalation of lithiated organic species with zinc salts.<sup>105,106</sup> Tetralithiotetraselenafulvalene is obtained by fourfold deprotonation of TSF with LDA and can be quenched by electrophiles such as disulfides or diselenides to produce the tetrachalcogenated TSFs.<sup>75</sup> Since this intermediate is stable, it should be possible to transmetalate the carbon-lithium bonds with zinc salts to obtain the tetrazincated TSF species, which in turn could be useful for Negishi coupling reactions with aryl halides. Negishi couplings were performed on monozincated TTF,<sup>82</sup> so applying the same conditions to TSF seemed promising. However, no conversion was observed when Pd(PPh<sub>3</sub>)<sub>4</sub> was used as the catalyst at RT as was reported for TTF (Table 5, Entry 5.1).<sup>82</sup> Equally ineffective were using PEPPSI-IPr or Pd(dibenzylideneacetone (dba))<sub>2</sub> in combination with 2-dicyclohexylphosphino-2'-(*N,N*-dimethylamino)biphenyl (DavePhos) (Entries 5.2–5.4). Only by increasing the temperature to 100 °C full conversion of TSF was observed but no products were formed, most likely due to decomposition of the metalated TSF at higher temperature (Entry 5.5). Using the strong kinetic bases 2,2,6,6-tetramethylpiperidinylmagnesium chloride lithium chloride (TMPMgCl · LiCl)<sup>107</sup> and 2,2,6,6-tetramethylpiperidinylzinc chloride lithium chloride (TMPZnCl · LiCl),<sup>108</sup> which allow the facile and regioselective deprotonation of (hetero-)aromatics, had no beneficial effect (Entries 5.9–5.11). A possible explanation for the lack of reactivity may be a poor rate of transmetalation of the tetrazincated (or lithiated) TSF species to oxidatively added aryl halide at palladium, or inhibited reductive elimination of the arylated product. Another reason may be the high charge on the tetrametalated TSF, for cross coupling reactions with multiple metalated substituents are rare.<sup>109</sup> Hence, the Negishi coupling strategy of metalated TSF was dismissed.

---

**Table 5.** Attempted Pd-catalyzed Negishi coupling of zincated TSF with ethyl 4-iodobenzoate. <sup>a</sup>No ZnCl<sub>2</sub>. <sup>b</sup>MgCl<sub>2</sub> used instead of ZnCl<sub>2</sub>. <sup>c</sup>1-methyl-2-pyrrolidone (NMP). <sup>d</sup>50 mol%. <sup>e</sup>10 mol%. <sup>f</sup>4 eq. <sup>g</sup>tri-(2-furyl)phosphine (tfp). <sup>h</sup>addition at 0 °C. <sup>i</sup>addition at RT. <sup>j</sup>ethyl 4-bromobenzoate was used.

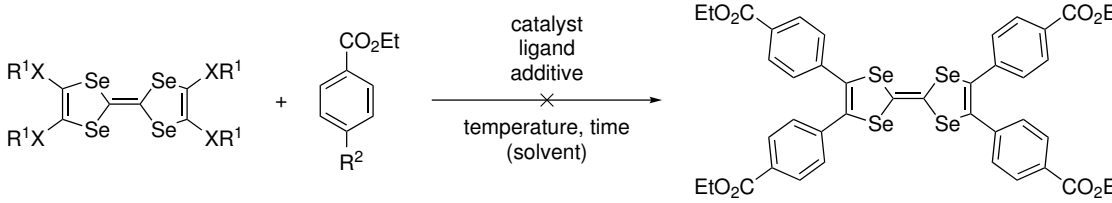


Entry	Catalyst	Ligand	Base	Additive	Solvent	T (°C)	Conv. (%)	Yield (%)
5.1	Pd(PPh <sub>3</sub> ) <sub>4</sub>		LDA		THF	RT	0	0
5.2	PEPPSI-IPr		LDA		THF	RT	0	0
5.3	PEPPSI-IPr		LDA		THF	RT	0	0 <sup>a</sup>
5.4	Pd(dba) <sub>2</sub> <sup>b</sup>	DavePhos	LDA		THF	RT	0	0 <sup>b</sup>
5.5	Pd(PPh <sub>3</sub> ) <sub>4</sub>		LDA		THF/NMP <sup>c</sup>	100	full	trace
5.6	Pd(P <sup>t</sup> Bu <sub>3</sub> ) <sub>2</sub> <sup>d</sup>		LDA		THF/NMP	100	full	0
5.7	CuI <sup>e</sup>		LDA	LiCl <sup>f</sup>	THF/DMF	100	0	0
5.8	Pd(dba) <sub>2</sub>	tfp <sup>g</sup>	LDA		THF	RT	full	0
5.9	Pd(dba) <sub>2</sub>	tfp	TMPMgCl · LiCl <sup>h</sup>		THF	RT	0	0
5.10	Pd(P <sup>t</sup> Bu <sub>3</sub> ) <sub>2</sub>		TMPZnCl · LiCl <sup>i</sup>		THF	50	full	0 <sup>a,j</sup>
5.11	PEPPSI-IPr		TMPZnCl · LiCl <sup>h</sup>		THF	80	full	0 <sup>a,j</sup>

### 3.4.2 Dechalcogenative Coupling

Since the high charge density on tetrametalated TSF was speculated to be problematic for the Negishi cross coupling, a solution would be to reverse the order of organic halide and transmetalation reagent, i.e., use a charge-neutral tetrahalogenated TSF with an aryl zinc reagent. However, tetrahalotetraselenafulvalene (chloro-, bromo-, iodo-) cannot be obtained by deprotonation of parent TSF with LDA and subsequent quenching with suitable halogen sources, but are synthesized from cyclization of trimethylsilylacetylene with selenium and CSe<sub>2</sub> to obtain the corresponding 1,3-diselenole-2-selenone, substitution of the trimethylsilyl group with another halogen, and final phosphite-mediated coupling.<sup>110</sup> The readily accessible tetrakis(thio- or selenoether)-substituted TSFs pose an attractive alternative to the tetrahalogenated TSFs, which are used in Liebeskind-Srogl type couplings for substrates where the halogenated congeners are unstable.<sup>88</sup> Three different chalcogen-etherified TSFs were tested for the coupling reactions: thiomethyl (–SMe), synthesized from quenching of Li<sub>4</sub>TSF with dimethyl disulfide, selenophenyl (–SePh), synthesized analogously using diphenyl diselenide, and selenobutyl (–SeBu), from dibutyl diselenide. Various transmetalation agents such as boronic acid or aryl zinc have been used, catalysts, ligands, and additives

**Table 6.** Attempted Pd-catalyzed Liebeskind-Srogl couplings of tetrachalcogenated TSF derivatives. <sup>a</sup>Copper(I) thiophene-2-carboxylate (CuTC). <sup>b</sup>with Zn(OAc)<sub>2</sub> (2 eq.). <sup>c</sup>with Cs<sub>2</sub>CO<sub>3</sub> (6 eq.). <sup>d</sup>2-dicyclohexylphosphino-2',6'-dimethoxybiphenyl (SPhos). <sup>e</sup>Cs<sub>2</sub>CO<sub>3</sub> (8 eq.) was used. <sup>f</sup>2-dicyclohexylphosphino-2',4',6'-triisopropylbiphenyl (XPhos). <sup>g</sup>2-dicyclohexylphosphino-2',6'-diisopropoxybiphenyl (RuPhos). <sup>h</sup>1,1'-ferrocenediyl-bis(diphenylphosphine) (dppf). <sup>i</sup>(oxydi-2,1-phenylene)-bis(diphenylphosphine) (DPE-Phos).



Entry	R <sup>1</sup>	R <sup>2</sup>	Catalyst (mol%)	Ligand (mol%)	Additive (eq.)	Solvent	T (°C)	Conv. (%)	Yield (%)
6.1	SMe	B(OH) <sub>2</sub>	Pd <sub>2</sub> dba <sub>3</sub> (20)	tfp (80)	CuTC <sup>a</sup> (5)	THF	90	little	0
6.2	SMe	B(OH) <sub>2</sub>	Pd(PPh <sub>3</sub> ) <sub>4</sub> (20)		CuTC (5)	dioxane	90	0	0
6.3	SMe	B(OH) <sub>2</sub>	Pd(PPh <sub>3</sub> ) <sub>4</sub> (20)		CuTC (5)	THF	90	0	0 <sup>b</sup>
6.4	SMe	B(OH) <sub>2</sub>	Pd(P <sup>t</sup> Bu <sub>3</sub> ) <sub>2</sub> (20)		CuTC (5)	THF	90	0	0
6.5	SMe	B(OH) <sub>2</sub>	Pd(P <sup>t</sup> Bu <sub>3</sub> ) <sub>2</sub> (20)		CuTC (5)	THF	90	0	0 <sup>c</sup>
6.6	SMe	ZnI · LiCl	Pd(OAc) <sub>2</sub> (10)	SPhos <sup>d</sup> (20)		THF	90	0	0
6.7	SMe	ZnI · LiCl	PEPPSI-IPr (10)			THF	RT	0	0
6.8	SePh	B(OH) <sub>2</sub>	Pd(PPh <sub>3</sub> ) <sub>4</sub> (40)		Cu(OAc) <sub>2</sub> (8)	DMF	80	little	trace
6.9	SePh	B(OH) <sub>2</sub>	Pd(OAc) <sub>2</sub> (40)	BINAP (60)	Cu(OAc) <sub>2</sub> (8)	DMF	80	0	0
6.10	SePh	B(OH) <sub>2</sub>	Pd(OAc) <sub>2</sub> (40)	BINAP (60)	Cu(OAc) <sub>2</sub> (8)	DMF	80	0	0 <sup>e</sup>
6.11	SePh	B(OH) <sub>2</sub>	Pd(OAc) <sub>2</sub> (40)	P <sup>t</sup> Bu <sub>3</sub> (60)	Cu(OAc) <sub>2</sub> (8)	DMF	80	0	0 <sup>e</sup>
6.12	SePh	B(OH) <sub>2</sub>	Pd(OAc) <sub>2</sub> (40)	XPhos <sup>f</sup> (60)	Cu(OAc) <sub>2</sub> (8)	DMF	80	0	0 <sup>e</sup>
6.13	SePh	B(OH) <sub>2</sub>	Pd(OAc) <sub>2</sub> (40)	SPhos (60)	Cu(OAc) <sub>2</sub> (8)	DMF	80	0	0 <sup>e</sup>
6.14	SePh	B(OH) <sub>2</sub>	Pd(OAc) <sub>2</sub> (40)	RuPhos <sup>g</sup> (60)	Cu(OAc) <sub>2</sub> (8)	DMF	80	0	0 <sup>e</sup>
6.15	SePh	B(OH) <sub>2</sub>	Pd(OAc) <sub>2</sub> (40)	dppf <sup>h</sup> (60)	Cu(OAc) <sub>2</sub> (8)	DMF	80	0	0 <sup>e</sup>
6.16	SeBu	ZnI · LiCl	Ni(acac) <sub>2</sub> (40)	DPE-Phos <sup>i</sup> (60)		DMF	80	0	0 <sup>e</sup>

(Table 6). In all cases, only little to no conversion of the corresponding TSF was observed, which points at a very high stability of these substituted TSFs compared to parent TSF. Therefore, this functionalization strategy was also dismissed.

### 3.5 CONCLUSION

In conclusion, the first cross coupling route of TSF with aromatic halides was established. Yields are comparatively low due to a competing destructive, ring-opening carbon-selenium coupling to form diaryl selenides, but yields can be increased by adjusting the reaction temperature and time. Other functionalization routes, such as Negishi coupling of zincated TSF, or Liebeskind-Srogl type couplings of chalcogenoether-substituted TSF failed to give any reaction. Although only one coupling partner was tested, for the motivation of the whole project laid in the preparation of TSF based MOFs that use carboxylic acids as linkers, it

can be expected that many more aryl iodides are suitable coupling partners. In the context of MOFs, however, the herein presented synthetic route is the most promising for the preparation of the H<sub>4</sub>TSFTB linker, which is believed to provide a new family of electrically interesting MOFs with unique properties.

---





# 4

## *Tuning Negative Thermal Expansion in Metal-Organic Frameworks*

### 4.1 INTRODUCTION

NTE describes the physical properties of some materials that show an unintuitive volume decrease with increasing temperatures.<sup>111-114</sup> The thermal expansion coefficient  $\alpha_V$ , which is defined as

$$\alpha_V = \frac{1}{V} \left( \frac{\partial V}{\partial T} \right)_p \quad (4.1)$$

describes the extent of the volume change  $V$  with temperature  $T$  (at constant pressure  $p$ ) and is  $< 0$  for NTE materials. Likewise, the linear thermal expansion coefficient  $\alpha_i$  describes the change in length  $l$  of one of the principal axes  $i$  with temperature, which is equal for all directions in isotropic (cubic) materials but may differ for materials with lower symmetry:

$$\alpha_i = \frac{1}{l_i} \left( \frac{\partial l_i}{\partial T} \right) \quad (4.2)$$

Typically, materials expand with increasing temperature because the additional energy input gives rise to the population of energetically higher vibrational states. This results in larger mean bond lengths between atoms due to the shape of the Morse potential, in which the slope for bond elongation is smaller, and thus energetically more favorable than bond contraction (Figure 23).<sup>115,116</sup> Although the same physical principles apply for the bond lengths in NTE materials, the

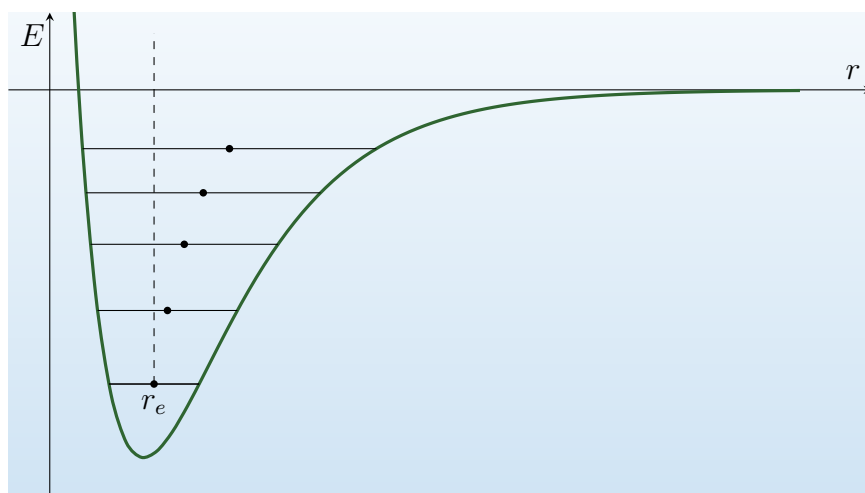


**Figure 23.** Illustration of the mean bond length ( $r_e$ ) increase with increasing temperature due to population of energetically higher vibrational states. The dashed line indicates the mean bond length at the initial temperature.

magnitude of bond length induced expansion is far outweighed by the effects of other mechanisms that ultimately lead to a volume contraction. These can be roughly divided into electronic or structural NTE mechanisms, of which the latter are arguably the most common.<sup>117</sup> More precisely, structural NTE is related to transverse vibrations of supramolecular units in rather flexible framework materials as in oxides,<sup>118–120</sup> perovskites,<sup>121–123</sup> or prussian blue analogues,<sup>124–126</sup> for example, in which corner-sharing polyhedra oscillate perpendicular to the bond direction, resulting in an effective contraction of the distances between the centers of mass of connected polyhedra (in spite of the atomic bond lengths increasing with temperature).<sup>113</sup> Additionally, polyhedra can also rotate along their connecting axis and cause effective volume contraction (Figure 24). A benchmark example for structural NTE is  $\text{ZrW}_2\text{O}_8$ , which consists of  $\text{ZrO}_6$  octahedra that are connected to six  $\text{WO}_4$  tetrahedra via corner-sharing oxygen atoms, and the  $\text{WO}_4$  tetrahedra are only connected to three other  $\text{ZrO}_6$  octahedra, so one oxygen remains uncoordinated (Figure 25).<sup>127</sup> Remarkably, this material exhibits an NTE temperature range of 0.3–1050 K because of the corner-sharing octahedra and tetrahedra tilting more when these transverse vibrational modes become more favorable with increasing temperature. Importantly, different transverse modes can contribute differently to the overall magnitude of NTE. Mathematically, this corresponds to the Grüneisen parameter  $\gamma$ , which correlates with  $\alpha$  according to<sup>112</sup>

$$\alpha_V = \frac{\gamma C_V}{BV} \quad (4.3)$$

where  $C_V$  is the specific heat capacity. The Grüneisen parameter  $\gamma$  itself is calculated using

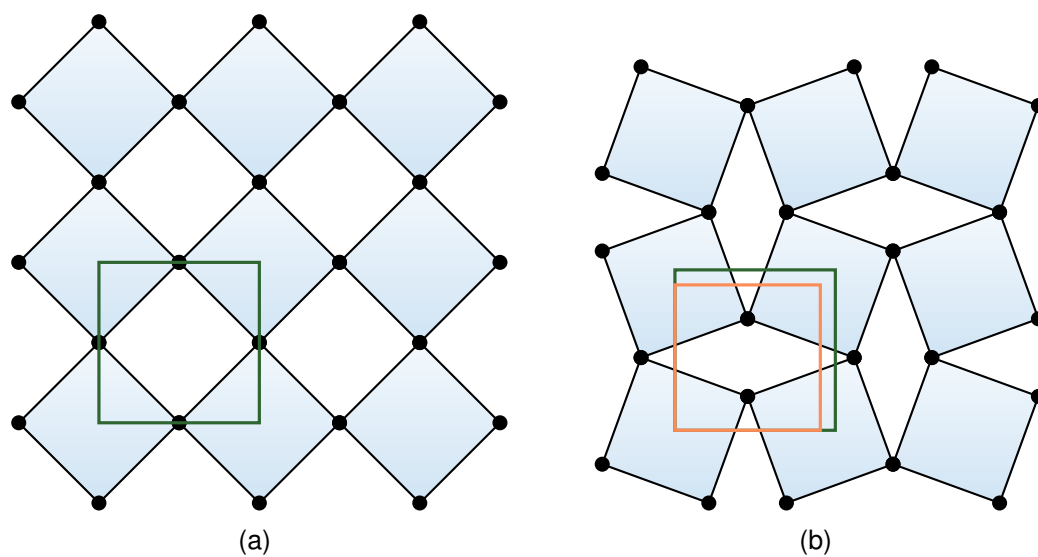


**Figure 24.** Illustration of volume shrinkage caused by rotation of equally sized tiles. The orange square on the right spans across the new tile centers and is smaller than the former (dark green) square when tile angles are  $90^\circ$ .

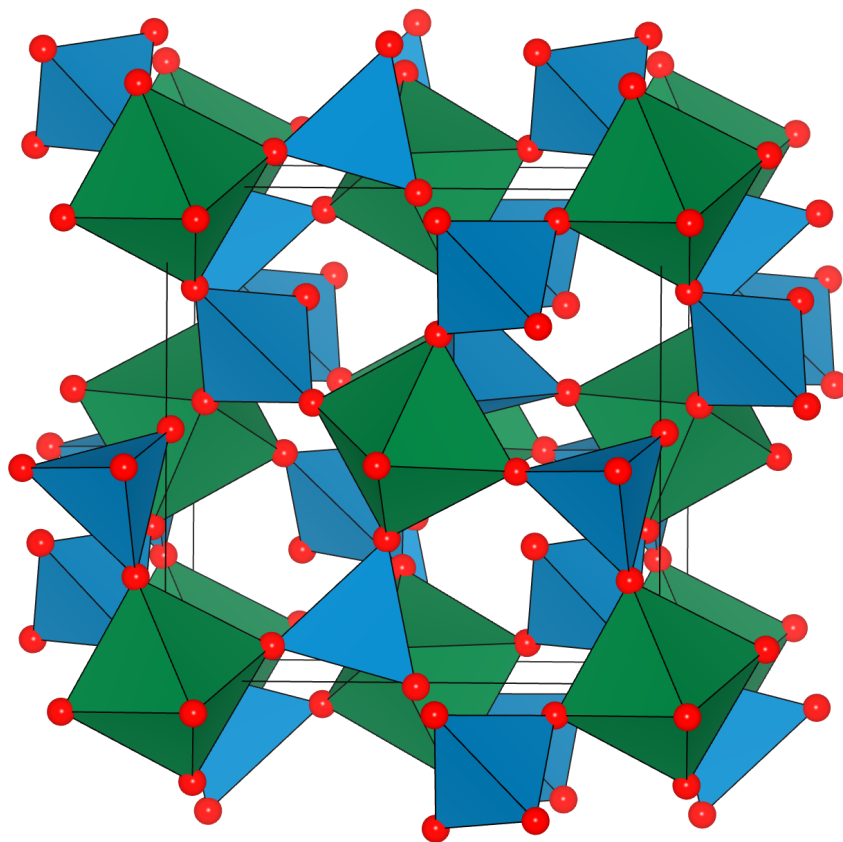


**Figure 25.** Crystal structure of  $ZrW_2O_8$  with corner-sharing  $ZrO_6$  octahedra (green) connected to six  $WO_4$  tetrahedra (blue).  $WO_4$  tetrahedra contain one terminal oxygen atom.

$$\gamma = -\frac{1}{2\omega^2} \frac{\partial \omega^2}{\partial s} \quad (4.4)$$

where  $\omega$  is the vibrational frequency and  $s$  is the applied strain on the solid during this vibration.<sup>112</sup> The two previous equations show that the sign of  $\gamma$  determines whether a mode leads to a negative or positive contribution to  $\alpha$ , and that the absolute value of  $\gamma$  increases for low frequency, that is, low energy modes. The implication of this relationship is that some mode contributions to NTE, which have higher  $\omega$ , are rather negligible compared to certain other modes. In other words, NTE materials contain rigid units in which modes are comparably stiff because they involve electrostatically unfavorable deformation of coordination polyhedra, and thus can be neglected for the interpretation of the NTE behavior in comparison to more flexible modes caused by linkages between rigid units, termed as rigid-unit modes (RUMs).<sup>112,113</sup>

MOFs are a new family of materials that generally exhibit NTE, as well.<sup>128–132</sup> The presence of RUMs in these materials may not seem surprising given the fact that flexible linkages between rigid units are innate to the concept of reticular chemistry, that is the modularity of MOFs composed of SBUs and organic linkers that self-assemble to supramolecular, porous architectures via coordination bonds (*cf.* Chapter 7). In comparison to structurally less complex oxides, the expansion between SBUs with carboxylates as linkers increases the number of possible modes that can contribute to NTE. Besides the transverse vibrational modes and rotations of coordination polyhedra or SBUs, the aromatic rings of the linkers are often found to exhibit a trampoline-like transverse motion that lead to NTE over a wide temperature range.<sup>131–134</sup> This is further amplified by the usually large void space in MOFs, which also typically exhibit a low bulk modulus because of their porosity and comparatively weak coordination bonds.<sup>117</sup> Consequently, NTE behavior is common in these materials.

Structural NTE in MOFs can be manipulated by interactions of the framework with guest molecules in the pore space. In fact, it was often discovered that fully evacuated MOFs show higher percentages of volume contraction, whereas pore filling with gases, solvent, or functional molecules can affect the expansion properties considerably. For example, decreased NTE of MOF-5 was observed after increasing the helium pressure, which was ascribed to a damping of the transverse linker motion when pores are filled.<sup>135</sup> Theoretical calculations suggest that the degree of NTE of MOF-5 can be controlled by the concentration of solvent molecules such as benzene or isopropanol, or other gases like propane in the MOF pores with possible switching between NTE and positive thermal expansion above a certain threshold.<sup>136</sup> A systematic study of the influence of host-guest interactions

---

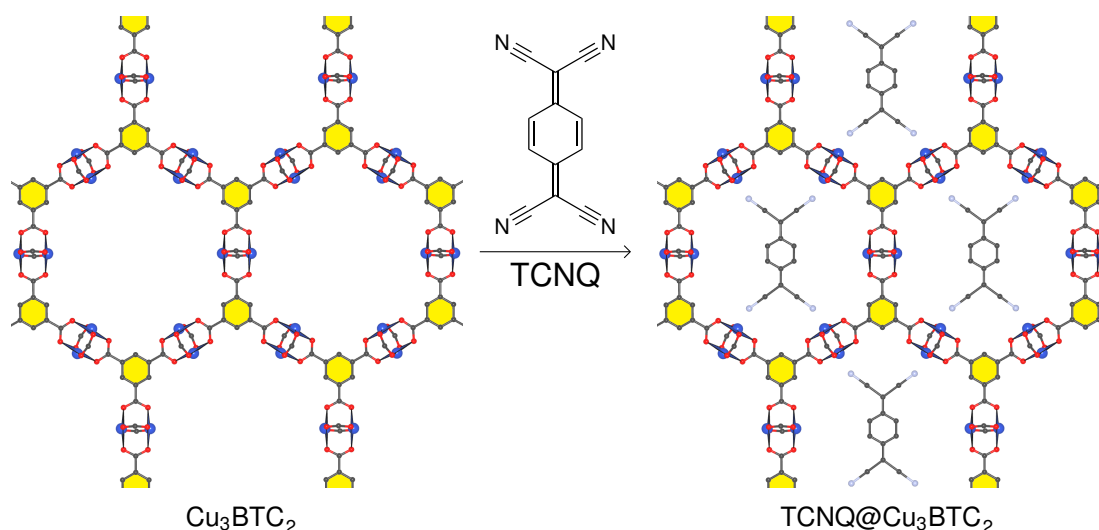


**Figure 26.** Retrofitting of  $\text{Cu}_3\text{BTC}_2$  with TCNQ. The guests are oriented within the crystallographic (111) plane of  $\text{Cu}_3\text{BTC}_2$ .

on NTE was conducted for the MOF  $\text{Cu}_3\text{BTC}_2$  that is filled with stoichiometric amounts of TCNQ to obtain the series  $x\text{TCNQ}@Cu_3\text{BTC}_2$  ( $x = 0.2, 0.4, 0.6, 0.8, 1.0$ ).<sup>137</sup>  $\text{TCNQ}@Cu_3\text{BTC}_2$  is known for its high increase of electrical conductivity after TCNQ is post-synthetically incorporated ("retrofitted"<sup>15,138</sup>) into the structure of electrically insulating  $\text{Cu}_3\text{BTC}_2$  (cf. Chapter 7).<sup>28,139</sup> Theoretical calculations and experimental data indicate that TCNQ coordinately bridges two OMS of two adjacent copper paddle-wheel SBUs to create additional linkages within the (111) crystallographic plane of the MOF (Figure 26).<sup>28,139,140</sup> Upon loading with TCNQ,  $\alpha_V$  of  $x\text{TCNQ}@Cu_3\text{BTC}_2$  increases gradually from  $-15.3 \times 10^{-6} \text{ K}^{-1}$  for  $x = 0$  to  $-8.4 \times 10^{-6} \text{ K}^{-1}$  for  $x = 1.0$ .<sup>137</sup> This was ascribed to an overall stiffening of the MOF accompanied by the cross-linking of SBUs with TCNQ, thereby increasing the bulk modulus of the material.

Subsequent work identified other dinitriles that are potentially suitable cross-linkers for retrofitting of  $\text{Cu}_3\text{BTC}_2$  via theoretical modeling of the nitrile- $\text{Cu}_3\text{BTC}_2$  interactions, and for some cases of the presented library such as 1,2-dicyanobenzene (DCB), 1,2,4,5-tetracyanobenzene (TCB), and 3,4-dicyanothiophene (DCT) the successful incorporation into the MOF was shown, as well.<sup>15</sup> The possibility of introducing several functional cross-linkers poses the question whether these dinitriles are also able to induce a decrease of NTE with increasing guest loading. Furthermore, a possible chemical influence on the retrofitted MOF properties, for instance via variation of sterics, or of the electronic structure and ligand donor strength of the applied cross-linker would further expand the toolbox of post-synthetic modification of NTE in MOFs. Accordingly, the following chapter deals with the synthesis and characterization of five different series of guest-loaded  $\text{Cu}_3\text{BTC}_2$ , using the guests DCB, TCB, DCT, as well as 2,3-dicyanonaphthalene

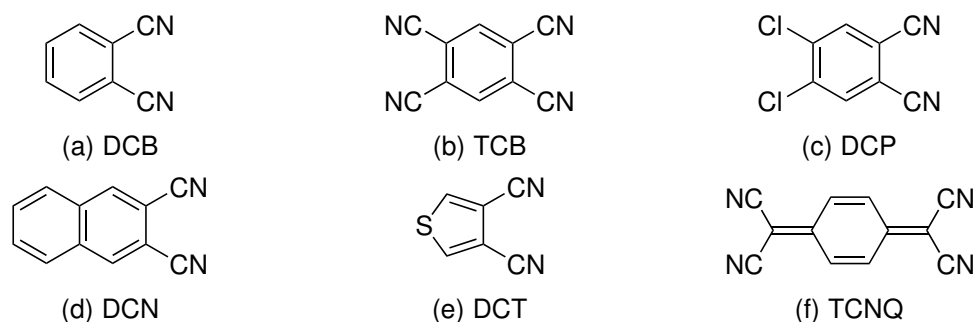


**Figure 27.** Cross-linkers used for the synthesis of  $(\text{Guest})_x\text{Cu}_3\text{BTC}_2$  ( $x = 0.5, 1.0$ ).

(DCN), 4,5-dichlorophthalonitrile (DCP), and TCNQ for a better comparability of the results with previous literature, using the VPI approach introduced in Chapter 2. The thermal expansion coefficients  $\alpha$  and relative volume changes are determined via variable temperature (VT)-PXRD of  $(\text{Guest})_x\text{Cu}_3\text{BTC}_2$  ( $x = 0.5, 1.0$ ) in a temperature range of 100–400 K and Pawley fitting of all obtained PXRD patterns to extract lattice parameters and cell volumes.

## 4.2 GUEST INFILTRATION OF $\text{Cu}_3\text{BTC}_2$ WITH OPEN METAL SITE BRIDGING DINITRILES

The different series of  $(\text{Guest})_x\text{Cu}_3\text{BTC}_2$  were obtained by enclosing stoichiometric amounts of activated  $\text{Cu}_3\text{BTC}_2$  and 0.5 or 1.0 eq. of dinitriles shown in Figure 27 in evacuated, flame-sealed ampules, which are then kept at 180 °C for 7 d in the oven. Under these conditions, the guest molecules sublime and diffuse into the highly porous structure of  $\text{Cu}_3\text{BTC}_2$ . The resulting powders are summarized in Table 7. Phase purity was confirmed by the absence of guest related reflections in the diffractograms of the host-guest complexes, which points at a full incorporation of the guests into  $\text{Cu}_3\text{BTC}_2$  (Figures 34–46). This is in line with previous observations that  $\text{Cu}_3\text{BTC}_2$  can accommodate up to 1.0 eq. of TCNQ, DCB, TCB, and DCT.<sup>15</sup> Lattice constants of the various host-guest complexes were obtained via Pawley profile fitting of the PXRD patterns in dependence of the measurement temperature (Figures 59–71) and are summarized in Tables 11–23. The absolute and relative volume changes of  $(\text{Guest})_x\text{Cu}_3\text{BTC}_2$  show varying temperature dependencies for different guests in the MOF pores (Figure 28). Pristine  $\text{Cu}_3\text{BTC}_2$  exhibits an  $\alpha_V$  value of  $-21.2 \pm 1.7 \times 10^{-6} \text{ K}^{-1}$ , which is in reasonable agreement with literature ( $-15.3 \times 10^{-6} \text{ K}^{-1}$ ,<sup>137</sup>  $-12.3 \times 10^{-6} \text{ K}^{-1}$ <sup>131</sup>). Generally, the incorporation of a guest molecule into the empty MOF leads to

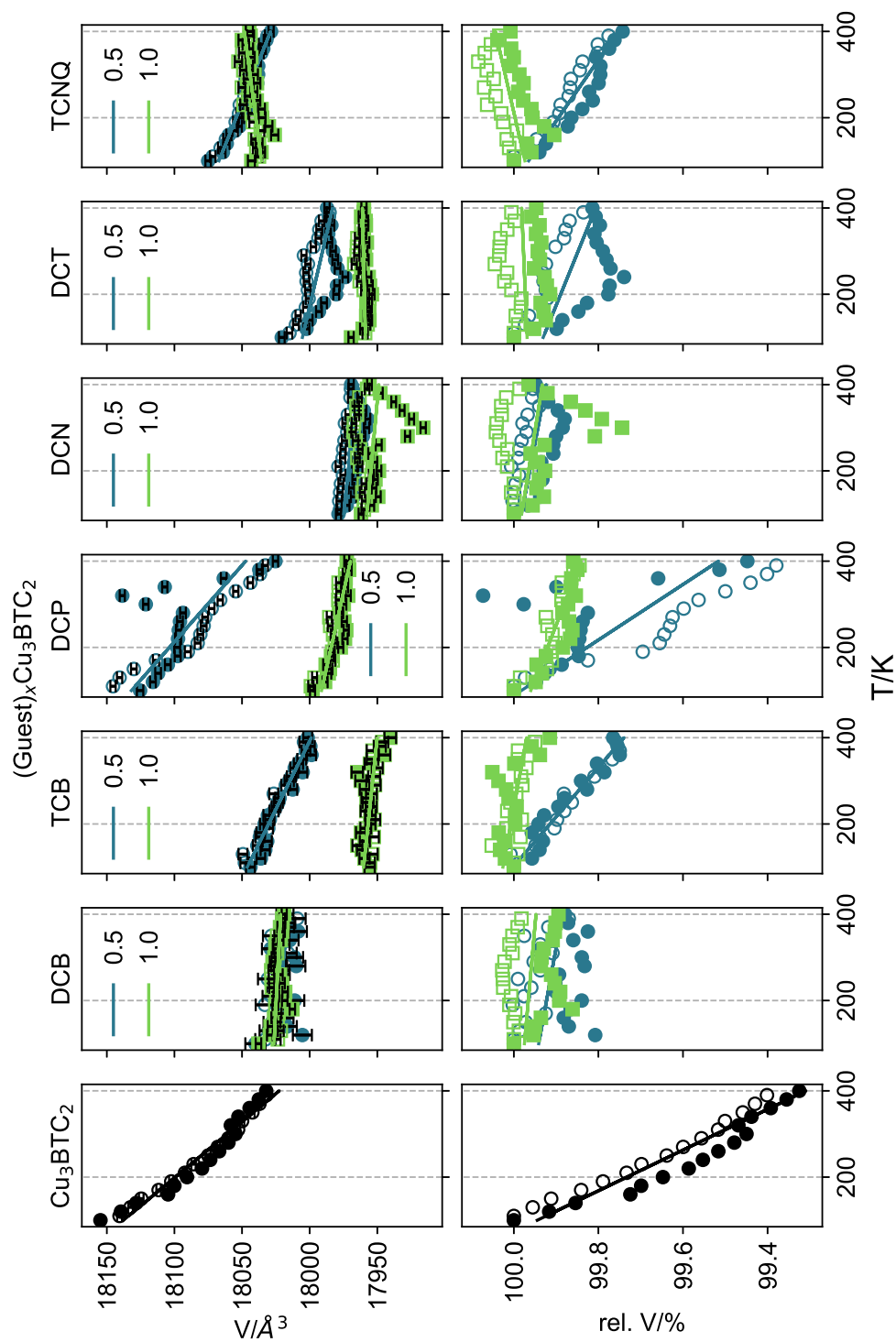


**Figure 28.** Absolute and relative volume changes of  $(\text{Guest})_x\text{Cu}_3\text{BTC}_2$  as a function of temperature. Guests are denoted above the subplots and different  $x$  are depicted in blue and green for 0.5 and 1.0 eq., respectively. Filled and empty markers correspond to the heating branch between 100 and 400 K in steps of 20 K and the cooling branch between 390 and 110 K in steps of 20 K, respectively.

**Table 7.** VPI of  $\text{Cu}_3\text{BTC}_2$  with 0.5 and 1.0 eq. of dinitriles at 180 °C for 10 d.
$$\text{Cu}_3\text{BTC}_2 \xrightarrow[180\text{ }^\circ\text{C, 7 d}]{\text{Guest}} (\text{Guest})_x\text{Cu}_3\text{BTC}_2$$

Dinitrile	No.	eq. of dinitrile
DCB	<b>I</b>	0.5
	<b>II</b>	1.0
TCB	<b>III</b>	0.5
	<b>IV</b>	1.0
DCP	<b>V</b>	0.5
	<b>VI</b>	1.0
DCN	<b>VII</b>	0.5
	<b>VIII</b>	1.0
DCT	<b>IX</b>	0.5
	<b>X</b>	1.0
TCNQ	<b>XI</b>	0.5
	<b>XII</b>	1.0

an increase of  $\alpha_V$  (decrease in NTE capability), as can be observed from the smaller volume changes in the VT-PXRD patterns (Figure 28), and increasing  $x$  enhances this effect even further. On one hand, this can be explained by the reduced pore volume and the presence of guest molecules within the pores that attenuate transverse motions of linkers and SBUs.<sup>135</sup> On the other hand, the dinitriles serve as bridging coordinating linkers of two copper paddle-wheels via their OMS and the resulting "retrofitting" enhances the bulk modulus of  $\text{Cu}_3\text{BTC}_2$ , and thus reduces  $\alpha_V$  according to equation 4.3.<sup>15,137</sup> Increasing the concentration of cross-linkers (increasing  $x$ ) reduces pore volumes even further and bridges more paddle-wheels, resulting in lower NTE capability. Focusing on the members of the  $(\text{Guest})_{0.5}\text{Cu}_3\text{BTC}_2$  series, interesting differences become apparent between the individual guests (Figure 29). For DCB and DCN, the respective compounds **I** and **VII** show the highest  $\alpha_V$  values of  $(-1.9 \pm 1.8)$  and  $-1.9 \pm 1.3 \times 10^{-6} \text{ K}^{-1}$ , followed by **IX** (DCT) and **XI** (TCNQ) with  $\alpha_V$  of  $(-4.1 \pm 2.2)$  and  $-7.0 \pm 0.8 \times 10^{-6} \text{ K}^{-1}$ . The last value is in good agreement with previously reported thermal expansion coefficients of  $0.5\text{TCNQ}@Cu_3\text{BTC}_2$  ( $\approx -9 \times 10^{-6} \text{ K}^{-1}$ ).<sup>137</sup> The lower absolute value observed in this study can be explained by a longer reaction time for the VPI, which is expected to give a better distribution of guests within individual MOF crystals and lead to a higher degree of retrofitting. This is emphasized even more by the comparison of  $\alpha_V$  of **XII** with  $1.0\text{TCNQ}@Cu_3\text{BTC}_2$  ( $2.3 \pm 1.1 \times 10^{-6} \text{ K}^{-1}$  vs.  $-8.4 \times 10^{-6} \text{ K}^{-1}$ ).<sup>137</sup> Looking at TCB and DCP, more striking thermal expansivities are observed for **III** and **V** with  $\alpha_V$  values of  $(-8.8 \pm 0.9)$  and  $-15.6 \pm 4.8 \times 10^{-6} \text{ K}^{-1}$ , the latter com-



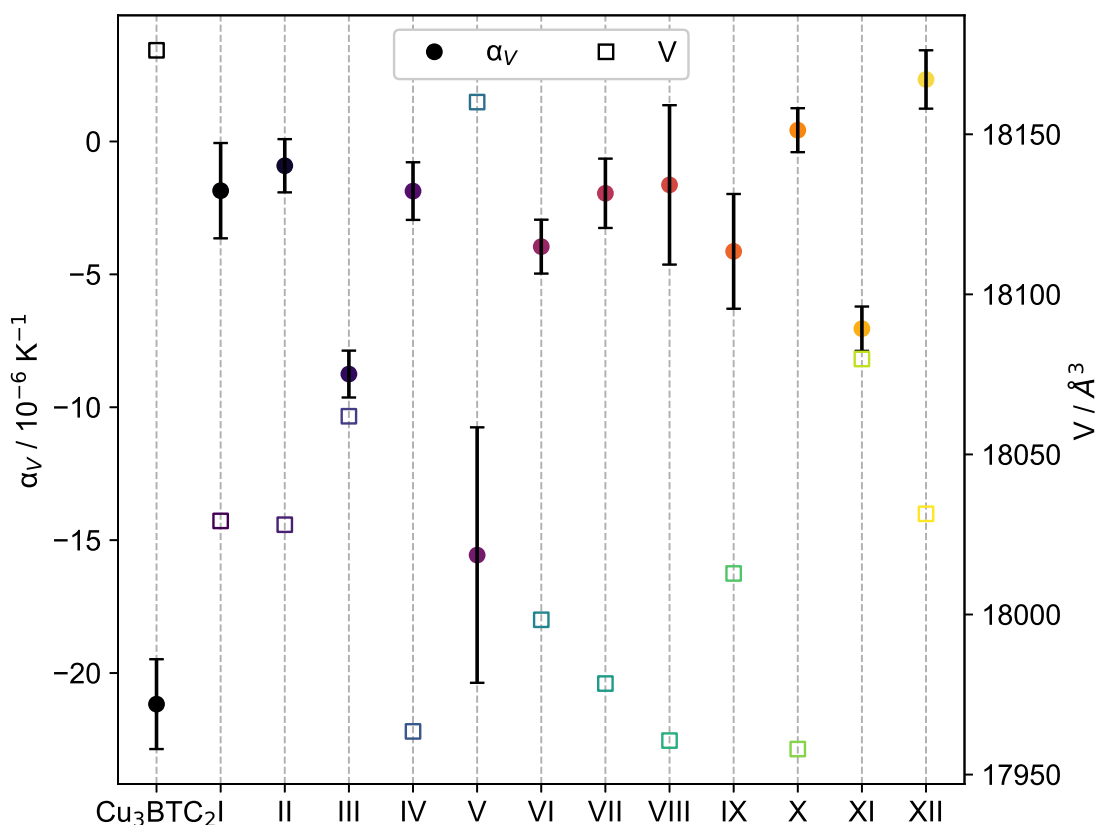


**Figure 29.** Thermal expansion coefficient  $\alpha_V$  and unit cell volume  $V$  at 100 K of (Guest)<sub>x</sub>Cu<sub>3</sub>BTC<sub>2</sub>.

pound showing considerably higher NTE compared to the other series members at equal concentrations. Note that the calculated  $\alpha_V$  values have comparatively high errors due to the hysteresis effects observed in the temperature-volume plots, which lead to a bad fit of the regression line through the measurement points (Figure 28). Nevertheless, the data shows clear differences in NTE behavior for different guests in Cu<sub>3</sub>BTC<sub>2</sub>.

### 4.3 VIBRATIONAL ANALYSIS OF RETROFITTED (GUEST)<sub>x</sub>CU<sub>3</sub>BTC<sub>2</sub>

A possible method to explain these differences has been previously discussed by describing the bridging cross-linkers as quasi-harmonic springs with different spring constants between two OMS at adjacent copper paddle-wheels, where higher spring constants correlated with a higher bulk modulus, and thus lower absolute thermal expansion coefficients.<sup>137</sup> In the previous study, higher spring constants were translated with increasing cross-linker concentrations within the MOF. However, these could also be described as different bond strengths between the cross-linker and OMS, where cross-linkers with different electronic structures

may yield architectures in which the cross-linkers interact more strongly with the framework than others. Note that this approximation ignores bond strength changes within the guest molecule, or other deformation processes that might occur. FTIR and Raman spectroscopy have previously been used to probe the phonon modes of  $\text{Cu}_3\text{BTC}_2$  in the far-infrared regime below  $400\text{ cm}^{-1}$ .<sup>133,137,141,142</sup> Additionally, screening of the nitrile stretching region between  $2100\text{--}2300\text{ cm}^{-1}$  of the different guests prior and after the VPI may also allow insight into the interaction of the nitrile functional group of the guest with the copper OMS. Nitriles are able to partake in  $\pi$ -backbonding in a coordination bond with a metal cation, and thus the nitrile stretching frequency can serve as a probe of the coordination bond strength.<sup>143,144</sup> Looking at the FTIR spectra of  $(\text{Guest})_x\text{Cu}_3\text{BTC}_2$ , only small shifts are observed between pristine guests and the host-guest complexes (Figure 30). Common for all samples except **XII**, the absorbances are all on a similarly low scale due to comparably low concentrations of the guest in the samples. In **XII**, the higher absorbances might be a result of the  $\text{Cu}(\text{TCNQ})$  side phase formation as indicated by the signal at  $2170\text{ cm}^{-1}$ .<sup>28</sup> While the concentration of dinitriles in **I** seems to be too low to detect any signal, this changes for higher loading amounts as in **II**. Interestingly, TCB-loaded MOFs (**III**, **IV**) and TCNQ-loaded MOFs (**XI**, **XII**) are the only samples that exhibit a red-shift of the  $\text{C}\equiv\text{N}$  stretching frequency with incorporation into  $\text{Cu}_3\text{BTC}_2$ , with the differences between the pristine guest and peak maximum in the spectrum of the host-guest complex increasing with increasing guest loading. For instance, while  $\Delta\nu$  is close to zero in the spectra of **III** and **XI**, it increases to  $-6$  and  $-17\text{ cm}^{-1}$  for **IV** and **XII**, respectively. A likely explanation for the different  $\Delta\nu$  values is that the electron affinity of TCNQ is higher than for TCB as can be deduced from the different reduction potentials of  $-0.25$  and  $-1.18\text{ V}$  (vs.  $\text{Fc}^{0/+}$ ) for TCNQ and TCB, respectively.<sup>145</sup> This could be interpreted as a stronger interaction between Cu and the  $\text{C}\equiv\text{N}$  bonds of TCNQ. On the other hand, the remaining host-guest complexes all exhibit a blue-shift of the  $\text{C}\equiv\text{N}$  stretching frequency compared to the pristine guest molecule. The  $\Delta\nu$  values for the higher loaded MOFs with DCB (**II**), DCP (**VI**), DCN (**VIII**), and DCT (**X**) are  $5$ ,  $4$ ,  $11$  and  $12\text{ cm}^{-1}$ , respectively, and similar values are obtained for the corresponding MOFs with lower guest contents. While this generally points at a weaker interaction between the guest and  $\text{Cu}_3\text{BTC}_2$ , it is not suitable to explain the striking differences between **V** and similarly behaving **I**, **VII** and **IX**. Nevertheless, these results indicate that at a substoichiometric level of guest within the MOF, the materials containing guests with electron-deficient substituents at the aromatic core, such as additional nitrile ligands or chlorine substituents as in **III**, **V**, and **XI**, combined with a low  $\Delta\nu$  in the FTIR spectrum, leads to smaller quenching of the RUM modes responsible for the NTE in  $\text{Cu}_3\text{BTC}_2$ . Note that only negligible

---

energetic differences have been observed computationally between DCB and TCB, so the mechanisms at play here go beyond a simple geometric matching of guests and coordination sites.<sup>15</sup> At higher guest concentrations, this effect is outweighed by the higher degree of retrofitting that inevitably increases the bulk modulus and leads to smaller thermal expansivity.

#### 4.4 CONCLUSION

In conclusion, a series of infiltrated  $(\text{Guest})_x\text{Cu}_3\text{BTC}_2$  with varying guests and  $x$  were obtained by using the VPI approach which allows easy control over the guest amount. VT-PXRD measurements revealed that crystallinity is retained and that the series members exhibit considerable residual NTE compared to the pristine MOF dependent on the nature of the guest, at least at lower concentrations. Analysis of the FTIR spectra shows that TCB and TCNQ exhibit a red-shift of the  $\text{C}\equiv\text{N}$  stretching frequency after incorporation into the MOF at high concentrations, which might be a result of CT to these highly electron-deficient ligands. The electron-deficiency seems to be a crucial parameter for the NTE behavior of  $(\text{Guest})_x\text{Cu}_3\text{BTC}_2$ , for the more electron-deficient linkers TCB, DCB, and TCNQ exhibit the strongest NTE in the host-guest complexes at substoichiometric amounts. At higher concentrations, these effects become largely irrelevant. At this stage, it is clear that there are other factors that have considerable effect on the changes of NTE because electronic considerations alone cannot explain the striking differences between less electron-deficient DCP in **V**. Looking forward, FTIR measurements in the far-infrared regime may yield further insight into the effects of the guests at the phonon modes of  $\text{Cu}_3\text{BTC}_2$  and how they are modulated by the presence of different guests. Computational studies may contribute further to the explanation of the mechanisms taking place. Altogether, the study shows that the potential of retrofitting reaches beyond structural aspects of MOF chemistry and that different functionalities and physical properties of applied cross-linkers may lead to clever post-synthetic design of MOFs exceeding the current state-of-the-art.

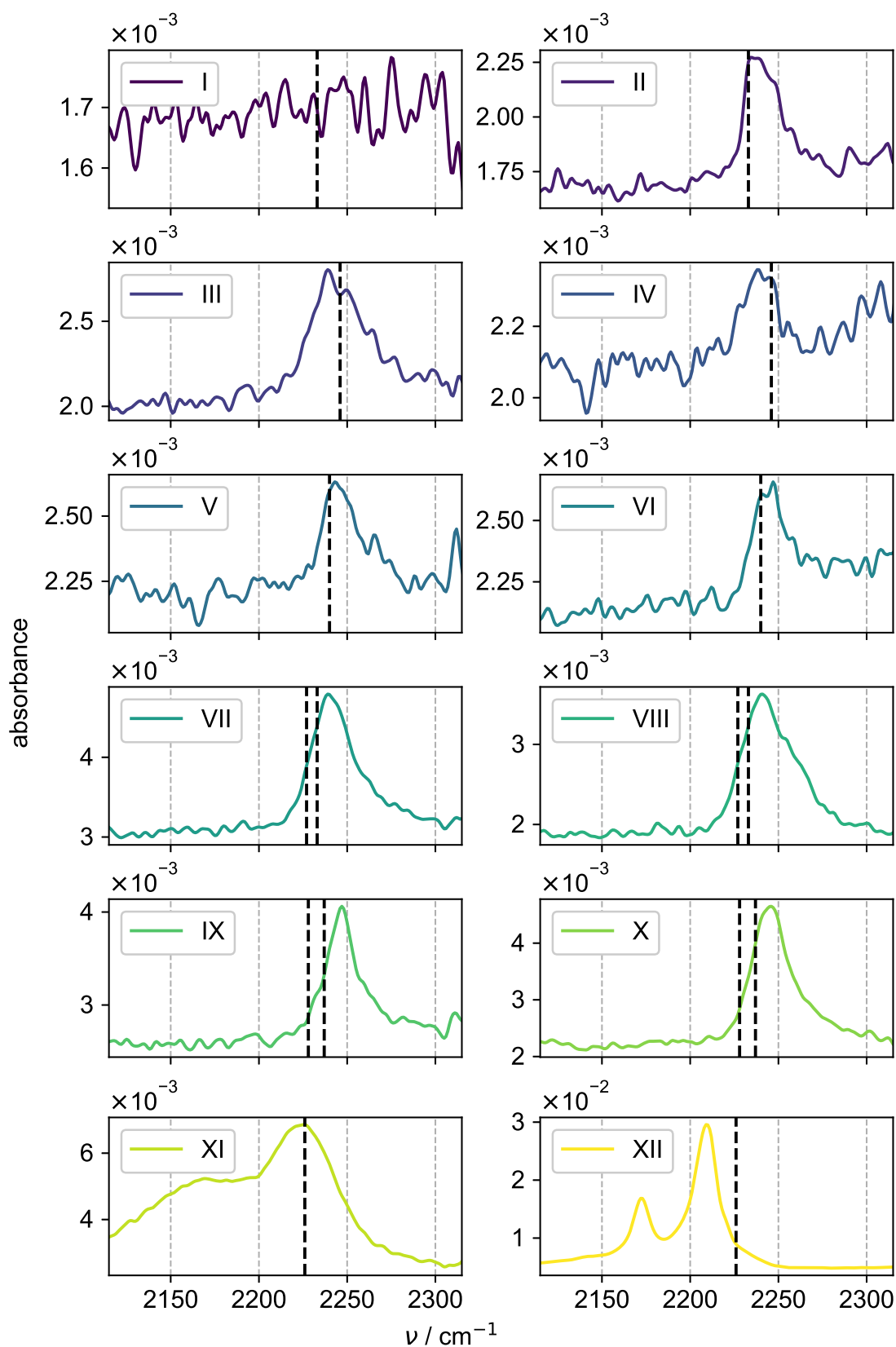


**Figure 30.** FTIR spectra of  $(\text{Guest})_x\text{Cu}_3\text{BTC}_2$  with focus on the nitrile stretching frequency region at  $2100\text{--}2300\text{ cm}^{-1}$ . Nitrile signals of free-standing guests are indicated as a black dashed line.

# 5

## *Conclusion*

MOFs have shown incredible potential in the design of multifunctional materials with modular structures and properties. Especially the exploitation of the pore space to introduce new functionality, which is not inherent in the pristine MOF, significantly expands the designing possibilities. However, this synthetic freedom also leaves behind a huge parameter space that is important to study in order to rationalize the effects of small changes between the interactions of MOFs and functional guests for the resulting material properties. The objective of this thesis was to unveil some of these influences and expand the knowledge of to which extent guests can alter the MOF host properties and how these changes can be manipulated in a controlled fashion.

In the first study, CT processes in the host-guest complexes of reducing TCNE and the  $M_2$ TTFTB ( $M^{2+} = \text{Zn, Cd}$ ) were at the center of attention. TCNE was expected to diffuse into the pores of  $M_2$ TTFTB during the VPI process and induce a CT from electron-rich TTFTB linkers to oxidizing TCNE, a process that is known to significantly enhance the electrical conductivity in other TTF-based CT complexes such as TTF-TCNQ. In fact, structural integrity was observed for TCNE-loaded MOFs, but their electrical conductivity showed significant differences based on the employed reaction conditions during VPI. These differences could be rationalized by a detailed vibrational spectroscopic analysis of the signals of TTFTB and TCNE, which present a probe of the oxidation state of these compounds due to the comparably large structural changes their bonds undergo upon a redox event. Especially the in-depth analysis of the  $\text{C}\equiv\text{N}$  stretching frequencies in  $(\text{TCNE})_x M_2 \text{TTFTB}$  gave a deep understanding of the composition of these host-guest complexes, which could be deduced from a deconvolution of the  $\text{C}\equiv\text{N}$  band into the corresponding contributions of neutral  $\text{TCNE}^0$  and radical-anionic  $\text{TCNE}^{\bullet-}$ . Strikingly, not the absolute concentration of  $\text{TCNE}^{\bullet-}$  in  $(\text{TCNE})_x M_2 \text{TTFTB}$ , but

rather the ratio between  $\text{TCNE}^0$  and  $\text{TCNE}^{\bullet-}$  was the determining factor in the electrical conductivity changes from pristine MOF to host-guest complex, and this ratio was dependent on the employed reaction condition. This study aimed at answering the first two research questions formulated in the beginning of this thesis, and it is believed to be a valuable contribution to the better understanding of host-guest interaction mechanisms and the control thereof.

In the second study, which is directly related to the topic of the first study, the higher goal was to investigate the electrical properties of a expectedly similar MOF using a TSF-based linker. CT complexes based on TSF are known for their higher electrical conductivity compared to their TTF congeners, so they are very interesting to explore. However, research on the functionalization of TSF, especially such including aromatic substituents, is surprisingly scarce. Not soon after the beginning of this study, it moved from a MOF related topic to a quest of finding a synthetic route towards aryl-substituted TSF. This is because the palladium-catalyzed direct arylation route of TTF to aryl-substituted derivatives, which initiated research of TTFTB-based MOFs, led to a full destruction of the TSF molecule. A library of different routes and reaction conditions were tested, which were mostly all ineffective or led to the destruction of TSF. Finally, a ligand-free copper-catalyzed direct arylation with aryl iodides as substrates was the long-awaited success, albeit with moderate yields. The target compound of these syntheses could be characterized using NMR and MS, but its isolation still proves to be challenging. Nevertheless, this study presents the first successful efforts to directly functionalize TSF and is encouraging subsequent work to improve yields. More research, including computational and mechanistic studies, are needed to fundamentally understand the peculiar reactivity of TSF and the mechanisms of the copper catalyzed direct arylation of the same.

In the last study, the NTE of  $\text{Cu}_3\text{BTC}_2$  was explored in the presence of different functional guests in its pores. This MOF is known to experience a reduced NTE capability when loaded with TCNQ, which was ascribed to a stiffening of the entire framework. Using this knowledge, the question arose how different guests with similar dinitrile moieties affect the resulting NTE of  $\text{Cu}_3\text{BTC}_2$ , which also serves the purpose of providing answers for the third research question of this thesis. Previous computational research showed that a whole library of dinitrile guests is able bridge adjacent copper paddle-wheels in  $\text{Cu}_3\text{BTC}_2$  with little energetic differences between them.<sup>15</sup> The study focused on the guests DCB, TCB, DCP, DCN and DCT, while also comparing to TCNQ-loaded  $\text{Cu}_3\text{BTC}_2$  as a reference. Generally, all host-guest complexes observed reduced NTE for  $(\text{Guest})_{1.0}\text{Cu}_3\text{BTC}_2$ , which is in line with previous literature.<sup>137</sup> On the other hand, differences appeared for the series of  $(\text{Guest})_{0.5}\text{Cu}_3\text{BTC}_2$ , i.e. with reduced concentration of guests

---

---

in the pores. Here, the generally more electron-deficient dinitriles containing electron-withdrawing substituents as in the case of TCB, DCP, and TCNQ were less effective in quenching the NTE in comparison to the more electron-rich guests DCB, DCN, and DCT. Vibrational analysis of the host-guest complexes showed a red-field shift of the  $C\equiv N$  stretching band for TCB and TCNQ, while the bands DCB, DCN, and DCT were blue-shifted, which may be an indicator of the different material properties. However, DCP with the strongest NTE in **V** also showed a blue-shifted  $C\equiv N$  band in the FTIR spectrum, which points at other mechanisms possibly playing a significant role which are still unknown at this stage. Taken as a whole, this study shows that supposedly small changes in the functional guest molecules can induce unexpectedly large differences in the resulting properties of the host-guest system, but more research is needed to quantify such effects. In conclusion, the thesis has provided some answers for the above-mentioned research question and has revealed the rich chemistry and analytical issues of host-guest complexes in MOFs. Providing general answers to how one guest will interact with a MOF may always remain difficult, but comparing different guests in a series and correlating the material properties of these series members with the guest concentration and nature allows to acquire some knowledge about interaction mechanisms and general reactivity trends. This is further complicated by how these interactions are often in a low-energy regime, and subtle changes in their physical and chemical properties are more difficult to extract from analytical data. The use of specific functional molecules that act as “tags” such as TCNE with redox-sensitive vibrational signals is of big advantage in these endeavors and the conclusions drawn from experiments with these systems can be also transferred to guests that are more difficult to study. Generally speaking, the ability to understand host-guest interactions in MOFs is strongly linked to the accuracy of theoretical models and strategies to make seemingly small energetic changes spectroscopically visible. Looking at possible applications of guest-loaded MOFs, this thesis underlines the potential of (fine-)tuning of physical and chemical properties of these highly diverse systems, a process which will be of large importance for their use as new multifunctional materials beyond the academic scale.

---





# 6

## *Experimental*

### 6.1 GENERAL

Unless otherwise stated, chemicals were obtained commercially and used without further purification. Organic solvents such as *n*-pentane, *n*-hexane, toluene, diethyl ether, THF, DCM, and acetonitrile were dried using a MBRAUN solvent purification system, in which solvents were passed through consecutive adsorbent columns by application of argon pressure gradients. All other solvents were dried using standard purification procedures, e.g., by passing through a column of activated alumina under inert atmosphere, storing over activated molecular sieves, or distillation. Such treated solvents exhibited a purity above 99% and water contents below 5 ppm, as verified by Karl-Fischer titration. Solvents were degassed by freeze-pump-thaw cycles and subsequent saturation with argon. Unless otherwise stated, column chromatographic purifications were carried out using silica gel (particle size distribution 60–210  $\mu\text{m}$ ). MOF synthesis was carried out in Schott flasks (100 mL volume) or teflon screw cap scintillation vials (20 mL). All MOF reactions were conducted in standard laboratory ovens (Mettler UN55). Air-sensitive samples were stored in an argon-filled glovebox (MBRAUN LAB-master Pro Glove Box Workstation, M. Braun Inertgas-Systeme GmbH; argon purity 99.996%, Westfalen AG; O<sub>2</sub> level < 0.5 ppm, H<sub>2</sub>O level < 0.5 ppm). VPI of M<sub>2</sub>TTFTB powder with TCNE, and Cu<sub>3</sub>BTC<sub>2</sub> with various dinitriles was performed in borosilicate glass ampules of approx. 10 cm length that were prepared from borosilicate glass tubes (10 mm diameter, 1 mm wall thickness). The tubes were dried in an oven at 120 °C before use. Then, they were transferred into the glovebox, filled with educts, and closed with a quick-fit. Outside of the glovebox, the tube was evacuated and flushed with argon one time and then evacuated

again until a pressure of ca.  $3 \times 10^{-2}$  mbar was reached. Next, the ampule was flame-sealed using a propane/O<sub>2</sub> burner, resulting in a closed, evacuated system. Reactions containing selenium often produced red or black coatings on the inner sides of the glass flask which could not be removed using standard KOH-isopropanol-water baths. These were cleaned using piranha solution (7:3 mixture of concentrated H<sub>2</sub>SO<sub>4</sub> and H<sub>2</sub>O<sub>2</sub> (30%)). Note that the forming water-soluble selenates are highly poisonous, so cleaning steps should be performed carefully wearing adequate safety equipment. Lithium bases such as LDA or lithium 2,2,6,6-tetramethylpiperidide (LiTMP) were titrated against menthol in diethyl ether at 0 °C in the presence of 1,10-phenanthroline (phen) as indicator prior to use. TMPMgCl · LiCl and TMPZnCl · LiCl were synthesized according to a literature procedure and titrated against benzoic acid in THF at 0 °C with 4-(phenylazo)diphenylamine as indicator.<sup>82</sup>

## 6.2 ANALYTICAL METHODS

### 6.2.1 Infrared Spectroscopy

FTIR measurements were performed with solid samples in air on a PerkinElmer Frontier FTIR spectrometer equipped with a Ge attenuated total reflectance unit at room temperature in the range from 700–4000 cm<sup>-1</sup> with a resolution of 4 cm<sup>-1</sup> and a deuterated triglycine sulfate (DTGS) detector. Twenty scans were recorded per measurement. Spectra were processed with the supplier software and further analyzed using Matplotlib (python program library), with the aid of the Imfit<sup>146</sup> and rampy<sup>147</sup> python packages. Absorption bands are consecutively reported as position (wavenumber in cm<sup>-1</sup>).

### 6.2.2 Raman Spectroscopy

Raman spectra were recorded on an inVia Reflex Raman microscope equipped with a research grade optical microscope (Leica DM2700M, magnification 50×) coupled to a high-performance Raman spectrometer (Renishaw). A 532 nm laser (RL532C, class 3b) was used as the excitation source. Samples were flame-sealed in borosilicate capillaries under inert atmosphere prior to the measurement. Spectra were processed with the supplier software and further analyzed using

---

Matplotlib (python program library). Absorption bands are consecutively reported as position (wavenumber in  $\text{cm}^{-1}$ ).

### 6.2.3 Nuclear Magnetic Resonance Spectroscopy

NMR spectra were recorded on a Bruker Advance III AV400 US spectrometer in  $\text{CDCl}_3$  or  $\text{DMSO}-d_6$ . Chemical shifts (in  $\delta$ ) are described in ppm and referenced to the residual solvent resonances as internal standards ( $^1\text{H}$ :  $\text{CDCl}_3$  7.26 ppm,  $\text{DMSO}-d_6$  2.50 ppm;  $^{13}\text{C}$ :  $\text{CDCl}_3$  77.16 ppm,  $\text{DMSO}-d_6$  39.52 ppm).  $^{13}\text{C}$ - and  $^{77}\text{Se}$ -NMR were conducted in fully proton decoupled modes. The spectra were processed and analyzed using the MestreNova (Mestrelab Research S. L.) software, version 14.2.1. Multiplicities are abbreviated as s = singlet, d = doublet, t = triplet, q = quartet, p = quintet, h = sextet, dd = doublet of doublets, m = multiplet.

### 6.2.4 X-Ray Diffraction

PXRD data were collected in a  $2\theta$  range of  $5^\circ$  to  $50^\circ$  in steps of  $0.01^\circ$  on a PANALYTICAL EMPYREAN equipped with a  $\text{Cu K}_{\alpha 1}$  radiation source ( $\lambda = 1.54059803 \text{ \AA}$ ) operated at 45 kV and 40 mA. Samples were filled into borosilicate capillaries of 0.7 mm diameter and placed in a capillary spinner. A focusing beam mirror equipped with a  $0.0625^\circ$  divergence slit and 0.02 rad soller slits was used as the incident beam optic. The diffracted beam was detected by a PIXcel1D detector in receiving slit mode equipped with a  $0.125^\circ$  antiscatter slit and 0.02 rad soller slits. Patterns were normalized to the highest intensity reflection. VT-PXRD was performed in capillary mode in transmission geometry on a STOE STADI P (Darmstadt, Germany) diffractometer equipped with a  $\text{Mo K}_{\alpha}$  radiation ( $\lambda = 0.7093 \text{ \AA}$ ) source, a curved  $\text{Ge}(111)$  monochromator and a DECTRIS Mythen 1K detector. Voltage and current were 50 kV and 40 mA, respectively. The measurement range was from  $2^\circ$  to  $30^\circ$  ( $2\theta$ ). An Oxford Habcryo-X Cryostream 700 Cobra was used for temperature control with steps of 20 K. The obtained diffraction patterns were analyzed by performing a Pawley profile fit analysis using TOPAS Academic v6 in combination with jEdit for creating the input files.<sup>148,149</sup>

### 6.2.5 Gas Sorption

Gas sorption experiments were performed on a Micromeritics 3flex. Approx. 40 mg of MOF was used, which was activated at 200 °C for pristine MOF samples and at 40 °C for (TCNE)<sub>x</sub>M<sub>2</sub>TTFTB prior to the first measurement on a SmartVacPrep. Purity of the gases used was 99.999%. Nitrogen isotherms were measured at 77 K. CO<sub>2</sub> isotherms were measured at 196 K. The BET surface area was calculated from data points in the relative pressure range from 0.01 to 0.1. Sorption data were processed using the 3Flex Software Version 5.01 of Micromeritics Instrument Corp. For the samples **1**, **3**, and **5**, it was not possible to measure the full relative pressure range due to long equilibration times and other indications pointing at strong helium adsorption in the remaining, ultra-narrow pore volume of these samples which was not accessible for N<sub>2</sub> and CO<sub>2</sub>. Combined with a generally low gas uptake, this leads to large systematic errors which only allow a semi-quantitative comparison of porosity changes between these materials.<sup>150</sup> Therefore, dead volumes of sample tubes was determined after the adsorption measurement using He to avoid interference effects and minimize errors.

### 6.2.6 Elemental Analysis

Elemental analysis for the elements C, H, N, and S was carried out on a EuroEA Elementaranalysator (HEKATECHANALYSENTECHNIK) at the microanalytical laboratory of the Technical University of Munich (TUM). The weight percentages  $\omega_E$  for each element in (Guest)<sub>x</sub>(MOF) were calculated according to

$$\omega_E = \frac{m_{E,t}}{m_t} = \frac{n_{E,t} \times M_E}{m_t} \quad (6.1)$$

where  $m_{E,t}$  is the total mass of an element  $E$  in the compound of total mass  $m_t$ , which can be rewritten as the total moles of atoms of said element  $n_{E,t}$  multiplied by the elemental molecular weight  $M_E$ . The total moles of elements is the sum of moles of elements from the MOF and the guest molecule, so

$$n_{E,t} = n_{E,MOF} + n_{E,Guest}. \quad (6.2)$$

These terms can be expressed in terms of the moles of MOF and guest via

$$n_{E,MOF} = i_{E,MOF} \times n_{MOF} \quad (6.3)$$

and

$$n_{E,Guest} = j_{E,Guest} \times n_{Guest} \quad (6.4)$$

where  $i, j$  are the coefficients of the element in the sum formula of MOF and guest, respectively. Rewriting  $n_{Guest}$  as

$$n_{Guest} = x \times n_{MOF} \quad (6.5)$$

leads to an expression independent of  $n_{MOF}$ :

$$\begin{aligned} \omega_E &= \frac{i_{E,MOF} \times n_{MOF} M_E + j_{E,Guest} \times x \times n_{MOF} M_E}{\sum_{E,i} i_{E,MOF} \times n_{MOF} M_E + \sum_{E,j} j_{E,Guest} \times x \times n_{MOF} M_E} \\ &= \frac{i_{E,MOF} \times M_E + j_{E,Guest} \times x \times M_E}{\sum_{E,i} i_{E,MOF} \times M_E + x \sum_{E,j} j_{E,Guest} \times M_E} \\ &= \frac{M_E (i_{E,MOF} + x j_{E,Guest})}{M_{MOF} + x M_{Guest}} \end{aligned} \quad (6.6)$$

Accordingly, the guest content  $x$  (in equivalents per formula unit of MOF) is calculated by solving the previous equation for  $x$  and inserting the experimentally determined value of  $\omega$ .

$$x = \frac{\omega_E M_{MOF} - M_E i_{E,MOF}}{M_E j_{E,Guest} - \omega_E M_{Guest}} \quad (6.7)$$

In the case of  $(TCNE)_x M_2 TTFTB$ , the pristine MOF does not contain nitrogen (i.e.,  $i_{E,MOF} = 0$ ), so the reaction is simplified even further (here:  $M = Zn$ ):

$$x = \frac{\omega_N \times 811.49 \text{ g mol}^{-1}}{14.01 \text{ g mol}^{-1} \times 4 - \omega_N \times 128.09 \text{ g mol}^{-1}} \quad (6.8)$$

### 6.2.7 Electron Microscopy

Top-view SEM images of MOF powders were obtained on a JEOL JSM-7500F field emission scanning electron microscope equipped with an EDS-System (Oxford Instruments) using an X-Max detector and INCA-Software and an accelerating voltage of 1 kV. Samples were not coated with metal prior to the measurement. DF-STEM micrographs and EDS elemental mapping were recorded with a JEM NEOARM microscope (JEOL) with a cold field-emission electron source operated at 200 kV. Samples were prepared by depositing a small amount of the crystalline products onto carbon coated copper grids (200 mesh), i.e., without using any solvent to prevent possible dissolving of the guest molecules.

### 6.2.8 Mass Spectrometry

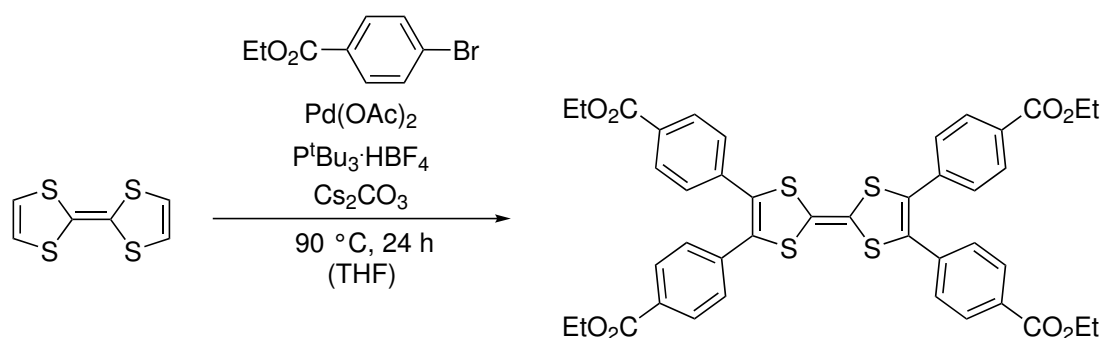
LIFDI-MS data were measured on an Exactive Plus Orbitrap system by Thermo Fisher Scientific equipped with an ion source (LIFDI) from LINDEN CMS GmbH. The samples were dissolved in either dry toluene or THF and filtered over a syringe filter under an inert atmosphere. Spectrometric data was processed using the supplier software and further analyzed using Matplotlib (python program library). MS results are given in  $m/z$ .

### 6.2.9 Electrical Conductivity

The two-contact probe method was used to measure the electrical conductivity of the series of  $(\text{TCNE})_x\text{M}_2\text{TTFTB}$ . Approximately 50 mg of the samples was pressed into pellets of 1 cm diameter between two hardened steel pistons, which also function as the electrodes, at a total pressure of 0.3 GPa in special cell casings that have been reported by Janek and coworkers.<sup>151</sup> They were mounted in aluminum frames with a 10 N m torque to maintain the pressure on the pellet. Current-voltage curves were recorded using a PGSTAT302N Metrohm potentiostat by measuring three cycles of the current-voltage response between  $-0.1-0.1$  V, starting from 0 V (open circuit voltage (OCV)). The thickness of the pellet was determined using a caliper gauge after the measurement.

---

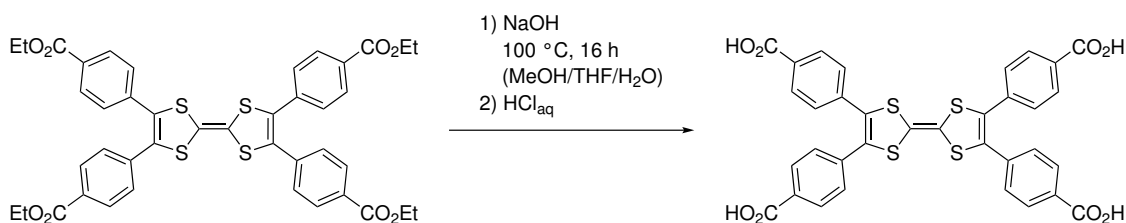
## 6.3 SYNTHETIC PROCEDURES

6.3.1 Tetraethyl tetrathiafulvalene tetrabenzoate ( $Et_4TFTB$ )**Scheme 16.** Reaction scheme for the synthesis of  $Et_4TFTB$ .

The compound was synthesized following a slightly modified literature procedure.<sup>86</sup> To a flame-dried two-neck round-bottom Schlenk flask (500 mL) were added anhydrous cesium carbonate,  $Cs_2CO_3$  (28.70 g, 88.09 mmol, 6 eq.), palladium acetate,  $Pd(OAc)_2$  (0.99 g, 4.40 mmol, 0.3 eq.), and tri-*tert*-butylphosphonium tetrafluoroborate,  $P^tBu_3 \cdot HBF_4$  (3.83 g, 13.21 mmol, 0.9 eq.) in the glovebox. To a separate Schlenk flask (250 mL), TTF (3.00 g, 14.68 mmol, 1 eq.) was added in the glovebox. After transfer to the Schlenk line, dry and degassed THF (100 mL) was added to the catalyst and base mixture via syringe. A flame-dried reflux condenser kept under argon and connected to an overpressure valve was mounted on the second neck of the flask. It was sealed and the mixture was stirred and heated to  $90\text{ }^\circ C$  for 45 min. During this period, the color of the solution lightened up from a red-brown to a bright yellow. In the meantime, dry and degassed THF (100 mL) was added to the second flask containing TTF, and ethyl 4-bromobenzoate (16.82 g, 12.0 mL, 73.41 mmol, 5 eq.) was added via syringe. The catalyst and base mixture was cooled down and the THF solution containing TTF and ethyl 4-bromobenzoate was added via Teflon cannula in one portion. Then, the flask was sealed again and heated to reflux conditions ( $90\text{ }^\circ C$ ) for 24 h. A dark red color indicating product formation forms rapidly at higher temperature. After that, the reaction was cooled down to RT. At this point, inert working conditions are no longer necessary. The mixture is filtered over a glass filter frit (porosity P4) and the filter cake is washed with DCM until the washings are colorless. The filtrate is concentrated using a rotary evaporator to a dark, crude oil, which is dissolved again in DCM (50 mL) and transferred to a separatory funnel. The organic phase is washed with brine ( $3 \times 50\text{ mL}$ ), dried over  $Na_2SO_4$ , then filtered and concentrated to a dark, crude oil. The compound is purified using column chromatography on silica gel ( $5 \times 20\text{ cm}$ )

using DCM as eluent until excess ethyl 4-bromobenzoate was eluted, then 0.5% ethyl acetate in DCM is used until Et<sub>4</sub>TTFTB is eluted ( $R_f = 0.17$ ). The product fractions are combined and concentrated on the rotary evaporator to obtain a dark red solid (8.78 g, 75%). <sup>1</sup>H-NMR (400 MHz, CDCl<sub>3</sub>):  $\delta$  (ppm) = 7.91 (d, <sup>3</sup> $J = 8.3$  Hz, 8 H, Ar–H), 7.26 (m, 8 H, Ar–H), 4.36 (q, <sup>3</sup> $J = 7.1$  Hz, 8 H, CH<sub>2</sub>CH<sub>3</sub>), 1.38 (t, <sup>3</sup> $J = 7.1$  Hz, 12 H, CH<sub>2</sub>CH<sub>3</sub>) (Figure 84).

### 6.3.2 Tetrathiafulvalene tetrabenzoic acid (H<sub>4</sub>TTFTB)



**Scheme 17.** Reaction scheme for the synthesis of tetrathiafulvalene tetrabenzoate (H<sub>4</sub>TTFTB).

The compound was synthesized following a slightly modified literature procedure.<sup>13</sup> Et<sub>4</sub>TTFTB (5.40 g, 6.78 mmol, 1 eq.) is added to a Schlenk flask (250 mL) and the flask is evacuated and flushed with argon three times. Then, dry and degassed THF (50 mL) and dry methanol (50 mL), which was degassed via five cycles of evacuation of the flask in an ultrasonication bath and subsequent flushing with argon, were used to dissolve Et<sub>4</sub>TTFTB. NaOH (3.43 g, 85.71 mmol, 12.7 eq.) solution in water (37 mL), which was degassed analogously to methanol, was added to the ester solution. A reflux condenser connected to an overpressure valve was mounted on top and flushed with argon, then the reaction mixture was refluxed (100 °C) for 16 h (over night). The red solution was concentrated *in vacuo* using the Schlenk line to obtain a red crude, which was acidified using 1 M HCl<sub>aq</sub> (220 mL). Immediately, a red precipitate is formed, which is filtered over a glass filter frit and washed with water until the washings are pH-neutral. The solid is dried *in vacuo* to obtain a dark red solid in nearly quantitative yield (4.59 g, 99%). <sup>1</sup>H-NMR (400 MHz, DMSO–d<sub>6</sub>):  $\delta$  (ppm) = 13.14 (broad s, 4 H, CO<sub>2</sub>H), 7.87 (d, <sup>3</sup> $J = 8.5$  Hz, 8 H, Ar–H), 7.35 (d, <sup>3</sup> $J = 8.5$  Hz, 8 H, Ar–H) (Figure 85).

### 6.3.3 Zn<sub>2</sub>TTFTB

The compound was synthesized following a literature procedure.<sup>13</sup> H<sub>4</sub>TTFTB (200 mg, 0.29 mmol, 1 eq.) was dissolved in a DMF-ethanol mixture (3:1, 32 mL) in a Schott flask (100 mL). Zn(NO<sub>3</sub>)<sub>2</sub> · 6 H<sub>2</sub>O (319 mg, 1.07 mmol, 3.7 eq.) was



dissolved in an ethanol-water mixture (1:1, 32 mL) and added slowly to the dark red linker solution while stirring. Then, the stirring bar is removed from the Schott flask, the flask is sealed and placed in the preheated oven at 75 °C for 72 h. A dark red to black precipitate has formed. The colorless supernatant is decanted and replaced with fresh DMF in which the product is left until the next day. This washing step is repeated three times. Then, the MOF is solvent-exchanged with ethanol three times. During the exchange processes, the precipitate is transferred to a smaller scintillation vial (20 mL). Finally, it is dried and activated at 200 °C *in vacuo* over night (Figure 31). Activated Zn<sub>2</sub>TTFTB was obtained in a yield of 154 mg (65% based on H<sub>4</sub>TTFTB) (Figure 47).

#### 6.3.4 Cd<sub>2</sub>TTFTB

The compound was synthesized following a literature procedure.<sup>14</sup> H<sub>4</sub>TTFTB (103 mg, 0.15 mmol, 1 eq.) was dissolved in a DMF-ethanol mixture (3:1, 8.4 mL) in a scintillation vial (20 mL). Cd(NO<sub>3</sub>)<sub>2</sub> · 4 H<sub>2</sub>O (172 mg, 0.56 mmol, 3.7 eq.) was dissolved in an ethanol-water mixture (1:1, 12 mL) and added slowly to the dark red linker solution while stirring. Then, the stirring bar is removed from the vial, it is sealed and placed in the preheated oven at 75 °C for 72 h. Dark red to black, long (several mm) needles have formed at the bottom (122 mg) (Figure 32). The colorless supernatant is decanted and replaced with fresh DMF in which the product is left until the next day. This washing step is repeated three times. Then, the MOF is solvent-exchanged with ethanol three times. Finally, it is dried and activated at 230 °C *in vacuo* over night (Figure 48).

#### 6.3.5 (TCNE)<sub>x</sub>M<sub>2</sub>TTFTB

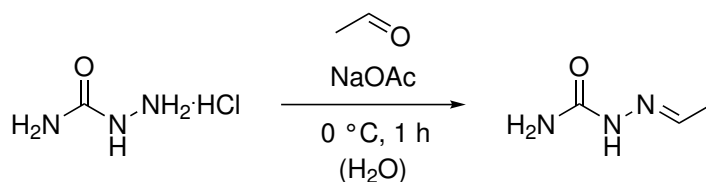
In the glovebox, powders of activated Zn<sub>2</sub>TTFTB (200 mg, 0.25 mmol, 1 eq.) or Cd<sub>2</sub>TTFTB (200 mg, 0.22 mmol, 1 eq.) were mixed with TCNE (0.5 or 1.0 eq. per formula unit of MOF) and ground in a mortar until a homogeneous mixture of MOF and TCNE were obtained. The mixtures were then transferred to a round-bottom glass tube using a glass funnel, ensuring that only the bottom of the tube was covered with sample and not the position of the tube where it would be sealed later. These tubes were capped with a quick-fit, taken out of the glovebox, and transferred to a Schlenk line where they were evacuated. In the meantime, the propane-O<sub>2</sub> burner flame was prepared. To ensure that volatile TCNE does not evaporate during the flame-sealing process, the bottom of the evacuated

**Table 8.** VPI of M<sub>2</sub>TTFTB (200 mg) with varying eq. TCNE, temperature, and reaction time.
$$\text{M}_2\text{TTFTB (M = Zn, Cd)} \xrightarrow[\text{T, time}]{\text{TCNE}} (\text{TCNE})_x\text{M}_2\text{TTFTB}$$

M	No.	$m_{\text{TCNE}}/\text{mg}$	$n_{\text{TCNE}}/\text{mmol}$	eq. TCNE used	time/days	T/°C
Zn	1	15.8	0.12	0.5	10	200
	2	31.6	0.25	1.0	10	200
	3	15.8	0.12	0.5	30	200
	4	31.6	0.25	1.0	30	200
	5	15.8	0.12	0.5	30	300
	6	31.6	0.25	1.0	30	300
Cd	7	14.2	0.11	0.5	10	200
	8	28.3	0.22	1.0	10	200
	9	14.2	0.11	0.5	30	200
	10	28.3	0.22	1.0	30	200

glass tube was kept in liquid N<sub>2</sub> for 1 min. The quick-fit stopcock was sealed and disconnected from the Schlenk line. Then, after quickly flame-sealing the glass tube, the evacuated system was placed in a sand bath and heated to a defined temperature for a certain amount of time in the oven. After cooling, black crystalline powders of (TCNE)<sub>x</sub>M<sub>2</sub>TTFTB were obtained. Excess TCNE resublimed at the colder side of the ampule. The samples were transferred to the glovebox and stored under argon (Table 8). Elemental analysis provided the values *x* for TCNE content in (TCNE)<sub>x</sub>M<sub>2</sub>TTFTB (Table 9). Profile fits of each sample were performed (Figure 49-58).

### 6.3.6 Acetaldehyde semicarbazone

**Scheme 18.** Reaction scheme for the synthesis of acetaldehyde semicarbazone.

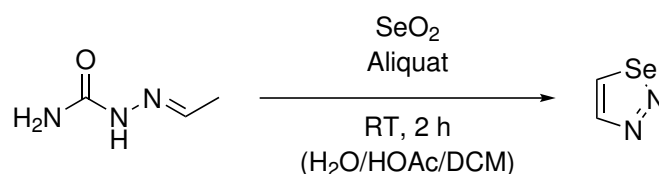
Semicarbazide hydrochloride (124 g, 1.11 mol, 1 eq.) and sodium acetate (142 g, 1.73 mol, 1.6 eq.) are dissolved in water (400 mL, ideally saturated solution) and cooled to 0 °C in an ice bath. Then, acetaldehyde (110 mL, 86.7 g, 1.97 mol, 1.8 eq.) is added in one portion. In some cases, immediate precipitation of a white solid occurs, in other cases it takes 1 h for the product to form. After 1 h, the

**Table 9.** Elemental analysis of (TCNE)<sub>x</sub>M<sub>2</sub>TTFTB with experimental values in wt.%, and simulated values in parentheses. *x* is calculated using equation 6.8, and simulated values using equation 6.6.

Entry	C	H	N	S	<i>x</i>
Zn <sub>2</sub> TTFTB	49.77 (50.32)	1.97 (1.99)	0 (0)	15.89 (15.81)	0
1	49.56 (50.66)	1.81 (1.87)	2.47 (2.48)	14.6–15.2 (14.91)	0.38
2	50.11 (50.99)	1.70 (1.76)	4.94 (4.96)	14.1–14.4 (14.01)	0.81
3	49.13 (50.72)	1.95 (1.85)	2.95 (2.96)	14.77 (14.74)	0.46
4	50.14 (51.03)	1.69 (1.75)	5.20 (5.23)	14.28 (13.92)	0.86
5	49.01 (50.76)	2.03 (1.84)	3.19 (3.20)	14.63 (14.65)	0.50
6	49.77 (51.00)	1.77 (1.76)	4.99 (5.01)	14.23 (13.99)	0.82
Cd <sub>2</sub> TTFTB	44.78 (45.10)	1.93 (1.78)	0.47 (0)	13.8–14.2 (14.16)	0
7	44.54 (45.79)	1.87 (1.67)	2.70 (2.73)	13.1–13.6 (13.28)	0.47
8	44.23 (45.94)	1.95 (1.65)	3.34 (3.32)	12.8–13.0 (13.09)	0.58
9	41.65 (45.79)	2.65 (1.67)	2.75 (2.73)	12.39 (13.28)	0.47
10	43.72 (45.97)	2.32 (1.64)	3.40 (3.42)	12.79 (13.06)	0.60

product is filtered over a Büchner funnel, washed with a little amount of cold water, and dried in air (80 g, 70%). <sup>1</sup>H-NMR (400 MHz, DMSO-d<sub>6</sub>): δ (ppm) = 9.79 (s, 1 H, NH), 7.15 (q, <sup>3</sup>J = 5.3 Hz, 1 H, CH), 6.10 (s, 2 H, NH<sub>2</sub>), 1.80 (d, <sup>3</sup>J = 5.4 Hz, 3 H, CH<sub>3</sub>) (Figure 86).

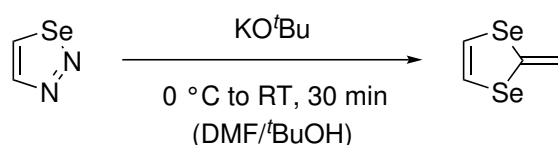
### 6.3.7 1,2,3-Selenadiazole

**Scheme 19.** Reaction scheme for the synthesis of 1,2,3-selenadiazole.

The compound was synthesized following a slightly modified literature procedure.<sup>58</sup> Acetaldehyde semicarbazone (30.0 g, 0.30 mol, 1 eq.) is placed in a round-bottom flask or Schott flask (1 L) and suspended in DCM (200 mL). The flask is covered with aluminum foil and placed in a water bath at RT. Ground selenium dioxide, SeO<sub>2</sub> (34.0 g, 0.31 mol) is dissolved in water (200 mL) in a separate flask and glacial acetic acid (10 mL) and Aliquat (mixture of different long-chain tetraalkylammonium salts, 10 mL) are added to the selenium dioxide solution. This solution is then added to the semicarbazone suspension in one portion, the top of the flask is also covered with aluminum foil, and the reaction is stirred at RT for 2 h. Immediately after the addition, gas evolution is observed (N<sub>2</sub>) and red selenium

starts to precipitate as byproduct. The reaction is generally done when gas evolution ceases. After that, the reaction mixture is filtered over a Büchner funnel in the dark to separate the red selenium from the two-phase mixture containing a pale yellow organic layer, which darkens over time due to the temperature sensitivity of the product and forms more red selenium byproduct. It is important to use a vacuum filtration during this step because the fine red selenium clogs up typical filter papers used for gravity filtration very quickly. The reaction flask is rinsed twice with a little amount of DCM and poured over the filter cake to extract more of the product. After that, the two-phase mixture was transferred to a separatory funnel, the aqueous phase is discarded, and the organic phase is washed with water (100 mL). It is advisable to use cold water to avoid even more decomposition of the product. After drying over  $\text{Na}_2\text{SO}_4$  and filtration into a (tared) Schlenk flask, the solution is concentrated without heating using the Schlenk line and an external cooling trap to remove DCM to obtain a dark, viscous oil. Note that the product is volatile, as well, so care should be taken to not extend this step further than necessary. The flask is flushed with argon and then connected to a second Schlenk flask of adequate size (25 mL) over a bent glass bridge. The apparatus is then evacuated through the stopcock of the second flask, then this flask is placed in liquid nitrogen, whereas the flask containing the crude oil is placed in the oil bath at RT. While stirring, the flask is then heated slowly to 70 °C. The distillation process is quite fast and begins already at ca. 40 °C, and hence the whole distillation is done when the oil bath has reached 70 °C. A black tar remains in the flask and frozen 1,2,3-selenadiazole is collected in the distillation flask, which quickly melts after removing the flask from the liquid nitrogen bath to yield a colorless or pale yellow oil (11.8 g, 30%). The density of the liquid was determined to be  $1.97 \text{ g mL}^{-1}$ . Furthermore, the product was stored at  $-32 \text{ °C}$  in the dark until further use; at these conditions, it is stable for long periods of time.  $^1\text{H-NMR}$  (400 MHz,  $\text{CDCl}_3$ ):  $\delta$  (ppm) = 9.41 (d,  $^3J = 3.8 \text{ Hz}$ , split into dd by  $^{77}\text{Se}$  with  $^2J = 40 \text{ Hz}$ , 1 H,  $\text{SeCHCH}$ ), 8.72 (d,  $^3J = 3.8 \text{ Hz}$ , 1 H,  $\text{SeCHCH}$ ) (Figure 87).

### 6.3.8 2-Methylene-1,3-diselenole

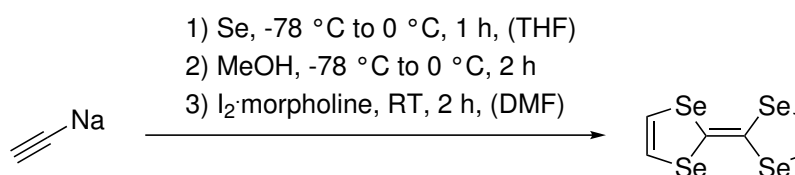


**Scheme 20.** Reaction scheme for the synthesis of 2-methylene-1,3-diselenole.

The compound was synthesized following a slightly modified literature procedure.<sup>56</sup> Under argon, a solution of 1,2,3-selenadiazole (6.1 mL, 12.0 g, 90.2 mmol, 1 eq.) in a dry and degassed mixture of DMF (240 mL) and *t*BuOH (40 mL) was cooled to 0 °C in an ice bath in the dark. Then, potassium *tert*-butoxide, KO<sup>*t*</sup>Bu (10.1 g, 90.2 mmol, 1 eq.) was added in small portions with waiting intervals in between until gas evolution ceases (N<sub>2</sub>). During this period the solution darkened from a yellow to a red-brown color. After the addition was complete, the ice-bath was removed and the reaction is stirred for 30 min at RT. In a next step, the solution is poured into ice-cold water (1 L). Full precipitation of the product takes up to 1 h. The white platelet crystals are filtered over a Büchner funnel and washed with water. They contained a brown impurity (<sup>1</sup>H-NMR (400 MHz, CDCl<sub>3</sub>): δ (ppm) = 4.75 (s)). The filtrate was transferred to a separatory funnel and extracted with hexane (3×150 mL), washed with water (3×150 mL), dried over Na<sub>2</sub>SO<sub>4</sub>, and filtered. To remove the impurity, the precipitated crystals were extracted with hexane and filtered, leaving behind a brown residue on the filter paper. This extract was dried over Na<sub>2</sub>SO<sub>4</sub>, filtered, and combined with the other hexane extract and concentrated *in vacuo* without heating using the Schlenk line and an external cooling trap. 2-Methylene-1,3-diselenole was obtained as an off-white product (8.5 g, 90%). The product can be stored for months without any noticeable decomposition at -32 °C. <sup>1</sup>H-NMR (400 MHz, CDCl<sub>3</sub>): δ (ppm) = 6.97 (s, split into dd by <sup>77</sup>Se with <sup>2</sup>*J* = 57 Hz, 2 H, CH), 5.66 (s, 2 H, CH<sub>2</sub>) (Figure 88a). At some point, only decomposition products of 2-methylene-1,3-diselenole were observed in NMR when CDCl<sub>3</sub> was used as solvent, the reasons of which are unknown. In those cases, an NMR of perfectly pure 2-methylene-1,3-diselenole was obtained in CD<sub>2</sub>Cl<sub>2</sub>. <sup>1</sup>H-NMR (400 MHz, CD<sub>2</sub>Cl<sub>2</sub>): δ (ppm) = 6.99 (s, split into dd by <sup>77</sup>Se with <sup>2</sup>*J* = 57 Hz, 2 H, CH), 5.66 (s, 2 H, CH<sub>2</sub>) (Figure 88b).

### 6.3.9 Tetraselenafulvalene

#### 6.3.9.1 Sodium acetylide route

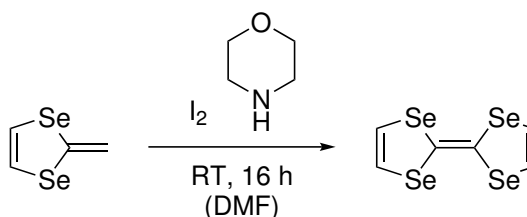


**Scheme 21.** Reaction scheme for the synthesis of TSF from sodium acetylide.

The synthesis of TSF from sodium acetylide was attempted following a literature

procedure.<sup>57</sup> Sodium acetylide (18 wt.% slurry in light mineral oil, 32 mL, 4.8 g, 0.1 mol, 1 eq.) was transferred via syringe to a flame-dried Schlenk flask and suspended in dry and degassed THF (100 mL) under argon in the dark. Then, the mixture was cooled to  $-78\text{ }^{\circ}\text{C}$  using a dry ice/acetone and powdered selenium (7.6 g, 0.1 mol, 1 eq.) was added in one portion. The cooling bath was removed and replaced with an ice bath at  $0\text{ }^{\circ}\text{C}$ , in which the mixture was stirred for 1 h. During this period, the color of the solution changed to dark brown. After that, the mixture was cooled again to  $-78\text{ }^{\circ}\text{C}$  and methanol (dried over magnesium/iodine and distilled on activated molecular sieves ( $3\text{ \AA}$ ), degassed via the ultrasonication method) (60 mL) was slowly added to the solution via syringe. An exothermic reaction was observed and the color darkened further. After the addition, the temperature was increased to  $0\text{ }^{\circ}\text{C}$  by switching back to the ice bath and the reaction was stirred at this temperature for 2 h. Water 120 mL was added and the mixture was transferred to a separatory funnel where the organics were extracted with pentane ( $4\times 80\text{ mL}$ ). Fast decomposition of the product was observed despite cooling, forming brown layers of material on the used glassware (presumably red selenium). The organic phase was washed with water ( $3\times 60\text{ mL}$ ), dried over  $\text{Na}_2\text{SO}_4$ , and concentrated *in vacuo* using the Schlenk line and an external cooling trap. A dark oil was obtained, which was used directly in the next step without further purification.<sup>57</sup> The oil was dissolved in dry and degassed DMF (stored over molecular sieves ( $3\text{ \AA}$ ), degassed using the ultrasonication method) (140 mL). In a separate dried flask under argon, iodine (26.5 g, 0.1 mol, 1 eq.) was dissolved in dry and degassed DMF (150 mL) and morpholine (dried over sodium, distilled on molecular sieves ( $4\text{ \AA}$ )) (27.5 mL, 27.2 g, 0.3 mol, 3 eq.) was added via syringe. This mixture was transferred via teflon cannula to a dropping funnel mounted on top of the flask containing 2-methylene-1,3-diselenole. The iodine-morpholine mixture was added drop-wise and the reaction flask was kept at RT using a water bath. After the addition was completed (ca. 1 h), the reaction was stirred for 2 h at RT. Then, water (100 mL) was added, the solution was transferred to a separatory funnel, the organics were extracted with DCM ( $4\times 50\text{ mL}$ ), washed with saturated  $\text{Na}_2\text{S}_2\text{O}_3 \cdot 5\text{ H}_2\text{O}$  solution ( $2\times 100\text{ mL}$ ), then with water ( $3\times 100\text{ mL}$ ) and concentrated *in vacuo* using the Schlenk line and an external cooling trap. A crude yield of 2.2 g was obtained which was purified using column chromatography on silica gel ( $5\times 20\text{ cm}$ ) using a hexane-DCM gradient ( $R_f = 0.4$ , hexane-DCM 2:1). The product fractions were combined and concentrated on the rotary evaporator to obtain TSF as a dark red to purple solid of only 2% (212 mg, lit. yield:<sup>57</sup> 2.2 g, 25%). Centrifugation of sodium acetylide and washing with pentane to remove the light mineral oil and isolate the intermediate product did not improve yields.  $^1\text{H-NMR}$  (400 MHz,  $\text{CDCl}_3$ ):  $\delta$  (ppm) = 7.21 (s, 4 H) (Figure 90).

## 6.3.9.2 Semicarbazone route



**Scheme 22.** Reaction scheme for the synthesis of TSF, starting from acetaldehyde semicarbazone.

Under argon and in the dark, 2-methylene-1,3-diselenole (8.5 g, 40.5 mmol, 1 eq.) was dissolved in a two-neck round-bottom Schlenk flask equipped with a dropping funnel using DMF (170 mL). Dry and degassed morpholine (23 mL, 22.9 g, 263 mmol, 6.5 eq.) was added to this solution. In a separate flask under argon, iodine (20.5 g, 81.0 mmol, 2 eq.) was dissolved in dry and degassed DMF (170 mL) and this solution was transferred to the dropping funnel. A water bath at RT is placed below the reaction flask and then the iodine solution was added drop-wise to 2-methylene-1,3-diselenole and morpholine while rapidly stirring. When the addition was complete, the reaction was stirred for further 16 h (over night). The dark reaction solution is quenched with brine (100 mL) and the organics were extracted with DCM (3×100 mL). The organic phase was washed with saturated aqueous Na<sub>2</sub>S<sub>2</sub>O<sub>3</sub> · 5 H<sub>2</sub>O solution (2×100 mL), brine (3×100 mL), dried over Na<sub>2</sub>SO<sub>4</sub>, filtered, and concentrated *in vacuo* using the rotary evaporator to obtain a dark oily residue. It was purified by performing two column chromatographic sequences, the first on neutral alumina and the second on silica gel (both 5×20 cm), using only DCM as eluent (due to poor solubility in hexane-DCM mixtures). Only the red band was collected, concentrated using the rotary evaporator. After the second column chromatography, a brilliant red solution was obtained which was concentrated to give shiny red crystals of pure TSF (1.0 g, 12%). TSF is generally air- but also temperature-sensitive, as samples were seen to considerably darken after leaving at RT even under argon in the dark. No darkening was observed for samples stored at -32 °C under air. Solid TSF can be handled in air at RT for short periods of time without noticeable decomposition, but should be stored under argon at -30 °C. <sup>1</sup>H-NMR (400 MHz, CDCl<sub>3</sub>): δ (ppm) = 7.21 (s, 4 H) (Figure 90). In some cases, CDCl<sub>3</sub> needed to be filtered over basic alumina to remove impurities which lead otherwise to instant decomposition of TSF as indicated by a color change from red to green (oxidation products).

### 6.3.10 Direct Arylation of Tetraselenafulvalene

#### 6.3.10.1 Palladium catalysis

All reactions were carried out under inert conditions in the presence of base (6 eq.), a palladium (pre-)catalyst (30 mol%), a suitable ligand (90 mol%), organic solvent (0.05 M), additive, as well as TSF (0.05 mmol) and an aryl halide (6 eq.) as coupling partner. The procedure was based on the direct arylation procedure of TTF.<sup>86</sup> The mixture was stirred at a defined temperature for 24 h. In all cases, the catalyst mixture was heated first prior to the addition of the coupling partners to ensure complete formation of the catalytically active species. After the addition of TSF, the reaction mixture quickly darkened. After the reaction was finished, the black solutions were quenched with saturated aqueous ammonium chloride solution and extracted with DCM. The organic phase was washed with brine three times, dried over Na<sub>2</sub>SO<sub>4</sub>, filtered, and concentrated using a rotary evaporator. The resulting crude was analyzed using thin-layer chromatography (TLC), NMR, and LIFDI-MS. In all cases where TSF was converted, bis(4-ethoxycarbonylphenyl) selenide was observed as the main product, indicating full destruction of the TSF molecule.

#### 6.3.10.2 Copper Catalysis

All reactions were carried out under inert conditions in the presence of base (6 eq.), a copper (pre-)catalyst (10 mol%), ligand (10 mol%), organic solvent (0.05 M), as well as TSF (0.05 mmol) and an aryl halide (6 eq.) as coupling partner. The procedure was based on procedures for the copper-catalyzed direct arylation of heteroarenes.<sup>152–154</sup> The mixture was stirred at a defined temperature for 24 h. After the addition of TSF, the reaction mixture quickly darkened. When the reaction was finished, the black solutions were quenched with saturated aqueous ammonium chloride solution and extracted with DCM. The organic phase was washed with brine three times, dried over Na<sub>2</sub>SO<sub>4</sub>, filtered, and concentrated using a rotary evaporator. The resulting crude was analyzed using TLC, NMR, and LIFDI-MS. Diethyl 4,4'-selenodibenzoate was observed as one of the products, indicating destruction of the TSF molecule to some extent during the reaction conditions; however, considerable amounts of the desired product are formed, as well.

---

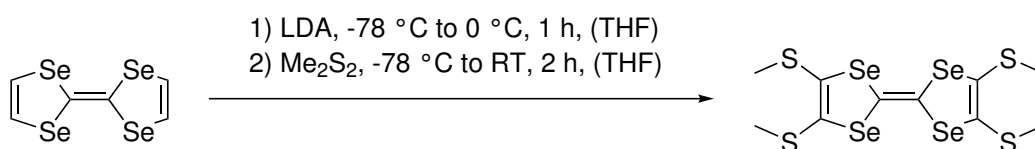


### 6.3.11 Cross Coupling of Functionalized Tetraselenafulvalene

#### 6.3.11.1 Negishi Coupling of Zincated Tetraselenafulvalene

All reactions were carried out under inert conditions in the presence of base (4.2 eq.), a palladium (pre-)catalyst (20 mol%), a ligand (60 mol%),  $\text{ZnCl}_2$  (4.3 eq.), organic solvent (0.1 M), additive, as well as TSF (0.13 mmol) and an aryl halide (5 eq.) as coupling partner. The procedure was based on the tetralithiation of TSF,<sup>75,76</sup> as well as the Negishi coupling of mono-functionalized TTF.<sup>82</sup> To a solution of LDA (0.87 M in THF, 4.2 eq.) cooled to  $-78\text{ }^\circ\text{C}$  was added TSF (1 eq.) in THF drop-wise and stirred at  $-78\text{ }^\circ\text{C}$  for 1 h. Immediately, the red TSF solution forms a yellow suspension. The dry ice-acetone bath is replaced with an ice bath and the reaction is stirred at  $0\text{ }^\circ\text{C}$  for 1 h. After cooling back to  $-78\text{ }^\circ\text{C}$ , anhydrous  $\text{ZnCl}_2$  solution in THF (0.5 M, 4.3 eq.) is added drop-wise and the reaction is stirred at the same temperature for 30 min, then warmed up to RT. A solution of catalyst, ligand, and aryl halide in THF is added to the reaction mixture and the reaction is stirred at RT for 24 h. After the reaction is done, it is quenched with saturated aqueous ammonium chloride solution, extracted with DCM, washed with brine, dried over  $\text{Na}_2\text{SO}_4$ , filtered, and concentrated *in vacuo*. The resulting crude was analyzed using TLC, NMR, and LIFDI-MS.

#### 6.3.11.2 Tetra(methylthio)tetraselenafulvalene (TSF(SMe)<sub>4</sub>)

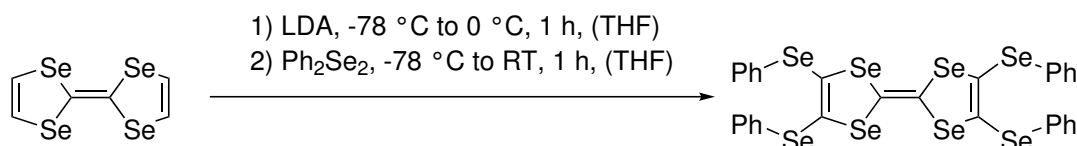


**Scheme 23.** Reaction scheme for the synthesis of  $\text{TSF}(\text{SMe})_4$ .

The compound was synthesized according to a modified literature procedure.<sup>76</sup> To a solution of LDA (0.87 M, 2.7 mL, 2.36 mmol, 4.2 eq.) cooled to  $-78\text{ }^\circ\text{C}$  was added a solution of TSF (220 mg, 0.56 mmol, 1 eq.) in dry and degassed THF (5 mL) under argon. The reaction was stirred at that temperature for 1 h, then warmed up to  $0\text{ }^\circ\text{C}$  and stirred again for 1 h. The yellow suspension was cooled back to  $-78\text{ }^\circ\text{C}$  and dimethyl disulfide (0.22 mL, 2.47 mmol, 4.4 eq.) was added in one portion. The reaction is stirred at  $-78\text{ }^\circ\text{C}$  for 1 h, warmed up to  $0\text{ }^\circ\text{C}$  and stirred at that temperature for 30 min during which the color of the solution changed from yellow to dark red, then stirred at RT for 1 h. The mixture was then diluted with toluene,

washed with water, then brine, dried over  $\text{Na}_2\text{SO}_4$ , filtered, and concentrated *in vacuo*. Purification over silica gel ( $3 \times 20$  cm) using hexane-toluene (5:1) yields an air-stable dark red solid (230 mg, 71%).  $^1\text{H-NMR}$  (400 MHz,  $\text{CDCl}_3$ ):  $\delta$  (ppm) = 2.45 (s, 12 H) (Figure 89).

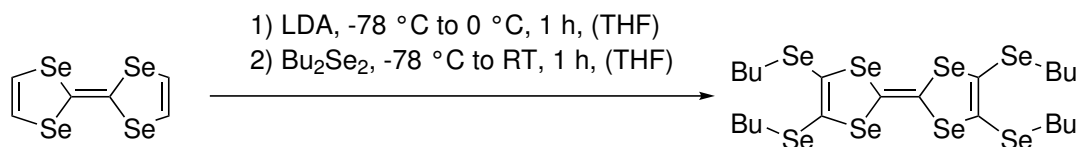
### 6.3.11.3 Tetra(phenylseleno)tetraselenafulvalene ( $\text{TSF}(\text{SePh})_4$ )



**Scheme 24.** Reaction scheme for the synthesis of  $\text{TSF}(\text{SePh})_4$ .

The compound was synthesized according to a modified literature procedure.<sup>75,155</sup> To a solution of LDA (0.87 M, 2.46 mL, 2.14 mmol, 4.2 eq.) cooled to  $-78$  °C was added a solution of TSF (200 mg, 0.51 mmol, 1 eq.) in dry and degassed THF (2 mL) under argon. The reaction was stirred at that temperature for 1 h, then warmed up to  $0$  °C and stirred again for 1 h. The yellow suspension was cooled back to  $-78$  °C and diphenyl diselenide (0.70 g, 2.24 mmol, 4.4 eq.) was added in one portion. The reaction is stirred at  $-78$  °C for 1 h, warmed up to  $0$  °C and stirred at that temperature for 30 min during which the color of the solution changed from yellow to dark red, then stirred at RT for 1 h. The mixture was then diluted with toluene, washed with water, then brine, dried over  $\text{Na}_2\text{SO}_4$ , filtered, and concentrated *in vacuo*. Recrystallization from THF-hexane (1:1) yields shiny air-stable dark purple crystals (332 mg, 76%).  $^1\text{H-NMR}$  (400 MHz,  $\text{CDCl}_3$ ):  $\delta$  (ppm) = 7.27-7.37 (m, 12 H, *m-/p*-Ar-H), 7.52-7.60 (m, 8 H, *o*-Ar-H) (Figure 91).

### 6.3.11.4 Tetra(butylseleno)tetraselenafulvalene ( $\text{TSF}(\text{SeBu})_4$ )



**Scheme 25.** Reaction scheme for the synthesis of  $\text{TSF}(\text{SeBu})_4$ .

The compound was synthesized according to a modified literature procedure.<sup>155</sup> To a solution of LDA (0.87 M, 2.46 mL, 2.14 mmol, 4.2 eq.) cooled to  $-78$  °C was added a solution of TSF (200 mg, 0.51 mmol, 1 eq.) in dry and degassed THF (2 mL) under argon. The reaction was stirred at that temperature for 1 h, then

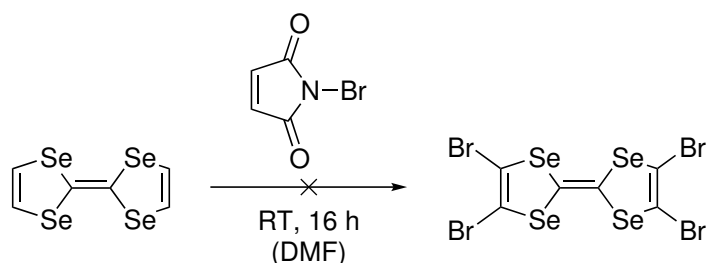
warmed up to 0 °C and stirred again for 1 h. The yellow suspension was cooled back to -78 °C and dibutyl diselenide (0.61 g, 2.24 mmol, 4.4 eq.) was added in one portion. The reaction is stirred at -78 °C for 1 h, warmed up to 0 °C and stirred at that temperature for 30 min during which the color of the solution changed from yellow to dark red, then stirred at RT for 1 h. The mixture was then diluted with toluene, washed with water, then brine, dried over Na<sub>2</sub>SO<sub>4</sub>, filtered, and concentrated *in vacuo*. Column chromatography on silica gel with gradient elution of hexane-toluene (9:1 to 4:1) yields a dark red oil ( $R_f = 0.5$ , hexane-toluene 4:1, 332 mg, 76%). <sup>1</sup>H-NMR (400 MHz, CDCl<sub>3</sub>):  $\delta$  (ppm) = 2.92 (t, <sup>3</sup> $J = 7.4$  Hz, 4 H, SeCH<sub>2</sub>), 1.72 (p, <sup>3</sup> $J = 7.4$  Hz, 4 H, Se-CH<sub>2</sub>-CH<sub>2</sub>), 1.43 (h, <sup>3</sup> $J = 7.4$  Hz, 4 H, CH<sub>2</sub>-CH<sub>3</sub>), 0.93 (t, <sup>3</sup> $J = 75.4$  Hz, 6 H, CH<sub>3</sub>) (Figure 92).

#### 6.3.11.5 Liebeskind-Srogl Type Coupling

All reactions were carried out under inert conditions in the presence of a palladium (pre-)catalyst, a ligand, an aryl boronic acid or arylzinc reagent (8 eq.) as coupling partner, additives, using either TSF(SMe)<sub>4</sub>, TSF(SePh)<sub>4</sub>, or TSF(SeBu)<sub>4</sub>. To a solution of tetrachalcogenated TSF (1 eq.) in THF, catalyst, ligand, additive, and aryl boronic acid or aryl zinc in THF is added to the reaction mixture and the reaction is stirred for 24 h with heating. After the reaction is done, it is quenched with saturated aqueous ammonium chloride solution, extracted with DCM, washed with brine, dried over Na<sub>2</sub>SO<sub>4</sub>, filtered, and concentrated *in vacuo*. The resulting crude was analyzed using TLC, NMR, and LIFDI-MS.

#### 6.3.12 Other Functionalizations of Tetraselenafulvalene

##### 6.3.12.1 Bromination with *N*-Bromosuccinimide

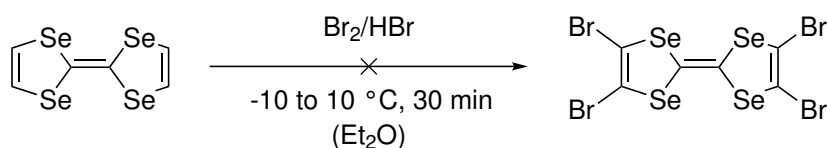


**Scheme 26.** Reaction scheme for the failed bromination of TSF using *N*-bromosuccinimide (NBS).

To a solution of TSF (50.0 mg, 0.13 mmol, 1 eq.) in dry and degassed DMF (4 mL) under argon was added NBS (99.9 mg, 0.56 mmol, 4.4 eq.) in one portion and the

reaction was stirred at RT for 16 h (over night) in the dark. The color of the solution changed to dark green. After addition of water, a sticky brown solid precipitated, which was filtered and washed with water. It was soluble in  $\text{CDCl}_3$  and the  $^1\text{H-NMR}$  showed an intense singlet signal at 4.75 ppm, very similar to the decomposition product observed during the synthesis of 2-methylene-1,3-diselenole, and the absence of TSF.

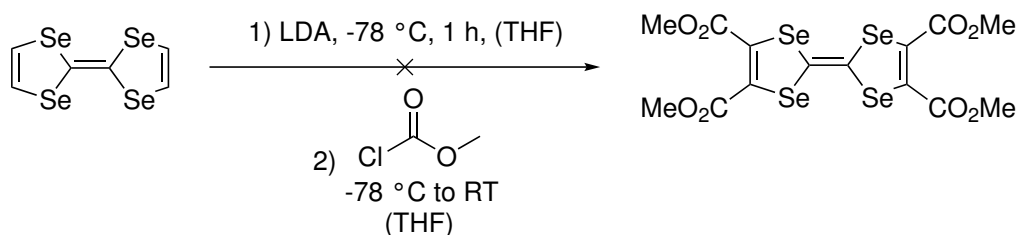
### 6.3.12.2 Bromination with Bromine



**Scheme 27.** Reaction scheme for the failed bromination of TSF with bromine.

The procedure followed here is based on the full bromination of TTF with bromine in the presence of HBr.<sup>156</sup> TSF (50.0 mg, 0.13 mmol, 1 eq.) is dissolved in degassed diethyl ether (3.6 mL) under argon and aqueous concentrated HBr (48%, 3.6 mL) is added. The solution immediately changes color from red to deep purple. Then, the solution is cooled to  $-10\text{ }^\circ\text{C}$  and a solution of bromine (101.9 mg, 0.64 mmol, 5 eq.) in diethyl ether (3.6 mL) is added drop-wise over 15 min via a syringe pump while stirring vigorously. A black solid precipitates, then the reaction is warmed up to  $10\text{ }^\circ\text{C}$  and stirred at that temperature for 30 min. The mixture is diluted with DCM and filtered. The obtained amorphous black slurry was uncharacterizable and the red color of the organic phase could be completely discolored by treating with saturated aqueous  $\text{Na}_2\text{S}_2\text{O}_3 \cdot 5\text{H}_2\text{O}$  solution, suggesting that TSF is fully converted and destroyed during the reaction.

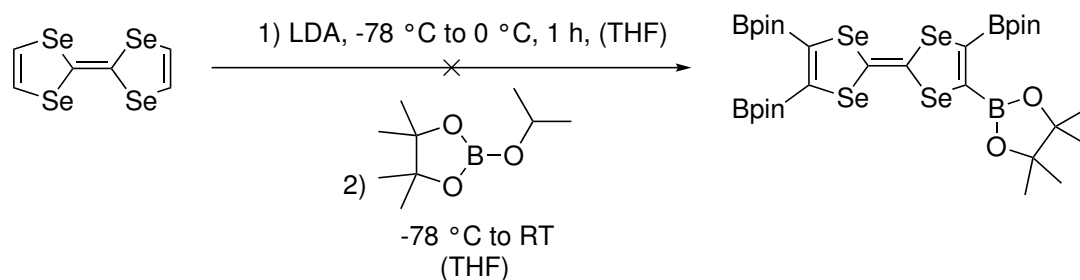
### 6.3.12.3 Tetracarboxylation



**Scheme 28.** Reaction scheme for the failed tetracarboxylation of TSF.

The synthesis of the compound was reported in the literature.<sup>75</sup> To a solution of LDA (0.87 M in THF, 0.06 mL, 48.3  $\mu\text{mol}$ , 4.2 eq.) cooled to  $-78\text{ }^{\circ}\text{C}$  was added TSF (4.5 mg, 11.5  $\mu\text{mol}$ , 1 eq.) and stirred at that temperature for 1 h, then at  $0\text{ }^{\circ}\text{C}$  for 1 h. After cooling back to  $-78\text{ }^{\circ}\text{C}$ , a solution of methyl chloroformate (0.5 M in THF, 0.1 mL, 50.6  $\mu\text{mol}$ , 4.4 eq.) was added in one portion. The color of the solution changes immediately from yellow to dark red-brown. The reaction was warmed up to RT and quenched with water. After usual workup, NMR and LIFDI-MS analysis showed that only a mixture of differently substituted TSF could be obtained ( $^1\text{H-NMR}$  (400 MHz,  $\text{CDCl}_3$ ):  $\delta$  (ppm) = 3.93 (s), 3.75 (s), 3.68 (s)). The product (Lit.:  $^1\text{H-NMR}$  (400 MHz,  $\text{CDCl}_3$ ):  $\delta$  (ppm) = 3.83 (s)<sup>75</sup>) was not detected.

#### 6.3.12.4 Tetraboronation

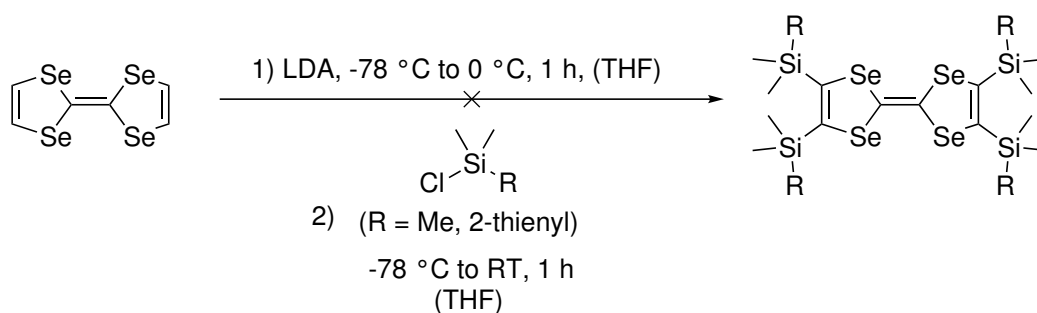


**Scheme 29.** Reaction scheme for the failed tetraboronation reaction of TSF with  $^i\text{PrO-Bpin}$ .

To a solution of LDA (0.87 M, 0.13 mL, 96.6  $\mu\text{mol}$ , 4.2 eq.) cooled to  $-78\text{ }^{\circ}\text{C}$  was added TSF (10 mg, 25.5  $\mu\text{mol}$ , 1 eq.) in dry and degassed THF (0.2 mL) drop-wise and the reaction was stirred at that temperature for 1 h, then at  $0\text{ }^{\circ}\text{C}$  for 1 h. After cooling again to  $-78\text{ }^{\circ}\text{C}$ , 2-isopropoxy-4,4,5,5-tetramethyl-1,3,2-dioxaborolane ( $^i\text{PrO-Bpin}$ ) was added (8 drops, excess). The reaction was stirred at the same temperature for 1 h, then warmed up to  $0\text{ }^{\circ}\text{C}$  and stirred for 30 min, then to RT and stirred for 16 h (over night). It was quenched with acetic acid, extracted with DCM, washed with brine, dried over  $\text{Na}_2\text{SO}_4$ , and concentrated *in vacuo*. NMR and LIFDI-MS showed the presence of only mono- and di-substituted product, indicating that the four-fold boronated product is unstable.

#### 6.3.12.5 Tetrasilylation

To a solution of LDA (0.87 M, 0.13 mL, 96.6  $\mu\text{mol}$ , 4.2 eq.) cooled to  $-78\text{ }^{\circ}\text{C}$  was added TSF (10 mg, 25.5  $\mu\text{mol}$ , 1 eq.) drop-wise and the reaction was stirred at that temperature for 1 h, then at  $0\text{ }^{\circ}\text{C}$  for 1 h. After cooling again to  $-78\text{ }^{\circ}\text{C}$ , trimethylsilyl



**Scheme 30.** Reaction scheme for the failed tetracarboxylation of TSF with various silyl chlorides.

chloride or (2-thienyl)dimethylsilyl chloride was added (excess). The reaction was stirred at the same temperature for 1 h, then warmed up to 0 °C and stirred for 30 min, then to RT and stirred for 16 h (over night). After usual workup, NMR and LIFDI-MS showed the presence of only mono- and di-substituted product.

### 6.3.13 $Cu_3BTC_2$

The compound was synthesized following a slightly modified literature procedure.<sup>157</sup>  $H_3BTC$  10 g, 48 mmol, 1 eq. and  $Cu(NO_3)_2 \cdot 3 H_2O$  (20.8 g, 86 mmol, 1.8 eq.) were dissolved in DMF-ethanol-water (1:1:1, 480 mL). After stirring for 15 min, the solution was separated into parts of 24 mL in twenty different Schott flasks (100 mL), the flasks were sealed and placed in the oven at 85 °C for 20 h. The blue crystals were filtrated while hot using a glass filter frit (P4) and washed with hot DMF. Then they were solvent-exchanged three times with DMF, three times with ethanol, and finally three times with DCM (each time leaving the sample in the solvent over night) prior to activation *in vacuo* at 180 °C (Figure 33).

### 6.3.14 $(Dinitrile)_x Cu_2BTC_2$

VPI of  $Cu_3BTC_2$  was based on a literature procedure.<sup>28</sup> Activated  $Cu_3BTC_2$  (100 mg, 0.17 mmol, 1 eq.) are mixed with various dinitriles, such as DCB, TCB, TCNQ, DCP, DCN, and DCT (0.5 or 1.0 eq. per formula unit of MOF) by grinding them in a mortar until a homogeneous mixture is obtained. This is transferred to round-bottom glass tube via a funnel, ensuring that the sample touches only the bottom of the tube. After evacuation and flame-sealing, the evacuated system was placed in a sand bath and heated to 180 °C for 10 d in the oven. After cooling, the crystalline powders were transferred to the glovebox and stored under argon (Table 10).

**Table 10.** VPI of  $\text{Cu}_3\text{BTC}_2$  (100 mg) with varying eq. of dinitriles at 180 °C for 10 d.

Dinitrile	No.	eq.-dinitrile	$m_{\text{dinitrile}}/\text{mg}$
DCB	<b>I</b>	0.5	10.6
	<b>II</b>	1.0	21.2
TCB	<b>III</b>	0.5	14.7
	<b>IV</b>	1.0	29.5
DCP	<b>V</b>	0.5	16.3
	<b>VI</b>	1.0	32.6
DCN	<b>VII</b>	0.5	14.7
	<b>VIII</b>	1.0	29.5
DCT	<b>IX</b>	0.5	11.1
	<b>X</b>	1.0	22.2
TCNQ	<b>XI</b>	0.5	16.9
	<b>XII</b>	1.0	33.8

## 6.4 CHARACTERIZATION

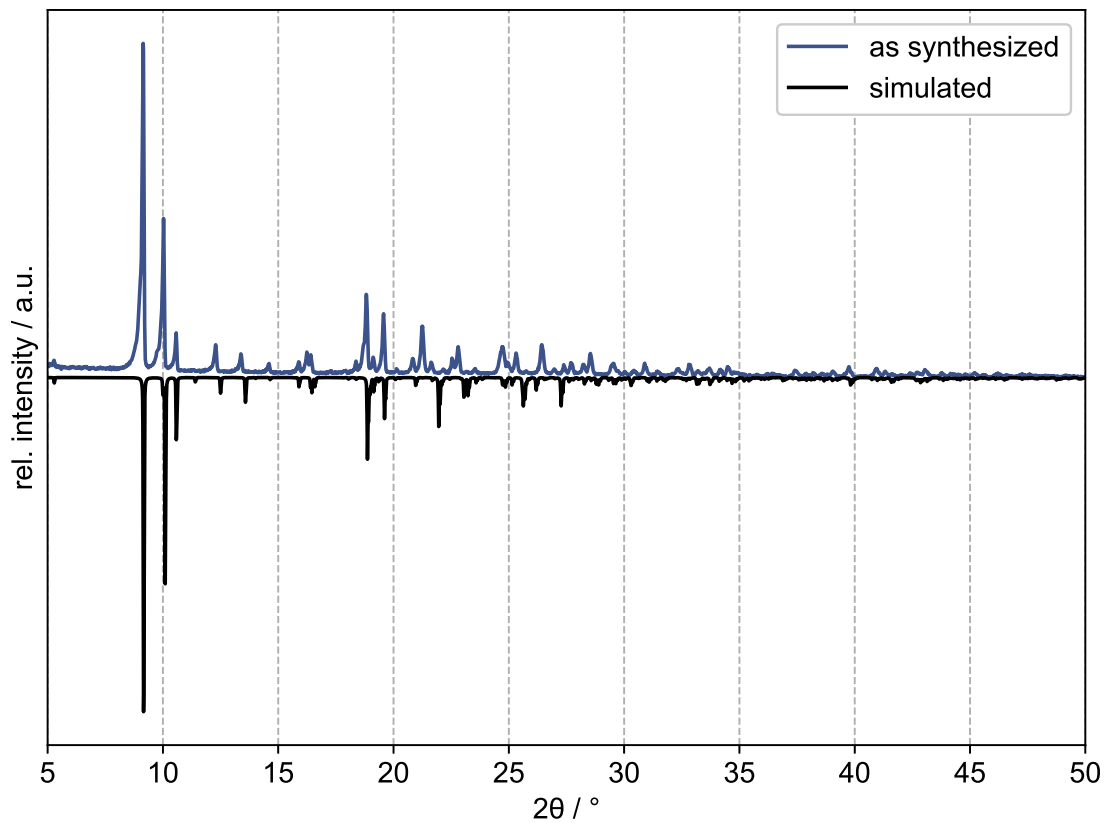


**Figure 31.** Simulated and as synthesized PXR D data of Zn<sub>2</sub>TTFTB in a range of 5° to 50°.

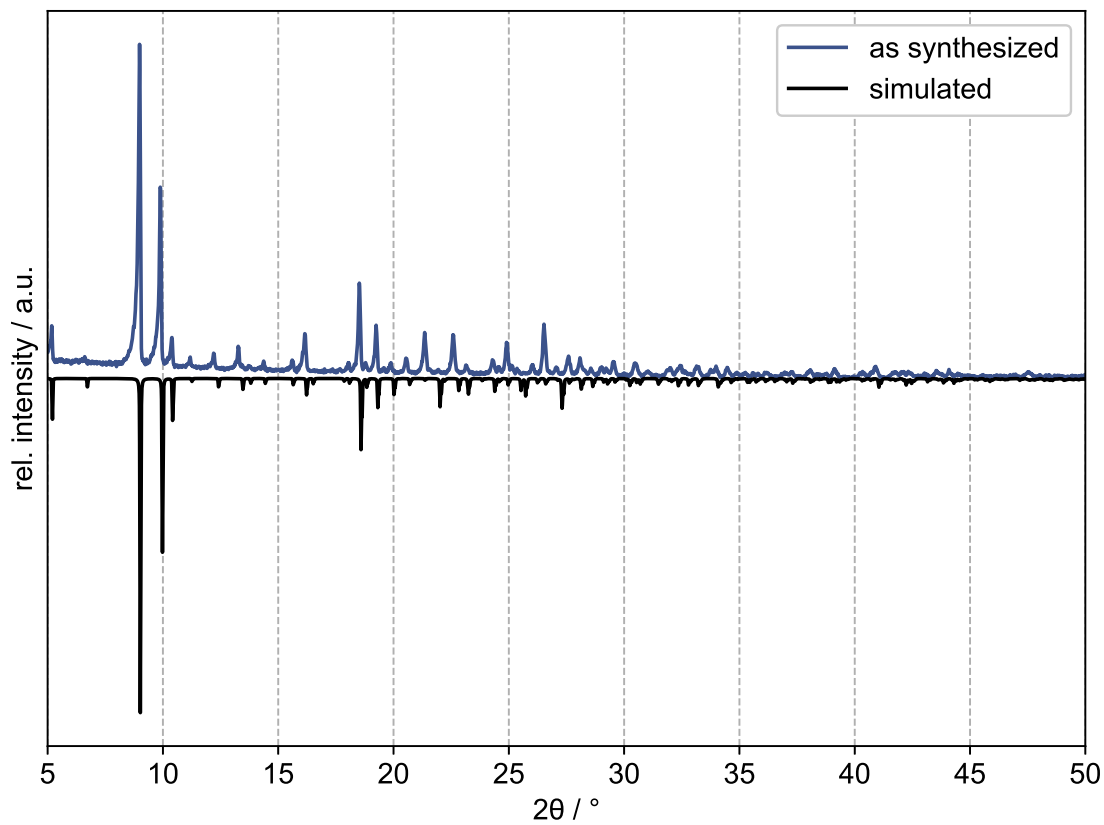


**Figure 32.** Simulated and as synthesized PXR D data of Cd<sub>2</sub>TTFTB in a range of 5° to 50°.



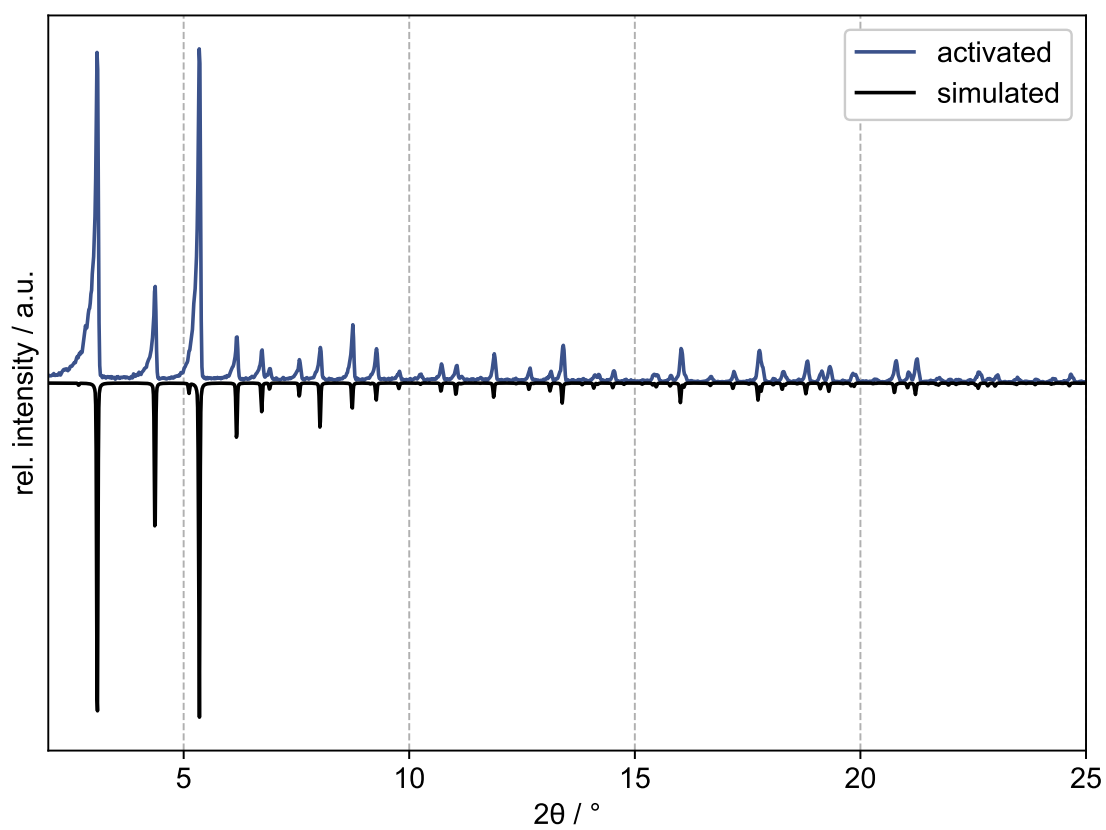


**Figure 33.** Simulated and as synthesized PXRD data of  $\text{Cu}_3\text{BTC}_2$  in a range of  $2^\circ$  to  $25^\circ$ .

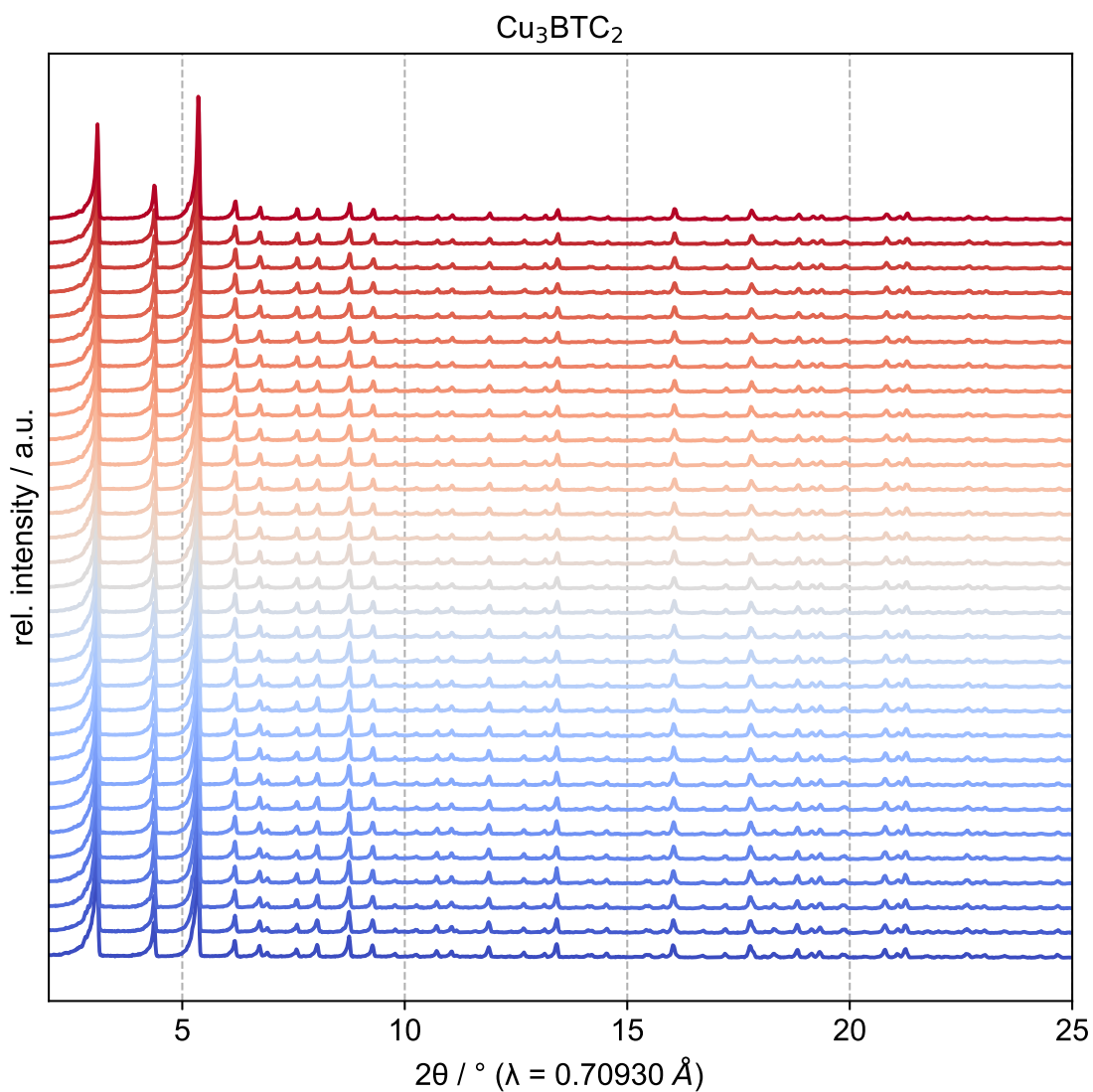


**Figure 34.** VT-PXRD data of  $\text{Cu}_3\text{BTC}_2$  in a range of  $2^\circ$  to  $25^\circ$  from 100–400 K. During heating between 100 and 400 K, measurements were performed in temperature steps of 20 K. For the cooling, measurements were performed between 390 and 110 K with the same temperature steps of 20 K.

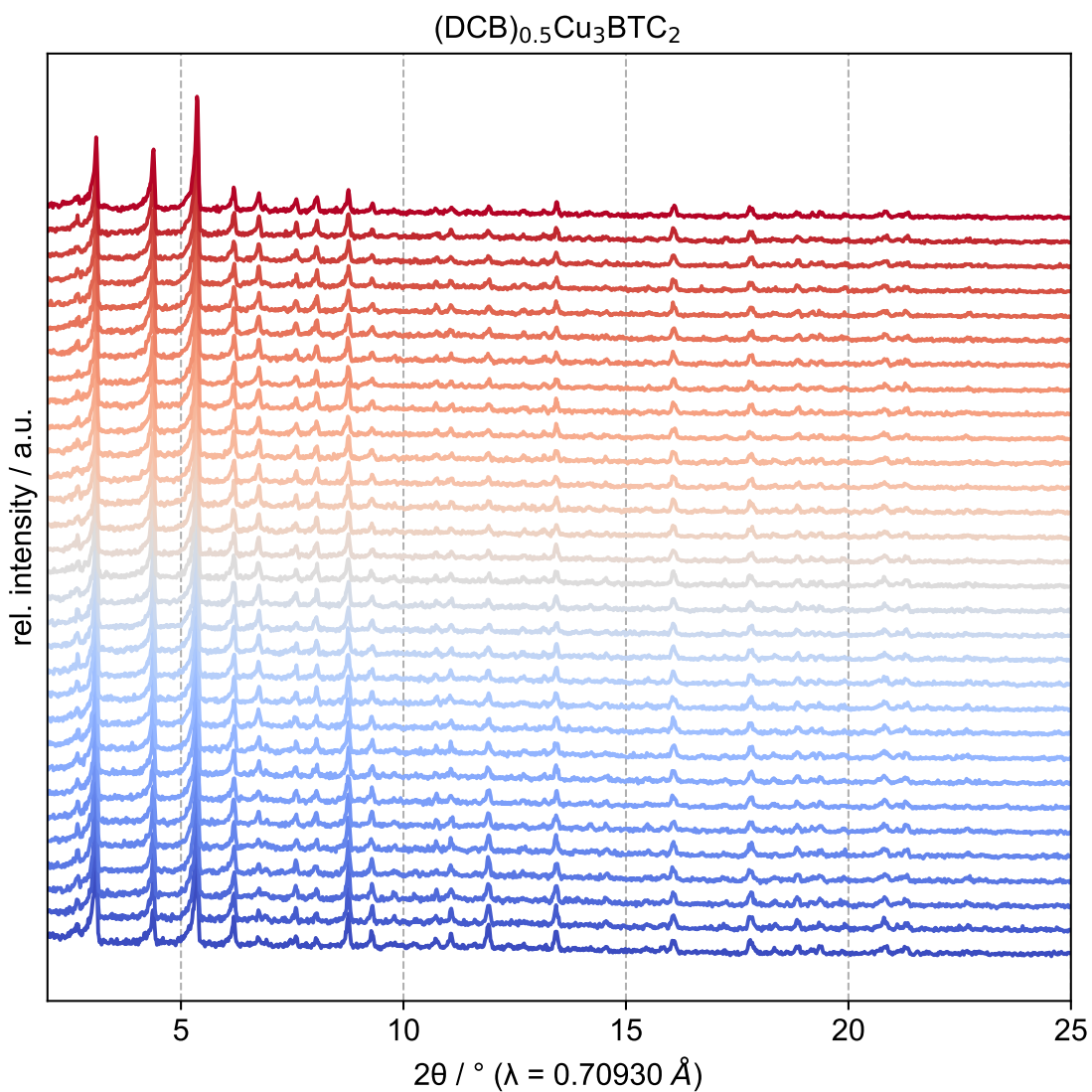


**Figure 35.** VT-PXRD data of **I** in a range of  $2^\circ$  to  $25^\circ$  from 100–400 K. During heating between 100 and 400 K, measurements were performed in temperature steps of 20 K. For the cooling, measurements were performed between 390 and 110 K with the same temperature steps of 20 K.

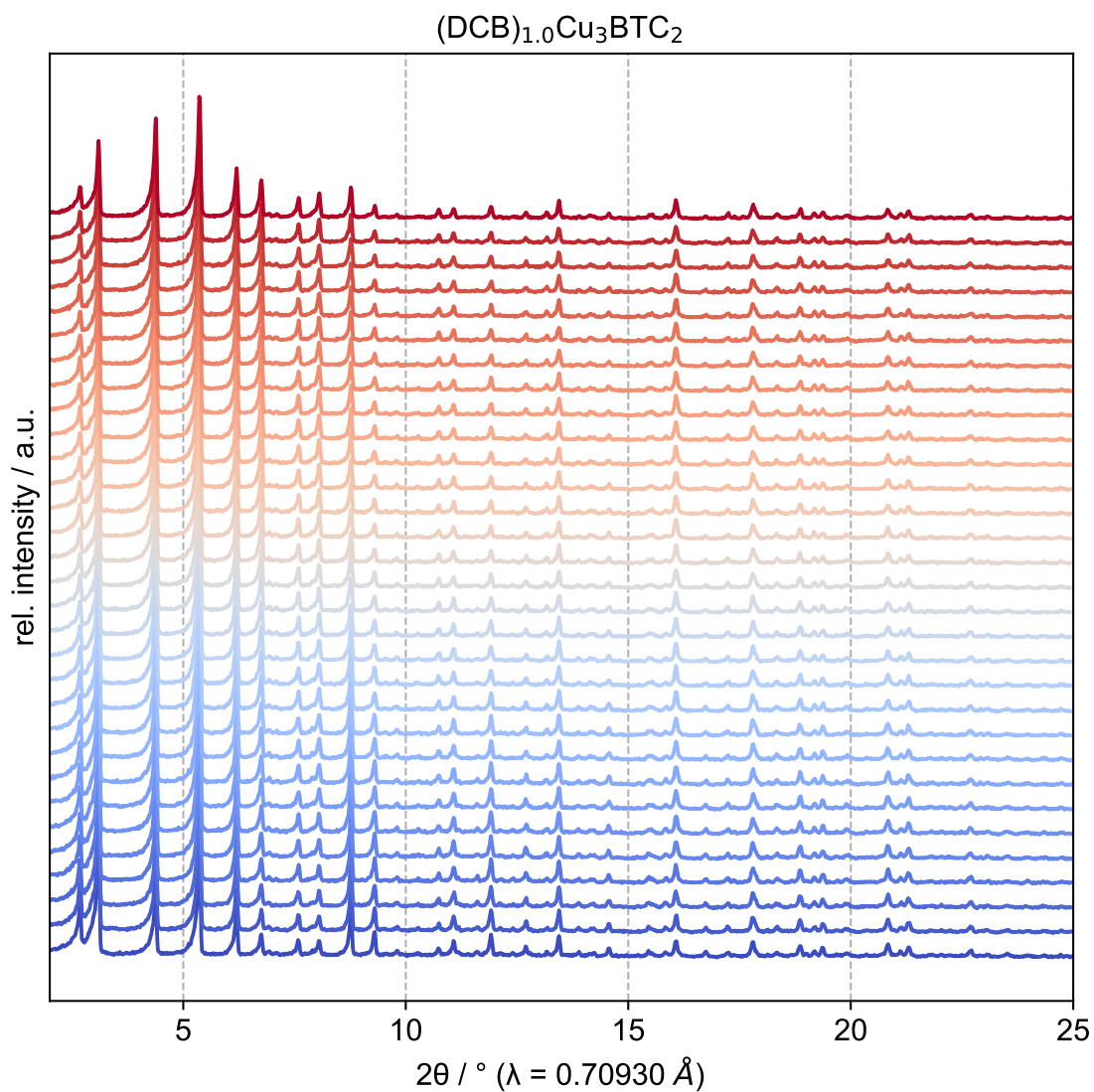


**Figure 36.** VT-PXRD data of **II** in a range of 2° to 25° from 100–400 K. During heating between 100 and 400 K, measurements were performed in temperature steps of 20 K. For the cooling, measurements were performed between 390 and 110 K with the same temperature steps of 20 K.

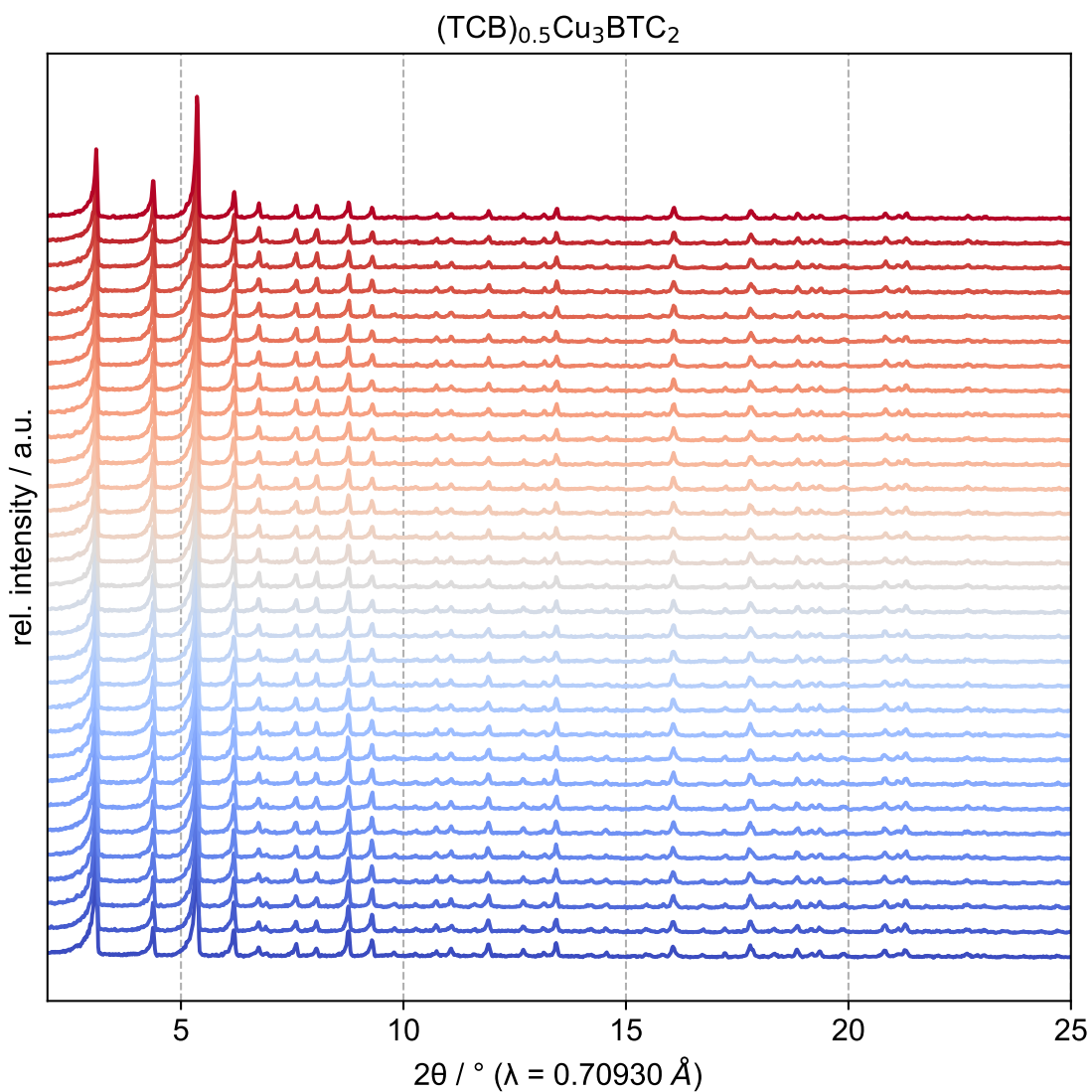


**Figure 37.** VT-PXRD data of **III** in a range of  $2^\circ$  to  $25^\circ$  from 100–400 K. During heating between 100 and 400 K, measurements were performed in temperature steps of 20 K. For the cooling, measurements were performed between 390 and 110 K with the same temperature steps of 20 K.

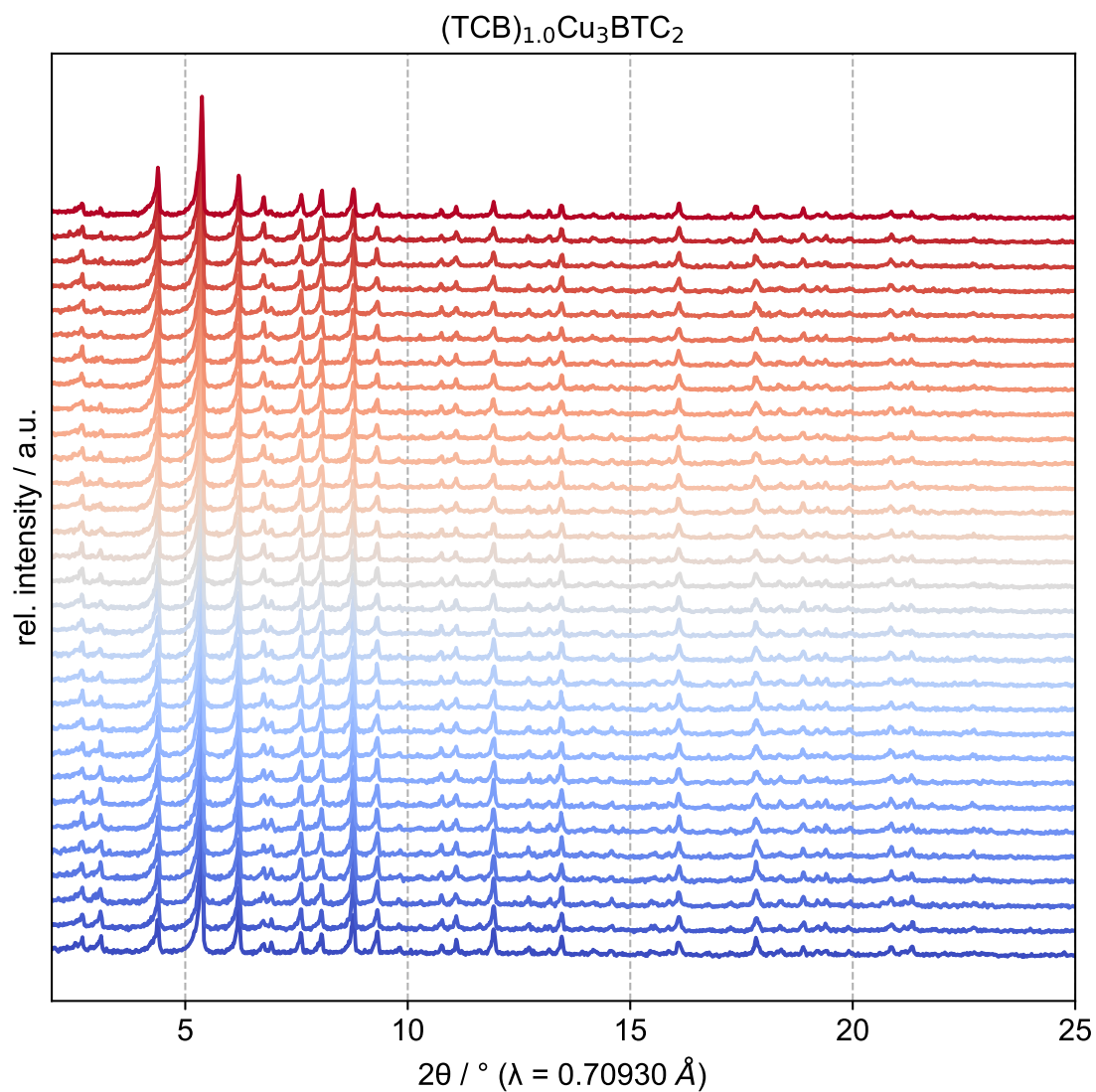


**Figure 38.** VT-PXRD data of **IV** in a range of  $2^\circ$  to  $25^\circ$  from 100–400 K. During heating between 100 and 400 K, measurements were performed in temperature steps of 20 K. For the cooling, measurements were performed between 390 and 110 K with the same temperature steps of 20 K.

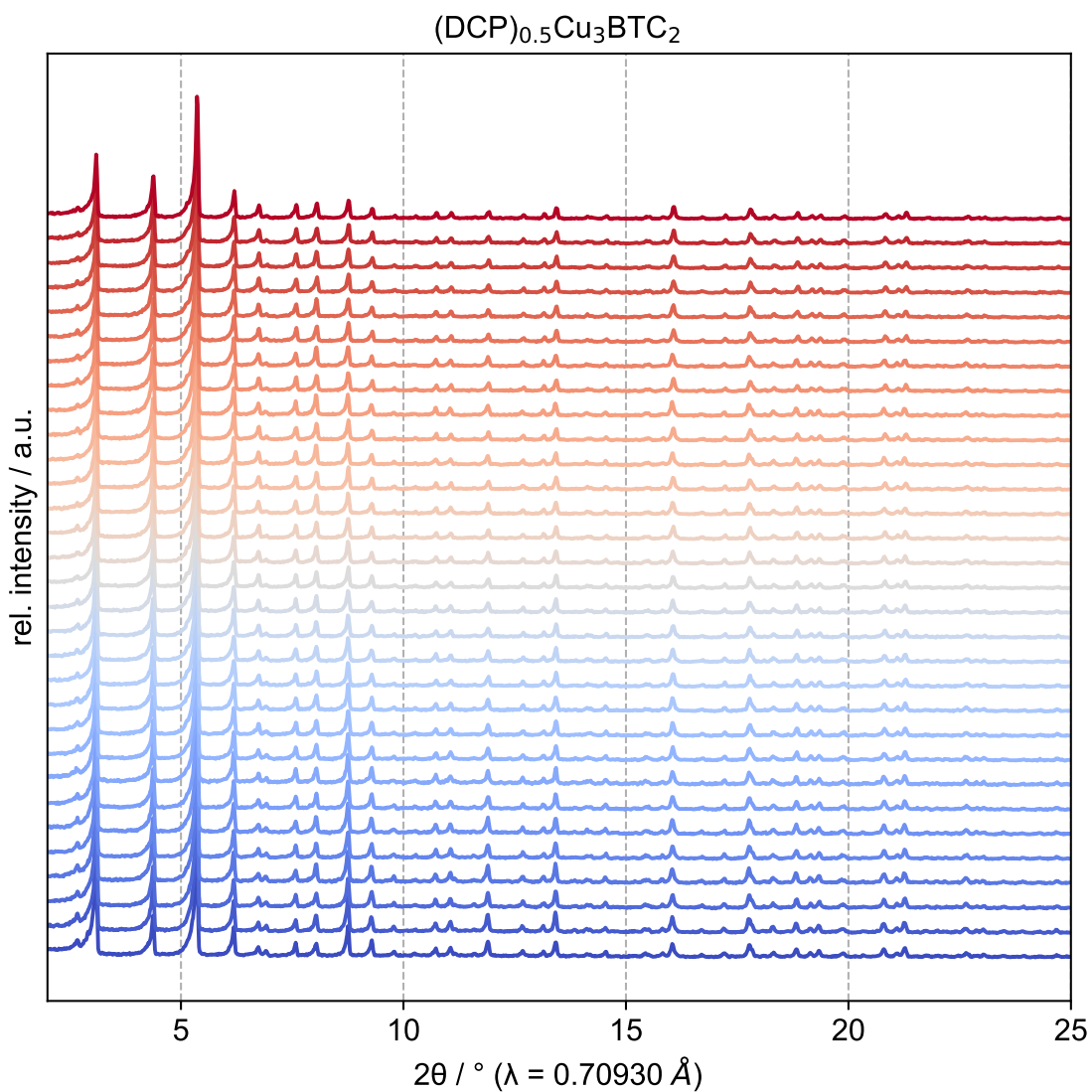


**Figure 39.** VT-PXRD data of **V** in a range of 2° to 25° from 100–400 K. During heating between 100 and 400 K, measurements were performed in temperature steps of 20 K. For the cooling, measurements were performed between 390 and 110 K with the same temperature steps of 20 K.

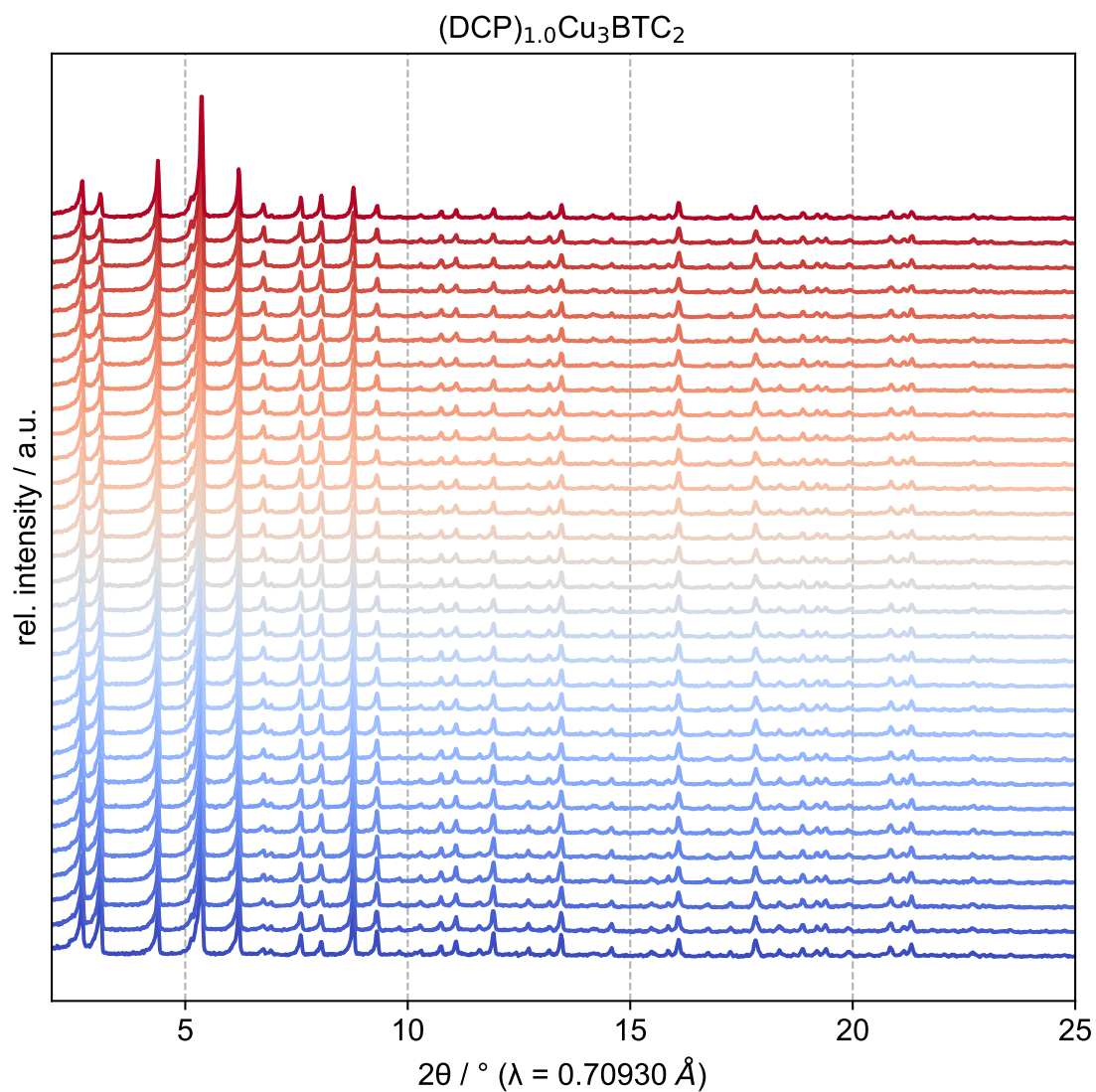


**Figure 40.** VT-PXRD data of **VI** in a range of 2° to 25° from 100–400 K. During heating between 100 and 400 K, measurements were performed in temperature steps of 20 K. For the cooling, measurements were performed between 390 and 110 K with the same temperature steps of 20 K.



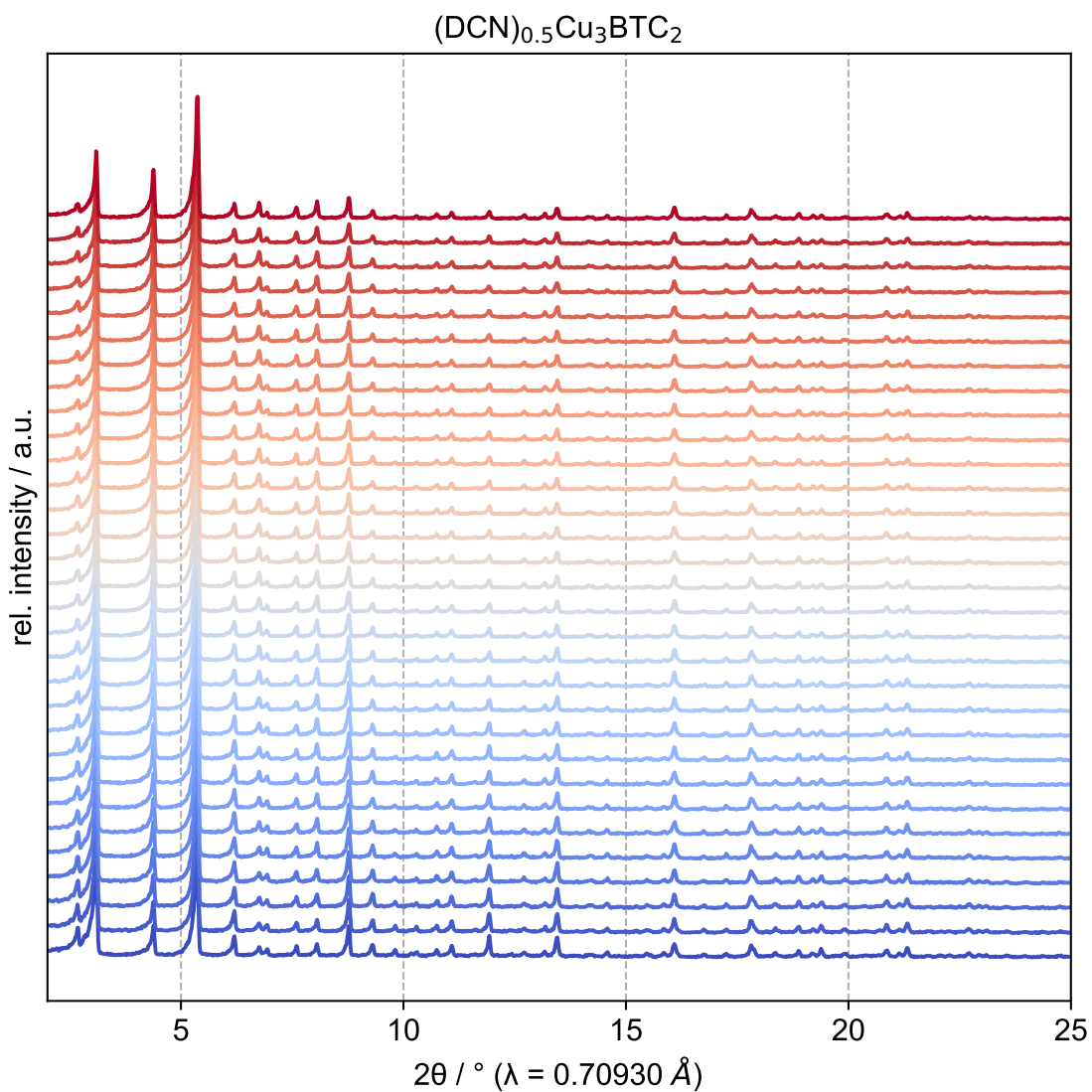


**Figure 41.** VT-PXRD data of **VII** in a range of 2° to 25° from 100–400 K. During heating between 100 and 400 K, measurements were performed in temperature steps of 20 K. For the cooling, measurements were performed between 390 and 110 K with the same temperature steps of 20 K.

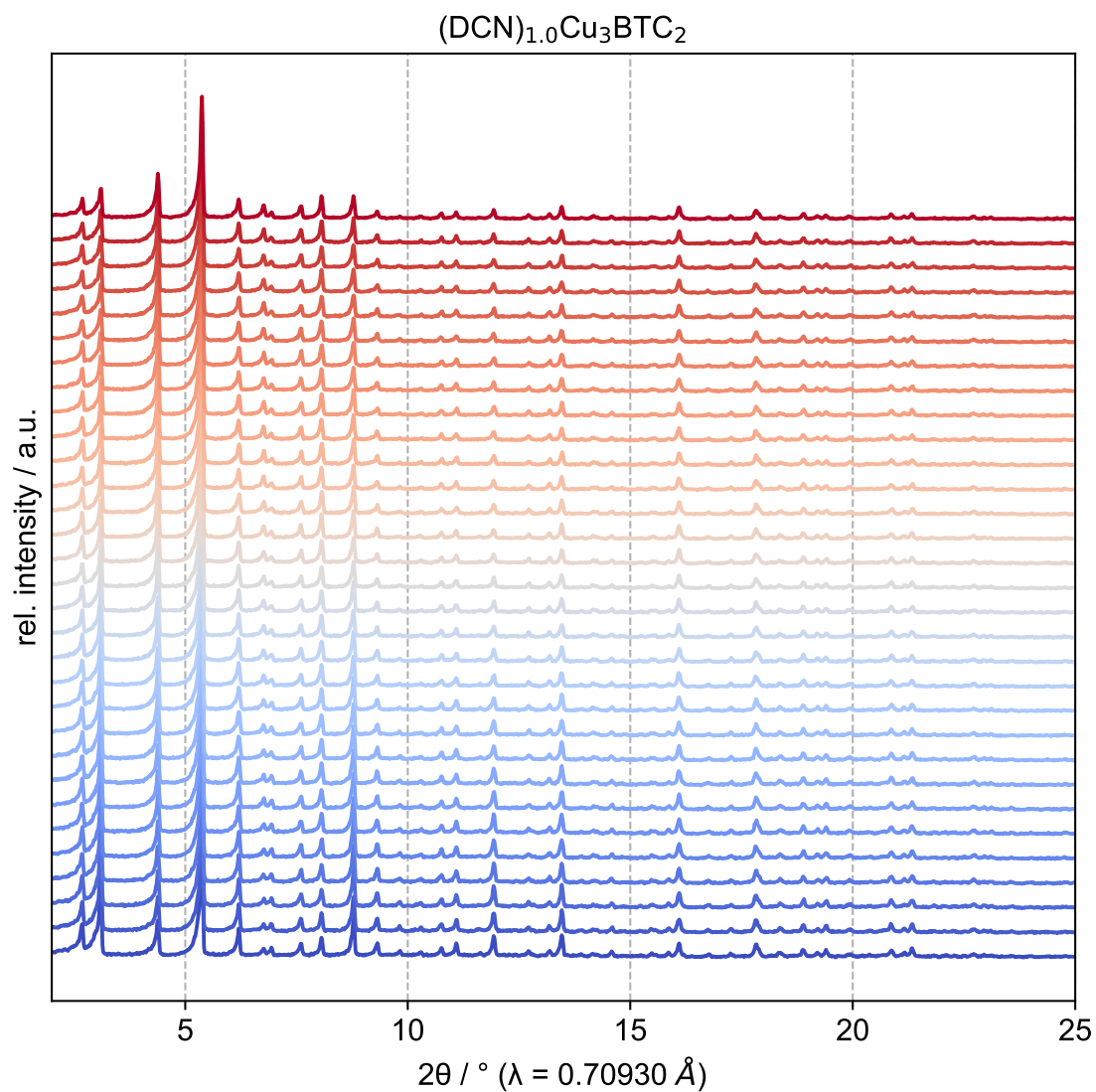


**Figure 42.** VT-PXRD data of **VIII** in a range of 2° to 25° from 100–400 K. During heating between 100 and 400 K, measurements were performed in temperature steps of 20 K. For the cooling, measurements were performed between 390 and 110 K with the same temperature steps of 20 K.

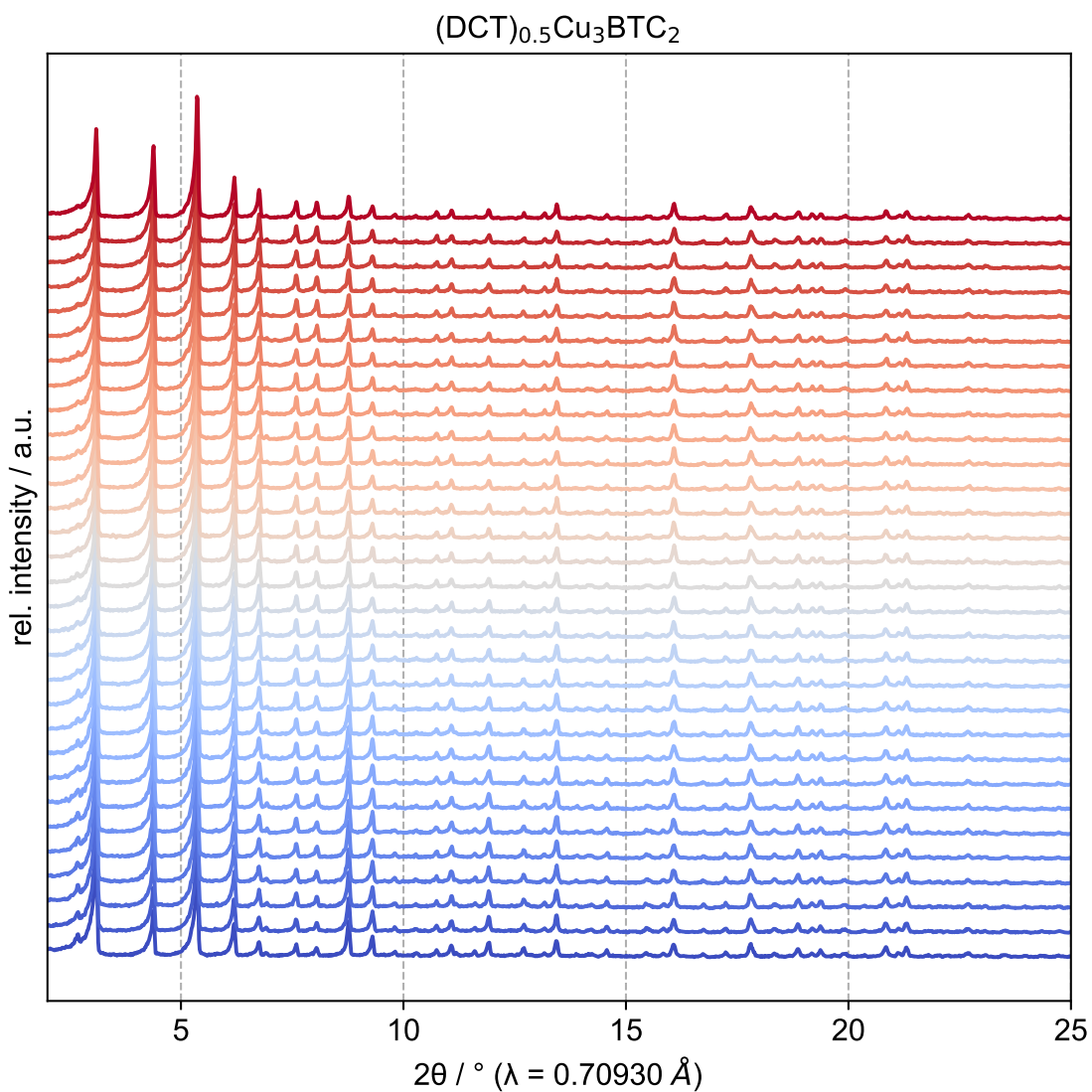


**Figure 43.** VT-PXRD data of **IX** in a range of 2° to 25° from 100–400 K. During heating between 100 and 400 K, measurements were performed in temperature steps of 20 K. For the cooling, measurements were performed between 390 and 110 K with the same temperature steps of 20 K.

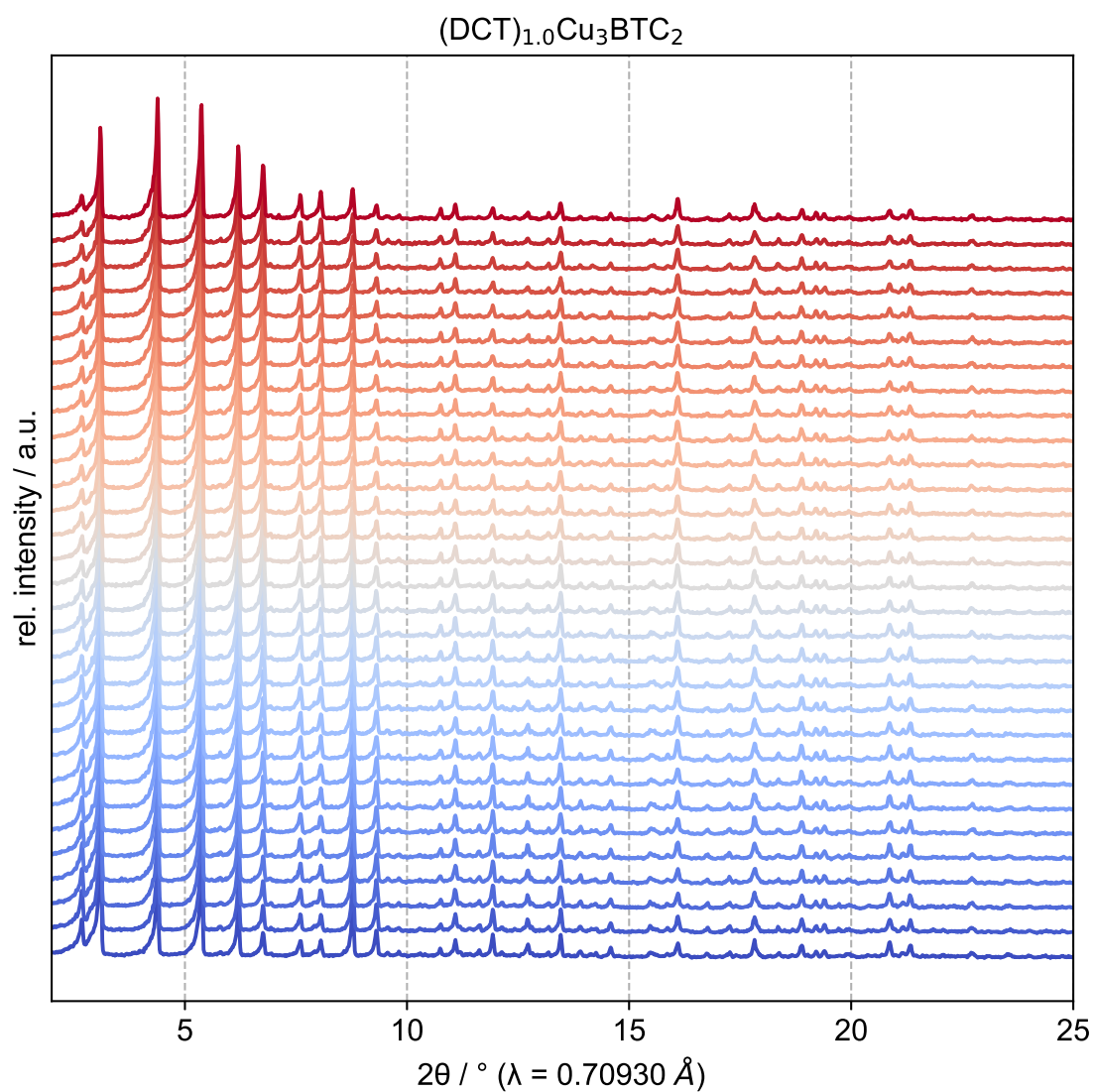


**Figure 44.** VT-PXRD data of **X** in a range of  $2^\circ$  to  $25^\circ$  from 100–400 K. During heating between 100 and 400 K, measurements were performed in temperature steps of 20 K. For the cooling, measurements were performed between 390 and 110 K with the same temperature steps of 20 K.

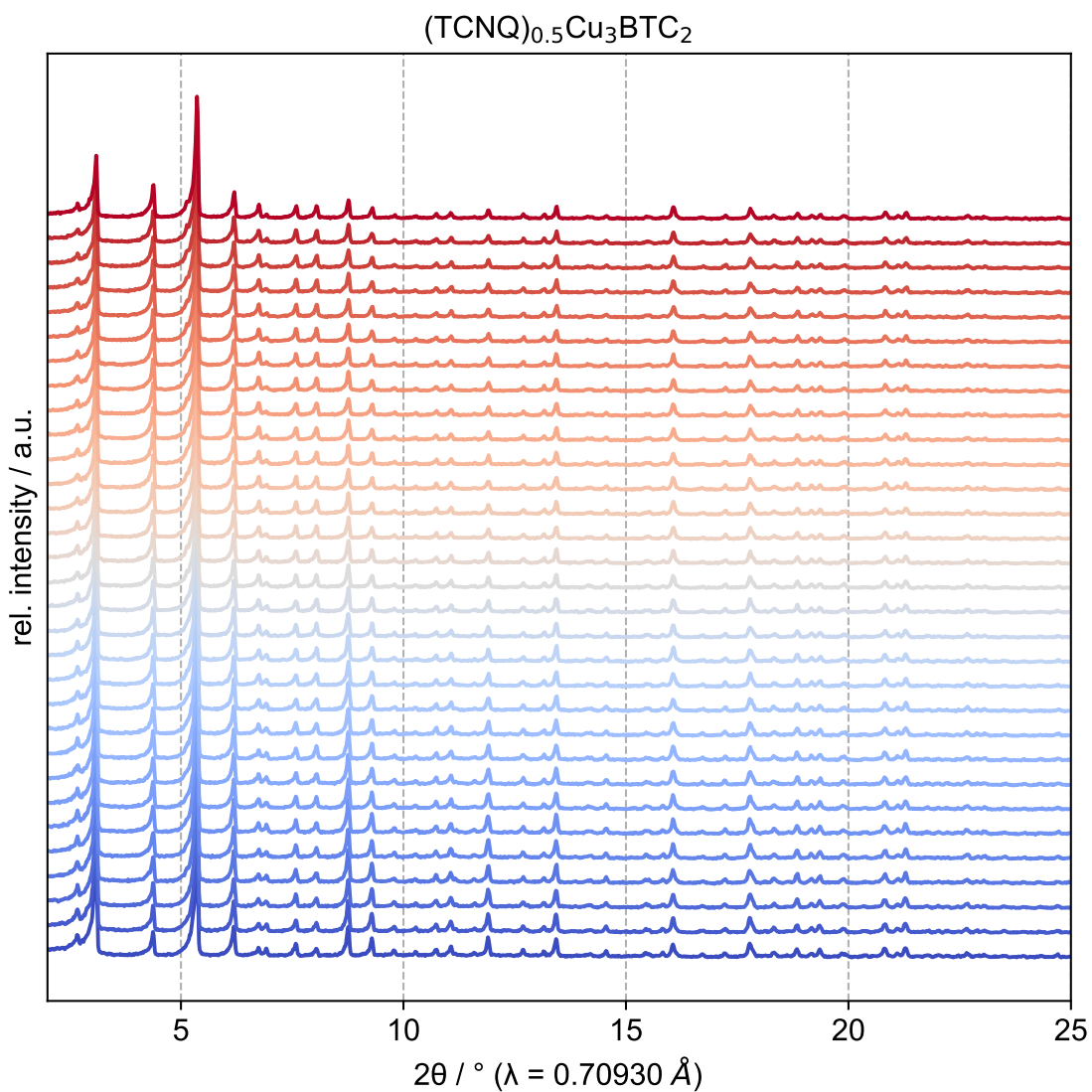


**Figure 45.** VT-PXRD data of **XI** in a range of 2° to 25° from 100–400 K. During heating between 100 and 400 K, measurements were performed in temperature steps of 20 K. For the cooling, measurements were performed between 390 and 110 K with the same temperature steps of 20 K.

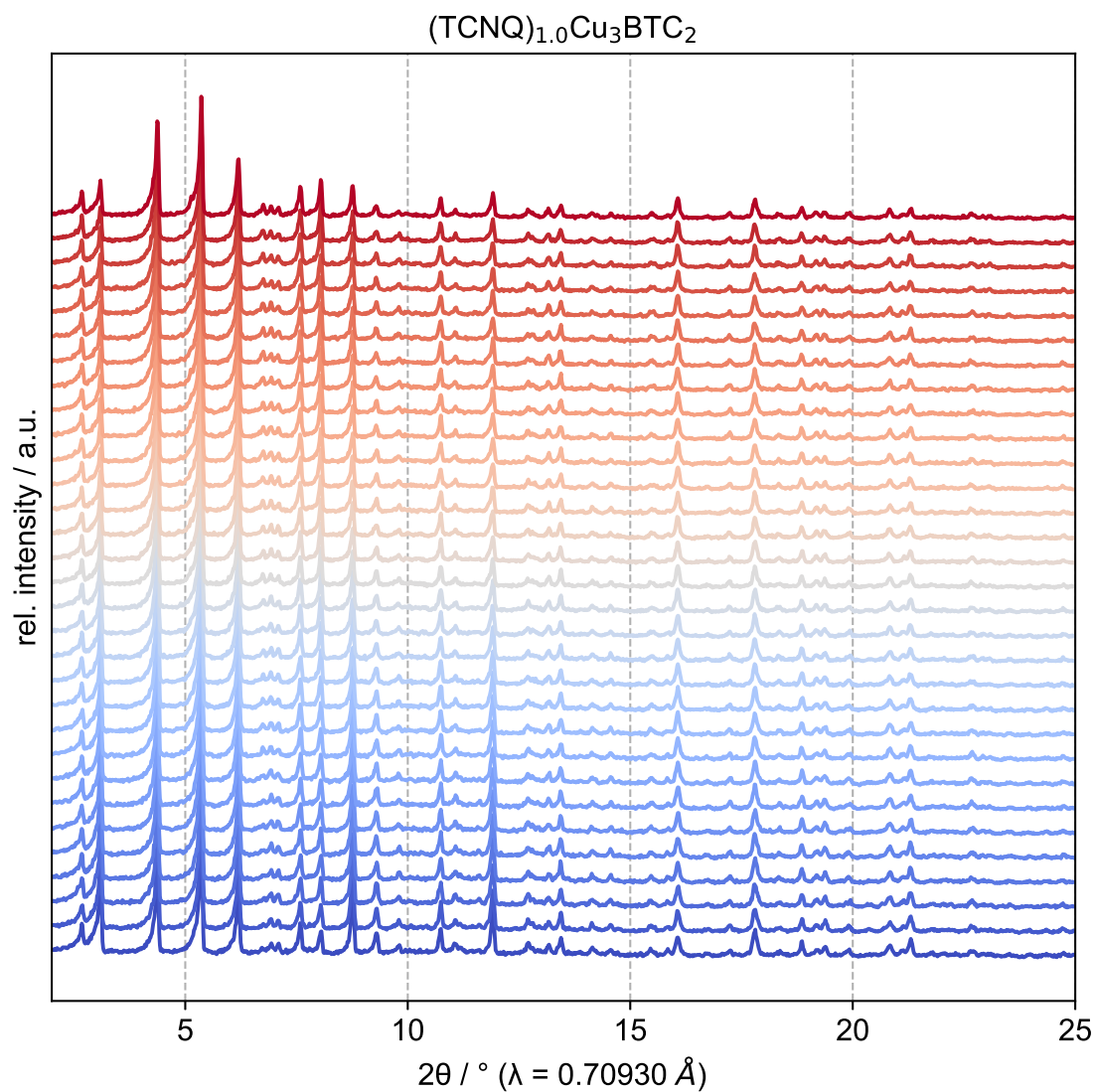


**Figure 46.** VT-PXRD data of **XII** in a range of  $2^\circ$  to  $25^\circ$  from 100–400 K. During heating between 100 and 400 K, measurements were performed in temperature steps of 20 K. For the cooling, measurements were performed between 390 and 110 K with the same temperature steps of 20 K.

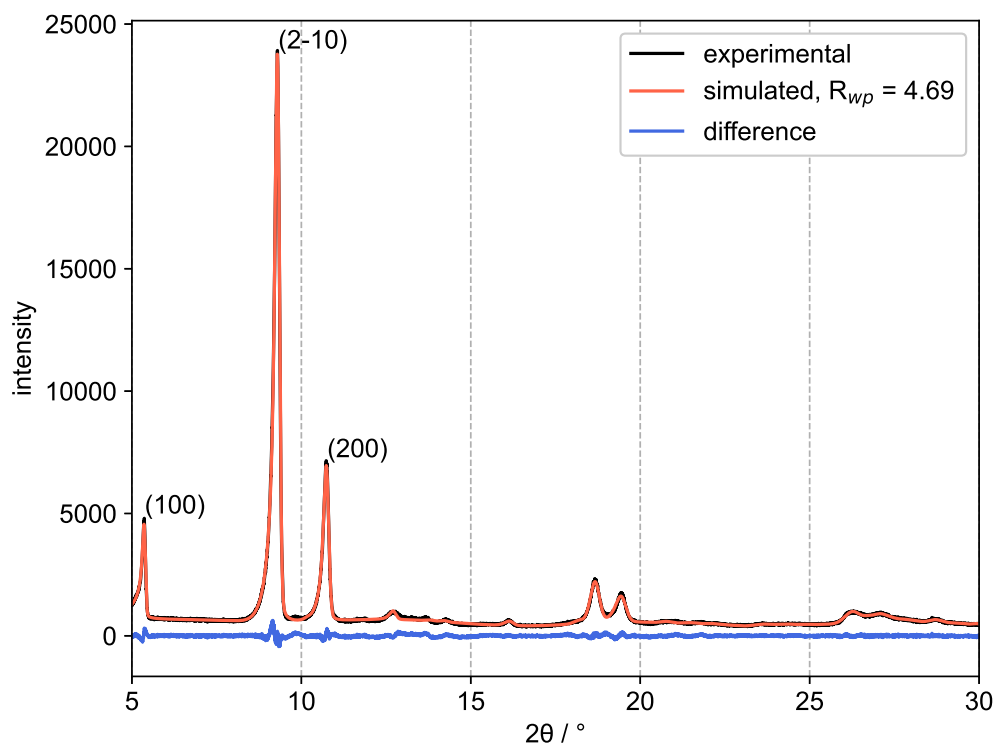


**Figure 47.** Pawley profile fit of activated Zn<sub>2</sub>TTFTB. The experimental data (black) was fitted (red) using the hexagonal space group  $P6_5$ . The difference curve is given in blue and the  $R_{wp}$  values are shown in the top right corner.

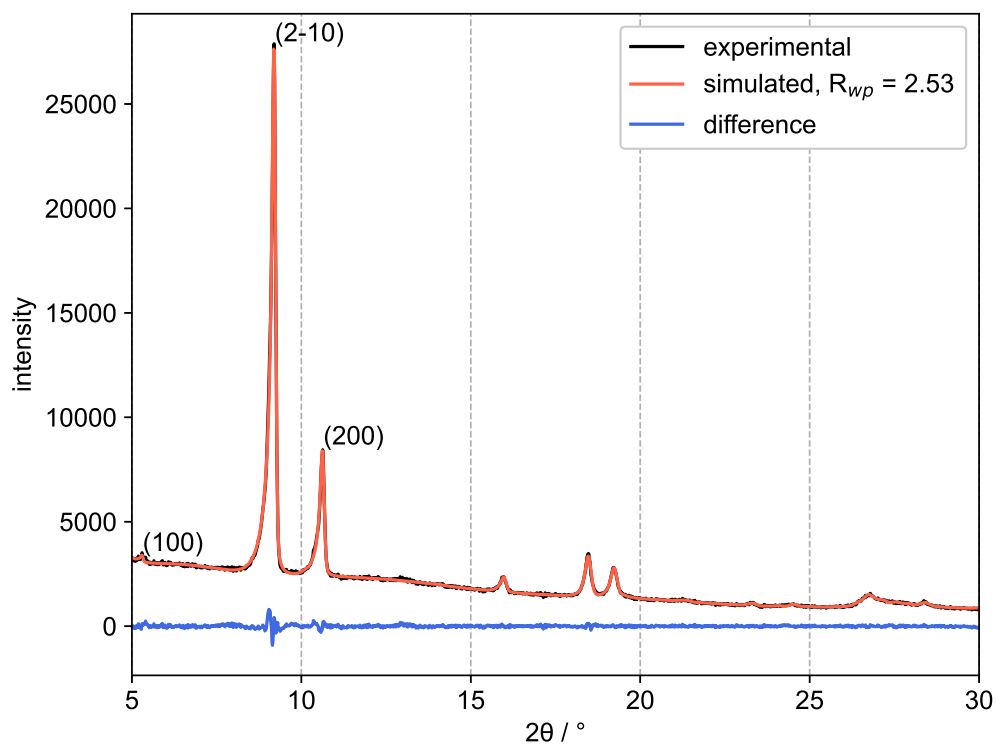


**Figure 48.** Pawley profile fit of activated Cd<sub>2</sub>TTFTB. The experimental data (black) was fitted (red) using the hexagonal space group  $P6_5$ . The difference curve is given in blue and the  $R_{wp}$  values are shown in the top right corner.

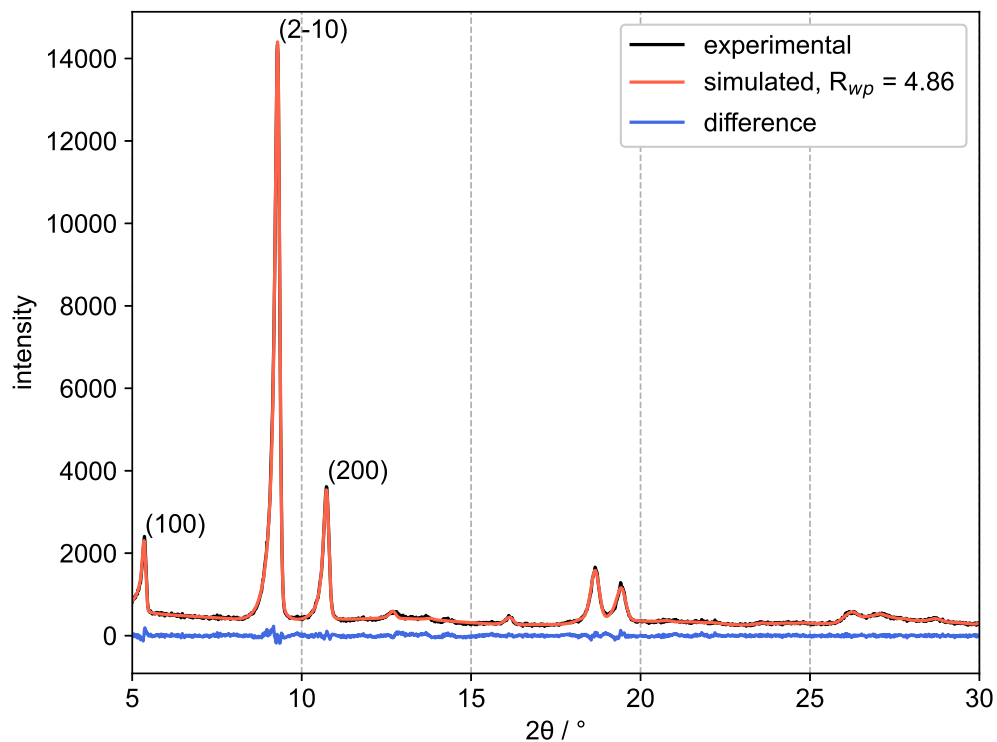


**Figure 49.** Pawley profile fit of 1. The experimental data (black) was fitted (red) using the hexagonal space group  $P6_5$ . The difference curve is given in blue and the  $R_{wp}$  values are shown in the top right.

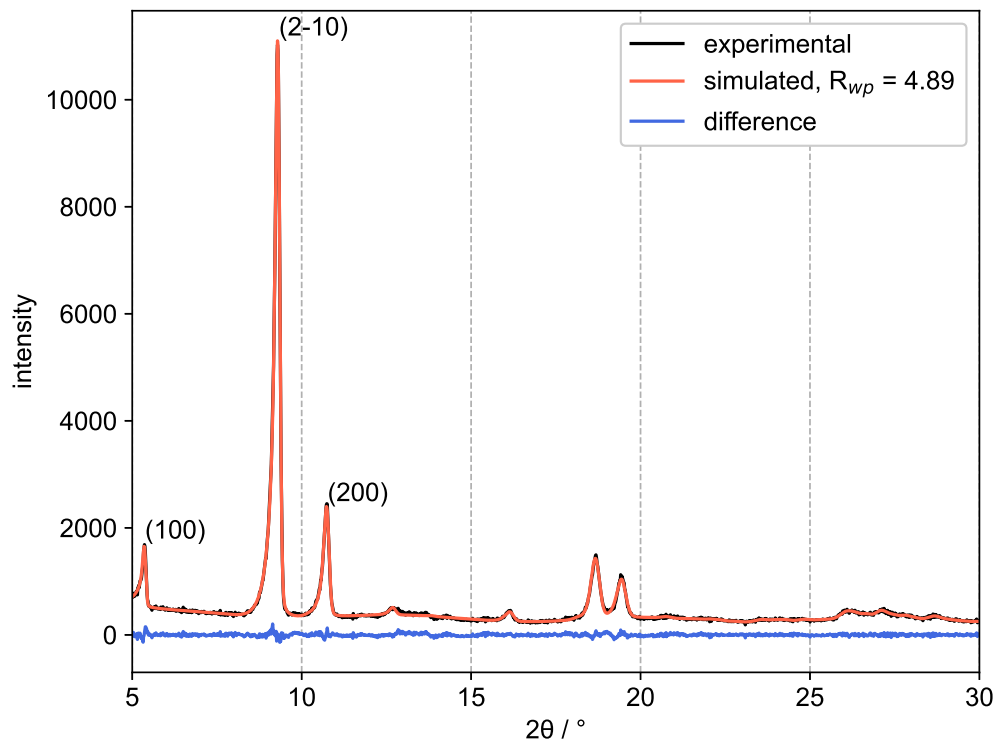


**Figure 50.** Pawley profile fit of 2. The experimental data (black) was fitted (red) using the hexagonal space group  $P6_5$ . The difference curve is given in blue and the  $R_{wp}$  values are shown in the top right.



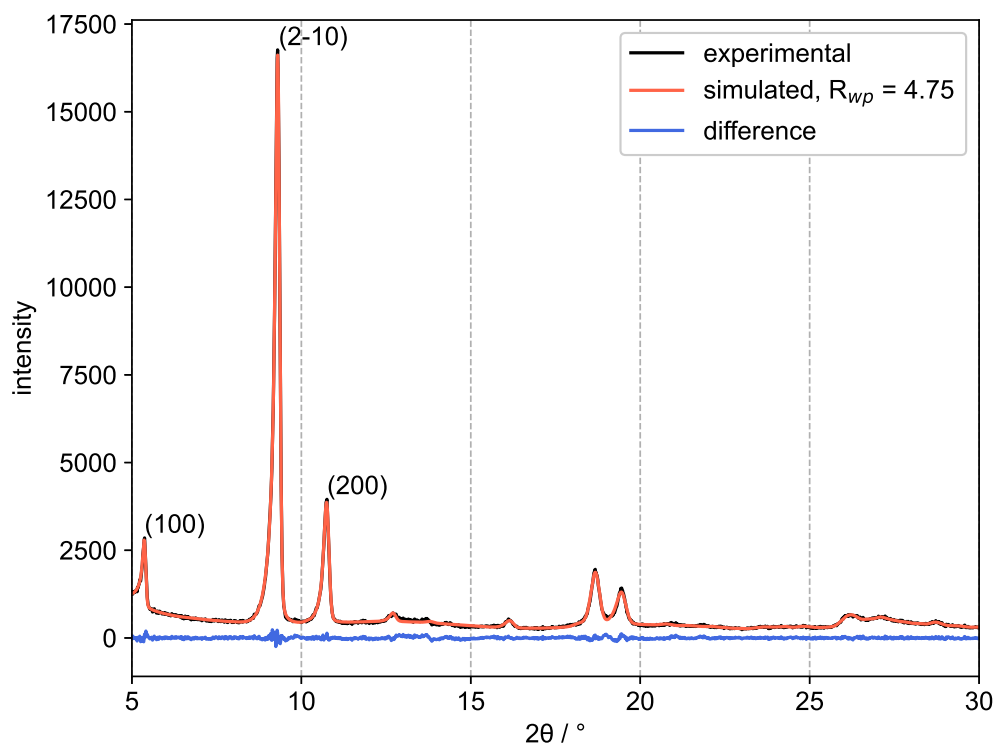


**Figure 51.** Pawley profile fit of **3**. The experimental data (black) was fitted (red) using the hexagonal space group  $P6_5$ . The difference curve is given in blue and the  $R_{wp}$  values are shown in the top right.

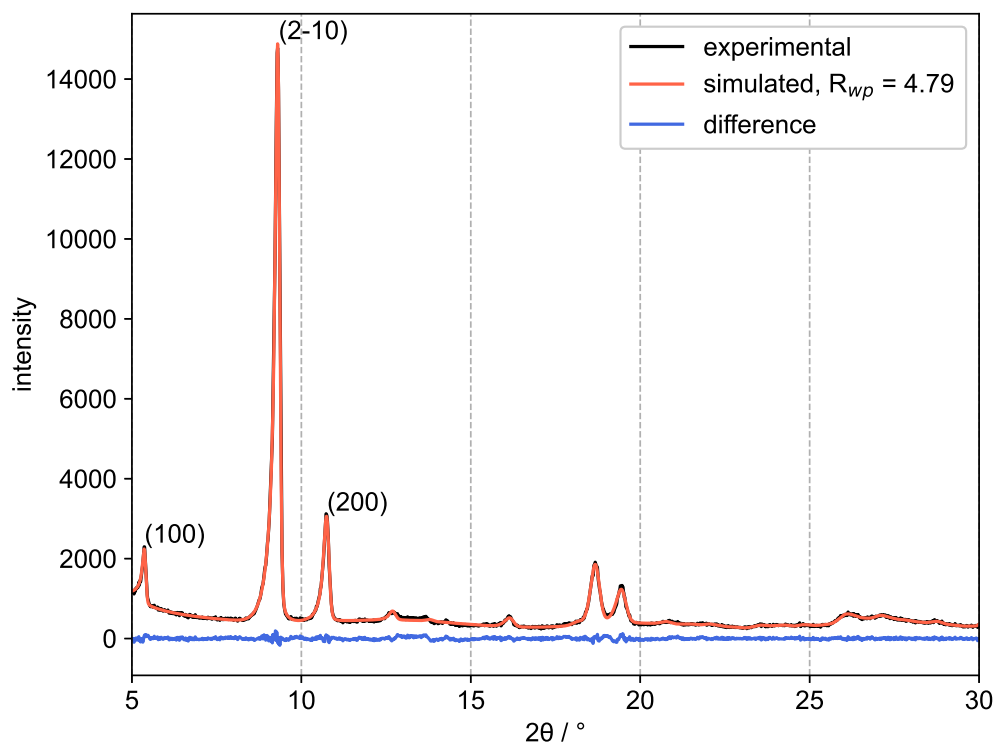


**Figure 52.** Pawley profile fit of **4**. The experimental data (black) was fitted (red) using the hexagonal space group  $P6_5$ . The difference curve is given in blue and the  $R_{wp}$  values are shown in the top right.

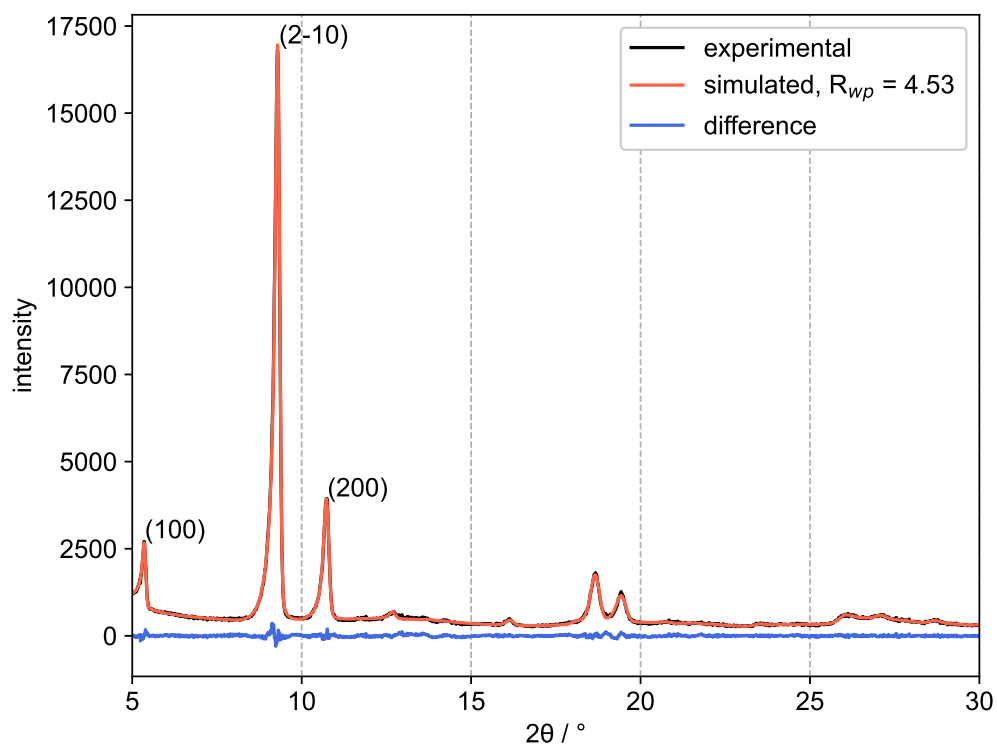


**Figure 53.** Pawley profile fit of **5**. The experimental data (black) was fitted (red) using the hexagonal space group  $P6_5$ . The difference curve is given in blue and the  $R_{wp}$  values are shown in the top right.

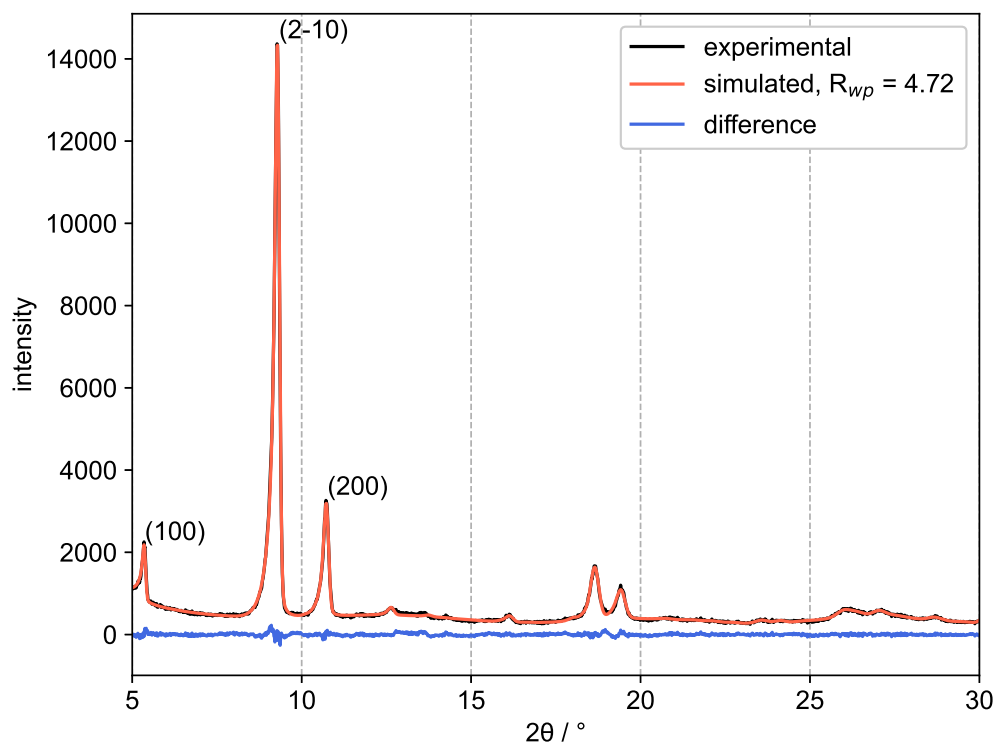


**Figure 54.** Pawley profile fit of **6**. The experimental data (black) was fitted (red) using the hexagonal space group  $P6_5$ . The difference curve is given in blue and the  $R_{wp}$  values are shown in the top right.

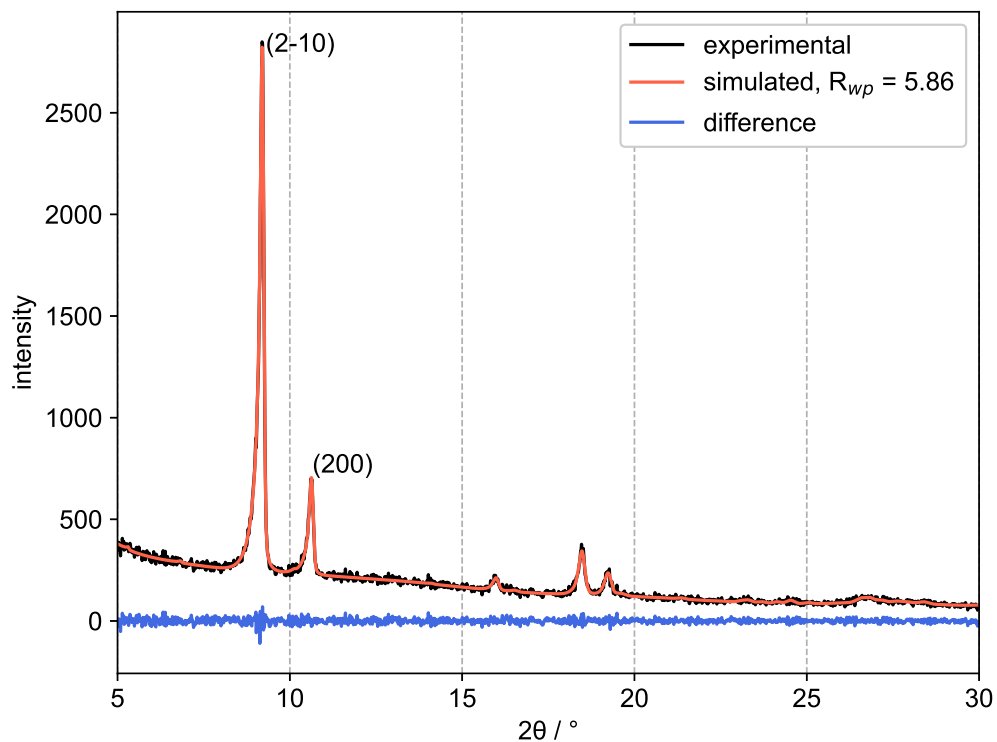


**Figure 55.** Pawley profile fit of **7**. The experimental data (black) was fitted (red) using the hexagonal space group  $P6_5$ . The difference curve is given in blue and the  $R_{wp}$  values are shown in the top right.

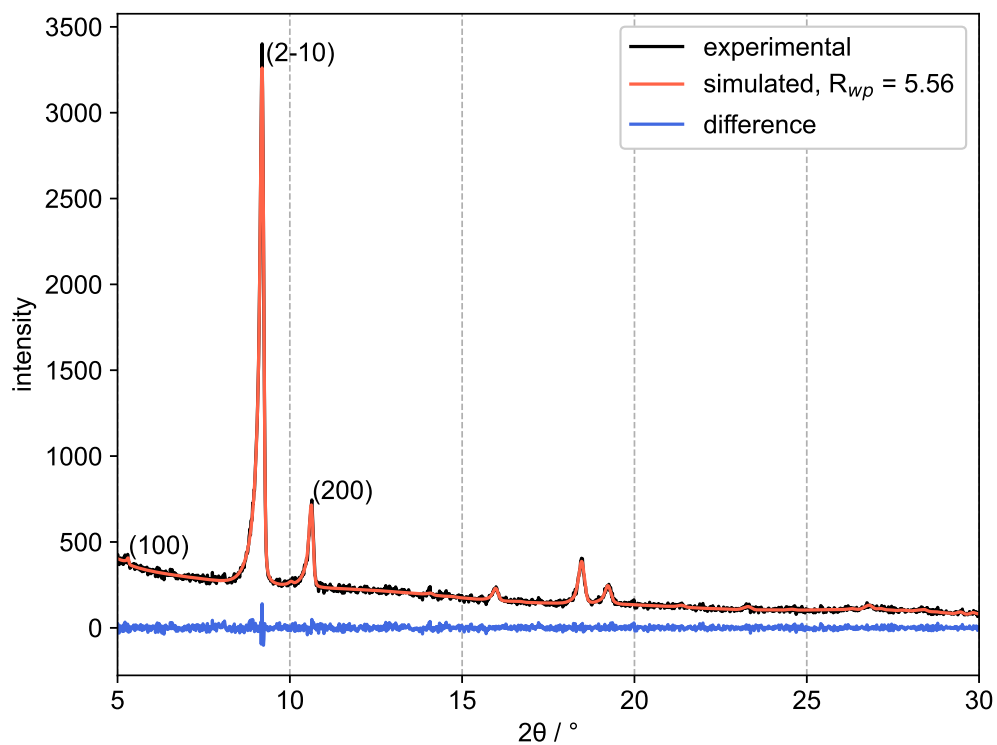


**Figure 56.** Pawley profile fit of **8**. The experimental data (black) was fitted (red) using the hexagonal space group  $P6_5$ . The difference curve is given in blue and the  $R_{wp}$  values are shown in the top right.

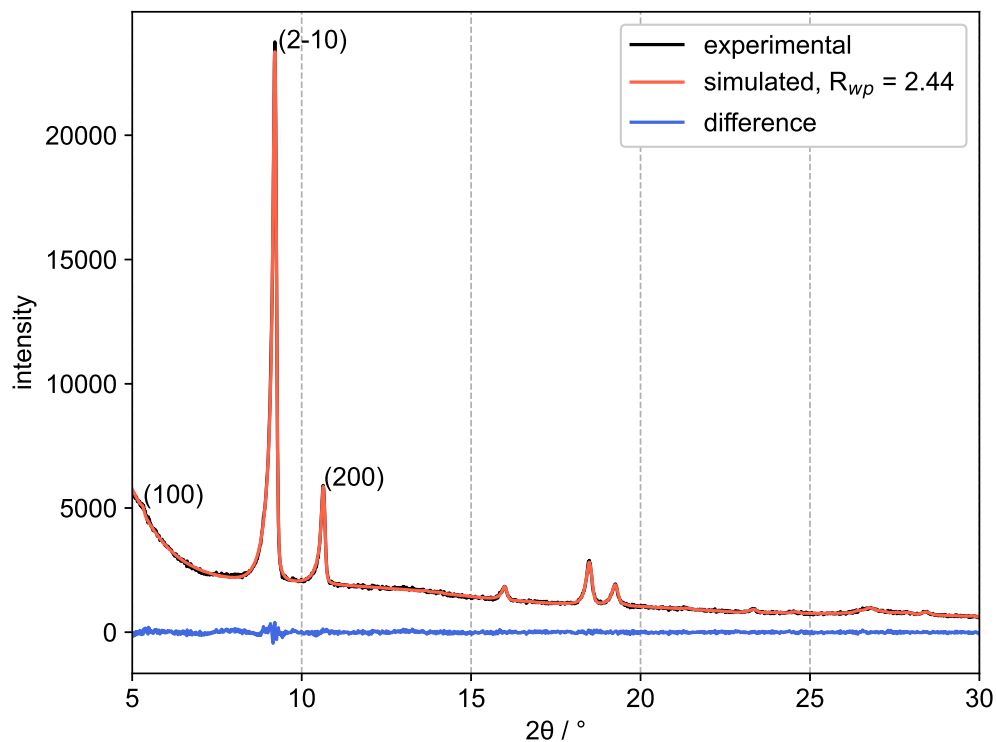


**Figure 57.** Pawley profile fit of **9**. The experimental data (black) was fitted (red) using the hexagonal space group  $P6_5$ . The difference curve is given in blue and the  $R_{wp}$  values are shown in the top right.

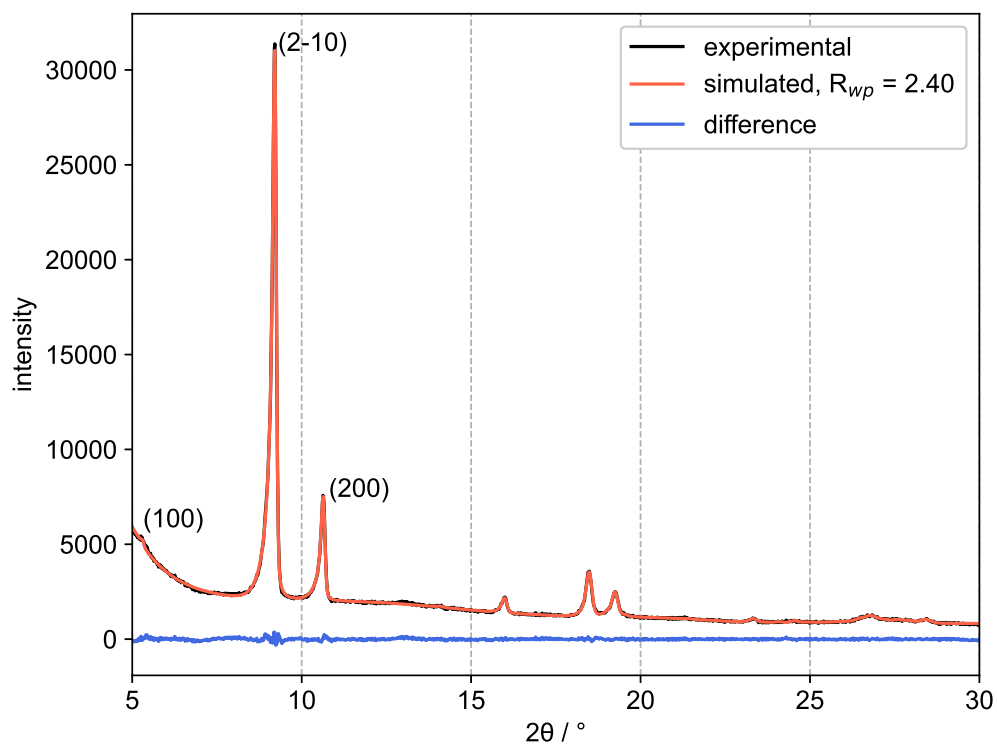


**Figure 58.** Pawley profile fit of **10**. The experimental data (black) was fitted (red) using the hexagonal space group  $P6_5$ . The difference curve is given in blue and the  $R_{wp}$  values are shown in the top right.

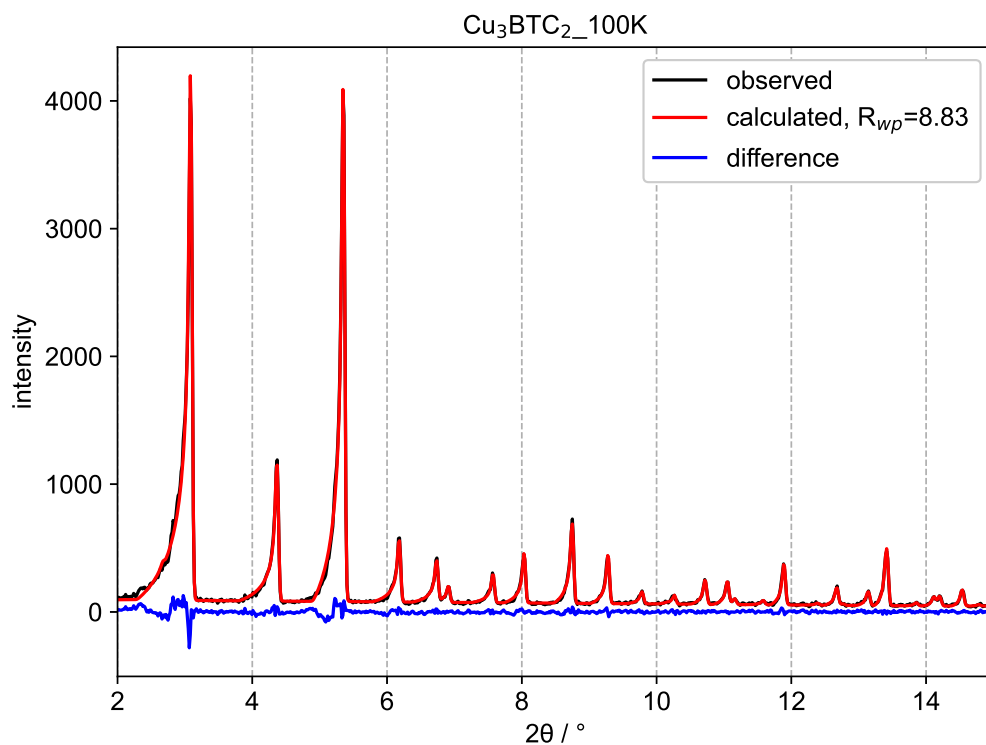


**Figure 59.** Pawley profile fit of  $\text{Cu}_3\text{BTC}_2$  at 100 K. The experimental data (black) was fitted (red) using the cubic space group Fm-3m. The difference curve is given in blue and the  $R_{wp}$  values are shown in the top right corner.

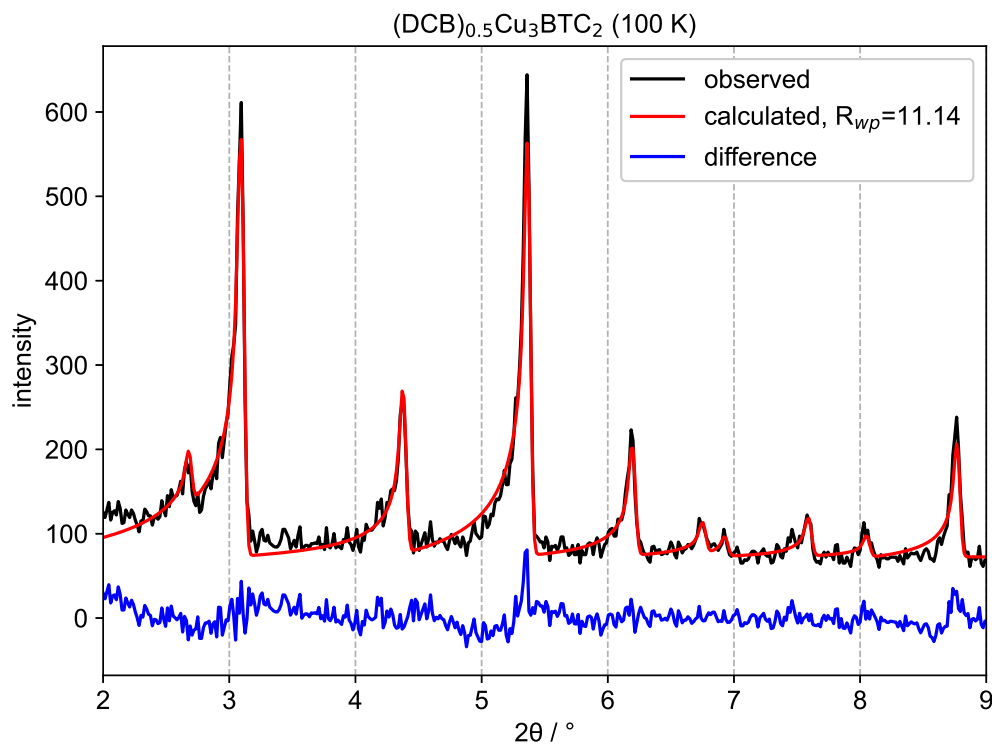


**Figure 60.** Pawley profile fit of **I** at 100 K. The experimental data (black) was fitted (red) using the cubic space group Fm-3m. The difference curve is given in blue and the  $R_{wp}$  values are shown in the top right corner.

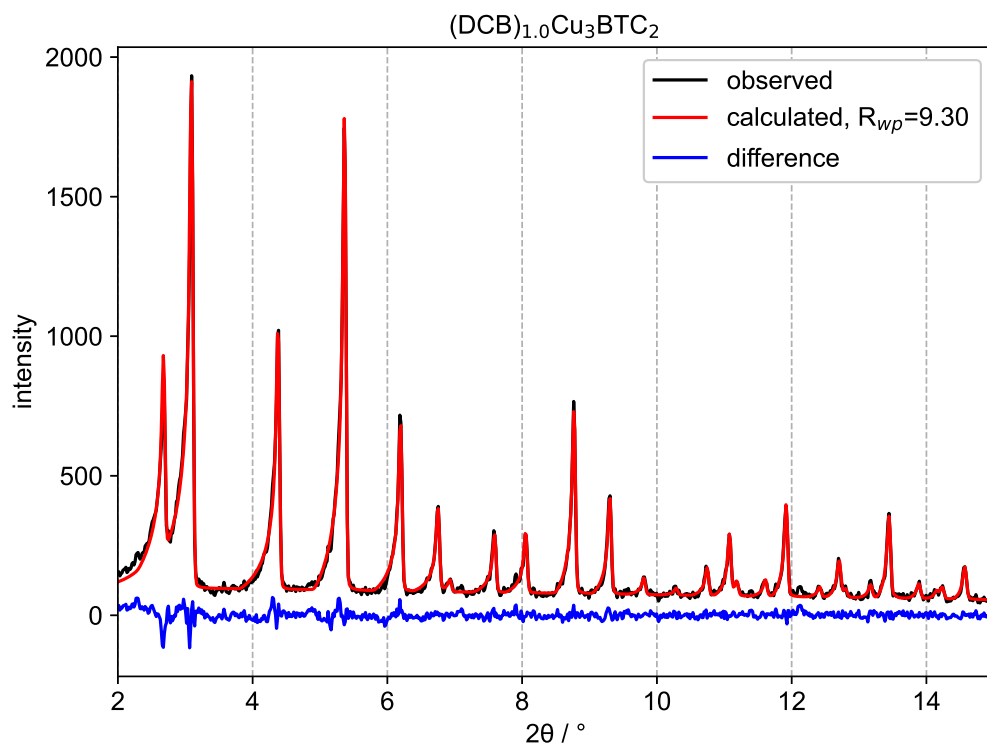


**Figure 61.** Pawley profile fit of **II** at 100 K. The experimental data (black) was fitted (red) using the cubic space group Fm-3m. The difference curve is given in blue and the  $R_{wp}$  values are shown in the top right corner.

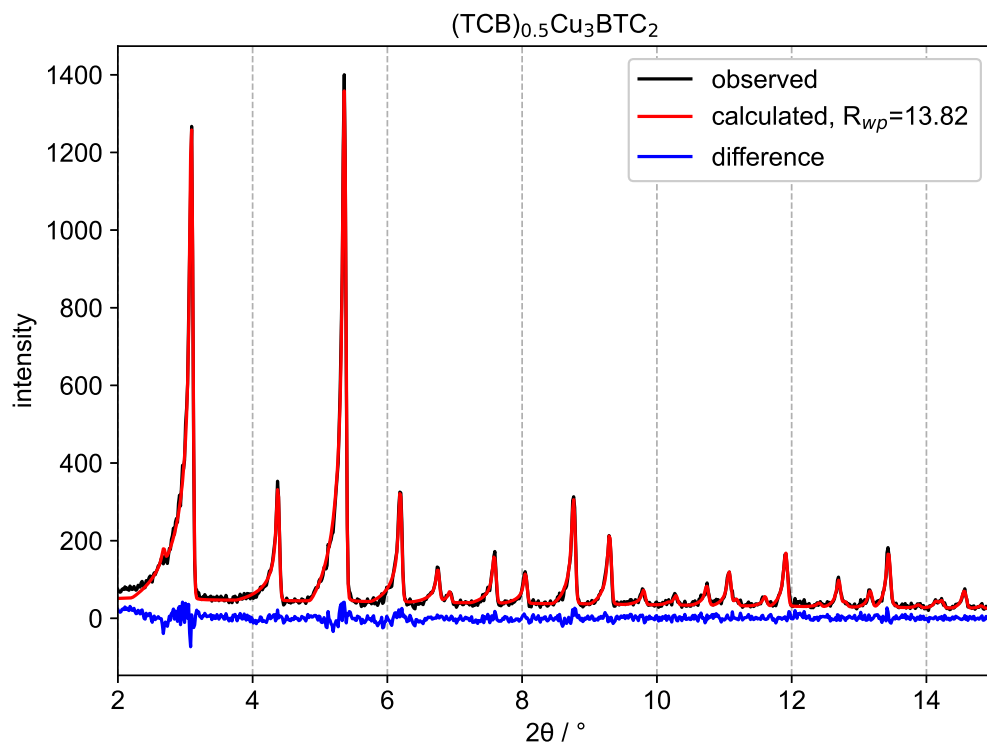


**Figure 62.** Pawley profile fit of **III** at 100 K. The experimental data (black) was fitted (red) using the cubic space group Fm-3m. The difference curve is given in blue and the  $R_{wp}$  values are shown in the top right corner.

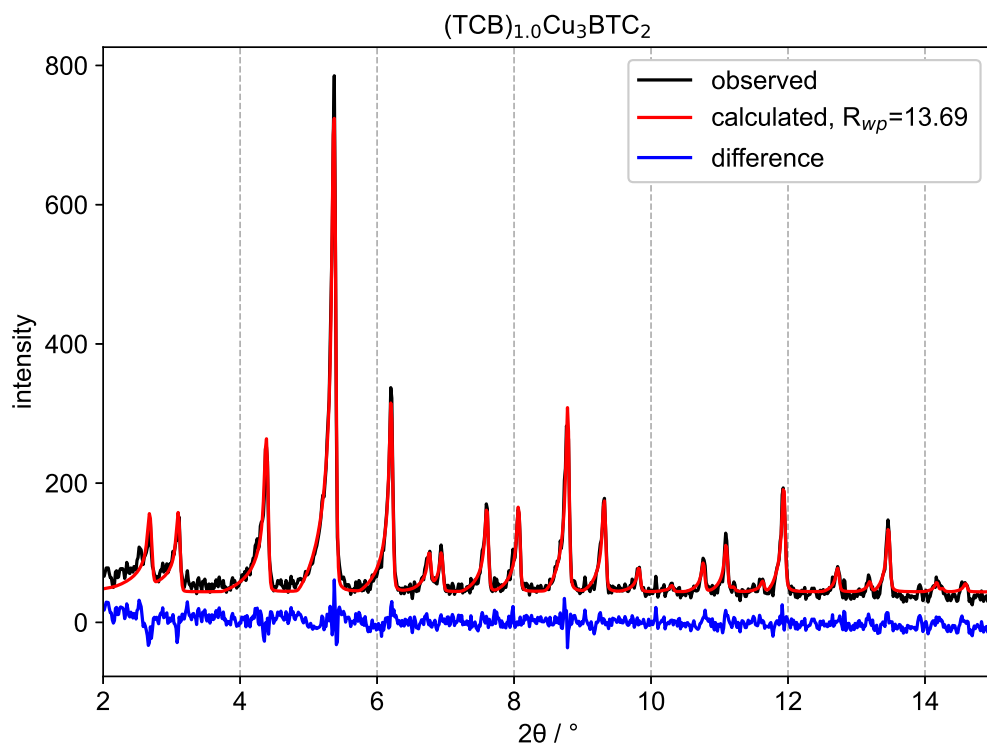


**Figure 63.** Pawley profile fit of **IV** at 100 K. The experimental data (black) was fitted (red) using the cubic space group Fm-3m. The difference curve is given in blue and the  $R_{wp}$  values are shown in the top right corner.

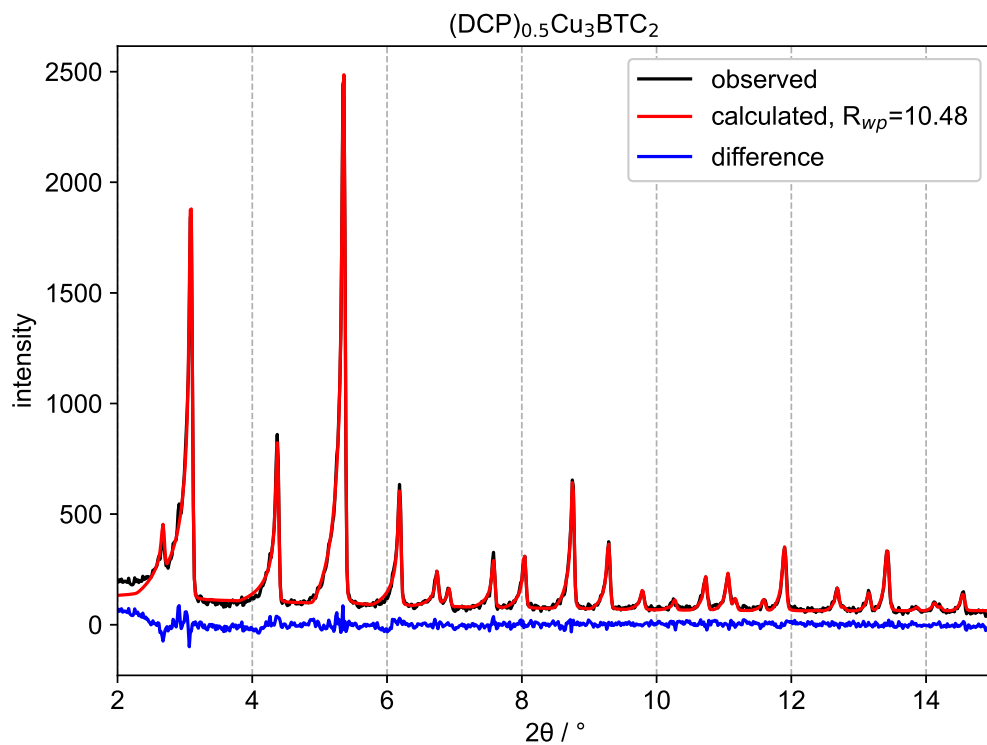


**Figure 64.** Pawley profile fit of **V** at 100 K. The experimental data (black) was fitted (red) using the cubic space group Fm-3m. The difference curve is given in blue and the  $R_{wp}$  values are shown in the top right corner.

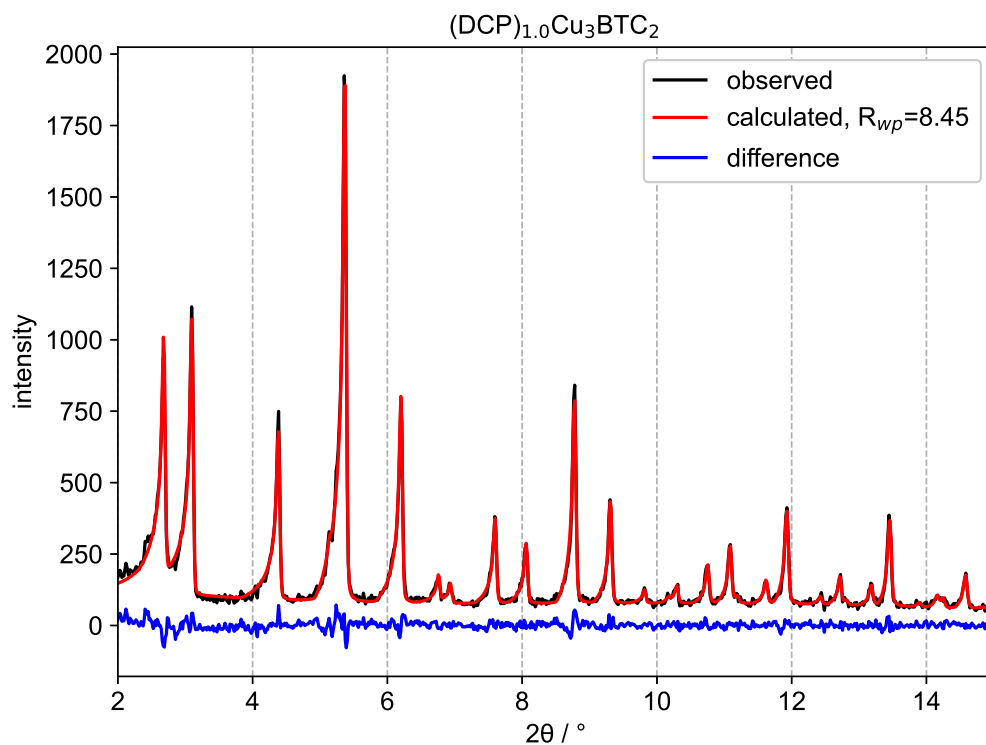


**Figure 65.** Pawley profile fit of **VI** at 100 K. The experimental data (black) was fitted (red) using the cubic space group Fm-3m. The difference curve is given in blue and the  $R_{wp}$  values are shown in the top right corner.

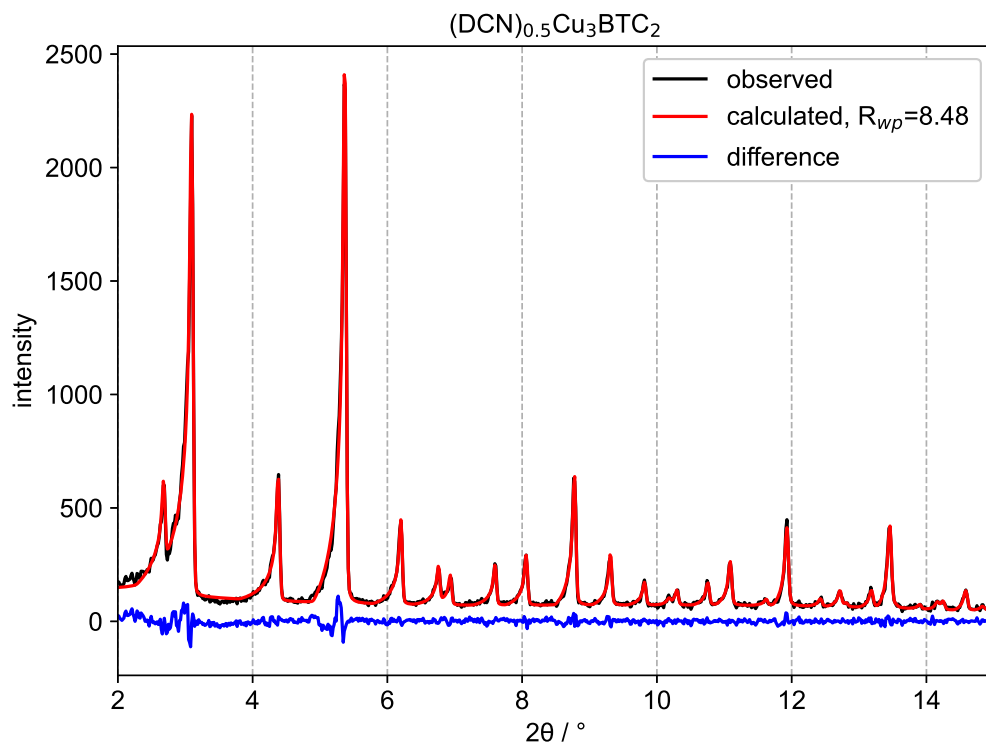


**Figure 66.** Pawley profile fit of **VII** at 100 K. The experimental data (black) was fitted (red) using the cubic space group Fm-3m. The difference curve is given in blue and the  $R_{wp}$  values are shown in the top right corner.



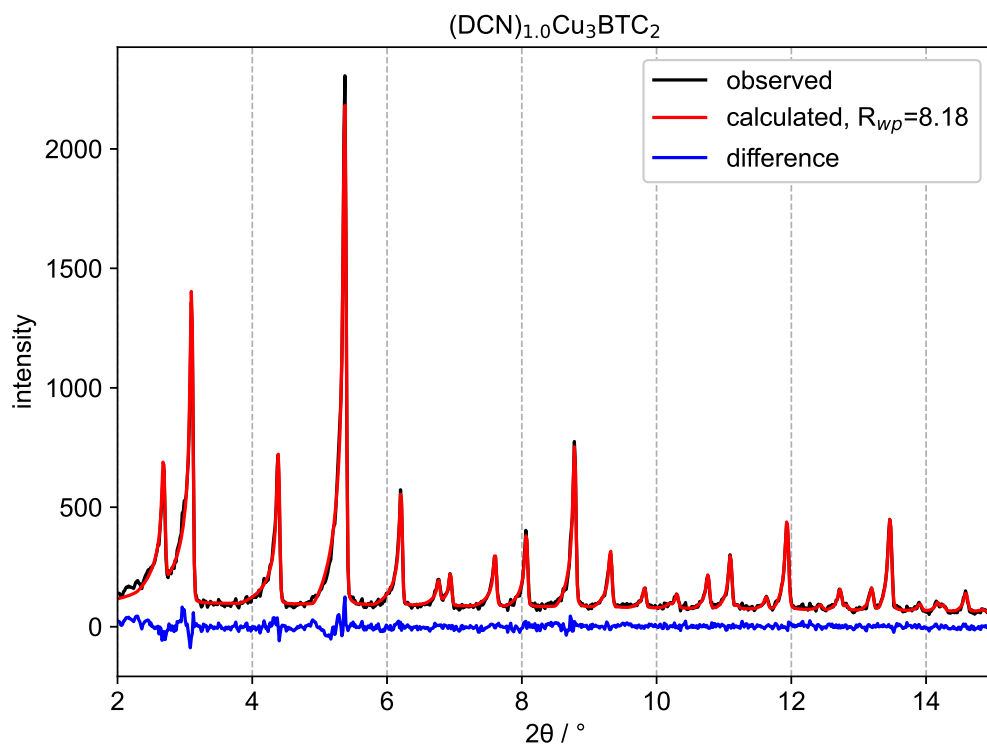


**Figure 67.** Pawley profile fit of **VIII** at 100 K. The experimental data (black) was fitted (red) using the cubic space group Fm-3m. The difference curve is given in blue and the  $R_{wp}$  values are shown in the top right corner.

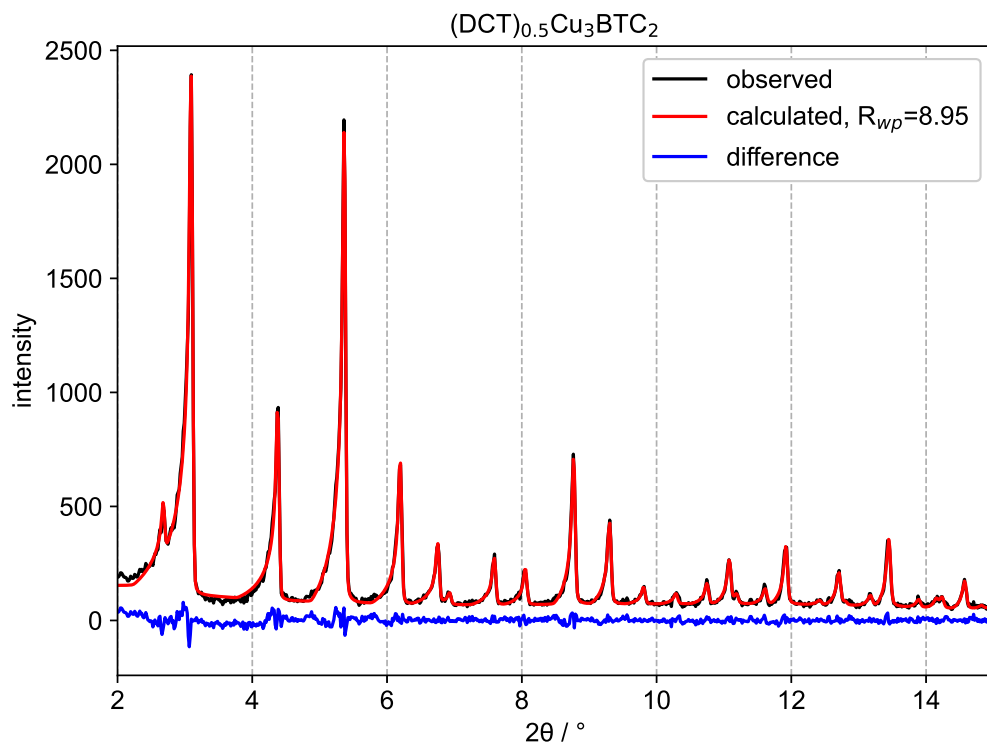


**Figure 68.** Pawley profile fit of **IX** at 100 K. The experimental data (black) was fitted (red) using the cubic space group Fm-3m. The difference curve is given in blue and the  $R_{wp}$  values are shown in the top right corner.

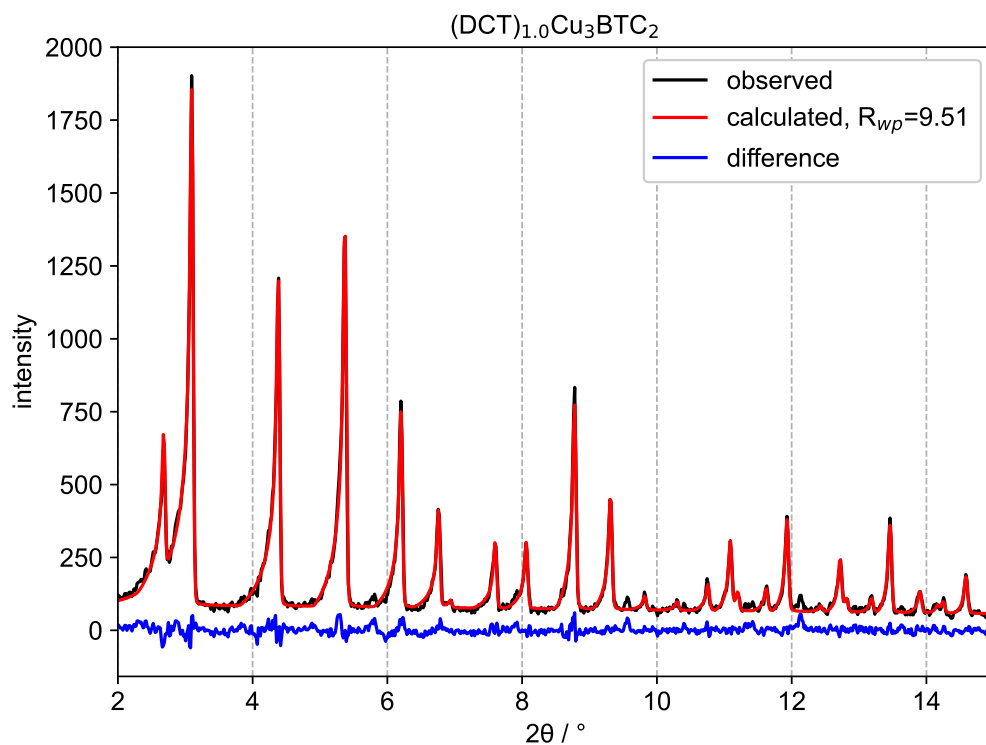


**Figure 69.** Pawley profile fit of **X** at 100 K. The experimental data (black) was fitted (red) using the cubic space group Fm-3m. The difference curve is given in blue and the  $R_{wp}$  values are shown in the top right corner.

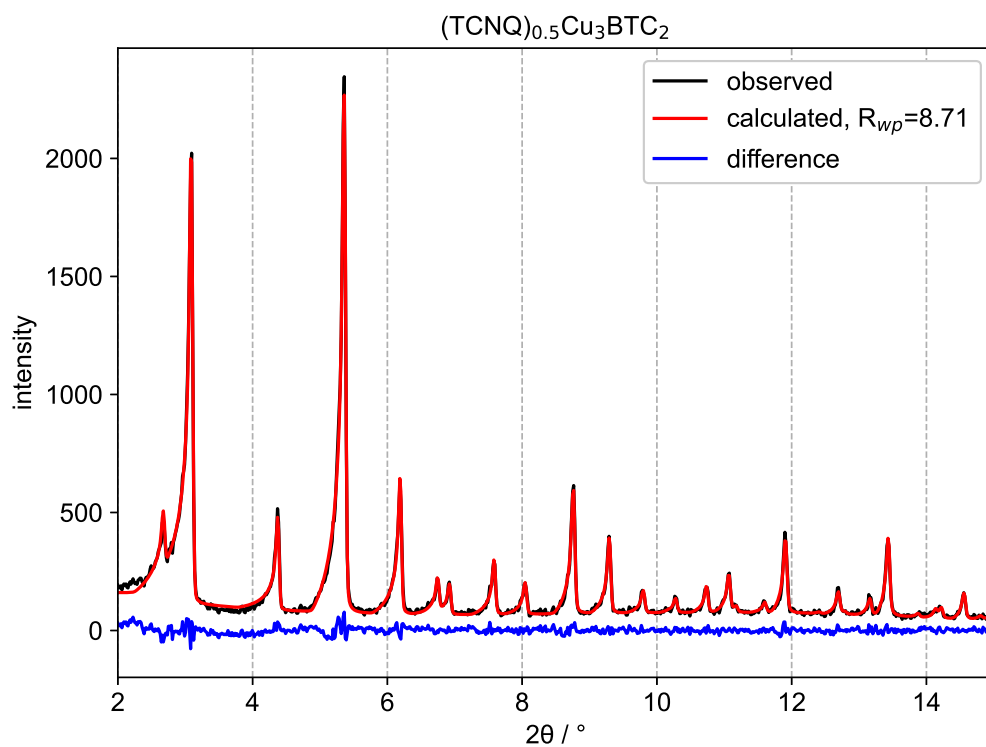


**Figure 70.** Pawley profile fit of **XI** at 100 K. The experimental data (black) was fitted (red) using the cubic space group Fm-3m. The difference curve is given in blue and the  $R_{wp}$  values are shown in the top right corner.

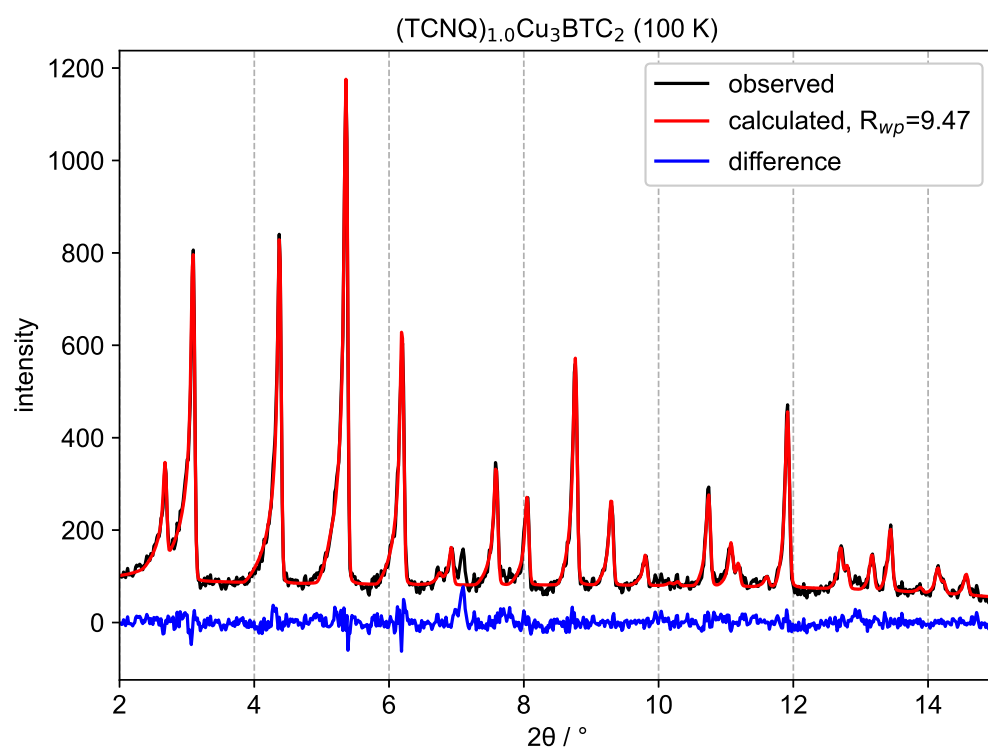


**Figure 71.** Pawley profile fit of **XII** at 100 K. The experimental data (black) was fitted (red) using the cubic space group Fm-3m. The difference curve is given in blue and the  $R_{wp}$  values are shown in the top right corner.

**Table 11.** Fitting parameters and crystallographic information for  $\text{Cu}_3\text{BTC}_2$ .

T/K	$R_{\text{wp}}$	$R_{\text{exp}}$	GOF	$a/\text{\AA}$	$V/\text{\AA}^3$
100	8.82616	7.06810	1.24873	26.28229±0.00079	18154.71524±1.64488
110	9.36690	7.05736	1.32725	26.27546±0.00085	18140.57775±1.76595
120	9.33702	7.13315	1.30896	26.27496±0.00086	18139.53379±1.77617
130	9.06971	7.07658	1.28165	26.27155±0.00082	18132.47956±1.69659
140	8.79414	7.12417	1.23441	26.26951±0.00080	18128.24319±1.65429
150	8.85152	7.10530	1.24576	26.26773±0.00082	18124.55889±1.70523
160	9.09744	7.10066	1.28121	26.25813±0.00084	18104.69384±1.73612
170	8.89957	7.12915	1.24834	26.26151±0.00082	18111.69619±1.69623
180	9.28001	7.12728	1.30204	26.25588±0.00086	18100.04612±1.77902
190	8.66203	7.14326	1.21262	26.25699±0.00079	18102.33768±1.63162
200	8.77650	7.10836	1.23467	26.25136±0.00082	18090.70776±1.68984
210	9.15335	7.14152	1.28171	26.25208±0.00083	18092.20095±1.71601
220	8.61269	7.13803	1.20659	26.24600±0.00077	18079.61638±1.59920
230	8.75718	7.16934	1.22148	26.24900±0.00080	18085.82746±1.65970
240	9.07890	7.13779	1.27195	26.24306±0.00082	18073.54554±1.70022
250	8.90988	7.15770	1.24480	26.24376±0.00081	18074.99015±1.67832
260	8.73568	7.13478	1.22438	26.23985±0.00079	18066.92051±1.62206
270	8.91303	7.15845	1.24511	26.24034±0.00082	18067.93279±1.68722
280	8.85064	7.15305	1.23732	26.23653±0.00081	18060.05670±1.68301
290	8.51412	7.18290	1.18533	26.23654±0.00076	18060.08320±1.57756
300	8.98825	7.15269	1.25662	26.23399±0.00081	18054.82124±1.66962
310	9.01274	7.16451	1.25797	26.23309±0.00082	18052.94954±1.69229
320	8.56562	7.16275	1.19586	26.23568±0.00078	18058.29886±1.60383
330	8.74062	7.18126	1.21714	26.23165±0.00079	18049.98373±1.62797
340	8.83147	7.16593	1.23242	26.23296±0.00080	18052.69585±1.65699
350	8.46729	7.16370	1.18197	26.22796±0.00077	18042.37580±1.59509
360	8.84971	7.16939	1.23437	26.22895±0.00081	18044.41563±1.66537
370	8.18243	7.16891	1.14138	26.22542±0.00074	18037.12999±1.53381
380	8.46338	7.18504	1.17792	26.22565±0.00078	18037.61148±1.59952
390	8.56595	7.18957	1.19144	26.22293±0.00078	18031.97965±1.60498
400	8.26728	7.17788	1.15177	26.22301±0.00074	18032.15815±1.53502

**Table 12.** Fitting parameters and crystallographic information for I.

T/K	$R_{wp}$	$R_{exp}$	GOF	$a/\text{\AA}$	$V/\text{\AA}^3$
100	11.14186	9.12666	1.22080	26.22687±0.00361	18040.12028±7.45935
110	11.53298	9.11107	1.26582	26.22326±0.00367	18032.66965±7.56185
120	11.49107	9.11056	1.26129	26.21004±0.00341	18005.40289±7.03527
130	11.10923	9.08290	1.22309	26.22207±0.00330	18030.22405±6.81664
140	11.46519	9.09234	1.26097	26.21550±0.00347	18016.66001±7.15617
150	11.13300	9.13890	1.21820	26.22079±0.00317	18027.58456±6.53473
160	11.35058	9.01859	1.25858	26.21655±0.00333	18018.83439±6.87437
170	11.39429	9.06686	1.25670	26.21667±0.00331	18019.07503±6.83171
180	11.79494	9.03462	1.30553	26.21513±0.00328	18015.91052±6.76104
190	11.55424	9.06192	1.27503	26.22348±0.00329	18033.12533±6.78861
200	12.22820	9.01991	1.35569	26.21283±0.00349	18011.15840±7.19302
210	11.27954	9.03487	1.24845	26.22116±0.00316	18028.33852±6.51330
220	10.74856	8.94500	1.20163	26.21817±0.00301	18022.17504±6.19828
230	11.71629	9.04001	1.29605	26.21965±0.00317	18025.22997±6.54431
240	11.54489	9.00027	1.28273	26.21829±0.00302	18022.41487±6.23110
250	11.96704	8.97092	1.33398	26.22241±0.00354	18030.91325±7.31246
260	11.29719	8.98858	1.25684	26.21752±0.00296	18020.82218±6.10600
270	11.52939	9.03321	1.27633	26.21777±0.00303	18021.35685±6.24878
280	11.90599	9.04658	1.31608	26.21223±0.00328	18009.93394±6.75213
290	12.05413	9.02057	1.33629	26.21916±0.00318	18024.21971±6.56889
300	11.88254	9.06644	1.31061	26.21281±0.00305	18011.12476±6.28069
310	12.08990	9.03943	1.33746	26.21526±0.00320	18016.18085±6.59054
320	12.05746	9.00150	1.33950	26.22137±0.00316	18028.76220±6.51180
330	12.39546	9.08357	1.36460	26.21778±0.00313	18021.37318±6.45408
340	11.91303	9.03769	1.31815	26.21457±0.00316	18014.75476±6.51991
350	11.62447	9.05691	1.28349	26.22112±0.00305	18028.24692±6.28804
360	11.69544	9.05041	1.29226	26.21156±0.00314	18008.53696±6.47424
370	11.63116	9.06192	1.28352	26.21613±0.00309	18017.96420±6.37714
380	11.31906	9.04808	1.25099	26.21564±0.00307	18016.96381±6.33534
390	11.29875	9.07516	1.24502	26.21190±0.00303	18009.24152±6.23778
400	11.39140	9.06753	1.25629	26.21628±0.00306	18018.26833±6.31238

**Table 13.** Fitting parameters and crystallographic information for II.

T/K	$R_{wp}$	$R_{exp}$	GOF	$a/\text{Å}$	$V/\text{Å}^3$
100	9.29928	7.65321	1.21508	26.22578±0.00099	18037.86780±2.04460
110	9.21112	7.63367	1.20664	26.21882±0.00099	18023.51553±2.03920
120	9.45392	7.68846	1.22962	26.22170±0.00103	18029.44327±2.12130
130	9.69722	7.67730	1.26310	26.21778±0.00104	18021.36611±2.13752
140	9.37556	7.71044	1.21596	26.22144±0.00102	18028.90590±2.10146
150	9.35637	7.68626	1.21729	26.21891±0.00101	18023.69011±2.09043
160	8.87216	7.71703	1.14969	26.22018±0.00096	18026.32084±1.97522
170	9.47026	7.66528	1.23547	26.21855±0.00100	18022.96454±2.05861
180	8.96466	7.67297	1.16834	26.21363±0.00098	18012.80944±2.01943
190	9.70941	7.66039	1.26748	26.21974±0.00103	18025.41380±2.13355
200	9.20158	7.63862	1.20461	26.21638±0.00100	18018.48435±2.05193
210	9.31477	7.63703	1.21968	26.21940±0.00101	18024.70346±2.09241
220	9.10912	7.61543	1.19614	26.21620±0.00099	18018.11894±2.04381
230	8.86299	7.63638	1.16063	26.22101±0.00095	18028.03202±1.95342
240	9.07710	7.61153	1.19255	26.21734±0.00100	18020.46854±2.05437
250	9.14000	7.62975	1.19794	26.22108±0.00099	18028.17264±2.05143
260	9.14175	7.61250	1.20089	26.21806±0.00096	18021.93883±1.97273
270	8.90989	7.61340	1.17029	26.22121±0.00098	18028.43583±2.01164
280	9.64361	7.59898	1.26907	26.22019±0.00102	18026.34273±2.10718
290	9.20428	7.61757	1.20830	26.22074±0.00098	18027.46861±2.02410
300	9.29358	7.57228	1.22732	26.22006±0.00101	18026.06777±2.08409
310	8.84143	7.61096	1.16167	26.21910±0.00095	18024.08307±1.95121
320	8.92238	7.61253	1.17206	26.21960±0.00095	18025.11394±1.96971
330	8.64435	7.61979	1.13446	26.21971±0.00091	18025.35572±1.88372
340	8.56844	7.61269	1.12555	26.21776±0.00094	18021.31733±1.93906
350	9.28204	7.61424	1.21904	26.21910±0.00098	18024.09679±2.03041
360	9.16093	7.60189	1.20509	26.21731±0.00099	18020.39257±2.03563
370	9.01801	7.60259	1.18618	26.21803±0.00098	18021.87833±2.01140
380	9.02945	7.58606	1.19027	26.21715±0.00098	18020.06123±2.02927
390	8.95967	7.60672	1.17786	26.21724±0.00099	18020.25873±2.04541
400	8.41073	7.61337	1.10473	26.21654±0.00090	18018.81968±1.86296

**Table 14.** Fitting parameters and crystallographic information for III.

T/K	$R_{wp}$	$R_{exp}$	GOF	$a/\text{Å}$	$V/\text{Å}^3$
100	13.81702	10.74028	1.28647	26.22866±0.00157	18043.80830±3.24833
110	13.92859	10.81973	1.28733	26.23065±0.00161	18047.91778±3.32455
120	13.80727	10.81810	1.27631	26.22491±0.00154	18036.08448±3.17353
130	13.86702	10.82532	1.28098	26.23134±0.00159	18049.33428±3.28357
140	14.17685	10.86141	1.30525	26.22335±0.00165	18032.85652±3.40171
150	14.16564	10.88773	1.30106	26.22619±0.00159	18038.70794±3.27910
160	14.26665	10.86636	1.31292	26.22263±0.00163	18031.38090±3.36590
170	14.44390	10.87754	1.32786	26.22526±0.00162	18036.80284±3.34476
180	13.96825	10.81337	1.29176	26.22494±0.00154	18036.13141±3.18739
190	14.71826	10.88804	1.35178	26.22226±0.00166	18030.60656±3.43380
200	14.56284	10.82042	1.34587	26.22357±0.00168	18033.30445±3.46143
210	14.73884	10.85341	1.35799	26.22171±0.00166	18029.48103±3.41683
220	14.44703	10.87226	1.32880	26.22240±0.00162	18030.89171±3.33285
230	14.78593	10.86722	1.36060	26.22022±0.00163	18026.39169±3.35471
240	14.58442	10.87849	1.34067	26.21946±0.00159	18024.82788±3.28023
250	14.47884	10.84910	1.33457	26.21866±0.00159	18023.18000±3.27410
260	14.59593	10.83349	1.34730	26.21821±0.00159	18022.25913±3.27010
270	14.45565	10.78528	1.34031	26.22030±0.00161	18026.56177±3.31234
280	14.66496	10.89628	1.34587	26.21352±0.00163	18012.57750±3.36596
290	14.89928	10.83544	1.37505	26.21598±0.00160	18017.64836±3.30410
300	15.09663	10.87565	1.38811	26.21476±0.00166	18015.13654±3.41607
310	14.95164	10.79806	1.38466	26.21396±0.00162	18013.49483±3.34087
320	15.19837	10.88291	1.39654	26.20993±0.00166	18005.18024±3.41272
330	14.79960	10.86384	1.36228	26.21277±0.00159	18011.04727±3.28187
340	14.94703	10.87581	1.37434	26.21145±0.00166	18008.32128±3.41658
350	14.78654	10.83271	1.36499	26.21026±0.00160	18005.86760±3.30615
360	14.87442	10.85153	1.37072	26.20674±0.00162	17998.62153±3.33922
370	14.66484	10.86549	1.34967	26.20874±0.00156	18002.73186±3.20596
380	14.39849	10.84465	1.32770	26.20717±0.00157	17999.50118±3.22969
390	15.01951	10.86455	1.38243	26.20946±0.00163	18004.20701±3.35241
400	14.87306	10.87210	1.36800	26.20811±0.00159	18001.43807±3.27170

**Table 15.** Fitting parameters and crystallographic information for IV.

T/K	$R_{wp}$	$R_{exp}$	GOF	$a/\text{\AA}$	$V/\text{\AA}^3$
100	13.69172	11.62217	1.17807	26.18588±0.00182	17955.65999±3.74973
110	13.12704	11.65967	1.12585	26.18572±0.00171	17955.34415±3.52100
120	13.77888	11.70343	1.17734	26.18770±0.00182	17959.41862±3.75061
130	13.12608	11.68149	1.12367	26.18484±0.00183	17953.52690±3.75964
140	13.17817	11.65977	1.13023	26.18871±0.00173	17961.48643±3.55030
150	12.96910	11.65278	1.11296	26.19028±0.00178	17964.72419±3.65317
160	13.35826	11.65365	1.14627	26.18762±0.00180	17959.24238±3.70626
170	13.48924	11.55834	1.16706	26.18437±0.00180	17952.56207±3.70877
180	13.85389	11.64397	1.18979	26.18900±0.00179	17962.07646±3.67944
190	14.05264	11.60499	1.21091	26.18725±0.00195	17958.47905±4.00378
200	13.71140	11.58207	1.18385	26.18560±0.00180	17955.09551±3.71163
210	14.27304	11.54455	1.23634	26.18409±0.00197	17951.99360±4.04365
220	14.06997	11.49658	1.22384	26.18562±0.00189	17955.13723±3.89412
230	14.43475	11.49342	1.25591	26.18708±0.00204	17958.12680±4.18832
240	14.41925	11.46349	1.25784	26.18530±0.00196	17954.47953±4.02440
250	14.53132	11.42172	1.27225	26.18642±0.00195	17956.78024±4.01531
260	14.48676	11.48283	1.26160	26.18696±0.00185	17957.89676±3.80020
270	14.59543	11.46155	1.27343	26.18523±0.00194	17954.33177±3.99977
280	14.20085	11.42766	1.24267	26.18746±0.00197	17958.91310±4.06050
290	15.07074	11.45758	1.31535	26.18397±0.00203	17951.72944±4.16605
300	14.90421	11.41871	1.30524	26.18904±0.00198	17962.17424±4.07012
310	15.63222	11.44186	1.36623	26.18425±0.00211	17952.30293±4.34712
320	14.69201	11.41515	1.28706	26.19032±0.00205	17964.79413±4.22798
330	13.92110	11.39851	1.22131	26.18315±0.00195	17950.04522±4.00555
340	14.49150	11.44103	1.26663	26.18577±0.00191	17955.44125±3.92195
350	15.34081	11.43947	1.34104	26.18484±0.00206	17953.52091±4.24706
360	14.99383	11.46312	1.30801	26.18051±0.00203	17944.61480±4.17791
370	15.07819	11.46672	1.31495	26.18484±0.00207	17953.52978±4.25254
380	15.03207	11.46349	1.31130	26.18222±0.00214	17948.13481±4.41037
390	14.95521	11.46533	1.30439	26.18133±0.00213	17946.30061±4.37997
400	15.18160	11.46155	1.32457	26.17845±0.00210	17940.37658±4.31830



**Table 16.** Fitting parameters and crystallographic information for V.

T/K	$R_{wp}$	$R_{exp}$	GOF	$a/\text{\AA}$	$V/\text{\AA}^3$
100	10.47811	7.73087	1.35536	26.26813±0.00114	18125.39498±2.36493
110	9.20986	7.68023	1.19916	26.27780±0.00095	18145.41031±1.97232
120	9.71182	7.78513	1.24748	26.26355±0.00103	18115.91073±2.12393
130	8.86037	7.87642	1.12492	26.27546±0.00095	18140.56456±1.96084
140	9.68944	7.80977	1.24068	26.26171±0.00102	18112.09950±2.10318
150	9.25134	8.00675	1.15544	26.27036±0.00101	18130.01813±2.08732
160	9.81296	7.83979	1.25169	26.25822±0.00103	18104.88241±2.13328
170	9.25361	8.47067	1.09243	26.26245±0.00111	18113.64432±2.29141
180	10.03959	7.80270	1.28668	26.25469±0.00108	18097.58998±2.23062
190	10.23889	7.78259	1.31562	26.25106±0.00109	18090.08743±2.24701
200	10.12728	7.80095	1.29821	26.25488±0.00105	18097.98278±2.16966
210	10.03734	7.77752	1.29056	26.24754±0.00107	18082.81484±2.20348
220	10.15485	7.81232	1.29985	26.25456±0.00108	18097.32571±2.23114
230	9.86428	7.75970	1.27122	26.24660±0.00104	18080.86525±2.14058
240	9.62134	7.78801	1.23541	26.25431±0.00101	18096.79782±2.09508
250	10.05343	7.74787	1.29757	26.24540±0.00105	18078.38710±2.16820
260	9.61209	7.77325	1.23656	26.25388±0.00102	18095.90913±2.11218
270	10.03146	7.75142	1.29415	26.24488±0.00107	18077.30996±2.20104
280	9.79334	7.79588	1.25622	26.25281±0.00103	18093.69942±2.12195
290	9.84639	7.76001	1.26886	26.24256±0.00102	18072.51388±2.10464
300	9.40070	7.80632	1.20424	26.26609±0.00097	18121.17310±2.00250
310	9.20242	7.75863	1.18609	26.23947±0.00095	18066.13855±1.95451
320	8.62970	7.82862	1.10233	26.27450±0.00092	18138.57622±1.90918
330	9.20790	7.76087	1.18645	26.23391±0.00095	18054.64581±1.95632
340	8.86514	7.80521	1.13580	26.25932±0.00092	18107.16234±1.91128
350	9.23635	7.76125	1.19006	26.22868±0.00096	18043.86230±1.98071
360	9.73094	7.76705	1.25285	26.23821±0.00103	18063.53557±2.13732
370	9.34330	7.74973	1.20563	26.22524±0.00098	18036.75169±2.02385
380	8.90614	7.76708	1.14665	26.22548±0.00094	18037.25863±1.93027
390	9.10707	7.80556	1.16674	26.22331±0.00095	18032.77513±1.95555
400	9.21676	7.78238	1.18431	26.21969±0.00095	18025.29662±1.96788

**Table 17.** Fitting parameters and crystallographic information for VI.

T/K	$R_{wp}$	$R_{exp}$	GOF	$a/\text{\AA}$	$V/\text{\AA}^3$
100	8.44635	7.77257	1.08669	26.20638±0.00091	17997.86138±1.88301
110	8.52529	7.76182	1.09836	26.20697±0.00095	17999.09236±1.95970
120	8.38977	7.79945	1.07569	26.20189±0.00091	17988.61631±1.86751
130	8.11597	7.76989	1.04454	26.20566±0.00089	17996.39155±1.83499
140	8.56311	7.79514	1.09852	26.20058±0.00092	17985.92230±1.89054
150	8.51269	7.81649	1.08907	26.20016±0.00093	17985.05604±1.90783
160	8.13965	7.76977	1.04761	26.20167±0.00090	17988.16781±1.86355
170	8.37495	7.80173	1.07347	26.19915±0.00091	17982.97923±1.87384
180	8.35259	7.76752	1.07532	26.19974±0.00090	17984.18563±1.85118
190	8.36976	7.77491	1.07651	26.19931±0.00091	17983.31122±1.86525
200	8.21996	7.73137	1.06320	26.19625±0.00091	17977.00312±1.88015
210	8.45355	7.76171	1.08913	26.19837±0.00090	17981.37539±1.85729
220	8.60251	7.71147	1.11555	26.19474±0.00096	17973.90258±1.96832
230	8.33078	7.71604	1.07967	26.19901±0.00089	17982.68081±1.82471
240	8.19990	7.70443	1.06431	26.19428±0.00091	17972.95129±1.87490
250	8.32890	7.70539	1.08092	26.20004±0.00089	17984.80404±1.83050
260	8.66715	7.66466	1.13079	26.19497±0.00094	17974.38017±1.92523
270	8.61374	7.68909	1.12025	26.20036±0.00092	17985.47146±1.89693
280	8.55728	7.68454	1.11357	26.19631±0.00093	17977.12086±1.91722
290	8.59383	7.70226	1.11575	26.19687±0.00093	17978.29264±1.91481
300	8.54197	7.68231	1.11190	26.19517±0.00093	17974.78635±1.90537
310	8.55484	7.68429	1.11329	26.19712±0.00093	17978.80258±1.90964
320	8.54579	7.68744	1.11166	26.19358±0.00092	17971.50719±1.90298
330	8.43750	7.67746	1.09900	26.19696±0.00089	17978.47189±1.83592
340	8.63663	7.67176	1.12577	26.19457±0.00094	17973.54945±1.94529
350	8.51508	7.67818	1.10900	26.19703±0.00092	17978.61614±1.89743
360	8.48674	7.68158	1.10482	26.19451±0.00090	17973.41948±1.85284
370	8.23922	7.68725	1.07180	26.19465±0.00090	17973.72085±1.85491
380	8.12221	7.66735	1.05933	26.19325±0.00088	17970.83190±1.81978
390	8.28901	7.69867	1.07668	26.19340±0.00090	17971.14750±1.85005
400	8.45094	7.71949	1.09475	26.19410±0.00090	17972.57971±1.84453

**Table 18.** Fitting parameters and crystallographic information for VII.

T/K	$R_{wp}$	$R_{exp}$	GOF	$a/\text{\AA}$	$V/\text{\AA}^3$
100	8.48437	7.70600	1.10101	26.19707±0.00092	17978.68824±1.90139
110	8.64695	7.74134	1.11698	26.19654±0.00093	17977.61316±1.91778
120	9.12594	7.73994	1.17907	26.19412±0.00100	17972.61559±2.05652
130	8.77548	7.74674	1.13280	26.19680±0.00098	17978.14860±2.00796
140	8.73777	7.74585	1.12806	26.19162±0.00097	17967.48163±1.99128
150	8.52156	7.74431	1.10036	26.19648±0.00093	17977.48920±1.92328
160	8.90176	7.75057	1.14853	26.19241±0.00099	17969.10900±2.04360
170	8.38678	7.73678	1.08401	26.19619±0.00091	17976.88927±1.86548
180	8.56840	7.74722	1.10600	26.19116±0.00093	17966.53168±1.91157
190	8.50409	7.72805	1.10042	26.19546±0.00093	17975.37937±1.91499
200	8.32519	7.71715	1.07879	26.19087±0.00090	17965.92911±1.84981
210	8.95575	7.73044	1.15850	26.19710±0.00098	17978.75342±2.02131
220	8.43190	7.71099	1.09349	26.19140±0.00091	17967.02989±1.87223
230	8.58270	7.70978	1.11322	26.19557±0.00094	17975.61282±1.93377
240	8.19247	7.69049	1.06527	26.18892±0.00089	17961.91578±1.83651
250	8.68598	7.70834	1.12683	26.19541±0.00096	17975.27394±1.97455
260	8.67197	7.68378	1.12861	26.18892±0.00095	17961.91329±1.95127
270	8.29369	7.69550	1.07773	26.19493±0.00091	17974.29897±1.86874
280	8.22012	7.67910	1.07045	26.18833±0.00090	17960.69928±1.85430
290	8.46072	7.70064	1.09870	26.19390±0.00091	17972.17065±1.87539
300	8.64450	7.66480	1.12782	26.18698±0.00095	17957.92838±1.95699
310	8.47535	7.67913	1.10369	26.19476±0.00092	17973.93079±1.89908
320	8.56865	7.67226	1.11684	26.18656±0.00092	17957.06265±1.88767
330	8.08175	7.67785	1.05261	26.19369±0.00088	17971.74325±1.81365
340	8.56243	7.69038	1.11339	26.18797±0.00093	17959.97121±1.90416
350	8.26446	7.68987	1.07472	26.19130±0.00090	17966.82441±1.85895
360	8.35374	7.70508	1.08419	26.18998±0.00090	17964.09398±1.86147
370	8.19963	7.71034	1.06346	26.19276±0.00091	17969.82369±1.87170
380	8.52491	7.69814	1.10740	26.19096±0.00095	17966.11748±1.95857
390	8.25836	7.70266	1.07214	26.19260±0.00091	17969.48429±1.87832
400	8.40772	7.71051	1.09042	26.19251±0.00093	17969.31011±1.91039

**Table 19.** Fitting parameters and crystallographic information for VIII.

T/K	$R_{wp}$	$R_{exp}$	GOF	$a/\text{\AA}$	$V/\text{\AA}^3$
100	8.17613	7.77730	1.05128	26.18897±0.00086	17962.03175±1.76695
110	8.31266	7.81624	1.06351	26.18795±0.00088	17959.91852±1.80975
120	8.09052	7.81068	1.03583	26.18510±0.00086	17954.06813±1.76566
130	8.31775	7.82739	1.06265	26.18780±0.00087	17959.62235±1.79665
140	8.18556	7.82739	1.04576	26.18278±0.00088	17949.28041±1.80124
150	7.43588	7.40794	1.00377	26.18849±0.00092	17961.04200±1.90100
160	7.91331	7.80046	1.01447	26.18431±0.00084	17952.43500±1.72300
170	8.04692	7.82225	1.02872	26.18794±0.00086	17959.91339±1.77673
180	8.06835	7.78461	1.03645	26.18379±0.00086	17951.36523±1.77867
190	7.53501	7.36796	1.02267	26.18524±0.00092	17954.34000±1.88700
200	8.13916	7.77545	1.04678	26.18253±0.00086	17948.77047±1.77446
210	7.93069	7.75781	1.02228	26.18932±0.00085	17962.74421±1.74340
220	8.40110	7.76771	1.08154	26.18404±0.00089	17951.88310±1.82143
230	8.07331	7.72202	1.04549	26.19028±0.00087	17964.71190±1.78419
240	7.83526	7.74017	1.01229	26.18551±0.00086	17954.90331±1.76884
250	7.87635	7.71517	1.02089	26.18928±0.00082	17962.66572±1.69589
260	7.84561	7.75527	1.01165	26.18263±0.00108	17948.97700±2.22400
270	8.32538	7.25387	1.14772	26.19092±0.00100	17966.02400±2.06200
280	8.39327	7.76998	1.08022	26.17224±0.00092	17927.63137±1.88969
290	7.91720	7.74852	1.02177	26.19164±0.00084	17967.51386±1.72864
300	8.98291	7.78259	1.15423	26.16662±0.00095	17916.06874±1.95591
310	7.88006	7.70507	1.02271	26.19149±0.00085	17967.21630±1.75049
320	8.47533	7.77531	1.09003	26.17080±0.00089	17924.65697±1.83591
330	7.78199	7.70288	1.01027	26.19046±0.00081	17965.08432±1.67434
340	8.12406	7.75089	1.04815	26.17420±0.00088	17931.65273±1.80964
350	7.94246	7.72211	1.02854	26.19054±0.00083	17965.26368±1.71594
360	8.07595	7.77165	1.03916	26.17722±0.00086	17937.85459±1.76834
370	7.81301	7.74658	1.00858	26.18952±0.00084	17963.14733±1.72281
380	8.05258	7.75623	1.03821	26.18203±0.00086	17947.75030±1.76258
390	8.00228	7.74854	1.03275	26.18677±0.00085	17957.49203±1.74371
400	7.76359	7.74846	1.00195	26.18592±0.00084	17955.74399±1.72146

**Table 20.** Fitting parameters and crystallographic information for **IX**.

T/K	$R_{wp}$	$R_{exp}$	GOF	$a/\text{\AA}$	$V/\text{\AA}^3$
100	8.94555	7.52263	1.18915	26.21742±0.00102	18020.62694±2.09904
110	8.95236	7.54649	1.18629	26.21467±0.00101	18014.95051±2.07240
120	9.23505	7.55884	1.22175	26.20856±0.00103	18002.37118±2.12233
130	9.48549	7.56573	1.25374	26.21233±0.00106	18010.12398±2.19342
140	9.02229	7.56038	1.19336	26.20739±0.00100	17999.94315±2.06908
150	8.51204	7.57012	1.12443	26.21156±0.00095	18008.53542±1.95113
160	9.21864	7.59024	1.21454	26.20408±0.00104	17993.12459±2.15192
170	9.00458	7.55332	1.19214	26.20878±0.00099	18002.80886±2.04392
180	9.45125	7.58058	1.24677	26.20228±0.00105	17989.42990±2.16045
190	9.09498	7.55515	1.20381	26.20780±0.00101	18000.78884±2.09064
200	9.24123	7.55706	1.22286	26.19788±0.00107	17980.36140±2.19313
210	9.04912	7.53871	1.20036	26.20807±0.00102	18001.34445±2.10135
220	8.60262	7.54935	1.13952	26.19761±0.00096	17979.81604±1.97664
230	9.11668	7.53263	1.21029	26.20853±0.00101	18002.30487±2.08788
240	9.11259	7.54403	1.20792	26.19462±0.00103	17973.64838±2.12550
250	9.10676	7.50497	1.21343	26.20868±0.00103	18002.60672±2.12380
260	8.90420	7.51826	1.18434	26.19741±0.00101	17979.40041±2.07144
270	8.58703	7.51422	1.14277	26.20803±0.00095	18001.27272±1.96227
280	9.16544	7.52067	1.21870	26.19826±0.00102	17981.13828±2.09213
290	8.46422	7.52208	1.12525	26.20948±0.00093	18004.26312±1.91597
300	9.00054	7.53763	1.19408	26.19902±0.00101	17982.70647±2.07201
310	8.40133	7.50801	1.11898	26.20606±0.00096	17997.21994±1.98421
320	8.89101	7.52428	1.18164	26.20030±0.00099	17985.34598±2.04009
330	8.99692	7.52491	1.19562	26.20429±0.00101	17993.55820±2.09081
340	8.77855	7.50650	1.16946	26.20075±0.00097	17986.27089±1.99875
350	9.40413	7.51218	1.25185	26.20397±0.00106	17992.89623±2.18389
360	9.17754	7.50637	1.22263	26.19962±0.00105	17983.94262±2.15971
370	8.71632	7.53497	1.15678	26.20314±0.00097	17991.18588±1.99776
380	8.97890	7.50201	1.19687	26.20050±0.00102	17985.75713±2.10454
390	8.83781	7.49462	1.17922	26.20028±0.00100	17985.29631±2.06047
400	8.30393	7.51479	1.10501	26.20118±0.00093	17987.15574±1.92080

**Table 21.** Fitting parameters and crystallographic information for **X**.

T/K	$R_{wp}$	$R_{exp}$	GOF	$a/\text{\AA}$	$V/\text{\AA}^3$
100	9.50693	7.87918	1.20659	26.19255±0.00094	17969.39379±1.93295
110	9.39658	7.87594	1.19307	26.18750±0.00096	17959.00238±1.96807
120	9.24514	7.88808	1.17204	26.18838±0.00093	17960.81854±1.91580
130	9.56324	7.91590	1.20810	26.18659±0.00097	17957.13096±1.99096
140	9.40196	7.92428	1.18648	26.18595±0.00096	17955.81969±1.97959
150	9.26896	7.96157	1.16421	26.18710±0.00095	17958.16901±1.94835
160	9.33771	7.95502	1.17381	26.18640±0.00093	17956.74181±1.90453
170	9.01786	7.95792	1.13319	26.18603±0.00094	17955.97159±1.93104
180	9.02286	7.94137	1.13618	26.18701±0.00094	17958.00076±1.92623
190	9.19119	7.93554	1.15823	26.18596±0.00096	17955.83225±1.97723
200	9.05751	7.93052	1.14211	26.18507±0.00095	17954.00599±1.94911
210	9.04082	7.95273	1.13682	26.18799±0.00096	17960.01522±1.97105
220	9.60314	7.93931	1.20957	26.18575±0.00098	17955.39033±2.02456
230	9.39053	7.92990	1.18419	26.18946±0.00097	17963.02150±2.00274
240	9.15508	7.93208	1.15418	26.18622±0.00095	17956.35757±1.95299
250	9.17678	7.95588	1.15346	26.18890±0.00093	17961.88302±1.91660
260	8.64413	7.93444	1.08945	26.18837±0.00089	17960.77867±1.83294
270	9.04741	7.90085	1.14512	26.19141±0.00094	17967.04903±1.93145
280	9.19287	7.93370	1.15871	26.18717±0.00095	17958.31212±1.95656
290	9.25063	7.91977	1.16804	26.19050±0.00095	17965.18108±1.96254
300	8.99334	7.93367	1.13357	26.18760±0.00094	17959.20539±1.93032
310	8.32667	7.93128	1.04985	26.19043±0.00087	17965.02635±1.78660
320	8.70836	7.92477	1.09888	26.18688±0.00091	17957.73144±1.86565
330	8.80830	7.90351	1.11448	26.19027±0.00090	17964.69018±1.85136
340	8.71005	7.94721	1.09599	26.18796±0.00092	17959.94258±1.89624
350	8.70006	7.92752	1.09745	26.18886±0.00089	17961.79413±1.83902
360	8.85700	7.90915	1.11984	26.18724±0.00091	17958.46040±1.86919
370	9.02291	7.91000	1.14070	26.18733±0.00096	17958.65352±1.96620
380	8.56163	7.95082	1.07682	26.18892±0.00090	17961.92753±1.84368
390	9.42123	7.93563	1.18721	26.18800±0.00099	17960.03527±2.03024
400	8.73287	7.95144	1.09828	26.18792±0.00092	17959.87189±1.89101

**Table 22.** Fitting parameters and crystallographic information for **XI**.

T/K	$R_{wp}$	$R_{exp}$	GOF	$a/\text{\AA}$	$V/\text{\AA}^3$
100	8.71372	7.74785	1.12466	26.24379±0.00098	18075.05788±2.02205
110	8.88493	7.67473	1.15769	26.24215±0.00099	18071.66824±2.05511
120	8.13498	7.77966	1.04567	26.23852±0.00093	18064.16471±1.92262
130	8.53672	7.72006	1.10578	26.23934±0.00094	18065.86284±1.93431
140	8.91325	7.78174	1.14541	26.23715±0.00101	18061.33105±2.08321
150	8.53327	7.70947	1.10686	26.23744±0.00095	18061.94474±1.96514
160	8.17842	7.77552	1.05182	26.23638±0.00092	18059.74037±1.89389
170	8.81539	7.70482	1.14414	26.23414±0.00097	18055.12269±1.99447
180	8.02430	7.75504	1.03472	26.23264±0.00091	18052.02312±1.86955
190	8.23537	7.74405	1.06345	26.23395±0.00094	18054.73625±1.93219
200	8.16033	7.70420	1.05921	26.23189±0.00093	18050.47458±1.92439
210	8.40443	7.71768	1.08898	26.23275±0.00096	18052.25006±1.97362
220	8.50307	7.70564	1.10349	26.22963±0.00094	18045.81849±1.94682
230	8.29176	7.68543	1.07889	26.23247±0.00093	18051.67844±1.91376
240	8.39735	7.68437	1.09278	26.22745±0.00094	18041.30744±1.93814
250	8.13793	7.68864	1.05843	26.23080±0.00090	18048.23684±1.86365
260	8.34975	7.68172	1.08696	26.22820±0.00093	18042.86261±1.91772
270	7.87715	7.68814	1.02459	26.23050±0.00089	18047.62031±1.84455
280	8.18246	7.70128	1.06248	26.22625±0.00091	18038.83325±1.86837
290	7.96404	7.69122	1.03547	26.23035±0.00089	18047.29329±1.84657
300	8.14334	7.69474	1.05830	26.22591±0.00091	18038.13073±1.87590
310	8.20515	7.70440	1.06499	26.22850±0.00091	18043.47328±1.87694
320	8.24317	7.67991	1.07334	26.22587±0.00094	18038.04530±1.93574
330	8.21029	7.67941	1.06913	26.22793±0.00092	18042.29661±1.89099
340	8.30517	7.68644	1.08050	26.22680±0.00093	18039.96511±1.92571
350	8.13694	7.69225	1.05781	26.22477±0.00089	18035.77603±1.84666
360	8.29036	7.70719	1.07567	26.22407±0.00094	18034.33201±1.93992
370	8.27356	7.70198	1.07421	26.22477±0.00092	18035.78037±1.89865
380	8.33862	7.70755	1.08188	26.22295±0.00094	18032.04053±1.93904
390	8.28881	7.69284	1.07747	26.22253±0.00093	18031.16909±1.90865
400	8.29330	7.69811	1.07732	26.22125±0.00092	18028.52798±1.89522

**Table 23.** Fitting parameters and crystallographic information for **XII**.

T/K	$R_{wp}$	$R_{exp}$	GOF	$a/\text{\AA}$	$V/\text{\AA}^3$
100	9.47226	8.43629	1.12280	26.22833±0.00124	18043.12305±2.56037
110	9.22831	8.45626	1.09130	26.22560±0.00118	18037.50033±2.44425
120	9.70716	8.45388	1.14825	26.22470±0.00129	18035.64976±2.66623
130	9.40021	8.48339	1.10807	26.22656±0.00120	18039.48781±2.48355
140	9.51960	8.50234	1.11964	26.22556±0.00124	18037.40665±2.56357
150	9.98057	8.51579	1.17201	26.22706±0.00129	18040.51771±2.67110
160	10.08917	8.50106	1.18681	26.21997±0.00130	18025.87664±2.67966
170	9.72280	8.48647	1.14568	26.22496±0.00126	18036.18659±2.60920
180	10.00377	8.49615	1.17745	26.22206±0.00129	18030.20093±2.66505
190	9.80486	8.50113	1.15336	26.22779±0.00124	18042.02077±2.56770
200	9.67074	8.48407	1.13987	26.22448±0.00123	18035.18277±2.53904
210	9.49796	8.50295	1.11702	26.22822±0.00121	18042.90529±2.49557
220	9.90612	8.49660	1.16589	26.22470±0.00124	18035.63970±2.55845
230	9.28230	8.47391	1.09540	26.23111±0.00120	18048.87093±2.48352
240	10.17026	8.47234	1.20041	26.22639±0.00127	18039.13696±2.62973
250	10.14813	8.49928	1.19400	26.22938±0.00125	18045.29711±2.58211
260	9.91629	8.46591	1.17132	26.22741±0.00123	18041.24233±2.54055
270	9.64555	8.46729	1.13915	26.23173±0.00122	18050.15746±2.51118
280	9.94554	8.46505	1.17489	26.22632±0.00122	18038.98300±2.51541
290	9.76857	8.45139	1.15585	26.22977±0.00125	18046.10351±2.58227
300	9.67944	8.46524	1.14343	26.22719±0.00121	18040.77572±2.50689
310	10.05169	8.47451	1.18611	26.23120±0.00125	18049.04987±2.57437
320	9.92541	8.45284	1.17421	26.22897±0.00122	18044.45817±2.52091
330	10.51400	8.48073	1.23975	26.23294±0.00131	18052.64911±2.70434
340	9.89488	8.47484	1.16756	26.22835±0.00120	18043.16970±2.47232
350	9.71359	8.47630	1.14597	26.23159±0.00121	18049.86798±2.49203
360	9.63345	8.48260	1.13567	26.22890±0.00119	18044.29838±2.46297
370	9.66079	8.47900	1.13938	26.23033±0.00119	18047.25961±2.44879
380	9.51905	8.49626	1.12038	26.23172±0.00121	18050.11977±2.49535
390	9.92334	8.50586	1.16665	26.22860±0.00124	18043.68028±2.55690
400	10.01307	8.50442	1.17740	26.22904±0.00125	18044.58838±2.58996



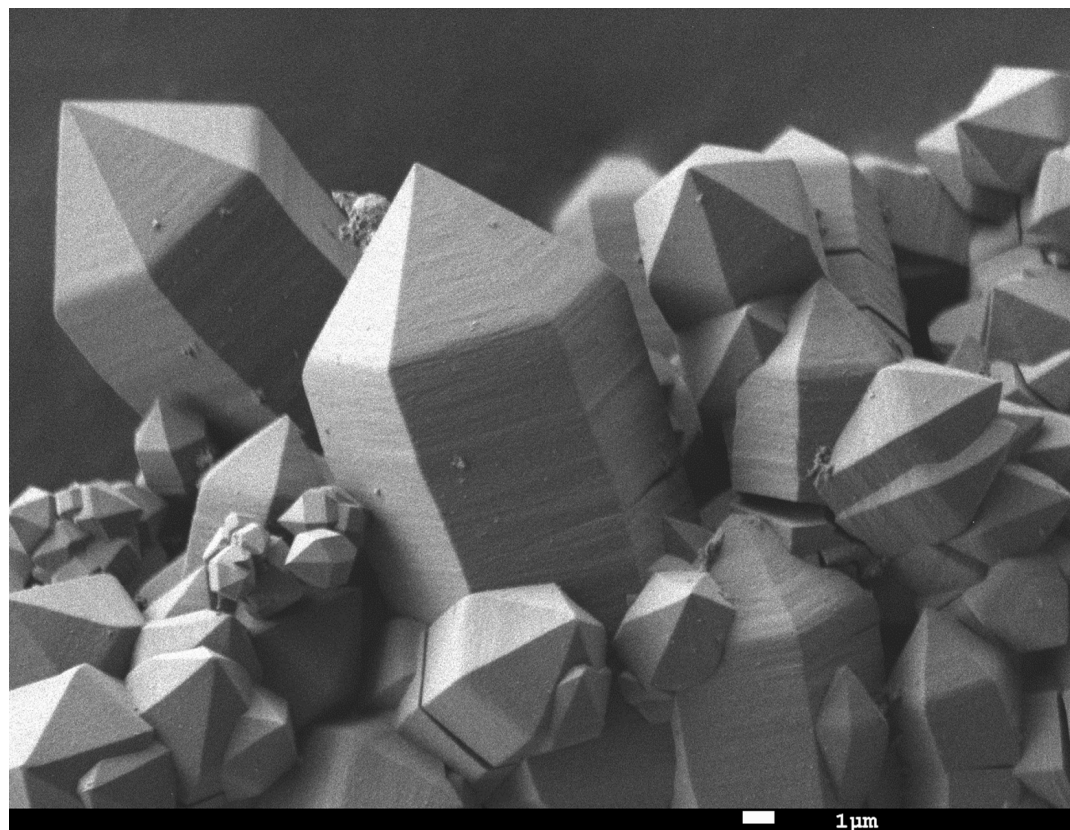


**Figure 72.** SEM picture of Zn<sub>2</sub>TTTB.

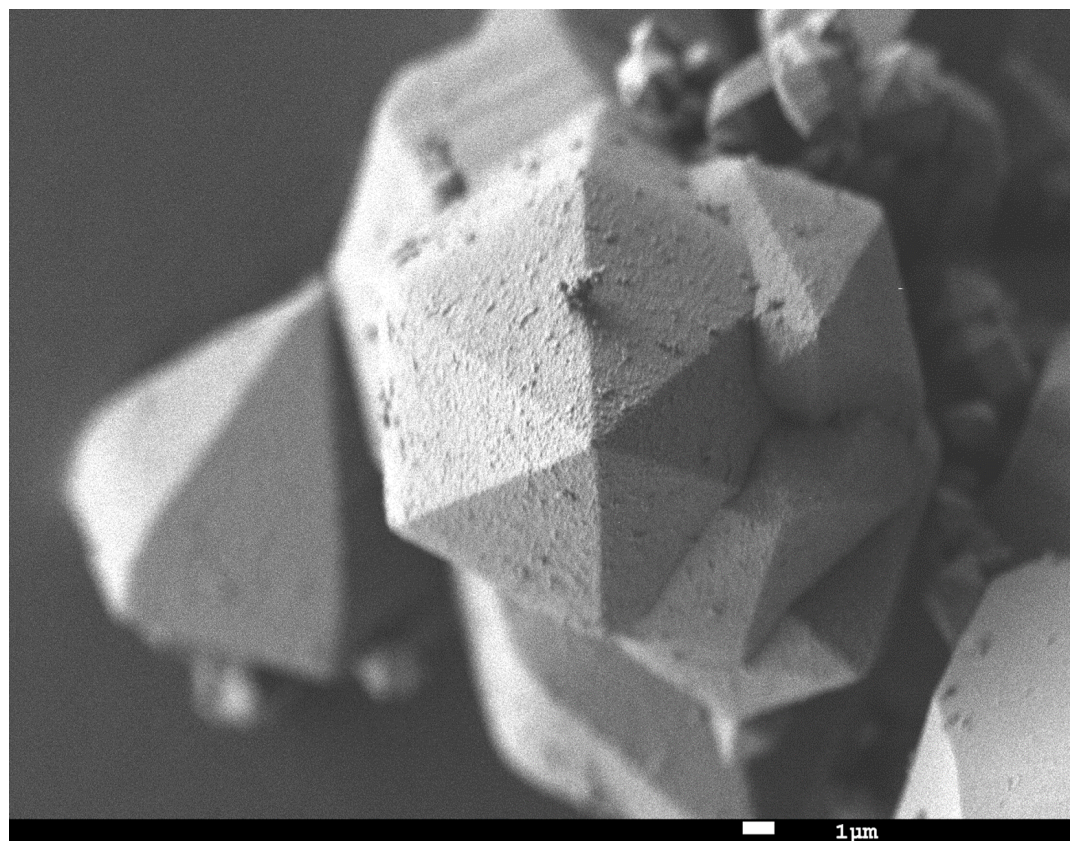


**Figure 73.** SEM picture of 1.



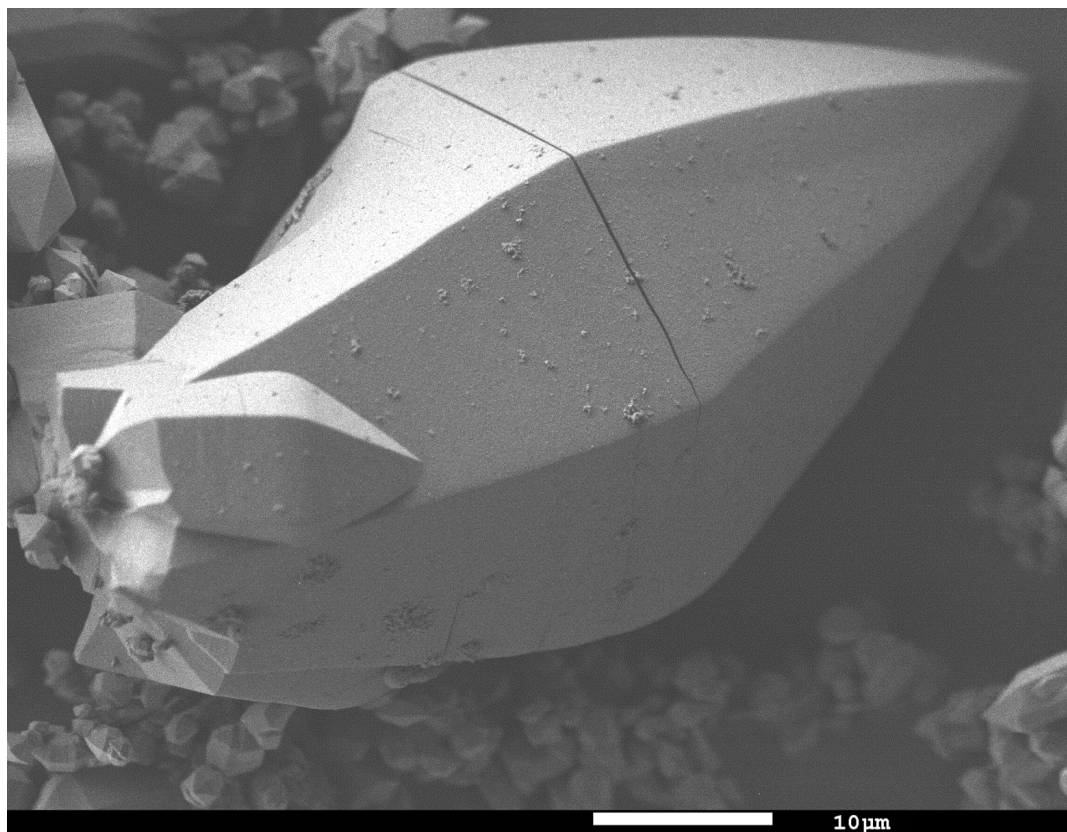


Figure 74. SEM picture of 2.

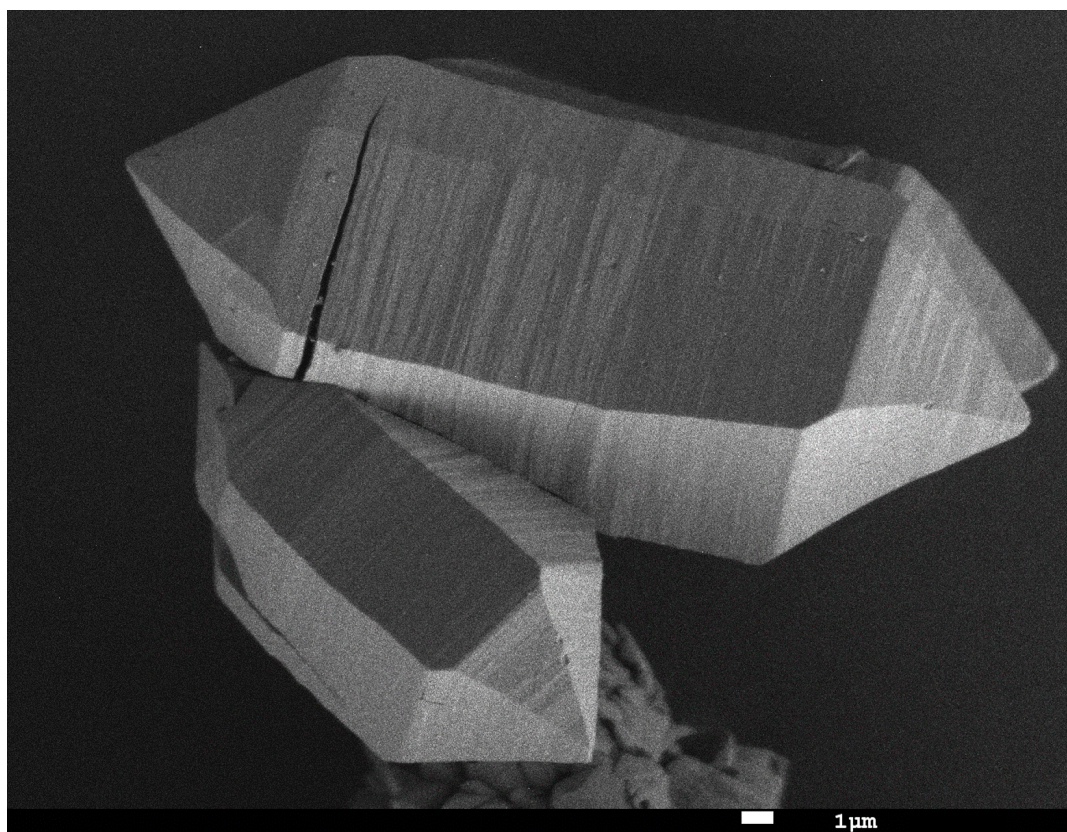


Figure 75. SEM picture of 3.



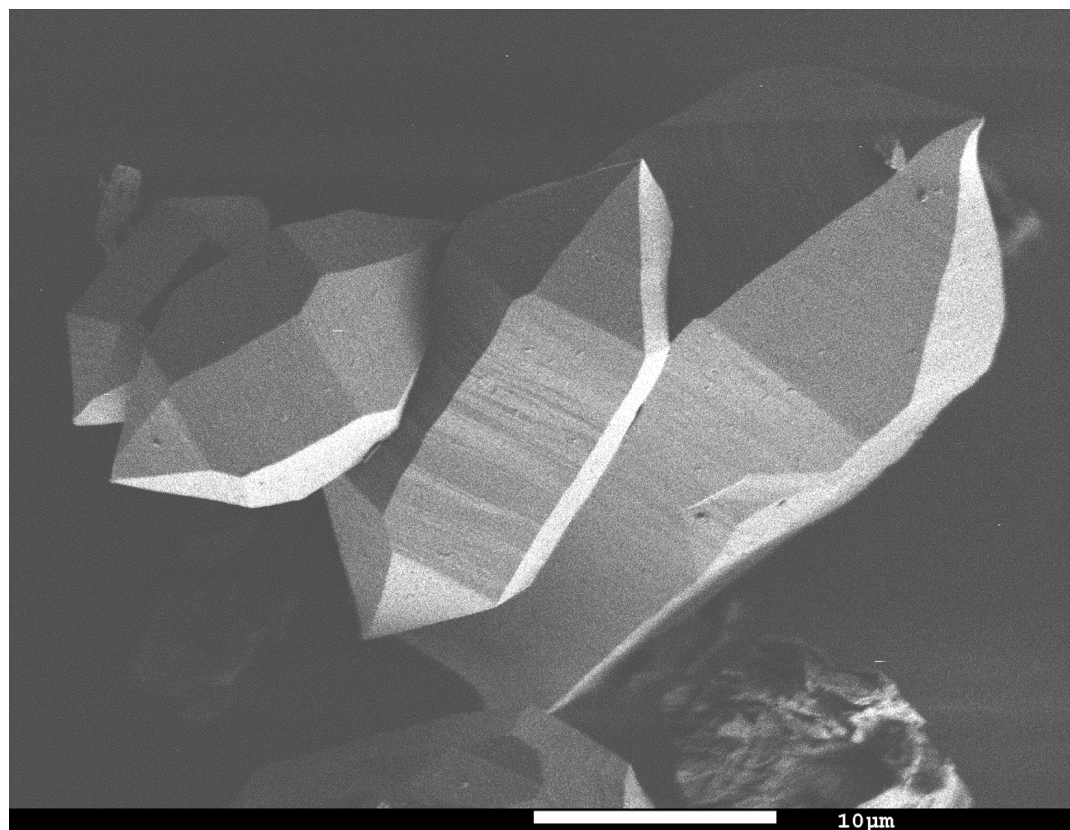


Figure 76. SEM picture of 4.

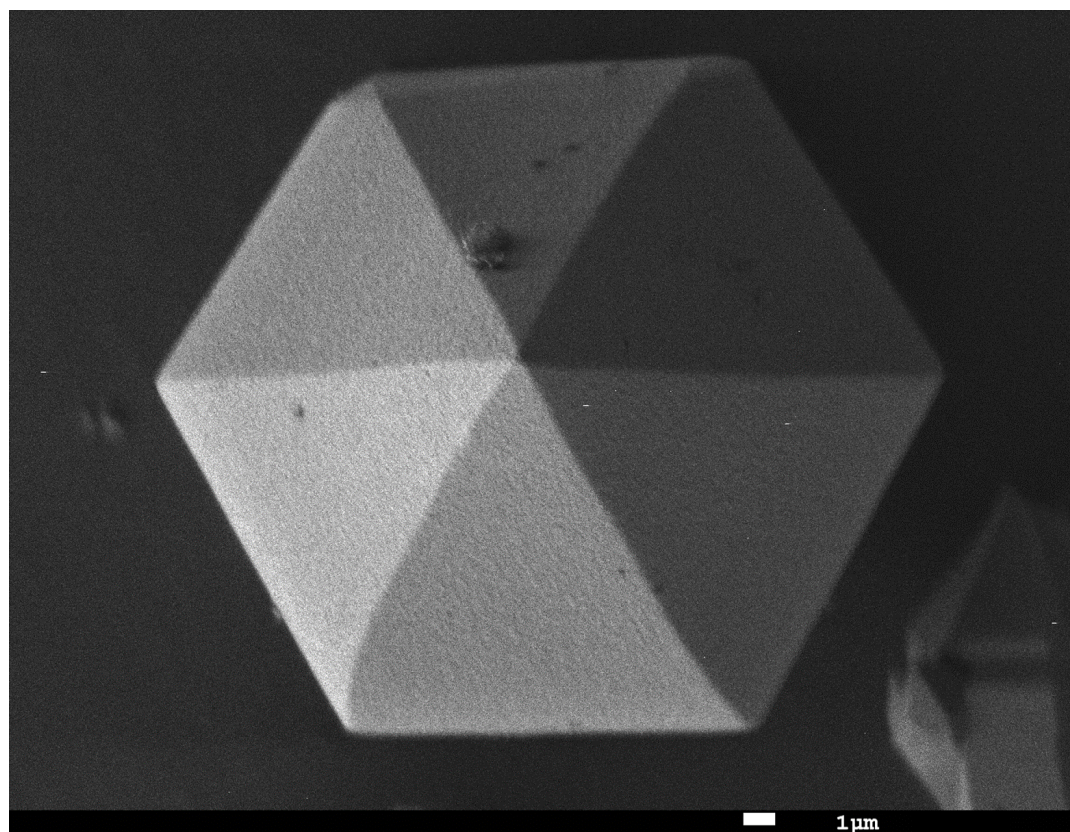
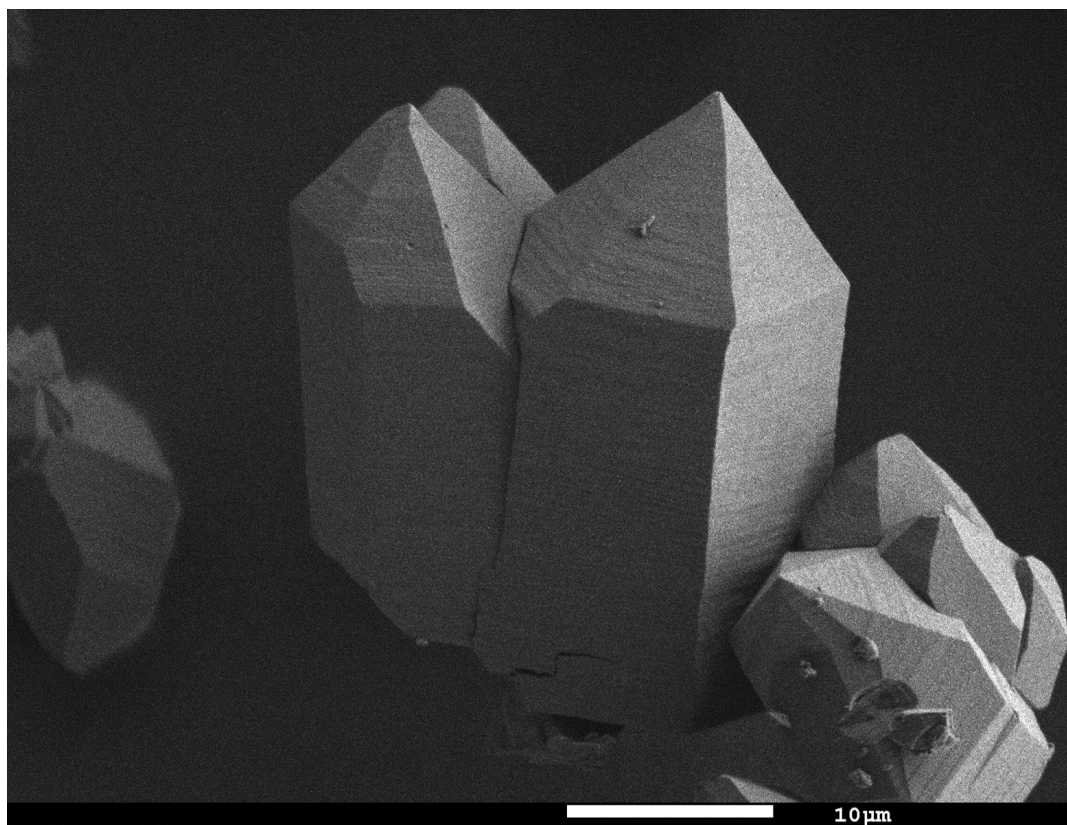
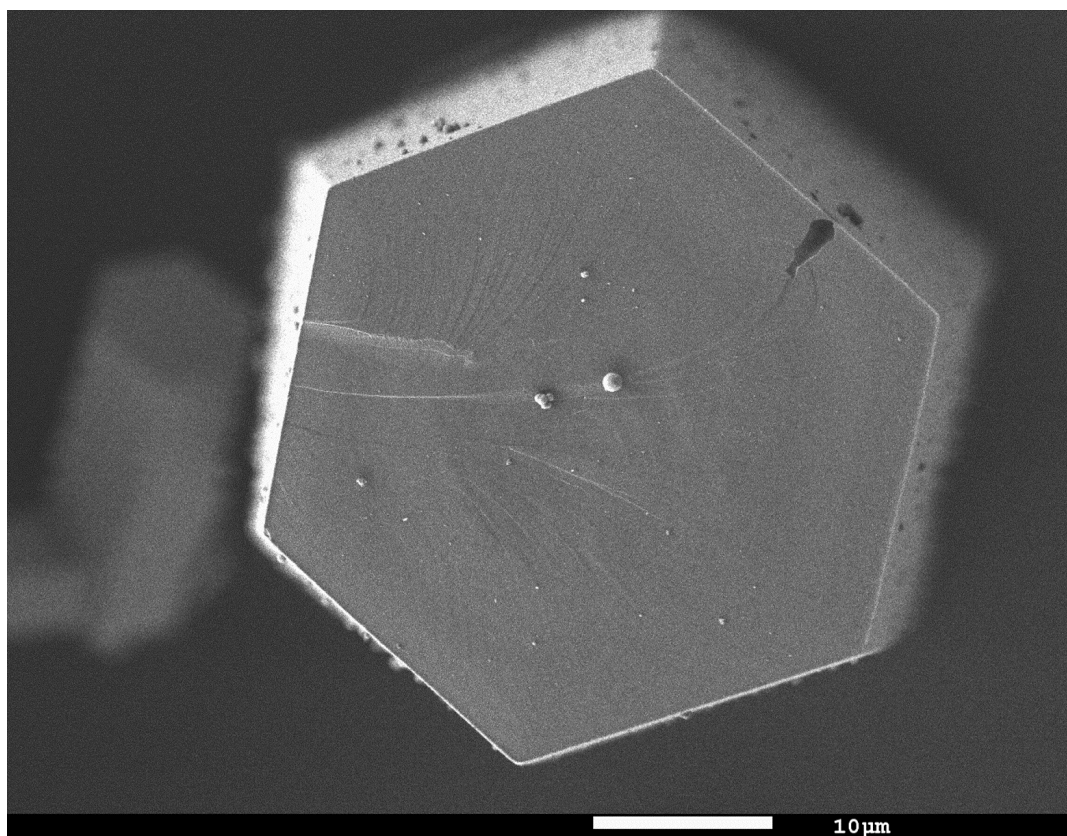


Figure 77. SEM picture of 5.





**Figure 78.** SEM picture of 6.



**Figure 79.** SEM picture of  $\text{Cd}_2\text{TFTB}$ .



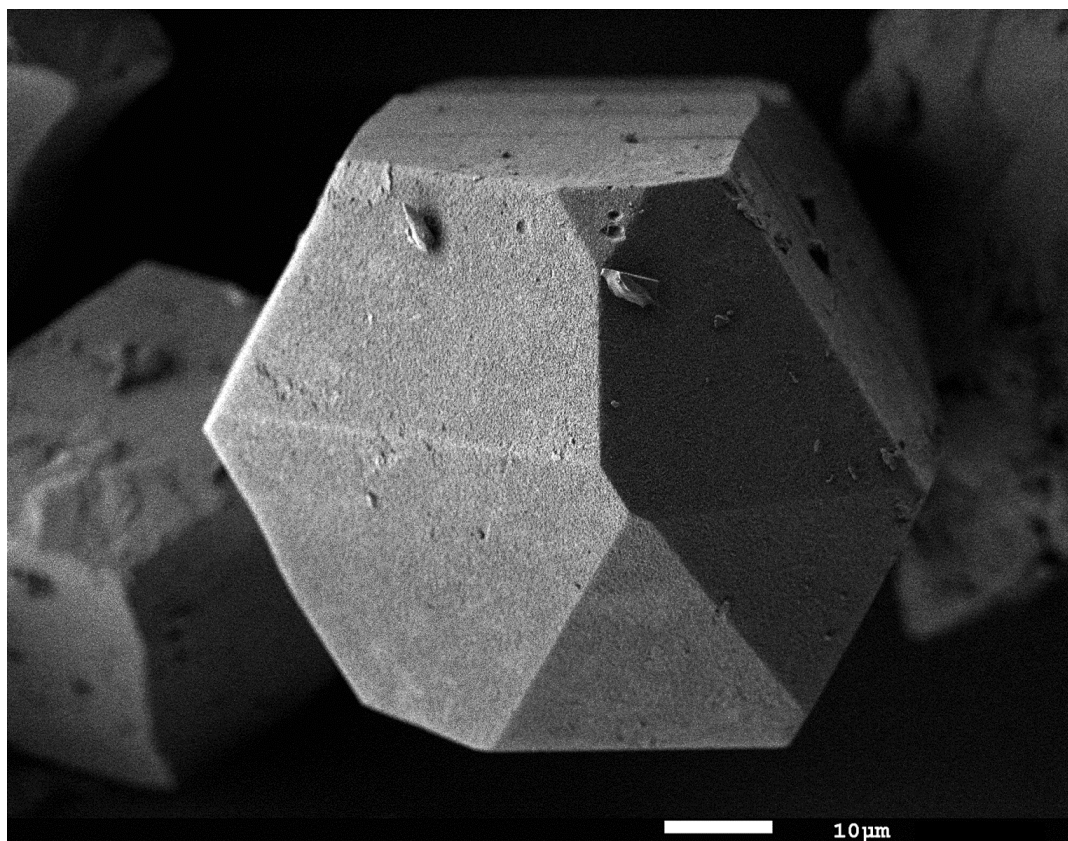


Figure 80. SEM picture of 7.

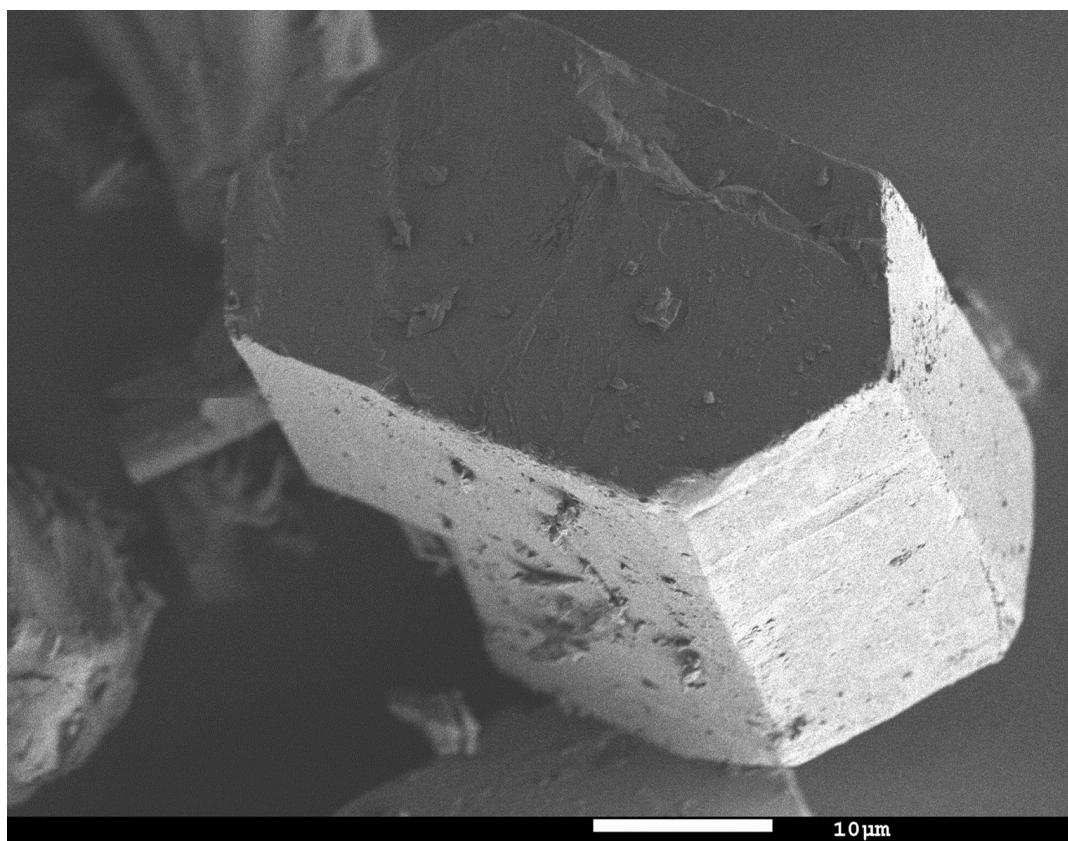


Figure 81. SEM picture of 8.



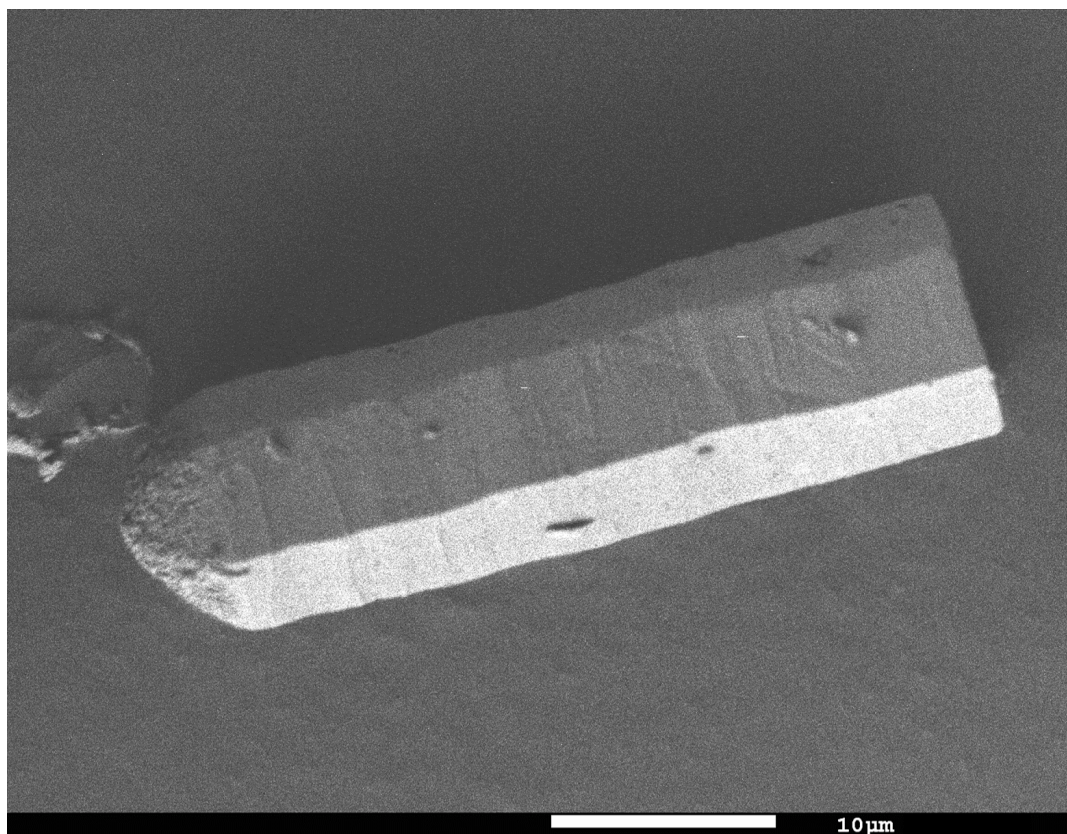


Figure 82. SEM picture of 9.

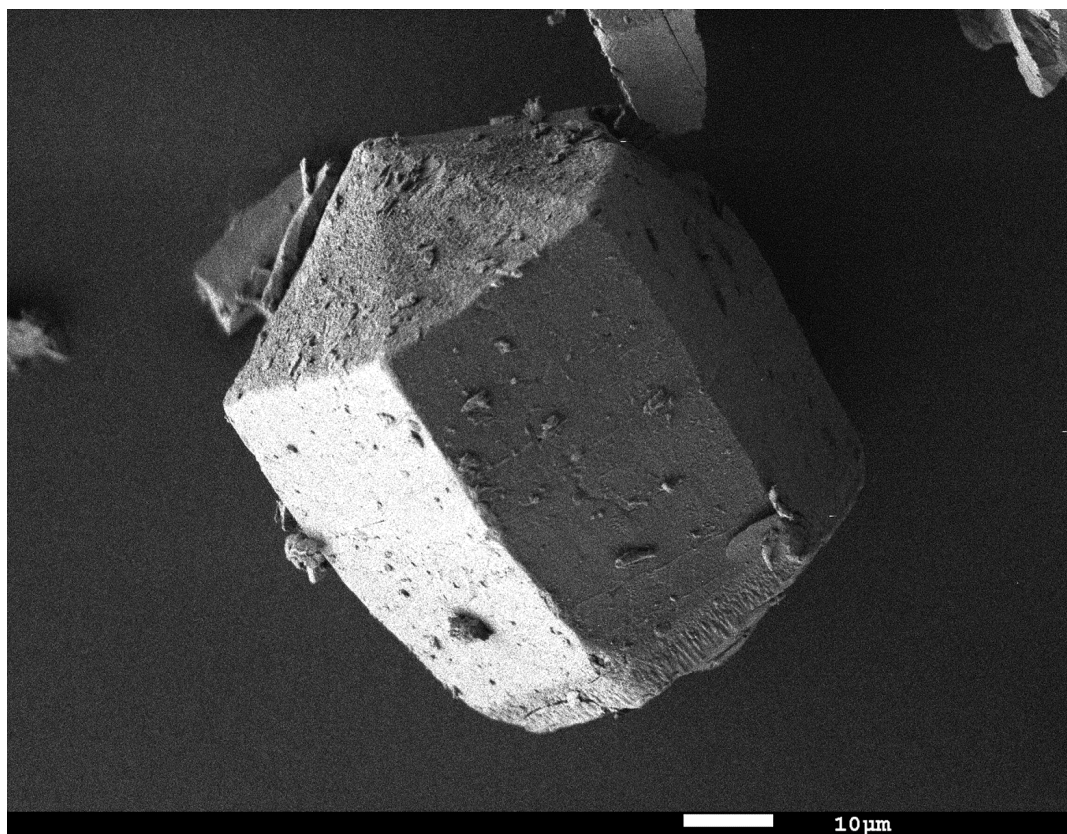


Figure 83. SEM picture of 10.

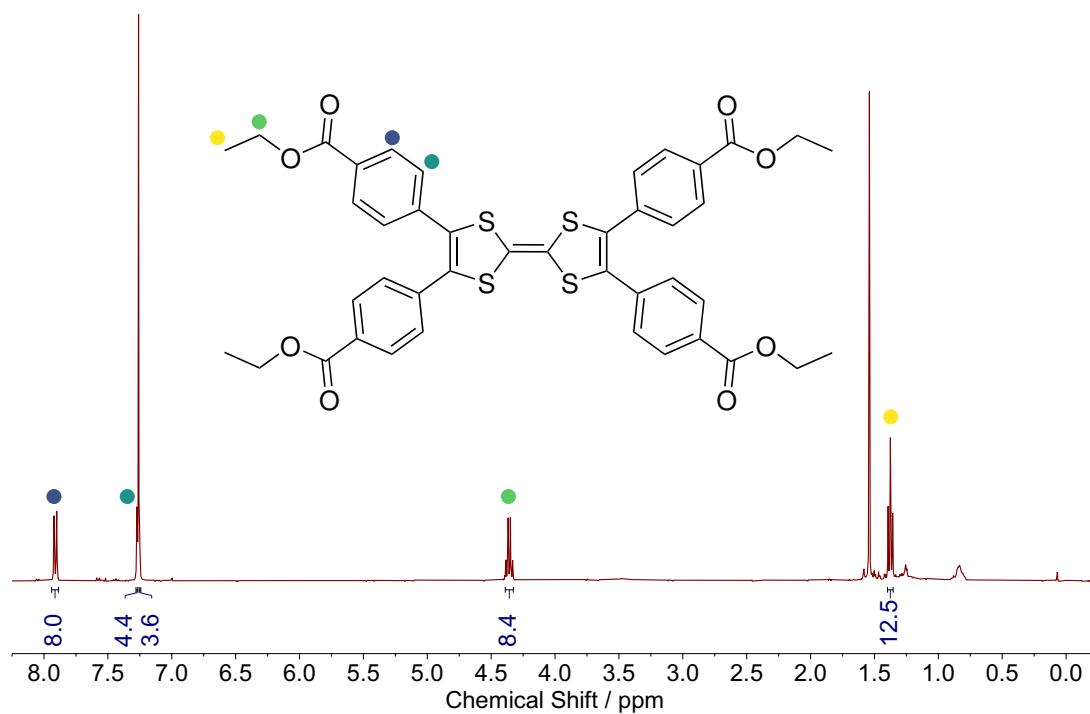


Figure 84. NMR spectrum of Et<sub>4</sub>TTFTB.

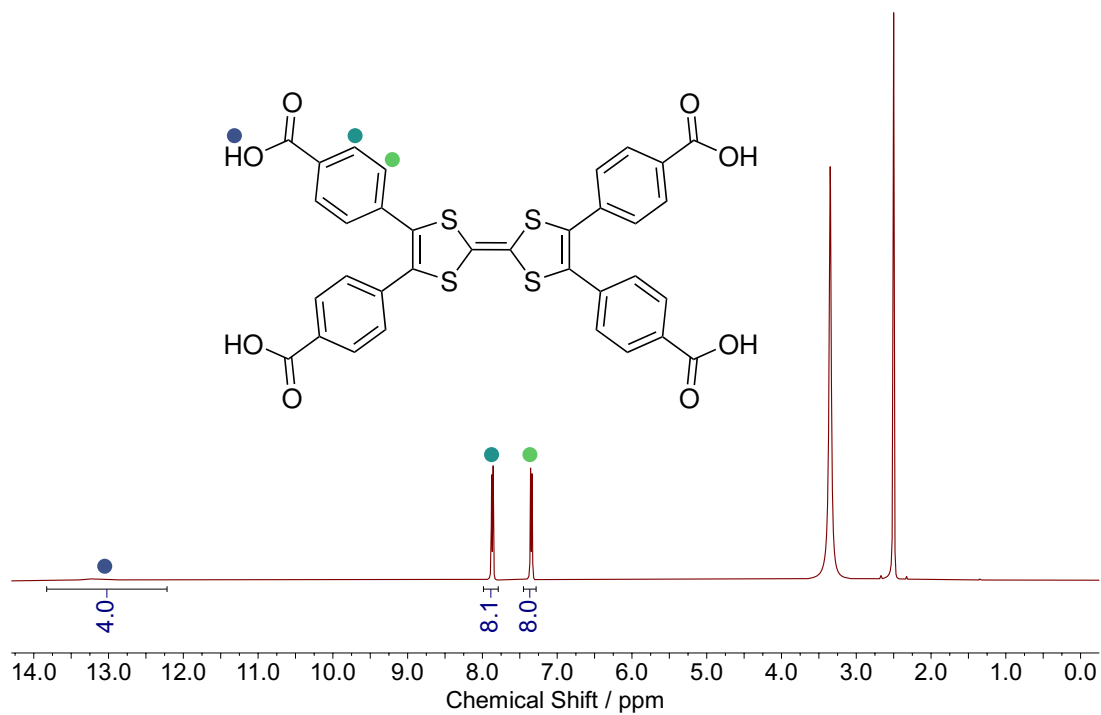
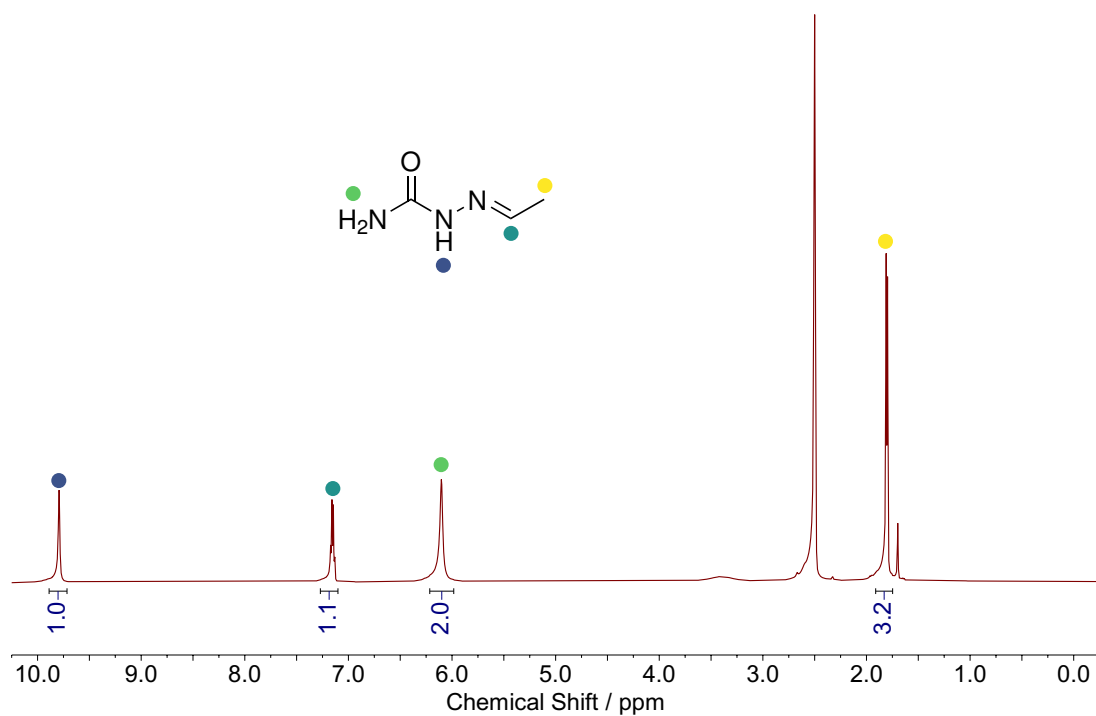
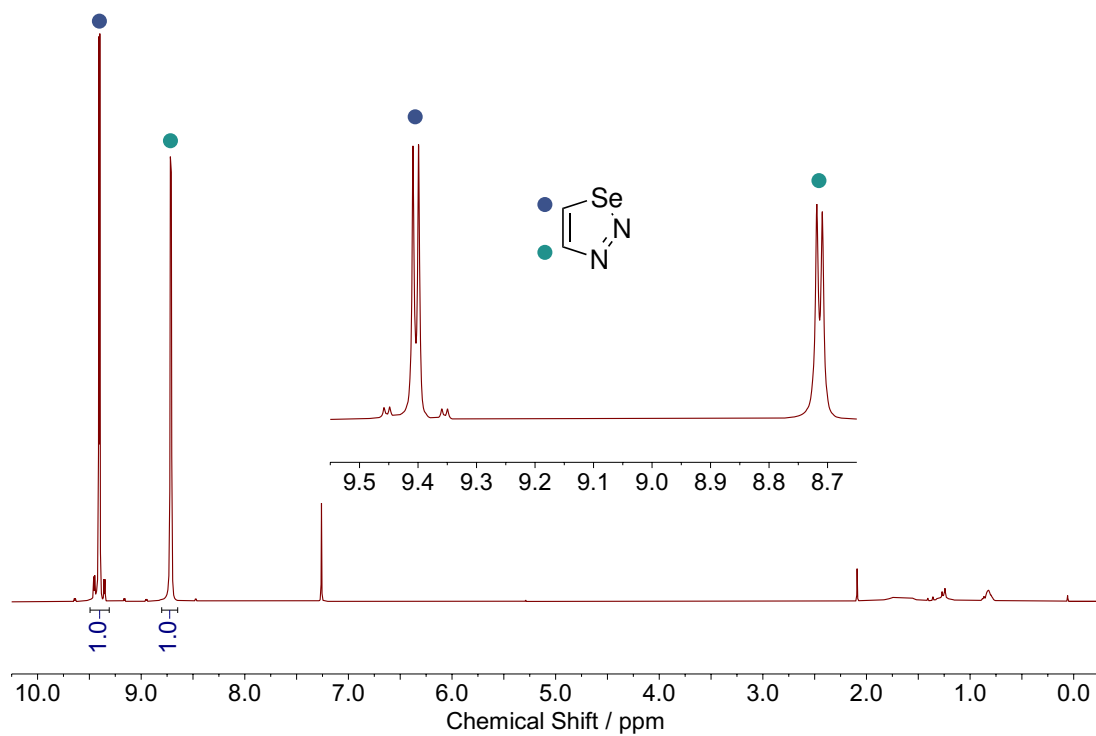


Figure 85. NMR spectrum of H<sub>4</sub>TTFTB.

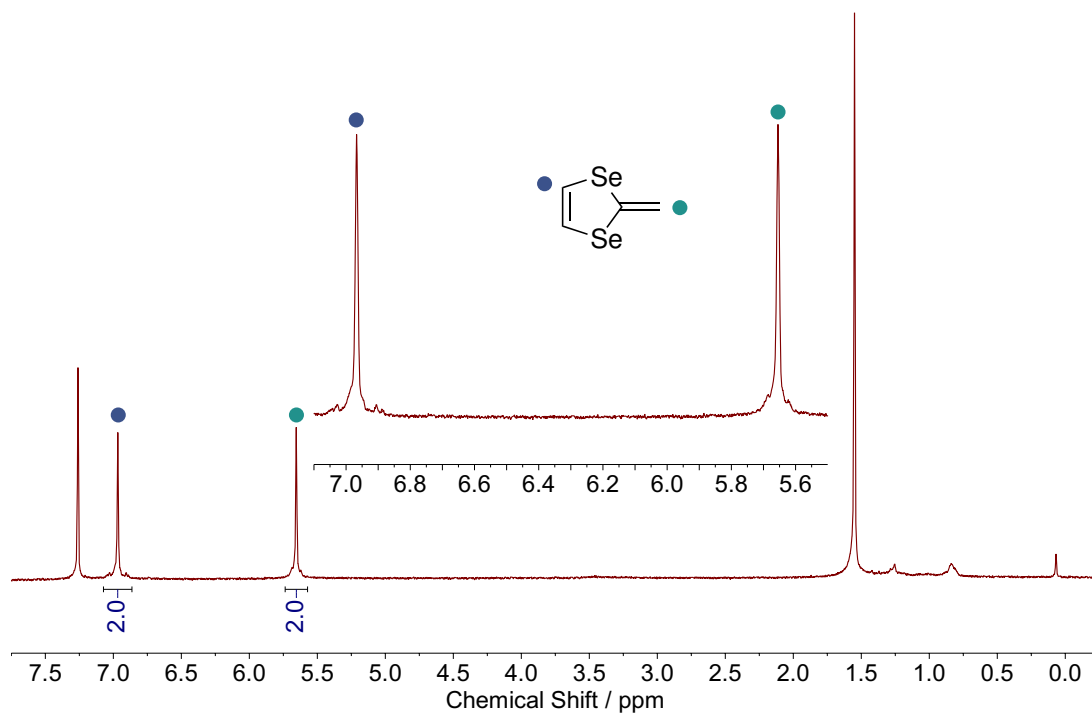


**Figure 86.** NMR spectrum of acetaldehyde semicarbazone.

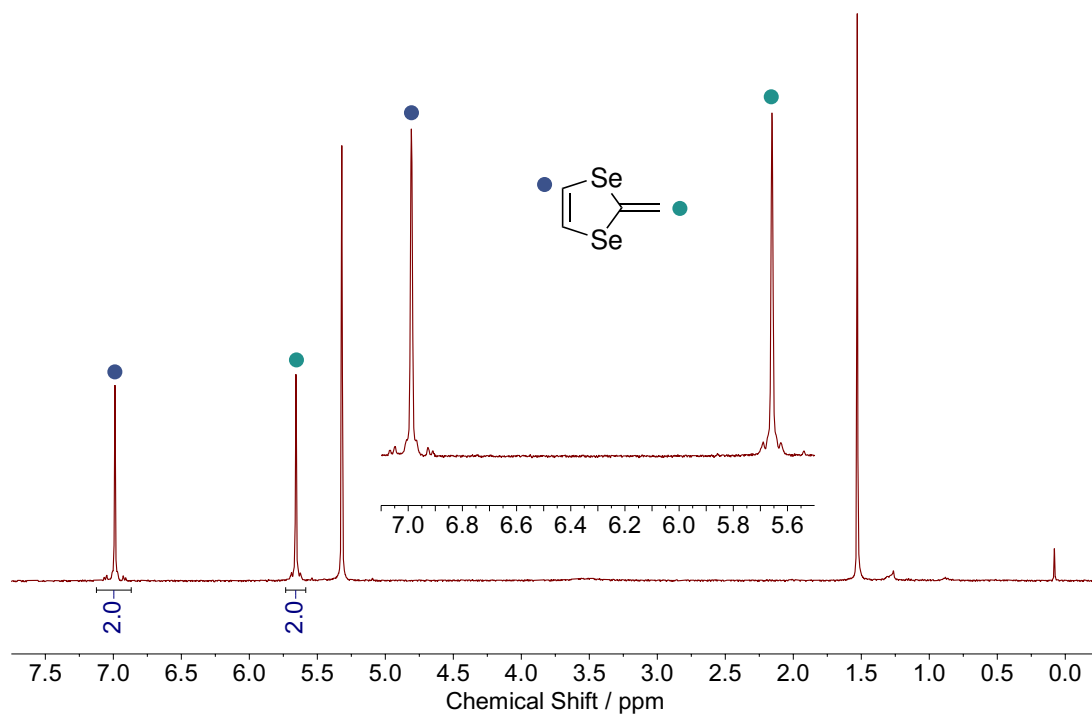


**Figure 87.** NMR spectrum of 1,2,3-selenadiazole.





(a)



(b)

**Figure 88.** NMR spectrum of 2-Methylene-1,3-diselenole in (a)  $\text{CDCl}_3$ , and (b)  $\text{CD}_2\text{Cl}_2$ .

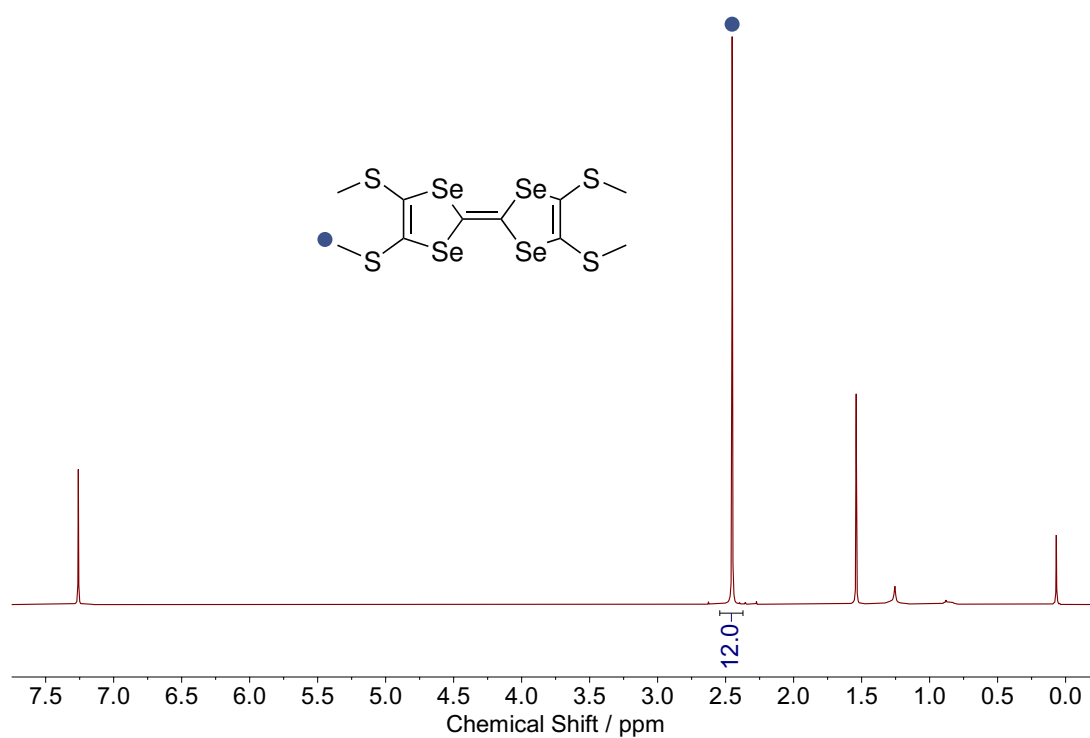


**Figure 89.** NMR spectrum of TSF(SMe)<sub>4</sub>.

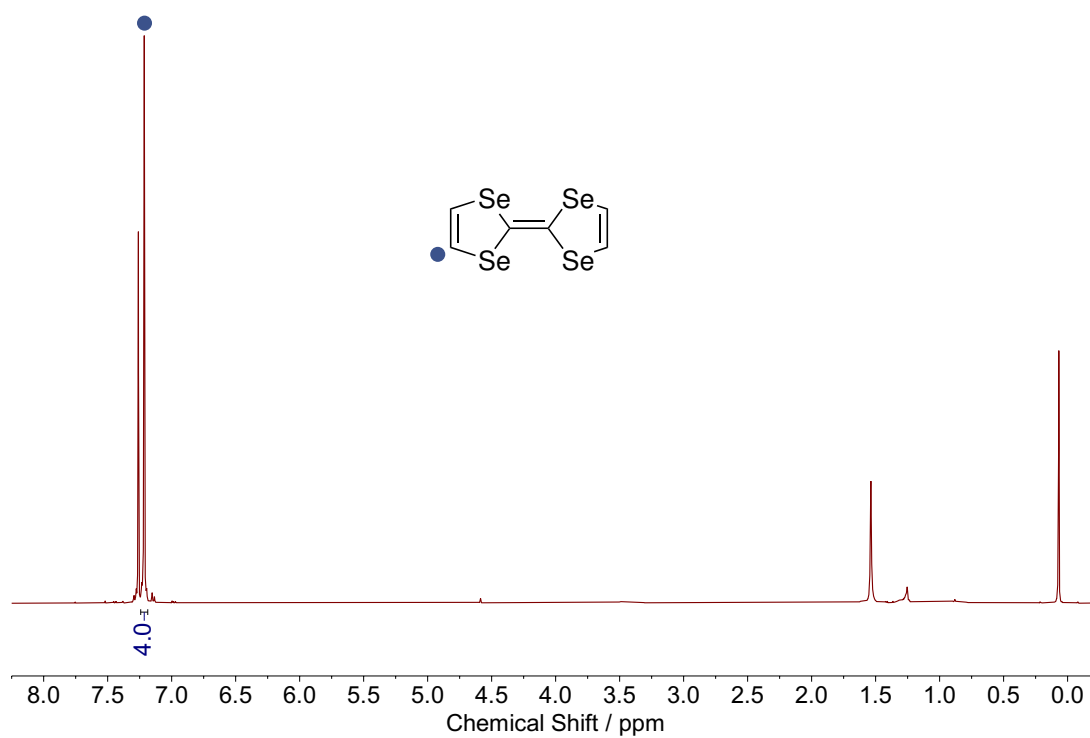


**Figure 90.** NMR spectrum of TSF.

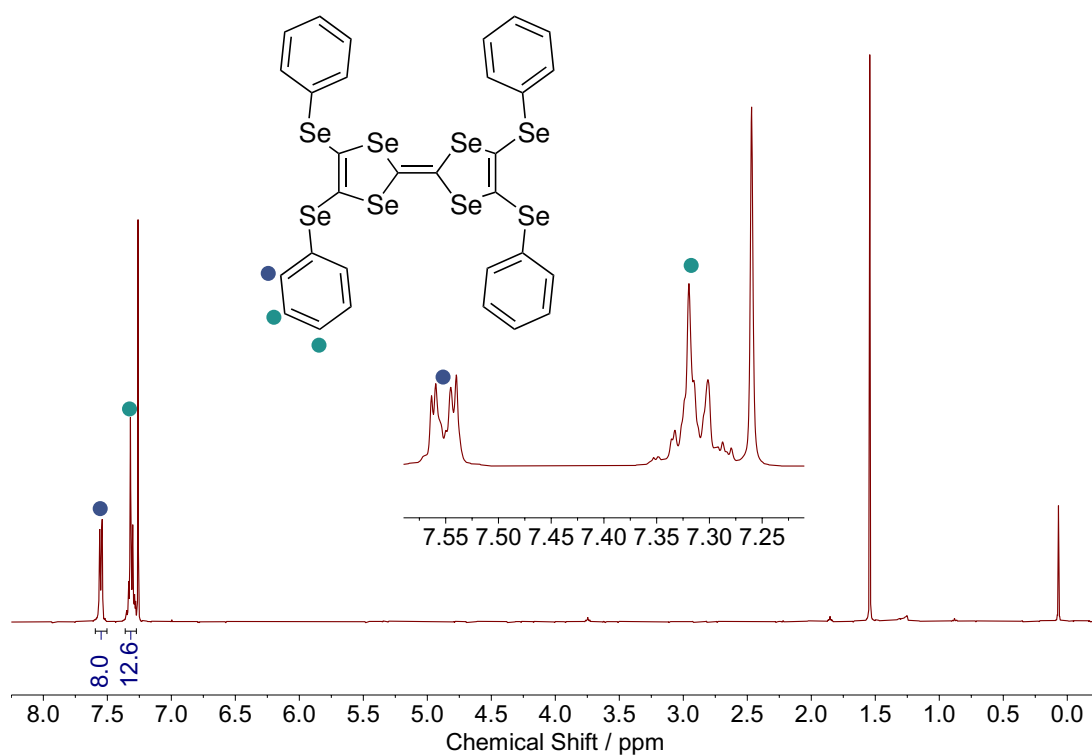


Figure 91. NMR spectrum of TSF(SePh)<sub>4</sub>.

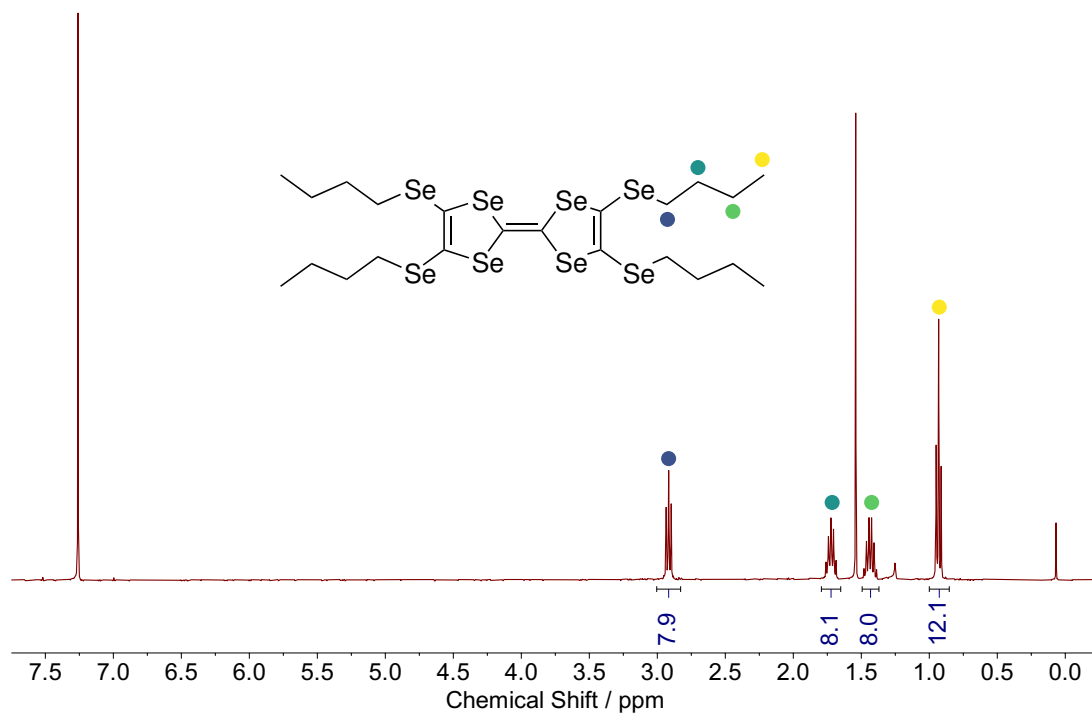
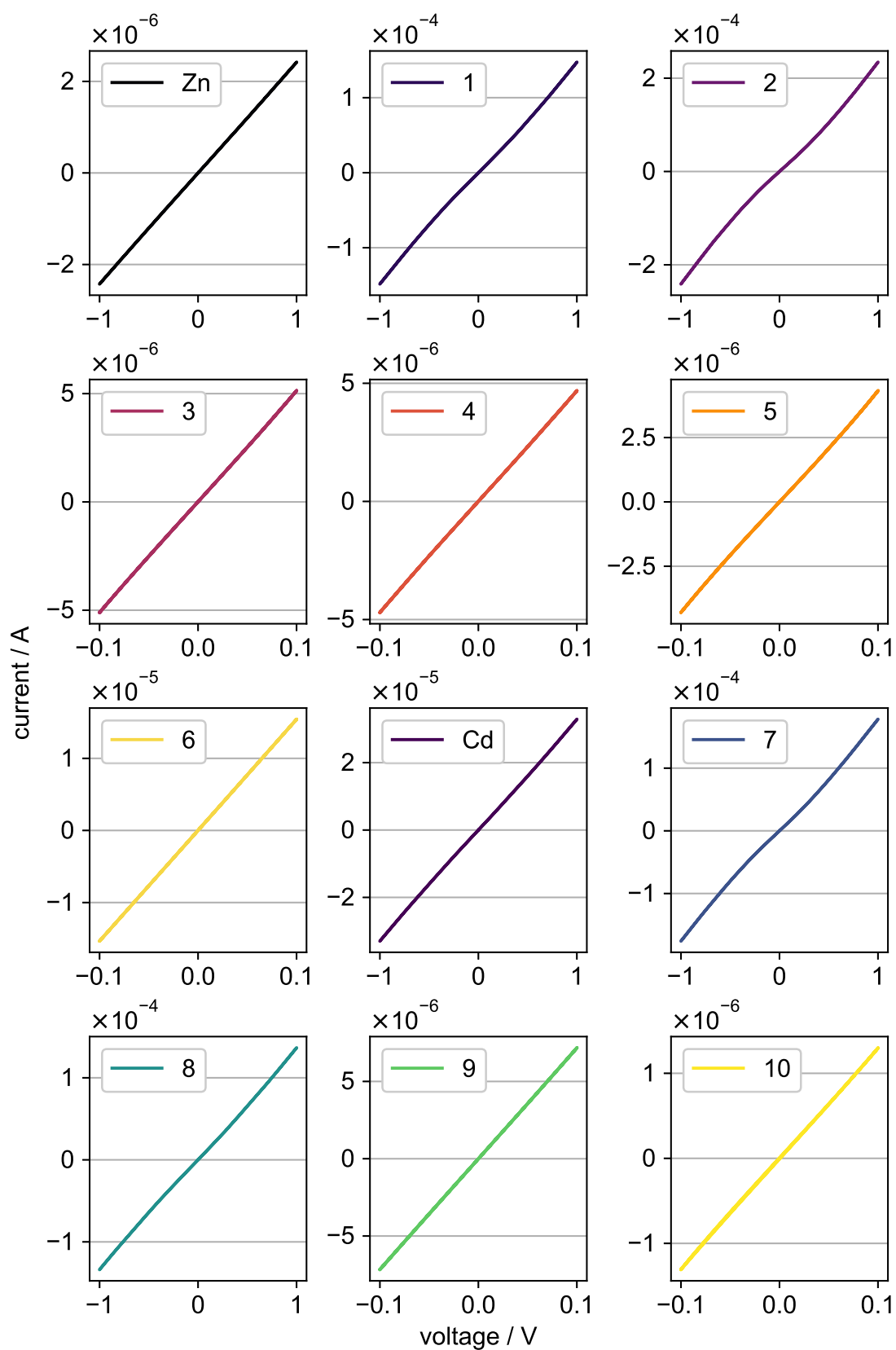
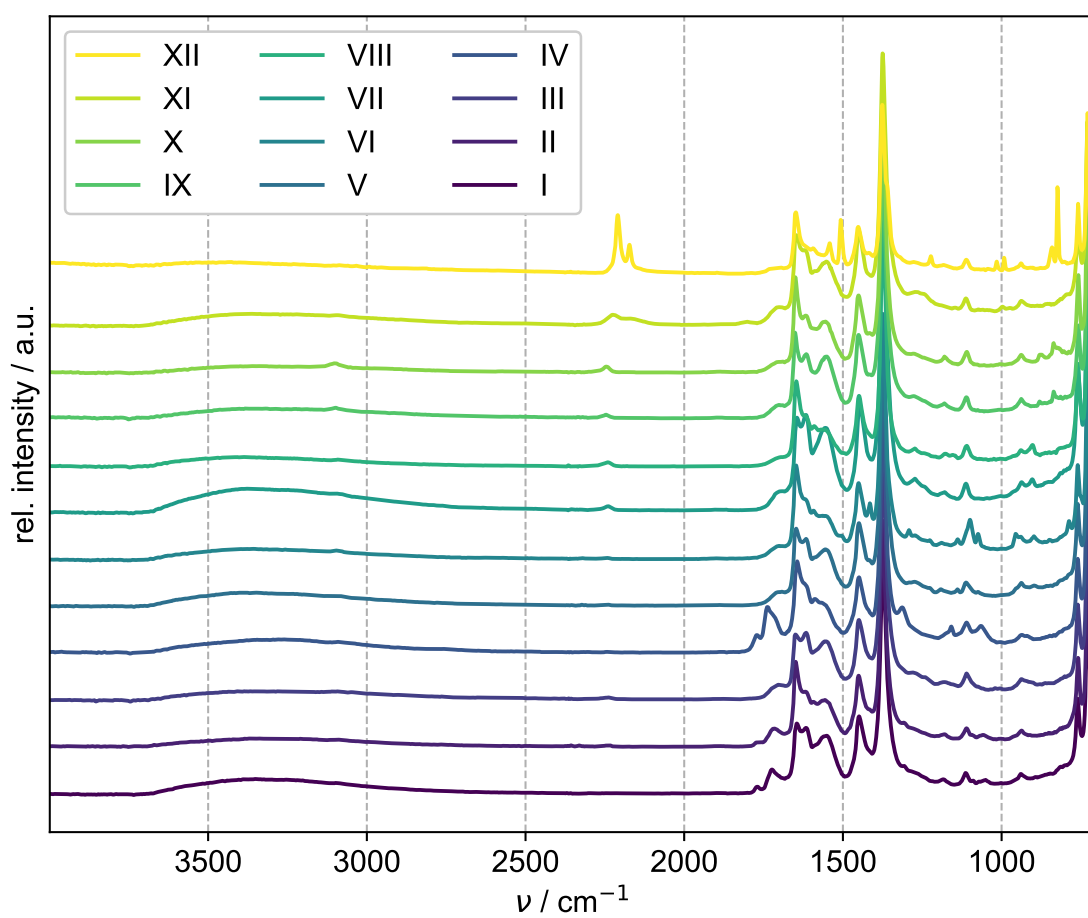


Figure 92. NMR spectrum of TSF(SeBu)<sub>4</sub>.



**Figure 93.** Current-voltage curves of  $(\text{TCNE})_x\text{M}_2\text{TTFTB}$ .



**Figure 94.** FTIR spectra of  $(\text{Guest})_x\text{Cu}_3\text{BTC}_2$ .

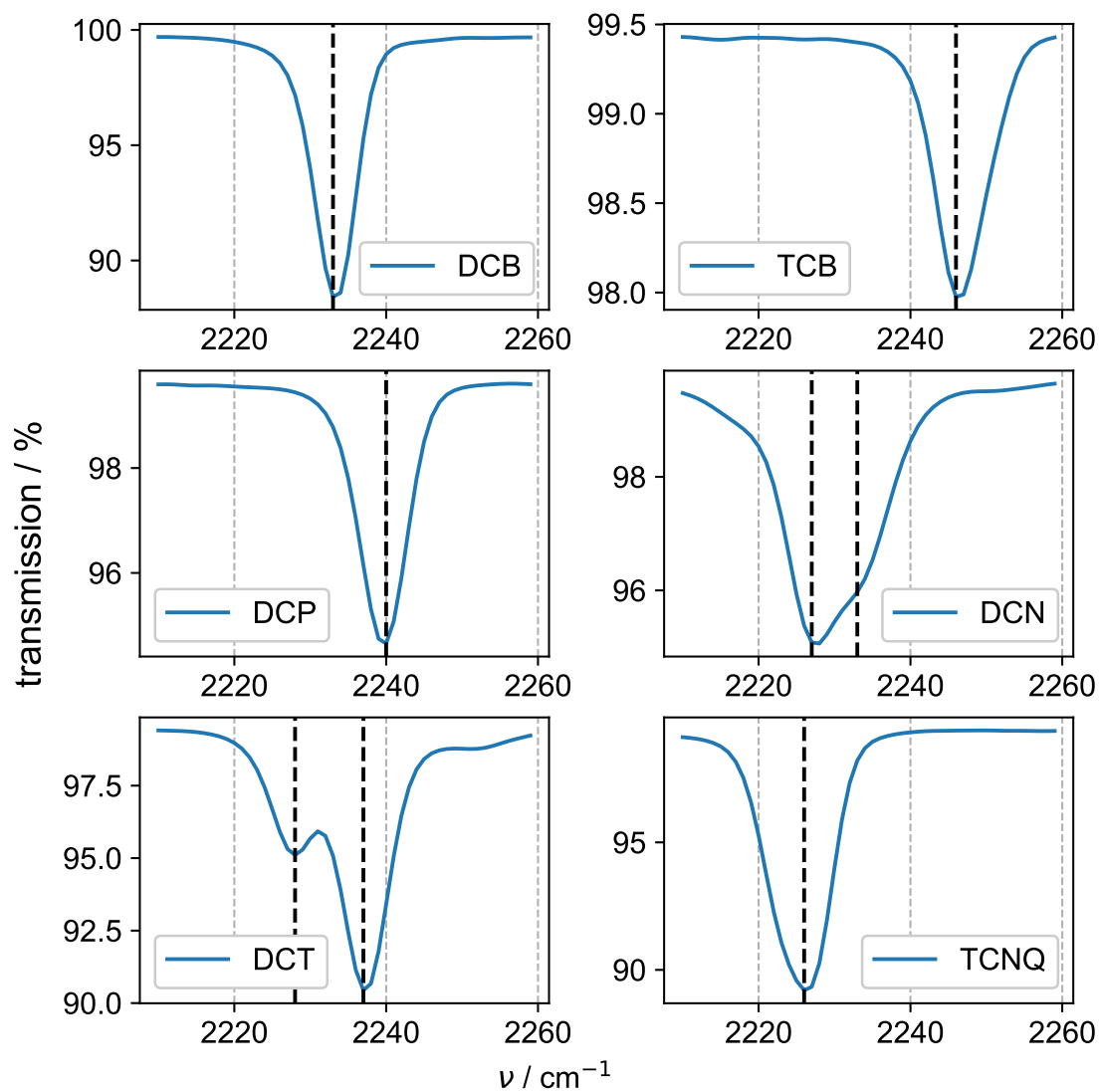


**Figure 95.** FTIR spectra of guests used for the VPI of  $\text{Cu}_3\text{BTC}_2$ . The peak maxima are indicated with a black dashed line.







# II

THEORY AND METHODOLOGY



# 7

## *Metal-Organic Frameworks*

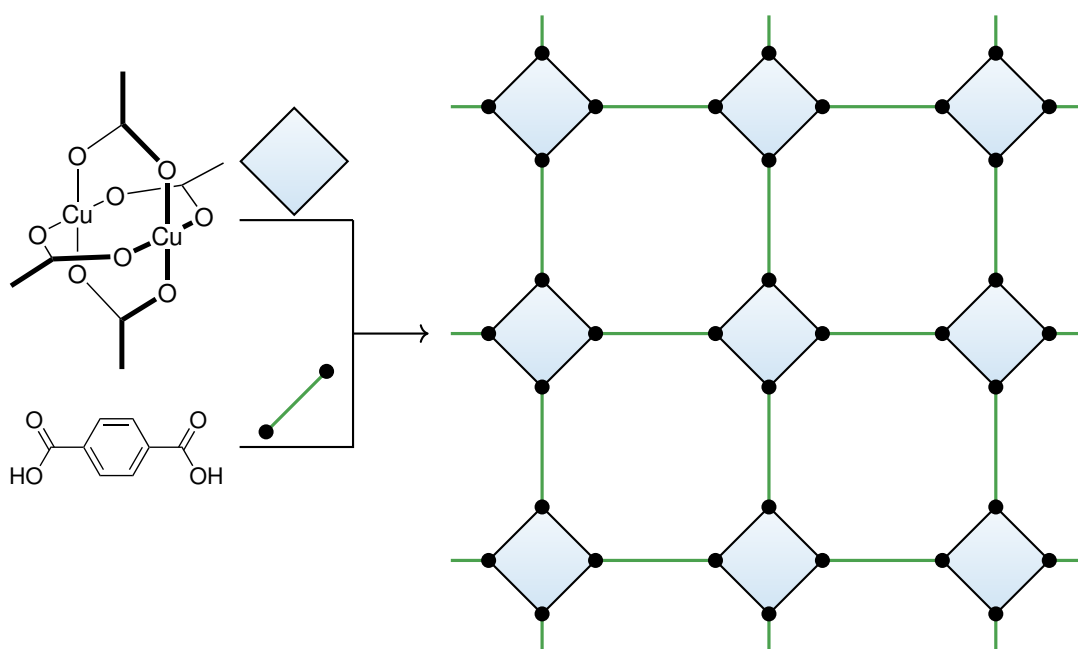
### 7.1 INTRODUCTION

Metal-organic frameworks (MOFs) are composed of single metal ions or polynuclear metal ion clusters that are interconnected by organic ligands (linkers) to form crystalline and porous coordination networks.<sup>5,6,158–160</sup> Their structures are highly defined due to the molecularly precise nature of the employed organic ligand, as well as the coordination chemistry of the discrete metal cations or clusters. Because of their high synthetic flexibility, MOFs have attracted exceptional attention in the past 20 years due to their potential applications in a vast spectrum of fields such as chemical separation,<sup>161,162</sup> gas storage,<sup>163</sup> catalysis,<sup>164,165</sup> and sensing.<sup>166–168</sup> In the following section, their formation, diverse physical properties, and chemical reactivities will be introduced to the reader prior to the discussion of their electronic structure and potential in the field of electronics.

### 7.2 TOPOLOGICAL DESCRIPTION

Generally, MOFs exhibit complex crystal structures with large unit cells containing many atoms which can complicate their analysis with respect to the arrangement of their constituents along with their connectivity to each other.<sup>169–171</sup> For this reason, it is advisable to simplify the crystal structures by reducing the information content gained by the structural analysis from an extensive and chemical representation (e.g., nature of atoms, intra- and intermolecular bond distances and angles) to a purely geometric image of the connectivity. This can be achieved by

a topological elucidation of a MOF structure in which the connectivity is described in terms of nets that consist of nodes and links.<sup>172–174</sup> These are defined by their points of extension; a node can make several connections depending on the symmetry and connectivity of the linkers and metal ions constructing the MOF (e.g., two connections for a ditopic linker with trigonal symmetry, four connections for a tetratopic metal ion with preferred square-planar coordination geometry), while a link connects two nodes via its two points of extension.<sup>175,176</sup> Importantly, a net is not characteristic when regarded as a sum of the connectivity and symmetry of nodes and links alone but also the spatial arrangement of the nodes relative to each other and the connectivity between them plays a large role. Additionally, nets are indifferent to bending and stretching and can only be transformed into each other via the breaking of connections. For example, four-connecting paddle-wheel complexes  $M_2(-COO)_4$  and two-connecting benzene dicarboxylate (BDC) can be topologically reduced to square-nodes and links, respectively, and arranged to an infinite two-dimensional array as indicated in Scheme 31.



**Scheme 31.** Illustration of the topological reduction of paddle-wheel complexes and linear dicarboxylates into squares and links and their connectivity.

The most prominent example for architecturally and chemically stable MOFs is MOF-5, which was published in 1999 by Yaghi *et al.*<sup>177</sup> In this MOF, inorganic units of octahedral  $Zn_4O(-COO)_6$  composed of four tetrahedral  $ZnO_4$  units sharing a central O atom are interconnected by ditopic BDC linkers to construct a three-dimensional coordination network with primitive cubic (**pcu**)<sup>178</sup> topology encompassing cubic pores of 15.1 and 11.0 Å size, respectively (Figure 96).

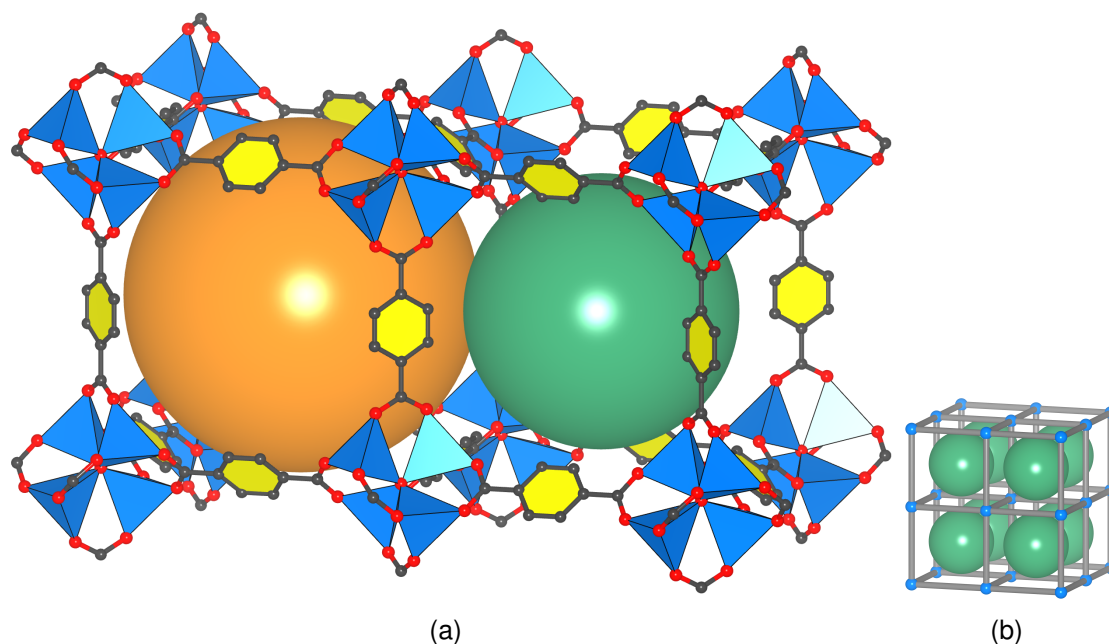


**Figure 96.** (a) Crystal structure of MOF-5. The different pore sizes of 15.1 and 11.0 Å are illustrated using an orange and a green sphere, respectively. (b) Illustration of the underlying **pcu** topology of MOF-5. Green spheres indicate the empty pore space. The Vesta3 software was used for crystal structure visualization.<sup>179</sup>

### 7.3 FORMATION OF METAL-ORGANIC FRAMEWORKS

Generally, the successful synthesis of MOFs is strongly dependent on the chosen reaction conditions, i.e., linker and metal source, concentration, molar ratios, temperature, time, solvent combinations, and the nature and concentration of additives.<sup>169,180–196</sup> Typically, the reactions are performed in high-boiling dipolar-aprotic amide solvents, e.g., DMF is used. Essential to obtaining highly crystalline products is a slow rate of formation of the framework, which increases with an increasing concentration of the linker that coordinates to a metal ion.<sup>197–201</sup> In the case of carboxylic acids as linkers, a deprotonation of the acidic proton at the carboxylic acid functional group needs to take place to release a carboxylate anion first, and thus forming the reactive, coordinating species. The amide solvent plays a crucial role since it is unstable at higher temperatures and decomposes in the presence of water to liberate a basic amine and a carboxylic acid (i.e., dimethylamine and formic acid in the case of DMF, respectively).<sup>202–205</sup> Both serve a specific purpose during the reaction; the base needed for the deprotonation of the carboxylic acid to generate the chelating carboxylate anion needed for the MOF formation. On the other hand, the carboxylic acid, which can be regarded as a monotopic linker, acts as a templating agent or modulator that slows down the formation rate of MOF and improves the crystallinity.<sup>206–210</sup> This is because the lower topicity of the linker does not allow the cross-linking of two metal nodes;

hence, the coordination process becomes more reversible. Thus, the nature of the amide solvent determines the base strength and modulating capability of liberated base and carboxylic acid, respectively, and the reaction temperature influences the rate of decomposition of the solvent into its hydrolysis products. After choosing the right reaction conditions, a crystalline and porous material is obtained together with solvent, potential side products and unreacted starting materials located both in the mother liquor (supernatant reaction solution) and inside the pores of the MOF. Thus, a "washing" treatment is necessary in which side products and unreacted starting materials are washed away with the solvent mixture used during the MOF synthesis, repeatedly. By soaking the materials in fresh portions of solvent, impurities inside the MOFs pores are gradually removed. Then, the encapsulated solvent molecules are replaced by repeated soaking of the as-synthesized material in a low-boiling solvent (e.g., acetone, ethanol, dichloromethane). This "solvent-exchange" procedure facilitates the evacuation process and prevents extensive adhesive (mechanical) forces between the solvent and the inner MOF surface when high-boiling solvents with large surface tension are to be removed from the pores. In a last activation step, the solvent molecules in the pores are removed either by subjecting the MOF to high temperatures and dynamic vacuum, or by applying more gentle evacuation techniques such as freeze-drying or super-critical CO<sub>2</sub> drying.<sup>7,177,211–216</sup>

## 7.4 RETICULAR CHEMISTRY

### 7.4.1 Historical Background

The topological deconstruction of crystal structures into nodes and links is not only useful to visualize structural arrangements of each component in a MOF, it also serves as a basis for the prediction of structures whose topology must be dictated by the topology and connectivity of incorporated linkers and metal components. Such a rational design of a coordination network by defining suitable nodes and links of compatible geometry and symmetry was pioneered by Robson *et al.* in 1989 with the publication of the synthesis and structural characterization of  $[\text{Cu}^{\text{I}}[\text{C}(\text{C}_6\text{H}_4\text{CN})_4]][\text{BF}_4] \cdot x \text{PhNO}_2$ .<sup>217</sup> They proposed that the connection of tetrahedral coordination centers with rod-like connecting units may yield coordination polymers with crystal structures based on either the cubic diamond or hexagonal lonsdaleite lattice. By substitution of the MeCN ligands in tetrahedrally coordinated  $\text{C}(\text{C}_6\text{H}_4\text{CN})_4$  with the nitrile substituents of tetrahedrally symmetric  $\text{C}(\text{C}_6\text{H}_4\text{CN})_4$ ,

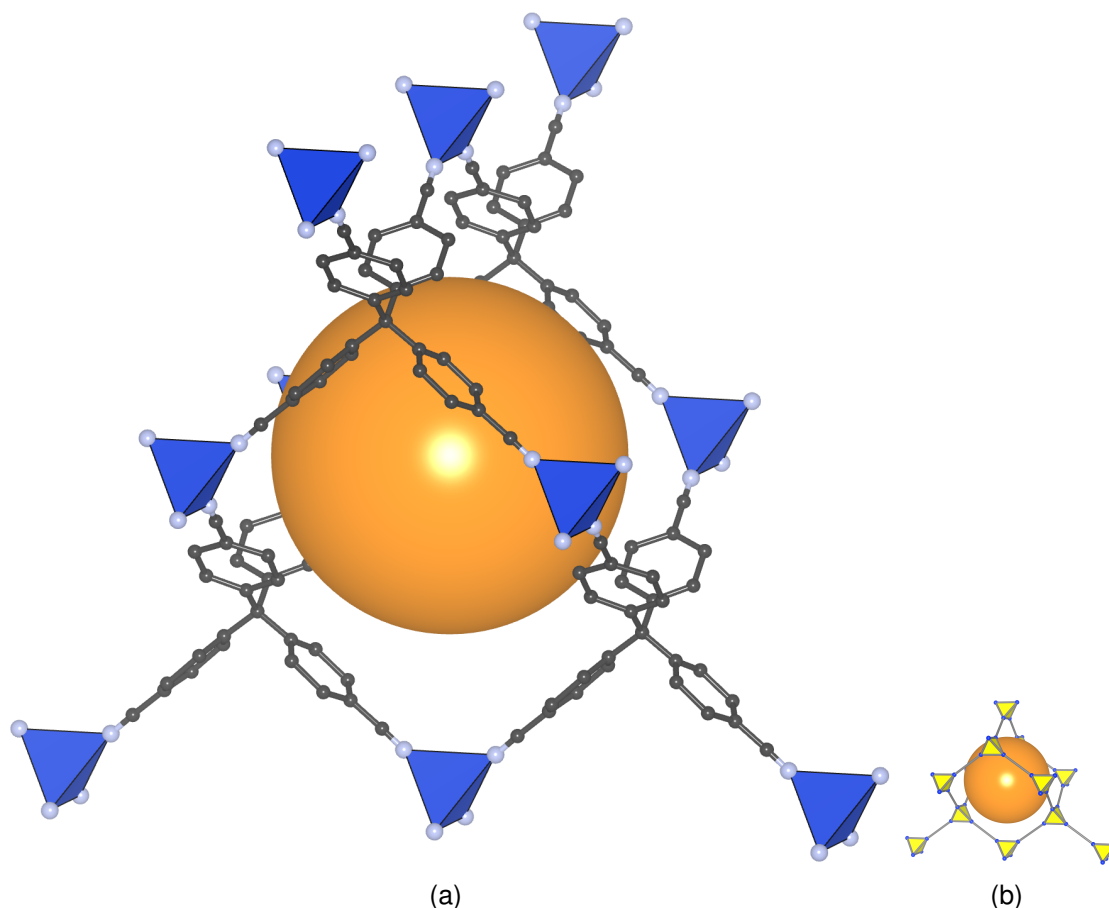


**Figure 97.** (a) Crystal structure of  $[\text{Cu}^{\text{I}}[\text{C}(\text{C}_6\text{H}_4\text{CN})_4]][\text{BF}_4] \cdot x \text{PhNO}_2 \cdot \text{H}$ ,  $\text{BF}_4^-$ , and  $\text{PhNO}_2$  are omitted. The orange sphere indicates the void space. (b) Illustration of the underlying **dia** topology in the cationic framework  $[\text{Cu}^{\text{I}}[\text{C}(\text{C}_6\text{H}_4\text{CN})_4]][\text{BF}_4] \cdot x \text{PhNO}_2$ .

a positively charged coordination network of diamond (**dia**)<sup>218</sup> topology charge balanced with  $\text{BF}_4^-$  anions and containing large cavities filled with solvent molecules precipitates out of the solution, one of the very first MOFs (Figure 97).

#### 7.4.2 Stable and Variable Metal-Organic Frameworks

It was proposed by the same group that connecting large and chemically functionalizable ligands in the same fashion could create materials with large cavities which render mass transport of various species within the void space possible, an important material property for applications such as molecular sieving and catalysis.<sup>219</sup> However, the so-called first-generation MOFs, based on neutral linkers such as bipyridines or dinitriles, are unstable to the removal of solvent molecules in the crystal cavities via evaporation (activation) due to the weak bond strength between the neutral ligand and the metal cations, leading to an architectural collapse and decomposition of the frameworks.<sup>220–224</sup> To address the stability

issues in MOFs, anionic linkers such as those containing carboxylate functional groups are used. These can form charge-balanced, neutral frameworks, obviating the need of counter-ions in the porous structure of the coordination network. Moreover, the higher bond strength between the metal ions and the linkers increases the salt-like character of the second generation MOFs, and thus the chemical, architectural, and thermal stability of the coordination network.<sup>5,169,225</sup> In many cases, the ligator atoms of the carboxylic acid linker molecules and the metal ions form metal-oxo clusters, so called SBUs, which further contribute to the stability of MOFs by forming chelated and charge-balanced polynuclear metal clusters with improved rigidity and directionality of such nodes in comparison to single metal cations.<sup>226–232</sup> The SBUs are formed during the reaction *in situ* at specific reaction conditions (e.g., temperature, concentration, ratio of metal ion to organic ligand, additives) spontaneously and reversibly through self-assembly.<sup>233–235</sup> During this process, comparatively strong coordination bonds are formed that increase the chemical stability of the resulting frameworks in comparison to those formed by neutral linkers, yet are sufficiently reversible to correct erroneous connections and create nearly defect-free architectures. Unlike single metal nodes, whose topologies are defined by the preferred coordination geometry of the metal ion, SBUs can adopt many different geometries with a vast range of connectivities, expanding the scope of possible topologies.<sup>162,231,232,236,237</sup> One of the most frequently occurring motifs is the four-connecting dinuclear paddle-wheel  $M_2(-COO)_4$ , which can be topologically reduced to a square-vertex (*cf.* Figure 31).<sup>238–242</sup> Here, each metal ion is coordinated by four oxygen atoms in a square-planar fashion and the carbon backbone from the acetate ligand serves as a bridge to form the  $\mu$ -carboxylato- $\kappa^2O,O'$  complexes known from inorganic acetate complexes of various divalent transition metals (copper, molybdenum, ruthenium, etc.).<sup>243</sup> Depending on the valence electron configuration of the complexed metal ions, metal-metal bonding can occur. The remaining axial coordination site is usually occupied by water. Both the topology and the coordination geometry of the inorganic nodes and organic ligands dictate the topology of the framework, and various topologies can be targeted. For example, the combination of the copper paddle-wheel SBU and a tritopic linker such as BTC yields the MOF  $Cu_3BTC_2$  (Hong Kong University of Science and Technology-1 (HKUST-1)) with the twisted boracite (**tbo**) topology (Figure 98).<sup>242</sup>  $Cu_3BTC_2$  crystallizes in the cubic space group  $Fm-3m$  and consists of two pores of distinct size, a smaller one with a diameter of 10 Å and a larger one with a diameter of 18 Å, as well as square pore openings with a diameter of 9 Å. Notably, there are two versions of the large pore which differ in the orientation of the Cu dimers. Only one half of those has  $Cu_2$  units whose Cu–Cu axis points to the center of the pore, while the other half



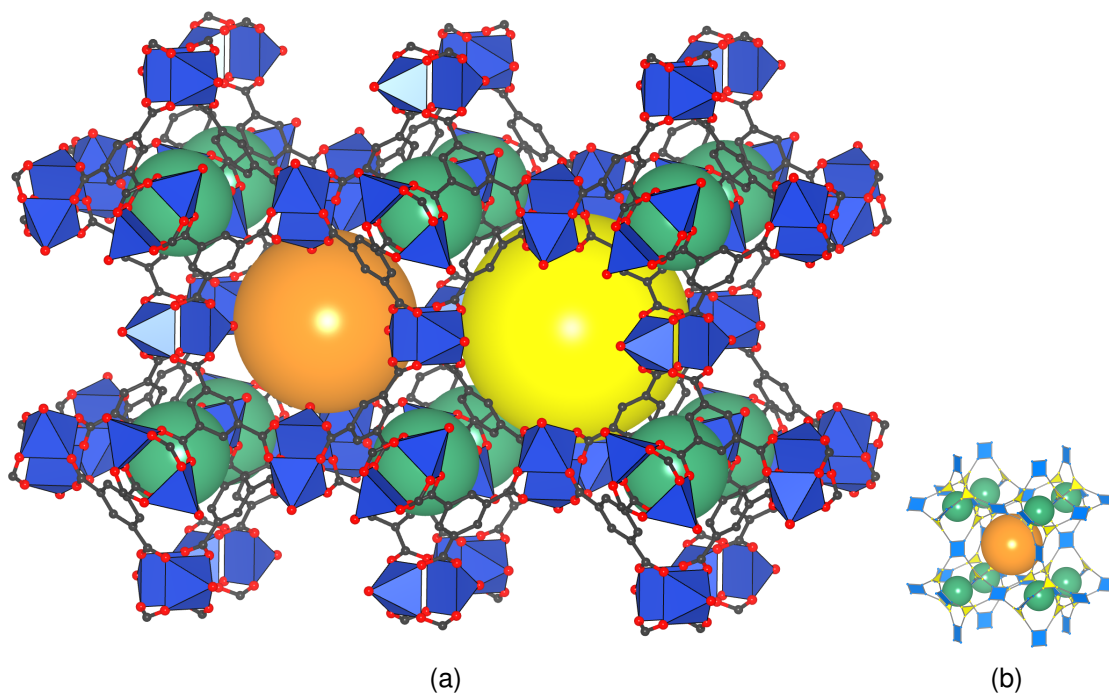


**Figure 98.** (a) Crystal structure of  $\text{Cu}_3\text{BTC}_2$ . The different pore sizes of are illustrated using an orange, green, and pink spheres. (b) Illustration of the underlying **tbo** topology of MOF-5. Orange and pink spheres indicate the empty pore space.

consists of Cu dimers with a tangential orientation. The axial water ligands at the Cu paddle-wheel SBU can be removed during the activation, affording OMS.<sup>244–249</sup> Even more, while maintaining the overall connectivity, it is possible to modify the building blocks (e.g., changing the metal ions of equal coordination geometry, substitution of SBUs with similar connectivity, introducing functional groups to linkers of equal topicity) without changing the MOF topology. This approach coined as "reticular chemistry" allows the formation of complex hybrid organic-inorganic materials with vast compositions and geometries in a highly precise and directed manner.<sup>6,169,250–254</sup>

## 7.5 RESPONSIVENESS TO EXTERNAL STIMULI

The third generation of MOFs, also called "soft porous crystals", contain flexible frameworks that respond to external stimuli and can change the shape of the pores without losing crystallinity or regularity of the framework.<sup>11,255–259</sup> The MOF termed Matériaux de l'Institut Lavoisier (MIL)-53 with the sum formula  $\text{M}(\text{BDC})(\text{OH})$  ( $\text{M} = \text{Cr}^{3+}, \text{Fe}^{3+}, \text{Al}^{3+}, \text{V}^{3+}$  contains  $\text{M}^{3+}$  cations octahedrally coordinated by four oxygen atoms coming from the two interconnecting BDC linkers and two hydroxyl groups in *trans* position which serve as the corner-sharing ligands for the formation

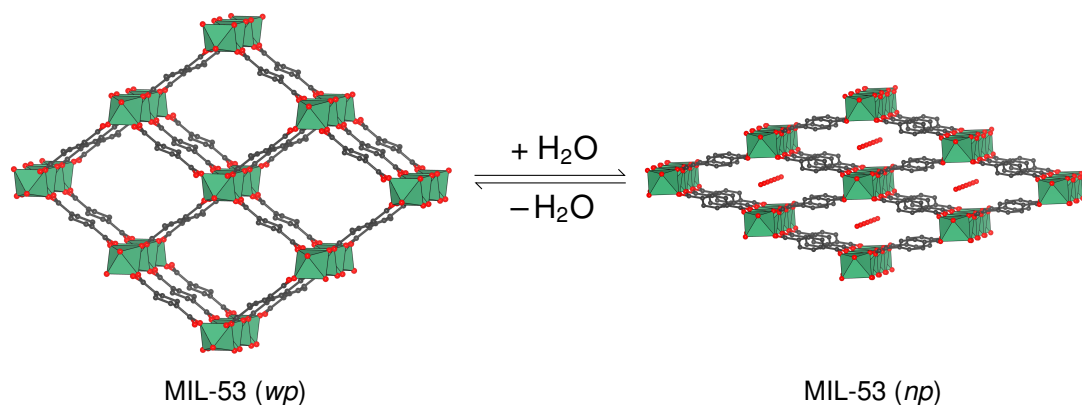


**Figure 99.** Breathing behavior of flexible MIL-53 in the presence of water.

of infinite, one-dimensional rod SBUs. Thus, a three-dimensional microporous structure with  $\text{SrAl}_2$  (**sra**)<sup>237,260</sup> topology and one-dimensional pores running along the SBUs are formed. These MOFs show reversible "breathing" behavior in the presence of guest molecules whereby the structures undergo a single crystal to single crystal (*scsc*) transition from one pore form to another with different unit cell parameters. For example,  $\text{Cr}(\text{BDC})(\text{OH})$  contracts upon adsorption of water from its activated wide pore (*wp*) form to the water-containing narrow pore (*np*) form.<sup>261</sup> One  $\text{H}_2\text{O}$  molecule is located at the center of every pore and stabilized via hydrogen bonding to the linker carboxylates (Figure 99).<sup>262</sup> Generally, the adsorption of gases induces a transition from *wp* to the thermodynamically more stable *np* form at low pressures and a reverse transition to the *wp* form at higher pressures, although the temperature ranges for the observation of these transitions differ for different probe gases.<sup>263–269</sup>

## 7.6 ISORETICULAR EXPANSION

MOFs have potential as next-generation materials in industrial applications because of their high crystallinity and chemical modularity combined with permanent porosity and surface area, which results from the steric demand of both the SBU and the organic linker.<sup>270,271</sup> Connecting elongated linkers through coordination bonds to metal nodes comes with the formation of pores of various sizes and shapes which can impart the resulting MOFs with different physical properties. Unlike other porous materials such as zeolites or carbons, the porosity of MOFs can be easily tuned by altering the organic building blocks without disturbing the original topology, enabling the formation of isostructural frameworks with different properties via pore engineering.<sup>272–276</sup> For example, the introduction of more func-

tional groups to the organic ligand increase the steric demand of the linker with the functional groups dangling in the pores of the MOF and reduce pore sizes in a controlled fashion. In addition, such functional groups can also introduce anchor sites for new chemical reactivities that are not inherent to the MOF structure (e.g., serve as anchoring point for post-synthetic modifications of MOFs, *vide infra*).<sup>277–280</sup> On the contrary, using longer organic ligands containing phenylene or acetylene units as spacer groups between the nodes and points of extension of the linker will extend the distance between the SBUs and give rise to structures with larger pores, and thus higher surface areas.<sup>281–286</sup> Such an "isorecticular expansion" was shown for the isorecticular metal-organic framework (IRMOF) series of MOF-5 (IRMOF-1), where elongated ditopic ligands were reticulated with  $Zn^{2+}$  ions at similar reaction conditions to obtain isostructural analogs of MOF-5 with altered pore dimensions or functionality (Figure 100).<sup>213</sup> In many cases, however, the resulting open space may influence the formation of additional frameworks that are identical in composition and topology but fill the voids of one framework, thereby forming mechanically entangled frameworks which cannot be separated from each other. This phenomenon described as "interpenetration" of MOFs is often concomitant with lower to no accessible surface area, and many topologies including the **pcu** topology is prone to interpenetration (e.g., IRMOF-1 is interpenetrated).<sup>287–292</sup> Conversely, some topologies do not exhibit interpenetration, such as the IRMOF series of MOF-74, which is a MOF built from one-dimensional SBUs connected by linear 2,5-dioxidoterephthalate (DOBDC) linkers forming a structure of composition  $M_2DOBDC$  ( $M^{2+} = Mg, Mn, Fe, Co, Ni, Zn$ ) with hexagonal channels.<sup>293</sup> The SBUs contain distorted octahedral  $M^{2+}$  centers which are coordinated by three oxygen atoms of three carboxyl groups, two hydroxy groups, and one terminal DMF ligand.<sup>237</sup> Symmetry is generally important for the successful isorecticular expansion of MOFs. This is nicely illustrated in  $Cu_3BTB_2$  or MOF-14, a MOF based on the copper paddle-wheel SBU and benzene tribenzoate (BTB), i.e., a phenylene-extended version of BTC.<sup>294</sup> Unlike  $Cu_3BTC_2$  it exhibits the platinum oxide (**pto**)<sup>295</sup> topology because of the differences in symmetry of the corresponding ligands. Whereas BTC contains carboxylic acid groups coplanar to the central benzene rings possessing  $D_{3h}$  symmetry, the benzoate groups in BTB are twisted with respect to the central aryl unit because of the steric repulsion of the aromatic hydrogen atoms and the molecular symmetry is reduced to  $C_3$ . In contrast, substitution of the CH units in the central ring in BTB with nitrogen groups gives triazine tribenzoate (TATB) which avoids steric repulsion of hydrogens and possesses  $D_{3h}$  like BTC. Thus, reticulation of TATB with  $Cu^{2+}$  results in the formation of  $Cu_3TATB_2$  or porous coordination network (PCN)-6 with **tbo** topology (Figure 101).<sup>281,296</sup>

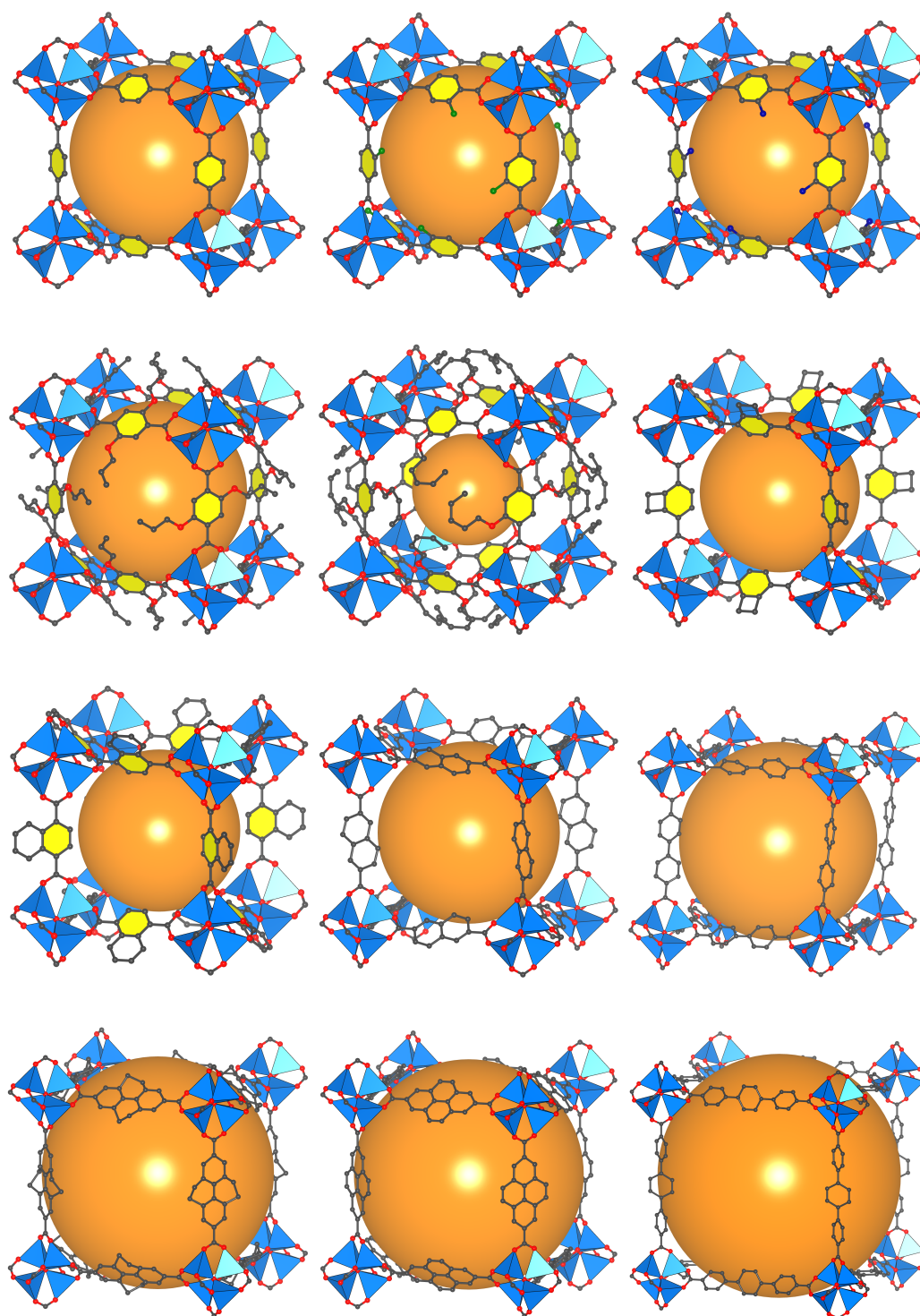


**Figure 100.** Isoreticular expansion of MOF-5.

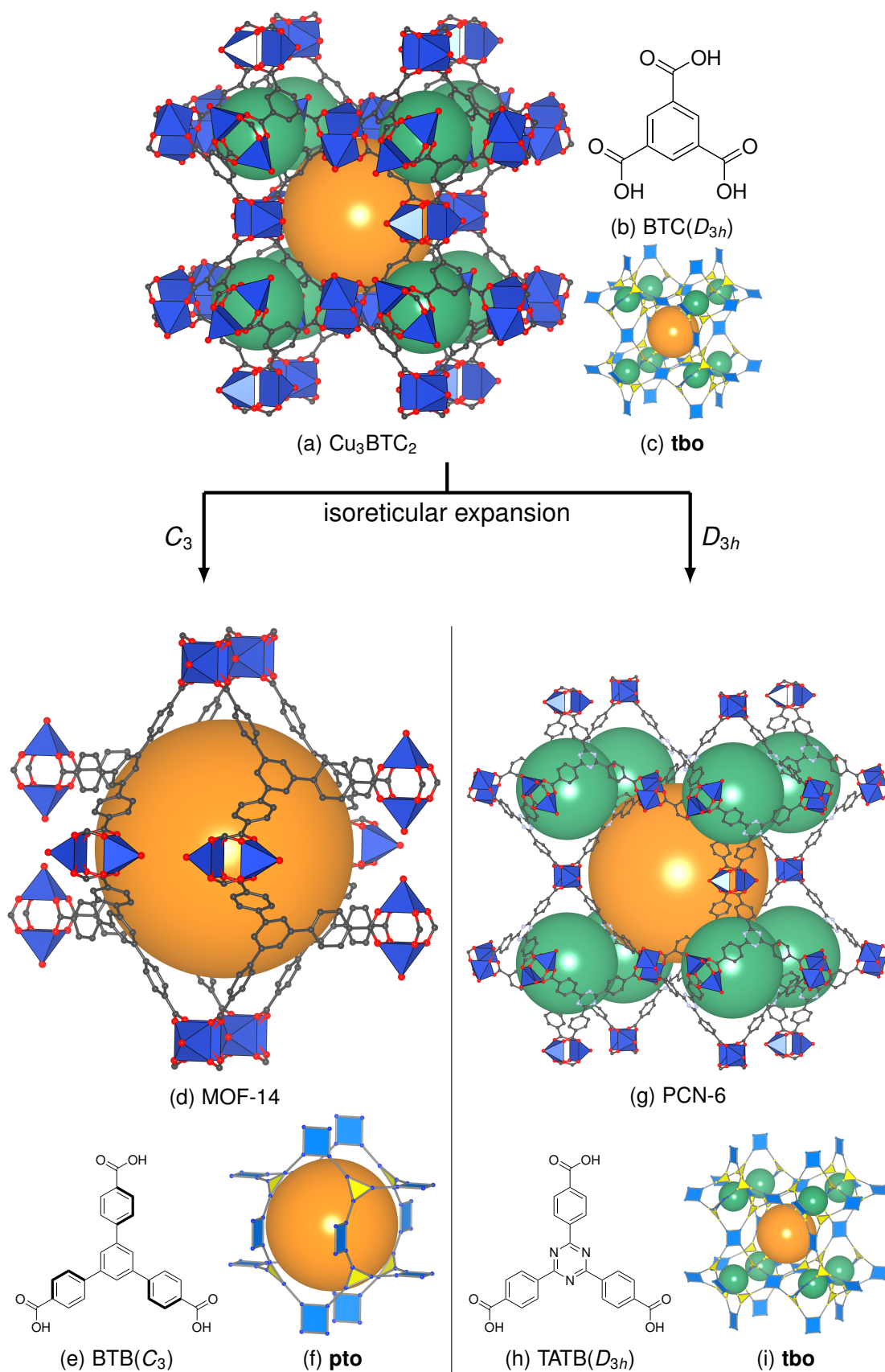


**Figure 101.** Dependence of the topology of MOFs obtained via isorecticular expansion on the linker symmetry.



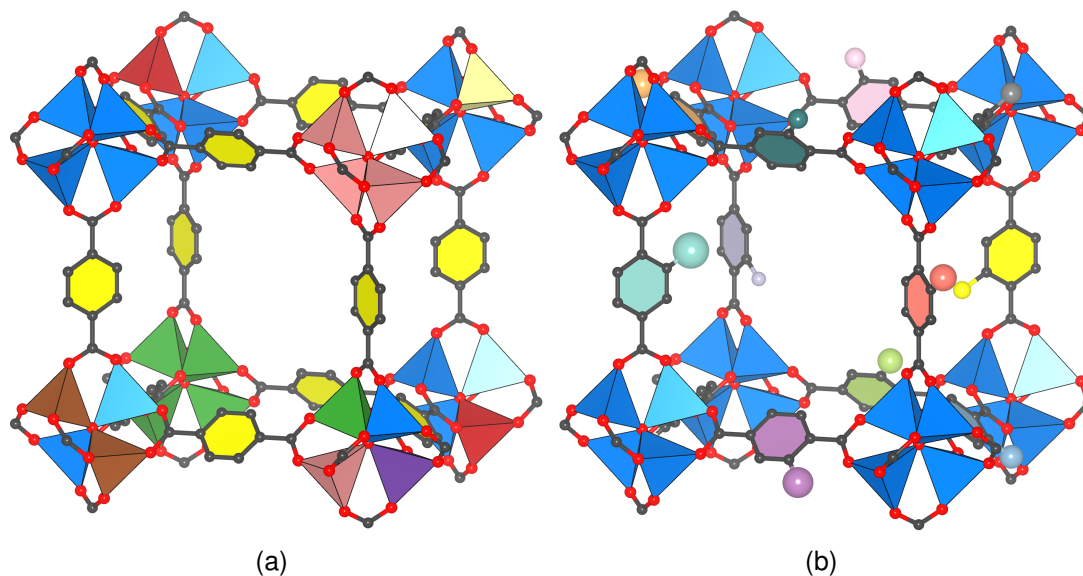


**Figure 102.** Conceptual illustration of MTV-MOF-5 containing (a) mixed-metal SBUs and (b) multiple linkers with a variety of functional groups (indicated with different colors).

## 7.7 CHEMICAL MODIFICATIONS

### 7.7.1 Pre-Synthetic Modifications

MOFs can be chemically modified by means of the reticular principle to obtain isostructural frameworks with different chemical and physical properties, e.g., by adding substituents with specific functional groups to the linker or substituting the metal ion with one of similar coordination geometry. Even more, multiple metal ions or linkers of equal dimensions and connectivity but containing different functional groups can be combined to form solid solutions of crystalline MOF materials (multi-variate metal-organic frameworks (MTV-MOFs)) with non-linear performance upgrades in adsorption properties or catalytic activities compared to the single-component MOFs.<sup>297–304</sup>

### 7.7.2 Post-Synthetic Modifications

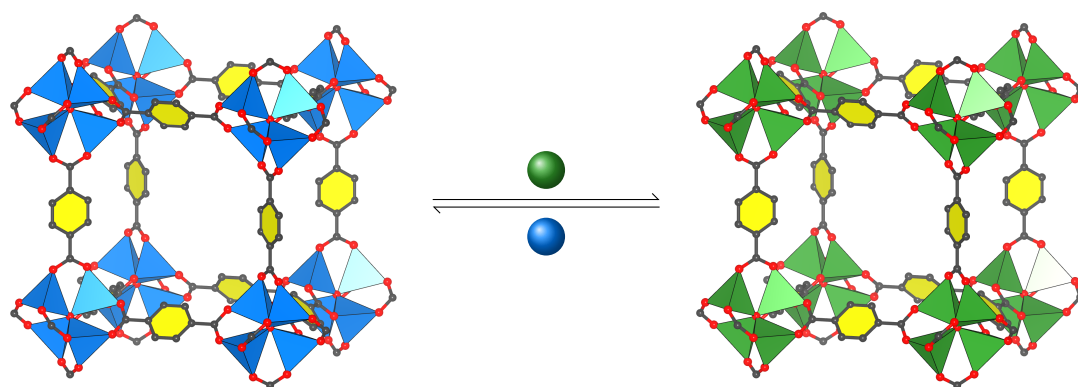
However, usually the presence of other functional groups in the linker can impede the MOF formation or lead to new structures with different topologies due to altered symmetry, geometry, and chemical properties, thereby posing a synthetic limitation of this methodology of modifying MOFs.<sup>10</sup> Similarly, the electronic structure of a different metal ion can have a large impact on the SBU formation, the reversibility of the coordination bond between the linker and metal, and thus the crystallinity of the resulting frameworks.<sup>305</sup> Another strategy is the "*in situ*"-functionalization

where a desired guest (functional (organic) molecule, nanoparticles, etc.) with specific chemical or physical activity is added to the reaction mixture of the MOF synthesis, but similar problems such as incompatibility of guests with the reaction conditions may occur.<sup>10,169</sup> Hence, it is advantageous to introduce new chemical functionality to the MOF "post-synthetically", i.e., after the MOF has been formed while simultaneously retaining its structure and crystallinity. Post-synthetic modification (PSM) can address all components of a MOF: the metal ions in a SBU,<sup>306–308</sup> the organic linker,<sup>306,309–313</sup> and the pore space.<sup>312,314,315</sup> During the post-synthetic metal-exchange (PSME)<sup>316,317</sup> and solvent-assisted linker exchange (SALE),<sup>318,319</sup> a controlled substitution of the components in the frameworks can be achieved by soaking MOFs in (saturated) solutions of the respective precursors for defined reaction temperatures and times to get modified systems which would otherwise not be accessible via a direct synthesis route. Ligands with specific coordinating anchor points (e.g., bipyridines, porphyrins) can be used for the post-synthetic metal incorporation (PSMI) to create discrete metal-organic complexes fixed to the pore walls of the MOF (Scheme 32).<sup>306,310,312</sup>

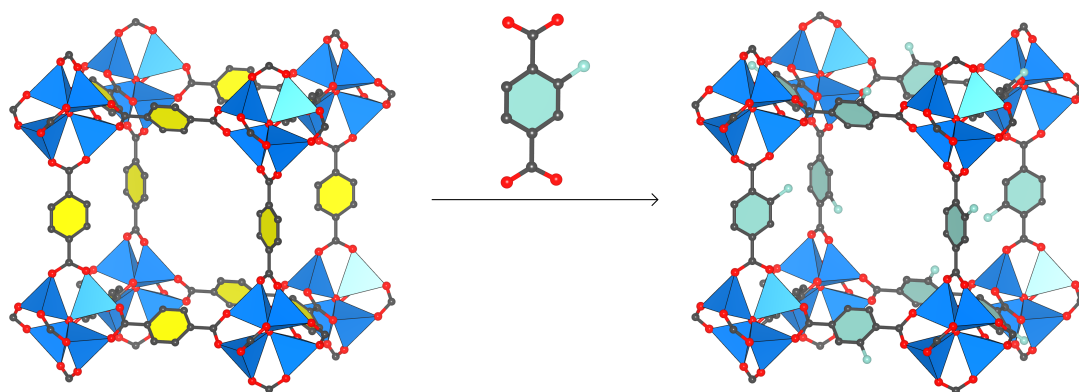
## 7.8 GUESTS IN METAL-ORGANIC FRAMEWORKS

### 7.8.1 Solvent Effects

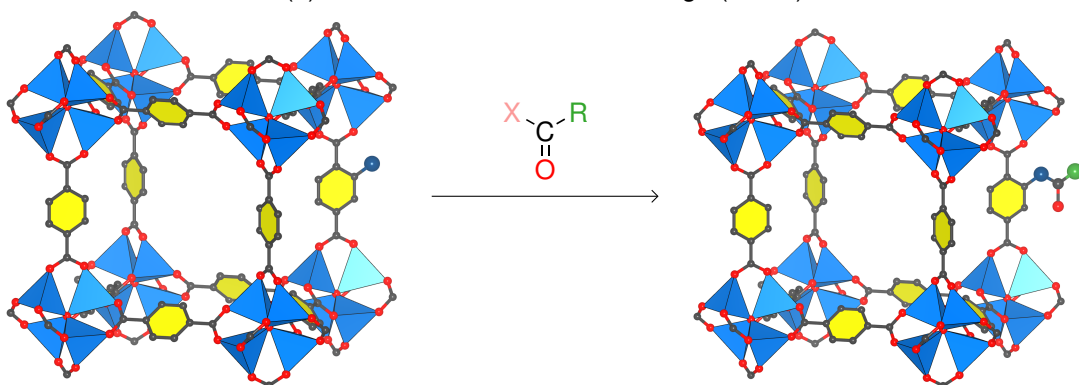
Not only the compositions and geometries of the SBU and linker, but also the presence of "extra-framework" guest species in the pores, i.e., compounds not bound to the framework via covalent or coordination bonds, can impart MOFs with new physical and chemical properties. This applies to seemingly trivial guests such as solvent molecules or counter ions for charge-balancing, as well. As outlined above, first-generation MOFs consist of charged frameworks in which counter ions and solvent molecules serve the purpose of providing chemical and architectural stability of the networks. In second-generation MOFs, the coordination bond strength between metal nodes and carboxylate linkers, the formation of SBUs, and the overall neutral charge of the frameworks provide sufficient stability, thereby obviating the need for stabilizing solvent in the pores. Nonetheless, a solvent-exchange process is performed prior to the removal of pore solvent via evacuation to replace high-boiling solvents with such that have low boiling points and low surface tension to facilitate the activation process. In this case, the replacement of internal guest solvent by means of PSM serves the purpose of



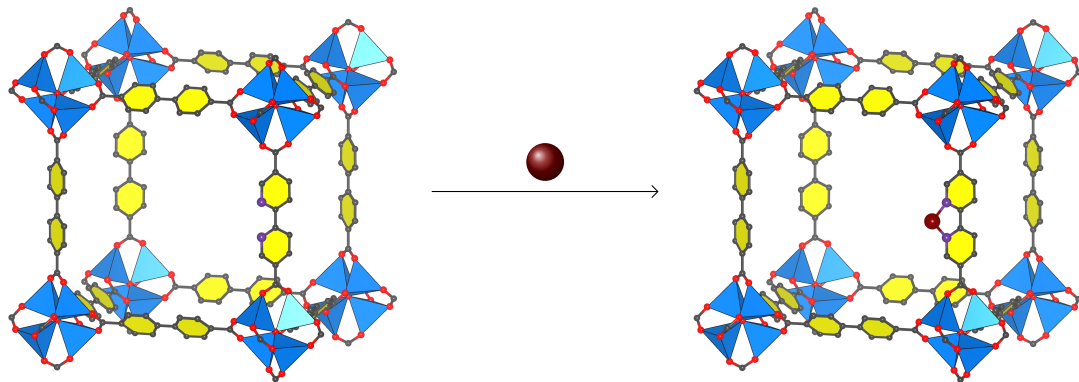
(a) Post-synthetic metal exchange (PSME)



(b) Solvent-assisted linker exchange (SALE)



(c) Tagging of linkers with new functional groups



(d) Post-synthetic metal incorporation (PSMI)

**Scheme 32.** Conceptual illustration of the diverse PSM strategies for MOF-5 analogs.



rendering the resulting frameworks more thermally and architecturally stable to high temperatures and vacuum. In third-generation MOFs, the mere presence of a guest in the pores induces structural transformations and imparts the frameworks with different material properties at proper temperatures and pressures.

### 7.8.2 Counter Ions

Another aspect is the presence of counter-ions in the pores which enables the use of MOFs as ion-exchange materials and affects the native properties of the framework.<sup>320</sup> An attractive feature is that MOFs could in principle be designed to show selectivity for one particular analyte in a pool of several ions, if the interactions and pore dimensions are tailored for an optimal interaction with a specific ion.<sup>321</sup> The first example of anion-exchange was demonstrated even in  $[\text{Cu}^{\text{I}}[\text{C}(\text{C}_6\text{H}_4\text{CN})_4]][\text{BF}_4] \cdot x \text{PhNO}_2$  (*cf.* Figure 97), the seminal work of rationalizing the design of coordination networks, where internal  $\text{BF}_4^-$  anions could be replaced with  $\text{PF}_6^-$  by soaking crystals of the network in a  $\text{NH}_4\text{PF}_6$  solution in  $\text{PhNO}_2$  as evidenced by FTIR.<sup>219</sup> After that, a series of other successful ion-exchange processes have been reported.<sup>322–326</sup> Particularly interesting are anion-exchanging MOFs with high selectivity towards environmentally problematic species such as the oxo-anions of heavy elements such as chromium, selenium, arsenic, etc. which can be used as toxin-capturing materials.<sup>327–329</sup> Moreover, the counter-ions can exert an influence on the physical material properties. For example, post-synthetically exchanging quaternary ammonium ions of negatively charged frameworks with lithium ions provides MOFs with altered performances in adsorption of various gases such  $\text{H}_2$ ,<sup>330</sup>  $\text{N}_2$ ,<sup>331</sup> and  $\text{CH}_4$ .<sup>332</sup>

### 7.8.3 Non-Native Guests

Moreover, non-native functionality can be introduced in the parent framework via the inherent properties of a guest or through its specific interaction with the hosting framework.<sup>12,333–335</sup> These guests can be of molecular,<sup>336–338</sup> polymeric,<sup>339–341</sup> or particle size dimensions.<sup>342–345</sup> While the possibilities are virtually limitless, a particularly interesting example for the encapsulation of functional species inside a MOF is the size-selective preparation of ligand-free nanoparticles of catalytically active metals such as palladium and platinum. Ultra-small particles in the nanometer regime are usually prone to agglomeration into architectures of reduced surface area and Ostwald ripening, i.e., the growth process of few

small particles to larger crystals with the concomitant dissolution of other smaller particles in order to achieve minimal surface energy.<sup>346</sup> Consequently, the use of stabilizing capping agents in solution<sup>347</sup> or of solid supports<sup>348</sup> is mandatory to prevent the above-mentioned decomposition routes. However, control of size and shape of such nanoparticles is difficult to achieve via conventional synthesis methods and poses a multi-parameter problem.<sup>349</sup> Here, the use of MOFs offers the advantage of nano-confinement of reactive species within the microporous structure with tunable pore properties to enable the successful synthesis of size-selective particles with superior properties.<sup>350,351</sup> For example, the encapsulation of Pt<sub>9</sub> carbonyl cluster compounds<sup>352</sup> into zeolitic imidazolate framework (ZIF)-8<sup>353</sup> affords stable Pt clusters containing 12 atoms and a diameter of 1.14 nm on average after carbonylation residing in the pores of the MOF.<sup>351</sup> After acidic dissolution of the framework, the intact clusters are transferred to a conductive carbon support and show high catalytic performance in the oxygen reduction reaction (ORR).<sup>354</sup>

#### 7.8.4 Retrofitting

As implied before, guests in MOFs do not necessarily impart new functionality to the parent material only due to the inherent properties of the guest, also the interaction of guest and framework are important. For instance, during post-synthetic ligand incorporation (PSLI) it is possible to create new linkages in the framework which are not accessible via *a priori* synthesis and improve the mechanical stability of the materials.<sup>355,356</sup> Such "retrofitting" of new linkers within existing MOF structures was illustrated in MOF-520 which was cross-linked with biphenyl dicarboxylic acid (BPDC) to yield retrofitted MOF-520-BPDC, a material stable to hydrostatic compression up to 5.5 GPa (Figure 103).<sup>138</sup> Furthermore, the activation of MOFs can form OMS at the SBUs serving as anchor points for coordinating guests. In Cu<sub>3</sub>BTC<sub>2</sub>, the OMS of two neighboring paddle-wheel SBUs are in close proximity accessible for bridging coordinating molecules. Thus, the retrofitting of Cu<sub>3</sub>BTC<sub>2</sub> with TCNQ affords TCNQ@Cu<sub>3</sub>BTC<sub>2</sub>, which was shown to exhibit increased electrical conductivity by seven orders of magnitude compared to the pristine MOF.<sup>139</sup> Similarly to MOF-520, the mechanical properties of TCNQ@Cu<sub>3</sub>BTC<sub>2</sub> are altered after the retrofitting the OMS with TCNQ in the crystallographic (111) plane of Cu<sub>3</sub>BTC<sub>2</sub> as shown in reduced NTE behavior of the framework with increasing guest content (Chapter 4, Figure 26).<sup>15,28,137</sup> In the field of electrically conductive MOFs, the interaction between a guest molecule and a framework host plays often a large role in the tuning of their electronic

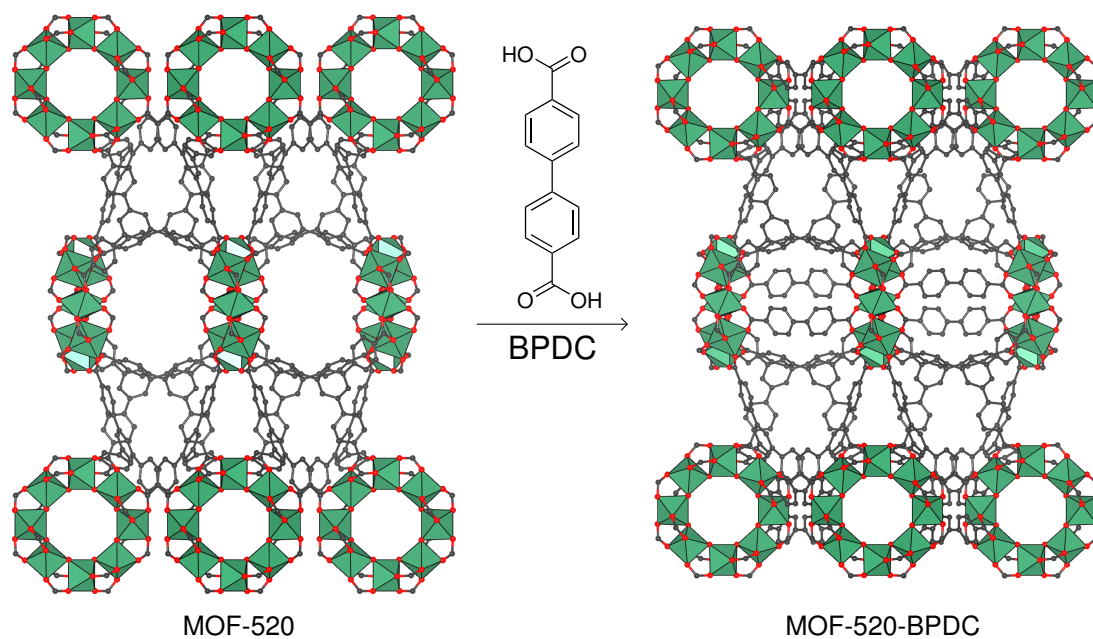


**Figure 103.** Retrofitting of BPDC in MOF-520.

properties. These will be discussed separately in the next chapter emphasizing the electrical conductivity in these materials.



# 8

## *Electrically Conductive Metal-Organic Frameworks*

### 8.1 INTRODUCTION

MOFs have sparked enormous interest in the exploitation of their diverse chemistry and possible applications in gas storage and separation as a natural consequence of their tunable and unprecedented porosity. Soon after, these properties have also become the center of focus with respect to the study of electronic properties of MOFs.<sup>9,27,270,271,357–361</sup> Their high crystallinity and synthetic flexibility concomitant with a tunable porosity and exceptional surface area provide a foundation for the discovery of electronic structure-property relationships in hybrid organic-inorganic materials combined with a rational and modular (reticular) adjustment of their electronic performances. Manifold applications of custom-designed MOFs can be envisioned, such as electrochemical supercapacitors where a combination of large surface areas and electrical conductivities could supersede state-of-the-art materials such as activated carbons, and related to that electrocatalytically active MOFs which combine a high electrical conductivity of the framework with metal ions or linkers in the MOF as active sites for electrocatalysis, among others.

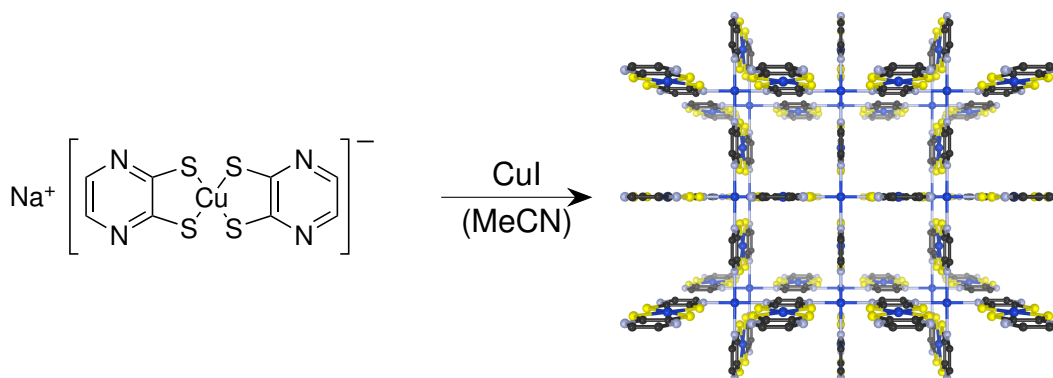
In spite of being an ideal platform for designing multi-functional materials that exhibit several chemical and physical properties at once, electrical conductivity is typically not inherent to MOFs. Generally, a high charge carrier density and mobility are required to produce materials with high electrical conductivity (*cf.* chapter 9). The charge mobility is proportional to the delocalization of electron density between the metal ions and coordinating linkers in a MOF, as well as within the organic linker itself and is dependent on the orbital overlap between two neighboring atoms. Commonly used  $\pi$ -delocalized, aromatic ligand systems of

MOFs provide a means of electronic communication within the organic backbone and are ideal, while aliphatic linker backbones with  $sp^3$ -hybridized carbons do not contribute free p-orbitals necessary to the conjugation of bonds in the ligand.<sup>362</sup> For the purpose of creating electronic overlap between the metal nodes and linkers, it is beneficial to use "soft" metals with high electron density, i.e., late transition metal cations from higher periods of the periodic table in low oxidation states, and  $\pi$ -conjugated ligands with similarly "soft" ligand atoms such as sulfur.<sup>363</sup> However, such coordination bonds of high bond energies come at the expense of the reversibility of the bond formation due to the larger covalent character of the coordination bond.<sup>364</sup> This in turn negatively impacts the formation of higher-dimensional architectures with high regularity and crystallinity, for the self-assembly of metal ions and linkers to form SBUs is too fast and irreversible, thereby promoting defect formation and amorphicity. MOFs on the other hand which are usually built from metal cations with high charge density and carboxylic acids as linkers provide this reversibility of the coordination bond. However, the resulting frameworks are highly ionic in their nature and low-energy CT pathways between the metal nodes and linkers are missing, yielding materials with poor electrical conductivity. Nonetheless, several approaches have been established to impart electrical conductivity in MOFs despite the various limitations listed before, and these will be discussed in the following sections with the aid of an exemplary selection of conductive structures.

## 8.2 THROUGH-BOND APPROACH

First, the through-bond approach tackles the orbital overlap between the metal node and the linker by introducing softer ligand atoms in the linker while simultaneously maintaining a good reversibility of the coordination bond to obtain crystalline products. One of the first electrically conductive MOFs based on a metal dithiolene unit was realized in the synthesis of  $Cu^{II}[Cu^{II}(2,3\text{-pyrazinedithiolate (pdt)})_2]$ . This MOF with a tetragonal lattice and pore openings of  $3.4 \text{ \AA} \times 3.4 \text{ \AA}$  is formed by the coordination of electron-accepting copper(III) 2,3-pyrazinedithiolate complex to electron-donating Cu(I) via its pyrazine N atoms and subsequent CT to form only Cu(II) ions. Here, the connectivity can be rationalized as a stacking of sheets of single-metal node Cu(II) centers which are coordinated by four pdt in a square-planar fashion to form an infinite two-dimensional sheet and which are spaced by the dimensions of the  $[Cu(pdt)_2]$  complex. The presence of only Cu(II) was proven via analysis of the bond distances between Cu and S ( $2.264 \text{ \AA}$

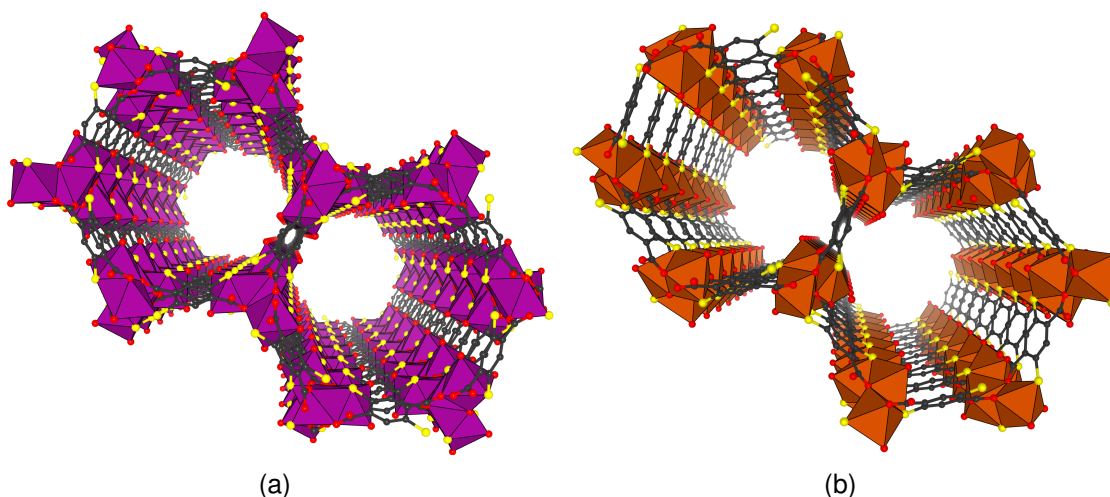
in  $\text{Cu}^{\text{II}}[\text{Cu}^{\text{II}}(\text{pdt})_2]$  vs. 2.182 Å in  $\text{Na}[\text{Cu}^{\text{III}}(\text{pdt})_2]$ , paramagnetic behavior observed in magnetic susceptibility measurements, and a CT band detected by FTIR. Electrical conductivity measurements showed semiconductive behavior with a room temperature conductivity of  $6 \times 10^{-4} \text{ S cm}^{-1}$  and an activation energy of 0.193 eV (Scheme 33).<sup>365</sup>



**Scheme 33.** Preparation of electrically conductive  $\text{Cu}^{\text{II}}[\text{Cu}^{\text{II}}(\text{pdt})_2]$  from  $\text{CuI}$  and  $\text{Na}[\text{Cu}^{\text{III}}(\text{pdt})_2]$  in MeCN.

Unlike  $\text{Cu}^{\text{II}}[\text{Cu}^{\text{II}}(\text{pdt})_2]$ , the isostructural  $\text{Cu}[\text{Ni}(\text{pdt})_2]$ , which can be obtained via a similar synthetic route, exhibits permanent porosity with a BET surface area of 385  $\text{m}^2$  after activation at 120 °C under dynamic vacuum as indicated via a type I sorption isotherm using  $\text{N}_2$  as probe gas at 77 K. However, the electrical conductivity of  $1 \times 10^{-8} \text{ S cm}^{-1}$  is comparatively low. Similarly to the  $\text{Cu}(\text{pdt})_2$  complex,  $\text{Ni}(\text{pdt})_2$  can be easily oxidized according to the reversible redox couple  $[\text{Ni}(\text{pdt})_2]^{2-/1-}$  at  $E_{1/2} = -0.391 \text{ eV}$  (vs.  $\text{Ag}/\text{AgCl}$ ). Thus, after subjecting an evacuated sample of  $\text{Cu}[\text{Ni}(\text{pdt})_2]$  to a suitable oxidant like  $\text{I}_2$  at 50 °C, the electrical conductivity increased to  $1 \times 10^{-4} \text{ S cm}^{-1}$ , and the activation energy decreased from  $E_a = 0.45 \text{ eV}$  to  $E_a = 0.18 \text{ eV}$ .<sup>366</sup>

The 2,5-dimercaptobenzene-1,4-dicarboxylate (DSBDC) linker, which is analogous to DOBDC except the two *o*-standing hydroxyl groups to the carboxylic acid group are replaced with two thiol groups, can be reticulated with divalent transition metal cations such as  $\text{Mn}^{2+}$  and  $\text{Fe}^{2+}$  to form MOFs of the composition  $\text{M}_2\text{DSBDC}$ .<sup>367</sup> These MOFs are isomorphous to MOF-74, but contain infinite one-dimensional  $(-\text{M}-\text{S}-)_n$  distorted helical chains. In  $\text{Mn}_2\text{DSBDC}$ , two crystallographically independent  $\text{Mn}^{2+}$  cations exist in the asymmetric unit where one is coordinated by four carboxylate oxygen atoms and two thiol sulfur atoms and the other by two carboxylate oxygen atoms, two thiol sulfur atoms, and two DMF molecules. In contrast, the  $\text{Fe}^{2+}$  cation in  $\text{Fe}_2\text{DSBDC}$  exhibits a similar coordination geometry as the cations in MOF-74 and is coordinated by three carboxylate oxygen atoms, two thiol sulfur atoms, and one DMF molecule (Figure 104).<sup>368</sup> They



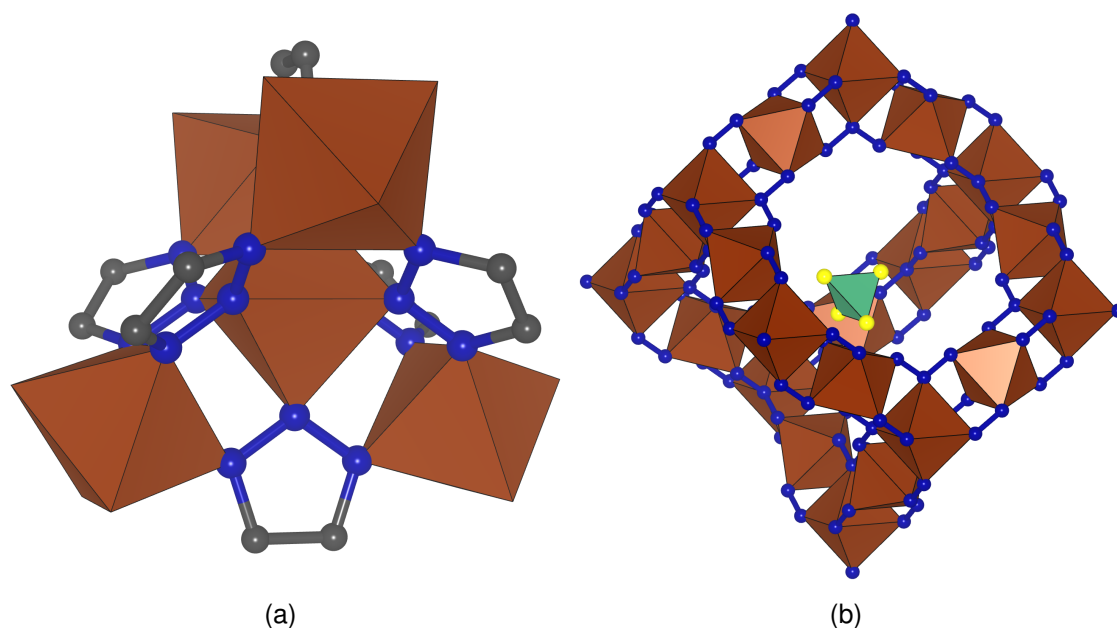
**Figure 104.** Crystal structures of  $M_2(\text{DSBDC})$  (a)  $M = \text{Mn}$ , (b)  $M = \text{Fe}$ .

exhibit permanent porosity with BET surface areas of  $232 \text{ m}^2 \text{ g}^{-1}$  and  $54 \text{ m}^2 \text{ g}^{-1}$  for  $\text{Mn}_2\text{DSBDC}$  and  $\text{Fe}_2\text{DSBDC}$ , respectively.  $\text{Mn}_2\text{DSBDC}$  shows ten-fold increased electrical conductivity of  $2.5 \times 10^{-12} \text{ S cm}^{-1}$  due to the improved charge mobility in the  $(-\text{M}-\text{S}-)_n$  chains, compared to  $3.9 \times 10^{-13} \text{ S cm}^{-1}$  in  $\text{Mn}_2\text{DOBDC}$ . Switching from Mn to Fe, the conductivity increases by over 6 orders of magnitude to a value of  $3.9 \times 10^{-6} \text{ S cm}^{-1}$ . While this was first ascribed to a change in the charge density in  $\text{Fe}_2\text{DSBDC}$  compared to  $\text{Mn}_2\text{DSBDC}$  because of the additional high-spin electron in  $\text{Fe}^{2+}$ , it was discovered later through Mössbauer spectroscopy that Fe atoms occupy mixed-valent 2+ and 3+ states which strongly enhances the charge carrier mobility of the system.<sup>369</sup> Consequently, a series of electrically conductive Fe-MOFs have been reported in which the conductivity mechanism relies on the redox-doping of Fe centers. Examples will be discussed in further detail in the following.

### 8.3 MIXED-VALENCY

Mixed-valency is another strategy to afford electrically conductive MOFs which is largely inspired by electronically completely delocalized, bimetallic organometallic complexes such as the Creutz-Taube ion,  $[\text{Ru}^{\text{II}}\text{Ru}^{\text{III}}(\text{NH}_3)_{10}(\text{pyrazine})]$ .<sup>370</sup> According to Robin and Day, class III compounds such as the Creutz-Taube ion are characterized by a completely delocalized valence due to strong electronic communication between the metal centers, leading to an average valence of  $\text{Ru}^{2.5+}$ .<sup>371</sup> In the context of MOFs, such electronic communication of metal ions through the linkers would positively affect the electronic properties of the material. An illustra-





**Figure 105.** (a) SBU of Fetri<sub>2</sub>. (b) Structure of Fe<sup>II</sup><sub>0.67</sub>Fe<sup>III</sup><sub>0.33</sub>(tri)<sub>2</sub>(BF<sub>4</sub>)<sub>0.33</sub> with **dia** topology.

tive example of the power of an electrically conductive, mixed-valent Fe-MOFs based on 1,2,3-triazolate (tri) is Fetri<sub>2</sub>.<sup>372</sup> Each N atom of tri coordinates to one Fe atom, which in turn is coordinated octahedrally by six tri ligands to form a tetrahedral SBU containing five Fe atoms. Connecting these affords the Fetri<sub>2</sub> with a **dia** topology and a pore diameter of 4.5 Å and a BET surface area of 450 m<sup>2</sup> g<sup>-1</sup> (type I, N<sub>2</sub>, 77 K). In the presence of air, the MOF exhibits an electrical conductivity of 0.77 × 10<sup>-4</sup> S cm<sup>-1</sup> as observed by a four-probe conductivity measurement on a pressed pellet, which can be increased further to 1.0 × 10<sup>-3</sup> S cm<sup>-1</sup> by exposure to I<sub>2</sub> vapor. However, it was later shown that Fetri<sub>2</sub> is highly air sensitive with immediate partial oxidation of Fe(II) to Fe(III) and that this mixed-valency resulted in the large electrical conductivity.<sup>369</sup> Fetri<sub>2</sub> prepared under air-free conditions exhibits only a conductivity of 1 × 10<sup>-10</sup> S cm<sup>-1</sup>. After post-synthetic oxidation with thianthrenium tetrafluoroborate, partially oxidized MOFs of the tunable composition Fe<sup>II</sup><sub>1-x</sub>Fe<sup>III</sup><sub>x</sub>(tri)<sub>2</sub>(BF<sub>4</sub>)<sub>x</sub> ( $x = 0.09, 0.22, 0.33$ ), where the maximum loading corresponds to one BF<sub>4</sub><sup>-</sup> ion per diamondoid pore, can be obtained which exhibit electrical conductivities of 0.03 ± 0.02 S cm<sup>-1</sup>, 0.2 ± 0.1 S cm<sup>-1</sup>, and 0.3 ± 0.1 S cm<sup>-1</sup>, respectively.<sup>373</sup> Mössbauer spectroscopy the absence of Fe(III) centers in pristine Fetri<sub>2</sub> and increasing concentrations with higher dopant contents. In addition, UV–Vis–NIR-spectroscopy shows the emergence of intervalence charge-transfer (IVCT) transition bands stemming from the interaction of Fe(II) and Fe(III) centers, pointing to a strong electronic delocalization within the doped MOF.<sup>373</sup> Another conductive Fe-MOF based on 5,5'-(1,4-phenylene)bis(1*H*-tetrazole) (BDT) is Fe<sub>2</sub>BDT<sub>3</sub> which forms Fe(III) centers after exposure to air and exhibits maxi-

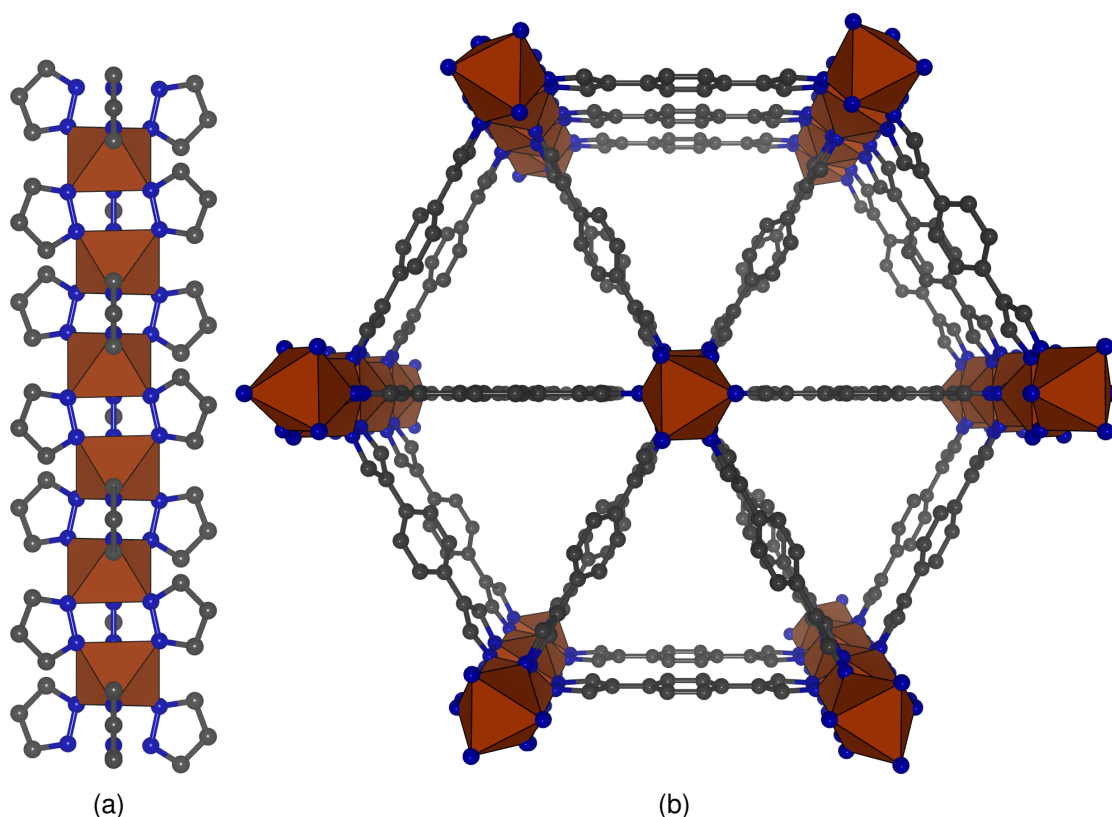


**Figure 106.** (a) One-dimensional chains of  $\text{FeN}_6$  octahedra bridged by pyrazolates as SBU. (b) Crystal structure of  $\text{Fe}_2\text{BDP}_3$ .

imum conductivities of  $1.2 \pm 0.4 \text{ S cm}^{-1}$ .<sup>374</sup> In contrast to the previous examples, reductive doping of a pure Fe(III)-MOF can result in mixed valency and high electrical conductivity, as well. Using 1,4-benzenedipyrazolate (BDP) as linker,  $\text{Fe}_2\text{BDP}_3$  is formed by reticulation with Fe(III) sources.<sup>375</sup> This MOF consists of octahedrally coordinated Fe(III) centers which are bridged by three pyrazolates along the crystallographic  $a$  axis to form one-dimensional chains of  $\text{FeN}_6$  octahedra as the rod-SBU. These are connected via the phenylene bridge of BDP to form a Kagome lattice with trigonally shaped pores aligned in parallel and a BET surface area of  $1230 \text{ m}^2 \text{ g}^{-1}$  (Figure 106). Stoichiometric reduction with potassium naphthalenide affords Fe(II) containing  $\text{K}_x\text{Fe}_2\text{BDP}_3$  ( $0 \leq x \leq 2.0$ ), which was experimentally proven by the emergence of additional doublets in the Mössbauer spectrum caused by Fe(II).<sup>376</sup> An increase of the electrical conductivity of five orders of magnitude was reported after the reduction, from  $3.5 \times 10^{-7} \text{ S cm}^{-1}$  for  $\text{Fe}_2\text{BDP}_3$  to  $7 \times 10^{-2} \text{ S cm}^{-1}$  for  $\text{K}_x\text{Fe}_2\text{BDP}_3$ , both for two-contact pellet measurement. Note that a four-contact pellet measurement of  $\text{Fe}_2\text{BDP}_3$  yielded an electrical conductivity of  $9.6 \times 10^{-3} \text{ S cm}^{-1}$ , illustrating the huge disadvantageous influence of grain boundary resistances on conductivity measurements of pressed pellets, as well as the large anisotropy of the conductivity pathway in this material (*cf.* section 9.4).

## 8.4 THROUGH-SPACE APPROACH

Secondly, the through-space approach comprises all efforts to increase the electrical conductivity of a MOF by enabling  $\pi$ - $\pi$ -interactions between the aromatic systems of the linkers which create low-energy charge transport pathways. For this purpose, linkers with extended aromatic or redox-active cores are used to increase the electronic communication between separate layers.<sup>44,377–379</sup> By reticulation of the TTFTB linker, which contains the redox-active and electron-donating TTF core, with divalent transition metal cations, isostructural MOFs of the composition  $M_2$ TTFTB ( $M^{2+} = \text{Mn, Co, Zn, Cd}$ ) can be obtained as hexagonal black needles.<sup>13,14</sup>  $M_2$ TTFTB contains one-dimensional helical columns of corner-sharing  $\text{MO}_6$ -octahedra as rod-SBUs. Helical  $\pi$ -stacks of the TTFTB-linkers, in which the TTF moieties are rotated to each other by an angle of  $60^\circ$ , connect the SBUs and form one-dimensional, cylindrical parallel pores with a van der Waals diameter of  $\approx 5$  nm. Here, the interplanar distances of the  $\pi$ -stacks ranging from 3.65–3.77 Å for  $\text{Cd}_2$ TTFTB and  $\text{Co}_2$ TTFTB, respectively, are typical for  $\pi$ - $\pi$ -interactions.<sup>380</sup> Moreover, the  $M_2$ TTFTB series exhibits permanent microporosity with type I sorption behavior and BET surface areas ranging from 625–730  $\text{m}^2 \text{g}^{-1}$  ( $\text{N}_2$ , 77 K). Electrical conductivity measurements reveal increasing values from  $4.0 \times 10^{-6}$ – $2.9 \times 10^{-4} \text{ S cm}^{-1}$  in  $\text{Zn}_2$ TTFTB and  $\text{Cd}_2$ TTFTB, respectively, which is attributed to the increase in ionic radii going from Zn to Cd, thereby decreasing the  $\pi$ - $\pi$ -interstacking and S–S distances between the helical columns of TTF and improving the orbital overlap. Charge carriers are generated by the *in situ* oxidation of TTF during the MOF synthesis as evidenced by electron paramagnetic resonance spectroscopy (EPR) which gives a signal at  $g = 2.006$  indicative for organic radicals.

In combination with lanthanide ions, different series of TTF-based MOFs can be obtained.<sup>381–384</sup> For example, the reaction of TTFTB with  $\text{Ln}^{\text{III}}(\text{NO}_3)_3$  ( $\text{Ln}(\text{III}) = \text{Tm, Yb, Lu}$ ) in a DMF/EtOH/water mixture affords the isostructural  $\text{Ln}_6$ TTFTB<sub>5</sub>.<sup>381</sup> The two SBUs contain each two Ln ions which are coordinated by eight O donor atoms, where six come from the carboxylate functional groups and the remaining ones from coordinating water of DMF molecules. Moreover, the unit cell contains of three crystallographically independent TTFTB linkers, two of which coordinate to four SBUs via their four carboxylate groups, whereas the third is only coordinated to two SBUs in a diagonal fashion. This leads to an arrangement of TTF cores where two units form a dimer which are separated by a distance of  $\approx 3.8$  Å. In between two dimers, the TTF core stemming from the two-coordinating TTFTB linker of the crystal structure is sandwiched perpendicular to the  $\pi$ -stacking direction of the dimers, with S–S distances between the central TTF unit and the dimers

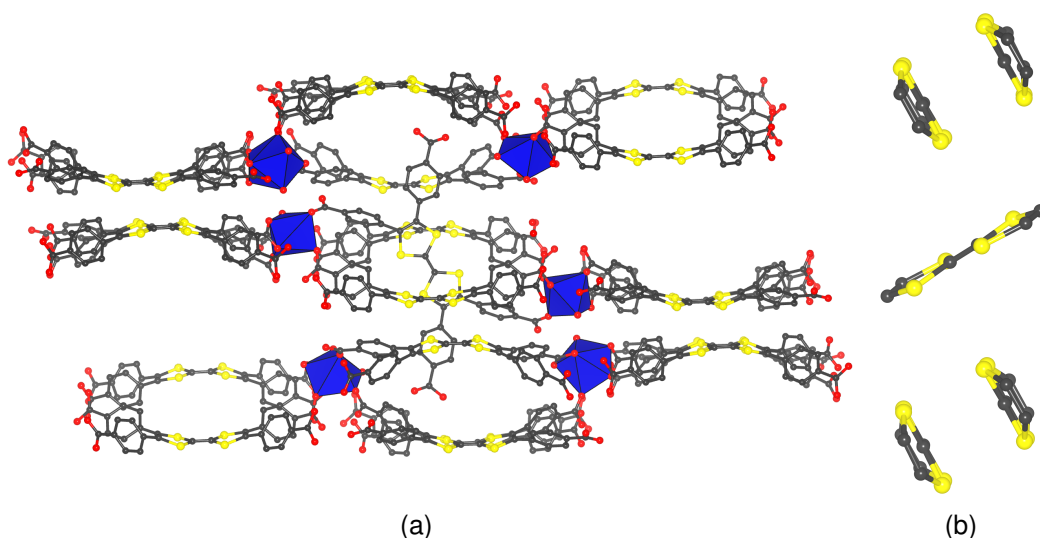


**Figure 107.** (a) Crystal structure and (b)  $\pi$ -stacking of TTF units in  $\text{Ln}_6\text{TTFTB}_5$  ( $\text{Ln} = \text{Tm}, \text{Yb}, \text{Lu}$ ).

ranging from 4.04–4.41 Å (Figure 107). Two-contact probe pressed pellet electrical conductivities measurements of  $\text{Ln}_6\text{TTFTB}_5$  revealed values of  $9 \pm 7 \times 10^{-7}$  and  $3 \pm 2 \times 10^{-7} \text{ S cm}^{-1}$  for  $\text{Ln} = \text{Yb}$  and  $\text{Lu}$ , respectively.<sup>381</sup>

Three MOFs of different topologies can be obtained with  $\text{La}(\text{III})$  ions and TTFTB as linker by slight variation of the reaction conditions.<sup>382</sup> Most notably, the TTF-TTF interplanar distances vary between the three phases, with the shortest S...S distances of 3.60 Å in  $\text{La}_4\text{HTTFTB}_4$ , to  $4.083 \pm 0.003$  Å between dimers in  $\text{LaHTTFTB}$ , increasing further to  $7.072 \pm 0.007$  Å between trimers in  $\text{La}_4\text{TTFTB}_3$  (Figure 108). Larger stacking distances between TTF moieties lead to smaller electronic communication and delocalization throughout a MOF crystal, which correlates well with the decreasing observed electrical conductivities, from  $2.5 \pm 0.7 \times 10^{-6} \text{ S cm}^{-1}$  in  $\text{La}_4\text{HTTFTB}_4$  over  $9 \pm 4 \times 10^{-7} \text{ S cm}^{-1}$  in  $\text{LaHTTFTB}$ , to  $1.0 \pm 0.5 \times 10^{-9} \text{ S cm}^{-1}$  in  $\text{La}_4\text{TTFTB}_3$ .<sup>382</sup>

Other linker motifs are known to form  $\pi$ -stacked conductive MOFs as well, for example  $N,N'$ -di(4-pyridyl)-1,4,5,8-naphthalenetetracarboxdiimide (NDI-py).<sup>385</sup> When a constant cathodic current is applied to a solution of NDI-py and  $\text{Cd}(\text{NO}_3)_2$  mixed in  $N,N$ -dimethyl acetamide (DMA), the redox-active and electron-accepting NDI-py is reduced *in situ* to radical-anions which tend to form  $\pi$ -stacks.<sup>386</sup> By coordination of the pyridinyl groups to  $\text{Cd}(\text{II})$  ions, one-dimensional chains of  $\text{Cd}$ -NDI-py which are connected to a three-dimensional arrangement via  $\pi$ -stacking along the crystallographic  $c$  axis and the  $60^\circ$  rotation of the chains with respect to each other, thereby forming triangular shaped pores (Figure 109). Interestingly, while this MOF exhibits an electrical conductivity of only  $7.6 \times 10^{-6} \text{ S cm}^{-1}$  at best, a pressed pellet of activated  $\text{Cd}$ -NDI-py shows values of up to  $3.7 \times 10^{-2} \text{ S cm}^{-1}$ , which was ascribed to a rearrangement to form two-dimensional  $\pi$ -stacking arrangements which give

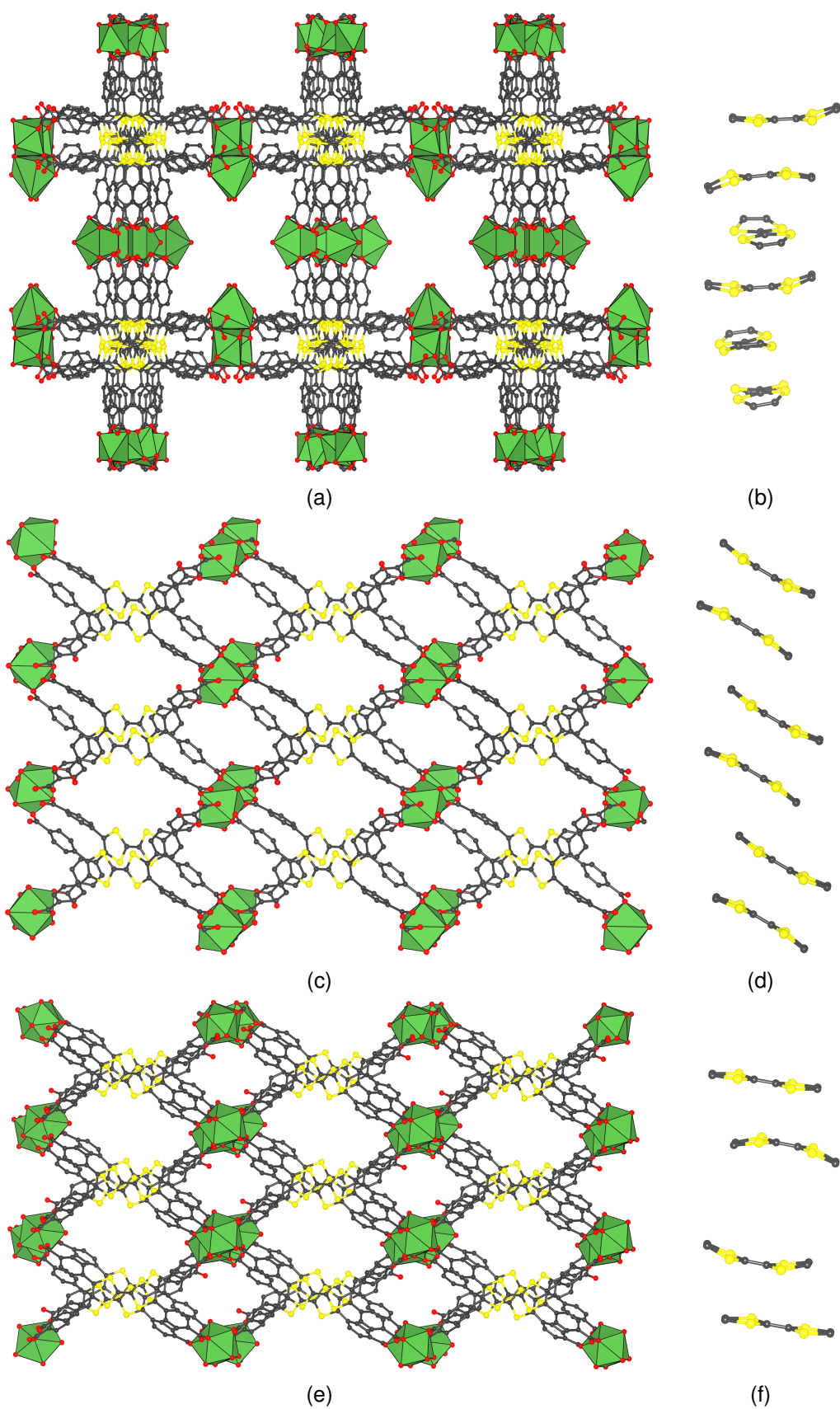


**Figure 108.** Crystal structures of (a)  $\text{La}_4\text{HTTFTB}_4$ , (c)  $\text{LaHTTFTB}$ , and (e)  $\text{La}_4\text{TTFTB}_3$ , and their respective TTF-TTF  $\pi$ -stacking motifs in (b), (d), and (f).



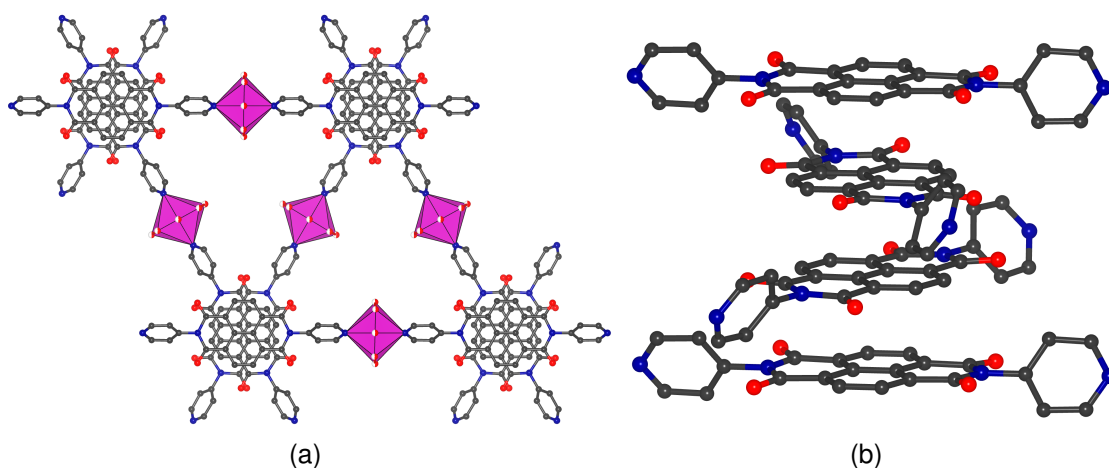


**Figure 109.** (a) Crystal structure and (b)  $\pi$ -stacking arrangement in Cd-NDI-py.

rise to improved electron mobilities and electrical conductivities across all crystallographic directions.<sup>386</sup> It is worth mentioning that such growth of electrically conductive structures via electrocrystallization is an often employed technique in the preparation of "organic metals" based on tetrachalcogenafulvalenes and other redox-active organic molecules with high propensity to form charged radical species, since mostly only conductive structures will grow on the electrode surfaces.<sup>387</sup>

## 8.5 EXTENDED CONJUGATION

Two-dimensional  $\pi$ -*d*-extended MOFs are a special case of electrically conductive frameworks that combine several of the above-mentioned strategies to achieve unparalleled electrical conductivities. They consist of multitopic redox-active ligands based on polyaromatic catecholates, diimines, or dithiolenes, which are linked to two-dimensional MOF sheets via the square-planar coordination to a single metal node.<sup>388–390</sup> The high oxidation potential of these ligand systems largely influences the electrical conductivity of resulting MOFs due to the formation of ligand-based radicals as charge carriers. Within the plane, they are characterized by significant delocalization of electron density over the linker  $\pi$ -systems and metal *d*-orbitals due to the large covalent nature of the coordination bond and beneficial orbital energy matching. Perpendicular to this plane, honeycomb-like  $\pi$ -stacks of polyaromatic scaffolds contribute to a large through-space delocalization of electron density, thereby increasing further the electronic mobility and conductivity in these systems.

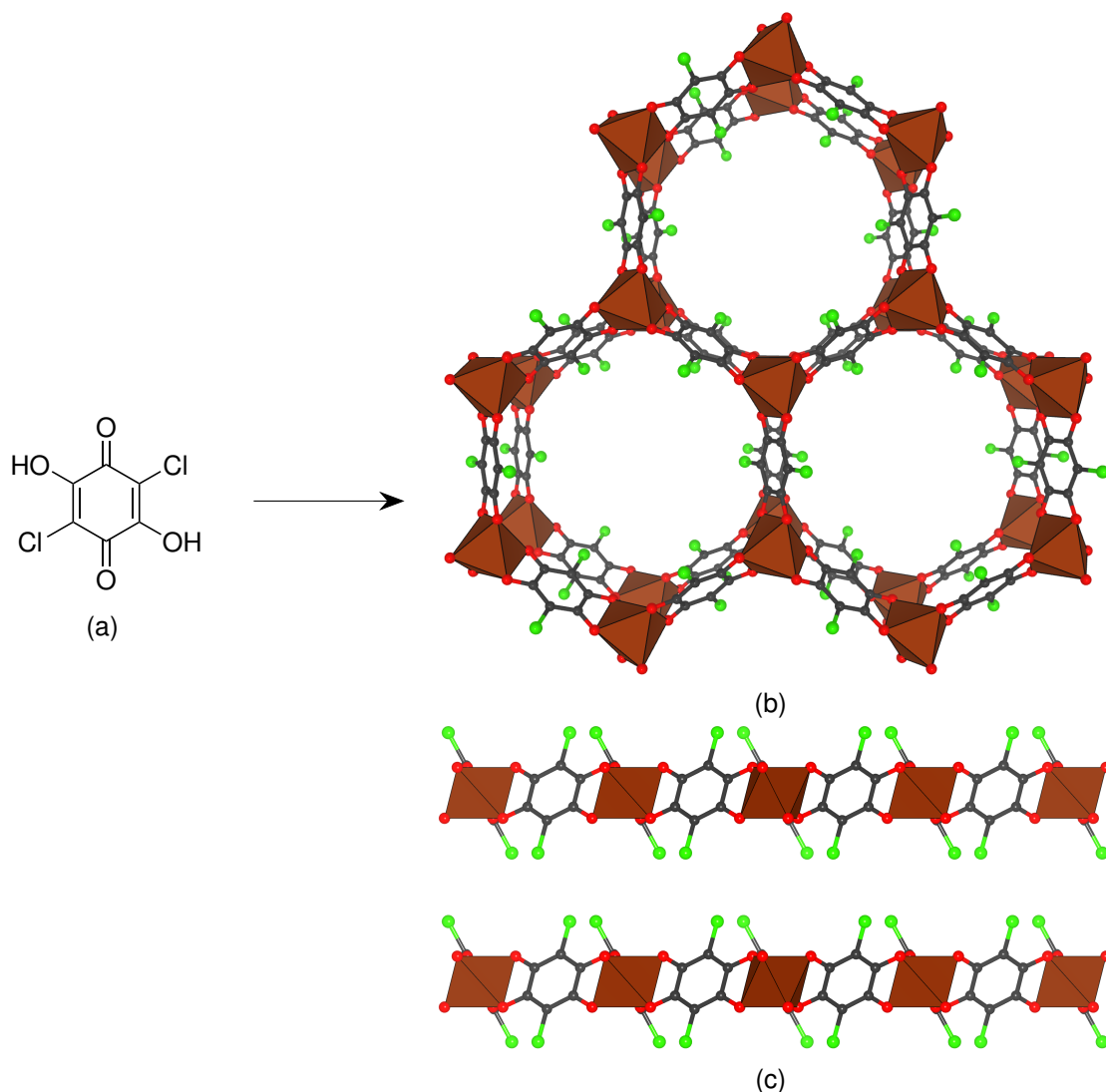
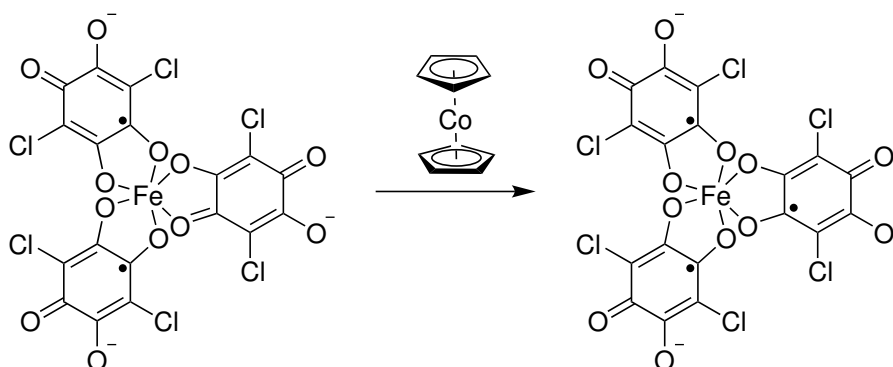


**Figure 110.** (a) Molecular structure of chloroanilic acid,  $\text{H}_2\text{Cl}_2\text{dhbq}$ . (b) Crystal structure of the MOF family  $[\text{M}_2\text{Cl}_2\text{dhbq}_3]^{2-}$  with view of the  $ab$  plane. (c) Stacking of two-dimensional sheets in  $[\text{M}_2\text{Cl}_2\text{dhbq}_3]^{2-}$  along the crystallographic  $c$  axis.

### 8.5.1 Dihydroxybenzoquinone Linkers

Reticulation of chloroanilate ( $\text{Cl}_2\text{dhbq}$ ) with Fe, Ti, and V gives a series of isostructural MOFs of composition  $[\text{M}_2(\text{Cl}_2\text{dhbq})_3]^{2-}$  (Figure 110).<sup>391–394</sup> Here, the metal ion is coordinated by six O atoms coming from three  $\text{Cl}_2\text{dhbq}$  linkers to form distorted isolated  $\text{MO}_6$  octahedra. These are connected by the ditopic linkers to form a two-dimensional sheet with hexagonal pores. Subsequent layers are stacked along the crystallographic  $c$  axis in an eclipsed fashion. For example, heating of a DMF solution containing  $\text{Fe}^{\text{II}}(\text{BF}_4)_2$  and  $\text{H}_2\text{Cl}_2\text{dhbq}$  gives black, hexagonal crystals of  $[\text{Me}_2\text{NH}_2][\text{Fe}_2(\text{Cl}_2\text{dhbq})_3]$  which can be activated without loss architectural collapse of the MOF structure and exhibits a BET surface area of  $1175 \pm 29 \text{ m}^2 \text{ g}^{-1}$ .<sup>391</sup> Here, Fe cations are only present in the +III oxidation state,

one of the  $\text{Cl}_2\text{dhbq}$  ligands is in its two-fold deprotonated, dianionic state, while the other two are reduced to the trianionic, radical-form. Upon subsequent post-synthetic reduction with dicyclopentadiene (Cp) cobalt(II) or cobaltocene,  $\text{Cp}_2\text{Co}$ ,  $(\text{Cp}_2\text{Co})_{1.43}(\text{Me}_2\text{NH}_2)_{1.57}(\text{Fe}_2(\text{Cl}_2\text{dhbq})_3)$  is obtained in a *scsc* fashion where all ligands are now reduced to the radical trianionic form (Scheme 34). Ligand-centered reduction was proven by the analysis of C–C and C–O bond distances obtained via single-crystal x-ray diffraction (SCXRD), as well as Raman spectroscopic analysis of the molecular vibrations.<sup>391</sup> Moreover, Mössbauer spectroscopy the absence of Fe(II) species in the material.



**Scheme 34.** Reduction reaction of mixed-valent  $[\text{Me}_2\text{NH}_2][\text{Fe}_2(\text{Cl}_2\text{dhbq})_3]$  to mono-valent  $(\text{Cp}_2\text{Co})_{1.43}(\text{Me}_2\text{NH}_2)_{1.57}(\text{Fe}_2(\text{Cl}_2\text{dhbq})_3)$  with cobaltocene.

Interestingly, two-contact probe electrical conductivity measurements of pressed pellets the as-synthesized, mixed-valent  $[\text{Fe}_2(\text{Cl}_2\text{dhbq})_3^{3-}(\text{Cl}_2\text{dhbq})_2^{2-}]^{2-}$  and the reduced, mono-valent  $[\text{Fe}_2(\text{Cl}_2\text{dhbq})_3^{3-}]^{3-}$  show that the electrical conductivity is reduced from  $1.4 \pm 0.7 \times 10^{-2} - 5.1 \pm 0.3 \times 10^{-4} \text{ S cm}^{-1}$ , respectively, possibly due to the removed beneficial mixed-valency. In comparison, the isostructural Zn(II)-based  $[\text{Me}_2\text{NH}_2][\text{Zn}_2\text{Cl}_2\text{dhbq}_3]$ , which contains ligands only in their dianionic, non-reduced form exhibits an electrical conductivity of  $1.5 \pm 0.3 \times 10^{-9} \text{ S cm}^{-1}$ , thereby emphasizing the importance of radical-containing systems, mixed-valency, and open-shell metal cations for improving the electron mobility and conductivity of MOFs.<sup>391</sup>

If a preformed, molecular  $[\text{Fe}^{\text{III}}(\text{Cl}_2\text{dhbq})_3]^{3-}$  complex containing only the non-reduced form of  $\text{Cl}_2\text{dhbq}$  is combined with a solution of  $\text{Fe}^{\text{II}}(\text{BF}_4)_2$  and phenazine (phz), MOFs of composition  $[(\text{H}_3\text{O})(\text{H}_2\text{O})(\text{phz})_3][\text{Fe}^{\text{II}}\text{Fe}^{\text{III}}(\text{Cl}_2\text{dhbq})_3]$ , identical connectivity and topology are obtained which contain metal-based mixed-valency in the form of Fe(II)/Fe(III) instead of  $\text{Cl}_2\text{dhbq}$ -based mixed-valency.<sup>392</sup> The Br-analog was obtained by employing bromoanilate ( $\text{Br}_2\text{dhbq}$ ) in the synthesis. Electrical conductivities of  $0.03 \text{ S cm}^{-1}$  and  $0.003 \text{ S cm}^{-1}$  were measured for single crystals of  $\text{Cl}_2\text{dhbq}$ - and  $\text{Br}_2\text{dhbq}$ -based MOF, respectively, when contacted parallel to the crystallographic *ab* plane (intra-layer conductivity). On the other hand, electrical



conductivities of only  $1 \times 10^{-4} \text{ S cm}^{-1}$  and  $6 \times 10^{-6} \text{ S cm}^{-1}$  were observed when single crystals of the respective MOFs were contacted along the crystallographic *c* axis (inter-layer conductivity), illustrating the large electrical anisotropy in these two materials.<sup>392</sup>

By heating divalent metal chlorides,  $\text{MCl}_2$  ( $\text{M} = \text{Ti}, \text{V}$ ) and  $\text{Cl}_2\text{dhbq}$  in DMF, black crystals of compositions  $(\text{H}_2\text{NMe}_2)_2\text{Ti}_2(\text{Cl}_2\text{dhbq})_3$  and  $(\text{H}_2\text{NMe}_2)_2\text{V}_2(\text{Cl}_2\text{dhbq})_3$  are obtained, respectively, which exhibit the same two-dimensional structure as shown in Figure 110.<sup>393</sup> FTIR of the Ti-MOF shows an absorption at  $1404 \text{ cm}^{-1}$  which is best described by a mixture of single- and double-reduced  $\text{Cl}_2\text{dhbq}$ ; thus, the composition of the Ti-MOF is best formulated as  $(\text{H}_2\text{NMe}_2)_2\text{Ti}^{\text{IV}}_2(\text{Cl}_2\text{dhbq})^{3-}_2(\text{Cl}_2\text{dhbq})^{4-}$  arising from a full metal-to-ligand charge-transfer (MLCT) of  $\text{Ti}^{2+}$  to  $\text{Cl}_2\text{dhbq}$ . Looking at the FTIR spectrum of the V-MOF, however, the assignment of ligand oxidation states is not possible due to a strong overlap with a broad absorbance which falls in the range of the interesting vibrational absorptions. Moreover, diffuse reflectance UV-Vis-NIR spectroscopy shows a broad absorbance over the mid-IR and near-IR region, which points at a fully delocalized electronic structure according to a Robin-Day class III compound, with intermediate oxidation states between the possible extremes  $[(\text{V}^{\text{III}})_2(\text{Cl}_2\text{dhbq}^{2-})(\text{Cl}_2\text{dhbq}^{3-})_2]^{2-}$  and  $[(\text{V}^{\text{III}})(\text{V}^{\text{IV}})(\text{Cl}_2\text{dhbq}^{3-})_3]^{2-}$ .<sup>393</sup> Consequently, two-contact probe electrical conductivity measurements with pressed pellets revealed much larger conductivities of  $0.45 \pm 0.03 \text{ S cm}^{-1}$  for the electronically more delocalized V-MOF compared to  $2.7 \pm 0.2 \times 10^{-3} \text{ S cm}^{-1}$ .<sup>393</sup> None of these MOFs are architecturally stable towards activation or exhibit permanent porosity.

Three-dimensional MOFs based on 2,5-dihydroxybenzoquinone (dhbq) can be obtained by the reaction of 2,5-diaminobenzoquinone and  $\text{FeSO}_4$  in the presence of water and tetrabutylammonium bromide to afford black cubic crystals of composition  $(\text{NBu}_4)_2[\text{Fe}^{\text{III}}_2(\text{dhbq})_3]$  (Figure 111).<sup>395</sup> This MOF also consists of distorted octahedrally coordinated  $\text{FeO}_6$  single metal nodes similarly to the MOFs based on  $\text{Cl}_2\text{dhbq}$ ; however, the dhbq linkers are not arranged in one plane but orthogonal to each other, thereby enabling translation of the connectivity along the third dimension. Furthermore, the structure is two-fold interpenetrated and remaining voids are filled with charge-balancing tetrabutylammonium cations, yielding a nonporous structure as evidenced by  $\text{N}_2$  sorption experiments. Analysis of the short Fe–O bonding distances obtained via SCXRD and Mössbauer spectroscopy of  $(\text{NBu}_4)_2[\text{Fe}^{\text{III}}_2(\text{dhbq})_3]$  revealed the presence of only Fe(III) species. Likewise, the absorption from  $1510\text{--}1450 \text{ cm}^{-1}$  and the presence of an IVCT at  $5200 \text{ cm}^{-1}$  in the UV-Vis-NIR spectrum can be assigned to the presence of mixed valent  $\text{dhbq}^{2-}$  and  $\text{dhbq}^{3-}$ , with another signal at  $4500 \text{ cm}^{-1}$  characteristic for Robin-Day class II/III compounds, pointing at a pronounced electronic delocalization within

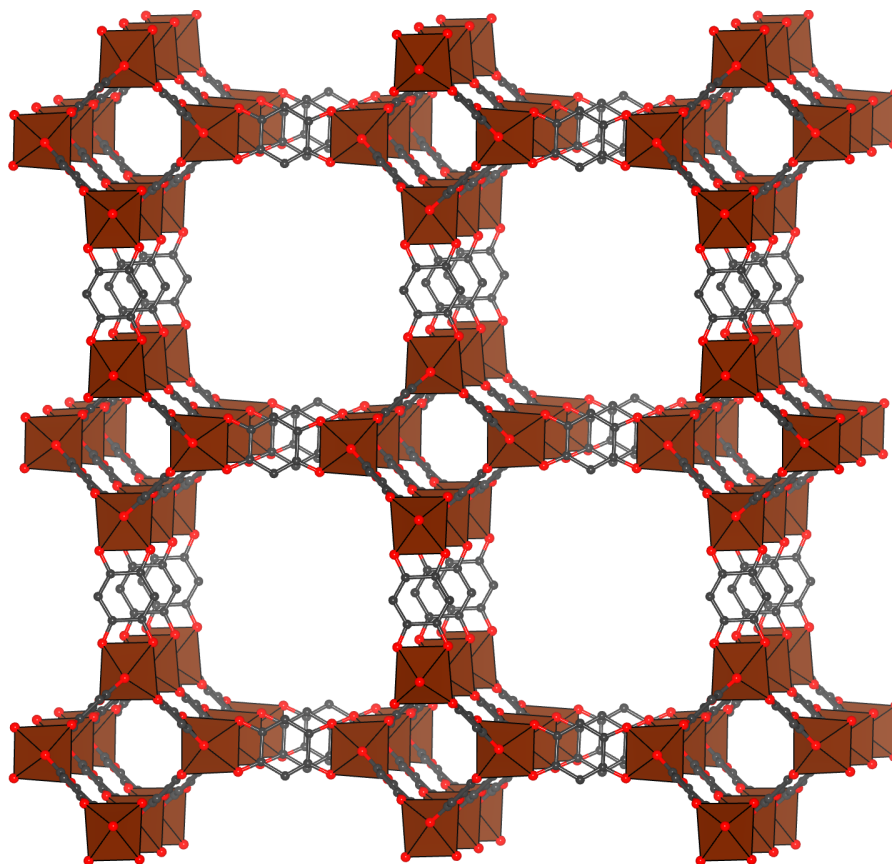


**Figure 111.** Crystal structure of  $(\text{NBu}_4)_2[\text{Fe}^{\text{III}}_2(\text{dhbq})_3]$ . For clarity, only one of the two entangled frameworks is shown. H atoms and tetrabutylammonium cations are omitted.

the MOF.<sup>395</sup> As a result, two-contact probe pressed pellet electrical conductivity measurements of  $(\text{NBu}_4)_2[\text{Fe}^{\text{III}}_2(\text{dhbq})_3]$  revealed a value of  $0.16 \pm 0.01 \text{ S cm}^{-1}$  and a temperature-activated electrical conductivity consistent with a hopping mechanism.<sup>395</sup>

### 8.5.2 Aromatic Catecholates

Triphenylene-based linkers are among the most studied systems in the formation of electrically conductive, two-dimensional MOFs.<sup>396–401</sup> One of the earliest works reported the synthesis of  $\text{Co}_3(2,3,6,7,10,11\text{-hexahydroxytriphenylene (HHTP)})_2$ . This MOF consists of two different layers. In one layer, an extended two-dimensional sheet consists of octahedrally coordinated  $\text{Co}(\text{II})\text{O}_6$  units connected by the triphenylene core to form a hexagonal structure, of which four of the O donor atoms stem from the two equatorial HHTP linkers and the remaining two come from axially coordinating water. In the other layer, isolated HHTP coordinates to three  $\text{Co}(\text{II})$  ions, and the remaining coordination sites are saturated by water (Figure 112). HHTP is in its single-reduced, radical state as evidenced

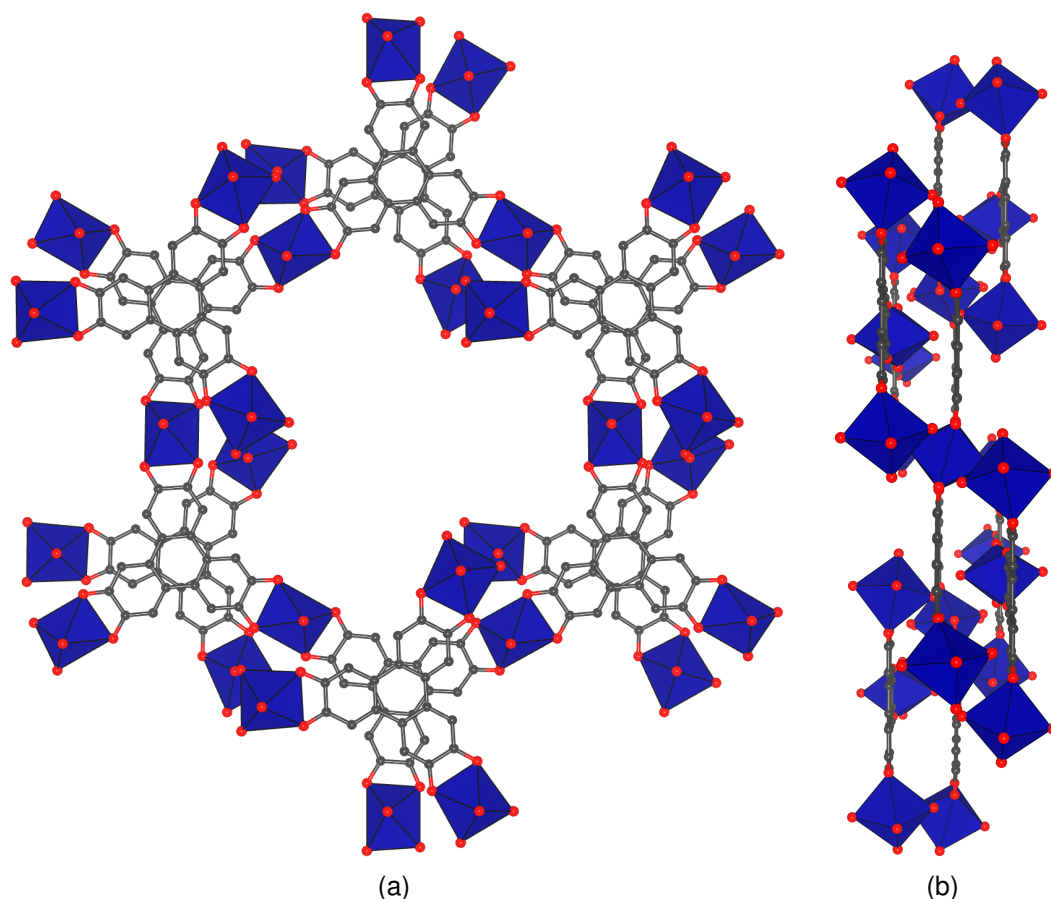


**Figure 112.** (a) Crystal structure of  $\text{Co}_3(\text{HHTP})_2$  viewed along the crystallographic  $c$  axis. (b) Stacking of extended and isolated layers of HHTP perpendicular to the  $c$  axis.

by EPR.<sup>398</sup> Electrical conductivities of  $1.8 \times 10^{-1} \text{ S cm}^{-1}$  and  $2.1 \times 10^{-1} \text{ S cm}^{-1}$  could be measured for two single crystals of  $\text{Co}_3(\text{HHTP})_2$  using a four-contact probe device. Ar sorption experiments performed at 87 K gave a BET surface area of  $490 \text{ m}^2 \text{ g}^{-1}$ .<sup>398</sup>

Isorecticular MOFs based on HHTP are obtained with Cu(II) and Ni(II) ions, although they exhibit different crystal structures as indicated via PXRD and high-resolution transmission electron microscopy (HR-TEM).<sup>401–403</sup> While  $\text{Ni}_3(\text{HHTP})_2$  is isostructural to  $\text{Co}_3(\text{HHTP})_2$ , the crystal structure of  $\text{Cu}_3(\text{HHTP})_2$  contains slipped parallel stacks of two-dimensional sheets of square-planar coordinated Cu(II) ions bridged by HHTP units.<sup>401</sup> Electrical conductivity measurements of  $\text{Cu}_3(\text{HHTP})_2$  parallel and perpendicular to the sheets revealed values of  $1.5 \text{ S cm}^{-1}$  and  $0.5 \text{ S cm}^{-1}$ , respectively, showing that the electronic structure is largely delocalized both within the layers as well as along the  $\pi$ -stacking direction.<sup>9,401</sup> For  $\text{Ni}_3(\text{HHTP})_2$ , four-point probe measurements showed an electrical conductivity of  $0.010 \pm 0.003 \text{ S cm}^{-1}$ .<sup>9,402</sup>

Moving to trivalent lanthanide ions, similar two-dimensional, hexagonal MOFs can be obtained by reticulation of HHTP with  $\text{Ln}^{3+} = \text{La}, \text{Nd}, \text{Ho}, \text{Yb}$ .<sup>404</sup> All MOFs

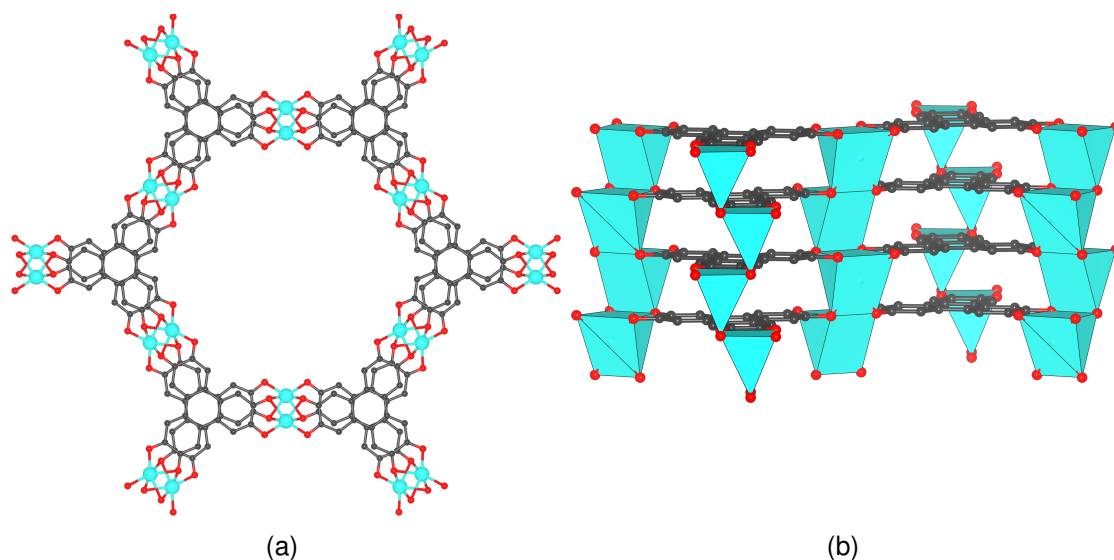


**Figure 113.** (a) Crystal structure of  $\text{Ln}_{1+x}\text{HHTP}$ . View of the hexagonal sheets in the  $ab$  plane. (b)  $\pi$ -stacking and edge-sharing  $\text{LnO}_6$  octahedra perpendicular to the sheets.

of composition  $\text{Ln}_{1+x}\text{HHTP}$  are isostructural, crystallizing in the similar hexagonal topology as for other two-dimensional MOFs and exhibit permanent porosity with BET surface areas of 325, 513, 208 and  $452 \text{ m}^2 \text{ g}^{-1}$  for La-, Nd-, Ho-, and Yb-MOF, respectively (Figure 113).<sup>404</sup> Remarkably, the Ln ions are not located within the organic sheet as for transition metal-based two-dimensional frameworks but in between, pinching the  $\pi$ -stacking distances between the HHTP sheets to 3.07, 3.06, 3.01 and 3.00 Å for La-, Nd-, Ho-, and Yb-MOF, respectively, which are shorter than in most extended two-dimensional MOFs.<sup>404</sup> As a consequence, the electronic structure of  $\text{Ln}_{1+x}\text{HHTP}$  is dominated by the metallic character of the Brillouin zone along the  $\pi$ -stacking direction, with little in-plane electronic delocalization.<sup>404</sup> Two-contact probe electrical conductivity measurements on pressed pellets of  $\text{Ln}_{1+x}\text{HHTP}$  revealed increasing conductivities with decreasing ionic radius of the employed lanthanide, ranging from  $0.9 \times 10^{-4}$ – $0.05 \text{ S cm}^{-1}$  for La- and Ho-MOF, respectively.<sup>404</sup>

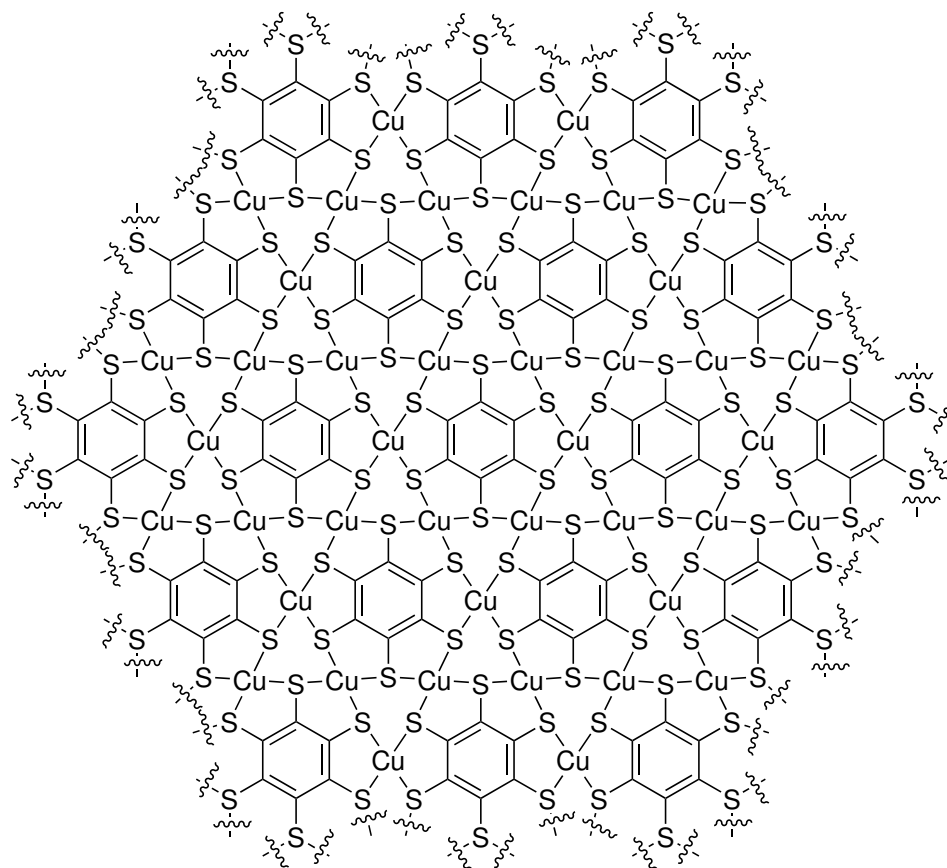
### 8.5.3 Aromatic Dithiolenes

Metal dithiolene complexes are well-known for forming electrically conductive discrete compounds due to their redox-activity and the improved electronic overlap between metal ions and the soft S donor ligands.<sup>405–407</sup> Likewise, extended, two-dimensional MOFs based on multitopic dithiolene linkers exhibit the highest known electrical conductivities in coordination networks as of today. For example, reticulation of Cu(II) with benzene-1,2,3,4,5,6-hexathiol (BHT) via an interfacial synthesis strategy gives a densely packed coordination layer as illustrated in

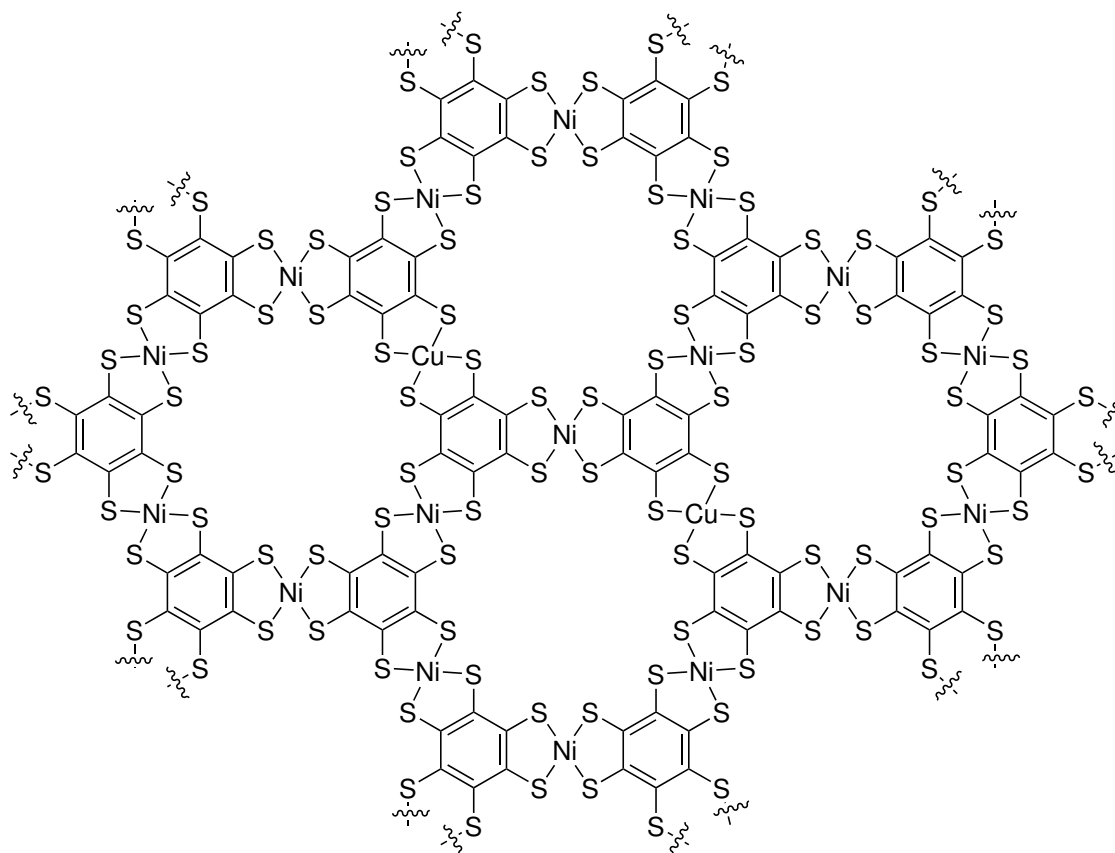
Scheme 35.<sup>408</sup> Here, Cu(II) are coordinated by four S ligands coming from two BHT linkers to complete the square-planar coordination geometry. The linker in turn coordinates to six Cu(II) in the same sheet, resulting in the overall composition  $\text{Cu}_3\text{BHT}$ . Electrical conductivity measurements were performed using the four-point probe method and values of  $1580 \text{ S cm}^{-1}$ .<sup>408</sup> On the other hand, the combination of Ni(II) and BHT yields the typical two-dimensional MOF structure with hexagonal pore windows along the crystallographic *c* axis (Scheme 35).<sup>409,410</sup> The electrical conductivity was found to be  $1.6 \times 10^2 \text{ S cm}^{-1}$  by performing conductivity measurements using the van-der-Pauw method. Density functional theory (DFT) calculations of the band electronic structure revealed a strong delocalization of electron density both within the plane and in the interlayer stacking direction, causing the material to be highly conductive.<sup>410</sup> Expanding the ligand leads to triphenylene-2,3,6,7,10,11-hexathiol (THT), which can be reticulated with Fe(II) ions via an interfacial synthesis to yield  $\text{Fe}^{\text{III}}_3\text{THT}_2(\text{NH}_4)_3$  (Scheme 36).<sup>399</sup> Similarly to previous examples, reducing Fe(II) ions undergo MLCT to redox-active THT upon coordination and hexagonal sheets with delocalized electronic structure are formed. Time-resolved terahertz spectroscopy (TRTS), which is a contact-free technique to probe the electrical conductivity, mobility, and mechanism of charge-transport in a material, revealed an electrical conductivity of  $0.034 \text{ S cm}^{-1}$  and an electron mobility of  $220 \text{ cm}^2 \text{ V}^{-1} \text{ s}^{-1}$ , which is the highest reported electron mobility for a MOF.<sup>399</sup>

#### 8.5.4 Aromatic Diimines

Analogs to the previously mentioned examples of two-dimensional MOFs are also known for linkers containing redox-active diimine units.<sup>400,401,411–413</sup> For example, 1,2,3,4,5,6-hexaaminobenzene (HAB) combines with Cu(II) and Ni(II) salts to give electrically conductive MOFs of compositions  $\text{M}_3\text{HAB}_2$  ( $\text{M}^{2+} = \text{Cu}, \text{Ni}$ ) under basic conditions in the presence of atmospheric oxygen. They contain eclipsed honeycomb sheets of square-planar coordinated metal ion by two HAB linkers, with pore sizes of  $\approx 0.8 \text{ nm}$  and BET surface areas ranging from  $180\text{--}350 \text{ m}^2 \text{ g}^{-1}$ .<sup>411</sup> The electrical conductivity of the Ni-MOF is  $0.70 \pm 0.15 \text{ S cm}^{-1}$  and higher than that of the Cu-MOF with  $0.11 \pm 0.03 \text{ S cm}^{-1}$ .<sup>411</sup> Conductive frameworks based on 2,3,6,7,10,11-hexaiminotriphenylene (HITP), such as  $\text{Cu}_3\text{HITP}_2$ <sup>413</sup> and  $\text{Ni}_3\text{HITP}_2$ <sup>400</sup>, are isorecticular expanded versions with a slipped parallel stacking structure (Figure 114) and two-contact probe pressed pellet electrical conductivities of  $0.2 \text{ S cm}^{-1}$  and  $2 \text{ S cm}^{-1}$ , respectively. Recently, a single-crystal four-point probe conductivity measurement of  $\text{Ni}_3\text{HITP}_2$  revealed a value of  $150 \text{ S cm}^{-1}$ .<sup>401</sup>

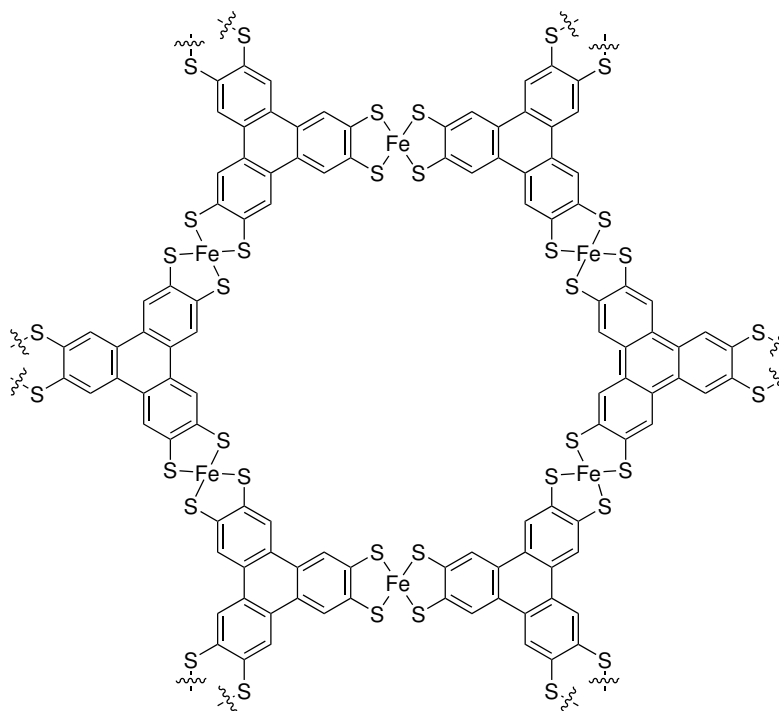


(a)



(b)

**Scheme 35.** Structure of the coordination polymer (a)  $\text{Cu}_3\text{BHT}$ , (b)  $\text{Ni}_3\text{BHT}_2$ .



**Scheme 36.** Structure of  $\text{Fe}_3\text{THT}_2(\text{NH}_4)_3$ .

### 8.5.5 Further Extended Metal-Organic Frameworks

Combination of redox-active pyrazine and highly reducing  $\text{Cr}^{\text{II}}\text{Cl}_2$  affords polycrystalline  $\text{Cr}^{\text{III}}\text{Cl}_2(\text{pyrazine})_2$ , a two-dimensional structure with staggered layers orthogonal to the crystallographic  $c$  axis in which  $\text{Cr}(\text{III})$  ions are coordinated by four pyrazine ligands via N coordination in a square-planar fashion in the equatorial  $ab$  plane, with two axial Cl ligands completing the octahedral coordination geometry (Figure 115). X-ray absorption spectroscopy (XAS) proved the oxidation of  $\text{Cr}(\text{II})$  to  $\text{Cr}(\text{III})$  in the MOF, whereas IVCT was observed in the UV-Vis-NIR spectra, showcasing another example of MOFs with delocalized structures. Here, an electrical conductivity of  $0.032 \text{ S cm}^{-1}$  was detected by two-contact probe conductivity measurements.<sup>414</sup>

## 8.6 GUEST-INDUCED ELECTRICAL CONDUCTIVITY

While the previous examples have proven to be effective strategies for realizing high electrical conductivity and porosity in MOFs, they demand an often tedious

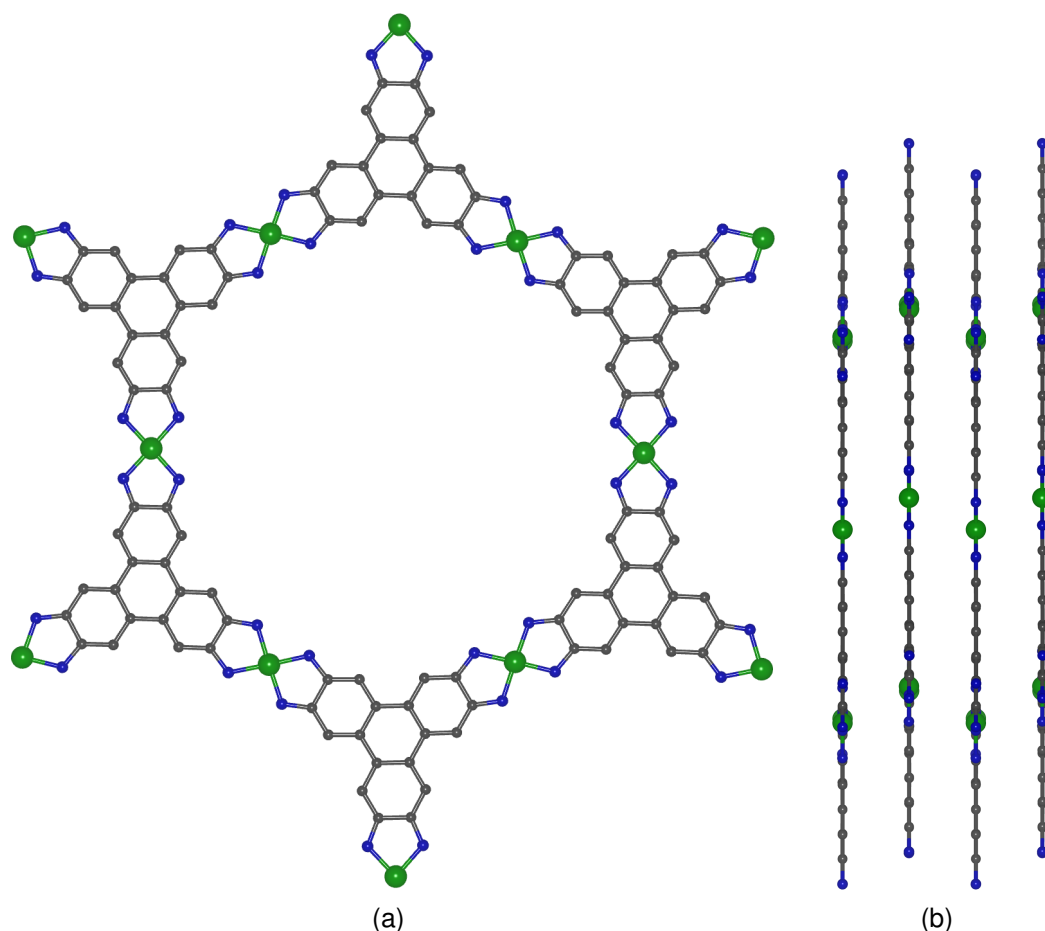


**Figure 114.** Simulated structure of  $\text{Ni}_3\text{HITP}_2$  (a) within the plane, (b) slipped-parallel stacking of the extended coordination sheets.

and time-consuming screening of suitable metal ion and linker combinations together with the optimization of synthetic conditions consisting of multiple reaction parameters (e.g., temperature, pH, solvents, etc.). On the contrary, a myriad of existing MOF structures with different properties and porosities could be rendered electrically conductive by the introduction of redox-active guests in a more modifiable, post-synthetic fashion as discussed above.

For example, the previously mentioned  $\text{TCNQ}@Cu_3\text{BTC}_2$  exhibits an electrical conductivity of  $0.07 \text{ S cm}^{-1}$  (thin film, four-probe), compared to  $1 \times 10^{-8} \text{ S cm}^{-1}$  of the pristine material (Figure 26).<sup>139</sup> To avoid a huge reduction in BET surface area (i.e.,  $214.0 \pm 0.5 \text{ m}^2 \text{ g}^{-1}$  for  $\text{TCNQ}@Cu_3\text{BTC}_2$  vs  $1844 \pm 4 \text{ m}^2 \text{ g}^{-1}$  for  $Cu_3\text{BTC}_2$ ) during the solution-infiltration of  $Cu_3\text{BTC}_2$ , it is also possible to expose activated polycrystalline  $Cu_3\text{BTC}_2$  to vapors of TCNQ in a VPI process. Thus,  $Cu_3\text{BTC}_2$  can be infused with defined stoichiometries of TCNQ to afford guest-loaded samples of the composition  $x\text{TCNQ}@Cu_3\text{BTC}_2$  ( $x = 0.1, 0.2, \dots, 1.0$ ) with a maximum electrical conductivity of  $1.5 \times 10^{-4} \text{ S cm}^{-1}$  for  $1.0\text{TCNQ}@Cu_3\text{BTC}_2$  (pellet, two-contact probe) and BET surface area of  $573.7 \text{ m}^2 \text{ g}^{-1}$ .<sup>28</sup>



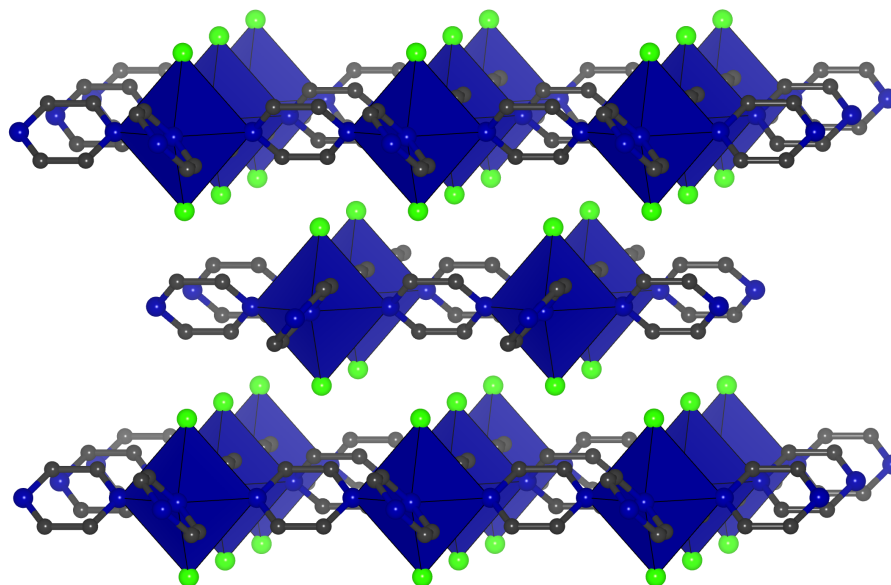


**Figure 115.** Crystal structure of  $\text{Cr}^{\text{III}}\text{Cl}_2(\text{pyrazine})_2$ .

Iodine is an often employed oxidizing dopant for the generation of electrical conductivity in MOFs.<sup>415–420</sup> For example, the redox-active V(III)-MOF based on biphenyl-3,3',5,5'-tetracarboxylic acid (BPTC), MFM-300(V<sup>III</sup>) or  $[\text{V}_2(\text{OH})_2\text{BPTC}]$ , consists of octahedrally coordinated V(III) ions, where four of the six O atoms come from the carboxylates and the remaining two are the  $\mu_2$ -OH groups, thereby forming a corner-sharing one-dimensional, helical rod-SBU. These are connected by the BPTC to form an open structure with square-shaped pores aligned in parallel to the SBUs along the crystallographic *c* axis. The isostructural V(IV)-analog contains bridging oxide ligands instead of hydroxyl groups.<sup>421,422</sup> By exposing the activated MOFs to  $\text{I}_2$  vapors at 70 °C for prolonged periods of time, they adsorb  $\text{I}_2$  and change colors from pale green and brown to dark brown for V(III) and V(IV), respectively. In the case of V(III), charge-transfer from V(III) to  $\text{I}_2$  to form a mixed-valent V(III)/V(IV)-MOF is observed upon adsorption as evidenced by the changes in V–O bond distances which are sensitive to the oxidation state of the central vanadium atom.<sup>422</sup> Moreover, x-ray photoelectron spectroscopy (XPS) indicates the presence of two different iodine species which are ascribed to  $\text{I}_2$  and  $\text{I}_3^-$ , whereas only one species corresponding to molecular  $\text{I}_2$  is observed in the V(IV)-MOF where no charge-transfer from the metal to the guest takes place.<sup>422</sup> Consequently, the electrical conductivities of MFM-300(V<sup>III</sup>), MFM-300(V<sup>IV</sup>), and  $\text{I}_2$ @MFM-300(V<sup>IV</sup>) are in the order of  $10^{-10} \text{ S cm}^{-1}$ , whereas the mixed valent  $\text{I}_2$ @MFM-300(V<sup>III/IV</sup>) shows increased conductivity by six orders of magnitude with values up to  $1.2 \times 10^{-4} \text{ S cm}^{-1}$ .<sup>422</sup>

Besides small organic molecules, it is also possible to infiltrate MOFs with large guests such as fullerene.<sup>423–425</sup> When activated NU-901, which consists

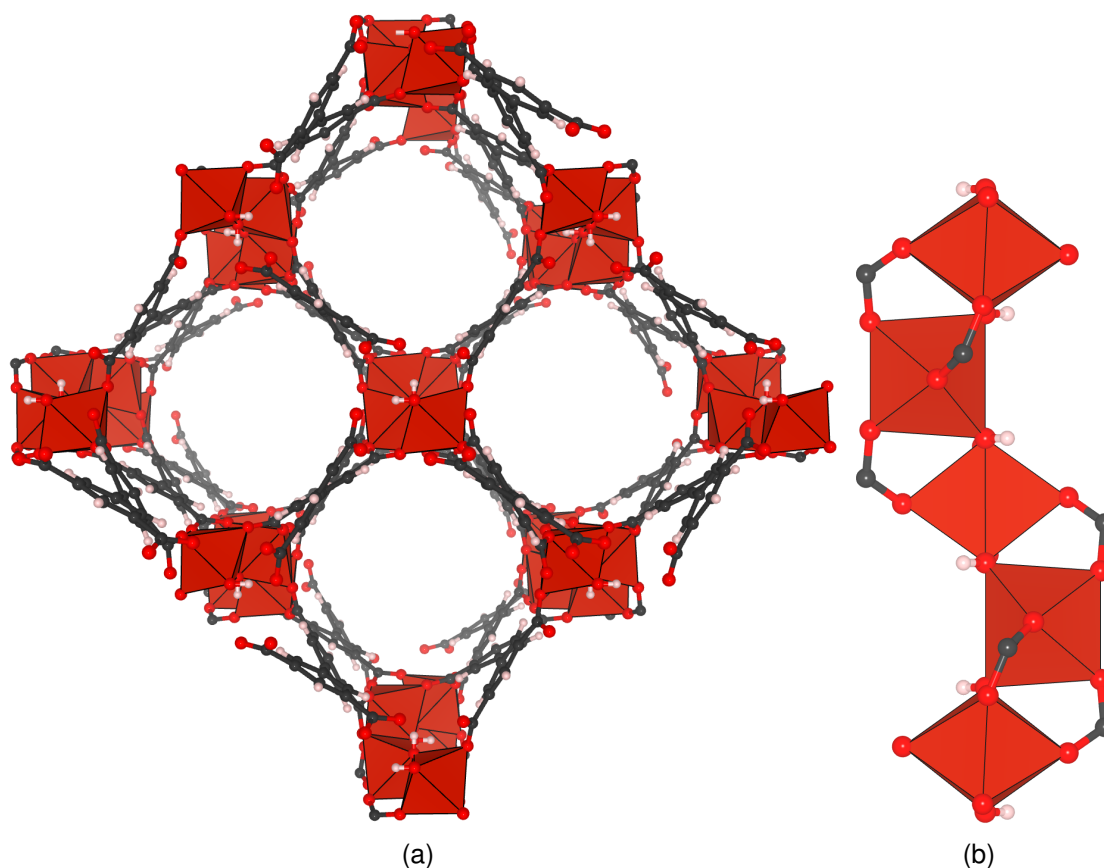


**Figure 116.** (a) Crystal structure and (b) helical rod-SBU in  $V_2(OH)_2BPTC$ .

of  $Zr_6(\mu_3-O)_4(\mu_3-OH)_4(H_2O)_4(OH)_4$  nodes and 1,3,6,8-tetrakis(*p*-benzoate)pyrene (TBAPy) as linker, is exposed to solutions of fullerene, the electrical conductivity increases from negligibly small values to  $10^{-3} \text{ S cm}^{-1}$ .<sup>426</sup> A charge-transfer occurs from electron-donating TBAPy to electron-accepting fullerene as evidenced via a charge-transfer band ranging from 500–700 nm in the UV-Vis spectrum, which increases the electronic delocalization in the system.<sup>426</sup>

# 9

## *Electron Theory*

### 9.1 INTRODUCTION

The electrical conductivity  $\sigma$  is an intrinsic physical property of a material that describes its ability to transport charge (electrons or holes) across an applied potential.<sup>427</sup> The range of electrical conductivities in solid materials can span many orders of magnitude and it is useful to introduce three material classes which best represent their physical properties: (1) conductive metals with conductivity values  $> 10^3 \text{ S cm}^{-1}$ ; (2) semiconductors exhibiting intermediate conductivity from  $10^{-5}$ – $10^3 \text{ S cm}^{-1}$ ; and (3) electrical insulators having conductivities even lower than  $10^{-15} \text{ S cm}^{-1}$ .<sup>428</sup> The differences in electrical conductivities between metals, semiconductors, and insulators are a direct consequence of their different electronic structures. In the following, the physical and quantum mechanical properties of an electron, as well as the electronic band theory will be introduced to the reader which is crucial for a better understanding of the underlying principles of electronic conduction. Then, the physics of electrical conductivity will be outlined based on the introduced band and hopping theory.<sup>429–434</sup>

### 9.2 QUANTUM MECHANICS OF THE ELECTRON

An electron is an elementary particle of charge  $e$  and is subject to the wave-particle dualism of elementary particles, i.e., different properties of the electron can be explained by either regarding the electron as a wave or a particle in space.<sup>435–437</sup>

The properties of an electron can be described by the Schrödinger equation:

$$\left(-\frac{\hbar^2}{2m}\nabla^2 + V\right)\psi = E\psi \quad (9.1)$$

where the total energy  $E$  of the electron is the sum of the kinetic ( $E_{kin}$ ) and potential energy ( $V$ ) of the electron, respectively,  $m$  the electron mass and

$$\nabla^2\psi = \frac{\partial^2\psi}{\partial x^2} + \frac{\partial^2\psi}{\partial y^2} + \frac{\partial^2\psi}{\partial z^2}. \quad (9.2)$$

### 9.2.1 Free Electron

A free electron moving in space in one direction with no potential energy,  $V = 0$  is described by:

$$-\frac{\hbar^2}{2m}\frac{\partial^2\psi}{\partial x^2} = E\psi \quad (9.3)$$

The solution to equation 9.3 is

$$\psi(x) = A \exp(i\alpha x) + B \exp(-i\alpha x), \quad E = \frac{\hbar^2}{2m}k^2 \quad (9.4)$$

where  $k = \frac{2\pi}{\lambda}$  is the wave vector in the  $x$ -dimension, corresponding to the momentum of the electron. This means that every energy of a free electron is permitted.<sup>438</sup>

### 9.2.2 Electron in a Box

In contrast, the energetic states of a bound electron, e.g., in an atom, do not form an energy continuum but are quantized into specific states. An electron that is confined in a potential well of potential energy  $V = 0$  and infinitely large potential barriers (i.e.,  $V = \infty$ ) is only located in the potential energy free zone (Figure 117).<sup>439,440</sup>

The wave equation is the same as in equation 9.4. For  $x = 0$ ,  $\psi = 0$ , so equation 9.4 is reduced to  $A = -B$ . Similarly, for  $x = a$ ,  $\psi = 0$ , and using the Euler equation  $\sin(x) = \frac{1}{2i}(e^{ix} - e^{-ix})$ , equation 9.4 gives:

$$0 = Ae^{i\alpha a} + Be^{-i\alpha a} = A(e^{i\alpha a} - e^{-i\alpha a}) = 2Ai \sin(\alpha a) \quad (9.5)$$

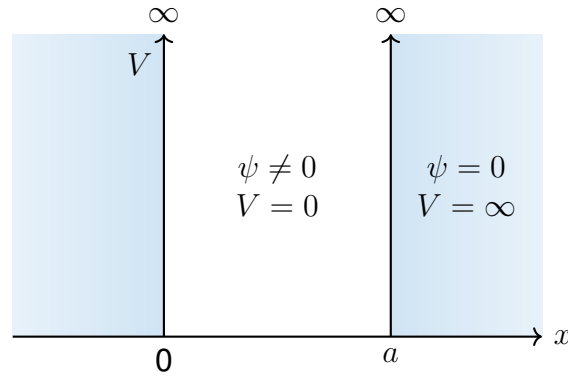


**Figure 117.** Schematic illustration of a bound electron in a potential well with infinitely large potential barriers. The probability function of the electron,  $\psi\psi^*$ , is zero in the forbidden blue area and on the border to the permitted white area.

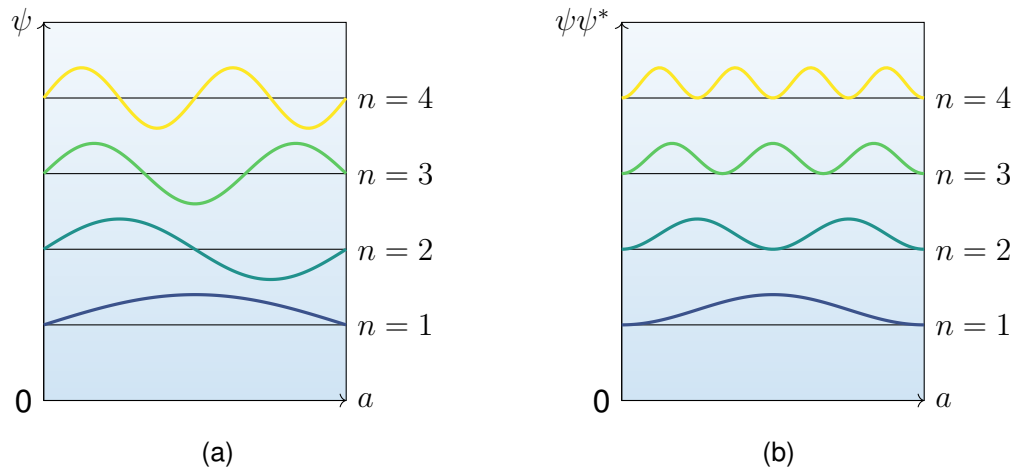


**Figure 118.** (a) Wave functions, and (b) probability functions for the energy levels of the bound electron with infinitely large potential barriers.

This can only be fulfilled when  $\sin \alpha a$  is zero, i.e., if  $\alpha a = n\pi$  ( $n = 0, 1, 2, 3, \dots$ ).  $n = 0$  can be neglected because that would lead to  $\psi = 0$ , meaning no electron density within the potential well which cannot be true by definition. This yields the following possible quantized energy states for the electron with the minimum energy for  $n = 1$ :

$$E_n = \frac{\hbar^2}{2m} \alpha^2 = \frac{\hbar^2 \pi^2}{2ma^2} n^2, \quad n = 1, 2, 3, \dots \quad (9.6)$$

The obtained wave functions and the probability to find an electron within the potential well,  $\psi\psi^* = 4A^2 \sin^2(\alpha x)$ , are analogous to the harmonic oscillator (Figure 118).<sup>441,442</sup>

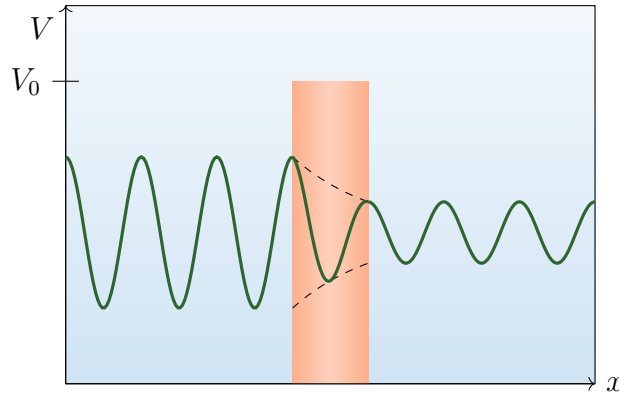


**Figure 119.** Tunneling of an electron through a potential barrier.

### 9.2.3 Tunnel effect

The probability of finding the electron within an energy barrier is not zero anymore if the barrier has a potential of finite height  $V_0$ . The Schrödinger equation of the potential free zone and its solution is the same as for the free electron, while the one for the potential barrier is

$$\left(-\frac{\hbar^2}{2m} \frac{\partial^2}{\partial x^2} + V_0\right) \psi = E\psi \quad (9.7)$$

and the solution is

$$\psi_V = De^{-\gamma x}, \quad \gamma = \sqrt{\frac{2m}{\hbar^2}(V_0 - E)}. \quad (9.8)$$

This shows that the wave function decreases exponentially in the potential barrier and can move through it and continue on the other side if  $V_0$  is small enough. This is known as the tunnel effect (Figure 119).<sup>443,444</sup>

### 9.2.4 Electron in the Solid State

The solid state is a periodic repetition of potential wells and potential barriers of finite height  $V_0$ . The solution to the Schrödinger equation in the solid state is

$$P \frac{\sin \alpha a}{\alpha a} + \cos \alpha a = \cos ka, \quad P = \frac{maV_0b}{\hbar^2} \quad (9.9)$$

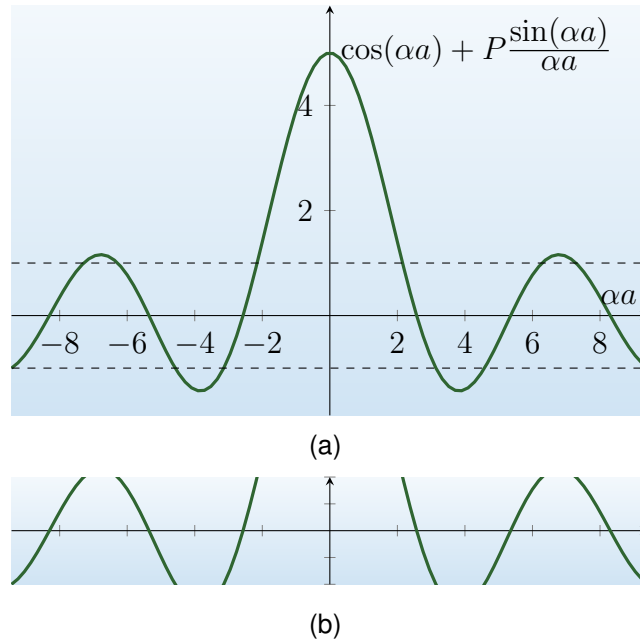


**Figure 120.** Formation of band gaps for an electron in a periodically varying potential field, also known as the Kronig-Penney model. (a) Function  $y = \cos(\alpha a) + P \frac{\sin(\alpha a)}{\alpha a}$  vs.  $\alpha a$  for  $P = 4$ . (b) Cutout of the above graph between  $-1 \leq y \leq 1$ .

where  $a$  and  $b$  are the length of the potential free zone and barrier, respectively. Plotting  $\cos(\alpha a) + P \frac{\sin(\alpha a)}{\alpha a}$  vs.  $\alpha a$  for an arbitrary value of  $P$  gives the following result (Figure 120). The dashed lines indicate that a solution is only defined for  $-1 \leq \cos(\alpha a) + P \frac{\sin(\alpha a)}{\alpha a} \leq 1$  because  $\cos(ka)$  cannot go beyond that range. This means that the electron in a periodically varying potential field can only occupy certain energy zones, also called bands, and areas outside of these bands are prohibited. The larger the term  $V_0 b$  (i.e., the higher the potential barrier), the narrower the bands will become and resemble sharp energy levels, whereas for small  $V_0 b$  values the bands become wider and the electrons more mobile.<sup>430,445,446</sup>

### 9.2.5 Energy Bands in Crystals

According to equation 9.4, the energy of a free electron is parabola-shaped with respect to the  $k$ -vector. In a crystal with a periodic potential field (equation 9.9) and for the case that  $P = 0$  (i.e.,  $V_0 = 0$ , free electron in a crystal), equation 9.9 is simplified to:

$$\cos(\alpha a) = \cos(k_x a) = \cos(k_x a + n2\pi), \quad n = 0, \pm 1, \pm 2, \dots \quad (9.10)$$

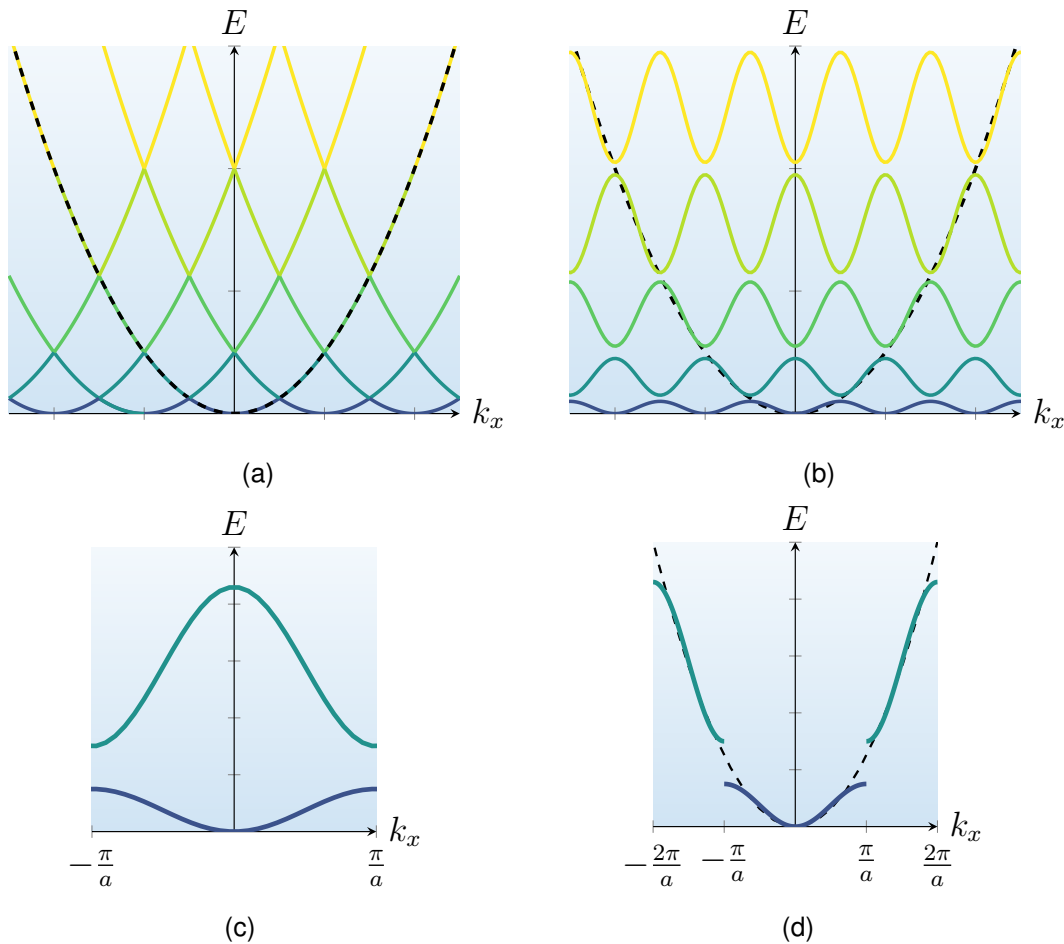


**Figure 121.** Energy profile of an electron in a crystal. (a) Repetition of the energy profile of a free electron with periodicity of  $\frac{2\pi}{a}$ . (b) Summation of the individual energy profiles into a periodic zone scheme. (c) Reduced zone scheme between  $k_x = \pm\frac{\pi}{a}$ . (d) Extended zone scheme showing both first and second Brillouin zones.

Hence,

$$k_x + n\frac{2\pi}{a} = \sqrt{\frac{2mE}{\hbar^2}} \quad (9.11)$$

and a periodic function of parabolas of periodicity  $\frac{2\pi}{a}$  is obtained (Figure 121a).<sup>447,448</sup> According to Figure 120 the electron exhibits energy discontinuities when  $\cos(k_x a) = \pm 1$ . This is only the case for  $k_x = n\frac{\pi}{a}$ ,  $n = \pm 1, \pm 2, \dots$  at the intersections of the different energy parabolas, leading to a new energy profile (Figure 121b). In the reduced zone scheme, only the section between  $\pm\frac{\pi}{a}$  is shown, which is called the first Brillouin zone (Figure 121c). In the extended zone scheme, the first and second ( $\frac{\pi}{a} < k_x < \frac{2\pi}{a}$  and  $-\frac{2\pi}{a} < k_x < -\frac{\pi}{a}$ ) Brillouin zones are shown and it is illustrated how electrons in a crystal behave like free electrons except close to or at  $k_x = n\frac{\pi}{a}$  (Figure 121d). Metals have characteristic parabola-shaped bands indicating that the electrons are very mobile similar to free electrons. Moreover,



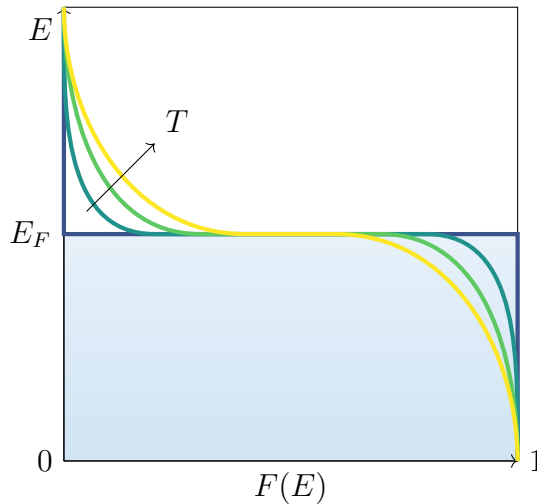


**Figure 122.** Fermi distribution functions. The line changes its shape from a horizontal line at  $T = 0$  (purple) to a curve with increasing temperature (yellow). Note that at  $E = E_F$ ,  $F(E) = 0.5$  for every temperature.

these bands overlap in metals resulting in no band gaps. In contrast, they do not overlap in the case of semiconductors and insulators and form the characteristic band gaps.

### 9.2.6 Fermi Distribution Function and Density of States

The probability that a certain energy level is occupied is given by the Fermi Function,  $F(E)$ :

$$F(E) = \frac{1}{\exp\left(\frac{E - E_F}{k_B T}\right) + 1} \quad (9.12)$$

where  $E$  is the energy level,  $E_F$  the Fermi energy where  $F(E_F) = 0.5$ ,  $k_B$  the Boltzmann constant, and  $T$  the temperature. Generally, the electrons in a solid occupy the available energetic states according to their energy level, beginning at the lowest available energy to succeeding higher levels. At  $T = 0$ , only the energetically lowest energy states are occupied and higher energetic states become accessible with increasing temperature (Figure 122).<sup>449</sup>

Each energy level is represented by the quantum number  $n$ . Since  $n$  is a three-dimensional vector with the elements  $n_x$ ,  $n_y$ , and  $n_z$  for the three space dimensions, the point  $n$  can be envisioned as the sum of the individual vectors in a quantum number sphere with the radius  $n$ , given that  $n^2 = n_x^2 + n_y^2 + n_z^2$  (Figure 123).<sup>430,438</sup> On the surface of the quantum number sphere with radius  $n$  are equal values of  $E_n$  with different quantum numbers. Consequently, the points within the sphere

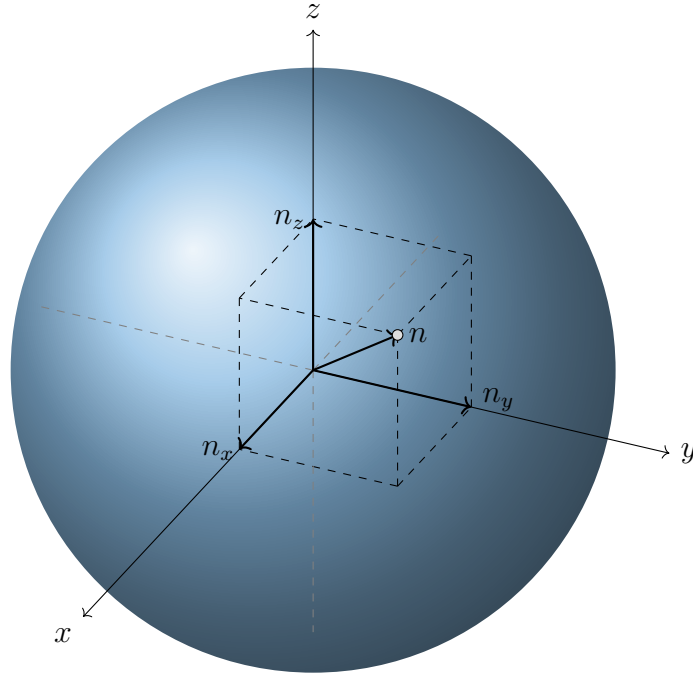


**Figure 123.** Energy state in quantum number space.

correspond to values of smaller  $n$  and  $E_n$ , and the number of energy states is larger when the surface area of the quantum number sphere is larger (i.e., when  $n$  is larger). The number of all states  $\eta$  is calculated as:

$$\eta = \frac{1}{8} \times \frac{4}{3} \pi n^3 = \frac{\pi}{6} \left( \frac{2ma^2}{\pi^2 \hbar^2} \right)^{\frac{3}{2}} E^{\frac{3}{2}} \quad (9.13)$$

The density of states  $Z(E)$  is the number of states  $\eta$  per energy increment  $dE$ :

$$\frac{d\eta}{dE} = Z(E) = \frac{\pi}{4} \left( \frac{2ma^2}{\pi^2 \hbar^2} \right)^{\frac{3}{2}} E^{\frac{1}{2}} = \frac{V}{4\pi^2} \left( \frac{2m}{\hbar^2} \right)^{\frac{3}{2}} E^{\frac{1}{2}} \quad (9.14)$$

where  $V = a^3$  (volume of the crystal). The density of states increases with energy, meaning that more states are available at higher energies for a free electron. In turn, this would lead to an infinitely high density of states for increasing energies. However, the energetic situation of electrons in real crystals is defined by the structure of the Brillouin zones. Here, the electrons behave like free electrons for low energies, whereas fewer states are available at higher energies and  $Z(E)$  becomes zero when the whole Brillouin zone is filled, giving rise to the characteristic profile seen in Figure 124a.<sup>430,445</sup>

The population density  $N(E)$  is the number of electrons per unit energy  $dE$  and obtained via combining equations 9.12, 9.14 and taking into account that every energy state can be occupied by two electrons according to the Pauli principle:

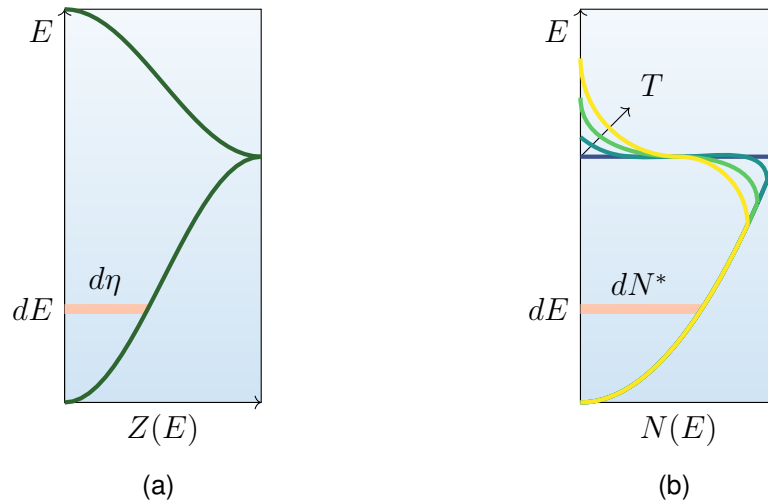


**Figure 124.** (a) Density of states and (b) population density within a band.

$$N(E) = 2Z(E)F(E) = \frac{V}{2\pi^2} \left( \frac{2m}{\hbar^2} \right)^{\frac{3}{2}} E^{\frac{1}{2}} \frac{1}{\exp\left(\frac{E - E_F}{k_B T}\right) + 1} \quad (9.15)$$

The number of electrons is represented by the population density in an energy increment (Figure 124b) and is calculated via:

$$dN^* = N(E) dE \quad (9.16)$$

Integration gives the total number of electrons (for  $T = 0$  and  $E = E_F$ ):

$$N^* = \int_0^{E_F} N(E) dE = \int_0^{E_F} \frac{V}{2\pi^2} \left( \frac{2m}{\hbar^2} \right)^{\frac{3}{2}} E^{\frac{1}{2}} dE = \frac{V}{3\pi^2} \left( \frac{2m}{\hbar^2} \right)^{\frac{3}{2}} E_F^{\frac{3}{2}} \quad (9.17)$$

From equation 9.17 the Fermi energy can be calculated:<sup>430,450,451</sup>

$$E_F = \left( 3\pi^2 \frac{N^*}{V} \right)^{\frac{2}{3}} \frac{\hbar^2}{2m} \quad (9.18)$$

## 9.3 ELECTRICAL CONDUCTIVITY

### 9.3.1 Classical Definition

The total electrical resistance  $R$  with the unit ohm  $\Omega$  is defined by Ohm's law as:<sup>431</sup>

$$R = \frac{V}{I} \quad (9.19)$$

where  $V$  is the applied voltage with the unit volt V and  $I$  the current with the unit ampere A passing through the material. Since  $R$  is dependent on the sample size dimensions such as length  $l$  and cross-sectional area  $A$ , the electrical resistivity  $\rho$  with the unit  $\Omega$  m describes the intrinsic, geometrically independent property as follows:

$$\rho = \frac{RA}{l} \quad (9.20)$$

$\sigma$  is then defined as the inverse of  $\rho$ , the corresponding unit is  $(\Omega \text{ m})^{-1}$  or  $\text{S m}^{-1}$ :

$$\sigma = \frac{1}{\rho} = \frac{l}{RA} = \frac{Il}{VA} \quad (9.21)$$

Resistance is the scattering of electrons in an electric field by lattice atoms or defects in the material. If the time between two scattering events is long, the resistance is low and *vice versa*. Additionally, the more electrons are capable of participating in the conduction process the lower the resistance. Thus,  $\sigma$  can be defined in classical physics microscopically as<sup>429–431</sup>

$$\sigma = \frac{Ne^2\tau}{m} = Ne\mu \quad (9.22)$$

where  $m$  is the electron mass,  $N$  is the number of electrons and  $\tau$  is the time between two scattering events.  $\mu$  is the electron mobility, which is defined as the velocity of charge carriers normalized to the electric field strength.

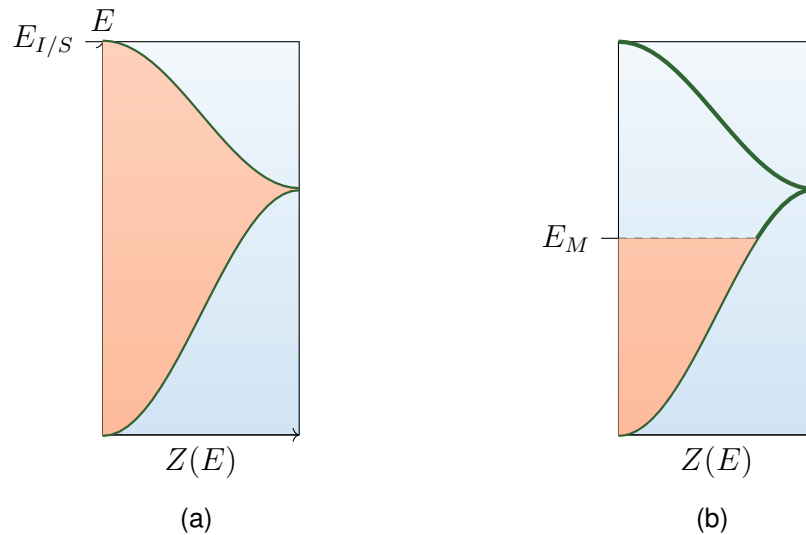


**Figure 125.** Band population and density of states for (a) insulators, semiconductors, and (b) metals.

### 9.3.2 Quantummechanical Aspects

The largest fraction of electrons possesses the Fermi energy  $E_F$  because the density of states  $Z(E)$  and population density  $N(E)$  are highest around the Fermi level.<sup>430</sup> Therefore, the velocity of the electrons can be approximated as the Fermi velocity  $v_F$  and the number of electrons participating in conduction is the number of electrons at the Fermi level  $E_F$  displaced by an energy increment  $\Delta E$ . After consideration of band theory, the following term for the electrical conductivity can be written:<sup>452</sup>

$$\sigma = \frac{1}{3} e^2 v_F^2 \tau N(E_F) \quad (9.23)$$

Equation 9.23 shows that the conductivity is dependent on the population density around the Fermi energy. In insulators and semiconductors, the valence band is completely filled and consequently the population density is very small, resulting in low electrical conductivities (Figure 125a). Unlike insulators, however, semiconductors show moderate electrical conductivity because they have small band gaps and excitation of electrons into the empty conduction band is possible via external stimuli of sufficiently large energy (*vide infra*). Looking at Figure 125b, it is evident that metals have only partially filled bands with high population density near the Fermi level and only little energy is needed to excite electrons into energetically larger states which is the reason for their large electrical conductivity.<sup>430,452</sup>

The electrical conductivity in metals decreases with increasing temperature. At higher temperatures, scattering of the electrons within the crystal occurs more

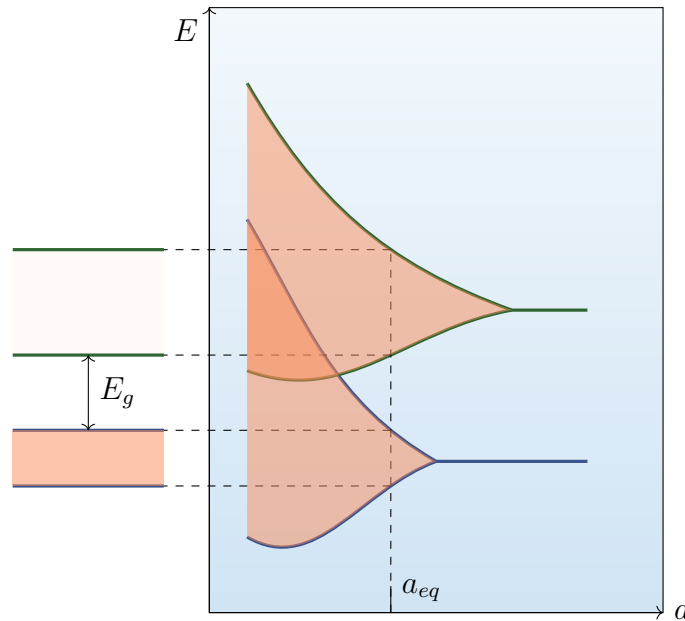


**Figure 126.** Band formation and overlap in a covalent solid with  $N$  atoms and interatomic bond distance  $a_{eq}$ .  $E_g$  is the energetic band gap between the filled valence band and empty conduction band.

frequently due to the increase in lattice energy, thereby reducing the relaxation time between two scattering events and according to equation 9.23 also the conductivity.<sup>431</sup>

### 9.3.3 Semiconductors

In a solid, the atomic energy levels of the individual atoms interact with each other the smaller the bond distances become, causing a widening of the energy levels into a band.<sup>429–431</sup> Importantly, the energetically higher valence electrons are first affected by this because the core electrons are more tightly bound to the atom. Silicon is the prototypical example of a covalent solid and semiconductor which crystallizes in the diamond-type crystal structure, i.e., one Si atom is bound via single bonds to four other Si atoms arranged tetrahedrally around the central Si atom. This bonding situation can be explained by a  $sp^3$ -hybridization in which the single 3s orbital and the three 3p orbitals of Si undergo hybridization into four  $sp^3$  orbitals, each containing one electron. Bonding to four neighboring Si atoms completes the electron shell of the central Si. For  $N$  Si atoms in a crystal, this means the valence band will contain  $4N$  electrons be completely filled, whereas the conduction band is empty. They are separated by a band gap (Figure 126).<sup>450,453</sup> Intrinsic semiconductors become conducting at higher temperatures when it is possible to excite electrons from the valence band into the

conduction band via a thermal energy input. Both the electron in the conduction band, as well as the hole in the valence band contribute to the resulting electrical conductivity. The Fermi energy  $E_F$  is located at in the center of the band gap because the same number of charge carriers is found in both bands, i.e.,  $n$  electrons in the conduction band and  $n$  holes in the valence band. The number of electrons in the conduction band can be calculated via<sup>430</sup>

$$N_e = \frac{1}{4} \left( \frac{2mk_B}{\pi\hbar^2} \right)^{\frac{3}{2}} T^{\frac{3}{2}} \exp \left( -\frac{E_g}{2k_B T} \right) = 4.84 \times 10^{15} T^{\frac{3}{2}} \exp \left( -\frac{E_g}{2k_B T} \right) \quad (9.24)$$

The exponential term shows that the number of electrons increases with increasing temperature and decreasing band gap. However, the number of electrons is relatively low in intrinsic semiconductors, resulting in moderate electrical conductivities. Both holes and electrons contribute to the conductivity, therefore:<sup>430,431</sup>

$$\sigma = N_e \mu_e e + N_h \mu_h e \quad (9.25)$$

Since the number of holes and electrons is equal, the following term for the conductivity is obtained after insertion of equation 9.24 in 9.25:

$$\sigma = 4.84 \times 10^{15} T^{\frac{3}{2}} e (\mu_e + \mu_h) \exp \left( -\frac{E_g}{2k_B T} \right) \quad (9.26)$$

Similarly to metals, the relaxation time of charge carriers in intrinsic semiconductors decreases with increasing temperature due to more frequent scattering of charges on the crystal lattice atoms. However, the number of charge carriers increases more strongly with increasing temperature, giving rise to an overall larger electrical conductivity (Figure 127).<sup>427,430,454</sup>

Extrinsic semiconductors contain dopants which modify the electron concentration within the material. Silicon is often mixed with little amounts of either group III or group V elements which can substitute a Si atom in the lattice and either add an additional electron (for group V elements such as P, As, or Sb), or lack one electron in comparison to Si (for group III elements such as B, Al, Ga or In). In  $n$ -doped Si, the additional electron provided by a group V element impurity provides a loosely bound electron of little binding energy which can be easily dissociated from its atom and moved around the crystal after application of an external electric field. These donor electrons can populate the empty conduction band of Si and increase the electrical conductivity. Similarly, an electron-accepting

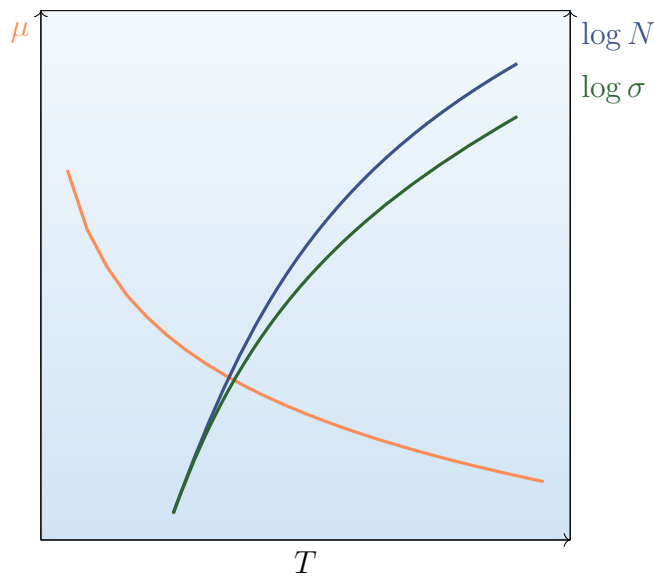


**Figure 127.** Relationships of charge carrier mobility, density, and electrical conductivity of intrinsic semiconductors vs. temperature.

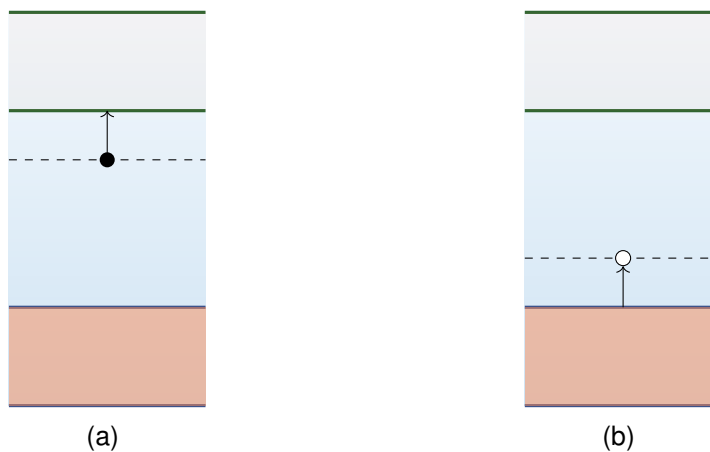


**Figure 128.** Donor and acceptor levels in (a) *n*-type and (b) *p*-type extrinsic semiconductors, respectively.

group III element provides a hole in *p*-doped Si and increase the electrical conductivity via conduction of positively charged holes (Figure 128).<sup>427,438</sup>

There are two types of charge carriers in extrinsic semiconductors. At  $T = 0$ , all donor levels are filled in *n*-type and all acceptor levels are empty in *p*-type semiconductors, respectively, and the conductivity is zero. With increasing temperature, the electrons from the donor levels in *n*-type semiconductors start populating the empty states in the conduction band, and similarly the the valence electrons will populate now the empty acceptor levels in *p*-type semiconductors. This will cause a fast increase in charge carrier density with increasing temperature until all possible electrons have been excited, then the number of charge carriers will remain constant until the intrinsic effects of the semiconductor start to become relevant. Consequently, the electrical conductivity of extrinsic semiconductors



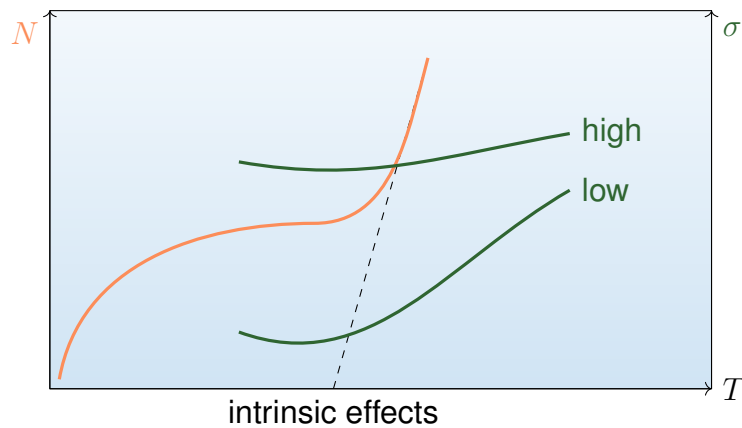


**Figure 129.** Relationship of charge carrier density and electrical conductivity with temperature for extrinsic semiconductors. The dashed lines indicate the temperature at which intrinsic effects become apparent. High doping increases the electrical conductivity.

is much larger in comparison to intrinsic ones and increases with higher doping. Similarly to metals and intrinsic semiconductors, the conductivity will first decrease with increasing temperature in the low temperature area because of increasing phonon scattering of electrons and holes, then increase because the thermal energy is now sufficient to excite electrons from the valence band into the conduction band. The temperature effect is less pronounced for highly doped extrinsic semiconductors due to a high concentration of donor electrons in the conduction band or holes in the valence band, respectively (Figure 129).<sup>451,452</sup> In addition, the Fermi energy of extrinsic semiconductors is also highly affected by the temperature. At low temperatures, more electrons are located in the conduction band than holes in the valence band for *n*-type, and more holes in the valence band than electrons in the conduction band for *p*-type extrinsic semiconductors, respectively. Therefore, the Fermi level is located between the dopant energy levels and the energetically closest band. With increasing temperature, the intrinsic effects become more dominant and the Fermi level will approach the value of intrinsic semiconductors, i.e., at higher temperatures the physical properties will resemble more and more those of an intrinsic semiconductor (Figure 130).<sup>430,452,455,456</sup>

#### 9.3.4 Hopping Transport

Hopping transport describes the physical phenomenon of electrical conduction in materials where localized charge carriers tunnel between specific sites within the material.<sup>457</sup> This type of charge transport dominates in materials where transport via delocalized states is not possible due to insufficient thermal activation. The hopping probability can be described by

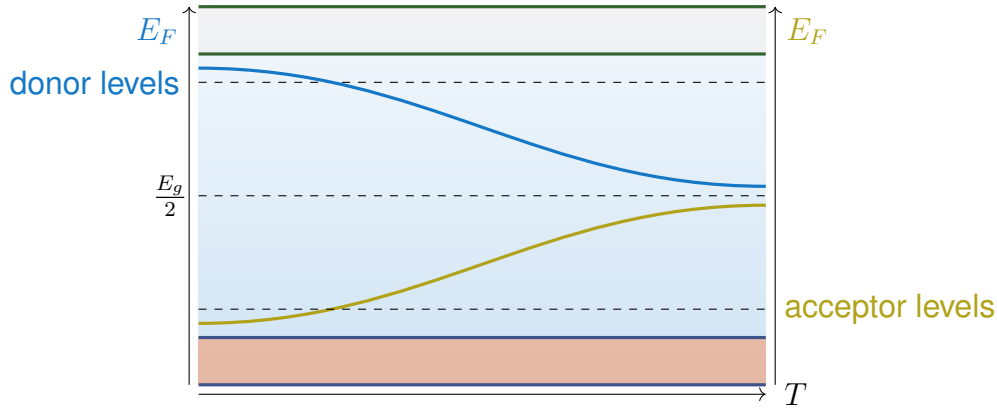


**Figure 130.** Dependence of the Fermi level on the temperature of  $n$ -type (blue) and  $p$ -type (yellow) extrinsic semiconductors.

$$\nu_{ij} = \nu_0 \exp\left(-\frac{2r_{ij}}{\alpha}\right) \quad (9.27)$$

where  $\nu_0$  is a constant,  $\alpha$  is the localization radius (i.e., half-width of the occupied localized electronic state), and  $r_{ij}$  is the distance between two centers  $i$  and  $j$ . This relationship shows that a tunneling transition becomes less likely with increasing separation between two localized states, and thus smaller electronic interaction between two wave functions. Hopping transport can be categorized into several types. In the simplest case, hopping occurs only between two nearest neighbors.<sup>458</sup> In this model, a hopping transition event takes only place from an occupied to an unoccupied electronic state and is dependent on the donor energy state  $E_D$  and the Fermi energy  $E_F$  and proportional to

$$\exp\left(-\frac{|E_F - E_D|}{T}\right) \quad (9.28)$$

This condition can be only fulfilled at high  $T$ , whereas the number of free neighbor states at low  $T$  is too low to match with experimental data. Thus, the variable-range hopping transport mechanism describes tunneling effects over all possible distances between two different electronic states. Applying percolation theory, the following term for the hopping electrical conductivity  $\sigma_h$  can be formulated

$$\sigma_h = \sigma_0 \exp\left(-\frac{T_0}{T}\right)^{(d+1)^{-1}} \quad (9.29)$$

where  $T_0$  and  $\sigma_0$  are material-dependent constants and  $d$  stands for the dimensionality of the material. Equation 9.29 shows that  $\sigma_h$  always increases with increasing  $T$ .<sup>457,458</sup>

## 9.4 MEASUREMENT OF ELECTRICAL CONDUCTIVITY

The electrical conductivity  $\sigma$  is a characteristic physical property that describes the ability of a material to conduct an electrical current, and it is dependent on the measurement conditions such as temperature, pressure, and applied current (*cf.* section 9.3).<sup>43,364</sup> It is calculated based on Ohm's law (equation 9.21) in a usually low voltage range since most materials exhibit ohmic behavior (i.e., the measured current at a defined voltage can be translated directly into the resistance of the sample) only for small applied potentials. There are several other problems that influence the measured values of electrical conductivity. Since most samples are obtained as polycrystalline powders, grain boundary resistances between individual crystallites accumulate and result in contact problems and reduced observed electrical conductivity values.<sup>459</sup> For this reason, pressed pellet electrical conductivities are usually a few orders of magnitude lower than those reported for single crystals. Related to that, a sufficient contact between electrodes and the sample can be problematic and appear as a sample-independent resistance (contact resistance) that influences the measurement. Likewise, the intrinsic electrical conductivity of the sample can also cause problems. If it is too low, the effectively measured value is the ohmic drop of the measurement instrument; if it is too large, the measured value will be limited by the contact resistance between sample and electrode.<sup>364</sup> Moreover, coordination polymers (CPs) often exhibit anisotropic properties, e.g., higher electrical conductivity along the axis of propagation in which a one-dimensional CP compared to directions perpendicular to that axis, which can affect the measurement, as well.

Consequently, different techniques were developed to measure the electrical conductivity of materials. The most commonly used measurement technique is the two-contact probe method where two probes are connected to a sample of known geometry (Figure 131a). This is often used for polycrystalline samples which are pressed into pellets and the opposite surfaces are connected to a thin metal foil with conductive adhesive paste such as silver paste. Then, the current and voltage are measured through these electrodes. In this case, the measured resistance corresponds to the resistance of the sample, the contacts, and the wires. These resistances are coupled with each other in series, and therefore, the sample resistance must be much larger to allow the contact and wire resistance to be negligible. Usually this technique is used for samples with high resistance and where sample quantities pose a problem. In the schematic case shown in Figure 131a, the conductivity is calculated according to<sup>9,43</sup>

$$\sigma = \frac{Il}{VA} = \frac{Il}{V_{ad}}. \quad (9.30)$$

In the four-contact probe method, four parallel in-line contacts are aligned in a row and connected to the sample by conductive, adhesive paste or pressure (Figure 131b). The two external ones are used to apply a current to the sample and two internal ones to measure the voltage drop. Advantageous to this method is the fact that only the sample resistance is measured while contact and wire resistances are avoided. This is particularly interesting for samples with low resistances and comes with a more precise determination of the real electrical conductivity value. However, a larger sample size is required for reasons of space for four electrodes compared to two. The electrical conductivity is calculated using equation 9.30. To account for limited sample amounts, the four-contact probe method can be replaced by a four-point probe method (Figure 131c). In this case, four small probes are placed on the surface of the sample separated by a defined, small distance, and the electrical conductivity is measured similarly to the four-contact probe method, using<sup>9,43</sup>

$$\sigma = \frac{I}{2\pi lV}. \quad (9.31)$$

The van-der-Pauw method is best for conductivity measurements of thin films that do not meet the requirements of the four-point probe method. Here, four small contacts are glued to the circumference of a thin film of continuous coverage of the substrate with uniform thickness in a fashion that they are arranged rectangular (Figure 131d). The electrical conductivity is calculated using<sup>9,43</sup>

$$\sigma = \left[ \frac{\pi d}{\ln 2} \times \left( \frac{1}{2} \left( \frac{V_{AB}}{I_{CD}} + \frac{V_{BC}}{I_{DA}} \right) \right) \times f \right]^{-1} \quad (9.32)$$

where  $V_{AB}$  and  $I_{CD}$  are the measured voltages and currents between the two specified points A and B (or C and D), respectively, and  $f$  is a correction factor.<sup>9,43</sup>

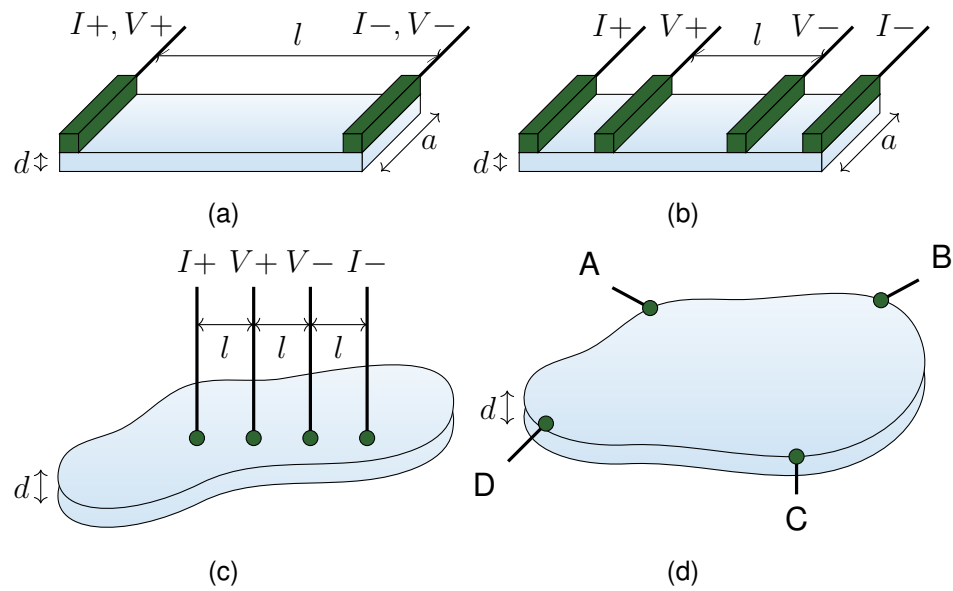


**Figure 131.** Measurement techniques for electrical conductivity. (a) Two-contact probe method. (b) Four-contact probe method. (c) Four-point probe method. (d) Van-der-Pauw method.



# 10

## *X-Ray Diffraction*

### 10.1 INTRODUCTION

XRD is an analytical technique used for the structure determination and confirmation of crystalline samples.<sup>460–464</sup> It takes advantage of the ordered and periodic arrangement of atoms in the crystalline state, with the interatomic distances being similar to the dimensions of x-ray wavelengths. Hence, they are suitable for the observation of interference effects of x-rays when scattered by crystallographic planes within the material. Importantly, diffraction leads to constructive interference only when the sample of interest is irradiated with x-rays at precisely defined angles, which in turn yields information about the positioning of atoms and the interplanar distances of crystallographic planes within a crystal.

### 10.2 CRYSTALLOGRAPHY

A crystal is defined as a solid with definite chemical composition in which its constituents (i.e., atoms or molecules) have an ordered arrangement.<sup>460</sup> It is based on one overall defining crystallographic unit or elementary cell which repeats itself in all three dimensions due to the translational symmetry inherent to crystals. This unit cell can be characterized with three non-orthogonal reference axes  $a$ ,  $b$ , and  $c$ , as well as the angles  $\alpha$ ,  $\beta$ , and  $\gamma$ , and is chosen in such a way as to best represent the symmetry of the crystal structure. Every crystal has an underlying geometrical lattice which is a regular and infinite arrangement of points.<sup>460</sup> There are 14 lattice types (Bravais lattices) based on seven crystal systems to describe

the arrangements of lattice points with unique, non-interchangeable symmetry (Figure 132). For example, a triclinic unit cell describes one with unequal lattice parameters  $a$ ,  $b$ ,  $c$ , and unequal angles  $\alpha$ ,  $\beta$ ,  $\gamma$  and contains the least symmetry elements at the lattice points, i.e., the identity and inversion operation,  $1$  and  $\bar{1}$ .<sup>460</sup> In a monoclinic unit cell,  $\alpha$  and  $\gamma$  are equal to  $90^\circ$ , and a two-fold rotation axis parallel to a mirror plane at the lattice points appear ( $2/m$ ). Besides the primitive cell containing atoms only at the corners of the lattice cell (P), monoclinic cells can also be face-centered (C). Orthorhombic cells with all angles equal to  $90^\circ$  exhibit mirror planes in all three dimensions ( $mmm$ ). The symmetry is further increased in tetragonal cells where all angles are  $90^\circ$  and  $a$  and  $b$  are of the same length, with an additional four-fold rotation axis along  $c$  ( $\frac{4}{m}mm$ ), and even more so in cubic cells where all angles are  $90^\circ$  and all edges are equal and a three-fold rotation axis and parallel mirror planes along the space diagonals become apparent ( $m\bar{3}m$ ). While orthorhombic cells can appear as primitive, base-centered, body-centered (I), and face-centered (F) cells, this is not possible for tetragonal cells allowing only primitive and body-centered cells because the four-fold symmetry allows the reduction of potential base-centered and face-centered tetragonal cells to primitive and body-centered cells with smaller unit volume, respectively.<sup>460</sup> Likewise, a base-centered cubic cell does not exist because it is equivalent to a primitive tetragonal cell. Thus, only primitive, body-centered, and face-centered cubic cells exist (Figure 132).<sup>460</sup> Hexagonal cells have equal  $a$  and  $b$ , as well as  $\alpha$  and  $\beta$  equal to  $90^\circ$ , with different parameter  $c$  and  $\gamma$  equal to  $120^\circ$ . Here, a six-fold rotation axis exists along  $c$  ( $\frac{6}{m}mm$ ). If this six-fold rotation symmetry does not exist, the symmetry is reduced to a trigonal cell with equal lattice parameters but only a three-fold rotation axis along  $c$  ( $\bar{3}m$ ). A special case is the rhombohedral unit cell where all lattice parameters are equal, and all angles are equal to each but unequal to  $90^\circ$  and less than  $120^\circ$ .<sup>460</sup>

## 10.3 X-RAYS

### 10.3.1 Generation of X-Rays

In an evacuated chamber, a high voltage ( $>40$  kV) is applied to a W cathode and a target anode (for example, Cu or Mo), respectively. As a result of the increasing temperature, the negatively charged, hot W filament emits electrons which are accelerated to the positively charged target anode. Importantly, the energy of the



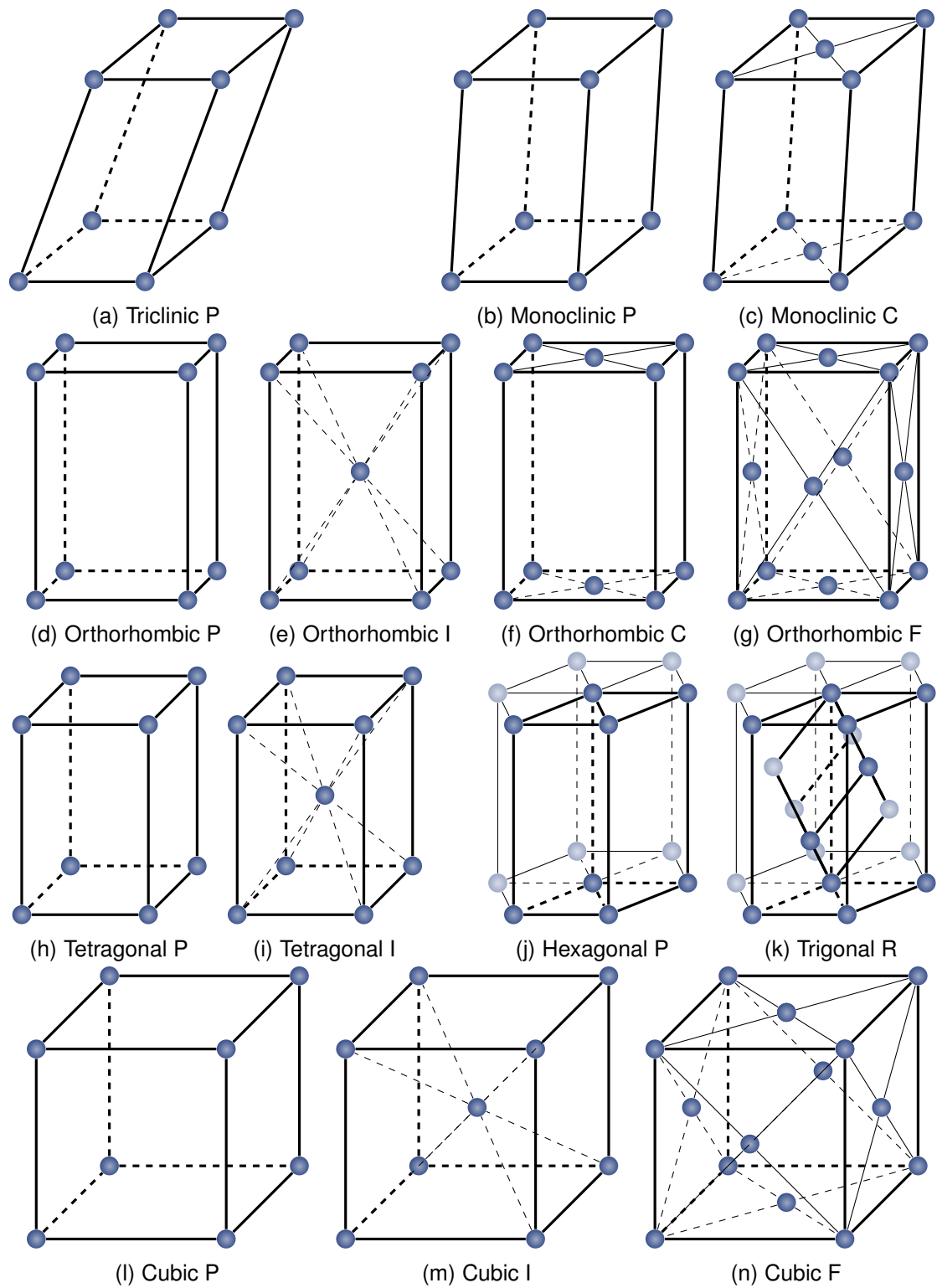


**Figure 132.** Crystal systems and Bravais lattices. Triclin:  $a \neq b \neq c$ ,  $\alpha \neq \beta \neq \gamma \neq 90^\circ, 120^\circ$ . Monoclin:  $a \neq b \neq c$ ,  $\alpha = \gamma = 90^\circ$ ,  $\beta \neq 90^\circ, 120^\circ$ . Orthorhombic:  $a \neq b \neq c$ ,  $\alpha = \beta = \gamma = 90^\circ$ . Tetragonal:  $a = b \neq c$ ,  $\alpha = \beta = \gamma = 90^\circ$ . Hexagonal:  $a = b \neq c$ ,  $\alpha = \beta = 90^\circ$ ,  $\gamma = 120^\circ$ . Trigonal:  $a = b = c$ ,  $\alpha = \beta = \gamma \neq 90^\circ, <120^\circ$ . Cubic:  $a = b = c$ ,  $\alpha = \beta = \gamma = 90^\circ$ . P: primitive, C: base-centered, I: body-centered, F: face-centered, R: rhombohedral.

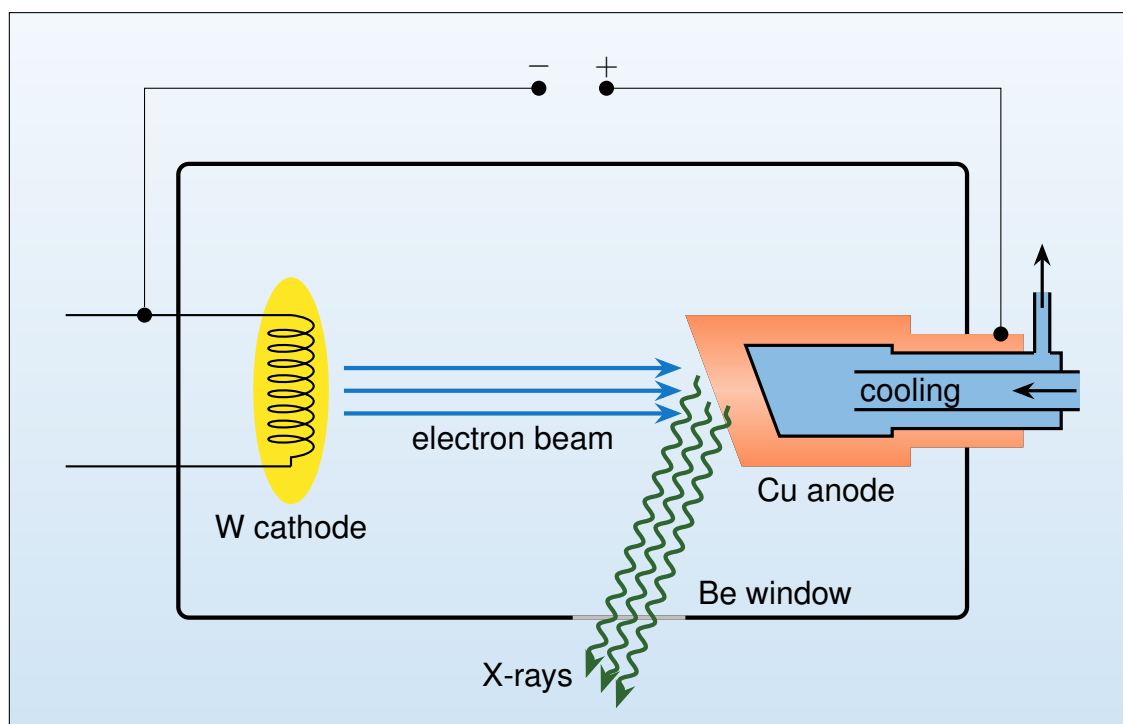


**Figure 133.** Schematic illustration of an x-ray source.

emitted electrons is directly proportional to the applied voltage. At small accelerating voltages the emitted electrons exhibit a spectrum of lower energies. When these hit the target material, they are strongly decelerated, resulting in the emission of x-ray quanta with a continuous distribution of energies and wavelengths ("white radiation"). However, at higher voltages the electron energies are sufficient enough to excite core electrons in the atoms of the target material, thereby creating holes in the lower energetic levels. These are immediately filled via the relaxation of an electron from higher energy levels, resulting in the emission of x-radiation of a precisely defined energy and wavelength characteristic of the material used for the target anode.

Two major contributions to the characteristic x-ray emissions stem from the relaxation of an electron from the L shell ( $n = 2$ ) to the K shell (principal quantum number  $n = 1$ ), and from the M shell ( $n = 3$ ) to the K shell, which are denoted as  $K_{\alpha}$  and  $K_{\beta}$ , respectively. Moreover, both  $K_{\alpha}$  and  $K_{\beta}$  are further split into two similar energies  $K_{\alpha 1}$  and  $K_{\alpha 2}$  (likewise,  $K_{\beta 1}$  and  $K_{\beta 2}$ ) due to the energy splitting in the L and M shells according to the azimuthal quantum number  $l = n - 1$  and the total angular momentum quantum number  $j = l \pm \frac{1}{2}$  (i.e.,  $j = \frac{1}{2}, \frac{3}{2}$  for  $l = 1$ ). The selection rule  $\Delta l = \pm 1$  applies. Thus, only electronic transitions from the  $l = 1$  energy levels in the L and M shells with only two possible  $j$  values are allowed to the K shell with  $l = 0$ , thereby giving rise to a fine splitting into two energies of the  $\alpha$  and  $\beta$  x-radiation.<sup>461</sup> For diffraction experiments, usage of monochromatic radiation is

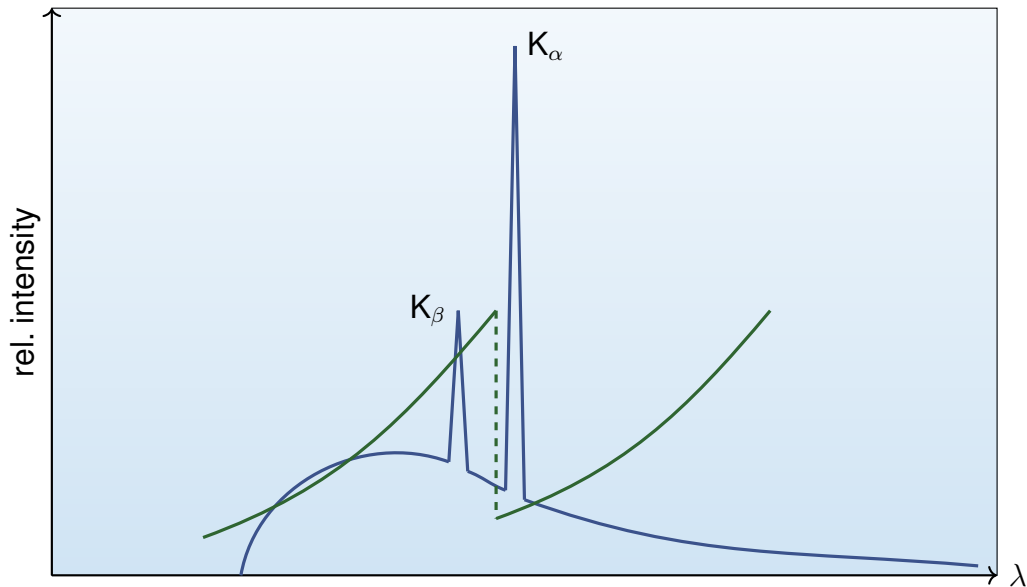


**Figure 134.** X-radiation spectrum for Cu. The green line indicates the absorption profile of Ni, with its absorption edge located between the  $K_{\alpha}$  and  $K_{\beta}$  lines indicated as a dashed green line.

mandatory (*vide infra*) and Ni foil is used to absorb most of the unwanted radiation from a Cu source. Ni fulfills two purposes: 1) it absorbs most of the white radiation due to the general absorption of x-radiation by all materials, and 2) at an energy between the  $K_{\alpha}$  and  $K_{\beta}$  lines of Cu, Ni exhibits an absorption edge due to the excitation and ejection of an electron from the Ni L shell, leading to a strong rise in absorption of the radiation which coincidentally diminishes the energies of the  $K_{\beta}$  rays to negligible values. Then, nearly monochromatic  $K_{\alpha}$  radiation (however, containing both  $K_{\alpha 1}$  and  $K_{\alpha 2}$ ) is obtained (Figure 134).<sup>460</sup>

### 10.3.2 Scattering at a Crystal - Bragg Conditions

During a scattering event of x-rays at a lattice with interplanar distances  $d$ , constructive interference can be observed only at specific incident angles  $\theta$  where the path difference  $\Delta$  between two scattered electromagnetic waves attains values of  $n\lambda$  ( $n = 1, 2, \dots$ ). According to Bragg's law, the following relationship is obtained for constructive interference (Figure 135):

$$2d \sin \theta = n\lambda \quad (10.1)$$

This shows that for every interplanar distance  $d$ , an angle  $\theta$  can be found which leads to constructive interference.  $d$  depends on the lattice parameters and the quadratic Bragg equation is used to calculate  $d^2$  based on the lattice parameters

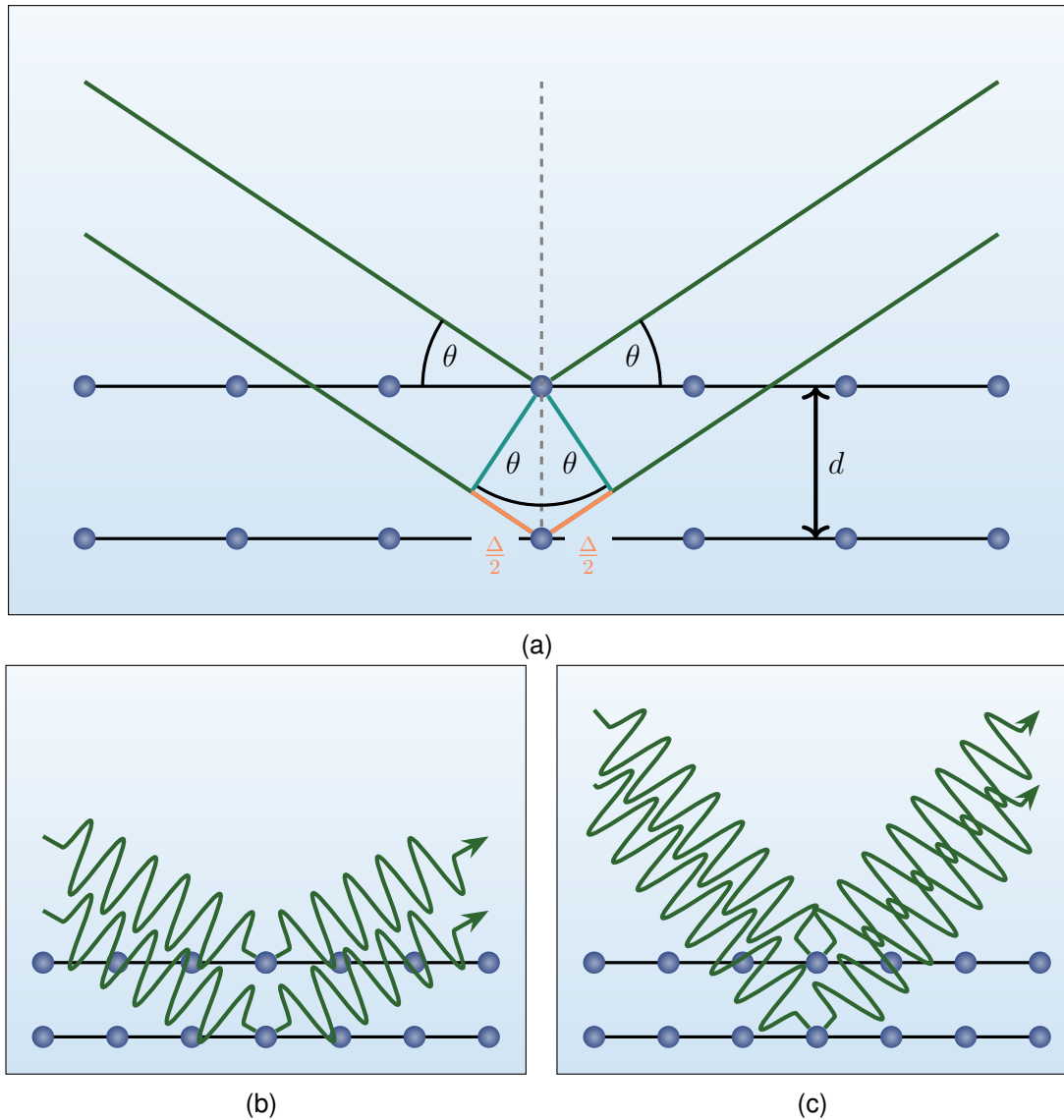


**Figure 135.** (a) Geometric illustration of Bragg's law. (b) Constructive interference. (c) Destructive interference.

and the  $h, k, l$  values or Miller indices (i.e., the intercepts of the crystallographic planes at  $\frac{1}{a}$ ,  $\frac{1}{b}$ , and  $\frac{1}{c}$ , respectively) as in

$$\sin^2 \theta = \frac{\lambda^2}{4} \times \frac{1}{d^2} \quad (10.2)$$

with  $\frac{1}{d^2}$  precisely defined for all seven crystal systems.<sup>461</sup>

### 10.3.3 Reciprocal Lattice and Ewald's Sphere

Reciprocal lattices are introduced to simplify the visualization and interpretation of diffraction patterns.<sup>460,461</sup> For instance, the infinite number of parallel crystal-

lographic planes described by the Miller indices  $(hkl)$  in the real space can be described by a single vector of length  $d^*$  (i.e., the interplanar distance) and aligned normal to the family planes. Generally, every point  $d^*$  in the reciprocal space can be described the reciprocal unit cell vectors  $a^*$ ,  $b^*$ , and  $c^*$ , which are normal to the  $bc$ ,  $ac$ , and  $ab$  planes, respectively. Thus, they are the vector products of the corresponding vectors in real space divided by the cell volume  $V$  to obtain reciprocal units in  $\text{\AA}^{-1}$ :

$$a^* = \frac{\vec{b} \times \vec{c}}{V} \quad (10.3)$$

$$b^* = \frac{\vec{a} \times \vec{c}}{V} \quad (10.4)$$

$$c^* = \frac{\vec{a} \times \vec{b}}{V} \quad (10.5)$$

From this follows that every point in the reciprocal space corresponds to a reflection with the Miller indices  $(hkl)$  (Figure 136). The orientation of the crystal determines the orientation of the reciprocal space. Angles  $\theta$  that lead to constructive interference can then be determined by construction of Ewald's sphere and the Bragg relationship

$$\sin \theta = \frac{d^*/2}{1/\lambda} \quad (10.6)$$

For instance, if a crystal at position  $K$  is irradiated with x-rays, then constructive interference will occur at an angle  $\theta$  where the phase difference of the scattered waves are a integer multiple of the used wavelength according to Bragg's law. Using Ewald's sphere and the reciprocal lattice, it is possible to assign the corresponding  $(hkl)$  family of planes to all angles  $\theta$  by rotation of the crystal, and hence, the reciprocal lattice, at a fixed point (the origin at 000) with respect to the x-ray beam. Constructive interference occurs when another point of the reciprocal lattice overlaps with Ewald's sphere; at this point,  $P$ , the Bragg condition for the  $P$  family of planes is fulfilled. An alternative interpretation is that the vector  $\vec{d}^*$  to a point  $P$  needs to lie on Ewald's sphere for constructive interference to occur (Figure 136).<sup>460,461</sup>

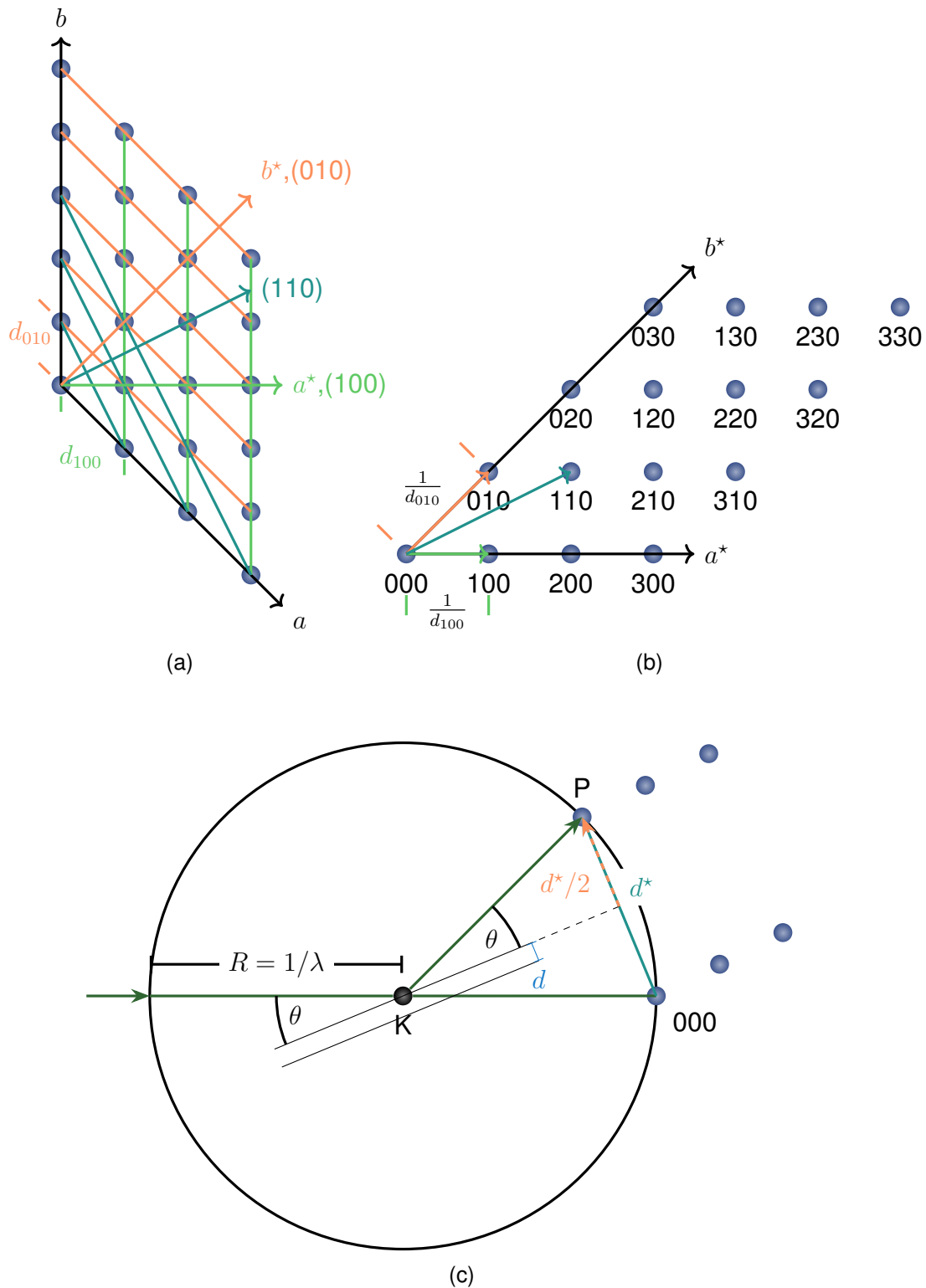


**Figure 136.** (a) Unit cell in real space. (b) Conversion of the real unit cell into the reciprocal unit cell. Each point in the reciprocal space corresponds to one family of planes in the real space.

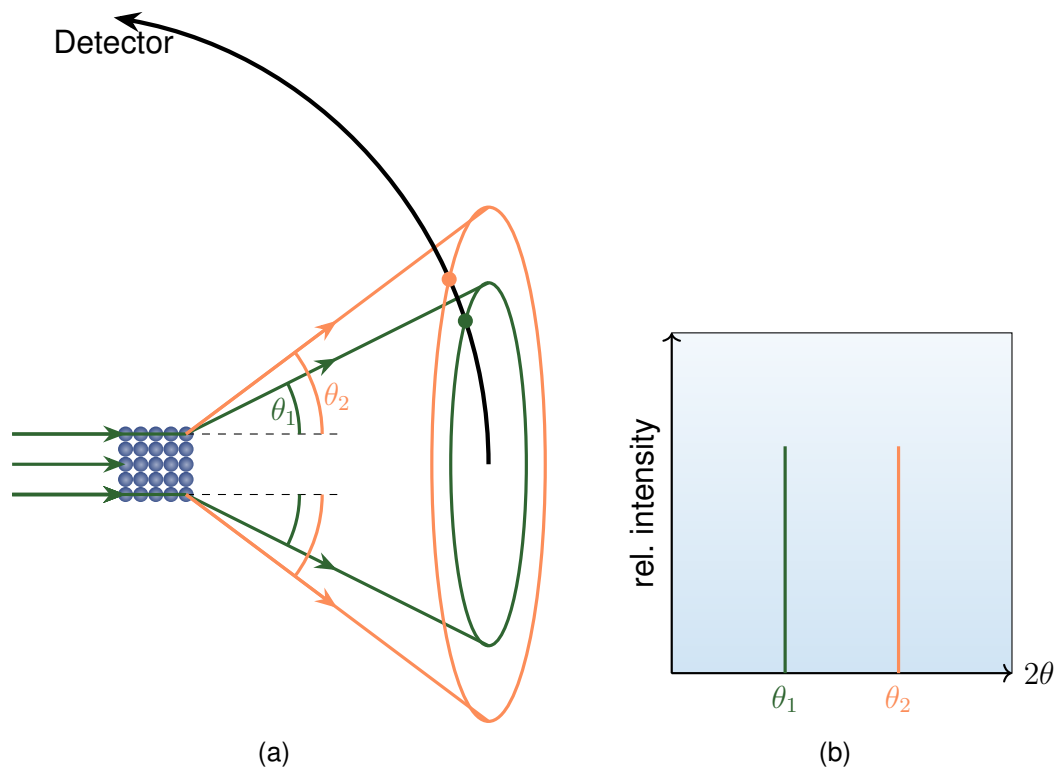


**Figure 137.** (a) Formation of diffraction cones from polycrystalline samples. (b) One-dimensional diffractogram obtained by scanning the  $2\theta$  diffraction range using a typical PXRD detector.

#### 10.3.4 Powder X-Ray Diffraction

A powder consists of many small crystallites that are randomly oriented with respect to the x-ray beam. Thus, a whole set of crystals will exhibit the correct orientation to allow diffraction of x-rays at the right angle  $\theta$ , thereby creating an entire ring of reflections at the detector plane consisting of the individual reflected x-rays for each crystallite. Typically, a line detector is used in PXRD to scan the  $2\theta$  range along one dimension, and diffracted x-rays are detected when the detector passes the diffraction cones (Debye-Scherrer rings), giving rise to a one-dimensional line diffractogram with contributions of the individual reflections (Figure 137).<sup>460,461</sup>





# 11

## *Gas Sorption*

### 11.1 INTRODUCTION

Gas sorption experiments are performed to analyze the porosity and surface of a material (adsorbent) at a constant temperature to obtain isotherms, i.e., the graphical relationship of the gas volumetric uptake of a material vs. the relative pressure  $p/p_0$  ( $p$ : equilibrium pressure,  $p_0$ : saturation vapor pressure of the probe gas (adsorptive) at the adsorption temperature). The interaction of gases with surfaces (adsorption) is an exothermic process though they can encompass a large magnitude of different interaction strengths, from weak electrostatic (van-der-Waals) interactions involved in physisorption to strong chemical bonds of species to surface atoms in chemisorption. While the latter is the preferred methodology when a surface is intended to be characterized with respect to its chemical reactivity (e.g., hydrogen under-potential deposition or carbon monoxide stripping to determine the electrochemically active surface area of platinum-based heterogeneous catalysts), physisorption of weakly interacting gases on surfaces is the commonly applied technique for the characterization of the whole surface. Advantages of physisorption are the low degree of specificity and directionality of the adsorption, which allow to probe the entire extent of the surface using different adsorptive gases, as well as the short equilibration times due to a low activation-energy barrier in this adsorption process. Gas molecules which are adsorbed on a surface are termed adsorbates.

Generally, it is useful to divide porous materials into three classes based on their pore dimensions: 1) microporosity describes pores  $< 2$  nm; 2) in mesoporous solids pore dimensions extend from 2–50 nm; and 3) macroporous materials exhibit pores with  $> 50$  nm size.

## 11.2 GENERAL EXPERIMENTAL PROCEDURE

For the experiment, porous samples are first degassed by applying a high vacuum at elevated temperatures to remove all adsorbed species on the surface of the material. Typically, the surface area is determined via manometric methods at constant, cryogenic temperature (e.g., 77 K for nitrogen gas, 87 K for argon). A defined amount of adsorptive is introduced to a confined and calibrated tube of known volume which contains a precisely weighed amount of adsorbent. Successive doses of gas are admitted to the measurement cell and the pressure change within the cell is detected; the pressure drops during the adsorption process until equilibrium is reached. With this, the adsorbed amount of gas is calculated as the difference between the dosed in gas and the amount of gas required to fill the dead space (the space around the adsorbent).<sup>465</sup>

## 11.3 SORPTION ISOTHERMS

The shape and dimensions of the pores can affect the behavior of adsorptives during the adsorption and desorption (reverse process), and six characteristic types of sorption isotherms are observed (Figure 138). For all pore types, a monolayer of adsorbate over the whole surface is first formed at low relative pressures, followed by pore filling. Type I isotherms are indicative of microporous materials where a steep increase in volumetric uptake to form a monolayer of adsorbate on the inner surface of the porous material is observed.<sup>466</sup> A distinction can be made between micropores in the dimensions of the adsorptive gas ( $< 1$  nm, Figure 138a) and those whose dimensions are somewhat larger than the kinetic diameter of the adsorptive ( $< 2.5$  nm, Figure 138b) based on the slope of the isotherm in the low relative pressure region. At the same time the micropores are filled with gas and a plateau in the volumetric uptake in the gas sorption isotherm is observed. Type II isotherms are indicative of monolayer formation on the inner surface of the porous material with subsequent multilayer formation according to the steep increase of the volumetric uptake at high relative pressures (Figure 138c). In type III isotherms adsorption occurs at higher relative pressures (Figure 138d). Both isotherm types are typically observed for nonporous or macroporous powders, but type II shows no limit in adsorption at relative pressures of  $p/p_0 = 1$ .<sup>465</sup> Another difference between type II and type III is that the heats of adsorption are less than the adsorbate heat of liquefaction in the latter, meaning that the adsorptive

---

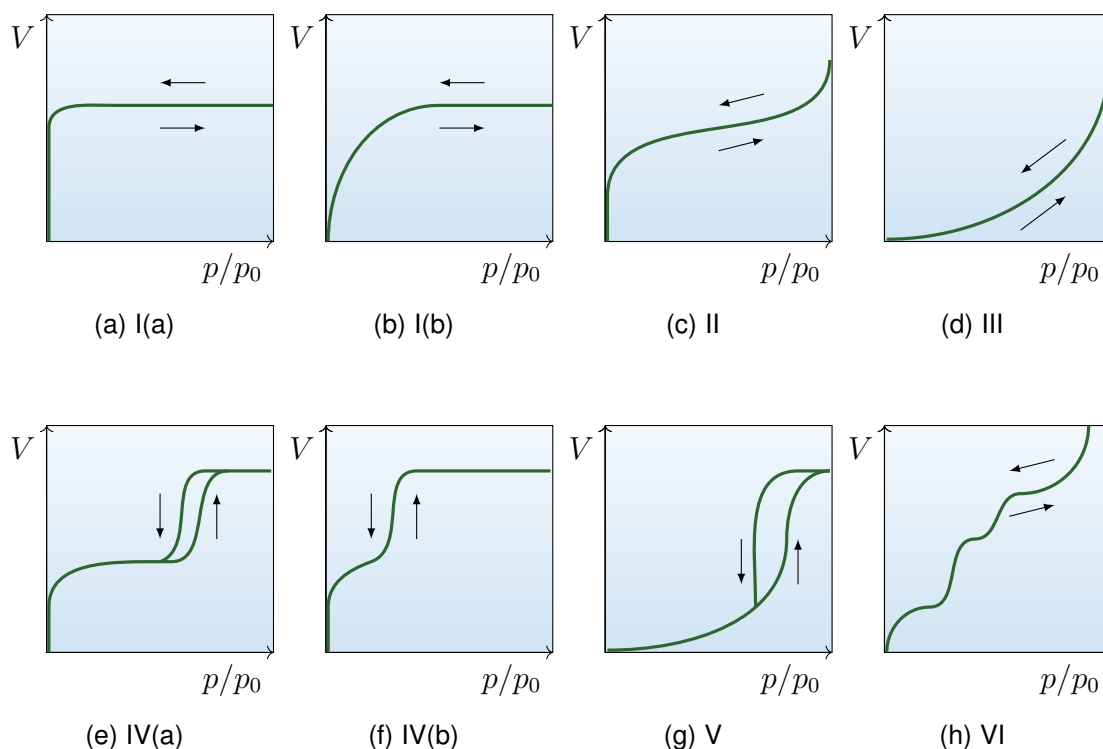


**Figure 138.** Isotherm types (volumetric uptake vs. relative pressure).

interacts preferably with an adsorbate layer rather than the adsorbent.<sup>467</sup> Mesoporous materials exhibit isotherm types IV and V and are influenced by adsorption phenomena and condensation of the adsorptive in the pores at lower relative pressures. Type IV isotherms resemble those of type II where monolayer coverage is achieved first until pore condensation occurs, giving rise to another steep increase in volumetric gas uptake at a specific relative pressure. Depending on the pore size, a hysteresis can be observed for mesopores  $> 4$  nm (Figure 138e), whereas a completely reversible isotherm is observed for pore sizes  $< 4$  nm (Figure 138f).<sup>465</sup> Type V isotherms resemble those of type III and are defined by a weak adsorbate-adsorbent interaction with subsequent pore condensation. Type VI is representative for layer-by-layer adsorption on nonporous solids.<sup>465</sup>

## 11.4 HYSTERESIS

Hysteresis is a result of the capillary condensation of gas in the pores. Unlike the adsorption branch, the desorption process can be described as a liquid-vapor transition of a system that is thermodynamically equilibrated.<sup>465</sup> The shape of the observed hysteresis loop allows to make statements about the pore geometry, connectivity, and size distribution found in the studied material. The most common

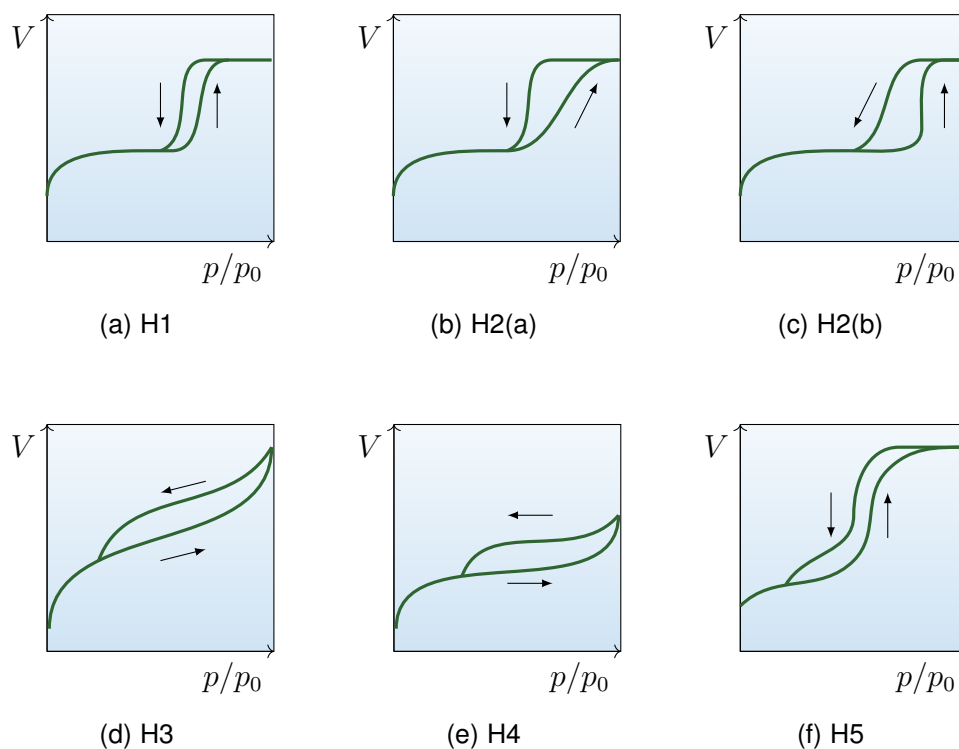


**Figure 139.** Hysteresis loops (volumetric uptake vs. relative pressure).

types of hysteresis loops are shown below (Figure 139). Type H1 loops are caused by materials with a narrow range of uniform, cylindrical mesopores with minimal network effects (Figure 139a). Type H2 loops are formed when network effects become important, with the distinction between pore-blocking at narrow pore necks (Figure 139b) and wide pore neck distributions (Figure 139c). Types H3 (Figure 139d) and H4 (Figure 139e) originate in non-rigid aggregates of plate-like particles and if the network consists of macropores are not completely filled with pore condensate and have an underlying type II or type I isotherm for H3 and H4 loops, respectively. H5 loops are consistent with structures containing both open and blocked mesopores (Figure 139f).<sup>465</sup>

## 11.5 BET MODEL AND SURFACE AREA DETERMINATION

The BET model describes the process of adsorption of gases on a surface on a microscopic level as well as the formation of multilayer adsorbates and allows the determination of a BET equivalent surface area of a porous material. It is based on the assumption that with increasing relative pressure more energetic adsorption centers (e.g., surfaces within small pores where the two Lennard-Jones potentials of each pore walls overlap, atoms with fewer surrounding atoms at surface edges)

are more likely to interact with the adsorptive to form an adsorbate layer. As the surface is increasingly covered with an adsorbate layer the probability increases that another layer forms on top of the first one despite of the incomplete coverage of the surface to form the first monolayer. Likewise, a third monolayer is more likely to form on top of a second one at a certain degree of coverage of the first monolayer with a second monolayer, respectively. Moreover, the highest layer is in a dynamic equilibrium with the vapor.<sup>467</sup>

The number of molecules  $\mathcal{N}$  which contact a square centimeter of surface per second is given as:

$$\mathcal{N} = \frac{\bar{N}p}{(2\pi\bar{M}RT)^{\frac{1}{2}}} = kp \quad (11.1)$$

where  $\bar{N}$  is Avogadro's constant,  $p$  and  $\bar{M}$  are the adsorbate pressure and molecular weight, respectively,  $R$  is the gas constant,  $T$  the temperature, and  $k$  the term containing all constants in equation 11.1. The number of contacts with uncovered surface atoms is

$$\mathcal{N}' = kp\theta_0 \quad (11.2)$$

where  $\theta_0$  is the fraction of surface atoms with no adsorbate layer on top of it. The number of contacts of the probe gas with uncovered atoms which then adsorb on the surface is

$$\mathcal{N}_{ads} = kp\theta_0 A_1 \quad (11.3)$$

where  $A_1$  is the condensation coefficient describing the probability of a molecule to adsorb on a surface after a contact. On the other hand, the number of adsorbed atoms desorbing from the surface is

$$\mathcal{N}_{des} = N_m \theta_1 \nu_1 e^{-\frac{E}{RT}} \quad (11.4)$$

where  $N_m$  is the number of adsorbed molecules of a completed monolayer,  $\theta_1$  is the fraction of the occupied surface,  $E$  is the energy of adsorption, and  $\nu_1$  is the vibrational frequency of the adsorbate. When the system is in equilibrium, the rates of adsorption (equation 11.3) and desorption (equation 11.4) are equal, leading to

$$N_m \theta_1 \nu_1 e^{-\frac{E}{RT}} = kp \theta_0 A_1. \quad (11.5)$$

$\theta_0 = 1 - \theta_1$ , so

$$N_m \theta_1 \nu_1 e^{-\frac{E}{RT}} = kp A_1 - kp \theta_1 A_1. \quad (11.6)$$

Rearrangement for  $\theta_1$  gives

$$\theta_1 = \frac{kp A_1}{N_m \nu_1 e^{-\frac{E}{RT}} + kp A_1}. \quad (11.7)$$

If

$$K = \frac{k A_1}{N_m \nu_1 e^{-\frac{E}{RT}}}, \quad (11.8)$$

then equation 11.7 is reduced to

$$\theta_1 = \frac{Kp}{1 + Kp}. \quad (11.9)$$

$\theta_1$  can be also described as

$$\theta_1 = \frac{N}{N_m} = \frac{W}{W_m} \quad (11.10)$$

where  $N$  and  $N_m$  are the number of molecules in the incomplete and complete monolayer, respectively, and  $W$  and  $W_m$  their corresponding weight. Equation (11.10) describes the Langmuir (type I) isotherm for a monolayer coverage of a surface. In the BET model, multiple layers can be formed, and the first layer can be described by equation 11.5

$$N_m \theta_1 \nu_1 e^{-\frac{E}{RT}} = kp \theta_0 A_1. \quad (11.11)$$

For the formation of  $n$  layers this gives

$$N_m \theta_n \nu_n e^{-\frac{E}{RT}} = kp \theta_{n-1} A_n. \quad (11.12)$$

All layers except the first one are considered to have the same values for  $\nu$ ,  $E$ , and  $A$ , so

$$N_m \theta_n \nu e^{-\frac{L}{RT}} = kp \theta_{n-1} A, \quad n > 1. \quad (11.13)$$

From this follows

$$\frac{\theta_1}{\theta_0} = \frac{kpA_1}{N_m \nu_1 e^{-\frac{E_1}{RT}}} = \alpha \quad (11.14)$$

and

$$\frac{\theta_n}{\theta_{n-1}} = \frac{kpA}{N_m \nu e^{-\frac{L}{RT}}} = \beta, \quad n > 1 \quad (11.15)$$

and

$$\theta_1 = \alpha \theta_0 \quad (11.16)$$

$$\theta_n = \beta \theta_{n-1} = \alpha \beta^{n-1} \theta_0 \quad (11.17)$$

At equilibrium the total number of adsorbed molecules is

$$N = N_m (\theta_1 + \dots + n \theta_n) \quad (11.18)$$

or

$$\frac{N}{N_m} = \alpha \theta_0 (1 + \dots + n \beta^{n-1}). \quad (11.19)$$

If

$$\alpha = C \beta \quad (11.20)$$

and

---

$$\frac{A_1\nu_2}{A_2\nu_1} e^{\frac{E_1-L}{RT}} = C \quad (11.21)$$

then

$$\frac{N}{N_m} = C\theta_0(\beta + \dots + n\beta^n). \quad (11.22)$$

After several other mathematical rearrangement, the following equation is obtained

$$\frac{N}{N_m} = \frac{C\beta}{(1-\beta)(1-\beta+C\beta)} \quad (11.23)$$

$\beta$  turns out to be the relative pressure  $p/p_0$ , so

$$\frac{N}{N_m} = \frac{C(p/p_0)}{(1-(p/p_0))(1-(p/p_0)+C(p/p_0))} = \frac{W}{W_m} \quad (11.24)$$

Rearrangement of equation 11.24 yields the BET equation in its final form:

$$\frac{1}{W[(p_0/p)-1]} = \frac{1}{W_m C} + \frac{C-1}{W_m C} (p/p_0) \quad (11.25)$$

Plotting  $\frac{1}{W[(p_0/p)-1]}$  vs  $p/p_0$  according to equation 11.25 gives a straight line (usually in the relative pressure regime  $0.05 < p/p_0 < 0.35$ ) and allows the determination of the weight of the adsorbed monolayer,  $W_m$  (Figure 140).

$W_m$  can be calculated using

$$W_m = \frac{1}{s+i}, \quad \text{with } s = \frac{C-1}{W_m C}, \quad i = \frac{1}{W_m C} \quad (11.26)$$

$C$  is the BET constant and calculated using

$$C = \frac{s}{i} + 1 \quad (11.27)$$

Finally, the specific surface area  $\mathcal{S}$  is calculated by

$$\mathcal{S} = \frac{W_m \bar{N} \mathcal{A}}{Mm} \quad (11.28)$$



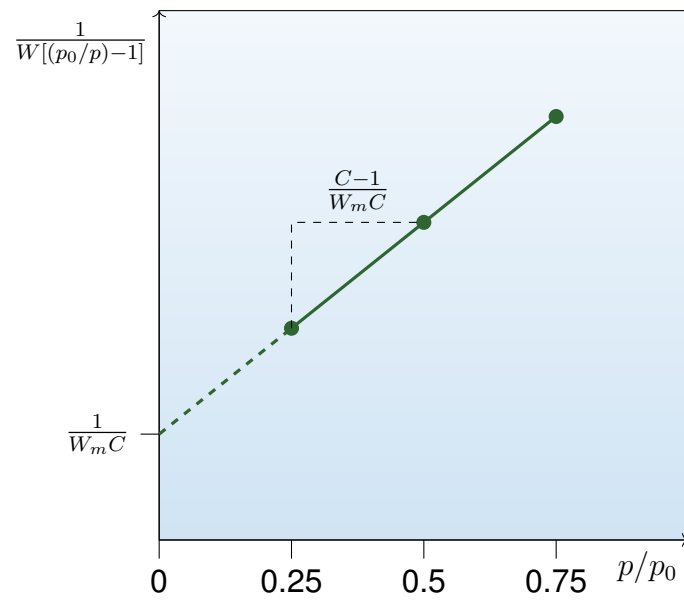


**Figure 140.** Schematic illustration of a BET plot.

where  $\mathcal{A}$  is the cross-section area and  $m$  is the weight of the sample.



# 12

## *Vibrational Spectroscopy*

### 12.1 INTRODUCTION

Vibrational spectroscopy is a field of study which describes the interaction of electromagnetic radiation with vibrations of chemical bonds. It allows the identification and quantification of the bond nature, strength, and presence of chemical functional groups by a characteristic location and intensity of a signal in the vibrational spectrum.<sup>429,431,468,469</sup> The most commonly employed techniques for obtaining vibrational spectra are infrared and Raman spectroscopy, which are complimentary techniques to obtain information about molecular vibrations in solids, liquids, and gases. Both spectra are a function of the absorbance vs. the frequency of the light given in reciprocal centimeters ( $\text{cm}^{-1}$ ) and yield similar chemical information, although they rely on different physical interaction mechanisms of the used light with the probed molecules.

### 12.2 MOLECULAR VIBRATIONS

Molecules consist of a specific arrangement of  $N$  atoms with element-specific mass which are connected by covalent or coordination bonds. Each atom has three (translational) degrees of freedom, and a molecule with  $N$  atoms has  $3N$  degrees of freedom. Again, three account for the translational, and another three for the rotational modes (for linear molecules, only two rotational modes exist). Thus,  $3N-6$  (or  $3N-5$ ) vibrational modes remain, which describe changes of the respective atom positions relative to each other. Specifically, different types

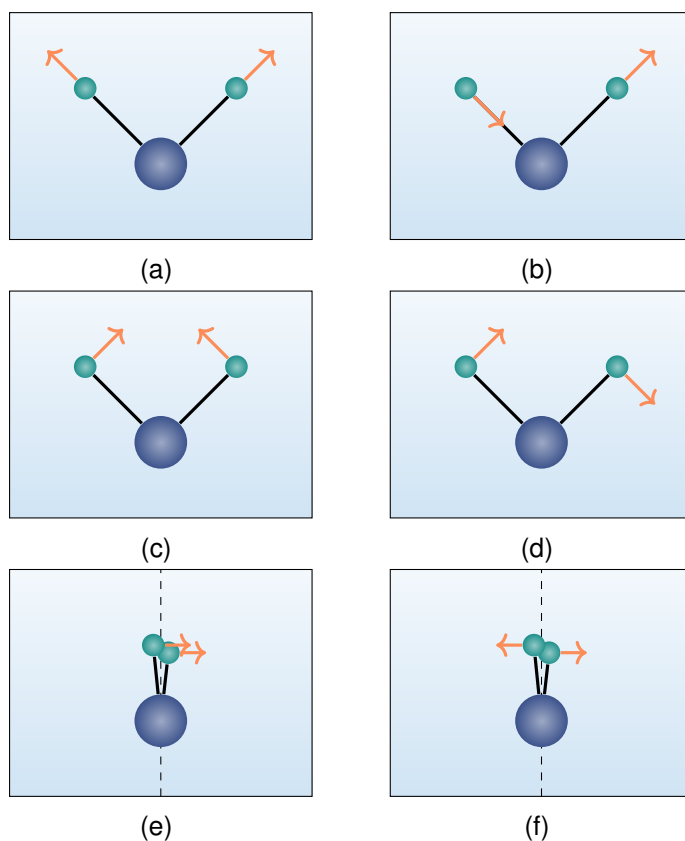


**Figure 141.** Vibrational modes: (a) symmetric stretching; (b) asymmetric stretching, (c) scissoring, (d) rocking, (e) wagging (out of plane), (f) twisting (out of plane).

of vibrations can change the bond distances and angles between two atoms: radial modes are the symmetric and asymmetric stretching, latitudinal modes are in plane bending modes such as scissoring and rocking, and longitudinal modes are the corresponding out of plane bending modes, wagging and twisting. (Figure 141).<sup>468</sup> Bonds can be classically described as two masses connected to each other via a spring with the force constant  $f$  (Figure 142a).<sup>468–470</sup> The force  $F$  needed to stretch the spring along a distance  $x$  is described by Hooke's law as

$$F = -f \times x \quad (12.1)$$

At the same time, the force can be described by applying Newton's law

$$F = m \times a = m \frac{d^2x}{dt^2} \quad (12.2)$$

where  $m$  is the mass. Combining and solving the differential equation gives

$$f = 4\pi^2\nu^2m \quad \text{or} \quad \nu = \frac{1}{2\pi} \sqrt{\frac{f}{m}} \quad (12.3)$$

where  $\nu$  is the vibrational frequency in [Hz]. In the diatomic case, the reduced mass needs to be considered according to

$$\frac{1}{m} = \frac{1}{m_1} + \frac{1}{m_2} \quad (12.4)$$

In addition,  $\nu$  needs to be divided by the vacuum speed of light,  $c$ , to obtain frequencies in the typical unit [ $\text{cm}^{-1}$ ]. Thus,

$$\tilde{\nu} = \frac{1}{2\pi c} \sqrt{f \left( \frac{1}{m_1} + \frac{1}{m_2} \right)}. \quad (12.5)$$

Integration of the force  $F$  over the distance  $x$  in equation 12.1 gives the harmonic potential energy of the vibration (Figure 142b)

$$E = \int f x dx = \frac{1}{2} f x^2. \quad (12.6)$$

However, real bonds cannot be infinitely stretched or compressed and compression is more energy-intensive than stretching which would lead eventually to bond dissociation. Therefore, a more correct description of the potential energy of a bond is the anharmonic Morse potential as in

$$E = D \left[ 1 - \exp \left( -\sqrt{f_e/2D} \times x \right) \right]^2 \quad (12.7)$$

where  $D$  is the bond dissociation energy and  $f_e$  the bond force constant at the potential minimum (Figure 142c).

According to quantum mechanics, vibrations are quantized into a ground and excited states.<sup>468,469</sup> For a harmonic potential, there are infinite vibrational states according to

$$E_i = h\nu \left( \nu_i + \frac{1}{2} \right) \quad (12.8)$$

where  $\nu_i = 0$  corresponds to the energetic ground state  $E_0 = \frac{1}{2}h\nu$ , while the number of vibrational states in the real anharmonic potential is limited by the bond dissociation energy  $D$ . Nevertheless, the harmonic potential is a good approximation for excitations from the ground state to the first excited state, which are the typically observed and most intense bands in vibrational spectra.

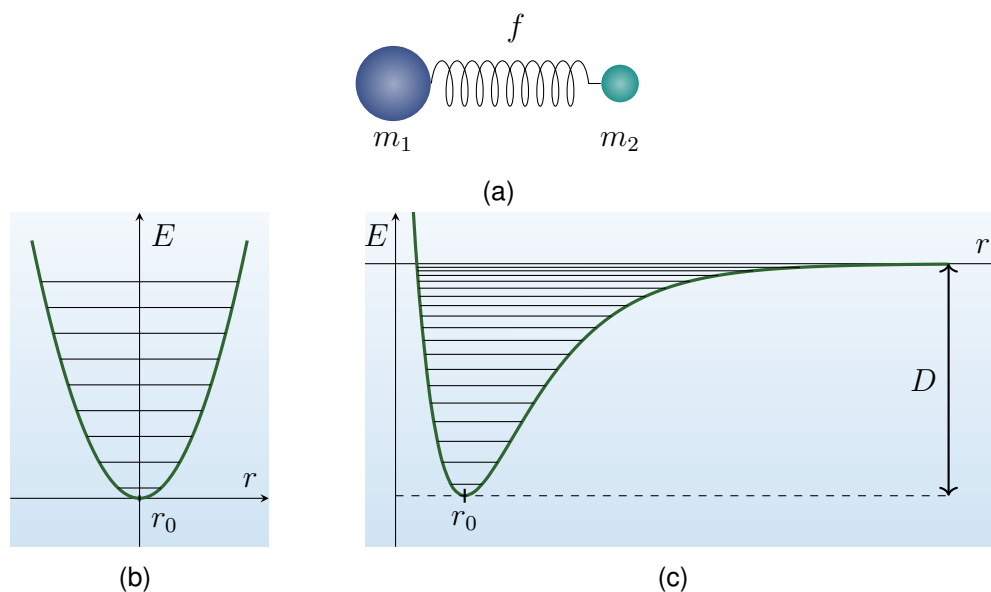


**Figure 142.** (a) Model for a chemical bond. (b) Harmonic potential energy of a bond with an equilibrium distance  $r_0$  and energetically equidistant vibrational states of the energy increment  $E_i = h\nu(0.5 + \nu_i)$ . (c) Anharmonic (Morse) potential with an equilibrium distance  $r_0$ , finite vibrational states and bond dissociation energy  $D$ .

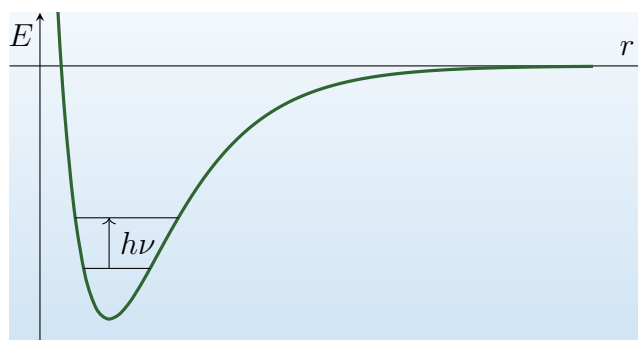


**Figure 143.** Model for an excitation of a vibration from the ground state to the first excited state using infrared light.

## 12.3 INFRARED SPECTROSCOPY

In infrared spectroscopy, a sample is irradiated with a spectrum of infrared light in the mid-infrared region ( $\tilde{\nu} = 4000\text{--}400\text{ cm}^{-1}$ ) which absorbs light with matching frequency for molecular vibrational excitations, typically from the ground state to the first excited state. Importantly, only certain vibrations are infrared active (i.e., will absorb infrared light), depending on the molecular electric dipole moment,  $\mu$ , of the vibration of interest. If the dynamic electric dipole moment (i.e., the polarity of the bond) is modulated by the vibration, then absorption of infrared light is possible and the absorption will become visible in the spectrum. If the dipole moment is not affected by the vibration, no absorption will occur and the band will remain invisible in the infrared spectrum (Figure 143).<sup>468,469</sup>

## 12.4 RAMAN SPECTROSCOPY

Raman spectroscopy takes advantage of the scattering of light at molecules. More accurately, the Raman effect is the inelastic scattering of light quanta with an energy much larger than those of molecular vibrations (usually in the visible region). When a sample is irradiated with a monochromatic light source (e.g., laser), the light can be either elastically scattered with no change in energy (Rayleigh scattering), or inelastically scattered and the change in energy corresponds to that of the excitation energy of the molecular vibration. Thus, in the first case, the molecule located in its vibrational ground state is excited to a virtual state and relaxes back into the ground state. The scattered light quantum  $h\nu_0$  is of the same energy as before the scattering event. In the second case, a relaxation from the virtual state into the first vibrational excited state results in an inelastically scattered light quantum of reduced energy  $h\nu_R = h\nu_0 - h\nu$  (Stokes shift). A third possible event is the excitation of a vibration in its first excited state to the virtual state followed by a relaxation to the vibrational ground state, where the scattered light quanta have increased energy  $h\nu_R = h\nu_0 + h\nu$  (Anti-Stokes shift); however, this event is less likely due to a lower amount of vibrations in the excited state compared to the ground state. Unlike the previous the case, the selection rule in Raman spectroscopy is not related to the electric dipole moment, but the polarizability (i.e., the extent of an induced dipole moment in a molecule in an electric field) of a vibration. Vibrations are only Raman active when the vibrations modulates the polarizability of the same; otherwise, they are inactive (Figure 144).<sup>468,469</sup>

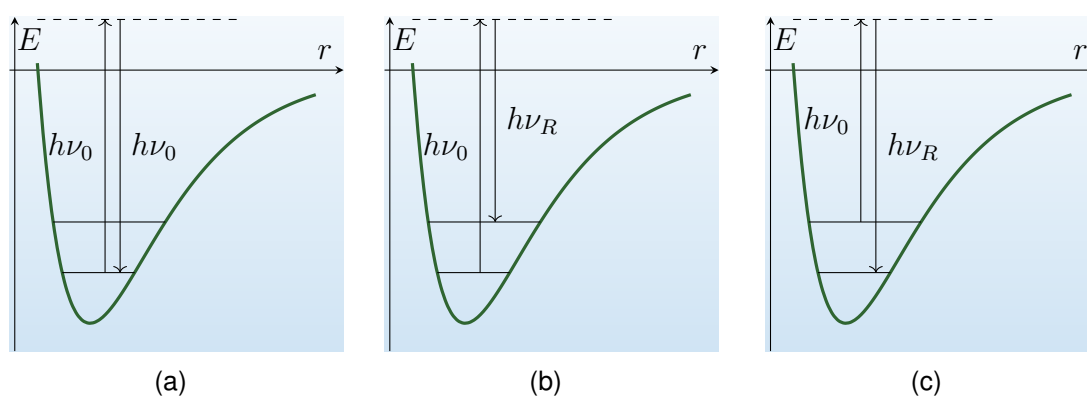


**Figure 144.** (a) Elastic (Rayleigh) scattering; Raman effect: (b) Inelastic (Stokes) scattering. (c) Inelastic (Anti-Stokes) scattering.





# 13

## *Electron Microscopy*

### 13.1 INTRODUCTION

Electron microscopy is an extremely versatile analytical field that goes beyond simply imaging objects which are too small to be studied by "conventional" visible-light microscopy, although that in itself is a powerful tool to gain insight into the topography, internal structure, (local) chemical composition and elemental distribution of solid materials in both qualitative and quantitative manners with (near) atomic resolution.<sup>471–473</sup> This is due to the fact that high-energy electrons accelerated by voltages of tens or hundreds of kV that can penetrate microns into a material are used to probe samples in the electron microscope, giving rise to corresponding de Broglie wavelengths of the incident electrons in the pm regime (*cf.* wave-particle dualism of electron, chapter 9). Hence, high-energy electrons are suitable for resolving distances in the atomic regime in comparison to visible light, which contains wavelengths from 400–700 nm. Many spectroscopic techniques are coupled to an electron microscope and take advantage of the interactions of electrons with solid materials to give information about specific material properties, which are outside the scope of this introduction. Moreover, the possibility of using electron diffraction at crystalline specimens for crystal structure determination is promising for the study of new materials which do not easily yield large single crystals suitable for XRD but will not be discussed here, either. Several types of electron microscopy exist which fundamentally differ in which kind of electrons are detected after being scattered by the specimen atoms and if the images are recorded statically or dynamically. For example, whereas in transmission electron microscopy (TEM) a fixed electron beam is used to illuminate a wider range of the sample and forward-scattered electrons are detected to form two-dimensional

"shadow projection" images of the three-dimensional sample, the SEM makes use of high-energy back-scattered electrons (BSEs) coming from the incident electron beam, or low-energy secondary electrons (SE) emitted from the sample after electron bombardment to form images with a three-dimensional appearance. In contrast to the fixed and relatively broad electron beam in TEM, SEM uses a sharply focused electron beam which is swept over the specimen surface point for point in a raster which is then combined to a final image. Finally, a STEM is a TEM instrument which uses the scanning operation mode from SEM. The following sections will outline the general interaction of electrons with specimen atoms and the nature of the signal detected in an electron microscope, the general setup and working principle of the instrument, as well as differences between TEM, SEM, and STEM.<sup>471–473</sup>

## 13.2 ELECTRON SCATTERING

Imaging small objects with electrons is based on the scattering of electrons coming from an incident beam due to Coulomb (electrostatic) interactions with positively charged atomic nuclei and negatively charged atomic electrons that exert an attractive or repulsive force on the incident electrons, respectively. This force is described by Coulomb's law as:

$$F = \frac{1}{4\pi\epsilon_0} \frac{q_1 q_2}{r^2} \quad (13.1)$$

where  $\epsilon_0$  is the electric constant,  $q_1$  and  $q_2$  are the charges of the involved particles and  $r$  is the distance between them.<sup>431</sup> Thus,  $q_1$  and  $q_2$  are both the elemental charge  $e$  for an electron-electron couple, and  $e$  and  $Ze$  for an electron-nucleus couple ( $Z$  as the atomic number of the element). An important characteristic of this scattering process is the deflection angle  $\theta$  with which the incident electron (primary) is deflected by an atomic nucleus or electron from its original trajectory (Fig. 145). Forward scattering occurs for  $\theta < 90^\circ$ , backscattering for  $\theta > 90^\circ$  (either via strong interaction with the nucleus or an atomic electron, or consecutive interactions which redirect the electron back).<sup>471,472</sup>

The probability of a scattering event at a single atom is influenced by its interaction cross section,  $\sigma$  (i.e., an effective area surrounding the atom in which scattering is possible, with the unit  $\text{m}^2$ ). For a single atom, this is:

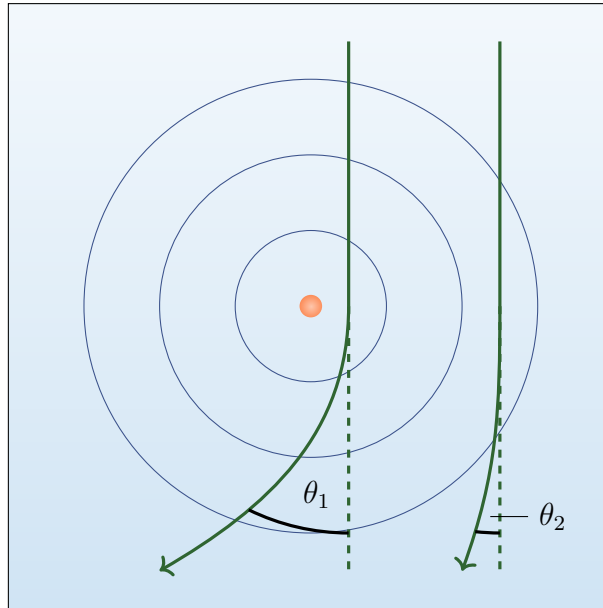


**Figure 145.** Scattering process of a primary electron (trajectory indicated in green) by atomic nucleus (surrounded by electron shells according to the Bohr atom model). The electric field is stronger closer to the nucleus, so the deflection angle  $\theta_1$  is greater for an electron passing closer to the nucleus than for one passing further away at an angle  $\theta_2$ .

$$\sigma_{atom} = \pi r_{eff}^2, \quad [\sigma_{atom}] = \text{m}^2 \quad (13.2)$$

where  $r_{eff}$  is the effective atomic radius. Thus, in a solid containing  $N$  atoms, the total cross section  $\sigma_{total}$  is the  $N$ -fold multiple of  $\sigma_{atom}$ . However, it is more intuitive to define the cross section in terms of scattering events per distance, so the number of atoms  $N$  per unit volume of solid is used:

$$\sigma_{total} = N\sigma_{atom} = \frac{N_0\delta}{Au}\sigma_{atom}, \quad [\sigma_{total}] = \text{m}^{-1} \quad (13.3)$$

$N$  can be described as the product of the Avogadro constant  $N_0$  and the density  $\delta$  of the solid, divided by the atomic mass number  $A$  and atomic mass unit  $u$ . Thus, large values of  $\sigma_{total}$  mean many scattering events occur per distance of the electron traveling through the solid and the corresponding scattering probability is high. The opposite is true for small values of  $\sigma_{total}$ , leading to a small scattering probability. Furthermore, by taking the thickness  $t$  of the sample into account, a dimensionless quantity  $P$  corresponding to the scattering probability is obtained:

$$P = \sigma_{total}t = \frac{N_0\delta t}{Au}\sigma_{atom} \quad (13.4)$$

where the term  $\delta t$  is called the mass-thickness of the specimen. This equation emphasizes the dependence of the scattering probability on the mass (i.e., the atomic number of the atoms involved in the scattering process) and the thickness of the specimen: electrons are scattered more strongly by thicker regions and those containing heavier atoms than vice versa. The inverse of  $\sigma_{total}$  with the unit m is the distance an electron can travel before it gets scattered, also known as the mean-free path of the electron.<sup>471,472</sup>

### 13.2.1 Elastic scattering

A distinction can be made between electron scattering in which no (measurable) energy transfer occurs during the process (elastic scattering) or if an energy transfer is involved (inelastic scattering). This can be calculated using

$$\frac{E}{E_0} = \frac{m_e}{m_N} \left[ 1 + \frac{v^2}{v_0^2} - 2 \left( \frac{v}{v_0} \right) \cos \theta \right] \quad (13.5)$$

where  $E_0$  and  $E$  are the energies of the electron, and  $v_0$  and  $v$  the electron velocities before and after the scattering event, respectively, and  $m_e$  and  $m_N$  are the masses of the electron and the nucleus, respectively (or more generally, the masses of the two particles involved in the scattering process).<sup>471</sup> Because of the huge differences in mass between the atomic nucleus and an electron, only a negligible fraction of energy is transferred from the incoming electron to the nucleus, and this interaction is mainly elastic. In contrast, the electron-electron interaction is much more likely to be an inelastic process due to the resulting independence of mass (they are equal). Elastically scattered electrons are mainly of interest in TEM where electrons are detected that transmit the sample; hence, it is the electron-nucleus interaction that mainly influences the resulting contrast (i.e., the difference in brightness of two points in the image) in TEM images. This interaction is determined by the Rutherford cross section:

$$\sigma_R(\theta) = \frac{e^4 Z^2}{16(4\pi\epsilon_0 E_0)^2} \frac{d\Omega}{\sin^4(\theta/2)} \quad (13.6)$$

where  $E_0$  is the beam energy,  $\theta$  is the deflection semi-angle, and  $d\Omega$  is the solid-angle (in three dimensions).<sup>472</sup> Several conclusions can be drawn from this equation: 1) the scattering is highly angle-dependent and is most likely for forward scattering ( $\theta = 0^\circ$ ), 2) the cross-section is proportional to  $Z^2$ ; thus, scattering is stronger at heavier atoms and in return the mean-free path  $\lambda$  is greater in

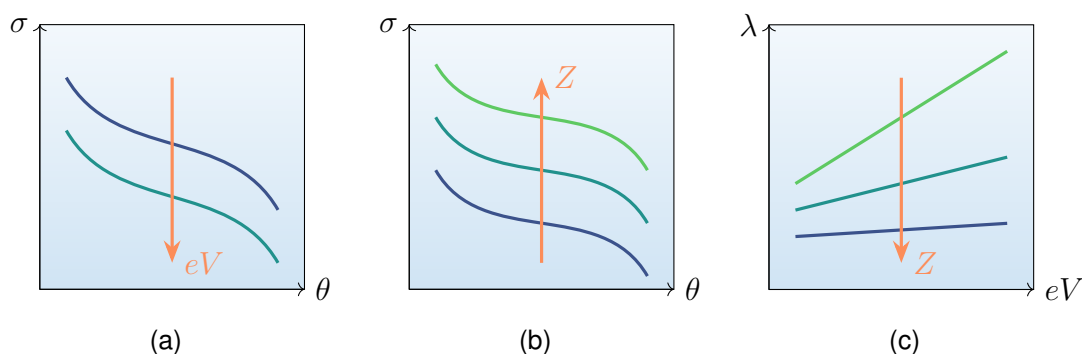


**Figure 146.** Relationship of (a) cross section  $\sigma$  and scattering angle  $\theta$  with varying beam energy  $eV$ , increasing beam energies decrease cross sections, (b)  $\sigma$  and  $\theta$  with varying atomic number  $Z$ , increasing  $Z$  increases  $\sigma$ , (c) the mean-free path  $\lambda$  and beam energy  $eV$  with varying  $Z$ ,  $\lambda$  decreases with increasing  $Z$ .

low- $Z$  specimens, and 3) it is inversely proportional to  $E_0^2$ , so high-energy electrons are less likely to be scattered compared to electrons with lower energy (Fig. 146).<sup>471,472</sup> In TEM, apertures are used to permit the collection of only a certain fraction of scattered electrons which are scattered by a specific range of scattering angles  $\theta_1 - \theta_2$ ; electrons scattered with an angle below or above this range are absorbed by the walls of the aperture. This results in a measurable contrast in the formed images due to the stronger scattering of electrons by regions of higher mass-thickness. Two types of images can be formed by careful positioning of the aperture. In the first case, the aperture is positioned in a way that permits only the direct electron beam and weakly scattered electrons through its central hole to travel through it whereas higher-angle electrons scattered by regions of the specimen with higher mass-thickness collide with the aperture walls and are "filtered". Thus, the resulting intensity in the image consists mostly of unscattered or weakly scattered electrons from regions of low mass-thickness, while regions of higher-mass thickness appear lower in intensity due to a reduced number of electrons being able to travel through the aperture. This leads to a "bright-field (BF)" image in TEM where dark spots indicate regions of higher  $Z$  or thickness. In the second case, the aperture can be horizontally displaced so that the permitted range of scattering angles does not include the direct, unscattered beam but only such of higher scattering angles. In this case, regions of higher mass-thickness scatter more electrons in the direction of the aperture hole, while unscattered electrons are absorbed by the aperture walls. In turn, a "DF" image is obtained in which only strongly scattering parts of the specimen appear bright in the image and areas containing no specimen or parts of low mass-thickness appear dark.<sup>471,472</sup>

As indicated by eqn. (13.6) and Fig. 146, a much smaller fraction of primary electrons is elastically backscattered (i.e.,  $\theta > 90^\circ$ ) because of the smaller interaction

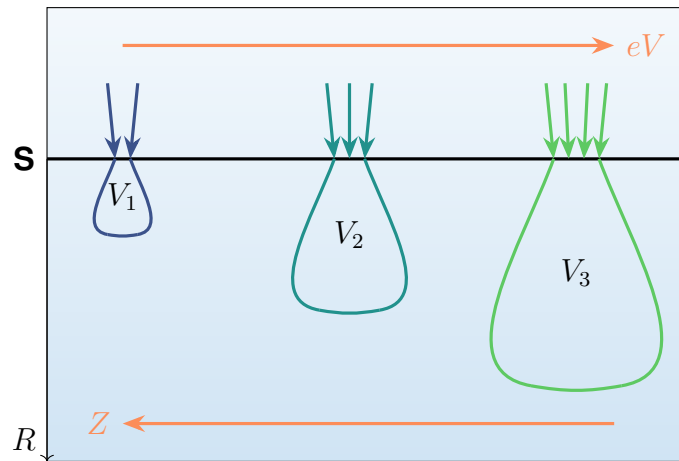


**Figure 147.** Penetration depth  $R$  of a primary electron (also a BSE) in a solid after impact with the surface  $S$  and characteristic pear-shape interaction volume  $V$ .  $R$  increases with increasing beam energy and decreasing  $Z$  (mass-thickness) of the specimen.

cross-section at higher angles. Their energy is generally close to the incident beam energy due to mostly energy loss-free scattering events that eject them out of the specimen at high angles. These can be detected as a backscattered-electron signal given that the kinetic energy of these electrons is sufficient enough to leave the specimen, and is one of the major signals collected in SEM. Other than the SE signal in SEM, BSE have a large penetration depth (i.e., the specimen volume in which the electron can move before it is brought to rest or absorbed due to inelastic scattering events) because of their high energy and imaging with BSE depicts mass-thickness-contrast in the specimen (see eqn. (13.6,  $Z^2$ -dependence); hence, they give information about the chemical composition and distribution. Accordingly, the penetration depth of the electron increases with increasing incident beam energy and decreasing mass-thickness of the specimen (Fig. 147).<sup>471,472</sup>

### 13.2.2 Inelastic scattering

Inelastic scattering is mostly caused by electron-electron interactions as indicated by eqn. (13.5), which is especially important for the generation of SE as the second major signal observed by SEM. SE are formed when the energy of a primary electron is transferred to an atomic electron in the specimen; then, a fraction of the incident energy  $E_0$  is converted to potential energy (ionization energy  $E_I$ ) that generates a free SE with the remainder of the incident energy as kinetic energy  $E_{kin} = E_0 - E_I$ , which is much smaller compared to the energy of BSE ( $< 50$  eV vs.  $\approx E_0$ ). Importantly, these SE will be repeatedly inelastically scattered, and the probability for a subsequent inelastic scattering event increases even further with decreasing energy of the SE (Fig. 146,  $\lambda$  decreases with decreasing energy  $eV$ ).

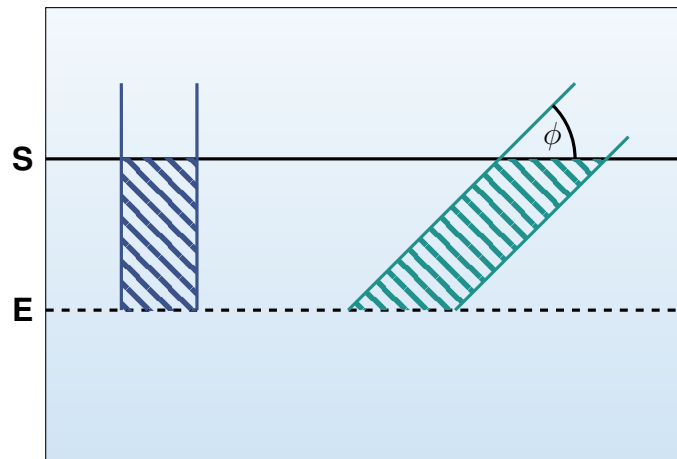


**Figure 148.** Oblique angle  $\phi$  of incident electron beam increases the specimen volume between the surface **S** and escape depth **E**, giving rise to higher SE yields.

Therefore, only SE that are formed close to the surface of the specimen have a higher probability for leaving the specimen and be detected. The escape depth (i.e., the distance that SE can travel in the solid without being absorbed) is much lower in comparison to BSE (<2 nm vs. hundreds of nm), and thus SE images are a depiction of the surface structure of the specimen with topological contrast. The secondary electron yield can be increased by tilting the sample away from the beam so that the specimen is not irradiated by the beam perpendicularly ( $\phi = 90^\circ$ ) but with an oblique angle ( $\phi < 90^\circ$ ) (Fig. 148). Thus, more of the sample is irradiated with electrons within the escape depth of the specimen. For protruding surface features of smaller size, a relatively large amount of SE can leave the specimen, making these features appear brighter in SEM images compared other parts of the specimen. Moreover, the tilting of the sample towards the detector increases the number of SE reaching the detector from areas of the specimen that are pointing towards the detector, making these appear brighter in SEM images as well compared to surfaces which are oriented differently.<sup>471–473</sup>

## 13.3 ELECTRON MICROSCOPES

### 13.3.1 General

Electron microscopes consist of an electron source (called electron gun), magnetic lenses to focus the electrons to a wide parallel beam (TEM) or into a narrow electron probe (SEM and STEM), optional scanning coils which are used to deflect the electron probe in scanning mode operation further to allow raster

scanning, the specimen stage and the imaging detectors.<sup>471–474</sup> The electron gun consists of a negatively charged cathode serving as the electron source which are accelerated by the anode and potential differences of hundreds of kV to obtain a beam of high kinetic energy electrons. Two types of electron sources are used. In the first case, a crystal of  $\text{LaB}_6$  with a fine tip as the cathode is heated to 1700 K at which a high current density of electrons is emitted into the surrounding vacuum via thermionic emission. In the second case, a tungsten crystal with a fine tip serving as the cathode is exposed to a very strong electric field in ultra-high vacuum at room temperature at which tunneling of electrons into the vacuum is possible via cold field-emission. These are then accelerated by a second anode to high kinetic energy. It is also possible to combine both thermionic and field-emission using a tungsten source treated with  $\text{ZrO}_2$  maintained at 1700 K where the work function of the cathode is sufficiently low to allow emission of electrons without tunneling (Schottky emission). While field-emission sources generate very narrow electron beams, thermionic emission currents are pre-focused by the so-called Wehnelt cylinder prior to the acceleration of electrons towards the anode. A negative bias is applied to the Wehnelt cylinder which contains a central hole so that it becomes more negative than the cathode. As the electron current emerges from the cathode, only the electrons generated very close at the tip are able to leave the Wehnelt through its central hole and are focused to a narrower beam whereas other electrons are deflected by the negative bias of the Wehnelt, collide with the cylinder walls and are absorbed. Both guns contain a circular anode plate with a central hole in which only a narrow fraction of the emitted beam parallel to the optic axis is able to pass through the anode plate. These electrons are then focused by magnetic lenses to a parallel beam onto the specimen. Often the lenses are covered with an aperture that limits the entry size into the lens to limit spherical and chromatic aberrations. This permits only electrons with a trajectory parallel to the optic axis to travel through the lens, so the resulting image appears less distorted and exhibits higher resolutions. Depending on the instrument, the electrons will then pass either more electron lenses with apertures (TEM) or be detected right after interaction with the specimen (SEM and STEM).<sup>471–474</sup>

### 13.3.2 Transmission Electron Microscope

In TEM, thin specimen are irradiated with a broad, homogeneous beam of electrons ( $\mu\text{m}$ -sized) to study forward-scattered electrons of low scattering angles  $\theta$ . Using a broad beam results in the entire image being recorded "all at once", and two-dimensional "shadow projection" images are obtained from three-dimensional

---



objects. After the scattered electrons leave the specimen, an aperture is used to filter allow only the transmission of electrons with certain deflection angles, resulting in either BF or DF TEM images (Fig. 149a).<sup>472</sup>

### 13.3.3 Scanning Electron Microscope

In SEM, samples are not limited by the thickness because BSE and SE are of interest instead of forward-scattered electrons. This is because the probability for the detection of a BSE increases with increasing mass-thickness of the sample (eqn. (13.6)) due to a higher number of possible scattering events. Moreover, the SE signal recorded in SEM is very surface-sensitive, and therefore independent of the specimen thickness. Unlike the broad parallel electron beam in TEM, SEM uses a smaller accelerating voltage ( $\leq 30$  kV) and a sharp electron probe (1–10 nm) which is deflected by magnetic scanning coils in two perpendicular directions to sweep over the specimen point by point in a raster, and so the image is also created sequentially. Due to the large depth of focus, images with three-dimensional appearances are created (Fig. 149b).<sup>471,473</sup>

### 13.3.4 Scanning Transmission Electron Microscope

A STEM combines the scanning technique of a SEM to study forward-scattered electrons by thin specimen like in TEM using a small electron probe (0.2 nm). Other than TEM, STEM detects the transmitted electrons directly instead of using apertures to select certain deflection angle ranges. Especially for DF images, STEM are equipped with a circular annular dark-field (ADF) detector which collects all azimuthal angles scattering, and hence, it is more efficient than DF signal collection in TEM. In high-angle annular dark-field (HAADF)-STEM, images reflecting only the  $Z$ -contrast in a specimen can be recorded with a better contrast and lower amount of noise than a conventional TEM, albeit at lower resolution (Fig. 149c).<sup>471,472,474</sup>

### 13.3.5 Energy-Dispersive X-ray Spectroscopy

EDS is based on the principle that inelastic scattering of electrons leading to the formation of SE leaves a hole in one of its energy states. This will be filled by the de-excitation of an electron with the concomitant emission of an x-ray photon whose energy is defined by the energetic difference of the two energy levels

---

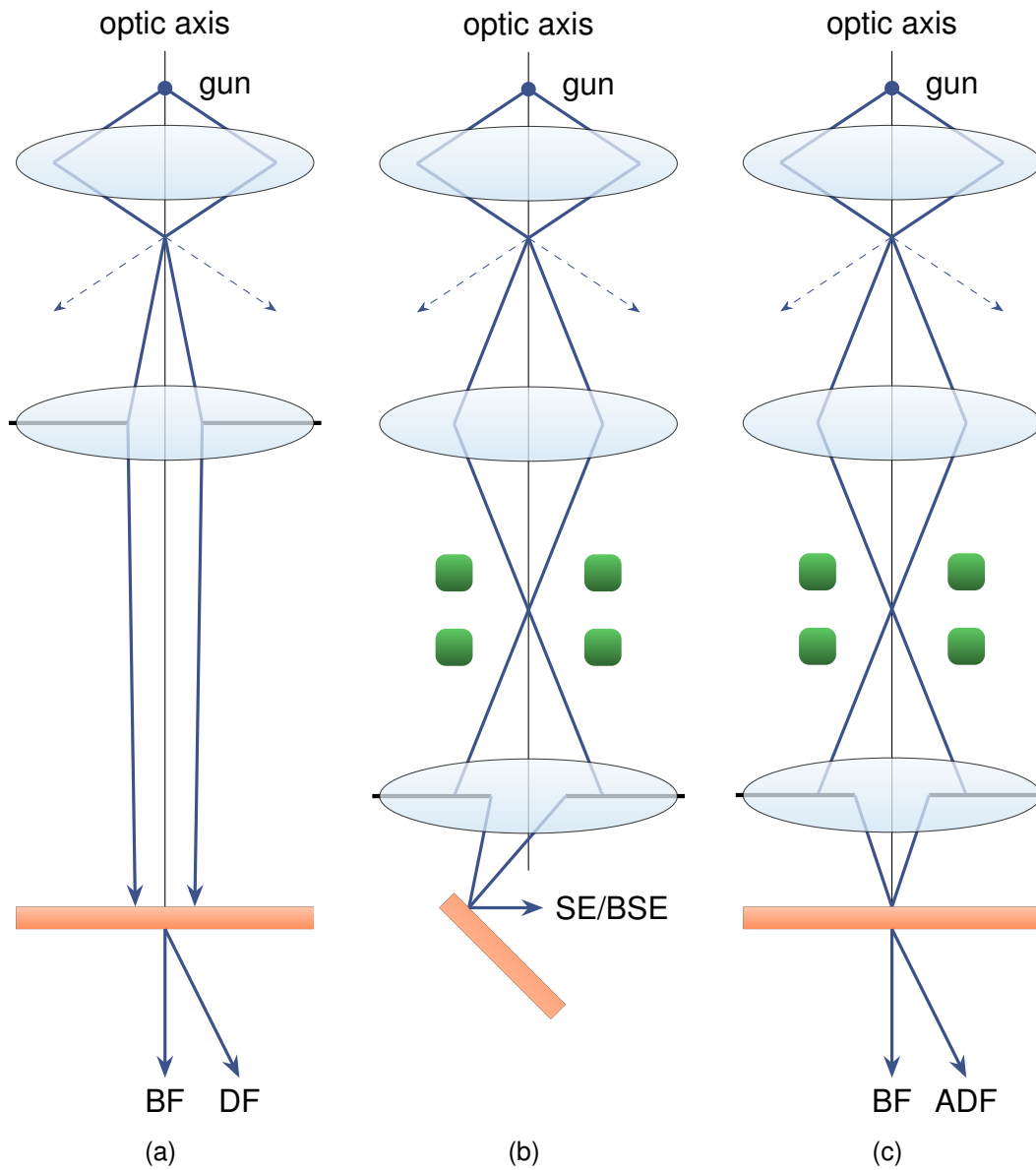


**Figure 149.** Schematic setups of (a) TEM, (b) SEM, and (c), STEM. Purple lines: electron trajectory, ellipses: magnetic electron lenses, green rectangles: scanning coils, orange rectangles: specimen.

---

involved and is characteristic for an element. This photon can be detected by an EDS system to provide qualitative and quantitative information about nature and amount of an element present within the sample. Importantly, low- $Z$  elements are less suitable for the detection with EDS due to their low fluorescence yield  $\omega$  (i.e., number of x-ray photons emitted per ionization).<sup>472</sup>

---



# 14

## *Nuclear Magnetic Resonance Spectroscopy*

### 14.1 INTRODUCTION

NMR is a field of study which describes the interaction of radio-frequency electromagnetic radiation with the spins of a set of nuclei in a strong external magnetic field.<sup>431,475–479</sup> Importantly, the electronic (chemical) environment of a magnetic nucleus in a sample influences the resonance frequencies observed by this spectroscopic technique. This allows the structure elucidation, precise identification of connectivities between individual atoms, and their quantification in organic molecules, organometallic complexes, or inorganic solids by analysis of the emerging signals together with multiplicities and coupling constants.

### 14.2 NUCLEAR SPIN

An atomic nucleus consists of  $Z$  protons and  $N$  neutrons, each with possible spin quantum numbers  $\pm\frac{1}{2}$ . The whole assembly has a resulting total spin angular momentum,  $I$ , with  $2I + 1$  possible magnetic spin orientations,  $m_I$  (multiplicity). Thus, a proton (or the nucleus of the  $^1_1\text{H}$  isotope) has two relative orientations of its spin, while a  $^{14}_7\text{N}$  nucleus with  $I = 1$  has three, and  $^{12}_6\text{C}$  with  $I = 0$  has zero magnetic moment. The value of  $I$  is generally dependent on  $Z$  and  $N$ . If both are even numbers, the individual spins are all paired and the resulting magnetic moment is zero. Such isotopes are undetectable by NMR. On the other hand, if both are odd numbers, the half-spins add up and the resulting total nuclear spin

quantum number is an integer. If only one is odd and the other even, a multiple of a half-integer is obtained for the total spin.<sup>431,479</sup>

### 14.3 NUCLEUS IN THE MAGNETIC FIELD

In a magnetic field of magnitude  $\mathcal{B}_0$ , the degenerate magnetic spin orientations split into states of different energy (nuclear Zeeman effect), which can be calculated using

$$E_{m_I} = -\gamma\hbar\mathcal{B}_0m_I \quad (14.1)$$

where  $\gamma$  is the magnetogyric ratio, an isotope dependent constant. For the proton, the two possible orientations,  $m_I = +\frac{1}{2}$  ( $\alpha$ ) and  $m_I = -\frac{1}{2}$  ( $\beta$ ) are lowered or raised in energy, respectively, and the energy separation between the levels is (Figure 150)

$$\Delta E = E_{-1/2} - E_{+1/2} = \frac{1}{2}\gamma\hbar\mathcal{B}_0 - \left(-\frac{1}{2}\gamma\hbar\mathcal{B}_0\right) = \gamma\hbar\mathcal{B}_0. \quad (14.2)$$

This is the resonance condition of NMR. If the energy of the electromagnetic radiation  $h\nu$  is lower than  $\gamma\hbar\mathcal{B}_0$ , no absorption can take place. The respective frequency is called the Larmor frequency,  $\nu_L$ , defined as<sup>431,479</sup>

$$\nu_L = \frac{\gamma\hbar\mathcal{B}_0}{h} = \frac{\gamma\mathcal{B}_0}{2\pi} \quad (14.3)$$

### 14.4 CHEMICAL SHIFT

In contrast to a bare proton, the nuclei in a molecule are surrounded by the electron clouds of the individual atoms which may interact further with neighboring atoms or groups of atoms. Applying an external magnetic field causes the circulation of these electrons in the orbitals, which results in a local, induced magnetic field,  $\mathcal{B}_i$ , that is oriented oppositely to the external field. Thus, the nuclei surrounded by electron density do not experience the full magnitude of the external field,  $\mathcal{B}_0$ ,

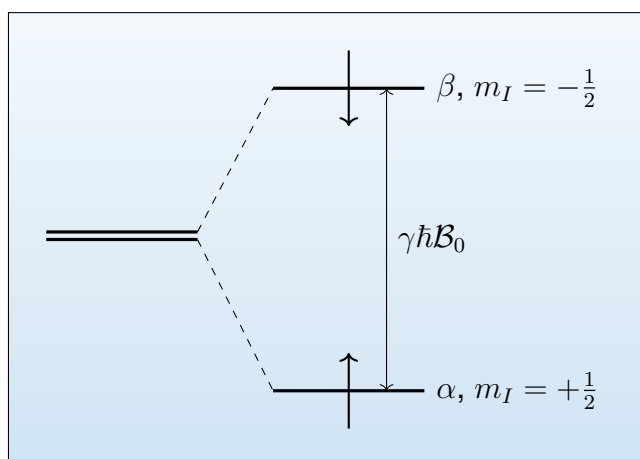


**Figure 150.** Energetic splitting of the magnetic orientations  $m_I$  in the field  $\mathcal{B}_0$ .

but a reduced local, effective magnetic field,  $\mathcal{B}_{eff}$ , which is the difference of the external and induced magnetic field according to

$$\mathcal{B}_{eff} = \mathcal{B}_0 - \mathcal{B}_i \quad (14.4)$$

Even more, this "shielding" of the nuclei from the external field is highly sensitive to the local electronic structure at the position of the nucleus of interest, and hence individual atoms in the same molecule experience different local magnetic fields and can be distinguished by the different resonance frequencies. The shielding can be expressed by introducing the shielding constant,  $\sigma$ , as in

$$\mathcal{B}_i = \sigma\mathcal{B}_0 \quad (14.5)$$

Unlike the value of  $\mathcal{B}_i$ , the shielding constant  $\sigma$  is not dependent on the magnitude of the applied external magnetic field but dimensionless and a representation of the local chemical environment of the nucleus. From this follows that

$$\mathcal{B}_{eff} = \mathcal{B}_0 - \sigma\mathcal{B}_0 = \mathcal{B}_0(1 - \sigma) \quad (14.6)$$

and

$$\nu_L = (1 - \sigma) \frac{\gamma\mathcal{B}_0}{2\pi} \quad (14.7)$$

This implies that a strongly shielded nucleus (i.e., large  $\sigma$ ) will experience only a fraction of the external field; hence, the magnetic spin orientations are less split in

energy and a smaller resonance frequency is observed. These signals appear on the right side of the NMR spectrum, which is the high-field side (because a high external field would be needed to observe the resonance of this nucleus at a given frequency). On the other hand, weakly shielded (or strongly deshielded) nuclei (i.e., small  $\sigma$ ) experience more of the full magnitude of the external magnetic field,  $\mathcal{B}_0$ , the spin orientations split up further in energy, the resonance frequency is large and found on the left, low-field side of the spectrum (a small external field is needed to observe the resonance of this nucleus at the same given frequency as above). To account for the field-dependent resonance frequencies, a field-normalized scale, the chemical shift,  $\delta$ , is introduced, which is defined as

$$\delta = \frac{\nu - \nu^0}{\nu^0} 10^6 \quad (14.8)$$

where  $\nu$  is the resonance frequency of a nucleus of interest and  $\nu^0$  the resonance frequency of a standard (e.g., tetramethylsilane (TMS) for  $^1\text{H}$  and  $^{13}\text{C}$ ).  $\delta$  can be also expressed as a function of  $\sigma$  as in

$$\delta = \frac{(1 - \sigma)\mathcal{B}_0 - (1 - \sigma^0)\mathcal{B}_0}{(1 - \sigma^0)\mathcal{B}_0} 10^6 = \frac{\sigma^0 - \sigma}{1 - \sigma^0} 10^6 \quad (14.9)$$

This relationship shows that  $\delta$  increases when  $\sigma$  decreases (strongly deshielded nuclei) and vice versa.<sup>431,479</sup>

## 14.5 FINE STRUCTURE

Signals in NMR spectra are often split into multiplets with equidistant separations between the individual lines. Other signals or groups thereof can be found in the spectrum which exhibit the same or other multiplets with the same separation of the individual lines. These are formed by spin-spin coupling of neighboring nuclei in the same molecule and indicate the connectivity of atoms within the compound. The energy of the interaction between neighboring nuclei can be described as

$$E_{m_1 m_2} = hJm_1 m_2 \quad (14.10)$$

where  $m_1$  and  $m_2$  are the magnetic spin orientations of the two nuclei, respectively. For example, an  $AX$ -system consisting of two nuclei  $A$  and  $X$  that are both spin- $\frac{1}{2}$



systems and have a large difference in chemical shifts couple in such a way that both nuclei show doublets in the NMR spectrum. In this case, the four possible spin states of the whole assembly are  $\alpha_A\alpha_X$ ,  $\alpha_A\beta_X$ ,  $\beta_A\alpha_X$ , and  $\beta_A\beta_X$ . Therefore, the energy levels are described as

$$E_{m_A m_X} = -h\nu_A m_A - h\nu_X m_X + hJ m_A m_X \quad (14.11)$$

where the last part of the sum describes the spin-spin coupling between  $A$  and  $X$ . If  $J > 0$ , then higher energies are obtained for the energy levels where both exhibit the same spin (i.e.,  $\alpha_A\alpha_X$  or  $\beta_A\beta_X$ ,  $m_A m_X > 0$ ) and lower energies when the spins are different (i.e.,  $\alpha_A\beta_X$  or  $\beta_A\alpha_X$ ). Thus, the resulting energy levels are

$$E_{\alpha_A\alpha_X} = -\frac{1}{2}h\nu_A - \frac{1}{2}h\nu_X + \frac{1}{4}hJ \quad (14.12)$$

$$E_{\alpha_A\beta_X} = -\frac{1}{2}h\nu_A + \frac{1}{2}h\nu_X - \frac{1}{4}hJ \quad (14.13)$$

$$E_{\beta_A\alpha_X} = +\frac{1}{2}h\nu_A - \frac{1}{2}h\nu_X - \frac{1}{4}hJ \quad (14.14)$$

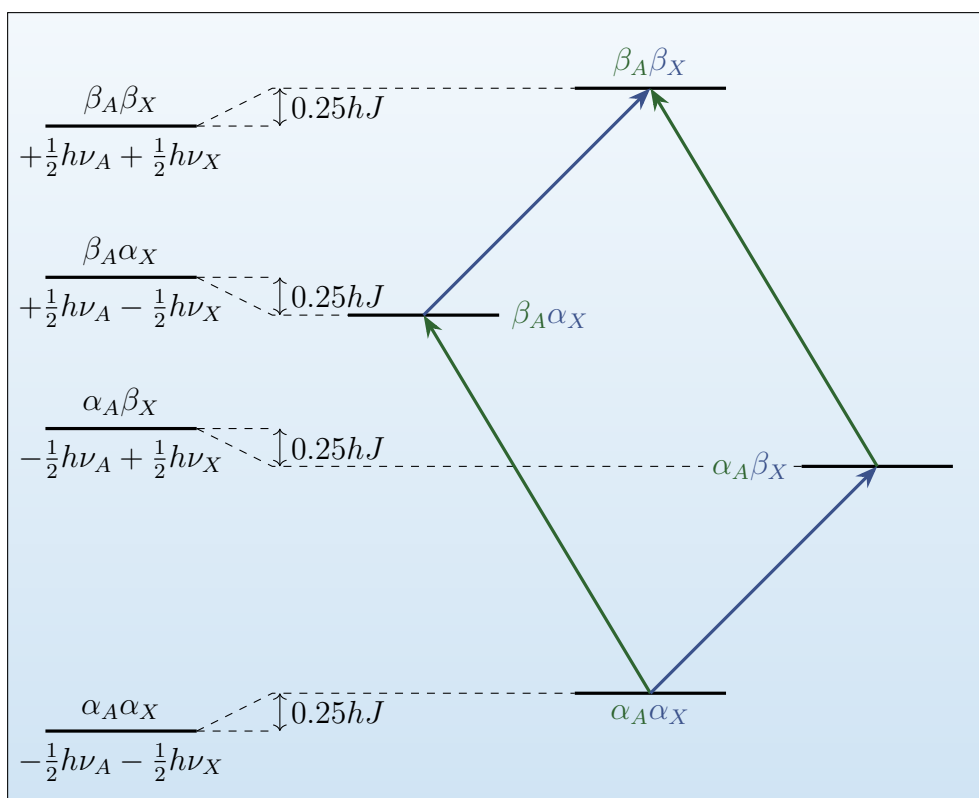
$$E_{\beta_A\beta_X} = +\frac{1}{2}h\nu_A + \frac{1}{2}h\nu_X + \frac{1}{4}hJ \quad (14.15)$$

A transition is only possible for one nucleus at a time. Therefore, resonance can only occur when the spin quantum number,  $m_I$ , of one nucleus is changed during the transition. In the  $AX$ -system, only two such transitions are possible for each nucleus, either when the other nucleus is in the  $\alpha$  or  $\beta$  state. Then, the corresponding differences of the energy levels (the resonance energies) for the transition of  $A$  are

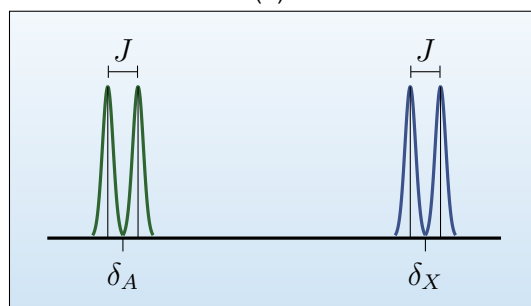
$$\begin{aligned} \Delta E_{A1} &= E_{\beta_A\alpha_X} - E_{\alpha_A\alpha_X} \\ &= +\frac{1}{2}h\nu_A - \frac{1}{2}h\nu_X - \frac{1}{4}hJ - \left(-\frac{1}{2}h\nu_A - \frac{1}{2}h\nu_X + \frac{1}{4}hJ\right) \\ &= h\nu_A - \frac{1}{2}hJ \end{aligned} \quad (14.16)$$

and

$$\Delta E_{A2} = E_{\beta_A\beta_X} - E_{\alpha_A\beta_X} = h\nu_A + \frac{1}{2}hJ \quad (14.17)$$



(a)



(b)

**Figure 151.** (a) Spin-spin coupling in an  $AX$ -system. (b) Illustration of the signal splitting in the NMR spectrum.

Likewise, the energies for the two  $X$  transitions are

$$\Delta E_X = h\nu_X \pm \frac{1}{2}hJ \quad (14.18)$$

Then, two doublets are observed for the resonances of  $A$  and  $X$  in the NMR spectrum, both with the same coupling constant  $J$  (Figure 151). For an  $AX_2$  system where the nuclei  $X$  are chemically and magnetically equivalent, the  $X$  resonance is again a doublet but with an integral (area under the signal) twice as high as for  $AX$ . The  $A$  resonance, in turn, is first a doublet with a coupling constant  $J$  where each of these lines is split by the interaction with the second  $X$

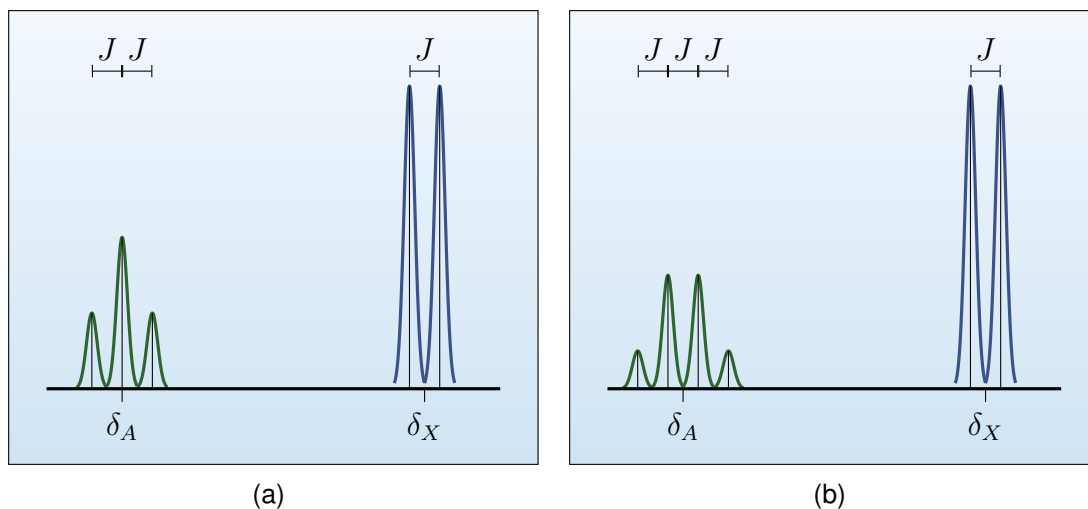


**Figure 152.** Spin-spin coupling in a (a)  $AX_2$ , (b)  $AX_3$ .

$n$						
0			1			singlet
1		1	1			doublet
2		1	2	1		triplet
3	1	3	3	1		quartet
4	1	4	6	4	1	quintet

**Figure 153.** Names and intensity ratios of multiplets defined by Pascal's triangle for  $n$  neighbors.

nucleus into another set of doublets with coupling constants  $J$ , thereby resulting in an overall formation of a triplet with intensity ratio 1:2:1. Similarly, the  $A$  resonance in  $AX_3$  gives a quartet with an intensity ratio of 1:3:3:1 (Figure 152). Generally, a  $A_nX_m$  species consisting of only spin- $\frac{1}{2}$  nuclei will form  $A$ -resonances of integral  $n$  and multiplicity  $m + 1$  and  $X$ -resonances of integral  $m$  and multiplicity  $n + 1$ , respectively, with the intensity ratios given by Pascal's triangle (Figure 153).<sup>431,479</sup>



# 15

## *Mass Spectrometry*

### 15.1 INTRODUCTION

MS is an analytical technique by which the molecular mass (or more precisely, the mass-to-charge ratio,  $m/z$ ) of an analyte can be determined. In contrast to other analytical techniques, MS can often unambiguously give the elemental composition of a molecule and is therefore an important complimentary analytical method for the structural elucidation of unknown compounds in combination with spectroscopy. Especially in the field of metal-organic chemistry, the splitting of peaks in the MS spectrum into isotopic patterns for compounds containing heavier elements with many isotopes is a valuable advantage of identifying these elements where commonly applied methods fail. A mass spectrometer consists of three stages: 1) an ion source in which the analyte of interest is ionized to create a positively (or negatively) charged ion, thereby bringing it to the gas phase, 2) a mass analyzer in which the generated ions by the source are separated according to their  $m/z$ , and 3) a detection system which translates the signal to readable output.<sup>480–484</sup>

### 15.2 ION SOURCES

#### *15.2.1 Electron/Chemical Ionization*

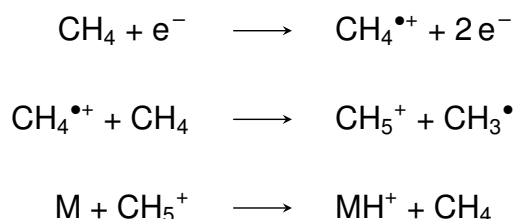
Electron ionization is the strategy of ionizing gas-phase or volatile analytes by directing an electron beam of suitable energy (70 eV) through a chamber held at

low pressure of the analyte. The electrons stem from a cathodic metal filament which is heated to high temperature within the vacuum and emits electrons that are accelerated towards the anode (*cf.* ch. 13). Inelastic interaction of the electrons from the electron beam with the atomic electrons of the analyte M leads to an emission of a secondary electron and the generation of a radical-cation of the analyte  $M^{\bullet+}$ . This energy-rich ion can undergo further fragmentation on the way to the mass analyzer, for example by cleavage of a radical-ion  $X^{\bullet}$  to generate a cation  $[M-X]^+$ , or by cleavage of a neutral fragment N to generate a radical-cation  $[M-N]^{\bullet+}$  (scheme 37).<sup>482-484</sup>



**Scheme 37.** Ionization and subsequent fragmentation pathways during electron ionization. Uncharged  $X^{\bullet}$  and N are not detected by MS.

Due to the strong fragmentation in electron ionization, the ion peak of the analyte may not be visible. However, if the analyte is exposed to an electron beam in the presence of an excess reagent gas (e.g.,  $CH_4$ ) at higher pressures as in chemical ionization, then this reagent gas is more likely interact with the electron beam first. Thus,  $CH_4$  is first oxidized to  $CH_4^{\bullet+}$  and then reacts with another equivalent of  $CH_4$  to the corresponding methyl radical,  $CH_3^{\bullet}$ , and carbonium ion,  $CH_5^+$ . This carbonium ion is able to transfer a proton to the analyte M, thereby forming the "pseudomolecular" ion  $MH^+$  which is detected by MS (scheme 38).<sup>482-484</sup>



**Scheme 38.** Ionization of the reagent gas and subsequent formation of the pseudomolecular ion  $MH^+$  in CI.

This strategy leads to less fragmentation and identifying the mass of the analyte is less complicated. A further improvement of the technique is atmospheric pressure chemical ionization where an analyte solution in a suitable solvent is introduced into the ionizing chamber as an electrically neutral spray and ionized at a corona discharged electrode in the presence of  $N_2$ .<sup>483</sup>

### 15.2.2 Field Ionization/Desorption

Field ionization makes use of the generation of very strong electric fields at electrodes containing sharp points which enables the ionization of molecules via tunneling of electrons in a very soft manner in very high vacuum (*cf.* field-emission source, ch. 13). In contrast to electron and chemical ionization, this technique produces true  $M^+$  ions (or  $M^-$  depending on the potential applied to the emitter). The emitter is a thin metal wire which is either covered with fine, conductive carbon needles (formed via the pyrolysis of benzonitrile vapors under inert conditions) or metal needles (formed via decomposition of metal carbonyls) with sharp tips which serve as the ionization sites where the electric field is strong enough for quantum mechanical tunneling to occur. When analytes are not gaseous or volatile, they are applied directly onto the emitter and this is then referred to as field desorption. One method is to use a microsyringe to apply a dilute solution of the analyte onto the emitter and subsequent evaporation of the solvent in the vacuum of the source, known as liquid injection field desorption ionization (LIFDI).<sup>483</sup>

### 15.2.3 Electrospray Ionization

In the electrospray ionization method, a dilute solution of the analyte is passed through a capillary at which a high potential is applied. This causes the formation of charged droplets of analyte solution containing either positively or negatively charged analyte ions (depending on the potential applied), a process called nebulisation. With the aid of a warm flow of  $N_2$  gas, the solvent in the droplets is continuously evaporating, giving rise to an increase of the charge density of the charged droplets and subsequent splitting into smaller particles due to the electrostatic repulsion. Eventually, all solvent has evaporated and only the charged analytes remain in the gas phase, which are moving through small holes of several skimmer cones that separate the atmospheric pressure spray chamber from the high vacuum mass analyzing stage. This technique is considered to be very softly ionizing, causing little to no fragmentation of the analyte ions.<sup>482,483</sup>

### 15.2.4 Matrix-Assisted Laser Desorption Ionization

An analyte can be ionized by short irradiation with a high-energy laser pulse. If the analyte is co-crystallized with an auxiliary compound (the matrix, typically an aromatic carboxylic acid), then this process is referred to as matrix-assisted

---

laser desorption ionization. Here, one of the softest ionization occurs due to the application of narrow pulse widths and fast expansion of the vaporized ions towards the mass analyzer.<sup>483</sup>

## 15.3 MASS ANALYZERS

### 15.3.1 Time-of-Flight

The time-of-flight (TOF) mass analyzer is based on the principle that ions of same kinetic energy but different mass have different velocities, and hence, they take different amounts of time to pass a certain distance (in very high vacuum). First, all ions are generated at the same time and then accelerated for a defined distance before they pass through a field-free drift area in which the ions are separated according to their velocity. The kinetic energy of the ions is caused by the acceleration of the electric field; hence,

$$E_{kin} = \frac{1}{2}mv^2 = zeV \quad (15.1)$$

where  $E_{kin}$  is the kinetic energy,  $m$  is the ion mass,  $v$  the ion velocity,  $z$  the number of elemental charges  $e$ , and  $V$  the accelerating voltage. Given  $v = \Delta x/\Delta t$ , where  $x$  is the distance and  $t$  the time needed for the ion to fly this distance, the time  $t$  for an ion is given by

$$\Delta t = \frac{\Delta x}{\sqrt{2eV}} \sqrt{\frac{m}{z}} \quad (15.2)$$

This equation shows that the TOF of an ion depends on  $m/z$  of an ion, which in turn allows the determination of  $m/z$  by precise measurement of TOF.<sup>480,482–484</sup>

### 15.3.2 Magnetic Sectors

A sector separates ions according to their  $m/z$  by means of the deflection of charged particles in a magnetic field by the Lorentz force,  $F_L$ . These are forced on a circular path when the magnetic field is oriented orthogonal to the trajectory of the ion and the Lorentz force is in equilibrium with the centrifugal force. Then,



$$F_L = zevB = \frac{mv^2}{r} \quad (15.3)$$

where  $B$  is the magnetic field strength and  $r$  is the radius of the circular path of the ion. After several transformations of this equation, the following relationship is obtained:

$$\frac{m}{z} = \frac{r^2 B^2 e}{2V} \quad (15.4)$$

This shows that, at constant magnetic field strength and accelerating voltage, ions of higher  $m/z$  must have a larger radius of their circular trajectory in the magnetic field, and therefore, they are less deflected by the magnetic field than ions of lower  $m/z$ . In practice, the radius  $r$  will be held constant to maintain the detector in place and the magnetic field strength  $B$  will be varied to detect different ions by which  $m/z$  is calculated.<sup>480,483</sup>

### 15.3.3 Quadrupoles

Quadrupoles consist of four separate rod electrodes of hyperbolic shape oriented in a square shape where the opposing rods are each held at the same potential consisting of a DC and an AC part. They separate ions of different  $m/z$  by taking advantage of the trajectory stability (or instability) of an ion in an oscillating electric field. When ions coming from the ion source enter the quadrupole, they are attracted to the rod of opposite charge. Because of the oscillating field, that ion will either timely switch directions and be attracted to the other pair of electrodes (stable trajectory) or will collide with the rods and be lost (unstable trajectory). Whether certain  $m/z$  values give stable or unstable pathways is determined by the magnitude of the potential and frequency.<sup>480,483,484</sup>

### 15.3.4 Ion Traps

An ion trap is related to the quadrupole but two of the opposing electrodes are replaced with a ring electrode and the other two rods are hyperbolic electrodes serving as end caps which are electrically connected. Again, the potential consists of a DC and AC part which create stable trajectories for ions of certain  $m/z$  while the rest collides with the walls of the trap or is ejected. The difference is that an ion

trap can store a whole range of  $m/z$ , which are then consecutively ejected using a specific AC voltage input to one of the end caps (resonant ejection).<sup>480,482–484</sup>

### 15.3.5 Fourier-Transform Ion Cyclotron Resonance

Fourier-Transform ion cyclotron resonance makes use of the fact that ions can be forced on a circular pathway in a very strong, orthogonal magnetic field (*cf.* sectors, *vide supra*). The frequency by which they oscillate is termed the cyclotron frequency,  $\omega$ , and is dependent only on their mass, not their velocity. This movement can be excited by a short-pulsed AC electric field of the same frequency  $\omega$  (i.e., an entire range of frequencies for the  $m/z$  range of interest). Ions that were moving on a circular path of small radius will increase their orbital radius and move closer to the walls of the device and induce an image current in the receiver plate walls. Soon after, de-excitation occurs and the ions move back to their original pathways. The signal consists of cyclotron frequencies of all ions, which can be extracted by Fourier transformation to obtain the individual contributions to the signal which are translated to corresponding  $m/z$  values of the individual ions.<sup>480,483</sup>

### 15.3.6 Orbitrap

An Orbitrap is an ion trap that operates similarly to Fourier transform ion cyclotron resonance where  $m/z$  values are determined based on Fourier transformation of frequencies of ion oscillations, but does not use magnetic fields or AC potentials. It consists of a spindle-shaped central electrode held at high potential surrounded by a coaxial, grounded outer electrode in which ions orbit around the central electrode in the radial electrostatic field and are confined axially by potentials applied to two end cap electrodes. The resulting oscillation induces an image current which is converted to an MS by Fourier transformation.<sup>480,482,484</sup>

---

## References

- (1) Yin, Y.; Rogers, J. A. Introduction: Smart Materials. *Chem. Rev.* **2022**, *122*, 4885–4886.
- (2) Lendlein, A.; Trask, R. S. Multifunctional materials: concepts, function-structure relationships, knowledge-based design, translational materials research. *Multifunct. Mater.* **2018**, *1*, 010201.
- (3) Goodall, R. E. A.; Lee, A. A. Predicting materials properties without crystal structure: deep representation learning from stoichiometry. *Nature Commun.* **2020**, *11*, 6280.
- (4) Koinuma, H.; Takeuchi, I. Combinatorial solid-state chemistry of inorganic materials. *Nat. Mater.* **2004**, *3*, 429–438.
- (5) Kitagawa, S.; Kitaura, R.; Noro, S.-i. Functional Porous Coordination Polymers. *Angew. Chem. Int. Ed.* **2004**, *43*, 2334–2375.
- (6) Yaghi, O. M.; O'keeffe, M.; Ockwig, N. W.; Chae, H. K.; Eddaoudi, M.; Kim, J. Reticular Synthesis and the Design of New Materials. *Nature* **2003**, *423*, 705–714.
- (7) Zhang, X.; Chen, Z.; Liu, X.; Hanna, S. L.; Wang, X.; Taheri-Ledari, R.; Maleki, A.; Li, P.; Farha, O. K. A historical overview of the activation and porosity of metal-organic frameworks. *Chem. Soc. Rev.* **2020**, *49*, 7406–7427.
- (8) Li, H.; Li, L.; Lin, R.-B.; Zhou, W.; Zhang, Z.; Xiang, S.; Chen, B. Porous metal-organic frameworks for gas storage and separation: Status and challenges. *EnergyChem* **2019**, *1*, 100006.
- (9) Xie, L. S.; Skorupskii, G.; Dincă, M. Electrically Conductive Metal-Organic Frameworks. *Chem. Rev.* **2020**, *120*, 8536–8580.
- (10) Mandal, S.; Natarajan, S.; Mani, P.; Pankajakshan, A. Post-Synthetic Modification of Metal-Organic Frameworks Toward Applications. *Adv. Funct. Mater.* **2020**, *31*, 2006291.

- (11) Schneemann, A.; Bon, V.; Schwedler, I.; Senkovska, I.; Kaskel, S.; Fischer, R. A. Flexible metal-organic frameworks. *Chem. Soc. Rev.* **2014**, *43*, 6062–6096.
- (12) Allendorf, M. D.; Foster, M. E.; Léonard, F.; Stavila, V.; Feng, P. L.; Doty, F. P.; Leong, K.; Ma, E. Y.; Johnston, S. R.; Talin, A. A. Guest-Induced Emergent Properties in Metal-Organic Frameworks. *J. Phys. Chem. Lett.* **2015**, *6*, 1182–1195.
- (13) Narayan, T. C.; Miyakai, T.; Seki, S.; Dincă, M. High Charge Mobility in a Tetrathiafulvalene-Based Microporous Metal-Organic Framework. *J. Am. Chem. Soc.* **2012**, *134*, 12932–12935.
- (14) Park, S. S.; Hontz, E. R.; Sun, L.; Hendon, C. H.; Walsh, A.; Voorhis, T. V.; Dincă, M. Cation-Dependent Intrinsic Electrical Conductivity in Isostructural Tetrathiafulvalene-Based Microporous Metal-Organic Frameworks. *J. Am. Chem. Soc.* **2015**, *137*, 1774–1777.
- (15) Schneider, C.; Bodesheim, D.; Keupp, J.; Schmid, R.; Kieslich, G. Retrofitting metal-organic frameworks. *Nature Commun.* **2019**, *10*, 4921.
- (16) Toyota, N.; Lang, M.; Müller, J.; Springer Series in Solid-State Sciences; Springer Berlin, Heidelberg: 2007.
- (17) Hatfield, W. E., Ed.; NATO conference series; Springer New York, NY: 1979.
- (18) Bryce, M. R.; Murphy, L. C. Organic metals. *Nature* **1984**, *309*, 119–126.
- (19) Ferraris, J. P.; Cowan, D. O.; Walatka, V. V.; Perlstein, J. H. Electron transfer in a new highly conducting donor-acceptor complex. *J. Am. Chem. Soc.* **1973**, *95*, 948–949.
- (20) Kistenmacher, T. J.; Phillips, T. E.; Cowan, D. O. The crystal structure of the 1:1 radical cation–radical anion salt of 2,2'-bis-1,3-dithiole (TTF) and 7,7,8,8-tetracyanoquinodimethane (TCNQ). *Acta Crystallogr. B: Struct. Sci. Cryst. Eng. Mater.* **1974**, *30*, 763–768.
- (21) Wudl, F. From organic metals to superconductors: managing conduction electrons in organic solids. *Acc. Chem. Res.* **1984**, *17*, 227–232.
- (22) Wang, W.; Luo, L.; Sheng, P.; Zhang, J.; Zhang, Q. Frontispiece: Multifunctional Features of Organic Charge-Transfer Complexes: Advances and Perspectives. *Chem. Eur. J.* **2021**, *27*.
- (23) Scott, B. A.; Placa, S. J. L.; Torrance, J. B.; Silverman, B. D.; Welber, B. The Crystal Chemistry of Organic Metals. Composition, Structure, and Stability in the Tetrathiafulvalinium-Halide Systems. *J. Am. Chem. Soc.* **1977**, *99*, 6631–6639.
- (24) Cowan, D. O.; Wiygul, F. M. The Organic Solid State. *Chem. Eng. News* **1986**, *64*, 28–45.

- (25) Wheland, R. C.; Gillson, J. L. Synthesis of electrically conductive organic solids. *J. Am. Chem. Soc.* **1976**, *98*, 3916–3925.
- (26) Clemente, D. A.; Marzotto, A. Structure of two polymorphs of the TTF-TCNE charge-transfer complex and the degree of ionicity. *J. Mater. Chem.* **1996**, *6*, 941–946.
- (27) Sun, L.; Campbell, M. G.; Dincă, M. Electrically Conductive Porous Metal–Organic Frameworks. *Angew. Chem. Int. Ed.* **2016**, *55*, 3566–3579.
- (28) Schneider, C.; Ukaj, D.; Koerver, R.; Talin, A. A.; Kieslich, G.; Pujari, S. P.; Zuilhof, H.; Janek, J.; Allendorf, M. D.; Fischer, R. A. High electrical conductivity and high porosity in a Guest@MOF material: evidence of TCNQ ordering within Cu<sub>3</sub>BTC<sub>2</sub> micropores. *Chem. Sci.* **2018**, *9*, 7405–7412.
- (29) Ukaj, D.; Bunzen, H.; Berger, J.; Kieslich, G.; Fischer, R. A. Charge-Transfer-Induced Electrical Conductivity in a Tetrathiafulvalene-Based Metal–Organic Framework. *Chem. Mater.* **2021**, *33*, 2532–2542.
- (30) Kini, A. M.; Parakka, J. P.; Geiser, U.; Wang, H.-H.; Rivas, F. M.; DiNino, E.; Thomas, S. Y.; Dudek, J. D.; Williams, J. M. Tetraalkyl- and dialkyl-substituted BEDT-TTF derivatives and their cation-radical salts: synthesis, structure, and properties. *J. Mater. Chem.* **1999**, *9*, 883–892.
- (31) Matsuzaki, S.; Moriyama, T.; Toyoda, K. Raman spectra of mixed valent TTF salts; relation between Raman frequency and formal charge. *Solid State Communications* **1980**, *34*, 857–859.
- (32) Bozio, R.; Zanon, I.; Girlando, A.; Pecile, C. Vibrational spectroscopy of molecular constituents of one-dimensional organic conductors. Tetrathiofulvalene (TTF), TTF<sup>+</sup>, and (TTF<sup>+</sup>)<sub>2</sub> dimer. *J. Chem. Phys.* **1979**, *71*, 2282–2293.
- (33) Hinkel, J. J.; Devlin, J. P. Vibronic interactions, resonance Raman spectra and bond strengths for the radical anion salts of tetracyanoethylene. *J. Chem. Phys.* **1973**, *58*, 4750–4756.
- (34) Dixon, D. A.; Miller, J. S. Crystal and molecular structure of the charge-transfer salt of decamethylcobaltocene and tetracyanoethylene (2:1): {[Co(C<sub>5</sub>Me<sub>5</sub>)<sub>2</sub>]<sup>+</sup>]<sub>2</sub>[(NC)<sub>2</sub>CC(CN)<sub>2</sub>]<sup>2-</sup>. The electronic structures and spectra of [TCNE]<sup>n</sup> (n = 0, 1–, 2–). *J. Am. Chem. Soc.* **1987**, *109*, 3656–3664.
- (35) Meneghetti, M.; Pecile, C. TTF-TCNE a charge transfer π-molecular crystal with partial ionic ground state: Optical properties and electron-molecular vibrations interaction. *J. Chem. Phys.* **1996**, *105*, 397–407.
- (36) Ashton, P. R.; Balzani, V.; Becher, J.; Credi, A.; Fyfe, M. C. T.; Mattersteig, G.; Menzer, S.; Nielsen, M. B.; Raymo, F. M.; Stoddart, J. F.; Venturi, M.;

- Williams, D. J. A Three-Pole Supramolecular Switch. *J. Am. Chem. Soc.* **1999**, *121*, 3951–3957.
- (37) Petersen, B. M.; Jørgensen, M.; Stein, P.; Jeppesen, J. O. Monopyrrolotetrathiafulvalenium dication and its complexation with 1,5-dinaphtho[38]-crown-10. *Supramol. Chem.* **2009**, *21*, 157–163.
- (38) Leong, C. F.; Wang, C.-H.; Ling, C. D.; D'Alessandro, D. M. A spectroscopic and electrochemical investigation of a tetrathiafulvalene series of metal–organic frameworks. *Polyhedron* **2018**, *154*, 334–342.
- (39) Usov, P. M.; Leong, C. F.; Chan, B.; Hayashi, M.; Kitagawa, H.; Sutton, J. J.; Gordon, K. C.; Hod, I.; Farha, O. K.; Hupp, J. T.; Addicoat, M. A.; Kuc, A. B.; Heine, T.; D'Alessandro, D. M. Probing charge transfer characteristics in a donor-acceptor metal-organic framework by Raman spectroelectrochemistry and pressure-dependence studies. *Phys. Chem. Chem. Phys.* **2018**, *20*, 25772–25779.
- (40) Souto, M.; Romero, J.; Calbo, J.; Vitorica-Yrezabal, I. J.; Zafra, J. L.; Casado, J.; Ortí, E.; Walsh, A.; Espallargas, G. M. Breathing-Dependent Redox Activity in a Tetrathiafulvalene-Based Metal–Organic Framework. *J. Am. Chem. Soc.* **2018**, *140*, 10562–10569.
- (41) Paxton, W. F.; Kleinman, S. L.; Basuray, A. N.; Stoddart, J. F.; Duyne, R. P. V. Surface-Enhanced Raman Spectroelectrochemistry of TTF-Modified Self-Assembled Monolayers. *J. Phys. Chem. Lett.* **2011**, *2*, 1145–1149.
- (42) Yin, W.-Y.; Weng, Y.-G.; Jiang, M.; Yu, S.-K.; Zhu, Q.-Y.; Dai, J. A Series of Tetrathiafulvalene Bismuth Chlorides: Effects of Oxidation States of Cations on Structures and Electric Properties. *Inorg. Chem.* **2020**, *59*, 5161–5169.
- (43) Sun, L.; Park, S. S.; Sheberla, D.; Dincă, M. Measuring and Reporting Electrical Conductivity in Metal-Organic Frameworks: Cd<sub>2</sub>(TTFTB) as a Case Study. *J. Am. Chem. Soc.* **2016**, *138*, 14772–14782.
- (44) Martín, N. Tetrathiafulvalene: the advent of organic metals. *Chem. Commun.* **2013**, *49*, 7025–7027.
- (45) Kagoshima, S. Peierls Phase Transition. *Jpn. J. Appl. Phys.* **1981**, *20*, 1617–1634.
- (46) Imada, M.; Fujimori, A.; Tokura, Y. Metal-insulator transitions. *Rev. Mod. Phys.* **1998**, *70*, 1039–1263.
- (47) Otsubo, T.; Takimiya, K.; Aso, Y. Synthetic Methods of Selenium- and Tellurium Variants of Tetrathiafulvalene Electron Donors. *Phosphorus Sulfur Silicon Relat. Elem.* **2001**, *171*, 231–253.
-

- (48) Cowan, D. O.; Mays, M. D.; Kistenmacher, T. J.; Poehler, T. O.; Beno, M. A.; Kini, A. M.; Williams, J. M.; Kwok, Y. K.; Carlson, K. D.; Xiao, L.; Novoa, J. J.; Whangbo, M.-H. Structural and Electronic Properties of TXF-TCNQ (X = S, Se, Te). *Mol. Cryst. Liq. Cryst.* **1990**, *181*, 43–58.
- (49) Engler, E. M.; Patel, V. V. Structure control in organic metals. Synthesis of tetraselenofulvalene and its charge transfer salt with tetracyano-p-quinodimethane. *J. Am. Chem. Soc.* **1974**, *96*, 7376–7378.
- (50) McCullough, R. D.; Kok, G. B.; Lerstrup, K. A.; Cowan, D. O. Tetratellurafulvalene(TTeF). *J. Am. Chem. Soc.* **1987**, *109*, 4115–4116.
- (51) Herr, D. E.; Mays, M. D.; Mccullough, R. D.; Bailey, A. B.; Cowan, D. O. Optimizing the Synthesis of Tetratellurafulvalene. *J. Org. Chem.* **1996**, *61*, 7006–7011.
- (52) Yamada, J.; Sugimoto, T., *TTF Chemistry: Fundamentals and Applications of Tetrathiafulvalene*; Springer Berlin Heidelberg: 2004.
- (53) Schukat, G.; Fanghänel, E. Synthesis, Reactions, and Selected Physico-Chemical Properties of 1,3- and 1,2-Tetrachalcogenafulvalenes. *Sulfur Rep.* **2003**, *24*, 1–190.
- (54) Lakshmikantham, M. V.; Cava, M. P. Alternate synthesis of tetraselenafulvalene. *J. Org. Chem.* **1976**, *41*, 882–882.
- (55) Pan, W.-H.; Fackler Jr., J. P.; Anderson, D. M.; Henderson, S. G. D.; Stephenson, T. A. In *Inorganic Syntheses*; John Wiley & Sons, Ltd: 1982, pp 6–11.
- (56) Jackson, Y. A.; White, C. L.; Lakshmikantham, M. V.; Cava, M. P. 2-Methylene-1,3-diselenole: A precursor of tetraselenafulvalene (TSeF). *Tetrahedron Lett.* **1987**, *28*, 5635–5636.
- (57) Takimiya, K.; Jeon, H. J.; Otsubo, T. A Practical Two-Step Synthesis of Tetraselenafulvalene (TSF). *Synthesis* **2005**, *2005*, 2810–2813.
- (58) Lakshmikantham, M. V.; Cava, M. P. Synthesis of sym-(E/Z)-diselenadithiafulvalene. *J. Org. Chem.* **1980**, *11*, 2632–2636.
- (59) Rajagopal, D.; Lakshmikantham, M. V.; Cava, M. P. 4-Phenyl-2-methylene-1,3-diselenole: Synthesis and reactions. *Sulfur Lett.* **2002**, *25*, 129–133.
- (60) Johannsen, I.; Lerstrup, K.; Henriksen, L.; Bechgaard, K. A novel exchange reaction between diselenides and bis(N,N-dialkylselenocarbamoyl)selenides. Application in the synthesis of tetraselenafulvalene (TSF). *J. Chem. Soc., Chem. Commun.* **1984**, 89–90.
- (61) Shu, P.; Bloch, A. N.; Carruthers, T. F.; Cowan, D. O. New synthesis of substituted diselenadithiafulvalenes (DSDTF) and tetraselenafulvalenes (TSF). *J. Chem. Soc., Chem. Commun.* **1977**, 505–506.

- (62) Wudl, F.; Nalewajek, D. Preparation of tetramethyltetraselenafulvalene without the use of carbon diselenide. *J. Chem. Soc., Chem. Commun.* **1980**, 866a–866a.
- (63) Chiang, L. Y.; Poehler, T. O.; Bloch, A. N.; Cowan, D. O. A modified synthesis of tetraselenafulvalenes. *J. Chem. Soc., Chem. Commun.* **1980**, 866b–867.
- (64) Moradpour, A.; Peyrussan, V.; Johansen, I.; Bechgaard, K. High-yield synthesis of tetramethyltetraselenafulvalene (TMTSF) avoiding the use of gaseous hydrogen selenide. *J. Org. Chem.* **1983**, *48*, 388–389.
- (65) Shaver, A. G.; McCall, J. M. Preparation and Variable-Temperature NMR Studies of the Metallocyclosulfanes  $Cp_2MS_5$  and  $(Me_5Cp)_2MS_3$ , where M = Ti, Zr and Hf. *Organometallics* **1984**, *16*, 1823–1829.
- (66) Bolinger, C. M.; Rauchfuss, T. B. Template syntheses of 1,2-alkene dichalcogenide chelates via the addition of activated acetylenes to biscyclopentadienyttitanium pentachalcogenides. *Inorg. Chem.* **1982**, *21*, 3947–3954.
- (67) Engler, E. M.; Patel, V. V.; Schumaker, R. R. Triselenathiafulvalenes: a novel sulphur–selenium interchange on trimethyl phosphite coupling of substituted 1,3-diselenole-2-thiones. *J. Chem. Soc., Chem. Commun.* **1977**, 835–836.
- (68) Walwyn, R.; Chan, B.; Usov, P. M.; Solomon, M. B.; Duyker, S. G.; Koo, J. Y.; Kawano, M.; Turner, P.; Kepert, C. J.; D'Alessandro, D. M. Spectroscopic, electronic and computational properties of a mixed tetrachalcogenafulvalene and its charge transfer complex. *J. Mater. Chem. C* **2017**, *6*, 1092–1104.
- (69) Imakubo, T.; Shirahata, T. CSe<sub>2</sub>-free synthesis of [1,3]diselenole-2-thione and its application to syntheses of iodinated tetraselenafulvalenes (TSeFs). *Chem. Commun.* **2003**, *15*, 1940–1941.
- (70) Kato, R.; Kobayashi, H.; Kobayashi, A. Synthesis and properties of bis(ethylenedithio)tetraselenafulvalene (BEDT-TSeF) compounds. *Synth. Met.* **1991**, *42*, 2093–2096.
- (71) Papavassiliou, G. C.; Gionis, V.; Yiannopoulos, S.; Zambounis, J. S.; Mousdis, G.; Kobayashi, K.; Umemoto, K. Some Nitrogen-Containing Tetraheterofulvalenes and a Few of Their Conductive Salts. *Mol. Cryst. Liq. Cryst.* **1988**, *156*, 277–287.
- (72) Okano, Y.; Sawa, H.; Aonuma, S.; Kato, R. Synthesis, Conductivity, and Structure of a Novel Organic Conductor (TMET-STF)<sub>2</sub>ClO<sub>4</sub>. Coexistence of One- and Two-dimensional Donor Columns. *Chem. Lett.* **1993**, *1993*, 1851–1854.



- (73) Okano, Y.; Iso, M.; Kashimura, Y.; Yamaura, J.-i.; Kato, R. A new synthesis of Se-containing TTF derivatives. *Synth. Met.* **1999**, *102*, 1703–1704.
- (74) Johannsen, I.; Bechgaard, K.; Mortensen, K.; Jacobsen, C. S. Dibenzotetraselenafulvalene (DBTSF). Synthesis and conducting salts. *J. Chem. Soc., Chem. Commun.* **1983**, 295–296.
- (75) Rajeswari, S.; Jackson, Y. A.; Cava, M. P. Tetralithiation of tetraselenafulvalene: a new synthesis of tetrasubstituted tetraselenafulvalenes. *J. Chem. Soc., Chem. Commun.* **1988**, 1089–1090.
- (76) Saito, G.; Yoshida, Y.; Murofushi, H.; Iwasawa, N.; Hiramatsu, T.; Otsuka, A.; Yamochi, H.; Isa, K.; Mineo-Ota, E.; Konno, M.; Mori, T.; Imaeda, K.; Inokuchi, H. Preparation, Structures, and Physical Properties of Tetrakis(alkylthio)tetraselenafulvalene (TTC<sub>n</sub>-TSeF, *n* = 1–15). *Bull. Chem. Soc. Jpn.* **2010**, *83*, 335–344.
- (77) Takimiya, K.; Kataoka, Y.; Niihara, N.; Aso, Y.; Otsubo, T. A General Method for the Synthesis of Alkylenedithio- and Bis(alkylenedithio)tetraselenafulvalenes. *J. Org. Chem.* **2003**, *68*, 5217–5224.
- (78) Colacot, T., *New Trends in Cross-Coupling, Theory and Applications*; Colacot, T., Ed.; Catalysis Series; The Royal Society of Chemistry: 2015.
- (79) De Meijere, A., Bräse, S., Oestreich, M., Eds.; John Wiley & Sons, Ltd: 2014.
- (80) Bates, R.; John Wiley & Sons, Ltd: 2012.
- (81) Iyoda, M.; Hara, K.; Rao, C. R. V.; Kuwatani, Y.; Takimiya, K.; Morikami, A.; Aso, Y.; Otsubo, T. Synthesis and properties of bitetraselenafulvalene. *Tetrahedron Lett.* **1999**, *40*, 5729–5730.
- (82) Nafe, J.; Auras, F.; Karaghiosoff, K.; Bein, T.; Knochel, P. Selective Functionalization of Tetrathiafulvalene Using Mg- and Zn-TMP-Bases: Preparation of Mono-, Di-, Tri-, and Tetrasubstituted Derivatives. *Org. Lett.* **2015**, *17*, 5356–5359.
- (83) Alberico, D.; Scott, M. E.; Lautens, M. Aryl-Aryl Bond Formation by Transition-Metal-Catalyzed Direct Arylation. *Chem. Rev.* **2007**, *107*, 174–238.
- (84) Ackermann, L.; Vicente, R.; Kapdi, A. R. Transition-Metal-Catalyzed Direct Arylation of (Hetero)Arenes by C-H Bond Cleavage. *Angew. Chem. Int. Ed.* **2009**, *48*, 9792–9826.
- (85) Schipper, D. J.; Fagnou, K. Direct Arylation as a Synthetic Tool for the Synthesis of Thiophene-Based Organic Electronic Materials. *Chem. Mater.* **2011**, *23*, 1594–1600.
- (86) Mitamura, Y.; Yorimitsu, H.; Oshima, K.; Osuka, A. Straightforward access to aryl-substituted tetrathiafulvalenes by palladium-catalysed direct C–H

- arylation and their photophysical and electrochemical properties. *Chem. Sci.* **2011**, *2*, 2017–2021.
- (87) Cheng, H.-G.; Chen, H.; Liu, Y.-E.; Zhou, Q. The Liebeskind–Srogl Cross-Coupling Reaction and its Synthetic Applications. *Asian J. Org. Chem.* **2018**, *7*, 490–508.
- (88) Prokopcová, H.; Kappe, C. O. The Liebeskind–Srogl C-C Cross-Coupling Reaction. *Angew. Chem. Int. Ed.* **2009**, *48*, 2276–2286.
- (89) Metzger, A.; Melzig, L.; Despotopoulou, C.; Knochel, P. Pd-Catalyzed Cross-Coupling of Functionalized Organozinc Reagents with Thiomethyl-Substituted Heterocycles. *Org. Lett.* **2009**, *11*, 4228–4231.
- (90) Stein, A. L. A.; Bilheri, F. N.; Zeni, G. R. Application of organoselenides in the Suzuki, Negishi, Sonogashira and Kumada cross-coupling reactions. *Chem. Commun.* **2015**, *51*, 15522–15525.
- (91) Klayman, D. L.; Griffin, T. S. Reaction of selenium with sodium borohydride in protic solvents. A Facile Method for the introduction of selenium into organic molecules. *J. Am. Chem. Soc.* **1973**, *95*, 197–199.
- (92) Tanini, D.; Capperucci, A. Synthesis and Applications of Organic Selenols. *Adv. Synth. Catal.* **2021**, *363*, 5360–5385.
- (93) Matsumura, M.; Kumagai, H.; Murata, Y.; Kakusawa, N.; Yasuike, S. Simple and efficient copper-catalyzed synthesis of symmetrical diaryl selenides from triarylbismuthanes and selenium under aerobic conditions. *J. Organomet. Chem.* **2016**, *807*, 11–16.
- (94) Yadav, D.; Dixit, A. K.; Raghothama, S.; Awasthi, S. K. Ni nanoparticle-confined covalent organic polymer directed diaryl-selenides synthesis. *Dalton Trans.* **2020**, *49*, 12266–12272.
- (95) Li, Y.; Nie, C.; Wang, H.; Li, X.; Verpoort, F.; Duan, C. A Highly Efficient Method for the Copper-Catalyzed Selective Synthesis of Diaryl Chalcogenides from Easily Available Chalcogen Sources. *Eur. J. Org. Chem.* **2011**, *2011*, 7331–7338.
- (96) Kumar, A. V.; Reddy, V. P.; Reddy, C. S.; Rao, K. S. R. Potassium selenocyanate as an efficient selenium source in C–Se cross-coupling catalyzed by copper iodide in water. *Tetrahedron Lett.* **2011**, *52*, 3978–3981.
- (97) Zhang, S.; Karra, K.; Heintz, C.; Kleckler, E.; Jin, J. Microwave-assisted Cu<sub>2</sub>O-catalyzed one-pot synthesis of symmetrical diaryl selenides from elemental selenium. *Tetrahedron Lett.* **2013**, *54*, 4753–4755.
- (98) Vardhan Reddy, K. H.; Reddy, V. P.; Madhav, B. T. P.; Shankar, J.; Nageswar, Y. V. D. Nano Copper Oxide Catalyzed Synthesis of Symmetrical Diaryl Selenides via Cascade Reaction of KSeCN with Aryl Halides. *Synlett* **2011**, *2011*, 1268–1272.

- (99) Zhao, D.; Wang, W.; Yang, F.; Lan, J.; Yang, L.; Gao, G.; You, J. Copper-Catalyzed Direct C Arylation of Heterocycles with Aryl Bromides: Discovery of Fluorescent Core Frameworks. *Angew. Chem. Int. Ed.* **2009**, *48*, 3296–3300.
- (100) Jia, N.-N.; Tian, X.-C.; Qu, X.-X.; Chen, X.-X.; Cao, Y.-N.; Yao, Y.-x.; Gao, F.; Zhou, X.-L. Copper-catalyzed Direct 2-Arylation of Benzoxazoles and Benzoimidazoles with Aryl Bromides and Cytotoxicity of Products. *Sci. Rep.* **2017**, *7*, 43758.
- (101) Do, H.-Q.; Daugulis, O. Copper-Catalyzed Arylation of Heterocycle C-H Bonds. *J. Am. Chem. Soc.* **2007**, *129*, 12404–12405.
- (102) Haas, D.; Hammann, J. M.; Greiner, R.; Knochel, P. Recent Developments in Negishi Cross-Coupling Reactions. *ACS Catal.* **2016**, *6*, 1540–1552.
- (103) Luzung, M. R.; Patel, J. S.; Yin, J. A Mild Negishi Cross-Coupling of 2-Heterocyclic Organozinc Reagents and Aryl Chlorides. *J. Org. Chem.* **2010**, *75*, 8330–8332.
- (104) Yang, Y.; Oldenhuis, N. J.; Buchwald, S. L. Mild and General Conditions for Negishi Cross-Coupling Enabled by the Use of Palladacycle Precatalysts. *Angew. Chem. Int. Ed.* **2013**, *52*, 615–619.
- (105) Menzel, K.; Fisher, E. L.; Dimichele, L.; Frantz, D. E.; Nelson, T.; Kress, M. H. An Improved Method for the Bromination of Metalated Haloarenes via Lithium, Zinc Transmetalation: A Convenient Synthesis of 1,2-Dibromoarenes. *J. Org. Chem.* **2006**, *71*, 2188–2191.
- (106) Yus, M.; Gomis, J. Negishi cross-coupling with functionalised organozinc compounds prepared by lithium-zinc transmetalation. *Tetrahedron Lett.* **2001**, *42*, 5721–5724.
- (107) Krasovskiy, A. L.; Krasovskaya, V.; Knochel, P. Mixed Mg/Li Amides of the Type  $R_2NMgCl \cdot LiCl$  as Highly Efficient Bases for the Regioselective Generation of Functionalized Aryl and Heteroaryl Magnesium Compounds. *Angew. Chem. Int. Ed.* **2006**, *45*, 2958–2961.
- (108) Mosrin, M.; Knochel, P.  $TMPZnCl \cdot LiCl$ : A New Active Selective Base for the Directed Zincation of Sensitive Aromatics and Heteroaromatics. *Org. Lett.* **2009**, *11*, 1837–1840.
- (109) Dostert, C.; Müller, T. J. J. A one-pot dilithiation-lithium-zinc exchange-Negishi coupling approach to 2,6-di(hetero)aryl substituted dithienothiazines a novel class of electronically fine-tunable redox systems. *Org. Chem. Front.* **2015**, *2*, 481–491.
- (110) Takimiya, K.; Kataoka, Y.; Morikami, A.; Aso, Y.; Otsubo, T. Halogen substituted tetraselenafulvalene derivatives. *Synth. Met.* **2001**, *120*, 875–876.

- (111) Lind, C. Two Decades of Negative Thermal Expansion Research: Where Do We Stand? *Materials* **2012**, *5*, 1125–1154.
- (112) Miller, W.; Smith, C. W.; Mackenzie, D. S.; Evans, K. E. Negative thermal expansion: a review. *J. Mater. Sci.* **2009**, *44*, 5441–5451.
- (113) Dove, M. T.; Fang, H. Negative thermal expansion and associated anomalous physical properties: review of the lattice dynamics theoretical foundation. *Rep. Prog. Phys.* **2016**, *79*, 066503.
- (114) Takenaka, K. Negative thermal expansion materials: technological key for control of thermal expansion. *Sci. Technol. Adv. Mater.* **2012**, *13*, 013001.
- (115) Chen, J.; Hu, L.; Deng, J. N.; Xing, X. Negative thermal expansion in functional materials: controllable thermal expansion by chemical modifications. *Chem. Soc. Rev.* **2015**, *44*, 3522–3567.
- (116) Liu, Z.; Gao, Q.; Chen, J.; Deng, J. N.; Lin, K.; Xing, X. Negative thermal expansion in molecular materials. *Chem. Commun.* **2018**, *54*, 5164–5176.
- (117) Coates, C. S.; Goodwin, A. L. How to quantify isotropic negative thermal expansion: magnitude, range, or both? *Mater. Horiz.* **2019**, *6*, 211–218.
- (118) Shi, N.; Sanson, A.; Gao, Q.; Sun, Q.; Ren, Y.; Huang, Q.; de Souza, D. O.; Xing, X.; Chen, J. Strong negative thermal expansion in a low-cost and facile oxide of  $\text{Cu}_2\text{P}_2\text{O}_7$ . *J. Am. Chem. Soc.* **2020**, *142*, 3088–3093.
- (119) Yamamura, Y.; Horikoshi, A.; Yasuzuka, S.; Saitoh, H.; Saito, K. Negative thermal expansion emerging upon structural phase transition in  $\text{ZrV}_2\text{O}_7$  and  $\text{HfV}_2\text{O}_7$ . *Dalton Trans.* **2011**, *40*, 2242–2248.
- (120) Sumithra, S.; Tyagi, A. K.; Umarji, A. M. Negative thermal expansion in  $\text{Er}_2\text{W}_3\text{O}_{12}$  and  $\text{Yb}_2\text{W}_3\text{O}_{12}$  by high temperature X-ray diffraction. *Mater. Sci. Eng. B* **2005**, *116*, 14–18.
- (121) Gao, H.; Wei, W.; Tan, Y.-h.; Tang, Y. Phase Transition and Negative Thermal Expansion in Guanidinium Magnesium-Hypophosphite Hybrid Perovskite. *Chem. Mater.* **2020**, *32*, 6886–6891.
- (122) Chen, W.-t.; Ablitt, C.; Bristowe, N. C.; Mostofi, A. A.; Saito, T.; Shimakawa, Y.; Senn, M. S. Negative thermal expansion in high pressure layered perovskite  $\text{Ca}_2\text{GeO}_4$ . *Chem. Commun.* **2019**, *55*, 2984–2987.
- (123) Yamamoto, H.; Imai, T.; Sakai, Y.; Azuma, M. Colossal Negative Thermal Expansion in Electron-Doped  $\text{PbVO}_3$  Perovskites. *Angew. Chem. Int. Ed.* **2018**, *57*, 8170–8173.
- (124) Shi, N.; Gao, Q.; Sanson, A.; Li, Q.; Fan, L.; Ren, Y.; Olivi, L.; Chen, J.; Xing, X. Negative thermal expansion in cubic  $\text{FeFe}(\text{CN})_6$  Prussian blue analogues. *Dalton Trans.* **2019**, *48*, 3658–3663.
- (125) Wang, C.; Chang, D.; Gao, Q.; Liu, C.; Wang, Q.; Huang, X.; Jia, Y. Large and tunable negative thermal expansion induced by a synergistic effect in

- $M_2^{II}[M^{IV}(CN)_8]$  Prussian blue analogues. *Phys. Chem. Chem. Phys.* **2020**, *22*, 18655–18662.
- (126) Chapman, K. W.; Chupas, P. J.; Kepert, C. J. Compositional dependence of negative thermal expansion in the Prussian Blue analogues  $M^{II}Pt^{IV}(CN)_6$  ( $M = Mn, Fe, Co, Ni, Cu, Zn, Cd$ ). *J. Am. Chem. Soc.* **2006**, *128*, 7009–7014.
- (127) Mary, T. A.; Evans, J. S. O.; Vogt, T.; Sleight, A. W. Negative Thermal Expansion from 0.3 to 1050 Kelvin in  $ZrW_2O_8$ . *Science* **1996**, *272*, 90–92.
- (128) Evans, J. D.; Dürholt, J. P.; Kaskel, S.; Schmid, R. Assessing Negative Thermal Expansion in Mesoporous Metal-Organic Frameworks by Molecular Simulation. *J. Mater. Chem. A* **2019**, *7*, 24019–24026.
- (129) Burtch, N. C.; Baxter, S. J.; Heinen, J.; Bird, A.; Schneemann, A.; Dubbeldam, D.; Wilkinson, A. P. Negative Thermal Expansion Design Strategies in a Diverse Series of Metal–Organic Frameworks. *Adv. Funct. Mater.* **2019**, *29*, 1904669.
- (130) Lock, N.; Christensen, M.; Wu, Y.; Peterson, V. K.; Thomsen, M. K.; Piltz, R. O.; Ramirez-Cuesta, A. J.; McIntyre, G. J.; Norén, K.; Kutteh, R. A.; Kepert, C. J.; Kearley, G. J.; Iversen, B. B. Scrutinizing negative thermal expansion in MOF-5 by scattering techniques and ab initio calculations. *Dalton Trans.* **2013**, *42*, 1996–2007.
- (131) Wu, Y.; Kobayashi, A.; Halder, G. J.; Peterson, V. K.; Chapman, K. W.; Lock, N.; Southon, P. D.; Kepert, C. J. Negative thermal expansion in the metal-organic framework material  $Cu_3(1,3,5\text{-benzenetricarboxylate})_2$ . *Angew. Chem. Int. Ed.* **2008**, *47*, 8929–8932.
- (132) Liu, Z.; Li, Q.; Zhu, H.; Lin, K.; Deng, J. N.; Chen, J.; Xing, X. 3D negative thermal expansion in orthorhombic MIL-68(In). *Chem. Commun.* **2018**, *54*, 5712–5715.
- (133) Lock, N.; Wu, Y.; Christensen, M.; Cameron, L. J.; Peterson, V. K.; Bridgeman, A. J.; Kepert, C. J.; Iversen, B. B. Elucidating Negative Thermal Expansion in MOF-5. *J. Phys. Chem. C* **2010**, *114*, 16181–16186.
- (134) Zhou, W.; Wu, H.; Yildirim, T.; Simpson, J. R.; Walker, A. R. H. Origin of the Exceptional Negative Thermal Expansion in Metal-Organic Framework-5  $Zn_4O(1,4\text{-benzenedicarboxylate})_3$ . *Phys. Rev. B* **2008**, *78*, 054114.
- (135) Lock, N.; Christensen, M.; Kepert, C. J.; Iversen, B. B. Effect of gas pressure on negative thermal expansion in MOF-5. *Chem. Commun.* **2013**, *49*, 789–791.
- (136) Balestra, S. R. G.; Bueno-Perez, R.; Hamad, S.; Dubbeldam, D.; Ruiz-Salvador, A. R.; Calero, S. Controlling Thermal Expansion: A Metal-Organic Frameworks Route. *Chem. Mater.* **2016**, *28*, 8296–8304.

- (137) Schneider, C.; Bodesheim, D.; Ehrenreich, M. G.; Crocellà, V.; Mink, J.; Fischer, R. A.; Butler, K. T.; Kieslich, G. Tuning the Negative Thermal Expansion Behavior of the Metal-Organic Framework  $\text{Cu}_3\text{BTC}_2$  by Retrofitting. *J. Am. Chem. Soc.* **2019**, *141*, 10504–10509.
- (138) Kapustin, E. A.; Lee, S.; Alshammari, A. S.; Yaghi, O. M. Molecular Retrofitting Adapts a Metal–Organic Framework to Extreme Pressure. *ACS Cent. Sci.* **2017**, *3*, 662–667.
- (139) Talin, A. A.; Centrone, A.; Ford, A. C.; Foster, M. E.; Stavila, V.; Haney, P. M.; Kinney, R. A.; Szalai, V. A.; Gabaly, F. E.; Yoon, H. P.; Léonard, F.; Allendorf, M. D. Tunable Electrical Conductivity in Metal-Organic Framework Thin-Film Devices. *Science* **2014**, *343*, 66–69.
- (140) Nie, X.; Kulkarni, A. R.; Sholl, D. S. Computational Prediction of Metal Organic Frameworks Suitable for Molecular Infiltration as a Route to Development of Conductive Materials. *J. Phys. Chem. Lett.* **2015**, *6*, 1586–1591.
- (141) Ryder, M. R.; Civalleri, B.; Cinque, G.; Tan, J.-C. Discovering connections between terahertz vibrations and elasticity underpinning the collective dynamics of the HKUST-1 metal-organic framework. *CrystEngComm* **2016**, *18*, 4303–4312.
- (142) Prestipino, C.; Regli, L.; Vitillo, J. G.; Bonino, F.; Damin, A.; Lamberti, C.; Zecchina, A.; Solari, P. L.; Kongshaug, K. O.; Bordiga, S. Local Structure of Framework Cu(II) in HKUST-1 Metallorganic Framework: Spectroscopic Characterization upon Activation and Interaction with Adsorbates. *Chem. Mater.* **2006**, *18*, 1337–1346.
- (143) Bresciani, G.; Biancalana, L.; Pampaloni, G.; Zacchini, S.; Ciancaleoni, G.; Marchetti, F. A Comprehensive Analysis of the Metal–Nitrile Bonding in an Organo-Diiron System. *Molecules* **2021**, *26*, 7088.
- (144) Cowley, R. E.; Christian, G.; Brennessel, W. W.; Neese, F.; Holland, P. L. A Reduced ( $\beta$ -Diketiminato)iron Complex with End-On and Side-On Nitriles: Strong Backbonding or Ligand Non-Innocence? *Eur. J. Inorg. Chem.* **2012**, *2012*, 479–483.
- (145) Kaim, W.; Moscherosch, M. H. The coordination chemistry of TCNE, TCNQ and related polynitrile  $\pi$  acceptors. *Coord. Chem. Rev.* **1994**, *129*, 157–193.
- (146) Newville, M. et al. Imfit/Imfit-py: 1.0.3, version 1.0.3, 2021.
- (147) Losq, C. L. Rampsy: a Python library for processing spectroscopic (IR, Raman, XAS...) data. Version 2, 2018.
- (148) Pawley, G. S. Unit-cell refinement from powder diffraction scans. *J. Appl. Cryst.* **1981**, *14*, 357–361.

- 
- (149) Coelho, A. A. TOPAS and TOPAS-Academic: an optimization program integrating computer algebra and crystallographic objects written in C++. *J. Appl. Cryst.* **2018**, *51*, 210–218.
- (150) Herrera, L. F.; Fan, C.; Do, D. D.; Nicholson, D. A. A revisit to the Gibbs dividing surfaces and helium adsorption. *Adsorption* **2011**, *17*, 955–965.
- (151) Zhang, W.; Weber, D. A.; Weigand, H.; Arlt, T.; Manke, I.; Schröder, D.; Koerver, R.; Leichtweiss, T.; Hartmann, P.; Zeier, W. G.; Janek, J. Interfacial Processes and Influence of Composite Cathode Microstructure Controlling the Performance of All-Solid-State Lithium Batteries. *ACS Appl. Mater. Interfaces* **2017**, *9*, 17835–17845.
- (152) Pandey, D. K.; Shabade, A. B.; Punji, B. Copper-Catalyzed Direct Arylation of Indoles and Related (Hetero)arenes: A Ligandless and Solvent-free Approach. *Adv. Synth. Catal.* **2020**, *362*, 2534–2540.
- (153) Yotphan, S.; Bergman, R. G.; Ellman, J. A. Application of Daugulis Copper-Catalyzed Direct Arylation to the Synthesis of 5-Aryl Benzotriazepines. *Org. Lett.* **2009**, *11*, 1511–1514.
- (154) Do, H.-Q.; Khan, R. M. K.; Daugulis, O. A General Method for Copper-Catalyzed Arylation of Arene C-H Bonds. *J. Am. Chem. Soc.* **2008**, *130*, 15185–15192.
- (155) Hsu, S.-y.; Chiang, L. Y. An efficient synthesis of alkyl and aryl chalcogenated derivatives of tetrathiafulvalene. *J. Org. Chem.* **1987**, *52*, 3444–3446.
- (156) Meline, R. L.; Elsenbaumer, R. L. The tuning of heterocyclic isomerization: additional routes to extended donors. *Synth. Met.* **1999**, *102*, 1658–1661.
- (157) Bhunia, M. K.; Hughes, J. T.; Fettingter, J. C.; Navrotsky, A. Thermochemistry of Paddle Wheel MOFs: Cu-HKUST-1 and Zn-HKUST-1. *Langmuir* **2013**, *29*, 8140–8145.
- (158) Zhou, H.-C.; Long, J. R.; Yaghi, O. M. Introduction to Metal-Organic Frameworks. *Chem. Rev.* **2012**, *112*, 673–674.
- (159) Stock, N.; Biswas, S. Synthesis of Metal-Organic Frameworks (MOFs): Routes to Various MOF Topologies, Morphologies, and Composites. *Chem. Rev.* **2012**, *112*, 933–969.
- (160) Batten, S. R.; Champness, N. R.; Chen, X.-M.; García-Martínez, J.; Kitagawa, S.; Öhrström, L.; O'keeffe, M.; Suh, M. P.; Reedijk, J. Terminology of Metal-Organic Frameworks and Coordination Polymers. *Pure and Applied Chemistry* **2013**, *85*, 1715–1724.
- (161) Li, J.-R.; Sculley, J. P.; Zhou, H. Metal-Organic Frameworks for Separations. *Chem. Rev.* **2012**, *112*, 869–932.
-

- (162) Furukawa, H.; Cordova, K. E.; O'keeffe, M.; Yaghi, O. M. The Chemistry and Applications of Metal-Organic Frameworks. *Science* **2013**, *341*.
- (163) Rosi, N. L.; Eckert, J.; Eddaoudi, M.; Vodak, D. T.; Kim, J.; O'keeffe, M.; Yaghi, O. M. Hydrogen Storage in Microporous Metal-Organic Frameworks. *Science* **2003**, *300*, 1127–1129.
- (164) Kornienko, N.; Zhao, Y.; Kley, C. S.; Zhu, C.; Kim, D.; Lin, S.; Chang, C. J.; Yaghi, O. M.; Yang, P. Metal-organic Frameworks for Electrocatalytic Reduction of Carbon Dioxide. *J. Am. Chem. Soc.* **2015**, *137*, 14129–14135.
- (165) Zhang, T.; Lin, W. Metal-Organic Frameworks for Artificial Photosynthesis and Photocatalysis. *Chem. Soc. Rev.* **2014**, *43*, 5982–5993.
- (166) Kreno, L. E.; Leong, K.; Farha, O. K.; Allendorf, M. D.; Duyne, R. P. V.; Hupp, J. T. Metal-Organic Framework Materials as Chemical Sensors. *Chem. Rev.* **2012**, *112*, 1105–1125.
- (167) Yi, F.-Y.; Chen, D.; Wu, M.-K.; Han, L.; Jiang, H.-L. Chemical Sensors Based on Metal-Organic Frameworks. *ChemPlusChem* **2016**, *81*, 675–690.
- (168) Liu, D.; Lu, K.; Poon, C.; Lin, W. Metal-Organic Frameworks as Sensory Materials and Imaging Agents. *Inorg. Chem.* **2014**, *53*, 1916–1924.
- (169) Yaghi, O.; Kalmutzki, M.; Diercks, C., *Introduction to Reticular Chemistry: Metal-Organic Frameworks and Covalent Organic Frameworks*; Wiley: 2019.
- (170) MacGillivray, L., *Metal-Organic Frameworks: Design and Application*; Wiley: 2010.
- (171) Kaskel, S., *The Chemistry of Metal-Organic Frameworks, 2 Volume Set: Synthesis, Characterization, and Applications*; The Chemistry of Metal-organic Frameworks: Synthesis, Characterization, and Applications Bd. 1; Wiley: 2016.
- (172) Wells, A. F. . The geometrical basis of crystal chemistry. Part 1. *Acta Crystallogr.* **1954**, *7*, 535–544.
- (173) Wells, A. F. . The geometrical basis of crystal chemistry. Part 2. *Acta Crystallogr.* **1954**, *7*, 545–554.
- (174) O'keeffe, M.; Peskov, M. A.; Ramsden, S.; Yaghi, O. M. The Reticular Chemistry Structure Resource (RCSR) Database of, and Symbols for, Crystal Nets. *Acc. Chem. Res.* **2008**, *41*, 1782–1789.
- (175) Kim, D.; Liu, X.; Lah, M. S. Topology analysis of metal-organic frameworks based on metal-organic polyhedra as secondary or tertiary building units. *Inorg. Chem. Front.* **2015**, *2*, 336–360.
-



- (176) O'keeffe, M.; Eddaoudi, M.; Li, H.; Reineke, T. M.; Yaghi, O. M. Frameworks for Extended Solids: Geometrical Design Principles. *IEEE J. Solid-State Circuits* **2000**, *152*, 3–20.
- (177) Li, H.; Eddaoudi, M.; O'keeffe, M.; Yaghi, O. M. Design and synthesis of an exceptionally stable and highly porous metal-organic framework. *Nature* **1999**, *402*, 276–279.
- (178) Friedrichs, O. D.; O'keeffe, M.; Yaghi, O. M. Three-periodic nets and tilings: regular and quasiregular nets. *Acta Crystallogr. A* **2003**, *59*, 22–27.
- (179) Momma, K.; Izumi, F. VESTA 3 for three-dimensional visualization of crystal, volumetric and morphology data. *J. Appl. Crystallogr.* **2011**, *44*, 1272–1276.
- (180) McKinstry, C.; Cussen, E. J.; Fletcher, A. J.; Patwardhan, S. V.; Sefcik, J. Effect of Synthesis Conditions on Formation Pathways of Metal Organic Framework (MOF-5) Crystals. *Cryst. Growth Des.* **2013**, *13*, 5481–5489.
- (181) Cheansirisomboon, A.; Salinas-Uber, J.; Massera, C.; Roubeau, O.; Youngme, S.; Gamez, P. One-Pot Multiple Metal-Organic Framework Formation: Concomitant Generation of Structural Isomers or of Drastically Distinct Materials. *Eur. J. Inorg. Chem.* **2014**, *2014*, 4385–4393.
- (182) Cook, T. R.; Zheng, Y.-R.; Stang, P. J. Metal-Organic Frameworks and Self-Assembled Supramolecular Coordination Complexes: Comparing and Contrasting the Design, Synthesis, and Functionality of Metal-Organic Materials. *Chem. Rev.* **2013**, *113*, 734–777.
- (183) Lin, J.; Xu, Y.-Y.; Qiu, L.; Zang, S.; Lu, C.; Duan, C.; Li, Y.-z.; Gao, S.; Meng, Q.-j. Ligand-to-metal ratio controlled assembly of nanoporous metal-organic frameworks. *Chem. Commun.* **2008**, *23*, 2659–2661.
- (184) Masaoka, S.; Tanaka, D.; Nakanishi, Y.; Kitagawa, S. Reaction-Temperature-Dependent Supramolecular Isomerism of Coordination Networks Based on the Organometallic Building Block  $[\text{Cu}^{\text{I}}_2(\mu_2\text{-BQ})(\mu_2\text{-OAc})_2]$ . *Angew. Chem. Int. Ed.* **2004**, *43*, 2530–2534.
- (185) Dong, Y.-B.; Jiang, Y.-Y.; Li, J. J.; Ma, J.; Liu, F.-L.; Tang, B.; Huang, R.-Q.; Batten, S. R. Temperature-Dependent Synthesis of Metal-Organic Frameworks Based on a Flexible Tetradentate Ligand with Bidirectional Coordination Donors. *J. Am. Chem. Soc.* **2007**, *129*, 4520–4521.
- (186) Xue, Z.; Sheng, T.; Wen, Y.; Wang, Y.; Hu, S.; Fu, R.; Wu, X. Effect of Anions on the Self-Assembly of Two Cd-Organic Frameworks: Syntheses, Structural Diversity and Photoluminescence Properties. *CrystEngComm* **2015**, *17*, 598–603.

- (187) Wang, Y.; Song, Y.; Liu, L.; Chen, J.; Wang, P.; Zhao, Y. From Interpenetration to Non-Interpenetration: A Series of Self-Assemblies Predominated by Reaction Conditions. *J. Mol. Struct.* **2018**, *1154*, 179–186.
- (188) Liu, B.; Vellingiri, K.; Jo, S.-H.; Kumar, P.; Ok, Y. S.; Kim, K.-H. Recent Advances in Controlled Modification of the Size and Morphology of Metal-Organic Frameworks. *Nano Res.* **2018**, *11*, 4441–4467.
- (189) Wang, F.-K.; Yang, S.-Y.; Dong, H.-Z. Influences of Mixed Solvent DMF/H<sub>2</sub>O or DMA/H<sub>2</sub>O on the Topologies of Coordination Polymers. *Inorg. Nano-Met. Chem.* **2020**, *51*, 1405–1410.
- (190) Akhbari, K.; Morsali, A. Effect of the Guest Solvent Molecules on Preparation of Different Morphologies of ZnO Nanomaterials from the [Zn<sub>2</sub>(1,4-bdc)<sub>2</sub>(dabco)] Metal-Organic Framework. *J. Coord. Chem.* **2011**, *64*, 3521–3530.
- (191) Li, L.; Wang, S.; Chen, T.; Sun, Z.; Luo, J.; Hong, M. Solvent-Dependent Formation of Cd(II) Coordination Polymers Based on a C<sub>2</sub>-Symmetric Tricarboxylate Linker. *Cryst. Growth Des.* **2012**, *12*, 4109–4115.
- (192) Banerjee, D.; Finkelstein, J. L.; Smirnov, A. V.; Forster, P. M.; Borkowski, L. A.; Teat, S. J.; Parise, J. B. Synthesis and Structural Characterization of Magnesium Based Coordination Networks in Different Solvents. *Cryst. Growth Des.* **2011**, *11*, 2572–2579.
- (193) Liu, B.; Yang, G.-P.; Wang, Y.; Liu, R.-t.; Hou, L.; Shi, Q.-z. Two New pH-Controlled Metal-Organic Frameworks Based on Polynuclear Secondary Building Units with Conformation-Flexible Cyclohexane-1,2,4,5-tetracarboxylate Ligand. *Inorg. Chim. Acta* **2011**, *367*, 127–134.
- (194) De Oliveira, C. A. F.; da Silva, F. F.; Malvestiti, I.; Malta, V. R. S.; Dutra, J. D. L.; da Costa, N. B.; Freire, R. O.; Junior, S. A. Effect of Temperature on Formation of Two New Lanthanide Metal-Organic Frameworks: Synthesis, Characterization and Theoretical Studies of Tm(III)-Succinate. *J. Solid State Chem.* **2013**, *197*, 7–13.
- (195) Chen, J.; Ohba, M.; Zhao, D.; Kaneko, W.; Kitagawa, S. Polynuclear Core-Based Nickel 1,4-Cyclohexanedicarboxylate Coordination Polymers as Temperature-Dependent Hydrothermal Reaction Products. *Cryst. Growth Des.* **2006**, *6*, 664–668.
- (196) Yin, P. X.; Zhang, J.; Qin, Y. Y.; Cheng, J.-K.; Li, Z.-j.; Yao, Y.-G. Role of Molar-Ratio, Temperature and Solvent on the Zn/Cd 1,2,4-Triazolate System with Novel Topological Architectures. *CrystEngComm* **2011**, *13*, 3536–3544.

- (197) Huang, L.; Wang, H.; Chen, J.; Wang, Z.; Sun, J.; Zhao, D.; Yan, Y. Synthesis, Morphology Control, and Properties of Porous Metal-Organic Coordination Polymers. *Microporous Mesoporous Mater.* **2003**, *58*, 105–114.
- (198) Li, H.; Eddaoudi, M.; Groy, T. L.; Yaghi, O. M. Establishing Microporosity in Open Metal-Organic Frameworks: Gas Sorption Isotherms for Zn(BDC) (BDC = 1,4-Benzenedicarboxylate). *J. Am. Chem. Soc.* **1998**, *120*, 8571–8572.
- (199) Li, H.; Davis, C. E.; Groy, T. L.; Kelley, D. G.; Yaghi, O. M. Coordinatively Unsaturated Metal Centers in the Extended Porous Framework of Zn<sub>3</sub>(BDC)<sub>3</sub>·6CH<sub>3</sub>OH (BDC = 1,4-Benzenedicarboxylate). *J. Am. Chem. Soc.* **1998**, *120*, 2186–2187.
- (200) Tranchemontagne, D. J.; Hunt, J. R.; Yaghi, O. M. Room temperature synthesis of metal-organic frameworks: MOF-5, MOF-74, MOF-177, MOF-199, and IRMOF-0. *Tetrahedron* **2008**, *64*, 8553–8557.
- (201) Ameloot, R.; Gobechiya, E. R.; Uji-i, H.; Martens, J. A.; Hofkens, J.; Alaerts, L.; Sels, B. F.; Vos, D. E. D. Direct Patterning of Oriented Metal-Organic Framework Crystals via Control over Crystallization Kinetics in Clear Precursor Solutions. *Adv. Mater.* **2010**, *22*, 2685–2688.
- (202) Embrechts, H.; Kriesten, M.; Hoffmann, K.; Peukert, W.; Hartmann, M.; Distaso, M. Elucidation of the Formation Mechanism of Metal-Organic Frameworks via in-Situ Raman and FTIR Spectroscopy under Solvothermal Conditions. *J. Phys. Chem. C* **2018**, *122*, 12267–12278.
- (203) Embrechts, H.; Hartmann, M.; Peukert, W.; Distaso, M. In Situ Monitoring of Particle Formation with Spectroscopic and Analytical Techniques Under Solvo-thermal Conditions. *Chem. Eng. Technol.* **2020**, *43*, 879–886.
- (204) Hausdorf, S.; Baitalow, F.; Seidel, J.; Mertens, F. Gaseous Species as Reaction Tracers in the Solvothermal Synthesis of the Zinc Oxide Terephthalate MOF-5. *J. Phys. Chem. A* **2007**, *111*, 4259–4266.
- (205) Zahn, G.; Zerner, P.; Lippke, J.; Kempf, F. L.; Lilienthal, S.; Schröder, C.; Schneider, A. M.; Behrens, P. Insight into the mechanism of modulated syntheses: in situ synchrotron diffraction studies on the formation of Zr-fumarate MOF. *CrystEngComm* **2014**, *16*, 9198–9207.
- (206) Rosnes, M. H.; Nesse, F. S.; Opitz, M.; Dietzel, P. D. C. Morphology control in modulated synthesis of metal-organic framework CPO-27. *Microporous and Mesoporous Mater.* **2019**, *275*, 207–213.
- (207) Hu, Z.; Castano, I.; Wang, S.; Wang, Y.; Peng, Y.; Qian, Y.; Chi, C.; Wang, X.; Zhao, D. Modulator Effects on the Water-Based Synthesis of Zr/Hf Metal-Organic Frameworks: Quantitative Relationship Studies between

- Modulator, Synthetic Condition, and Performance. *Cryst. Growth Des.* **2016**, *16*, 2295–2301.
- (208) Thür, R.; Velthoven, N. V.; Lemmens, V.; Bastin, M.; Smolders, S.; Vos, D. E. D.; Vankelecom, I. F. J. Modulator-Mediated Functionalization of MOF-808 as a Platform Tool to Create High-Performance Mixed-Matrix Membranes. *ACS Appl. Mater. Interfaces* **2019**, *11*, 44792–44801.
- (209) Webber, T. E.; Desai, S. P.; Combs, R. L.; Bingham, S.; Lu, C. C.; Penn, R. L. Size Control of the MOF NU-1000 through Manipulation of the Modulator/Linker Competition. *Cryst. Growth Des.* **2020**, *20*, 2965–2972.
- (210) Forgan, R. S. Modulated self-assembly of metal-organic frameworks. *Chem. Sci.* **2020**, *11*, 4546–4562.
- (211) Mondloch, J. E.; Karagiari, O.; Farha, O. K.; Hupp, J. T. Activation of metal-organic framework materials. *CrystEngComm* **2013**, *15*, 9258–9264.
- (212) Farha, O. K.; Hupp, J. T. Rational Design, Synthesis, Purification, and Activation of Metal-Organic Framework Materials. *Acc. Chem. Res.* **2010**, *43*, 1166–1175.
- (213) Eddaoudi, M.; Kim, J.; Rosi, N.; Vodak, D. T.; Wachter, J.; O’keeffe, M.; Yaghi, O. M. Systematic Design of Pore Size and Functionality in Isoreticular MOFs and Their Application in Methane Storage. *Science* **2002**, *295*, 469–472.
- (214) Nelson, A.; Farha, O. K.; Mulfort, K. L.; Hupp, J. T. Supercritical Processing as a Route to High Internal Surface Areas and Permanent Microporosity in Metal-Organic Framework Materials. *J. Am. Chem. Soc.* **2009**, *131*, 458–460.
- (215) Ma, L.; Jin, A.; Xie, Z.; Lin, W. Freeze Drying Significantly Increases Permanent Porosity and Hydrogen Uptake in 4,4-Connected Metal-Organic Frameworks. *Angew. Chem. Int. Ed.* **2009**, *48*, 9905–9908.
- (216) Howarth, A. J.; Peters, A. W.; Vermeulen, N. A.; Wang, T. C.; Hupp, J. T.; Farha, O. K. Best Practices for the Synthesis, Activation, and Characterization of Metal-Organic Frameworks. *Chem. Mater.* **2017**, *29*, 26–39.
- (217) Hoskins, B. F.; Robson, R. Infinite Polymeric Frameworks Consisting of Three Dimensionally Linked Rod-Like Segments. *J. Am. Chem. Soc.* **1989**, *111*, 5962–5964.
- (218) Friedrichs, O. D.; O’keeffe, M.; Yaghi, O. M. Three-periodic nets and tilings: semiregular nets. *Acta Crystallogr. A* **2003**, *59*, 515–525.
- (219) Hoskins, B. F.; Robson, R. Design and construction of a new class of scaffolding-like materials comprising infinite polymeric frameworks of 3D-linked molecular rods. A reappraisal of the zinc cyanide and cadmium cyanide structures and the synthesis and structure of the diamond-related

- frameworks [N(CH<sub>3</sub>)<sub>4</sub>] [CuI<sub>2</sub>ZnII(CN)<sub>4</sub>] and CuI[4, 4', 4'', 4''']-tetracyano-tetraphenylmethane]BF<sub>4</sub> · x C<sub>6</sub>H<sub>5</sub>NO<sub>2</sub>. *J. Am. Chem. Soc.* **1990**, *112*, 1546–1554.
- (220) Rasheed, T.; Rizwan, K.; Bilal, M.; Iqbal, H. M. N. Metal-Organic Framework-Based Engineered Materials – Fundamentals and Applications. *Molecules* **2020**, *25*, 1598.
- (221) Liu, J.; Chen, L.; Cui, H.; Zhang, J.; Zhang, L.; Su, C. Applications of metal-organic frameworks in heterogeneous supramolecular catalysis. *Chem. Soc. Rev.* **2014**, *43*, 6011–6061.
- (222) Kitagawa, S.; Kondo, M. Functional Micropore Chemistry of Crystalline Metal Complex-Assembled Compounds. *Bull. Chem. Soc. Jpn.* **1998**, *71*, 1739–1753.
- (223) Uemura, K.; Matsuda, R.; Kitagawa, S. Flexible microporous coordination polymers. *J. Solid State Chem.* **2005**, *178*, 2420–2429.
- (224) Kitagawa, S.; Munakata, M.; Tanimura, T. Synthesis of the novel infinite-sheet and -chain copper(I) complex polymers {[Cu(C<sub>4</sub>H<sub>4</sub>N<sub>2</sub>)<sub>3/2</sub>(CH<sub>3</sub>CN)](PF<sub>6</sub>)<sub>6</sub>}.cntdot.0.5C<sub>3</sub>H<sub>6</sub>O}.infin. and {[Cu<sub>2</sub>(C<sub>8</sub>H<sub>12</sub>N<sub>2</sub>)<sub>3</sub>](ClO<sub>4</sub>)<sub>2</sub>}.infin. and their x-ray crystal structures. *Inorg. Chem.* **1992**, *31*, 1714–1717.
- (225) Garcia, H.; Navalon, S., *Metal-Organic Frameworks: Applications in Separations and Catalysis*; Wiley: 2018.
- (226) Kalmutzki, M. J.; Hanikel, N.; Yaghi, O. M. Secondary building units as the turning point in the development of the reticular chemistry of MOFs. *Sci. Adv.* **2018**, *4*, 9180.
- (227) Ha, J.; Lee, J. H.; Moon, H. R. Alterations to secondary building units of metal-organic frameworks for the development of new functions. *Inorg. Chem. Front.* **2020**, *7*, 12–27.
- (228) Eddaoudi, M.; Moler, D. B.; Li, H.; Chen, B. B.; Reinecke, T. M.; O'keeffe, M.; Yaghi, O. M. Modular Chemistry: Secondary Building Units as a Basis for the Design of Highly Porous and Robust Metal-Organic Carboxylate Frameworks. *Acc. Chem. Res.* **2001**, *34*, 319–330.
- (229) Bu, X.; Zaworotko, M.; Zhang, Z., *Metal-Organic Framework: From Design to Applications*; Topics in Current Chemistry Collections; Springer International Publishing: 2020.
- (230) Mozafari, M., *Metal-Organic Frameworks for Biomedical Applications*; Elsevier Science & Technology: 2020.
- (231) Tranchemontagne, D. J.; Mendoza-Cortes, J. L.; O'keeffe, M.; Yaghi, O. M. Secondary building units, nets and bonding in the chemistry of metal-organic frameworks. *Chem. Soc. Rev.* **2009**, *38*, 1257–1283.

- (232) Schoedel, A.; Li, M.; Li, D.; O'keeffe, M.; Yaghi, O. M. Structures of Metal-Organic Frameworks with Rod Secondary Building Units. *Chem. Rev.* **2016**, *116*, 12466–12535.
- (233) Cantu, D. C.; McGrail, B. P.; Glezakou, V.-A. Formation Mechanism of the Secondary Building Unit in a Chromium Terephthalate Metal-Organic Framework. *Chem. Mater.* **2014**, *26*, 6401–6409.
- (234) Xu, H.; Sommer, S.; Broge, N. L. N.; Gao, J.; Iversen, B. B. The Chemistry of Nucleation: In Situ Pair Distribution Function Analysis of Secondary Building Units During UiO-66 MOF Formation. *Chem. Eur. J.* **2019**, *25*, 2051–2058.
- (235) Vleet, M. J. V.; Weng, T.; Li, X.; Schmidt, J. R. In Situ, Time-Resolved, and Mechanistic Studies of Metal-Organic Framework Nucleation and Growth. *Chem. Rev.* **2018**, *118*, 3681–3721.
- (236) Perry, J. J.; Perman, J. A.; Zaworotko, M. J. Design and synthesis of metal-organic frameworks using metal-organic polyhedra as supermolecular building blocks. *Chem. Soc. Rev.* **2009**, *38*, 1400–1417.
- (237) Rosi, N. L.; Kim, J.; Eddaoudi, M.; Chen, B.; O'keeffe, M.; Yaghi, O. M. Rod Packings and Metal-Organic Frameworks Constructed from Rod-Shaped Secondary Building Units. *J. Am. Chem. Soc.* **2005**, *127*, 1504–1518.
- (238) Mori, W.; Inoue, F.; Yoshida, K.; Nakayama, H.; Takamizawa, S.; Kishita, M. Synthesis of New Adsorbent Copper(II) Terephthalate. *Chem. Lett.* **1997**, *1997*, 1219–1220.
- (239) Dybtsev, D. N.; Chun, H.; Kim, K. Rigid and Flexible: A Highly Porous Metal-Organic Framework with Unusual Guest-Dependent Dynamic Behavior. *Angew. Chem. Int. Ed.* **2004**, *43*, 5033–5036.
- (240) Lee, J. Y.; Pan, L.; Huang, X.; Emge, T. J.; Li, J. A Systematic Approach to Building Highly Porous, Noninterpenetrating Metal-Organic Frameworks with a Large Capacity for Adsorbing H<sub>2</sub> and CH<sub>4</sub>. *Adv. Funct. Mater.* **2011**, *21*, 993–998.
- (241) Zhao, Y.; Wu, H.; Emge, T. J.; Gong, Q.; Nijem, N.; Chabal, Y. J.; Kong, L.; Langreth, D. C.; Liu, H.; Zeng, H.; Li, J. Enhancing Gas Adsorption and Separation Capacity through Ligand Functionalization of Microporous Metal-Organic Framework Structures. *Chem. Eur. J.* **2011**, *17*, 5101–5109.
- (242) Chui, S. S.-Y.; Lo, S. M. F.; Charmant, J. P. H.; Orpen, A. G.; Williams, I. D. A chemically functionalizable nanoporous material [Cu<sub>3</sub>(TMA)<sub>2</sub>(H<sub>2</sub>O)<sub>3</sub>]<sub>n</sub>. *Science* **1999**, *283*, 1148–1150.
- (243) Köberl, M.; Cokoja, M.; Herrmann, W. A.; Kühn, F. E. From molecules to materials: molecular paddle-wheel synthons of macromolecules, cage

- compounds and metal-organic frameworks. *Dalton Trans.* **2011**, *40*, 6834–6859.
- (244) Kökcam-Demir, Ü.; Goldman, A.; Esrafilı, L.; Gharib, M.; Morsali, A.; Weingart, O.; Janiak, C. Coordinatively unsaturated metal sites (open metal sites) in metal-organic frameworks: design and applications. *Chem. Soc. Rev.* **2020**, *49*, 2751–2798.
- (245) Moon, H. R.; Kobayashi, N.; Suh, M. P. Porous Metal-Organic Framework with Coordinatively Unsaturated Mn<sup>II</sup> Sites: Sorption Properties for Various Gases. *Inorg. Chem.* **2006**, *45*, 8672–8676.
- (246) Wu, H.; Zhou, W.; Yildirim, T. High-Capacity Methane Storage in Metal-Organic Frameworks M<sub>2</sub>(dhtp): The Important Role of Open Metal Sites. *J. Am. Chem. Soc.* **2009**, *131*, 4995–5000.
- (247) Guo, Z.; Wu, H.; Srinivas, G.; Zhou, Y.; Xiang, S.; Chen, Z.; Yang, Y.; Zhou, W.; O'keeffe, M.; Chen, B. A Metal-Organic Framework with Optimized Open Metal Sites and Pore Spaces for High Methane Storage at Room Temperature. *Angew. Chem. Int. Ed.* **2011**, *50*, 3178–3181.
- (248) Dietzel, P. D. C.; Besikiotis, V.; Blom, R. Application of metal-organic frameworks with coordinatively unsaturated metal sites in storage and separation of methane and carbon dioxide. *J. Mater. Chem.* **2009**, *19*, 7362–7370.
- (249) Bae, Y.-S.; Lee, C. Y.; Kim, K. C.; Farha, O. K.; Nickias, P. N.; Hupp, J. T.; Nguyen, S. T.; Snurr, R. Q. High Propene/Propane Selectivity in Isostructural Metal-Organic Frameworks with High Densities of Open Metal Sites. *Angew. Chem. Int. Ed.* **2012**, *51*, 1857–1860.
- (250) Yaghi, O. M. Reticular Chemistry in All Dimensions. *ACS Cent. Sci.* **2019**, *5*, 1295–1300.
- (251) Yaghi, O. M. Reticular Chemistry-Construction, Properties, and Precision Reactions of Frameworks. *J. Am. Chem. Soc.* **2016**, *138*, 15507–15509.
- (252) Qin, J.-s.; Du, D.; Li, M.; Lian, X.; Dong, L.-Z.; Bosch, M.; Su, Z.; Zhang, Q.; Li, S.; Lan, Y.; Yuan, S.; Zhou, H.-C. Derivation and Decoration of Nets with Trigonal-Prismatic Nodes: A Unique Route to Reticular Synthesis of Metal-Organic Frameworks. *J. Am. Chem. Soc.* **2016**, *138*, 5299–5307.
- (253) Inge, A. K.; Köppen, M.; Su, J.; Feyand, M.; Xu, H.; Zou, X.; O'keeffe, M.; Stock, N. Unprecedented Topological Complexity in a Metal-Organic Framework Constructed from Simple Building Units. *J. Am. Chem. Soc.* **2016**, *138*, 1970–1976.
- (254) Alezi, D.; Spanopoulos, I.; Tsangarakis, C.; Shkurenko, A.; Adil, K.; Belmabkhout, Y.; Keffe, M. O.; Eddaoudi, M.; Trikalitis, P. N. Reticular Chemistry at Its Best: Directed Assembly of Hexagonal Building Units into the Awaited

- Metal-Organic Framework with the Intricate Polybenzene Topology, pbz-MOF. *J. Am. Chem. Soc.* **2016**, *138*, 12767–12770.
- (255) Horike, S.; Shimomura, S.; Kitagawa, S. Soft Porous Crystals. *Nat. Chem.* **2009**, *1*, 695–704.
- (256) Krause, S.; Hosono, N.; Kitagawa, S. Chemistry of Soft Porous Crystals - Structural Dynamics and Gas Adsorption Properties. *Angew. Chem. Int. Ed.* **2020**, *59*, 15325–15341.
- (257) Kaur, J.; Kaur, G. Review on Flexible Metal-Organic Frameworks. *ChemistrySelect* **2021**, *6*, 8227–8243.
- (258) Coudert, F.-X. Responsive Metal-Organic Frameworks and Framework Materials: Under Pressure, Taking the Heat, in the Spotlight, with Friends. *Chem. Mater.* **2015**, *27*, 1905–1916.
- (259) Li, Y.; Wang, Y.; Fan, W.; Sun, D. Flexible metal-organic frameworks for gas storage and separation. *Dalton Trans.* **2022**.
- (260) Blatov, V. A.; Carlucci, L.; Ciani, G.; Proserpio, D. M. Interpenetrating metal-organic and inorganic 3D networks: a computer-aided systematic investigation. Part I. Analysis of the Cambridge structural database. *CrystEngComm* **2004**, *6*, 377–395.
- (261) Serre, C.; Millange, F.; Thouvenot, C.; Nogués, M.; Marsolier, G.; Louër, D.; Férey, G. Very Large Breathing Effect in the First Nanoporous Chromium(III)-Based Solids: MIL-53 or  $\text{Cr}^{\text{III}}(\text{OH}) \cdot \{\text{O}_2\text{C}-\text{C}_6\text{H}_4-\text{CO}_2\} \cdot \{\text{HO}_2\text{C}-\text{C}_6\text{H}_4-\text{CO}_2\text{H}\}_x \cdot \text{H}_2\text{O}_y$ . *J. Am. Chem. Soc.* **2002**, *124*, 13519–13526.
- (262) Loiseau, T.; Serre, C.; Huguenard, C.; Fink, G.; Taulelle, F.; Henry, M.; Bataille, T.; Férey, G. A Rationale for the Large Breathing of the Porous Aluminum Terephthalate (MIL-53) Upon Hydration. *Chem. Eur. J.* **2004**, *10*, 1373–1382.
- (263) Boutin, A.; Springuel-Huet, M.-A.; Nossov, A.; Gédéon, A.; Loiseau, T.; Volkringer, C.; Férey, G.; Coudert, F.-X.; Fuchs, A. H. Breathing Transitions in MIL-53(Al) Metal–Organic Framework Upon Xenon Adsorption. *Angew. Chem. Int. Ed.* **2009**, *48*, 8314–8317.
- (264) Llewellyn, P. L.; Maurin, G.; Devic, T.; Loera-Serna, S.; Rosenbach, N.; Serre, C.; Bourrelly, S.; Horcajada, P.; Filinchuk, Y.; Férey, G. Prediction of the Conditions for Breathing of Metal Organic Framework Materials Using a Combination of X-ray Powder Diffraction, Microcalorimetry, and Molecular Simulation. *J. Am. Chem. Soc.* **2008**, *130*, 12808–12814.
- (265) Férey, G.; Serre, C. Large breathing effects in three-dimensional porous hybrid matter: facts, analyses, rules and consequences. *Chem. Soc. Rev.* **2009**, *38*, 1380–1399.



- (266) Boutin, A.; Coudert, F.-X.; Springuel-Huet, M.-A.; Neimark, A. V.; F'erey, G.; Fuchs, A. H. The Behavior of Flexible MIL-53(Al) upon CH<sub>4</sub> and CO<sub>2</sub> Adsorption. *J. Phys. Chem. C* **2010**, *114*, 22237–22244.
- (267) Coudert, F.-X.; Jeffroy, M.; Fuchs, A. H.; Boutin, A.; Mellot-Draznieks, C. Thermodynamics of Guest-Induced Structural Transitions in Hybrid Organic-Inorganic Frameworks. *J. Am. Chem. Soc.* **2008**, *130*, 14294–14302.
- (268) Coudert, F.-X.; Mellot-Draznieks, C.; Fuchs, A. H.; Boutin, A. Double Structural Transition in Hybrid Material MIL-53 upon Hydrocarbon Adsorption: The Thermodynamics Behind the Scenes. *J. Am. Chem. Soc.* **2009**, *131*, 3442–3443.
- (269) Coudert, F.-X.; Mellot-Draznieks, C.; Fuchs, A. H.; Boutin, A. Prediction of Breathing and Gate-Opening Transitions Upon Binary Mixture Adsorption in Metal-Organic Frameworks. *J. Am. Chem. Soc.* **2009**, *131*, 11329–11331.
- (270) Allendorf, M. D.; Schwartzberg, A. M.; Stavila, V.; Talin, A. A. A Roadmap to Implementing Metal-Organic Frameworks in Electronic Devices: Challenges and Critical Directions. *Chem. Eur. J.* **2011**, *17*, 11372–11388.
- (271) Stassen, I.; Burtch, N. C.; Talin, A. A.; Falcaro, P.; Allendorf, M. D.; Ameloot, R. An updated roadmap for the integration of metal-organic frameworks with electronic devices and chemical sensors. *Chem. Soc. Rev.* **2017**, *46*, 3185–3241.
- (272) Kim, Y.; Huh, S. Pore engineering of metal-organic frameworks: Introduction of chemically accessible Lewis basic sites inside MOF channels. *CrystEngComm* **2016**, *18*, 3524–3550.
- (273) Feng, Y.; Wang, Z.; Fan, W.; Kang, Z.; Feng, S.; Fan, L.; Hu, S.; Sun, D. Engineering the pore environment of metal-organic framework membranes via modification of the secondary building unit for improved gas separation. *J. Mater. Chem.* **2020**, *8*, 13132–13141.
- (274) Wang, J.; Zhang, Y. S.; Su, Y.; Liu, X.; Zhang, P.; Lin, R.-B.; Chen, S.; Deng, Q.; Zeng, Z.; Deng, S.; Chen, B. Fine pore engineering in a series of isorecticular metal-organic frameworks for efficient C<sub>2</sub>H<sub>2</sub>/CO<sub>2</sub> separation. *Nat. Commun.* **2022**, *13*, 200.
- (275) Lin, R.-B.; Zhang, Z.; Chen, B. Achieving High Performance Metal-Organic Framework Materials through Pore Engineering. *Acc. Chem. Res.* **2021**, *54*, 3362–3376.
- (276) Du, R.; Wu, Y.; Yang, Y.; Zhai, T.-t.; Zhou, T.; Shang, Q.; Zhu, L.; Shang, C.; Guo, Z. Porosity Engineering of MOF-Based Materials for Electrochemical Energy Storage. *Adv. Energy Mater.* **2021**, 2100154.

- (277) Lu, W.; Wei, Z.; Gu, Z.-Y.; Liu, T.-F.; Park, J.; Park, J.; Tian, J.; Zhang, M.; Zhang, Q.; Gentle, T. M.; Bosch, M.; Zhou, H.-C. Tuning the structure and function of metal-organic frameworks via linker design. *Chem. Soc. Rev.* **2014**, *43*, 5561–5593.
- (278) Razavi, S. A. A.; Morsali, A. Linker functionalized metal-organic frameworks. *Coord. Chem. Rev.* **2019**, *399*, 213023.
- (279) Kim, D.; Kang, M.; Ha, H.; Hong, C. S.; Kim, M. Multiple functional groups in metal-organic frameworks and their positional regioisomerism. *Coord. Chem. Rev.* **2021**, *438*, 213892.
- (280) Ji, Z.; Wang, H.; Canossa, S.; Wuttke, S.; Yaghi, O. M. Pore Chemistry of Metal-Organic Frameworks. *Adv. Funct. Mater.* **2020**, *30*, 2000238.
- (281) Furukawa, H.; Go, Y. B.; Ko, N.; Park, Y. K.; Uribe-Romo, F. J.; Kim, J.; O'keeffe, M.; Yaghi, O. M. Isoreticular Expansion of Metal-Organic Frameworks with Triangular and Square Building Units and the Lowest Calculated Density for Porous Crystals. *Inorg. Chem.* **2011**, *50*, 9147–9152.
- (282) Cavka, J. H.; Jakobsen, S. N.; Olsbye, U.; Guillou, N.; Lamberti, C.; Bordiga, S.; Lillerud, K. P. A New Zirconium Inorganic Building Brick Forming Metal Organic Frameworks with Exceptional Stability. *J. Am. Chem. Soc.* **2008**, *130*, 13850–13851.
- (283) Surblé, S.; Serre, C.; Mellot-Draznieks, C.; Millange, F.; Férey, G. A new iso-reticular class of metal-organic-frameworks with the MIL-88 topology. *Chem. Commun.* **2006**, *3*, 284–286.
- (284) Yuan, D.; Zhao, D.; Sun, D.; Zhou, H.-C. An Isoreticular Series of Metal-Organic Frameworks with Dendritic Hexacarboxylate Ligands and Exceptionally High Gas-Uptake Capacity. *Angew. Chem. Int. Ed.* **2010**, *49*, 5357–5361.
- (285) He, Y.; Zhou, W.; Yildirim, T.; Chen, B. A series of metal-organic frameworks with high methane uptake and an empirical equation for predicting methane storage capacity. *Energy Environ. Sci.* **2013**, *6*, 2735–2744.
- (286) Fan, W.; Zhang, X.; Kang, Z.; Liu, X.; Sun, D. Isoreticular chemistry within metal-organic frameworks for gas storage and separation. *Coord. Chem. Rev.* **2021**, *443*, 213968.
- (287) Gong, Y.-N.; Zhong, D.-C.; Lu, T.-B. Interpenetrating metal-organic frameworks. *CrystEngComm* **2016**, *18*, 2596–2606.
- (288) Jiang, H.-L.; Makal, T. A.; Zhou, H.-C. Interpenetration control in metal-organic frameworks for functional applications. *Coord. Chem. Rev.* **2013**, *257*, 2232–2249.
-

- (289) Nguyen, T. T. T.; Le, H. M.; Kawazoe, Y.; Nguyen, H. L. Reticular control of interpenetration in a complex metal-organic framework. *Mater. Chem. Front.* **2018**, *2*, 2063–2069.
- (290) Verma, G.; Butikofer, S.; Kumar, S.; Ma, S. Regulation of the Degree of Interpenetration in Metal-Organic Frameworks. *Top. Curr. Chem.* **2019**, *378*, 4.
- (291) Gupta, M.; Vittal, J. J. Control of interpenetration and structural transformations in the interpenetrated MOFs. *Coord. Chem. Rev.* **2021**, *435*, 213789.
- (292) Sezginel, K. B.; Asinger, P. A.; Babaei, H.; Wilmer, C. E. Thermal Transport in Interpenetrated Metal-Organic Frameworks. *Chem. Mater.* **2018**, *30*, 2281–2286.
- (293) Deng, H.; Grunder, S.; Cordova, K. E.; Valente, C.; Furukawa, H.; Hmadeh, M.; Gandara, F.; Whalley, A. C.; Liu, Z.; Asahina, S.; Kazumori, H.; O'keeffe, M.; Terasaki, O.; Stoddart, J. F.; Yaghi, O. M. Large-Pore Apertures in a Series of Metal-Organic Frameworks. *Science* **2012**, *336*, 1018–1023.
- (294) Chen, B.; Eddaoudi, M.; Hyde, S. T.; O'keeffe, M.; Yaghi, O. M. Interwoven Metal-Organic Framework on a Periodic Minimal Surface with Extra-Large Pores. *Science* **2001**, *291*, 1021–1023.
- (295) Delgado-Friedrichs, O.; O'keeffe, M.; Yaghi, O. M. Three-periodic nets and tilings: edge-transitive binodal structures. *Acta Crystallogr. A* **2006**, *62*, 350–355.
- (296) Sun, D.; Ma, S.; Ke, Y.; Collins, D. J.; Zhou, H. An Interweaving MOF with High Hydrogen Uptake. *J. Am. Chem. Soc.* **2006**, *128*, 3896–3897.
- (297) Deng, H.; Doonan, C. J.; Furukawa, H.; Ferreira, R. B.; Towne, J. C.; Knobler, C. B.; Wang, B.; Yaghi, O. M. Multiple Functional Groups of Varying Ratios in Metal-Organic Frameworks. *Science* **2010**, *327*, 846–850.
- (298) Kong, X.; Deng, H.; Yan, F.; Kim, J.; Swisher, J. A.; Smit, B.; Yaghi, O. M.; Reimer, J. A. Mapping of Functional Groups in Metal-Organic Frameworks. *Science* **2013**, *341*, 882–885.
- (299) Wang, L.; Deng, H.; Furukawa, H.; Gándara, F.; Cordova, K. E.; Peri, D.; Yaghi, O. M. Synthesis and Characterization of Metal–Organic Framework-74 Containing 2, 4, 6, 8, and 10 Different Metals. *Inorg. Chem.* **2014**, *53*, 5881–5883.
- (300) Fracaroli, A. M.; Siman, P.; Nagib, D. A.; Suzuki, M.; Furukawa, H.; Toste, F. D.; Yaghi, O. M. Seven Post-synthetic Covalent Reactions in Tandem Leading to Enzyme-like Complexity within Metal-Organic Framework Crystals. *J. Am. Chem. Soc.* **2016**, *138*, 8352–8355.

- (301) Xia, Q.; Li, Z.; Tan, C.; Liu, Y.; Gong, W.; Cui, Y. Multivariate Metal-Organic Frameworks as Multifunctional Heterogeneous Asymmetric Catalysts for Sequential Reactions. *J. Am. Chem. Soc.* **2017**, *139*, 8259–8266.
- (302) Aguirre-Díaz, L. M.; Gándara, F.; Iglesias, M.; Snejko, N.; Gutiérrez-Puebla, E.; Monge, M. Á. Tunable Catalytic Activity of Solid Solution Metal-Organic Frameworks in One-Pot Multicomponent Reactions. *J. Am. Chem. Soc.* **2015**, *137*, 6132–6135.
- (303) Zhang, Y.-B.; Furukawa, H.; Ko, N.; Nie, W.; Park, H. J.; Okajima, S.; Cordova, K. E.; Deng, H.; Kim, J.; Yaghi, O. M. Introduction of Functionality, Selection of Topology, and Enhancement of Gas Adsorption in Multivariate Metal-Organic Framework-177. *J. Am. Chem. Soc.* **2015**, *137*, 2641–2650.
- (304) Ji, Z.; Li, T.; Yaghi, O. M. Sequencing of metals in multivariate metal-organic frameworks. *Science* **2020**, *369*, 674–680.
- (305) Cohen, S. M. The Postsynthetic Renaissance in Porous Solids. *J. Am. Chem. Soc.* **2017**, *139*, 2855–2863.
- (306) Yin, Z.; Wan, S.-Y.; Yang, J.; Kurmoo, M.; Zeng, M.-H. Recent advances in post-synthetic modification of metal-organic frameworks: New types and tandem reactions. *Coord. Chem. Rev.* **2019**, *378*, 500–512.
- (307) Das, S.; Kim, H.; Kim, K. Metathesis in Single Crystal: Complete and Reversible Exchange of Metal Ions Constituting the Frameworks of Metal-Organic Frameworks. *J. Am. Chem. Soc.* **2009**, *131*, 3814–3815.
- (308) Brozek, C. K.; Dincă, M. Cation exchange at the secondary building units of metal-organic frameworks. *Chem. Soc. Rev.* **2014**, *43*, 5456–5467.
- (309) Cohen, S. M. Postsynthetic Methods for the Functionalization of Metal-Organic Frameworks. *Chem. Rev.* **2012**, *112*, 970–1000.
- (310) Wang, Z.; Cohen, S. M. Postsynthetic modification of metal-organic frameworks. *Chem. Soc. Rev.* **2009**, *38*, 1315–1329.
- (311) Burrows, A. D.; Frost, C. G.; Mahon, M. F.; Richardson, C. Post-Synthetic Modification of Tagged Metal-Organic Frameworks. *Angew. Chem. Int. Ed.* **2008**, *47*, 8482–8486.
- (312) Tanabe, K. K.; Cohen, S. M. Postsynthetic modification of metal-organic frameworks—a progress report. *Chem. Soc. Rev.* **2011**, *40*, 498–519.
- (313) Karagiari, O.; Bury, W.; Tylanakis, E.; Sarjeant, A. A.; Hupp, J. T.; Farha, O. K. Opening Metal-Organic Frameworks Vol. 2: Inserting Longer Pillars into Pillared-Paddlewheel Structures through Solvent-Assisted Linker Exchange. *Chem. Mater.* **2013**, *25*, 3499–3503.
- (314) An, J.; Rosi, N. L. Tuning MOF CO<sub>2</sub> Adsorption Properties via Cation Exchange. *J. Am. Chem. Soc.* **2010**, *132*, 5578–5579.

- (315) Wang, Z.; Cohen, S. M. Postsynthetic Covalent Modification of a Neutral Metal-Organic Framework. *J. Am. Chem. Soc.* **2007**, *129*, 12368–12369.
- (316) Brozek, C. K.; Bellarosa, L.; Soejima, T.; Clark, T. V.; López, N.; Dincă, M. Solvent-Dependent Cation Exchange in Metal-Organic Frameworks. *Chem. Eur. J.* **2014**, *20*, 6871–6874.
- (317) Sun, D.; Liu, W.; Qiu, M.; Zhang, Y.; Li, Z. Introduction of a mediator for enhancing photocatalytic performance via post-synthetic metal exchange in metal-organic frameworks (MOFs). *Chem. Commun.* **2015**, *51*, 2056–2059.
- (318) Islamoglu, T.; Goswami, S.; Li, Z.; Howarth, A. J.; Farha, O. K.; Hupp, J. T. Postsynthetic Tuning of Metal-Organic Frameworks for Targeted Applications. *Acc. Chem. Res.* **2017**, *50*, 805–813.
- (319) Liu, C.; Zeng, C.; Luo, T.-Y.; Merg, A. D.; Jin, R.; Rosi, N. L. Establishing Porosity Gradients within Metal-Organic Frameworks Using Partial Postsynthetic Ligand Exchange. *J. Am. Chem. Soc.* **2016**, *138*, 12045–12048.
- (320) Noori, Y.; Akhbari, K. Post-synthetic ion-exchange process in nanoporous metal-organic frameworks; an effective way for modulating their structures and properties. *RSC Adv.* **2017**, *7*, 1782–1808.
- (321) Custelcean, R.; Moyer, B. A. Anion Separation with Metal-Organic Frameworks. *Eur. J. Inorg. Chem.* **2007**, *2007*, 1321–1340.
- (322) Carlucci, L.; Ciani, G.; Maggini, S.; Proserpio, D. M.; Visconti, M. Heterometallic Modular Metal-Organic 3D Frameworks Assembled via New Tris- $\beta$ -Diketonate Metalloligands: Nanoporous Materials for Anion Exchange and Scaffolding of Selected Anionic Guests. *Chem. Eur. J.* **2010**, *16*, 12328–12341.
- (323) Ma, J.; Yu, Y.; Dong, Y.-B. Fluorene-based Cu(II)-MOF: a visual colorimetric anion sensor and separator based on an anion-exchange approach. *Chem. Commun.* **2012**, *48*, 2946–2948.
- (324) Custelcean, R.; Haverlock, T. J.; Moyer, B. A. Anion Separation by Selective Crystallization of Metal-Organic Frameworks. *Inorg. Chem.* **2006**, *45*, 6446–6452.
- (325) Liu, T.; Lü, J.; Tian, C. B.; Cao, M.; Lin, Z.-J.; Cao, R. Porous Anionic, Cationic, and Neutral Metal-Carboxylate Frameworks Constructed from Flexible Tetrapodal Ligands: Syntheses, Structures, Ion-Exchanges, and Magnetic Properties. *Inorg. Chem.* **2011**, *50*, 2264–2271.
- (326) Xiong, S.; Li, S.; Wang, S.; Wang, Z. Multi-functional metal-organic frameworks based on H<sub>4</sub>mdip: Crystal structure, photoluminescence, selective ion-exchange and catalysis. *CrystEngComm* **2011**, *13*, 7236–7245.

- (327) Sharma, S.; Desai, A. V.; Joarder, B.; Ghosh, S. K. A Water-Stable Ionic MOF for the Selective Capture of Toxic Oxoanions of Se<sup>VI</sup> and As<sup>V</sup> and Crystallographic Insight into the Ion-Exchange Mechanism. *Angew. Chem. Int. Ed.* **2020**, *59*, 7788–7792.
- (328) Fei, H.; Bresler, M. R.; Oliver, S. R. J. A New Paradigm for Anion Trapping in High Capacity and Selectivity: Crystal-to-Crystal Transformation of Cationic Materials. *J. Am. Chem. Soc.* **2011**, *133*, 11110–11113.
- (329) Maji, T. K.; Matsuda, R.; Kitagawa, S. A flexible interpenetrating coordination framework with a bimodal porous functionality. *Nat. Mater.* **2007**, *6*, 142–148.
- (330) Yang, S.; Lin, X.; Blake, A. J.; Walker, G. S.; Hubberstey, P.; Champness, N. R.; Schröder, M. Cation-induced kinetic trapping and enhanced hydrogen adsorption in a modulated anionic metal-organic framework. *Nat. Chem.* **2009**, *1*, 487–493.
- (331) Yang, S.; Martin, G. S.; Titman, J. J.; Blake, A. J.; Allan, D. R.; Champness, N. R.; Schröder, M. Pore with Gate: Enhancement of the Isothermic Heat of Adsorption of Dihydrogen via Postsynthetic Cation Exchange in Metal-Organic Frameworks. *Inorg. Chem.* **2011**, *50*, 9374–9384.
- (332) Akhbari, K.; Morsali, A. Modulating methane storage in anionic nanoporous MOF materials via post-synthetic cation exchange process. *Dalton Trans.* **2013**, *42*, 4786–4789.
- (333) Chen, L.; Luque, R.; Li, Y. Controllable design of tunable nanostructures inside metal-organic frameworks. *Chem. Soc. Rev.* **2017**, *46*, 4614–4630.
- (334) Allendorf, M. D.; Medishetty, R.; Fischer, R. A. Guest molecules as a design element for metal-organic frameworks. *Mrs Bull.* **2016**, *41*, 865–869.
- (335) Juan-Alcañiz, J.; Gascón, J.; Kapteijn, F. Metal-organic frameworks as scaffolds for the encapsulation of active species: state of the art and future perspectives. *J. Mat. Chem.* **2012**, *22*, 10102–10118.
- (336) Zhuang, J.; Young, A. P.; Tsung, C.-K. Integration of Biomolecules with Metal-Organic Frameworks. *Small* **2017**, *13*, 1700880.
- (337) Mallakpour, S.; Nikkhoo, E.; Hussain, C. M. Application of MOF materials as drug delivery systems for cancer therapy and dermal treatment. *Coord. Chem. Rev.* **2022**, *451*, 214262.
- (338) Li, H.; Zhao, S.-n.; Zang, S.; Li, J. Functional metal-organic frameworks as effective sensors of gases and volatile compounds. *Chem. Soc. Rev.* **2020**, *49*, 6364–6401.
-

- 
- (339) Kalaj, M.; Bentz, K. C.; Ayala, S.; Palomba, J. M.; Barcus, K. S.; Katayama, Y.; Cohen, S. M. MOF-Polymer Hybrid Materials: From Simple Composites to Tailored Architectures. *Chem. Rev.* **2020**, *120*, 8267–8302.
- (340) Schmidt, B. V. Metal-Organic Frameworks in Polymer Science: Polymerization Catalysis, Polymerization Environment, and Hybrid Materials. *Macromol. Rapid Commun.* **2019**, *41*, 1900333.
- (341) Kitao, T.; Uemura, T. Polymers in Metal-Organic Frameworks: From Nanostructured Chain Assemblies to New Functional Materials. *Chem. Lett.* **2020**, *49*, 624–632.
- (342) Wang, T.; Gao, L.; Hou, J.; Hérou, S.; Griffiths, J. T.; Li, W.; Dong, J.; Gao, S.; Titirici, M.-M.; Kumar, R. V.; Cheetham, A. K.; Bao, X.; Fu, Q.; Smoukov, S. K. Rational approach to guest confinement inside MOF cavities for low-temperature catalysis. *Nature Commun.* **2019**, *10*, 1340.
- (343) Rösler, C.; Fischer, R. A. Metal-organic frameworks as hosts for nanoparticles. *CrystEngComm* **2015**, *17*, 199–217.
- (344) Meilikhov, M.; Yussenko, K. V.; Esken, D.; Turner, S.; van Tendeloo, G.; Fischer, R. A. Metals@MOFs - Loading MOFs with Metal Nanoparticles for Hybrid Functions. *Eur. J. Inorg. Chem.* **2010**, *2010*, 3701–3714.
- (345) Hermes, S.; Schröter, M. K.; Schmid, R.; Khodeir, L.; Muhler, M.; Tissler, A. D.; Fischer, R. W.; Fischer, R. A. Metal@MOF: Loading of Highly Porous Coordination Polymers Host Lattices by Metal Organic Chemical Vapor Deposition. *Angew. Chem. Int. Ed.* **2005**, *44*, 6237–6241.
- (346) Ostwald, W., *Lehrbuch Der Allgemeinen Chemie*; Lehrbuch Der Allgemeinen Chemie Bd. 2, Teil 3; W. Engelmann: 1896.
- (347) Kang, H.; Buchman, J. T.; Rodriguez, R. S.; Ring, H. L.; He, J.; Bantz, K. C.; Haynes, C. L. Stabilization of Silver and Gold Nanoparticles: Preservation and Improvement of Plasmonic Functionalities. *Chem. Rev.* **2019**, *119*, 664–699.
- (348) Ndolomingo, M. J.; Bingwa, N.; Meijboom, R. Review of supported metal nanoparticles: synthesis methodologies, advantages and application as catalysts. *J. Mater. Sci.* **2020**, *55*, 6195–6241.
- (349) Lisiecki, I. Size, Shape, and Structural Control of Metallic Nanocrystals. *J. Phys. Chem. B* **2005**, *109*, 12231–12244.
- (350) Fortea-Pérez, F. R.; Mon, M.; Ferrando-Soria, J.; Boronat, M.; Leyva-Pérez, A.; Corma, A.; Herrera, J. M.; Osadchii, D.; Gascón, J.; Armentano, D.; Pardo, E. The MOF-driven synthesis of supported palladium clusters with catalytic activity for carbene-mediated chemistry. *Nature Mater.* **2017**, *16*, 760–766.
-

- (351) Kratzl, K.; Kratky, T.; Günther, S.; Tomanec, O.; Zbořil, R.; Michalička, J.; Macák, J. M.; Cokoja, M.; Fischer, R. A. Generation and Stabilization of Small Platinum Clusters Pt<sub>12±x</sub> inside a Metal-Organic Framework. *J. Am. Chem. Soc.* **2019**, *141*, 13962–13969.
- (352) Dragonetti, C.; Ceriotti, A.; Roberto, D.; Ugo, R. Surface-Mediated Organometallic Synthesis: The Role of the Oxidation State and of Ancillary Ligands in the High-Yield and Selective Syntheses of Platinum Carbonyl Dianions [Pt<sub>3</sub>(CO)<sub>6</sub>]<sub>n</sub><sup>2-</sup> (n = 6, 5, 4, 3) by Reductive Carbonylation under Mild Conditions and in the Presence of Surface Basicity of Various Silica-Supported Pt(IV) or Pt(II) Compounds. *Organometallics* **2007**, *26*, 310–315.
- (353) Cravillon, J.; Münzer, S.; Lohmeier, S.-J.; Feldhoff, A.; Huber, K.; Wiebcke, M. Rapid Room-Temperature Synthesis and Characterization of Nanocrystals of a Prototypical Zeolitic Imidazolate Framework. *Chem. Mater.* **2009**, *21*, 1410–1412.
- (354) Garlyyev, B.; Kratzl, K.; Rück, M.; Michalička, J.; Fichtner, J.; Macák, J. M.; Kratky, T.; Günther, S.; Cokoja, M.; Bandarenka, A. S.; Gagliardi, A.; Fischer, R. A. Optimizing the Size of Platinum Nanoparticles for Enhanced Mass Activity in the Electrochemical Oxygen Reduction Reaction. *Angew. Chem. Int. Ed.* **2019**, *58*, 9596–9600.
- (355) Zhang, L.; Yuan, S.; Fan, W.; Pang, J.; Li, F.; Guo, B.; Zhang, P.; Sun, D.; Zhou, H.-C. Cooperative Sieving and Functionalization of Zr Metal-Organic Frameworks through Insertion and Post-Modification of Auxiliary Linkers. *ACS Appl. Mater. Interfaces* **2019**, *11*, 22390–22397.
- (356) Xu, W.; Tu, B.; Liu, Q.; Shu, Y.; Liang, C.-C.; Diercks, C. S.; Yaghi, O. M.; Zhang, Y.-B.; Deng, H.; Li, Q. Anisotropic reticular chemistry. *Nature Rev. Mater.* **2020**, *5*, 764–779.
- (357) Silva, C. G.; Corma, A.; García, H. Metal-organic frameworks as semiconductors. *J. Mater. Chem.* **2010**, *20*, 3141–3156.
- (358) Hendon, C. H.; Tiana, D.; Walsh, A. Conductive metal-organic frameworks and networks: fact or fantasy? *Phys. Chem. Chem. Phys.* **2012**, *14*, 13120–13132.
- (359) Stavila, V.; Talin, A. A.; Allendorf, M. D. MOF-based electronic and optoelectronic devices. *Chem. Soc. Rev.* **2014**, *43*, 5994–6010.
- (360) D'Alessandro, D. M.; Kanga, J. R. R.; Caddy, J. S. Towards Conducting Metal-Organic Frameworks. *Aust. J. Chem.* **2011**, *64*, 718–722.
- (361) Dincă, M.; Léonard, F. Metal-organic frameworks for electronics and photonics. *MRS Bull.* **2016**, *41*, 854–857.



- (362) Haberkorn, H.; Naarmann, H.; Penzien, K.; Schlag, J.; Simak, P. Structure and conductivity of poly(acetylene). *Synth. Met.* **1982**, *5*, 51–71.
- (363) Pearson, R. G. HARD AND SOFT ACIDS AND BASES. *J. Am. Chem. Soc.* **1963**, *85*, 3533–3539.
- (364) Givaja, G.; Amo-Ochoa, P.; Gomez-Garcia, C. J.; Zamora, F. Electrical conductive coordination polymers. *Chem. Soc. Rev.* **2012**, *41*, 115–147.
- (365) Takaishi, S.; Hosoda, M.; Kajiwara, T.; Miyasaka, H.; Yamashita, M.; Nakanishi, Y.; Kitagawa, Y.; Yamaguchi, K.; Kobayashi, A.; Kitagawa, H. Electroconductive Porous Coordination Polymer Cu[Cu(pdt)<sub>2</sub>] Composed of Donor and Acceptor Building Units. *Inorg. Chem.* **2009**, *48*, 9048–9050.
- (366) Kobayashi, Y.; Jacobs, B. W.; Allendorf, M. D.; Long, J. R. Conductivity, Doping, and Redox Chemistry of a Microporous Dithiolene-Based Metal-Organic Framework. *Chem. Mater.* **2010**, *22*, 4120–4122.
- (367) Sun, L.; Miyakai, T.; Seki, S.; Dincă, M. Mn<sub>2</sub>(2,5-disulfhydrylbenzene-1,4-dicarboxylate): A Microporous Metal-Organic Framework with Infinite (-Mn-S)<sub>∞</sub> Chains and High Intrinsic Charge Mobility. *J. Am. Chem. Soc.* **2013**, *135*, 8185–8188.
- (368) Sun, L.; Hendon, C. H.; Minier, M. A.; Walsh, A.; Dincă, M. Million-Fold Electrical Conductivity Enhancement in Fe<sub>2</sub>(DEBDC) versus Mn<sub>2</sub>(DEBDC) (E = S, O). *J. Am. Chem. Soc.* **2015**, *137*, 6164–6167.
- (369) Sun, L.; Hendon, C. H.; Park, S. S.; Tulchinsky, Y.; Wan, R.; Wang, F.; Walsh, A.; Dincă, M. Is iron unique in promoting electrical conductivity in MOFs? *Chem. Sci.* **2017**, *8*, 4450–4457.
- (370) Creutz, C.; Taube, H. Direct approach to measuring the Franck-Condon barrier to electron transfer between metal ions. *J. Am. Chem. Soc.* **1969**, *91*, 3988–3989.
- (371) Robin, M. B.; Day, P. Mixed Valence Chemistry-A Survey and Classification. *Adv. Inorg. Chem. Radiochem.* **1968**, *10*, 247–422.
- (372) Gándara, F.; Uribe-Romo, F. J.; Britt, D. K.; Furukawa, H.; Lei, L.; Cheng, R.; Duan, X.; O’keeffe, M.; Yaghi, O. M. Porous, Conductive Metal-Triazolates and Their Structural Elucidation by the Charge-Flipping Method. *Chem. Eur. J.* **2012**, *18*, 10595–10601.
- (373) Park, J. G.; Aubrey, M. L.; Oktawiec, J.; Chakarawet, K.; Darago, L. E.; Grandjean, F.; Long, G. J.; Long, J. R. Charge Delocalization and Bulk Electronic Conductivity in the Mixed-Valence Metal-Organic Framework Fe(1,2,3-triazolate)<sub>2</sub>(BF<sub>4</sub>)<sub>x</sub>. *J. Am. Chem. Soc.* **2018**, *140*, 8526–8534.
- (374) Xie, L. S.; Sun, L.; Wan, R.; Park, S. S.; DeGayner, J. A.; Hendon, C. H.; Dincă, M. Tunable Mixed-Valence Doping toward Record Electrical Con-

- ductivity in a Three-Dimensional Metal-Organic Framework. *J. Am. Chem. Soc.* **2018**, *140*, 7411–7414.
- (375) Herm, Z. R.; Wiers, B. M.; Mason, J. A.; van Baten, J. M.; Hudson, M. R.; Zajdel, P.; Brown, C. M.; Masciocchi, N.; Krishna, R.; Long, J. R. Separation of Hexane Isomers in a Metal-Organic Framework with Triangular Channels. *Science* **2013**, *340*, 960–964.
- (376) Aubrey, M. L. et al. Electron delocalization and charge mobility as a function of reduction in a metal–organic framework. *Nature Mater.* **2018**, *17*, 625–632.
- (377) Koo, J. Y.; Yakiyama, Y.; Lee, G. R.; Lee, J.; Choi, H. C.; Morita, Y.; Kawano, M. Selective Formation of Conductive Network by Radical-Induced Oxidation. *J. Am. Chem. Soc.* **2016**, *138*, 1776–1779.
- (378) Kuang, X.; Chen, S.; Meng, L.; Chen, J. L.; Wu, X.; Zhang, G.-D.; Zhong, G.; Hu, T.; Li, Y.; Lu, C. Supramolecular aggregation of a redox-active copper-naphthalenediimide network with intrinsic electron conduction. *Chem. Commun.* **2019**, *55*, 1643–1646.
- (379) Johnson, D.; Hof, F., *Aromatic Interactions: Frontiers in Knowledge and Application*; ISSN; Royal Society of Chemistry: 2016.
- (380) Janiak, C. A critical account on  $\pi$ - $\pi$  stacking in metal complexes with aromatic nitrogen-containing ligands. *J. Chem. Soc., Dalton Trans.* **2000**, 3885–3896.
- (381) Xie, L. S.; Dincă, M. Novel Topology in Semiconducting Tetrathiafulvalene Lanthanide Metal-Organic Frameworks. *Israel Journal of Chemistry* **2018**, *58*, 1119–1122.
- (382) Xie, L. S.; Alexandrov, E. V.; Skorupskii, G.; Proserpio, D. M.; Dincă, M. Diverse  $\pi$ - $\pi$  stacking motifs modulate electrical conductivity in tetrathiafulvalene-based metal-organic frameworks. *Chem. Sci.* **2019**, *10*, 8558–8565.
- (383) Castells-Gil, J.; Mañas-Valero, S.; Vitorica-Yrezabal, I. J.; Ananias, D.; Rocha, J.; Santiago, R.; Bromley, S. T.; Baldoví, J. J.; Coronado, E.; Souto, M.; Espallargas, G. M. Electronic, Structural and Functional Versatility in Tetrathiafulvalene-Lanthanide Metal-Organic Frameworks. *Chem. Eur. J.* **2019**, *25*, 12636–12643.
- (384) Su, J.; Hu, T.; Murase, R.; Wang, H.-Y.; D'Alessandro, D. M.; Kurmoo, M.; Zuo, J. Redox Activities of Metal-Organic Frameworks Incorporating Rare-Earth Metal Chains and Tetrathiafulvalene Linkers. *Inorg. Chem.* **2019**, *58*, 3698–3706.
- (385) Qu, L.; Iguchi, H.; Takaishi, S.; Habib, F.; Leong, C. F.; D'Alessandro, D. M.; Yoshida, T.; Abe, H.; Nishibori, E.; Yamashita, M. Porous Molecular Conductor: Electrochemical Fabrication of Through-Space Conduction

- Pathways among Linear Coordination Polymers. *J. Am. Chem. Soc.* **2019**, *141*, 6802–6806.
- (386) Kobaisi, M. A.; Bhosale, S. V.; Latham, K.; Raynor, A. M.; Bhosale, S. V. Functional Naphthalene Diimides: Synthesis, Properties, and Applications. *Chem. Rev.* **2016**, *116*, 11685–11796.
- (387) Batail, P.; Boubekour, K.; Fourmigué, M.; Gabriel, J.-C. P. Electrocrystallization, an Invaluable Tool for the Construction of Ordered, Electroactive Molecular Solids. *Chem. Mater.* **1998**, *10*, 3005–3015.
- (388) Kaim, W. The transition metal coordination chemistry of anion radicals. *Coord. Chem. Rev.* **1987**, *76*, 187–235.
- (389) Kaim, W.; Schwederski, B. Non-innocent ligands in bioinorganic chemistry - An overview. *Coord. Chem. Rev.* **2010**, *254*, 1580–1588.
- (390) Lyaskovskyy, V.; de Bruin, B. Redox Non-Innocent Ligands: Versatile New Tools to Control Catalytic Reactions. *ACS Catal.* **2012**, *2*, 270–279.
- (391) DeGayner, J. A.; Jeon, I.-R.; Sun, L.; Dincă, M.; Harris, T. D. 2D Conductive Iron-Quinoid Magnets Ordering up to  $T_c = 105$  K via Heterogenous Redox Chemistry. *J. Am. Chem. Soc.* **2017**, *139*, 4175–4184.
- (392) Benmansour, S.; Abhervé, A.; Gómez-Claramunt, P.; Vallés-García, C.; Gómez-García, C. J. Nanosheets of Two-Dimensional Magnetic and Conducting Fe(II)/Fe(III) Mixed-Valence Metal-Organic Frameworks. *ACS Appl. Mater. Interfaces* **2017**, *9*, 26210–26218.
- (393) Ziebel, M. E.; Darago, L. E.; Long, J. R. Control of Electronic Structure and Conductivity in Two-Dimensional Metal-Semiquinoid Frameworks of Titanium, Vanadium, and Chromium. *J. Am. Chem. Soc.* **2018**, *140*, 3040–3051.
- (394) Jeon, I.-R.; Negru, B.; Duyne, R. P. V.; Harris, T. D. A 2D Semiquinone Radical-Containing Microporous Magnet with Solvent-Induced Switching from  $T_c = 26$  to 80 K. *J. Am. Chem. Soc.* **2015**, *137*, 15699–15702.
- (395) Darago, L. E.; Aubrey, M. L.; Yu, C.-J.; Gonzalez, M. I.; Long, J. R. Electronic Conductivity, Ferrimagnetic Ordering, and Reductive Insertion Mediated by Organic Mixed-Valence in a Ferric Semiquinoid Metal-Organic Framework. *J. Am. Chem. Soc.* **2015**, *137*, 15703–15711.
- (396) Rubio-Giménez, V.; Galbiati, M.; Castells-Gil, J.; Almora-Barrios, N.; Navarro-Sánchez, J.; Escorcía-Ariza, G.; Mattera, M.; Arnold, T.; Rawle, J.; Tatay, S.; Coronado, E.; Martí-Gastaldo, C. Bottom-Up Fabrication of Semiconductive Metal-Organic Framework Ultrathin Films. *Adv. Mater.* **2018**, *30*, 1704291.

- (397) Campbell, M. G.; Liu, S. F.; Swager, T. M.; Dincă, M. Chemiresistive Sensor Arrays from Conductive 2D Metal-Organic Frameworks. *J. Am. Chem. Soc.* **2015**, *137*, 13780–13783.
- (398) Hmadeh, M. et al. New Porous Crystals of Extended Metal-Catecholates. *Chem. Mater.* **2012**, *24*, 3511–3513.
- (399) Dong, R. et al. High-mobility band-like charge transport in a semiconducting two-dimensional metal-organic framework. *Nat. Mater.* **2018**, *17*, 1027–1032.
- (400) Sheberla, D.; Sun, L.; Blood-Forsythe, M. A.; Er, S.; Wade, C. R.; Brozek, C. K.; Aspuru-Guzik, A.; Dincă, M. High Electrical Conductivity in Ni<sub>3</sub>(2,3,6,7,10,11-hexamino-triphenylene)<sub>2</sub>, a Semiconducting Metal-Organic Graphene Analogue. *J. Am. Chem. Soc.* **2014**, *136*, 8859–8862.
- (401) Day, R. W.; Bediako, D. K.; Rezaee, M.; Parent, L. R.; Skorupskii, G.; Arguilla, M. Q.; Hendon, C. H.; Stassen, I.; Gianneschi, N. C.; Kim, P.; Dincă, M. Single Crystals of Electrically Conductive Two-Dimensional Metal-Organic Frameworks: Structural and Electrical Transport Properties. *ACS Cent. Sci.* **2019**, *5*, 1959–1964.
- (402) Smith, M. K.; Jensen, K. E.; Pivak, P. A.; Mirica, K. A. Direct Self-Assembly of Conductive Nanorods of Metal-Organic Frameworks into Chemiresistive Devices on Shrinkable Polymer Films. *Chem. Mater.* **2016**, *28*, 5264–5268.
- (403) Ko, M.; Mendecki, L.; Mirica, K. A. Conductive two-dimensional metal-organic frameworks as multifunctional materials. *Chem. Commun.* **2018**, *54*, 7873–7891.
- (404) Skorupskii, G.; Trump, B.; Kasel, T. W.; Brown, C. M.; Hendon, C. H.; Dincă, M. Efficient and tunable one-dimensional charge transport in layered lanthanide metal-organic frameworks. *Nat. Chem.* **2019**, *12*, 131–136.
- (405) Kato, R. Conducting Metal Dithiolene Complexes: Structural and Electronic Properties. *Chem. Rev.* **2004**, *104*, 5319–5346.
- (406) Kato, R. Development of  $\pi$ -Electron Systems Based on [M(dmit)<sub>2</sub>] (M = Ni and Pd; dmit: 1,3-dithiole-2-thione-4,5-dithiolate) Anion Radicals. *Bull. Chem. Soc. Jpn.* **2014**, *87*, 355–374.
- (407) Robertson, N.; Cronin, L. Metal bis-1,2-dithiolene complexes in conducting or magnetic crystalline assemblies. *Coord. Chem. Rev.* **2002**, *227*, 93–127.
- (408) Huang, X.; Sheng, P.; Tu, Z.; Zhang, F.; Wang, J.; Geng, H.; Zou, Y.; Di, C.-a.; Yi, Y.; Sun, Y.; Xu, W.; Zhu, D. A two-dimensional  $\pi$ -d conjugated coordination polymer with extremely high electrical conductivity and ambipolar transport behaviour. *Nature Commun.* **2015**, *6*, 7408.

- (409) Kambe, T.; Sakamoto, R.; Hoshiko, K.; Takada, K.; Miyachi, M.; Ryu, J.-H.; Sasaki, S.; Kim, J.; Nakazato, K.; Takata, M.; Nishihara, H.  $\pi$ -Conjugated Nickel Bis(dithiolene) Complex Nanosheet. *J. Am. Chem. Soc.* **2013**, *135*, 2462–2465.
- (410) Kambe, T.; Sakamoto, R.; Kusamoto, T.; Pal, T.; Fukui, N.; Hoshiko, K.; Shimojima, T.; Wang, Z.; Hirahara, T.; Ishizaka, K.; Hasegawa, S.; Liu, F.; Nishihara, H. Redox Control and High Conductivity of Nickel Bis(dithiolene) Complex  $\pi$ -Nanosheet: A Potential Organic Two-Dimensional Topological Insulator. *J. Am. Chem. Soc.* **2014**, *136*, 14357–14360.
- (411) Feng, D. et al. Robust and conductive two-dimensional metal-organic frameworks with exceptionally high volumetric and areal capacitance. *Nat. Energy* **2018**, *3*, 30–36.
- (412) Dou, J.-H.; Sun, L.; Ge, Y.; Li, W.; Hendon, C. H.; Li, J.; Gul, S.; Yano, J.; Stach, E. A.; Dincă, M. Signature of Metallic Behavior in the Metal-Organic Frameworks  $M_3(\text{hexaiminobenzene})_2$  ( $M = \text{Ni}, \text{Cu}$ ). *J. Am. Chem. Soc.* **2017**, *139*, 13608–13611.
- (413) Campbell, M. G.; Sheberla, D.; Liu, S. F.; Swager, T. M.; Dincă, M.  $\text{Cu}_3(\text{hexaiminotriphenylene})_2$ : An Electrically Conductive 2D Metal-Organic Framework for Chemiresistive Sensing. *Angew. Chem. Int. Ed.* **2015**, *54*, 4349–4352.
- (414) Pedersen, K. S. et al. Formation of the layered conductive magnet  $\text{CrCl}_2(\text{pyrazine})_2$  through redox-active coordination chemistry. *Nat. Chem.* **2018**, *10*, 1056–1061.
- (415) Li, G.-P.; Zhang, K.; Zhao, H.; Hou, L.; Wang, Y.-Y. Increased Electric Conductivity upon  $\text{I}_2$  Uptake and Gas Sorption in a Pillar-Layered Metal-Organic Framework. *ChemPlusChem* **2017**, *82*, 716–720.
- (416) Zeng, M.-H.; Yin, Z.; Tan, Y.; Zhang, W.-X.; He, Y.-P.; Kurmoo, M. Nanoporous Cobalt(II) MOF Exhibiting Four Magnetic Ground States and Changes in Gas Sorption upon Post-Synthetic Modification. *J. Am. Chem. Soc.* **2014**, *136*, 4680–4688.
- (417) Lee, D. Y.; Kim, E.-K.; Shrestha, N. K.; Boukhvalov, D. W.; Lee, J.-K.; Han, S.-H. Charge Transfer-Induced Molecular Hole Doping into Thin Film of Metal-Organic Frameworks. *ACS Appl. Mater. Interfaces* **2015**, *7*, 18501–18507.
- (418) Yin, Z.; Wang, Q.-x.; Zeng, M.-H. Iodine Release and Recovery, Influence of Polyiodide Anions on Electrical Conductivity and Nonlinear Optical Activity in an Interdigitated and Interpenetrated Bipillared-Bilayer Metal-Organic Framework. *J. Am. Chem. Soc.* **2012**, *134*, 4857–4863.

- (419) Hao, Z.; Yang, G.; Song, X.-Z.; Zhu, M.; Meng, X.; Zhao, S.-n.; Song, S.; Zhang, H. A europium(III) based metal–organic framework: bifunctional properties related to sensing and electronic conductivity. *J. Mater. Chem. A* **2014**, *2*, 237–244.
- (420) Zeng, M.-H.; Wang, Q.-x.; Tan, Y.; Hu, S.; Zhao, H.; Long, L.-s.; Kurmoo, M. Rigid Pillars and Double Walls in a Porous Metal-Organic Framework: Single-Crystal to Single-Crystal, Controlled Uptake and Release of Iodine and Electrical Conductivity. *J. Am. Chem. Soc.* **2010**, *132*, 2561–2563.
- (421) Lu, Z. et al. Modulating supramolecular binding of carbon dioxide in a redox-active porous metal-organic framework. *Nat. Commun.* **2017**, *8*, 14212.
- (422) Zhang, X.; da Silva, I.; Fazzi, R. B.; Sheveleva, A. M.; Han, X.; Spencer, B. F.; Sapchenko, S. A.; Tuna, F.; McInnes, E. J. L.; Li, M.; Yang, S.; Schröder, M. Iodine Adsorption in a Redox-Active Metal-Organic Framework: Electrical Conductivity Induced by Host-Guest Charge-Transfer. *Inorg. Chem.* **2019**, *58*, 14145–14150.
- (423) Saura-Sanmartín, A.; Martínez-Cuezva, A.; Marín-Luna, M.; Bautista, D.; Berná, J. Effective Encapsulation of C<sub>60</sub> by Metal-Organic Frameworks with Polyamide Macrocyclic Linkers. *Angew- Chem. Int. Ed.* **2021**, *60*, 10814–10819.
- (424) Meng, H.; Zhao, C.; Nie, M.; Wang, C.; Wang, T. Changing the Hydrophobic MOF Pores through Encapsulating Fullerene C<sub>60</sub> and Metallofullerene Sc<sub>3</sub>C<sub>2</sub>@C<sub>80</sub>. *J. Phys. Chem. C* **2019**, *123*, 6265–6269.
- (425) Souto, M.; Calbo, J.; Mañas-Valero, S.; Walsh, A.; Espallargas, G. M. Charge-transfer interactions between fullerenes and a mesoporous tetra-thiafulvalene-based metal-organic framework. *Beilstein J. Nanotechnol.* **2019**, *10*, 1883–1893.
- (426) Goswami, S.; Ray, D.; Otake, K.-i.; Kung, C.-W.; Garibay, S. J.; Islamoglu, T.; Atilgan, A.; Cui, Y.; Cramer, C. J.; Farha, O. K.; Hupp, J. T. A porous, electrically conductive hexa-zirconium(IV) metal-organic framework. *Chem. Sci.* **2018**, *9*, 4477–4482.
- (427) Kasap, S.; Capper, P., *Springer Handbook of Electronic and Photonic Materials*; Springer Handbooks; Springer International Publishing: 2017.
- (428) Webster, J., *Wiley Encyclopedia of Electrical and Electronics Engineering*; A Wiley-interscience publication Bd. 1-24; John Wiley: 1999.
- (429) Callister, W.; Rethwisch, D., *Fundamentals of Materials Science and Engineering: An Integrated Approach, Binder Ready Version*; John Wiley & Sons, Incorporated: 2008.
- (430) Hummel, R., *Electronic Properties of Materials*; Springer New York: 2004.
-

- 
- (431) Atkins, P.; de Paula, J., *Atkins' Physical Chemistry*; OUP Oxford: 2010.
- (432) Mizutani, U., *Introduction to the Electron Theory of Metals*; Introduction to the Electron Theory of Metals; Cambridge University Press: 2001.
- (433) Mori, T., *Electronic Properties of Organic Conductors*; Springer Japan: 2016.
- (434) Harrison, W., *Electronic Structure and the Properties of Solids: The Physics of the Chemical Bond*; Dover Books on Physics; Dover Publications: 1989.
- (435) Greiner, W.; Bromley, D., *Quantum Mechanics: An Introduction*; Springer Berlin Heidelberg: 2011.
- (436) Eisberg, R.; Eisberg, R.; Resnick, R.; Caldwell, D.; Derrin, E.; Christman, J., *Quantum Physics of Atoms, Molecules, Solids, Nuclei, and Particles*; Quantum Physics of Atoms, Molecules, Solids, Nuclei and Particles; Wiley: 1985.
- (437) Griffiths, D.; Schroeter, D., *Introduction to Quantum Mechanics*; Cambridge University Press: 2018.
- (438) Sutton, A., *Electronic Structure of Materials*; Clarendon Press: 1993.
- (439) Cohen-Tannoudji, C.; Diu, B.; Laloë, F.; Streubel, J.; Balla, J.; Lippert, K.; Henkel, C., *Quantenmechanik*; De Gruyter Studium; De Gruyter: 2019.
- (440) Bransden, B.; Joachain, C., *Quantum Mechanics*; Prentice Hall: 2000.
- (441) Liboff, R., *Introductory Quantum Mechanics*; Addison-Wesley: 2003.
- (442) Hall, B., *Quantum Theory for Mathematicians*; Graduate Texts in Mathematics; Springer New York: 2013.
- (443) Razavy, M., *Quantum Theory of Tunneling*; World Scientific: 2003.
- (444) Sakurai, J.; Napolitano, J., *Modern Quantum Mechanics*; Cambridge University Press: 2017.
- (445) Ashcroft, N.; W, A.; Mermin, N.; Mermin, N.; Company, B. P., *Solid State Physics*; HRW international editions; Holt, Rinehart and Winston: 1976.
- (446) Kittel, C., *Introduction to Solid State Physics*; Wiley series on the science and technology of materials; Wiley: 1959.
- (447) Elliott, S., *The Physics and Chemistry of Solids*; Wiley: 1998.
- (448) Ibach, H.; Lüth, H., *Solid-State Physics: An Introduction to Principles of Materials Science*; Springer Berlin Heidelberg: 2009.
- (449) Reif, F., *Fundamentals of Statistical and Thermal Physics*; Waveland Press: 2009.
- (450) Harrison, W., *Elementary Electronic Structure*; Elementary Electronic Structure; World Scientific: 2004.
- (451) Marder, M.; Isihara, A., *Condensed Matter Physics*; Dover books o physics; Wiley: 2000.
-

- (452) Omar, M., *Elementary Solid State Physics: Principles and Applications*; Addison-Wesley series in solid state sciences; Addison-Wesley Publishing Company: 1993.
- (453) Holleman, A.; Wiberg, E.; Wiberg, N., *Lehrbuch der anorganischen Chemie*; de Gruyter: 1995.
- (454) Irene, E., *Electronic Materials Science*; Wiley: 2005.
- (455) Yacobi, B., *Semiconductor Materials: An Introduction to Basic Principles*; Microdevices; Springer US: 2013.
- (456) YU, P.; Cardona, M., *Fundamentals of Semiconductors: Physics and Materials Properties*; Graduate Texts in Physics; Springer Berlin Heidelberg: 2010.
- (457) Baranovski, S., *Charge Transport in Disordered Solids with Applications in Electronics*; Wiley Series in Materials for Electronic & Optoelectronic Applications; Wiley: 2006.
- (458) Gantmakher, V.; Gantmacher, F.; Man, L.; Press, O. U., *Electrons and Disorder in Solids*; International Series of Monographs on Physics; OUP Oxford: 2005.
- (459) Pike, G. E.; Seager, C. H. The dc voltage dependence of semiconductor grain-boundary resistance. *J. Appl. Phys.* **1979**, *50*, 3414–3422.
- (460) Ladd, M.; Palmer, R., *Structure Determination by X-ray Crystallography: Analysis by X-rays and Neutrons*; Springer US: 2013.
- (461) Massa, W., *Kristallstrukturbestimmung*; Studienbücher Chemie; Vieweg+Teubner Verlag: 2010.
- (462) Spiess, L.; Teichert, G.; Schwarzer, R.; Behnken, H.; Genzel, C., *Moderne Röntgenbeugung: Röntgendiffraktometrie für Materialwissenschaftler, Physiker und Chemiker*; Vieweg Studium; Vieweg+Teubner Verlag: 2009.
- (463) Giacovazzo, C.; Monaco, H.; Artioli, G.; Viterbo, D.; Milanesio, M.; Gilli, G.; Gilli, P.; Zanotti, G.; Ferraris, G.; Catti, M., *Fundamentals of Crystallography*; International Union of Crystallography Texts on Crystallography; OUP Oxford: 2011.
- (464) Borchardt-Ott, W.; Sowa, H., *Kristallographie: Eine Einführung für Studierende der Naturwissenschaften*; Springer-Lehrbuch; Springer Berlin Heidelberg: 2018.
- (465) Thommes, M.; Kaneko, K.; Neimark, A. V.; Olivier, J. P.; Rodriguez-Reinoso, F.; Rouquerol, J.; Sing, K. S. Physisorption of gases, with special reference to the evaluation of surface area and pore size distribution (IUPAC Technical Report). *Pure Appl. Chem* **2015**, *87*, 1051–1069.
- (466) Glover, T.; Mu, B., *Gas Adsorption in Metal-organic Frameworks: Fundamentals and Applications*; CRC Press/Taylor & Francis Group: 2018.
-



- 
- (467) Lowell, S.; Shields, J., *Powder Surface Area and Porosity*; Particle Technology Series; Springer Netherlands: 2013.
- (468) Schrader, B., *Infrared and Raman Spectroscopy: Methods and Applications*; Wiley: 2008.
- (469) Stuart, B., *Infrared Spectroscopy: Fundamentals and Applications*; Analytical Techniques in the Sciences (AnTs); Wiley: 2004.
- (470) Hesse, M.; Meier, H.; Zeeh, B., *Spektroskopische Methoden in der organischen Chemie*; Thieme electronic book library; Thieme: 2005.
- (471) Egerton, R., *Physical principles of electron microscopy: an introduction to TEM, SEM, and AEM*; Physical Principles of Electron Microscopy; Springer: 2005.
- (472) Williams, D.; Carter, C., *Transmission Electron Microscopy: A Textbook for Materials Science*; Cambridge library collection Bd. 1; Springer: 2009.
- (473) Goldstein, J.; Goldshtain, Y.; GOLDSTEIN, J.; Media, S. S.; Newbury, D.; Joy, D.; Echlin, P.; Lyman, C.; Lifshin, E., et al., *Scanning Electron Microscopy and X-Ray Microanalysis: Third Edition*; Scanning Electron Microscopy and X-ray Microanalysis; Springer US: 2003.
- (474) Pennycook, S.; Nellist, P., *Scanning Transmission Electron Microscopy: Imaging and Analysis*; Springer New York: 2011.
- (475) Keeler, J., *Understanding NMR Spectroscopy*; Wiley: 2011.
- (476) Levitt, M., *Spin Dynamics: Basics of Nuclear Magnetic Resonance*; Wiley: 2008.
- (477) Derome, A., *Modern NMR Techniques for Chemistry Research*; Organic Chemistry Series - Pergamon Press; Elsevier Science & Technology Books: 1987.
- (478) Friebolin, H., *Ein- und zweidimensionale NMR-Spektroskopie*; Wiley: 1992.
- (479) Macomber, R., *A Complete Introduction to Modern NMR Spectroscopy*; A Wiley-Interscience publication; Wiley: 1998.
- (480) Gross, J., *Mass Spectrometry: A Textbook*; Springer International Publishing: 2017.
- (481) Becker, S., *Inorganic Mass Spectrometry: Principles and Applications*; Wiley: 2008.
- (482) Ekman, R.; Silberring, J.; Westman-Brinkmalm, A.; Desiderio, D.; Nibbering, N.; Kraj, A., *Mass Spectrometry: Instrumentation, Interpretation, and Applications*; Wiley Series on Mass Spectrometry; Wiley: 2008.
- (483) Henderson, W.; McIndoe, J., *Mass Spectrometry of Inorganic and Organometallic Compounds: Tools - Techniques - Tips*; Inorganic Chemistry: A Textbook Series; Wiley: 2005.
-

- (484) De Hoffmann, E.; Stroobant, V., *Mass Spectrometry: Principles and Applications*; Wiley: 2007.
-

## *List of Scientific Contributions*

The following list shows a summary of publications and presentations of the author of this thesis (sorted by date). The entries marked with an asterisk are results of the above presented work.

### POSTER PRESENTATIONS

**Ukaj, D.**; Kieslich, G.; Fischer, R. A. Charge-Transfer Induced Electrical Conductivity in a Tetrathiafulvalene-Based Metal-Organic Framework. 1<sup>st</sup> International School on Advanced Porous Materials (MOFSchool), Como, Italy, June 2019.

**Ukaj, D.**; Kieslich, G.; Fischer, R. A. Charge-Transfer Induced Electrical Conductivity in a Tetrathiafulvalene-Based Metal-Organic Framework. 3<sup>rd</sup> International Conference on Metal Organic Frameworks and Porous Polymers, Paris, France, October 2019.

### PUBLICATIONS

*Works of this thesis:*

\***Ukaj, D.**; Bunzen, H.; Berger, J.; Kieslich, G.; Fischer, R. A. Charge-Transfer Induced Electrical Conductivity in a Tetrathiafulvalene-Based Metal-Organic Framework. *Chem. Mater.* **2021**, *33*(7), 2532–2542.

*Contributions to other projects:*

Schneider, C.; **Ukaj, D.**; Koerver, R.; Talin, A. A.; Kieslich, G.; Pujari, S. P.; Zuilhof, H.; Janek, J.; Allendorf, M. D.; Fischer, R. A. High electrical conductivity and high porosity in a Guest@MOF material: evidence of TCNQ ordering within  $\text{Cu}_3\text{BTC}_2$  micropores. *Chem. Sci.* **2018**, 9(37), 7405–7412.

OVERVIEW OF THE AUTHOR CONTRIBUTION TO WORK IN THIS  
THESIS:

*Chapter 2*

- Synthesis and characterization of  $\text{M}_2\text{TTFTB}$  and TCNE-infiltrated  $\text{M}_2\text{TTFTB}$
- Infrared- and Raman analysis of TCNE-infiltrated samples via Imfit+rampy python libraries
- Measurement of electrical conductivity
- STEM-measurements were performed by H. Bunzen
- BET-measurements were performed by J. Berger

*Chapter 3*

- Synthesis and characterization of all reaction products

*Chapter 4*

- Synthesis and characterization of all  $\text{Cu}_3\text{BTC}_2$  and guest-infiltrated MOF samples
  - Pawley profile fitting via Topas and jEdit
-